

https://dspace.org/

Deformation and partial melting in the Central Zone of the Damara Orogen, Namibia

Goslin, Lechelle Morgan

2019
https://hdl.handle.net/10539/29652

Downloaded from a DSpace repository. https://dspace.org/

Deformation and partial melting in the Central Zone of the Damara Orogen, Namibia

Lechelle Morgan Goslin



WITS
UNIVERSITY

A Dissertation submitted to the Faculty of Science, University of the Witwatersrand, in fullfillment of the requirements for the degree of Master of Science

Johannesburg,

2019

I declare that this Dissertation is my own, unaided work. It is being submitted for the Degree of Master of Science at the University of the Witwatersrand, Johannesburg. It has not been submitted before for any degree or examination at any other University.



Lechelle Morgan Goslin

5th day of July 2019 in Johannesburg

"It is our choices… that show what we truly are, far more than our abilities"

J.K. Rowling,

Harry Potter and the Chamber of Secrets

Abstract

The southern Central Zone of the Damara Belt, Namibia is characterised by northeast-southwest trending basement-cored domes. The Palmenhorst Dome is the largest of these basement-cored domes and the northern extent of this dome forms the focus of this research. Previous studies have shown that these Palaeoproterozoic domes have varied stratigraphies, including infolded Damaran metasediments or they may not be cored by basement lithologies at all. This study aims to re-evaluate the lithologies of the Abbabis Complex in the northern Palmenhorst Dome by means of integrating remote sensing, field mapping, petrographic analysis, whole rock geochemistry and U-Pb-Hf geochronology.

Eight major spectral domains were noted in the field area which comprise the Abbabis Complex (domains 1 – 3) within the core surrounded by Damaran metasediments (domains 4 - 8). Several units of the Damara Supergroup were identified in the field area including the Etusis (domain 4), Khan (domains 5 and 6), Rössing (domain 7) and Chuos (domain 8) formations. Anomalous rafts were identified in the basement lithologies and are proposed to be infolded Damaran metasediments or amphibolite dykes. Field work confirmed that these anomalies did in fact represent a combination of these domains. The Abbabis Complex domes yielded compositional heterogeneities and were found to contain textural and compositional variations of granites and orthogneisses, which was confirmed by field mapping, petrographic studies and geochemistry. Detailed zircon U-Pb dating revealed *ca.* 2 Ga genesis for the Abbabis Complex (1998.6 ± 14.9 Ma, 2002.5 ± 13.9 Ma and 2071.39 ± 5.39 Ma, upper intercept regression ages), confirmed to be of Narubis Granitoid Complex affinity.

The succession of metasedimentary units in the field study area is similar to those proposed by previous studies. Lower Damaran units , namely metasediments of the Etusis, Khan, Rössing and Chuos formations, were identified in D2 synclines infolded into the basement-cored domes. The synclines identified in this study include the Ostrich Gorge, Hinge and Dorob synclines. The Etusis Formation yielded detrital age peaks of 1 and 2 Ga, which are correlatable to sedimentary rocks analysed in other studies along the southern Congo Craton edge. Unradiogenic εHf values indicate that the Etusis Formation had three main provenance sources and a minor Abbabis Complex affinity. The three main source regions include a younger 1 Ga source that was formed from recycled (εHf = -25 to -28) Archaean (3.3 – 3.6 Ga) sources (Et1), another 1 Ga source that was crustally derived (and recycled; εHf= -11 to -17) from Archaean (2.6 - 2.9 Ga) sources (Et2), a juvenile source (εHf= + 4 to +9) that was extracted from the Depleted Mantle and crystallised new Eburnean crust (2.2 - 2.4 Ga) (Et3). These sources can be attributed to the Congo Craton. Zircon Hf isotope systematics (εHf of 2.8

to -8.8 with DM model ages of 3.1 to 2.8 Ga) suggest a Congo Craton affinity for the Abbabis Complex.

The Damaran granitoids (red granites, grey granites and sheeted leucogranites) are comparable to those found by other workers and the amphibolite dykes were found to be Damaran in age (550.48 ± 0.85 Ma, zircon concordia age) and are associated with the Goas Intrusive Suite. The syn-tectonic red (535.77 ± 0.96 Ma, zircon concordia age) and grey granites were emplaced shortly after the amphibolite dykes during early phases of collision and are typically associated with M1 metamorphism. The sheeted leucogranites were variably emplaced as post-tectonic granites during orogenic collapse (D2 and D3). These Damaran granitoids were found to be a result of biotite-dehydration melting and exhibited various modes of crystallisation from cumulates (enriched REE, positive Eu anomaly) to fractional crystallisation as final melts (REE enrichment, negative Eu anomaly). All these granitoids and the amphibolites show unradiogenic εHf values, which indicate crustal reworking of variably aged Archaean- to Mesoproterozoic-aged crust during the Pan-African orogeny.

Detailed structural and lithological mapping revealed pre-Damaran and Damaran deformational histories. However, except for a pre-Damaran fabric, the pre-Damaran deformation is not always identifiable. The Damaran deformation is divided into four main events (D1 to D4). The main features associated with each event include (D1) a regional fabric with intrafolial folds (560 – 540 Ma), (D2) recumbent southwest verging folds, associated limb parallel high strain zones (525 – 510 Ma) from orogenic collapse, (D3) upright and open interference folds which lead to dome formation and (D4) brittle deformation associated with conjugate sets of faults/joints. These main events correlate to the main phases of the Damara Orogen from Khomas Ocean closure to Congo-Kalahari collision. An early metamorphic event (M1) is associated with the emplacement of the red granites and D1, with U-Pb concordia ages established from multiple metamorphic zircons (560 – 540 Ma). The second, and most prominent metamorphic event (M2) outlived D2 deformation and resulted in post-tectonic leucogranites. This event was constrained by the U-Pb concordia ages for type C' sheeted leucogranites of 525.72 ± 1.91 Ma and regressed metamorphic zircons from various granites (525 – 510 Ma).

Acknowledgments

Firstly, I would like to thank my supervisors Prof. Robert Bolhar and Prof. Paul Nex for their continued support and guidance throughout this project. If it were not for your feedback and sometimes personal time, this project would not be what it is today. Thank you for sharing a beer or two with me at Tiger Reef and giving me the opportunity to discover the complexities and wonders of the rocks of Namibia. I would also like to thank Prof. Judith Kinnaird for her time spent with me in the field, odd bit of advice and encouraging push whenever I needed it.

This project would not have been possible without the financial assistance provided from the National Research Fund's Centre of Excellence for Integrated Mineral and Energy Resource Analysis (Cimera). I would also like to thank Dr. Guy Freemantle and Mr. Berti Roesner from Husab Mine for always being willing to provide access to their permits in the Khan River and use of their road. Without this, the drive into the field every day, would have been much more treacherous. Additionally, a special thanks goes to Dr. Guy Freemantle for providing me with hyperspectral imagery which formed an integral component of my project. The Geological Survey of Namibia, the Namibian Ministry of Mines and Energy and the Dorob National Park were always helpful with providing permits for access and exportation of samples.

A big thanks goes to the technical staff at Wits (School of Geosciences and Earth Lab) for their patience and for always being willing to help. Thank you to Mr. Joe Aphane for assistance and guidance with mineral separation and Mr. Marlin Patchappa for providing whole rock geochemical data. To Mr. Caiphus Majola - thank you for preparing many a thin section for me and providing me with countless laughs during the course of my project! Your jokes made the days go quicker. Again, thank you to Robert Bolhar for the many hours of assistance on the laser. Without your help with the ICP-MS, data reduction and interpretation of my U-Pb data I would not be at this point today. Ms. Henriette Ueckermann thank you for all the help and patience with the MC- ICP- MS at the University of Johannesburg and collection of my Lu-Hf data.

Dr. Clarisa Voster - you have been a friend in more ways than one! Firstly, thank you for sacrificing some of your SEM time for me - without it nothing would have progressed. But most of all, thank you for always being willing to listen to the trials of my project. The laughs and glasses of wine saw me through to the end.

Loic Le Bras you made walking through the dessert sand an enjoyable experience. My second field season would not have been as productive if it were not for you. I found a true friend while searching

for shade patches in the desert. Thank you for always being up for a cup of coffee and Saturday morning work sessions- they kept me sane especially through the last push.

To my friends in Geosciences who I shared many a beer with at the PiG. Thank you for always being available to bounce ideas off of and for keeping my mind off work when needed. There are too many to thank individually, but please know your encouragement and a friendly smile always went a long way.

To my parents. Without your financial support and emotional encouragement my entire university career would not have been possible. I will always be grateful for the opportunities you gave me and the sacrifices you have made to get me to this point. I owe this all to you.

Most importantly, I need to thank Dr. Cameron Penn-Clarke. You have been a rock through all of this. Your encouragement and patience has been unending. You may not care much for high -grade mush but you have always been willing to assist me in the field, listen to my ideas, selflessly edit and read over my ramblings, which all made this dissertation into what it is today. Thank you for pushing me, always reassuring me that my love for rocks had not been extinguished and that I had it in me to get this dissertation done.





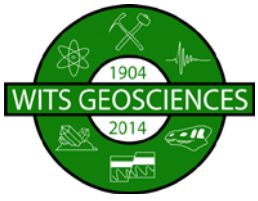


Table of Contents

1. Introduction 1

1.1 The Pan-African Orogeny 1

1.2 The Damara Orogen 4

1.2.1 Stratotectonic zones of the Damara Belt 5

1.2.2 Basement Inliers 8

1.3 Project locality 9

1.4 Research problem and aims 9

1.5 Thesis organisation 12

2. Geological Setting and previous work on the southern Central Zone 13

2.1 Introduction 13

2.2 Abbabis Complex 15

2.2.1 Accepted stratigraphy of the Abbabis Complex at the type locality 15

2.3 Damara Supergroup in the southern Central Zone 18

2.3.1 Nosib Group 19

2.3.2 Swakop Group 20

2.4 Metamorphism 21

2.5 Structure and Deformation 22

2.5.1 Damaran deformation 22

2.5.1 Pre-Damaran deformation 24

2.5.2 Dome formation 24

2.6 Associated magmatism 24

2.7 Field mapping of the Palmenhorst Dome 25

2.8 Geochronology of the Abbabis Complex 29

3. Remote Sensing 31

3.1 Introduction 31

3.2 Methods and Materials 31

3.2.1 Pre-processing of Landsat 8 data 33

3.2.2 Processing of Landsat 8 data 34

3.2.3 Selection of Hymap images 36

3.2.4 Maps and image creation 36
3.3 Landsat 8 Results 37
3.3.1 Landsat 8 Domains 37
3.4 Hyperspectral Imagery 41
3.4.1 Domain refinements and anomalies 42
3.4.2 Domain compositions from Mineral Maps 45
3.5 Delineation of Rafts 48
3.6 Discussion 49
3.7 Conclusions 60
4. Field studies 62
4.1 Introduction 62
4.2 Stratigraphy 62
4.2.1 Abbabis Complex (AC) 65
4.2.2 The Damara Supergroup 68
4.2.3 Lithological mapping of the synclinal infolds 80
4.3 Structure 83
4.3.1 Pre-Damaran Deformation in the Abbabis Complex 83
4.3.2 Damaran Deformation 84
4.4 Pavement map: synthesis of cross-cutting deformational and intrusive relationships 94
4.5 Intrusive Rocks 96
4.5.1 Basement granites 97
4.5.2 Amphibolites 99
4.5.3 Red granites 100
4.5.4 Grey granites 102
4.5.5 Sheeted leucogranites 104
4.6 Migmatites of the Palmenhorst Dome 110
4.7 Discussion 119
4.7.1 The Abbabis Complex and associated magmatism 121
4.7.2 The Damara Supergroup 122
4.7.3 Structure and Metamorphism 125
4.7.4 Early Damaran Intrusives 128

4.7.5 Damaran sheeted leucogranites 129
4.7.6 Migmatites 129
4.8 Conclusions 132
5. Petrology 135
5.1 Introduction 135
5.2 Basement and Damaran Lithologies 135
5.2.1 Abbabis Complex 136
5.2.2 The Damara Supergroup 139
5.3 Intrusions related to the Abbabis Complex and the Damara Belt 150
5.3.1 Basement granites 150
5.3.2 Amphibolites 151
5.3.3 Red granites 152
5.3.4 Grey granites 154
5.3.5 Sheeted Leucogranites 155
5.4 Possible indicators for the presence of remnant partial melt 157
5.5 Discussion 159
5.5.1 The Abbabis Complex 159
5.5.2 The Damaran metasediments 161
5.5.3 Early Damaran Granites 162
5.5.4 Damaran sheeted leucogranites 162
5.5.5 Structure and metamorphism 163
5.5.6 Evidence for partial melting 163
5.6 Conclusions 164
6. Geochemistry 166
6.1 Introduction 166
6.2 Laboratory Methods 166
6.3 Whole-rock geochemistry 167
6.3.1 Major oxide geochemical classification of field lithologies 168
6.3.2 Trace Element Geochemistry 172
6.3.3 Provenance links between the Abbabis Complex and Damaran metasediments 178
6.4 Discussion 181

6.4.1 The Abbabis Complex 181
6.4.2 The Damaran metasediments 182
6.4.3 The Damaran Granitoids and their petrogenesis 184
6.4.4 Tectonic setting and petrogenesis of the Palaeoproterozoic amphibolite dykes and the Damaran granitoids 186
6.5 Conclusions 187
7. Geochronology 189
7.1 Introduction 189
7.2 Methodology 195
7.3 U-Pb Geochronology Results 197
7.3.1 Abbabis Complex 197
7.3.2 Amphibolites 203
7.3.3 Etusis Formation 207
7.3.4 Red granites 213
7.3.5 Sheeted leucogranites 216
7.4 Lu-Hf isotope analysis 220
7.5 Discussion 222
7.5.1 The Abbabis Complex 223
7.5.2 Amphibolite dykes 227
7.5.3 The Etusis Formation 229
7.5.4 Red granites 233
7.5.5 Sheeted leucogranites 234
7.6 Conclusions 235
8. Synthesis and Conclusions 238
8.1 The evolution of the northern Palmenhorst Dome in the context of the southern Central Zone of the Damara Belt 238
8.1.1 The Abbabis Complex and associated intrusives 240
8.1.2 Comparison between the quartzofeldspathic Abbabis Complex and the Etusis Formation 242
8.1.3 The Damara Supergroup 244
8.1.4 Structure and Metamorphism 245
8.1.5 Damaran amphibolite dykes and granitoids 248
8.1.6 Partial melting in the northern extent of the Palmenhorst Dome 251

8.2 Future studies on the Abbabis Complex and the southern Central Zone:..... 253
9. References 254
10. Appendices..... 263

List of Figures

Figure 1.1: Reconstruction of Gondwana showing East and West Gondwana with associated shields and Neoproterozoic to Mesozoic-Tertiary Orogens (after Gray *et al.*, 2008; Malone *et al.*, 2008; Rankin, 2015). Note DB – Damara Belt, LA- Lufilian Arc, RP- Rio de la Plata, SF- São Francisco.....2
Figure 1.2: Tectonic evolution and geodynamic model of the Damara Belt involving the Kalahari and Congo Cratons. The model illustrates the rifting, northward subduction through to collisional phases of the cratons, with the tectonostratigraphic zones of the Damara Belt labelled as NF- Northern Foreland, NZ- Northern Zone, CZ- Central Zone, SZ- Southern Zone, SMZ- Southern Marginal Zone, and SF- Southern Foreland (modified after Gray *et al.*, 2007).....3
Figure 1.3: Illustration showing the colliding cratons that formed the Damara Orogen: Damara Belt, Gariep Belt and the Kaoko Belt. Pan-African orogenic belts are indicated by their respective suturing ages (modified after Gray *et al.*, 2008). Inset demonstrates where the Damara Belt is situated between the Congo and Kalahari cratons (modified after Oliver, 1994).....5
Figure 1.4: Map of the Damara Belt showing the subdivisions of the stratotectonic zones, major lineaments and basement inliers or pre-Damaran rocks (modified after Miller, 2008).....6
Figure 1.5: Schematic of various lithostratigraphic variations and correlations across the different stratotectonic zones of the Damara Belt with general ages of the stratigraphy (modified after Miller, 2008). ..7
Figure 1.6: Locality of field area. (A) A hyperspectral image of the area with the Khan River and B2 Access Road. (B) A detailed geological map of the Palmenhorst Dome of the sCZ indicating the location of the field area in context of the larger Palmenhorst Dome (WGS84, Zone 33K) (modified after Lehtonen *et al.*, 1995; Longridge *et al.*, 2011).....10
Figure 2.1: Simplified stratigraphic column of the sCZ of the Damara Belt, showing lithologies, approximate depositional ages and general contact relationships (modified after Brandt, 1987; Badenhorst, 1992; Hoffmann *et al.*, 2004; Longridge *et al.*, 2011).....13
Figure 2.2: Detailed geological map of the Central Zone showing the distribution of the Damara Supergroup, Abbabis Complex (basement) and the associated intrusives. Domes of the area are also indicated (WGS84, Zone 33K; modified after Lehtonen *et al.*, 1995 and Longridge *et al.*, 2011). Specific basement-cored domes are referred to in text.....14
Figure 2.3: Simplified stratigraphic column of the sCZ with the main lithological differences for each Formation of the Damara Supergroup (Nosib and Swakop Groups) and the Abbabis Complex (modified after Hoffman *et al.*, 2004; Miller, 2008).....19
Figure 2.4: Simplified representation of peak metamorphic assemblages in the Damara Orogen (modified after Goscombe *et al.*, 2004).....21

Figure 2.5: Distribution and comparison of the Abbabis Complex and Damara Supergroup (Rössing, Khan and Etusis formations) in the Khan-River Dome (or Palmenhorst Dome). Maps after (A) Smith (1965), (B) Barnes (1981) and (C) Longridge (2012) show considerable differences in the distribution of the Abbabis Complex and Damara Supergroup from undifferentiated basement cores to complex patterns of crustal elements within the basement. Modified after Longridge (2012).....26
Figure 2.6: A map of the northern extent of the Palmenhorst Dome illustrating (A) Poli's (1997) proposed Tsawisis Formation of the Abbabis Complex showing rafted quartzites, amphibolite, conglomerate and marble within granites, and (B) a revised lithological map (Longridge, 2012) indicating a complete lower Damara Supergroup sequence correlated with the proposed rafts by Poli (1997). Damaran-aged granites (as indicated in grey) are omitted in illustration B (modified after Longridge; 2012). The inset shows an overview of the Palmenhorst Dome and where maps A and B are approximately located in terms of the larger Palmenhorst Dome.....28
Figure 2.7: A geological cross section along the southern extent of the Palmenhorst Dome from Goanikontes to the Ida Dome. The geological cross section indicates "lower, middle and upper units" (after Toe *et al.*; 2013).
.....29
Figure 3.1: Schematic of the workflow used on Landsat 8 and Hymap hyperspectral imagery. The five images used for interpretation include the (1) Principal Component Analysis (PCA), (2) Maximum Noise Fraction (MNF), (3) statistical composite 761, and (4 and 5) two band ratio (5:7/5:1/5:4*3:4 and 4:3/5:2/3:1) images MNF= Maximum Noise Fraction; Inv. MNF= Inverse MNF; VNIR= Visible and Near-infrared; SWIR= Short-wave Infrared; FLAASH= Fast Line-of-sight Atmospheric Analysis of Hypercubes; ROI= Region of Interest; PCA= Principal Component Analysis; NOFEOX= no iron oxides. 32
Figure 3.2: Landsat 8 Image of the Palmenhorst Dome. The pink colour highlights the Palmenhorst Dome and the red box indicates the northern extent of the dome, which is subject of this study. (Area is approximately 38 km^2). 33
Figure 3.3: Images of multiple band ratios used for discriminating between different rock types showing minimal variability in their discrimination potential (from Simon *et al.*, 2016). 35
Figure 3.4: Processed Landsat 8 images used in the interpretation of the spectral domains and geological base map. Image (B) indicates the boundaries (white) for the spectral domains labelled from 1 to 8. These domains apply to all images. The inset, in the bottom right hand corner, illustrates the general orientation of the fold axial trace within the mapped area. Rafts are traced in white within domains 2 and 3 with the rafts in domain 3 displaying a folded geometry. Note the extension of thin slivers of domain 4 into domain 1 and 2 along the contact in the northern extent of domain 2.....38
Figure 3.5: The three hyperspectral images used for the refinement of Landsat 8 domains: (A) MNF VNIR 236, (B) MNF SWIR 245 and (C) Decorrelation Stretch 114/108/33. Landsat domains 1 to 8 are also indicated on image B. 43
Figure 3.6: Decorrelation Stretch 114/108/33 (A) with the interpretive RGB ternary plot (B) showing mafic MgOH minerals and carbonates, felsic minerals, AlOH clays and micas as well as iron oxides and ferrous Fe minerals using RGB colours.....45

Figure 3.7: Multi-mineral Rule Classified Map NOFEOX (No Iron Oxide included) image of the northern extent of the Palmenhorst Dome. Mineral varieties that were noted from previous Hymap processing are indicated in brackets, but more common equivalents are noted. The spectral signatures are estimates and mineral identification was not performed in this study. Hyperspectral imagery was already processed. Montmorillonite is a type of clay mineral. 47
Figure 3.8: Landsat 8 images and Hymap images illustrating the isolated rafts within domains 1 to 3. (A) Landsat 8 MNF, (B) Landsat 8 band ratio 5/7:5/1:5/4x3/4, (C) Hymap MNF VNIR 236 and (D) Hymap MNF SWIR 245. Rafts shown as black lines in all images. 48
Figure 3.9: The Hymap MNF VNIR image of the greater Palmenhorst Dome illustrates the presence of rafts within the dome – outlined by white lines for the greater extent of the dome and traced by black lines within the field area. 49
Figure 3.10: Geological map of the Nose Structure (modified after Lehtonen *et al.*, 1995 and Longridge *et al.*, 2011). 50
Figure 3.11: A Landsat image of the Nose Structure (in pink), showing the axial traces of the D2 and D3 folds. The inset, top left corner, shows the location of the Nose Structure as part of the greater Palmenhorst Dome (also shown in pink). A Karoo-aged dyke has been traced (green) from synthesis between the Landsat image and previous geological maps (Smith, 1965; Lehtonen *et al.,* 1995). 51
Figure 3.12: Stratigraphic column summarising rock types and associated mineral assemblages of the Abbabis Complex and Damara Supergroup (modified from Brandt, 1987; Badenhorst, 1992; Hoffman *et al.*, 2004; Miller, 2008; Longridge *et al.*, 2011; Rankin, 2015). N.G.C - Narubis Granitoid Complex. 52
Figure 3.13: Different maps produced by (a) Smith (1965), (b) Volkman *et al.* (1988) and (c) Lehtonen *et al.* (1995) of the northern extent of the Palmenhorst Dome showing the evolution of mapping. These maps have been traced and do not necessarily indicate a migrating Khan River but rather highlights how there are varying outcrop patterns according to different authors. 55
Figure 3.14: Proposed geological base map integrating spectral domain interpretation and stratigraphic subdivision from published geological maps (Lehtonen *et al.*, 1995 and Longridge, 2012). Domains are numbered from 1 to 8. 56
Figure 3.15: MNF VNIR image showing the Nose structure as part of the larger Palmenhorst Dome with proposed supracrustal components found in this study (outlined in black and white). The white rafts correlate with infolded lower Damaran sequences proposed by Longridge (2012). Overlain geology: Yellow= Etusis Formation, Blue= Khan Formation, Orange= Rössing Formation and Green= Chuos Formation. Proposed axial traces of the folded rafts are indicated (yellow) and a trace of the Karoo-aged dyke (red) is also shown. 58
Figure 4.1 (on following page): Geological map produced from this study of the Nose Structure at the northeast end of the Palmenhorst Dome. Geological map with inset of the Palmenhorst Dome showing only the Abbabis Complex (as undifferentiated), the lower Damara Supergroup (Etusis, Khan, Rössing and Chuos Formation) and the field area within context of the greater Palmenhorst Dome on the top right and a cross section from A to B (indicated by the blue line on main geological map) along the right-hand margin. 62
Figure 4.2 (on previous page): Outcrop field photographs of the various gneisses of the Abbabis Complex. (A) Banded orthogneiss within the HSZ displaying folding of foliation and strained K-feldspar-rich leucocratic

segregations. Examples of folded leucocratic segregations traced in white. (B) Characteristic pencil cleavage of the augen gneiss. Examples of augen, comprising quartz, plagioclase and K-feldspar, are outlined in white in the bottom left hand corner. Sheets of augens are seen as weathered fragments in the picture. (C) A fine-grained banded orthogneiss in the HSZ. Alternating bands of biotite-rich and plagioclase -rich bands (< 1 – 2 mm thick) are convoluted and folded, but still maintain the general banded orientation. (D) Banded paragneiss/grey orthogneisses with SLGs intruding parallel to banding orientation. These feldspar-rich SLGs are convoluted and often nebulitic. (E) Folded HSZ paragneiss/grey orthogneisses with strained SLGs folded and extended into isolated leucocratic blebs. FA= fold axis indicating the axial trace orientation. (F) Boudinaged gneiss within leucosomes of fine-grained white migmatites in the core of the boudin (indicated in photograph). Main extension direction is indicated by the dashed line. (G) orthogneiss with SLG (type A) associated with a cross-cutting dextral shear zone. (H) Granite-gneiss with a defined biotite foliation (indicated with the white dashed line). Red K-feldspar, plagioclase and quartz are weakly aligned. 68
Figure 4.3: Field photograph illustrating the difficulty in identifying the contact between the Abbabis Complex and the Etusis Formation due to their similar compositional and textural characteristics. 70
Figure 4.4: A simplified geological map of the field area highlighting the distribution of the Etusis Formation with a summary of the lithologies identified (lower right) for the Etusis Formation in the field area. The column height is not drawn to scale, but the quartzite is more common in the field area and therefore has an increased representation. Colours in the column do not correspond to those shown in the alongside map. 71
Figure 4.5: Outcrop field photographs of the Etusis Formation. (A) A banded quartzite with heavy mineralisation (white arrow). (B) A banded quartzite with heavy mineralisation (white arrow) and pebble lags. Pebbles comprise flattened quartz grains 1-2 cm in length. (C) Isolated carbonate layer in banded quartzite to gritstone. Calcite (grey) and quartz-rich (red-brown) interbeds are present. (D) A banded arkose showing interbeds of quartz-rich (light brown to tan - indicated in yellow) and K-feldspar-rich layers (pink). Cross-cutting brittle joints are present. (E) An arkose with sillimanite teeth forming a lineation. Teeth are traced in fine black dashes indicated by the yellow arrow. (F) Sillimanite-quartz-biotite schist interlayered with meta-arkose. Sillimanite lineation is defined by the dashed red line. 72
Figure 4.6: A simplified geological map of the field area highlighting the distribution of the Khan Formation with a summary of the lithologies identified (lower right) for the Khan Formation in the field area. The column height is not drawn to scale and the colours in the column do not correspond to those shown in the alongside map. 73
Figure 4.7: Outcrop field photographs of the Khan Formation. (A) A stromatic and net-textured diopside-amphibole-(biotite-cordierite) schist. This semi-pelitic schist contains migmatitic bands of leucosomes and palaeosomes giving it the distinctive white and dark green-grey colour, respectively. (B) A diopside-amphibole-(biotite-cordierite) schist is present with nodular cordierite in a biotite-amphibole matrix. (C) A banded gneiss showing gneissic bands of diopside and K-feldspar. Attenuated diopside layers are present. (D) Folded banded diopside-K-feldspar gneiss with orange calcite (white arrow) and associated (folded) type C′ SLGs. Dashed black line indicates fold axis orientation (strike of plane= 050°). (E) Green calcsilicate with accumulations of cross-cutting diopside-amphibole vein-like feature with cross-cutting parallel K-feldspar and plagioclase-rich boudin controlled SLG. (F) Weathered calcsilicate with interbeds of calcite-rich (red arrow)

and quartzite (white arrow) layers with replacement of calcite with diopside (yellow arrow). These layers are convolute and show a positive-negative weathering relief. 74
Figure 4.8: A simplified geological map of the field area highlighting the distribution of the Rössing Formation with a summary of the lithologies identified (lower right) for the Rössing Formation in the field area. The column height is not drawn to scale and the colours in the column do not correspond to those shown in the alongside map. 76
Figure 4.9: Outcrop photographs of the Rössing Formation. (A) Two white to tan marble units of the Rössing Formation interbedded with the pelitic schists of the Khan Formation. This highlights the gradational contact. (B) A calcsilicate with calcite (grey), biotite (dark brown to black) and radial laths of green-blue scapolite (white arrow). (C) Interbedded marble (white lithology with scale on it), quartzite, semi-pelitic schists and garnet-sillimanite-quartz schist (red quartzite). Red quartzite is highly foliated. Lateral facies change along strike. (D) Interbedded marble layers and foliated sillimanite-garnet schist (red quartzite). Marble is attenuated, and foliation is continuous indicating increased deformation. (E) Interbeds of quartzite- and calcite-rich layers that are folded (dashed white lines). Calcite-rich layer is thicker. (F) A shear zone cross-cutting and bending the foliation of the maroon pelitic schist with sillimanite and garnet porphyroblasts. Deflection of the foliation is only on one side of the shear. 77
Figure 4.10: A simplified geological map of the field area highlighting the distribution of the Chuos Formation with a summary of the lithologies identified (lower right) for the Chuos Formation in the field area. The column height is not drawn to scale and the colours in the column do not correspond to those shown in the alongside map. 79
Figure 4.11: Outcrop field (A to D) and hand sample (E) photographs of the Chuos Formation. (A) Iron-rich interbeds of calcite-rich layers (grey) and iron-rich quartzite in a thin iron-formation. (B) Cross sectional view of strained clasts from the Chuos diamictites. Flattened clasts that are folded and granular quartz in composition. (C) Down dip view of the Chuos Formation showing flattened clasts (yellow arrow) in a semi-pelitic matrix and interbeds of marble layers (white arrow). (D) Cross sectional view of an upright open fold. The diamictite is folded with both the foliation and clasts folded. Black dashed line is approximate fold axis with the yellow trace highlighting the folded layers. (E) A garnet-biotite-amphibole-quartz schist with white sillimanite or plagioclase blebs.....80
Figure 4.12: Geological map showing the synclinal infolds and their associated lower Damaran stratigraphic units in each syncline. The Hinge, Dorob and Ostrich Gorge Synclines are illustrated in the stratigraphic sections. Thicknesses are not representative. X indicates missing formations in the stratigraphic sections. ...82
Figure 4.13: Field photograph of the Abbabis Complex augen and/or orthogneiss displaying an early fabric and later Damaran fabric cross-cutting one another resulting in the characteristic pencil cleavage that creates the jagged weathering profile of the gneisses. The yellow line indicates the Abbabis Complex gneissic fabric, while the white line indicates an axial planar foliation from the open folding event. 84
Figure 4.14: An example of the early regional fabric, identified in the field, that is reoriented by later D2 and D3 events. The foliation is traced in a solid black line and the orientation, of the undeformed and bedding parallel portion, is given alongside. 85

Figure 4.15: Field photographs (A to C), equal area stereonet plot of the D2 folds (D) and geological map of the Hinge Syncline. (A) Folded sillimanite-biotite schist, of the Etusis Formation, with two fold generations. D2 (red) is recumbent and tight meanwhile D3 (yellow) has reoriented the axial planes but is open and more upright. (B) Intrafolial isoclinal and recumbent D2 folds (red) of SLG. A D3 open fold (black) that has folded the foliation and displays two fold axial planes. (C) Discordant sinistral shear zone that has cross-cut basement granites. (D) An equal area stereoplot of the poles of fold axial planes (maroon triangles) measured from parasitic isoclinal folds, axial planar foliation (purple circle) and northeast gently dipping lineation (green diamonds). The circles, and their colours correspond to conical best fit projections of each data set with the centre and enlarged points indicating the average. The average fold axial plane (FAP) shows a northeast dipping and north-south striking fold axial plane. The black filled circle shows the pole to the FAP. The in-set in the bottom right shows the Hinge Syncline where there is a large scale D2 syncline refolded by the D3 folding event. Pink= Abbabis Complex; purple= amphibolites; yellow= Etusis Formation; blue=Khan Formation; orange= Rössing Formation; white= recent deposits. 87
Figure 4.16: Field photographs of the D2 HSZ. (A) A grey granite being extended into the strain direction as zig-zag edges attenuate the granite into the basement gneiss. (B) The area in image A indicated by the black box, showing a more detailed image of the of the strain extending the granite into the gneiss. (C) Bedding parallel foliation within a HSZ. Foliation spacing is thinned and now continuous. (D) HSZ gneisses (HSZ) with foliation parallel and cross-cutting type A SLG (pink) being extended into the gneissic fabric by the strain. Discordant sinistral shear zone intruded by the SLG. Stretching and boudinage (red) are in a northeast-southwest direction parallel to compressive direction. 89
Figure 4.17: Field photographs of boudinage parallel to the northeast-southwest trending HSZ. (A) Strained Rössing Formation showing bedding parallel foliation with boudinage. SLG present in the core of the extension site. (B) Sillimanite porphyroblasts, in the Etusis Formation, are boudinaged and extened into the HSZ extension direction. (C) Basement rocks within the HSZ, and associated SLG boudinaged and extended into the direction of stretching. 90
Figure 4.18 (on previous page): Field photographs of the D3 interference folds (A to C and E), stereoplots (D) and geological map of the field area. (A) Open and steeply dipping folds of amphibolite dykes and SLGs cross-cutting basement rocks. Two foliations are present: axial planar foliation (black dashed line) and one folded (red line). (B) A parasitic open fold with a bent fold axial plane (plane line) due to interference patterns in the Chuos Formation. Surrounding biotite and amphibole foliation folded too. (C) Dome-like interference patterns from outcrop scale folds in a HSZ gneiss. Red fold axial plane (D2) is refolded by D3 (white) fold to form a basement-cored fold. (D) Equal area stereoplot showing measured poles of fold axial planes (red triangles), axial planar foliation (purple circles) and stretching lineation (green diamonds) with the fold average fold axial plane (FAP; black) derived from the conical best fit average of the fold axial plane pole measurements. average pole indicated by the black circle. Circles, in the same colours as the datasets, are conical best fit projections with the average poles indicated in slightly enlarged symbols. (E) Cross section of a folded outcrop. Basement-cored domes (pink) with surrounding Etusis Formation (yellow) is a result of fold interference patterns between D2 and D3 at the outcrop scale. Top right inset: interference fold pattern of recumbent D2 (yellow=

limbs; red= fold axial plane) folds being refolded by D3 open and vertical folds (white). Inset is enlargement of black box outlined on the left. 93
Figure 4.19: Field photographs of the brittle deformation associated with D4. (A) Brittle sinistral faulting displacing various SLGs. The zone has cleavage within the displacement zone. (B) Low angle conjugate joints within the Rössing Formation. (C) Brittle joints associated with chlorite and/or epidote alteration along the joint planes (indicated by the yellow arrow). This joint cross-cuts basement rocks and a SLG in this picture.. 94
Figure 4.20: Pavement outcrop map of the HSZ, summarising the cross-cutting relationships between the supracrustals, basement rocks, granites and deformational features. The lower right inset shows the locality of the pavement map in the northern extent of the field area. Residual layering is present within xenoliths of palaeosomes. 95
Figure 4.21: Simplified geological map of the field area, modified from figure 4.1, highlighting the estimated extent of the basement granites. 97
Figure 4.22: Outcrop photographs of the basement granites. (A) Weathered outcrop of a basement granite, in the Ostrich Gorge Intrusion, showing the distinct light pink to musky pink colour of the microgranite. Late stage joints (dashed yellow line) cross-cut the granite. (B) Polished basement granites cross-cut by type A SLGs (white dashed line) and B, with type B cross-cutting type A SLGs. All granites are sheared by a sinistral shear (red dashed line and arrows= shear; red solid line= sense of movement). (C) basement granite cross-cut by red granite. Foliations within both granites (white dashed line= basement granite foliation; red dashed line= red granite foliation) are sub-parallel. (D) basement granite cross-cut by two generations of SLGs, namely type B and then by type E. 98
Figure 4.23: Outcrop photographs of the amphibolite dykes. (A) Foliated amphibolite dyke with cross-cutting tabular type C′ SLGs. (B) Red stained and lighter grey amphibolite dyke with intruding type E SLGs. Both lithologies have been boudinaged. (C) Folded amphibolite dyke with associated intruded type C′ SLGs. Leucosome, melanosome and palaeosome are all identified. (D) Large outcrop (10 m across) of amphibolite dyke intruded by type C′ SLGs. The type C′ SLGs have an anastomosing and sheeted morphology with rafts of melanosomes and palaeosomes within the granitic intrusion. (E) Near upright open folded amphibolite dyke with parallel type B SLGs. Approximate fold axial plane (dashed yellow line) with parallel axial planar foliation (solid yellow line) associated with folded amphibolite foliation (white dashed line). 100
Figure 4.24: Field photographs of the red granites. (A) Polished red granite showing the distinctive deep red colour with a quartz pod (traced in white) that is refolded by tight to isoclinal folds. (B) Granular red granites with sillimanite knots (white dashed line). (C) A foliation (white line) that is folded. Xenoliths of proposed Rössing Formation are present that contain a sillimanite lineation that extend to the granite. The lineation remains parallel and are at an angle to the foliation. (D) A photo illustrating the homogeneous texture of the red granite intruding into the orthogneisses of the Abbabis Complex. Contact indicated in red. 101
Figure 4.25: Outcrop photographs of the grey granites. (A) Melanocratic type 1 grey granite with cross-cutting more felsic type 3 grey granites and type C′ SLGs. (B) Melanocratic type 1 grey granite with a moderate foliation cross-cut by tabular type B SLGs. The sheeted body has rafts of the grey granite. (C) Porphyritic type 2 grey granite with a plagioclase lineation and a defined foliation. (D) Light type 3 grey granite with associated

sheeted plagioclase veins. Tabular cross-cutting type F SLG is present. (E) Type 3 grey granite with associated plagioclase veins. Cross-cutting type B SLG, which is cross-cut by type E SLG. 103
Figure 4.26: Outcrop field photographs of the type C' SLGs. (A) Homogeneous and tabular type C' SLG intruded bedding parallel. (B) Near vertical and tabular type C' SLG highlighting the homogeneous nature. (C) Amorphous and deformed type C' SLG cross-cutting the grey granites and cross-cut by type F SLG. (D) Type C' SLG cross-cutting red granites, and cross-cut by type A SLG. Type A and C are both sheared, strained and cross-cutting relationships are not always apparent. 105
Figure 4.27: Outcrop field photographs of the type A SLGs. (A) Bedding parallel and thin type A SLGs cross-cutting Damaran metasediments. The intrusion is associated with boudinage and occurs within the dilation features (yellow arrow). (B) Convoluted and folded type A intrusion cross-cutting Abbabis Complex gneisses. The SLGs are folded by two folding events because there are two-fold axial planes (yellow dashed line). (C) Continuous and discordant type A intrusions folded into gently inclined tight folds (fold axial planes= white dashed lines). (D) Rootless isoclinal and gently inclined folds, indicated by the red outline, of type A SLG. . 106
Figure 4.28: Field photographs of type B SLGs. (A) Homogeneous white type B SLGs which cross-cut Khan Formation semi-pelitic schists. type E SLG cross-cuts both the Khan Formation and type B SLGs. Sharp intrusive contact between the two SLGs are indicated in red. (B) Diffuse contact (black dashed line) between type B SLGs and E, in the HSZ, with type E cross-cutting type B. (C) Type B SLG leucosome cross-cutting grey granites type 1. Yellow arrow indicates the porphyroblastic garnet and amphibole. The SLG is openly folded. (D) A sharp intrusive contact between basement granites and type B SLG. The SLG is an openly folded Z-fold (fold axial trace= black dashed lines). 107
Figure 4.29: Field photographs of the type E SLGs. (A) Rootless openly folded type E SLGs (outlined in pink) cross-cut the foliation in the HSZ. The foliation (white dashed line) is bent and folded as well as truncated by the type E intrusion. Fold axial trace= yellow dashed line. (B) Granular pegmatitic K-feldspar and quartz appear to be scattered over the basement rocks and cross-cut the type B SLG. 108
Figure 4.30: Satellite image of the northern extent of the field area showing a portion of the basement and Damara cover sequence. Some examples of type F SLG pegmatites are indicated by the red lines. Other SLGs observed may be Type F SLGs, however only a few examples have been traced so not all the examples were obscured by the traced lines. The yellow shaded area indicates the HSZ and the location of the pavement map (Fig 4.20) in the black box. The in-set (bottom right) shows a geological map of the area in the satellite image (pink= Abbabis Complex; yellow= Etusis Formation; blue= Khan Formation; orange= Rössing Formation; green= Chuos Formation). 109
Figure 4.31: Field photographs of the type F SLGs. (A) A sharp contact of the type F SLG and the red granite. Pegmatitic SLGs with shiny cleavage plane of K-feldspar. (B) Cross-cutting type F SLGs with shears, foliation and type B SLG. The shear is a set of two dextral shears (dashed black lines; kinematics indicated by yellow arrow) with S-C fabric in between the shears (solid black line). Foliation is bent by shears. Type B SLG in the shear and sheared by the deformational feature. 110
Figure 4.32: Schematic illustration of the 4 groups of migmatites identified in the Palmenhorst Dome. These types include (A) intrusive bedding and foliation parallel metatexites, (B) intrusive sheeted granites, (C) sheeted granites with rafted palaeosomes and (D) homogeneous granite diatexites and plutons. 111

Figure 4.33: Geological map of the field area showing localities of metatexite and diatexite outcrops. Metatexites are largely concentrated in the north of the field area and along the basement-cover contact. In contrast, the diatexites are concentrated in the south of the field area, although similarly, transitional diatexites are seen at the basement-cover contact. Proposed zones of metatexite, transitional and diatexite migmatites are outlined in the top left inset (metatexite= pale orange with blank and solid banding; transitional= peach with hatched and lined banding; diatexite= pink with crosses; banding orientations do not represent a preferred orientation but is used for distinction between the domains). Section A-B is indicated on the map which correlates to the cross section in section 4.7.5. 112
Figure 4.34: Field photographs of the intrusive bedding and foliation parallel metatexites. (A) In situ patch neosome (yellow arrow) weakly developed in a dilational structure cross-cutting the HSZ basement. (B) Dilation to net-textured leucosomes (yellow arrow) with a biotite melanosome. Both in-source leucosome and palaeosome has been boudinaged. (C) Net-textured migmatite showing elongate palaeosome blocks with two directions of intrusive leucosomes (white arrow). (D) Stromatic migmatite with dismembered boudins of palaeosome, Khan Formation. Meter-rule for scale. 114
Figure 4.35: Field photographs of the intrusive sheeted granites metatexites. (A) Amorphous leucocratic vein structured migmatite, outlined in red, in contact with the basement gneisses. (B) Two generations of migmatites forming a stromatic texture (white arrow). Palaeosome is present as Abbabis Complex gneisses. (C) Anastomosing vein-structured migmatite, which has still preserved the palaeosome. Contacts are sharp. (D) Anastomosing vein-structured migmatite showing the intrusive nature yet the contacts are diffuse in some instances. 115
Figure 4.36: Field photographs of the sheeted granites with rafted palaeosome diatexites. (A) Schollen of amphibolite dykes (examples outlined in red) as the palaeosome within a schlieren dominated leucosome. (B) An example of a smaller raft (outlined in yellow) that is a lozenge shaped. The foliation in the palaeosome truncates the leucosome at a low angle (white lines truncated by the yellow outline of the raft). Melanosomes are present at the contact between the palaeosome and leucosomes and is developed as a concentration of biotite and amphibole platy dark minerals (red arrow) and in this case is similar to the palaeosome due to the protolith mineralogy. (C) A wall of multiple partial melt generations with schollen of dark palaeosomes. ... 117
Figure 4.37: Field photographs of the homogeneous granite diatexites and pluton migmatites. (A) A gorge wall of a diatexite intruding into the basement gneisses. Homogeneous red granites are observed. (B) Khan River Gorge outcrop of multiple generations of migmatites or SLGs coalesced to form diatexites. Resister lithologies are present and examples are outlined in white. 118
Figure 4.38: Lithological distributions in the Nose Structure from various authors and this study. (A) Smith (1965); (B) Volkman *et al.* (1988); (C) Lehtonen *et al.* (1995) and (D) lithological distributions from this study showing the new distribution of Damara metasediment-cored synclines within the basement rocks. 125
Figure 4.39: Schematic block diagrams of cross-sections of D2 and D3 deformational events. Folding and associated fabrics and intrusions are noted. (D2) Southwest verging northeast plunging to recumbent folds resulting in basement-cored nappes, high strain zones (HSZ) on the attenuated and upright limb of the folds. Southwest-northeast compression and northwest-southeast extension. (D3) Northwest-southeast compression and northeast-southwest extension is orthogonal to D2 with open upright folds (D3 FAP= red

dashed line). D2 nappe-like structures are refolded (D2 FAP= black dashed line) by D3 folds resulting in dome formation. The interference fold pattern and parasitic folds yield similar outcrop extents seen in the geological map produced for the Nose Structure (yellow rectangle) and the northern extent of the Palmenhorst Dome from other studies (plan view of northern margin folds after Longridge, 2012). 127
Figure 4.40: Northwest-southeast schematic cross section of the field area showing the stratification of the intrusions based on the distribution of the migmatites in the field area. First order classification of the migmatites are shown, based on a function of the fraction of melt present, in the top diagram. The uniform, rigid spheres (URS) and non-uniform in size and shape (NUP) models are illustrated after Renner *et al.* (2000) and Sawyer (2008). The distribution of the four different groups of migmatites, described in section 4.4, within the crust is indicated in the middle by the black distribution bars. Cross section from A-B (see figure 4.35) is showing the basement and cover lithologies and the types of partial melt associated with each. 131
Figure 5.1: Overview photomicrographs of thin sections from the Abbabis Complex. (A) Cross-polarised light (XPL) photomicrograph showing overall rock texture of an orthogneiss with an associated sheeted leucogranite outlined with dashed yellow lines. Biotite foliation= white dashed lines. Two foliations are present - one is parallel to the yellow dashed line and younger than the foliation at an angle. Red dashed line indicates microcline compositional layering direction and distribution. (B) A plane polarised light (PPL) photomicrograph showing biotite foliation, mineral alignment and opaque mineral distribution in the area indicated by the white box in image (A). (C) Overview photomicrograph showing a granite-gneiss with elongate, poikiloblastic quartz indicated by the dashed red lines. Biotite accumulations and foliations are indicated with the white dashed line (XPL). (D) Biotite accumulations in the area indicated by the white box in image (C) (PPL). (E) Overall rock texture of a grey orthogneiss with grain size banding. Increase in grain size, with respect to the other grains= yellow dashed line; Biotite foliation= white dashed line (XPL). (F) Opaque and biotite alignment (red dashed line) in the area indicated by the white box in image (E) (PPL). 137
Figure 5.2: Photomicrographs of the Abbabis Complex gneisses. (A) Dusty and altered microcline, foliated biotite being replaced by chlorite (white arrow) and cuspate lobate grain boundaries (PPL). (B) Altered quartz and plagioclase. Seritisation replacing remnant plagioclase twinning, along with alteration along cracks within quartz (white arrows). Rounded inclusions within plagioclase (red arrow). (C) Cream quartz, microcline, biotite, plagioclase and magnetite. Rounded inclusions of quartz within altered plagioclase (red arrow). Poikiloblastic and elongate quartz is also present (XPL). (D) Granoblastic quartz and biotite. Biotite has altered and replaced remnant plagioclase (white arrow), which then has undergone seritisation. (XPL) (E) Microcline and plagioclase replaced by biotite as microcline remnants are present within biotite laths. Microcrystalline rims along cuspate grain boundaries (white arrow). Plagioclase is altered to sericite. (XPL) (F) Large plagioclase grain with cuspate lobate grain boundaries (yellow arrow). Granophyric intergrowths within the plagioclase grain (white arrow) (XPL). Mineral abbreviations are after Kretz (1983). 138
Figure 5.3: Overview photomicrographs of thin sections from the Etusis Formation meta-siliciclastic rocks. (A) Banded quartzite showing a granoblastic polygonal texture, comprising mainly quartz and feldspar (white arrow). Large quartz are aligned with banding (XPL). (B) Ilmenite banding is indicated by the yellow dashed line in the PPL image of area indicated by white box in image (A). Ilmenite is indicated by the red arrows. (C) Sillimanite-quartz-biotite schist showing the sillimanite-biotite lineation and foliation within a quartz and

minor feldspar matrix. Quartz elongation direction (red lines) is parallel to the foliation; microcline= yellow arrow (XPL). (D) Sillimanite knots (grey fibrous texture) and distinct biotite foliation (red arrow) in PPL image of area in (C). Mineral abbreviations are after Kretz (1983). 140
Figure 5.4: Photomicrographs of the Etusis Formation meta-siliciclastic rocks. (A) Granoblastic quartzite with quartz, plagioclase and ilmenite and minor biotite (XPL). (B) Sillimanite-quartz-biotite schist with quartz, microcline, sillimanite and biotite (XPL). Microcrystalline rims around quartzofeldspathic minerals (red arrow). (C) Sillimanite-quartz-biotite schist with elongate quartz laths, as well as biotite and sillimanite knots. Altered and replaced plagioclase (XPL). (D) Biotite-sillimanite porphyroblast as red-brown and pink-grey, respectively. The bright quartz shows the anastomosing nature of the sillimanite-biotite lineation (PPL). (E) Sillimanite-quartz-biotite schist showing the fibrous nature of the sillimanite and how it replaces the biotite. Intergrowth and alignment of quartz with the sillimanite and biotite (PPL). (F) Sillimanite-quartz-biotite schist with elongate poikiloblastic quartz and alignment of ilmenite with a S-C fabric (yellow dashed line). Mineral abbreviations are after Kretz (1983). 142
Figure 5.5: Overview photomicrographs of thin sections from the Khan Formation. (A) Hornblende-diopside-plagioclase-quartz-biotite schist showing an alignment of poikiloblastic hornblende and diopside (yellow dashed lines) and biotite laths (white dashed line). Quartz is also faintly aligned (XPL). (B) Poikiloblastic nature and distribution of hornblende (dark green) and diopside (tan) is best illustrated in PPL. (C) Banded diopside-hornblende-microcline-(quartz) gneiss. The gneiss shows compositional banding (white dashed line) with alternating banding of diopside + microcline + quartz-rich and hornblende + microcline + quartz + minor diopside banding. Alignment of diopside and hornblende is present (XPL). (D) Poikiloblastic and aligned (yellow dashed line) diopside and hornblende is best illustrated in PPL. (E) Calcsilicate unit comprising calcite, quartz and diopside. The quartz is polycrystalline with undulose extinction. The calcite and diopside are interstitial to the quartz (XPL). (F) PPL photomicrograph of the area in (E) The green diopside appears along quartz grain boundaries and as interstitial minerals to quartz. Calcite is grey and shows faint cross-hatching from calcite twinning (PPL). Mineral abbreviations are after Kretz (1983). 143
Figure 5.6: Photomicrographs of the Khan Formation lithologies. (A) The pelitic schist comprising diopside, hornblende, biotite, plagioclase and quartz. Poikiloblastic diopside and hornblende are aligned with rounded inclusions of quartz and plagioclase. Biotite cross-cuts the diopside and hornblende (yellow arrow) (PPL). (B) The pelitic schist with inclusions of plagioclase within hornblende and diopside. Aligned biotite truncates hornblende and diopside. Magnetite is present in minor amounts (PPL). (C) The banded gneiss showing diopside + microcline + quartz-rich bands in the top right corner, and a small portion of the hornblende + quartz + microcline band in the bottom left corner. Amalgamated diopside encloses microcline and quartz (XPL). (D) Granoblastic polygonal quartz with hornblende and diopside in a banded gneiss. Altered microcline is present (XPL). (E) Polycrystalline quartz (yellow arrow) with undulose extinction. Calcite and diopside are interstitial to quartz (XPL). (F) Quartz, diopside, and calcite in a calcsilicate. Quartz grains are largest with interstitial calcite and diopside (PPL). Mineral abbreviations are after Kretz (1983). 145
Figure 5.7: Photomicrographs of the Rössing Formation. (A) Garnet-cordierite-sillimanite-pyrite-biotite schist with aligned cubic pyrite and biotite with cordierite, quartz and fibrous sillimanite (XPL). (B) Aligned pyrite and biotite is highlighted (dashed white lines) (PPL). (C) Garnet-cordierite-sillimanite-pyrite-biotite schist with

acicular sillimanite replacing biotite. Quartz matrix is present (PPL). (D) Garnet-cordierite-sillimanite-pyrite-biotite schist showing porphyroblastic garnet enclosing biotite laths (yellow arrow) and rounded biotite inclusions (white arrow). Quartz is poikiloblastic and elongate with biotite inclusions. Biotite is concentrated along grain boundaries of quartz and garnet with two foliations (red dashed line) directions (PPL). Mineral abbreviations are after Kretz (1983). 146
Figure 5.8: Overview photomicrographs of thin sections from the Chuos Formation. (A) Diamictite clasts showing the asymmetrical morphology of the quartz clast. Biotite and quartz make up most the matrix (XPL). (B) PPL image of the same area shown in (A) highlighting the clast elongation direction (younger foliation; yellow dashed line) and the biotite foliation (red dashed line) at an angle to the older foliation direction (PPL). (C) Biotite-garnet-hornblende-quartz-sillimanite-(cordierite) schist. A younger biotite foliation (dashed yellow line) and an older crenulation cleavage (white dashed line), which is kinked, is present (XPL). (D) PPL image of the same area in image (C). Mineral abbreviations are after Kretz (1983) 148
Figure 5.9: Photomicrographs of the Chuos Formation. (A) A diamictite showing the edge of the quartz clasts and biotite accumulations along the clast boundary. Biotite defines the main foliation. Rounded quartz grains (100 µm in diameter) are concentrated adjacent to the the larger grains of the clast (XPL). (B) Diamictite showing a quartz clast with inclusions of biotite and ilmenite along the clast boundary (white arrow) (XPL). (C) Poikiloblastic hornblende in a diamictite. The poikiloblasts have inclusions of quartz, biotite and occasionally sillimanite (XPL). (D) Biotite-garnet-hornblende-quartz-sillimanite-(cordierite) schist. Cordierite, aligned biotite, microcline and sillimanite are present. Microcline is replaced by sillimanite and the cordierite shows small inclusions within the grain. Cuspate-lobate grain boundaries are present (white arrow) (XPL). (E) Biotite-garnet-hornblende-quartz-sillimanite-(cordierite) schist highlighting the two biotite foliations: younger deep red-brown biotite (dashed yellow line) and younger tan-brown biotite (white dashed line). Garnet porphyroblasts contain rounded inclusions of quartz (XPL). (F) Ilmenite inclusions in cordierite. Other minerals include microcline altered to sillimanite (white arrow), quartz and biotite (XPL). Mineral abbreviations are after Kretz (1983) 149
Figure 5.10: Photomicrographs of the basement granites. (A) XPL Alignment of quartz (dashed yellow line) and surrounding finer-grained granoblastic polygonal microcline (XPL). (B) Irregular elongate quartz (Qtz) grain boundary with cuspate-lobate features (white arrow) between microcline. Thin rims of quartz are present (XPL). (C) Large quartz grain boundary with microcline that is cuspate-lobate (white arrow). Fractures with sericite are present (XPL). (D) Altered quartz, plagioclase and microcline. Granite is affected by sericitic alteration (yellow arrow). Chlorite (red arrow) is present within fractures (blue arrow). Quartz phenocrysts and microcline have cuspate-lobate boundaries (white arrow) (XPL). Mineral abbreviations are after Kretz (1983). 151
Figure 5.11: Photomicrograph of the amphibolite dykes. (A) Overall rock texture and aligned poikiloblastic hornblende (yellow dashed line), biotite (red dashed line), plagioclase and quartz. Accessory ilmenite and epidote are present (PPL). (B) Interstitial hornblende to plagioclase (black arrow). Biotite is present, along with altered plagioclase (PPL). (C) Aligned chlorite, biotite and hornblende with altered plagioclase. Inclusions of rounded quartz in biotite. Chlorite enclosed in biotite (PPL). (D) Overall rock texture comprising plagioclase,

quartz, biotite and hornblende. Alignment of main rock forming minerals. Accessory epidote and ilmenite Epidote is enclosed in biotite (white arrow) (XPL). Mineral abbreviations are after Kretz (1983). 152
Figure 5.12: Photomicrographs of the red granites. (A) Larger quartz with anhedral microcline. Cuspate-lobate grain boundaries are prevalent in quartz (XPL). (B) Monocrystalline quartz overgrowing rounded quartz. Microcline and cordierite surround the quartz grains. Minor altered biotite is present. (C) Aligned chlorite as tabular laths of amorphous accumulations. Altered microcline, large anhedral quartz and accessory magnetite is present. (D) Quartz displays cuspate-lobate grain boundaries. Overgrown quartz or plagioclase by sillimanite, with tabular subhedral chlorite and altered microcline. Mineral abbreviations are after Kretz (1983). 153
Figure 5.13: Photomicrographs of the grey granites. (A) XPL image of biotite, hornblende, plagioclase, quartz and cordierite. Biotite and hornblende are aligned and form a foliation (white dashed line). A second foliation is present, indicated by the yellow dashed line, within the cordierite and is defined by the biotite inclusions. Rounded magnetite inclusions (yellow arrow) are also present within the cordierite porphyroblast. (B) PPL image of quartz, plagioclase, biotite, hornblende and magnetite. The PPL image shows the biotite, hornblende and plagioclase foliation best. Plagioclase shows seritisation in PPL. (C) Cuspate-lobate textures between quartz and microcline in a XPL image. Hornblende and plagioclase also show minor anatexis. (D) XPL image of poikiloblastic microcline with granophyric intergrowths between microcline and quartz (Qtz; yellow arrow). Microcrystalline rims, around granophyric textures, occur within the microcline grain. Mineral abbreviations are after Kretz (1983). 154
Figure 5.14: Photomicrographs of the type C′ SLGs. (A) Large monocrystalline quartz and microcline with interstitial biotite and magnetite. Fractures and joints cross-cut the quartz and microcline (XPL). (B) The sharp and intrusive contact between the basement orthogneisses (bottom) and the type C′ SLG (top), which is indicated by the yellow line. Quartz and plagioclase truncate the biotite foliation and microcline, quartz and plagioclase of the orthogneiss (XPL). Mineral abbreviations are after Kretz (1983). 155
Figure 5.15: Photomicrographs of the type A SLGs. (A) Quartz, microcline and plagioclase, all of which are compartmentalised by the spaced biotite foliation (XPL). (B) Microcline, quartz and biotite. Sericite alteration microcline along grain boundaries (yellow arrow) (XPL). Mineral abbreviations are after Kretz (1983)..... 156
Figure 5.16: Photomicrographs of the type B SLGs. (A) Quartz and plagioclase sheeted granite, with associated aligned biotite (XPL). Cuspate-lobate grain boundaries are sometimes present (white arrow). (B) Quartz and plagioclase with minor microcline. Interstitial biotite to plagioclase and quartz. Plagioclase and quartz surround microcline (white arrow) (XPL). Mineral abbreviations are after Kretz (1983). 157
Figure 5.17: Streckeisen diagram showing modal mineral abundances for of the Abbabis Complex, red granites, grey granites and SLGs. The various gneisses of the Abbabis Complex and quartzofeldspathic Etusis Formation sample are compared to establish modal mineralogy differences. Intrusions reported by Nex and Kinnaird (1995) and Longridge (2012) from the Palmenhorst Dome are also shown. 159
Figure 6.1: Localities of the samples collected in the field and surrounding areas. Sample localities are indicated by red circles. Geology (modified after Lehtonen *et al.*, 1995 with additions from this study) of the Palmenhorst Dome (Abbabis Complex) and enveloping Damara Supergroup (Etusis, Khan, Chuos and Rössing formations) superimposed over a Landsat 8 satellite image..... 167

Figure 6.2: Whole rock geochemical plots of the Abbabis Complex gneisses and migmatites, amphibolites, Etusis Formation, red granites, grey granites and sheeted leucogranites (SLGs) from the study area. (A) QAP diagram of the CIPW normalised Abbabis Complex gneisses and granites, amphibolites and Damaran Granites (Streckeisen, 1976). Metasedimentary rocks of the Etusis Formation are shown for comparison, but a classification is not applied. (B) TAS classification diagram (Le Maitre *et al.*, 1989). (C) Molecular normative values plotted on the An-Ab-Or diagram (Barker, 1979). (D) Shand index (Shand, 1927) classification showing the peraluminous nature of the lithologies. A/CNK= $Al_2O_3/(CaO+Na_2O+K_2O)$ molar and A/NK= $Al_2O_3/(Na_2O+K_2O)$ molar.....169
Figure 6.3: Major element discrimination diagram distinguishing between paragneisses or orthogneisses of the Abbabis Complex lithologies (Werner, 1987; Passchier *et al.,* 1990). 170
Figure 6.4: Stacked major element oxides versus SiO_2 for the Damaran Granitoids. 171
Figure 6.5: REE chondrite-normalised diagrams (Anders and Grevesse, 1989): (A) Abbabis Complex granite-gneisses, (B) amphibolites, (C) Damaran metasediments, (D) red granites, (E) grey granites and (F) the SLGs. Samples that contained both leucosomes (L) and melanosomes (M; dashed lines) are indicated by the sample number and suffix. 173
Figure 6.6: Stacked large ion lithophile element versus SiO_2 plots for the Damaran granitoids.....175
Figure 6.7: Rb/Sr versus (A) Sr and (A) Ba with plagioclase fractionation (A) and biotite fractionation trends (B) (after McDermott *et al.,* 1996 and references within) of the SLGs.....176
Figure 6.8: N-MORB normalised multi-element plots of the (A) amphibolite dykes, Abbabis Complex gneisses (and granites) and (B) the Damaran Granitoids. Elemental array after Kamber *et al.* (2002) and normalisation values after Hofmann (1988). 177
Figure 6.9: Th/Yb versus Nb/Yb plot of the amphibolite dykes to show crustal contamination. OIB-MORB array after Pearce (2008). 177
Figure 6.10: SiO_2/10, CaO + MgO and Na2O + K2O plot (Taylor and McLennan, 1985) showing the Abbabis Complex lithologies and amphibolite dykes, which represent possible felsic to mafic end members. An array, of the Damaran metasediments, is observed from the basement gneisses to the amphibolite dykes. Abbabis Complex gneisses and amphibolite dykes are plotted from Longridge (2012) to use a more homogenous representation. Most the whole rock data for the Khan and Chuos formations (not bolded) are from Nex (pers. comm.) and data collected from this study (bolded) can be seen in Appendix 3.A.....179
Figure 6.11: Stacked Th/Sc and La/Sc versus Zr/Sc binary plots after Taylor and McLennan (1985). Most the trace element data for the Khan and Chuos formations are from Nex (pers. comm.) and data collected from this study (bolded) can be seen in Appendix 3.A. 180
Figure 6.12: Diagrams comparing geochemical data for whole rock samples from this study and published studies. Classification schemes include (A) QAP, (B) An-Ab-Or, (C) TAS plots.....181
Figure 6.13: (A) Stacked Rb/Sr and Ba/Sr versus combined Fe_2O_3 and MgO after McDermott *at al.* (1996) for the Damaran granitoids determining plagioclase- and biotite-limited melting regimes. Lu/Th versus combined Fe_2O_3 and MgO (McDermott *et al.,* 1996) used to established biotite- or muscovite-dehydration melting. .. 185

Figure 7.1: Landsat 8 image with overlain simplified geology of the Palmenhorst Dome showing locations of samples selected for geochronology (geology modified after Lehtonen *et al.*, 1995 and Longridge *et al.*, 2011). 193
Figure 7.2: (A) CL images of selected zircons with spot placement and $^{207}Pb/^{206}Pb$ ages (only near-concordant data with < 10% discordance shown). Concordia age plots of (B) magmatic and (C) metamorphic domains for a basement granite sample (K05) from the Abbabis Complex. Colourless error ellipses were excluded from the regression calculations. MSWD= Mean Square of Weighted Deviates. 200
Figure 7.3: (A) CL images of selected zircons with spot placement and $^{207}Pb/^{206}Pb$ ages (only near-concordant data with < 10% discordance shown). Concordia age plots of (B) magmatic and (C) metamorphic domains for an orthogneiss sample (R06) from the Abbabis Complex. Colourless error ellipses were excluded from the regression calculations. MSWD= Mean Square of Weighted Deviates. 201
Figure 7.4: (A) CL images of selected zircons with spot placement and $^{207}Pb/^{206}Pb$ ages (only near-concordant data with < 10% discordance shown). Concordia age plots of (B) magmatic and (C) metamorphic domains for a grey orthogneiss sample (PA02) from the Abbabis Complex. Colourless error ellipses were excluded from the regression calculations. MSWD= Mean Square of Weighted Deviates. 202
Figure 7.5: Th/U ratios for zircons from various lithologies of the Abbabis Complex. Line indicate constant Th/U ratios where Th/U ratios below 0.1 may be considered to indicate metamorphic zircon growth (Rubatto and Gebauer, 2000). 203
Figure 7.6: (A) CL images of selected zircons with spot placement and $^{206}Pb/^{238}U$ ages (only near-concordant data with < 10% discordance shown). Concordia age plots of (B) all domains (C) magmatic and (D) metamorphic domains for amphibolite sample 7.3 from the amphibolites. Colourless error ellipses were excluded from the concordia calculations as they represent outliers. MSWD= Mean Square of Weighted Deviates. Inset in lower right of figure (B) shows a detailed plot of the *ca.* 600 Ma to 500 Ma population of both magmatic and metamorphic ages. 205
Figure 7.7: (A) CL images of selected zircons with spot placement and $^{206}Pb/^{238}U$ ages (only near-concordant data with < 10% discordance shown). Concordia age plots of (B) magmatic and (C) metamorphic domains for amphibolite sample R02. Colourless error ellipses were excluded from the concordia calculations. MSWD= Mean Square of Weighted Deviates. Inset in upper left of figure (B) shows closely related magmatic (blue) and metamorphic (green) events around 550 Ma. 206
Figure 7.8: Th/U ratios for zircons from the amphibolites. Line indicate constant Th/U ratios where Th/U ratios below 0.1 may be considered to indicate metamorphic zircon growth (Rubatto and Gebauer, 2000). 207
Figure 7.9: Detrital U-Pb geochronology results for arkosic quartzite sample 1.1 from the Etusis Formation. (A) CL images of selected zircons showing spot placement and $^{207}Pb/^{206}Pb$ age dates. (B) Wetherill diagrams showing two populations (1, 2 Ga) for magmatic and metamorphic domains. Ages with > 10% discordance are omitted in both diagrams. 210
Figure 7.10: Detrital U-Pb geochronology results for sillimanite-biotite pelitic schist sample PA01 from the Etusis Formation. (A) CL images of selected zircons showing spot placement and $^{207}Pb/^{206}Pb$ age dates. (B) Wetherill diagrams showing a more concordant magmatic population (2 Ga) and younger discordant metamorphic domains. Ages with > 10% discordance are omitted in both diagrams. 211

Figure 7.11: Detrital age spectra for the Etusis Formation displayed as histograms and relative density probability plots. $^{207}Pb/^{206}Pb$ ages with < 10% discordance were utilised with a bin size of 20 myr. (A) Histogram for sample 1.1 showing two populations of ages, at *ca.* 1 and *ca.* 2 Ga, and associated density curve (solid green line) highlighting these peaks. Bin 1000 - 1020 Ma displays the highest frequency of ages, with a second peak at 2000 - 2020 Ma. (B) Histogram for sample PA01 showing three populations at *ca.* 1860 to *ca.* 1960 Ma and *ca.* 2 Ga (density curve as solid blue line). The relative density curve shows a fourth peak at 1900 Ma. Bin 2020 - 2040 Ma displays the highest frequency of ages, with less significant peaks at 1860 - 1880 Ma and 1960 - 1980 Ma. (C) Comparison of relative density distributions for both samples (green solid line: sample 1.1, blue solid line: sample PA01). 212
Figure 7.12: Th/U ratios for zircons from sillimanite-biotite pelitic schist and arkosic quartzite. Line indicate constant Th/U ratios where Th/U ratios below 0.1 may be considered to indicate metamorphic zircon growth (Rubatto and Gebauer, 2000). 213
Figure 7.13: (A) CL images of selected zircons with spot placement and $^{206}Pb/^{238}U$ ages (only near-concordant data with < 10% discordance shown). Concordia age plots of (B) all data (including inheritance), (C) magmatic and (D) metamorphic domains for sample K06 from the red granites. Colourless error ellipses were excluded from the concordia calculations. MSWD= Mean Square of Weighted Deviates. Figure (D) highlights three possible metamorphic populations (1 to 3) and a final pooled metamorphic age. 215
Figure 7.14: Th/U ratios for zircons from the red granite. Line indicate constant Th/U ratios where Th/U ratios below 0.1 may be considered to indicate metamorphic zircon growth (Rubatto and Gebauer, 2000). 216
Figure 7.15: (A) CL images of selected zircons with spot placement and $^{206}Pb/^{238}U$ ages (only near-concordant data with < 10% discordance shown). Concordia age plots of (B) magmatic and metamorphic domains for sample K07 from the type C' SLGs. (C) Regression of two metamorphic populations with detailed concordia age plots of (D) regression 1 and (E) regression 2. Colourless error ellipses were excluded from the concordia calculations. MSWD= Mean Square of Weighted Deviates. 218
Figure 7.16: (A) CL images of selected zircons with spot placement and $^{207}Pb/^{206}Pb$ ages (only near-concordant data with < 10% discordance shown). Concordia age plots of (B) metamorphic domains for sample PA03 from the type E SLGs. MSWD= Mean Square of Weighted Deviates. 220
Figure 7.17: Th/U ratios for zircons from various SLGs. Line indicate constant Th/U ratios where Th/U ratios below 0.1 may be considered to indicate metamorphic zircon growth (Rubatto and Gebauer, 2000). 220
Figure 7.18: εHf vs U-Pb ages (Ma) plot showing all samples. $^{207}Pb/^{206}Pb$ ages were used for spots that yielded ages older than 1 Ga and $^{207}Pb/^{238}U$ ages were used for spots that yielded ages younger than 1 Ga. Evolution curves for Chondrite Uniform Reservoir (CHUR) (after Bouvier *et al.,* 2008) and Depleted Mantle (DM) (after Gerdes and Zeh, 2006) are shown in grey and red, respectively. Ranges for DM model ages are indicated by different coloured and labelled bars. Dots below bars indicate individual model ages calculated. These are plotted to show clusters and breaks within the ranges. AC= Abbabis Complex, A= amphibolites, Et= Etusis Formation, RG= red granites, SLG= sheeted leucogranites. The Etusis Formation defines three populations translating into three distinct ranges of model ages. 222
Figure 7.19: Summary of the U-Pb age data for the lithologies in chronological order. Ages are concordia or regression ages (latter indicated by the symbol *). Ages in brackets are less reliable. Type E SLG U-Pb ages

show inheritance (see discussion text) and not a true crystallisation age. Red dashed lines indicate unreliable ages, which have been considered in the text. 223
Figure 7.20: Comparison of U-Pb and Lu-Hf isotopic data from this and previous studies (both εHf and εNd). Superimposed fields for various εHf values from (1) Foster *et al.* (2015), (2) Milani *et al.* (2015) and (3) Longridge *et al.* (2018). Numbers (1 to 3) correspond to those in the diagram. DM model age histograms for the Damaran granitoids (red), Congo (blue) and Kalahari (green) Cratons are taken from compilation by Longridge *et al.* (2018; references therein). Histograms do not correspond to the y-axis scale. For original scaling see Longridge *et al.* (2018). Abbreviations: AC= Abbabis Complex; A= amphibolites; Et= Etusis Formation; Kh= Khan Formation; RG= red granites; GG= grey granites; SLG= sheeted leucogranites. Et1 to 3 populations of the Etusis Formation. Solid horizontal bars indicate DM model age ranges (colours correspond to model age range bars that correspond to the different lithology types). CHUR and DM evolution curves after Bouvier *et al.* (2008) and Gerdes and Zeh (2006), respectively. 226
Figure 7.21: Comparison of detrital zircon age spectra of Damaran sediments from the Congo and Kalahari Craton edges (after Foster *et al.*, 2015) and of the Etusis Formation (this study). The signatures show that the Etusis Formation show similarities to the Congo Craton Damara Sequence as the peaks at *ca.* 2015 Ma and 1020 Ma overlap with the Congo Craton peaks at 2060 Ma to 1970 Ma and 1150 Ma and 1000 Ma, respectively. Blue and green curves correspond to samples 1.1 and PA01; orange curves and arrows correspond to the Congo Craton Damara Sequence; pink curves and arrows correspond to the Kalahari Craton Damara Sequence. 231
Figure 8.1: A summary of the deformational, metamorphic and emplacement events that took affected the sCZ as well as age constraints from other studies (modified after Goscombe *et al.,* 2017b and references within) and this one. Where there was no evidence found from this study correlations to the synthesis established from Goscombe *et al.* (2017b) were performed and other references were utilised (Hoffman *et al.,* 1996; Longridge, 2012; Lehmann *et al.,* 2016). 239

List of Tables

Table 2.1: Comparison between stratigraphy schemes for the Abbabis Complex (modified after Brandt, 1987). 17
Table 2.2: Summary of deformation from early workers in the Central Zone (modified after Longridge, 2012; authors indicated by *) and a recent detailed study on the Palmenhorst Dome after Longridge, 2012. 23
Table 2.3: A comparison of various granite classification schemes by various authors (modified after Longridge, 2012). 25
Table 3.1: Table summarising the spectral colour responses from each spectral domain for all Landsat 8 processed images, namely the PCA, MNF, statistical composite, band ratio 5/7:5/1:5:4x3:4, and band ratio 4/3:5:2/3:1, as well as alluvium and cross-cutting dykes. Standardised RGB colours were used. A reference table can be accessed for comparison of the colours from https://www.rapidtables.com/web/color/RGB_Color.html. 39

Table 3.2: Detailed summary of the spectral colour responses from the eight spectral domains for the three hyperspectral composites MNF VNIR 236, MNF SWIR 245 and the Decorrelation Stretch 114/108/33, as well as alluvium and cross-cutting dykes. A reference table can be accessed from https://www.rapidtables.com/web/color/RGB_Color.html for comparison of standardised RGB colours used as descriptors. 44
Table 3.3: Table showing the RGB normalised values (quoted in percentages), established from the mean colour within each domain and then plotted on the RGB ternary plot in figure 3.6.A. Using the RGB normalised values, the average composition was determined with the greatest percentage compositions constituting the most likely composition of the domain. Most abundant spectral responses are listed in the mean composition row with brackets around the next most abundant spectral signature. 46
Table 3.4: Table summarising the minerals found in each domain in the Multi-Mineral Rule Classified Map of figure 3.7....47
Table 4.1: Table showing the characteristic features of the lower Damara Supergroup formations with the pitfalls associated with these characteristics (modified after Martin, 1965; Smith, 1965; Nash, 1971; Jacob, 1974; Sawyer, 1981; Henry, 1992; De Kock, 2001; Miller, 2008; Longridge, 2012). 65
Table 4.2: Table detailing the different dome formation arguments presented by various authors with their respective characteristics....83
Table 4.3: Classification of granites based on field characteristics in the study area using the nomenclature of Smith (1965), Marlow (1983), Brandt (1985), McDermott (1986) and Nex (1997) with the table modified after Freemantle (2017). 96
Table 4.4: Table showing the relative timing of the multiple intrusions, deformational and metamorphic events based on cross-cutting relationships from field observations. 120
Table 4.5: Summary table of previous workers' stratigraphies correlated by Longridge (2012), and this study's stratigraphy correlated with previous work. 123
Table 5.1: Summary of possible indicators for the presence of crystallised partial melt or intrusive features for each lithology examined under thin section. Textures indicating the presence of partial melt are adopted from Sawyer (2008). The table describes the oldest to youngest lithologies as outlined in previous sections (5.2 – 5.3). 158
Table 7.1 (on following page): Summary of published crystallisation and metamorphic ages for various lithologies of the Damara Belt. Table modified after Longridge (2012), with recent age dates included. Reported ages are magmatic ages except for the metamorphic ages at the bottom of the table. U-Pb "discordia zircon" ages are from upper intercepts between regression and concordia curve. A more extensive summary on geochronological work in the Damara is provided by Milani *et al.* (2015)....189
Table 7.2: A list of samples chosen for for U-Pb geochronology. Sample numbers correspond to the localities in figure 7.1. Samples from outside the field area (Nose Structure, Northern Palmenhorst Dome) are indicated in the table. SLG= sheeted leucogranite. 194

List of Abbreviations

CL	cathodoluminescence
DCS	Decorrelation Stretch
FLAASH	Fast Line-of-sight Atmospheric Analysis of Hypercubes
HSZ	high strain zone
ICP-MS	Inductively Coupled Plasma Mass Spectrometry
Inv. MNF	Inverse Maximum Noise Fraction
MNF	Maximum Noise Fraction
MSWD	Mean Square of Weighted Deviates
NOFEOX	No Iron Oxides
PCA	Principal Component Analysis
ROI	Region of Interest
sCZ	southern Central Zone
SLG	sheeted leucogranite
SWIR	Short-wave Infrared
VNIR	Visible and Near-infrared
XRF	X-ray fluorescence

1. Introduction

The basement-cored domes are a characteristic feature of the southern Central Zone of the Damara Belt, Namibia (Smith, 1965) and are typically described to be undifferentiated granite-gneisses of the Abbabis Complex; the basement lithologies of the southern Central Zone (Smith, 1965). However, these domes have been variously revised to comprise a simplified pre-Damaran stratigraphy (Smith, 1965; Brandt, 1987) and lower Damaran metasediments (Oliver and Kinnaird, 1996). or are observed to include infolded Damaran metasediments in Abbabis Complex gneisses (Longridge, 2012). These basement-cored domes occur within the core of the Damara Belt and have been subjected to the most intense deformation and peak metamorphism (Goscombe *et al.,* 2017b), making the interpretation of the evolution of these domes challenging. This study evaluates aspects of these domes to understand aspects of the evolution of one of these domes within the context of the Damara Orogen adopting a multi-disciplinary approach.

1.1 The Pan-African Orogeny

The Pan-African orogenic event is a major orogenic event that involved the amalgamation of Gondwana (Fig. 1.1) and occurred between *ca.* 820 and 500 Ma (Kennedy, 1964; Miller, 2008; Merdith *et al.,* 2017). This orogenic event involved the accretion of a number of continental fragments to form collisional orogenic belts, which cross-cut and surround the African continent today (Kennedy, 1964; Miller, 2008; Merdith *et al.,* 2017). The Damara Belt is the northeast-southwest trending arm of a network of Pan-African orogenic belts located in Namibia with extensions into Botswana, Angola and the Democratic Republic of Congo (Martin and Porada, 1977; Miller, 2008); and is of interest to this study. These Pan-African orogenic belts formed from multiple events of rifting, drifting and continent-continent collision to represents a Wilsons Cycle affecting the crust (Miller, 2008; Wilson *et al.,* 1997).

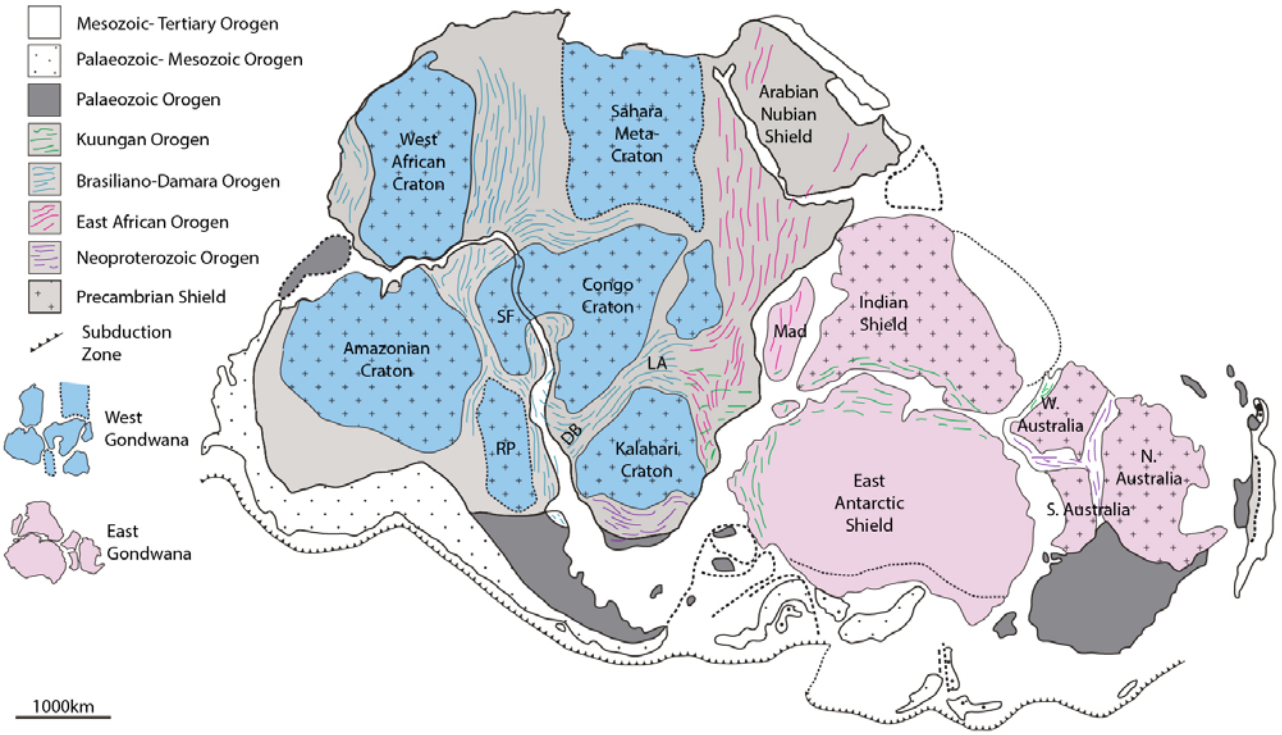


Figure 1.1: Reconstruction of Gondwana showing East and West Gondwana with associated shields and Neoproterozoic to Mesozoic-Tertiary Orogens (after Gray *et al.*, 2008; Malone *et al.*, 2008; Rankin, 2015). Note DB – Damara Belt, LA- Lufilian Arc, RP- Rio de la Plata, SF- São Francisco.

The tectonic evolution and geodynamic model of the Damara Belt is represented by the opening and closing of the Adamastor and Khomas oceans (Fig. 1.2). The Adamastor and Khomas oceans were formed by the rifting of Rodinia (*ca.* 1100–800 Ma: Jacobs *et al.,* 2008; 750 Ma: Hoffman *et al.,* 1994) which involved the Kalahari, Congo and Rio de la Plata cratons (Hartnady *et al.*, 1985; Wilson *et al.*, 1997). The spreading of the Khomas Ocean continued until *ca.* 609 Ma (Nagel, 1999), until collisional tectonics superseded extension. The Pan African collisional event involved the closure of these oceans resulting in three collisional belts at a triple junction; the Kaoko Belt, Gariep Belt and the most widely studied Damara Belt (Miller, 2008). Northward subduction (*ca.* 580 Ma; Gray *et al.*, 2007) of the Kalahari plate beneath the Congo plate resulted in the closure of the Khomas Ocean leading to crustal thickening. These mobile belts were formed as a result of the collision between the Kalahari, Congo and Rio de la Plata cratons (Hoffman, *et al.*, 1994), resulting in the suturing of West Gondwana (Merdith *et al.,* 2017).

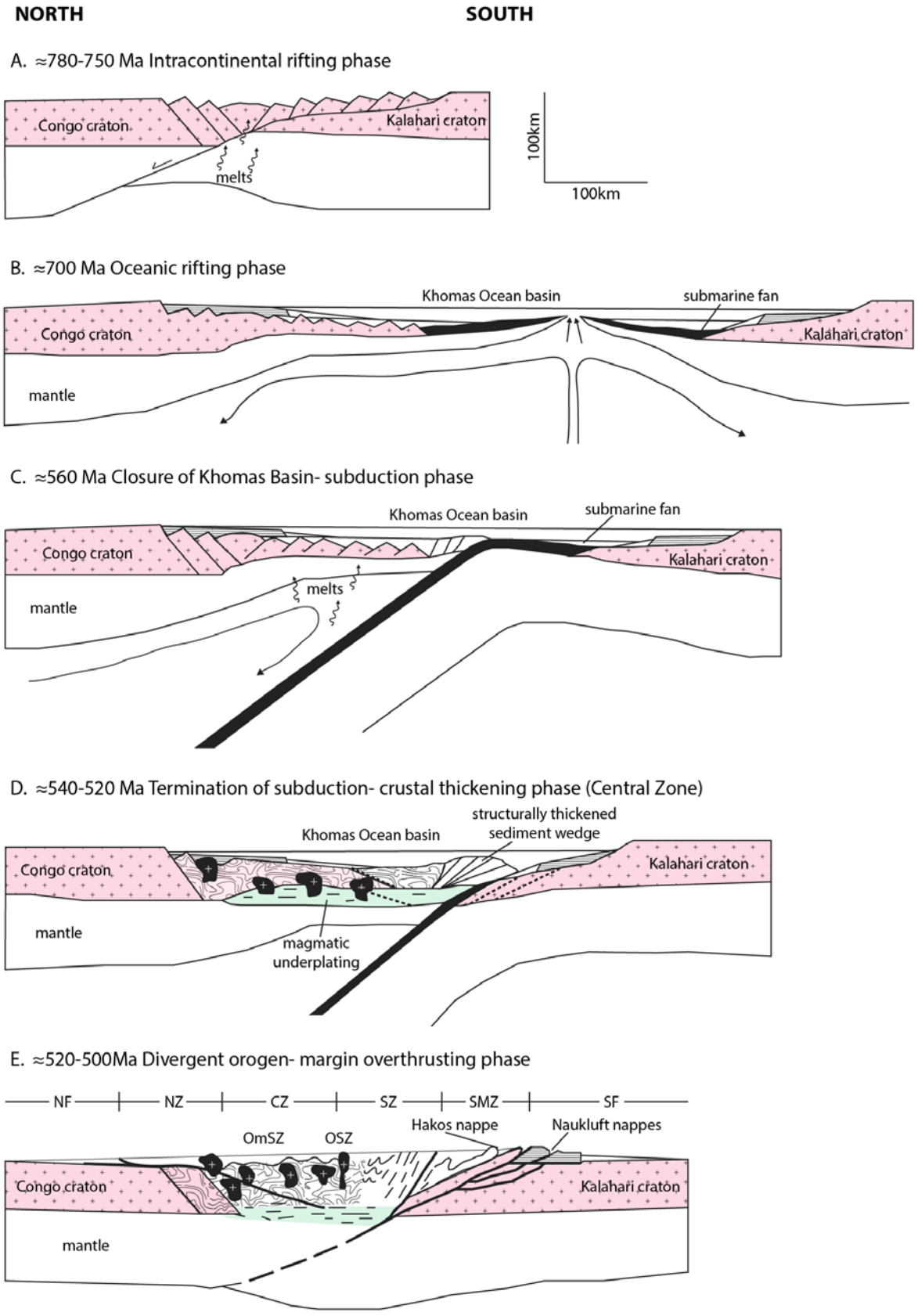


Figure 1.2: Tectonic evolution and geodynamic model of the Damara Belt involving the Kalahari and Congo Cratons. The model illustrates the rifting, northward subduction through to collisional phases of the cratons, with the tectonostratigraphic zones of the Damara Belt labelled as NF- Northern Foreland, NZ- Northern Zone, CZ- Central Zone, SZ- Southern Zone, SMZ- Southern Marginal Zone, and SF- Southern Foreland (modified after Gray *et al.*, 2007).

1.2 The Damara Orogen

The Damara orogen is a network of orogenic belts of Namibia, which preserves multiple deformational and metamorphic histories (Poli and Oliver, 2001). In Namibia, the Pan-African age orogen consists of three belts (Fig. 1.3): (i) a north-south trending coastal belt, named the Kaoko Belt, which runs along the Atlantic coast from Angola through Namibia (Kennedy, 1964). This belt connects the Gariep and Malmesbury belts in South Africa. (ii) the Gariep Belt extends in a south-north direction and forms the southern extension of the orogen along the Atlantic coastline from Walvis Bay (Miller, 2008). (iii) The Damara Belt, the northeast trending intracontinental branch, which stretches over 400 km between the Congo and Kalahari cratons (Martin and Porada, 1977). These belts represent suture zones, along which continental fragments amalgamated during the Pan-African orogeny to form Gondwana (Martin and Porada, 1977). The Kaoko Belt and Damara Belt are contiguous with each other and share certain lithostratigraphic units (Miller, 2008). In contrast, the Gariep Belt, originally continuous with the Damara, has distinct lithological differences when compared to the Damara Belt (Miller, 2008).

Extending from Namibia into Angola and the Democratic Republic of the Congo, the Kaoko Belt (Fig. 1.3) comprises the Eastern, Central, Western and Southern Kaoko Zones (Miller, 1983). The Eastern Kaoko Zone is linked to the Damara Belt by the shallow water Otavi deposits of the Northern Platform (Miller, 2008), however the collision and metamorphism (580-550 Ma) predates orogenic activity in the Damara Belt (Goscombe *et al.*, 2003). The coastal belt forms the suture (Fig. 1.3) between the Congo and Rio de la Plata cratons (Porada, 1979) and is interpreted as a sinistral transpressional orogeny (Goscombe *et al.*, 2003). It comprises an orogenic core and bounding transpressional shear zones that exposed high-grade rocks and granitoids in half flower structures (Goscombe *et al.*, 2005).

The Damara Belt (Fig. 1.3) of Namibia extends into northern Botswana to the Zambezi belt and links with the north-south Mozambique Belt via the Lufilian Arc and Zambezi Belt (Miller, 2008). Miller (1983) subdivided the belt into stratotectonic zones separated by geophysical lineaments. The Damara Supergroup includes sediments that were either deposited on the Congo or Kalahari cratons (Miller, 2008). These sediments of the supergroup are observed throughout the Damara Belt.

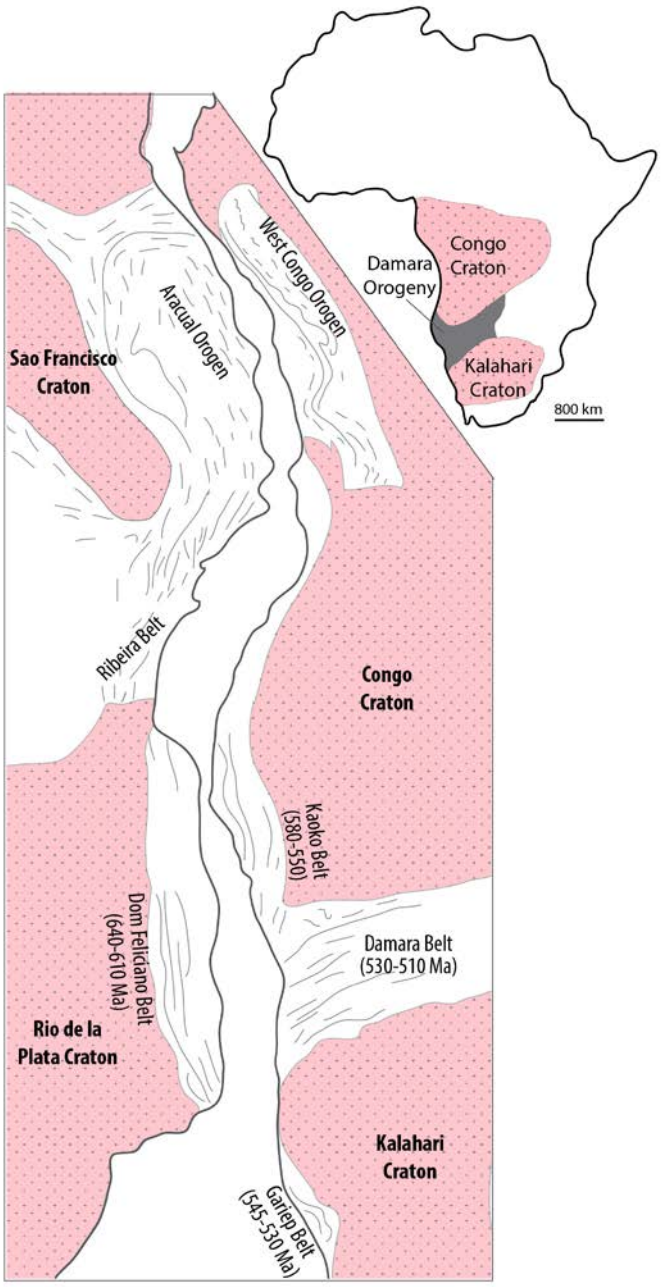


Figure 1.3: Illustration showing the colliding cratons that formed the Damara Orogen: Damara Belt, Gariep Belt and the Kaoko Belt. Pan-African orogenic belts are indicated by their respective suturing ages (modified after Gray *et al.*, 2008). Inset demonstrates where the Damara Belt is situated between the Congo and Kalahari cratons (modified after Oliver, 1994).

1.2.1 Stratotectonic zones of the Damara Belt

The inland orogenic belt is divided into a number of stratotectonic zones (Fig. 1.4) based on variations in stratigraphy, structure, metamorphic grade, igneous activity, geochronology and aeromagnetic expressions (Barnes and Sawyer, 1980; Miller, 1983), with the boundaries between zones defined by geophysical lineaments (Corner, 2008). The regional lineaments, predominantly thrusts, faults, mylonite belts, stratigraphic boundaries or zones where rapid facies variations are observed (Miller, 2008) coincide with prominent aeromagnetic anomalies (Frimmel *et al.*, 2011). De

Kock (2001) proposed that particular regional lineaments and structures may have controlled sedimentary deposition within the different zones during the collision of the Kalahari and Congo cratons. The stratotectonic zones include (from north to south) the Northern Platform, Northern Margin Zone, Northern Zone, northern Central Zone, southern Central Zone, Okahandja Lineament Zone, Southern Zone, Southern Margin Zone and the Southern Foreland (Miller, 2008), with their lithostratigraphic correlations displayed in figure 1.5. For the purposes of this study the Central Zone and basement inliers (Fig. 1.4) are only considered but a detailed description of the stratotectonic zones can be found in Miller (2008).

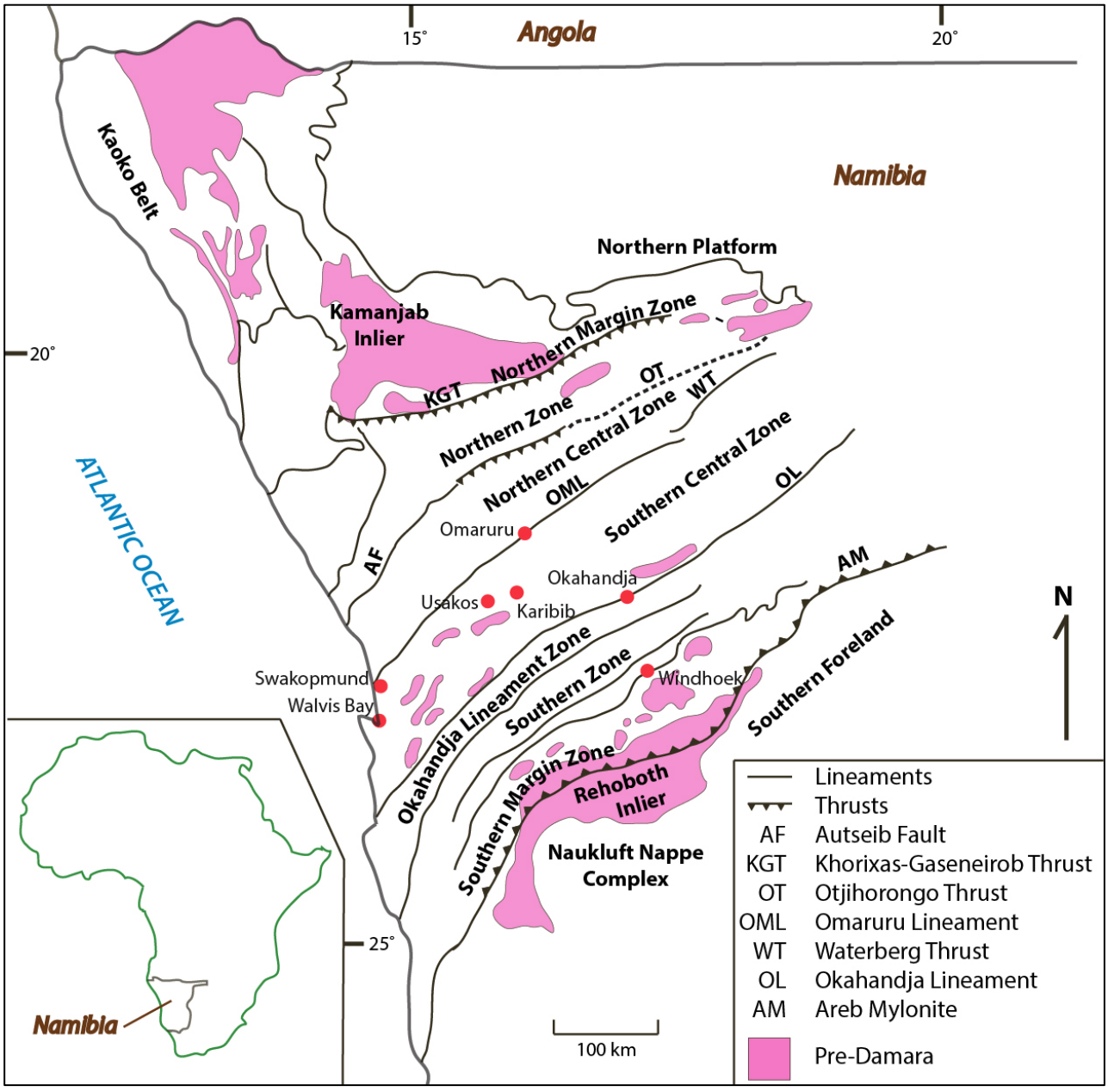


Figure 1.4: Map of the Damara Belt showing the subdivisions of the stratotectonic zones, major lineaments and basement inliers or pre-Damaran rocks (modified after Miller, 2008).

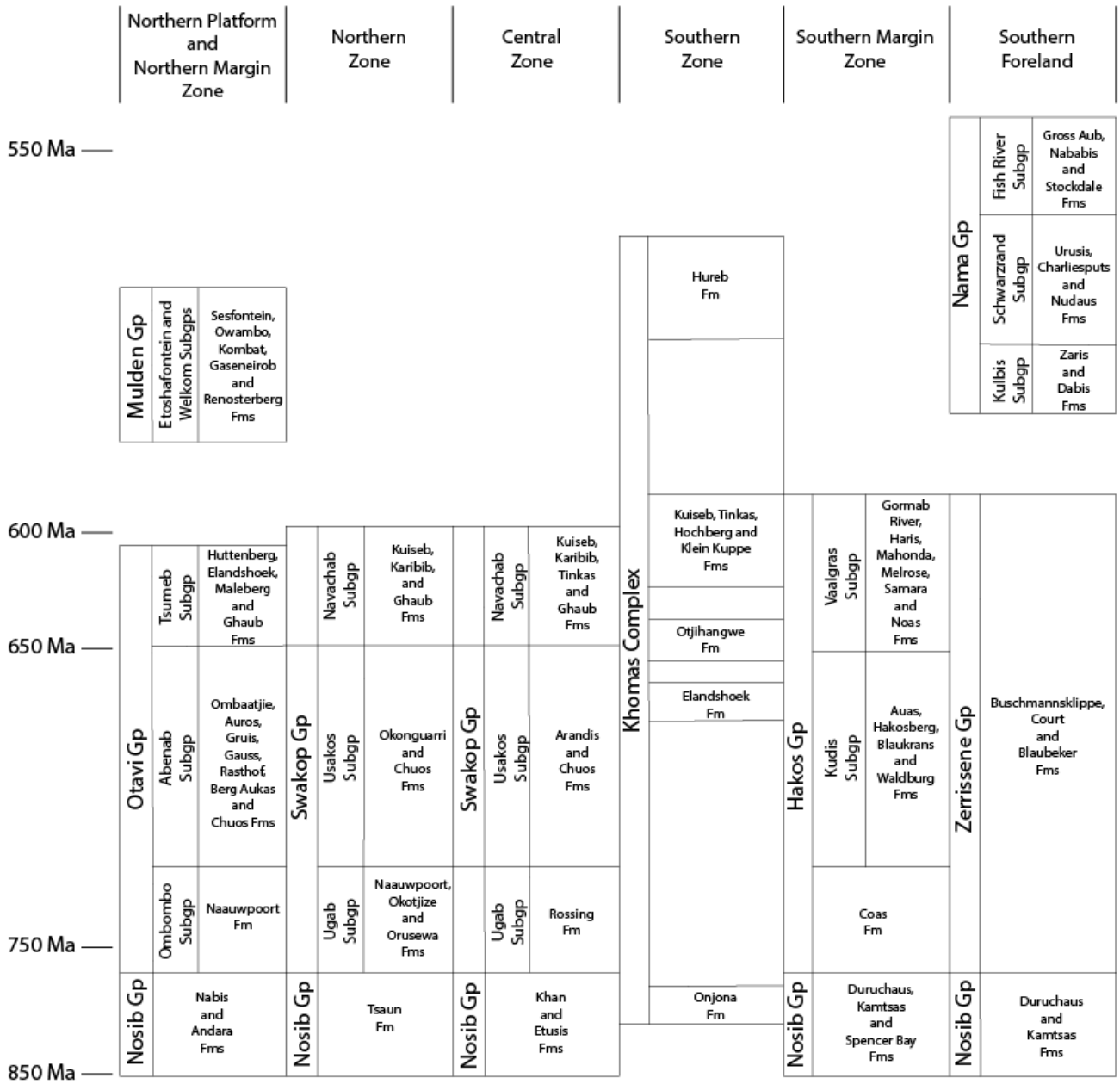


Figure 1.5: Schematic of various lithostratigraphic variations and correlations across the different stratotectonic zones of the Damara Belt with general ages of the stratigraphy (modified after Miller, 2008).

The Central Zone is metamorphically and structurally distinct from the other zones and forms the core of the orogen (Goscombe *et al.,* 2017b). It is characterised by high temperature, low pressure metamorphism (Basson and Greenway, 2004; Goscombe *et al.,* 2017a; Longridge *et al.,* 2017) and domal structures (Smith, 1965; Miller, 2008). The metamorphism within the orogen core is associated with Pan-African collisional events and reaches granulite facies towards the west (Basson and Greenway, 2004; Miller, 2008). The Central Zone can be subdivided into the southern and northern Central Zone separated by the Omaruru Lineament (Miller, 2008) (Fig. 1.4). Both of these exhibit a distinct northeast elongation and syn- to post-tectonic granitic intrusions (Oliver, 1994). However, within the southern Central Zone (sCZ) the domal structures are characteristically cored

by pre-Damaran granitic basement, whereas the northern Central Zone and the Omururu Lineament are marked by domes cored by Karibib Formation marbles and Usakos Subgroup calc silicates, marbles and schists (Fig. 1.5) (Miller, 2008). The northern Central Zone contains a thick succession of Karibib Formation carbonates and Kuiseb Formation schists deformed into abundant basin and dome structures (Miller, 2008). These metasediments are stratigraphically higher than those of the Nosib Group of the sCZ (Miller, 2008). The sCZ comprises clastic and chemical schists of the Nosib Group, which unconformably overlie the pre-Damaran Abbabis Complex (Smith, 1965). The Nosib Group has been purported to have been sourced from the underlying Abbabis Complex (Smith, 1965; McDermott and Hawkesworth, 1990; Foster *et al.,* 2015; Nascimento *et al.,* 2017). Metamorphosed sandstones, tillites and pelites of the Swakop Group unconformably overlie the Nosib Group (Smith, 1965; Miller, 2008). This succession contains the glaciomarine basal conglomerates of the Chuos Formation (Kukla and Stanistreet, 1991). Further review of the sCZ is discussed in following sections.

1.2.2 Basement Inliers

Basement inliers are observed throughout the Damara Belt and range in age from Mesoproterozoic to Palaeoproterozoic (Miller, 2008). These basement inliers (Fig. 1.4) include the Kamanjab Inlier along the southwestern extent of the Congo Craton and the Rehoboth Inlier along the northwestern margin of the Naukluft Nappe Complex of the Kalahari Craton (Jacobs *et al.*, 2008).

The Mesoproterozoic Rehoboth Inlier (Fig. 1.4) comprises the volcano-sedimentary Rehoboth Group, Sinclair Supergroup and associated intrusives (Becker and Schalk, 2008; Miller, 2008). Within the Rehoboth Subprovince, the Damaran lithologies are thrust over the rocks of the Sinclair Supergroup (Hoffman, 1989). This basement inlier is interpreted as being a younger northwest extension of the Abbabis Complex (Miller, 2008). However, this Kalahari Craton link is mainly based on a single 1 Ga age determination (Kröner *et al.,* 1991) for the Abbabis Complex in the sCZ, which is otherwise regarded as Palaeoproterozoic in age (Jacob *et al.*, 1978; De Kock *et al.,* 2000; Tack *et al.,* 2002; Longridge, 2012; Longridge *et al.,* 2018).

The Palaeoproterozoic Kamanjab Inlier comprises the northern low-grade Khoabendus Group (meta-volcanoclastic) and southern high-grade Huab Metamorphic Complex (metasediments, orthogneisses and amphibolites) (Kleinhanns *et al.,* 2013). Jacob *et al.* (1978) proposed that the Abbabis Complex could be correlated to the Franzfontein Granite (Huab Complex) due to similar Palaeoproterozoic ages.

The Abbabis Metamorphic Complex (Fig. 1.4) is the largest of the pre-Damaran basement inliers and is restricted to the sCZ (Miller, 2008). These basement inliers form numerous anticlines manifesting as basement-cored domes that are surrounded by Damaran sediments (Miller, 2008). The range in U-Pb ages for the Abbabis Complex have resulted in various interpretations for the affinity of these basement lithologies. Additionally, contention surrounds stratigraphic interpretations (Smith, 1965; Brandt, 1987; Oliver and Kinnaird, 1996; Longridge, 2012; Toe *et al.,* 2013) and the nature of the formation of these domes (Smith, 1965; Oliver, 1995; Poli, 1997; Barnes, 1981; Coward, 1981; Jacob *et al.,* 1983; Kisters *et al.,* 2004; Longridge, 2012). These basement-cored domes are characteristic of the sCZ and form an important component of the Damaran evolution in terms of the structural implications, and whether the Abbabis Complex has a Congo or Kalahari craton affinity.

1.3 Project locality

The study area is located along the Khan River and B2 Access Road for the Husab Mine at the edge of the Namib-Naukluft National Park, Namibia, approximately 50 km northeast from Swakopmund (Fig. 1.6). The area of study traverses the basement-cored domes mapped as the Abbabis Complex and the surrounding Damara Supergroup which also provides abundant outcrop ideal for remote sensing. This area is located along the northern extent of the Palmenhorst Dome (Fig. 1.6) of the sCZ of the Damara Belt, which includes the "Nose structure" and anticlinal core of the Palmenhorst Dome. The Khan River Gorge and B2 Access Road in the Ostrich Gorge provide excellent exposures of the basement and Damara lithologies ideal for detailed field mapping.

1.4 Research problem and aims

The basement-cored domes of the sCZ have typically been described as undifferentiated granite-gneisses (Smith, 1965; Miller, 2008) as these basement-cored domes tend to be intruded by multiple generations of partial melt (Toe *et al.,* 2013), making it challenging to unravel the exact nature of these domes. However, after the identification of a simplified stratigraphy in the type locality of the Abbabis Complex (Smith, 1965) other authors described similar stratigraphies in various domes across the zone (Sawyer, 1981; Marlow, 1981; Brandt, 1987; Poli, 1997). In contrast, the Rössing Dome was remapped to contain various lithologies of the Etusis Formation (Oliver and Kinnaird, 1996), the Palmenhorst Dome was proposed to contain Nosib Group lithologies with limited basement lithologies (Barnes, 1981) and infolded Damaran metasediments were identified in the Palmenhorst Dome (Longridge, 2012).

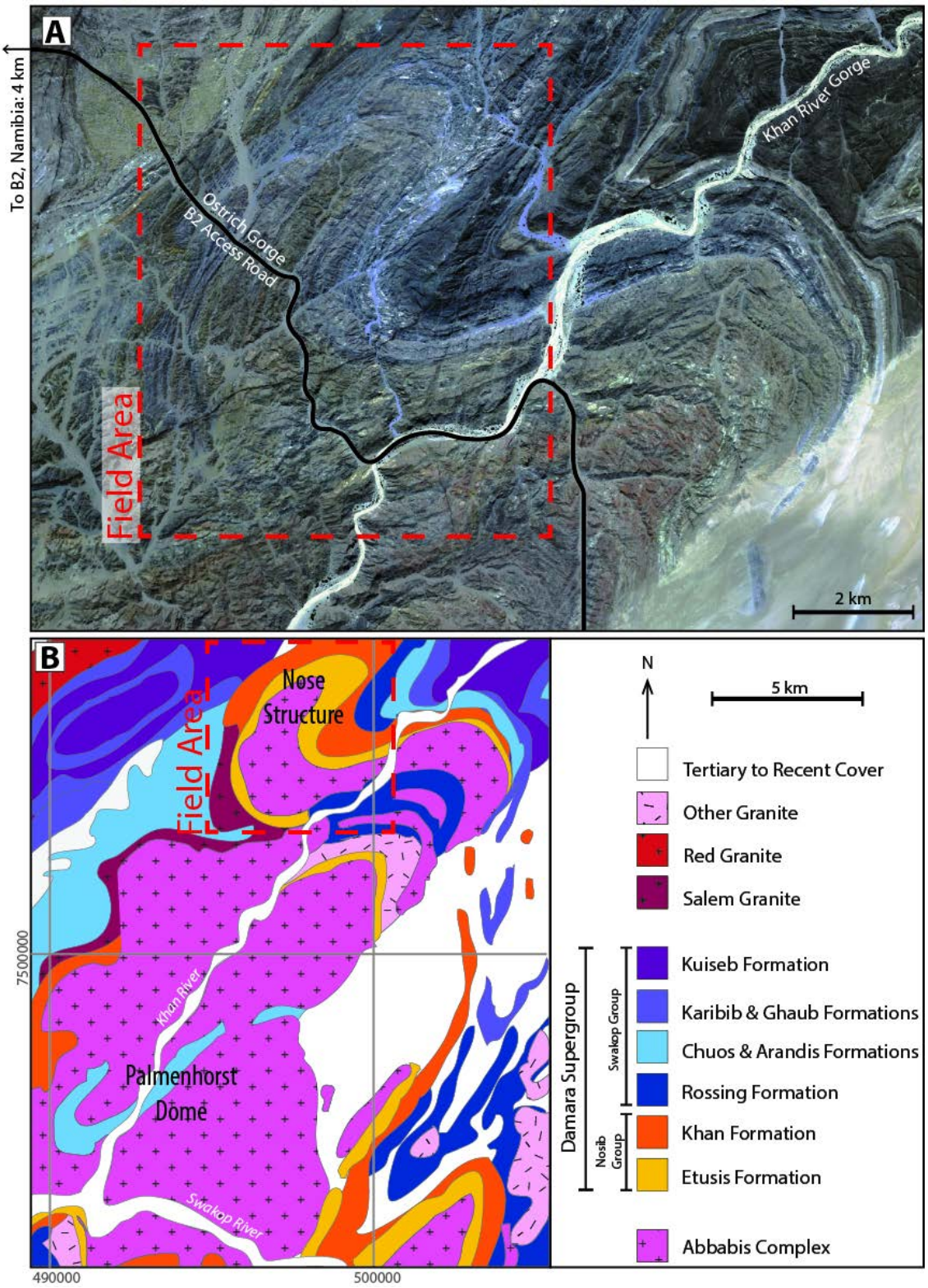


Figure 1.6: Locality of field area. (A) A hyperspectral image of the area with the Khan River and B2 Access Road. (B) A detailed geological map of the Palmenhorst Dome of the sCZ indicating the location of the field area in context of the larger Palmenhorst Dome (WGS84, Zone 33K) (modified after Lehtonen *et al.*, 1995; Longridge *et al.*, 2011).

These different ideas highlight the contention and evolving ideas of the basement-cored domes in the area and justifies the need for some detailed work on these basement lithologies. The question of whether these domes are actually cored by basement rocks has implications for the evolution of

the Damara Belt. The Abbabis Complex lithologies, usually proposed to be of Congo Craton affinity (Jacob *et al.,* 1978; Hawkesworth and Marlow, 1983; Tack *et al.,* 2002; Miller, 2008; Longridge, 2012; Longridge *et al.,* 2018) have been incorporated into geodynamic models for the evolution of the orogenic belt involving aspects of dome formation, the ensalic nature of the crust, and the possible source for the Nosib Group meta-sedimentary rocks.

Therefore, the aim of this research was to revaluate the geology of the northern extent of the Palmenhorst Dome by adopting a multi-disciplined approach. These various aims and objectives include:

1. Remote sensing and detailed lithological mapping were performed in order to establish a base map for targeted more detailed mapping of the Nose Structure and assessment of the nature of the lithological distribution of the dome. This included detailed descriptions of various lithologies for correlations to other studies as the field area preserves high-grade metamorphism, extensive partial melting and intense deformation.
2. Lithological and structural mapping assessed the relative timing and cross-cutting relationships of pre-Damaran to Damaran-aged partial melt generations, deformation, metamorphism and intrusions in order to determine the exact relationship between the assumed basement lithologies and the supracrustal rocks (Damara Supergroup). This approach was also used to assess possible dome formation processes.
3. Textural descriptions along with understanding of the spatial distribution, processes and extent of various migmatites was employed to help establish the extent of the basement and supracrustal lithologies as these domes tend to be intruded by pervasive partial melts.
4. Detailed petrographic analysis was performed to establish relative timing of deformation, metamorphism and partial melting at a microscopic scale, classify various lithologies (basement granite-gneisses, supracrustals and intrusives) in order to correlate with previous studies.
5. Geochemical analysis was utilised to characterise intrusives and orthogneisses in order establish correlations with previous studies. Major and trace elements were used to assess crystallisation and melting processes for the intrusive rocks and sediment provenance for the metasediments.
6. Cathodoluminesce (CL) imaging guided zircon U-Pb LA-ICPMS (Laser Ablation Inductively Coupled Plasma Mass Spectrometry) dating was used to establish a geochronological framework for key lithologies identified in the field as well as placing the Palmenhorst Dome into context of the Damara Belt. Age constraints on the formation of the Abbabis Complex and various intrusions were used to date deformation. Metamorphic zircons were used to

fingerprint metamorphic histories. Detrital ages for the Etusis Formation were established in order to assess the suggested provenance (the Abbabis Complex) of these metasediments.

7. Lu-Hf isotopic measurements of U-Pb dated zircons were used to assess the crustal evolution of the Abbabis Complex, amphibolite dykes and various Damaran intrusives as well as the provenance for the Etusis Formation. Limited studies exist for Lu-Hf work in the Central Zone.

1.5 Thesis organisation

This thesis is organised into eight chapters including this introductory chapter. The chapters dealing with results (3 to 7) all contain brief introductions, results and discussions. The chapters are as follows:

Chapter 2: A summary of previous work in the southern Central Dome, but more specifically the Abbabis Complex.

Chapter 3: Results from a remote sensing examination of to the Nose Structure, which attempts to define outcropping extents of formations and basement lithologies as well as delineate possible anomalies/rafts in the basement lithologies.

Chapter 4: Detailed descriptions of lithological units, intrusives, structure and migmatite textures from field-based results. Field mapping utilised the base map produced from remote sensing.

Chapter 5: Petrographic analysis of key lithologies with a focus on characterisation, microscopic partial melt textures and microstructures.

Chapter 6: Major and trace element results from key lithologies.

Chapter 7: U-Pb-Hf results augmented by CL interpretations in order to determine a geochronological framework for the study area.

Chapter 8: Synthesis and conclusions of all the discussions from previous chapters placed into the evolution of the sCZ of the Damara Belt.

2. Geological Setting and previous work on the southern Central Zone

2.1 Introduction

The sCZ of the Damara Belt comprises metamorphosed Damaran supracrustal successions of the Nosib and Swakop Groups which unconformably overlie the Abbabis Metamorphic Complex, a pre-Damaran gneissic basement (Miller, 2008) (Fig. 2.1). Owing to the structural complexity of this area, numerous gneissic basement-cored domal structures characterise the sCZ (Miller, 2008) (Fig. 2.2).

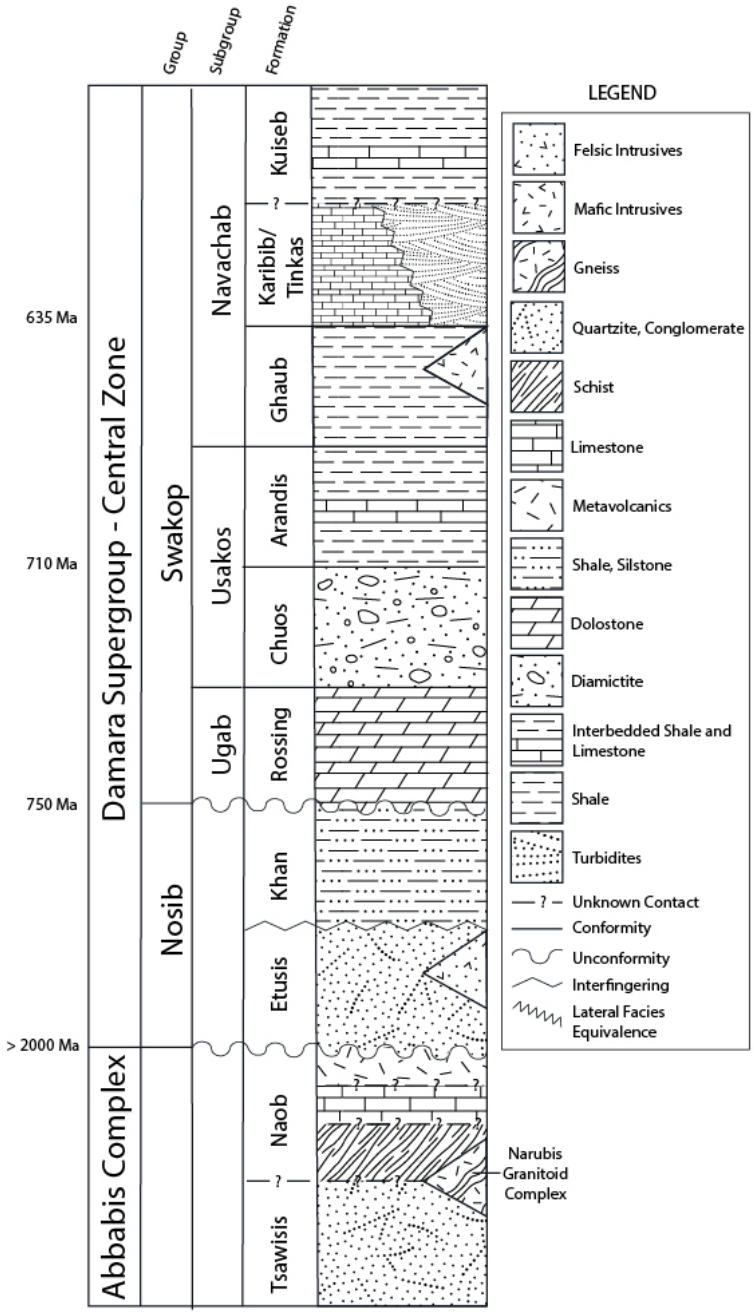


Figure 2.1: Simplified stratigraphic column of the sCZ of the Damara Belt, showing lithologies, approximate depositional ages and general contact relationships (modified after Brandt, 1987; Badenhorst, 1992; Hoffmann *et al.*, 2004; Longridge *et al.*, 2011).

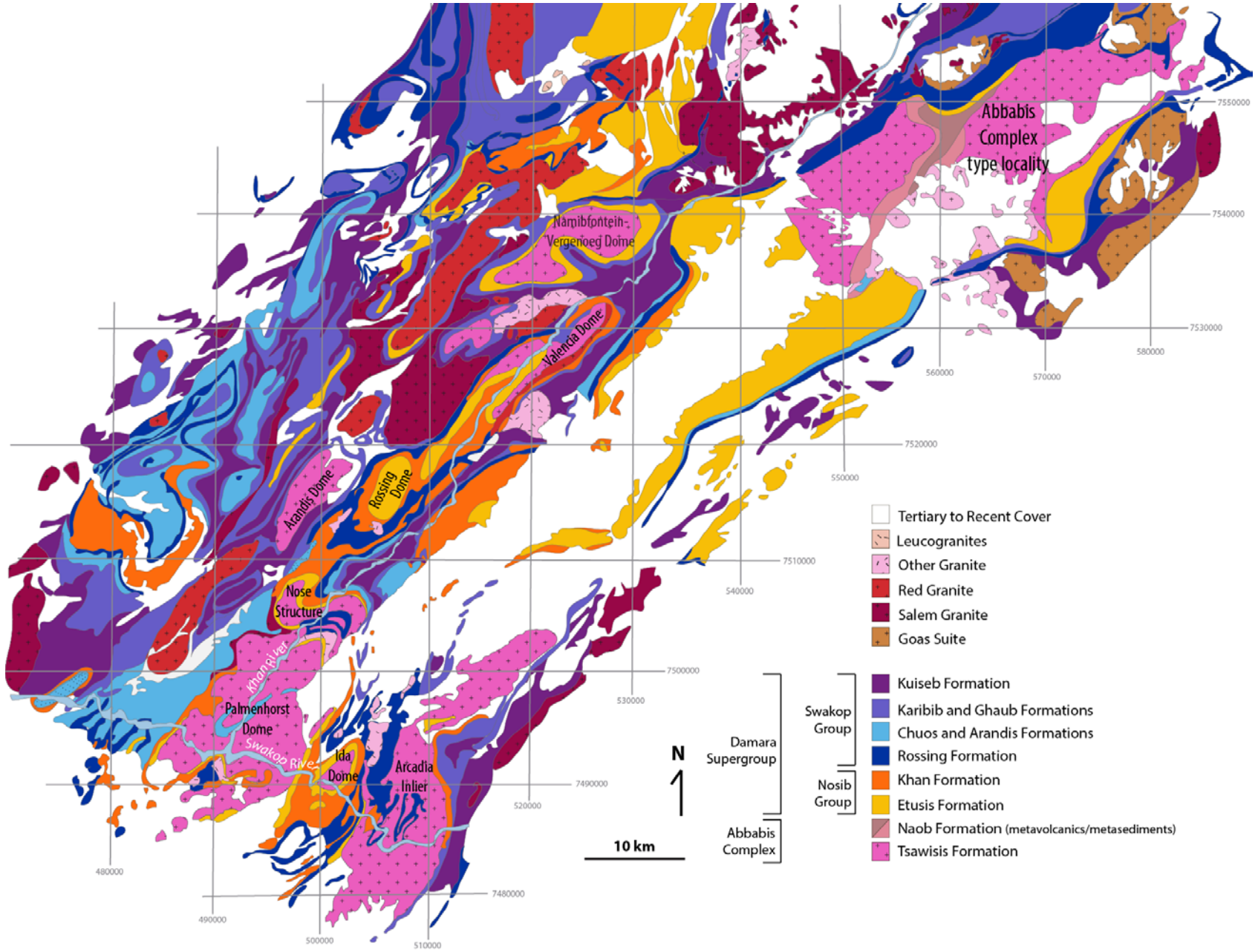


Figure 2.2: Detailed geological map of the Central Zone showing the distribution of the Damara Supergroup, Abbabis Complex (basement) and the associated intrusives. Domes of the area are also indicated (WGS84, Zone 33K; modified after Lehtonen *et al.*, 1995 and Longridge *et al.*, 2011). Specific basement-cored domes are referred to in text.

2.2 Abbabis Complex

The Palaeoproterozoic Abbabis Complex was first described by Gevers (1931) on the farm "Abbabis 70" (22°08'25.5"S;15°35'37.5"E) situated approximately 20 km southwest of Karibib (Fig. 2.2). At its type section in the sCZ of the Damara Belt, the Abbabis Complex is unconformably overlain by metasediments of the Damara Supergroup (Gevers, 1931; Smith, 1965). The Abbabis Complex consists of a variety of metasediments, metavolcanics and granitic gneisses, the latter being the most dominant (Smith, 1965). The basement, supracrustal and intrusive rocks typically form gneissic domes and anticlinoria (Jacob *et al.*, 1978) These anticlinoria are cored by basement lithologies and form widespread northeast-southwest trending domes framed by folded Damaran metasediments (Smith, 1965; Brandt, 1987). In many cases, the unconformity between the pre-Damaran basement and Damara Supergroup is indistinguishable and appears most frequently as a paraconformity (Gevers, 1931; Smith, 1965). This is due to the large degree of deformation, metamorphism and partial melting that affected both the pre-Damaran basement and Damaran supracrustals (Smith, 1965). A review of previous work on the Abbabis Metamorphic Complex is outlined below.

2.2.1 Accepted stratigraphy of the Abbabis Complex at the type locality

The Abbabis Complex was first identified by means of a basal tillite of the Damara Sequence, which contains clasts of Abbabis Complex gneisses at its type locality (Gevers, 1931). Gevers (1931) recognised this contact to be unconformable and that the basement complex underlying the Damaran diamictite to be pre-Damaran in origin. Later, Smith (1965) further mapped and described the contact between the Damaran metasediments and Abbabis Complex and found Abbabis gneisses as clasts within the overlying Etusis Formation. This constituted the first line of evidence that the Etusis Formation was derived from these basement lithologies. This work produced the first descriptive stratigraphic framework and subdivision for the Abbabis Complex into the Abbabis Gneiss, Dolomitic Marble and Calcsilicate Group, Biotite Schist Group as well as associated intrusives of Abbabis age (Gevers, 1931; Smith, 1965) (Table 2.1).

Coeval rocks were proposed to exist in the cores of various domes of the sCZ. However, due to the migmatised nature of the zone, the rocks of the Abbabis System are often indistinguishable from the cover sequences or voluminous granites (Smith, 1965; Jacob, 1974). This is due to the general conformity of foliation within the Abbabis and Damaran sequences and similarity of certain rock types found within basement and overlying supracrustals (Smith, 1965). Smith (1965) proposed that as a result of the tectonic complexity and intensity of gneissification of the Abbabis rocks it is difficult to unravel the stratigraphic succession. Additionally, this author proposed a possible link between

the Kaokoveld, Abbabis and Marienhof systems, although the similarities established between the different basement complexes were largely lithological.

Brandt (1987) reviewed previous stratigraphic relationships and classifications (Smith, 1965; Marlow, 1981; Sawyer, 1981) in order to better characterise specific stratigraphic relationships and lithological groupings within the Abbabis Inlier, which lead to stratigraphic nomenclature. The Abbabis Complex (SACS, 1980) was subdivided into the Tsawisis Formation, Naob Formation and the intrusive Narubis Granitoid Complex (Brandt, 1987; Table 2.1.). Due to the large variety of the rocks in the various parts of the sCZ adequate recognition of these basement rocks remained problematic (Smith, 1965). Additionally, the complexity of the structure, metamorphism and deformation (Miller, 2008) and the often migmatised basement-cover contact added to the difficulty in identifying the pre-Damaran basement. Certain sedimentological (e.g. cross beds) and volcanological features were used to identify the supracrustal nature of lithologies within the Gamgamichabberg syncline, which also helped to clarify stratigraphic relationships (Brandt, 1987). Descriptions of the various stratigraphic divisions are detailed in table 2.1.

Amphibolite dykes have commonly been associated with the Abbabis Complex (Smith, 1965; Brandt, 1978; Marlow, 1981) and were often used as a diagnostic tool to help identify the basement lithologies. However, based on the first U-Pb ages for these amphibolites from the sCZ (Longridge *et al.,* 2014), two phases of amphibolite dykes were identified. These include Palaeoproterozoic-aged amphibolite dykes belonging to the Abbabis Complex as well as Damaran amphibolite dykes (557 Ma) proposed to be related to the Goas Suite (Longridge *et al.,* 2014).

Tsawisis Formation

This constitutes the lowermost unit of the Abbabis Complex and consists mainly of coarse-grained feldspathic quartzite, paragneiss, biotite schist and biotite-sillimanite schists with minor locally confined calcsilicate units (Smith, 1965; Brandt, 1987). The thickness of the Tsawisis Formation is indeterminable as there is no base present locally in the Abbabis Inlier, in addition to intense deformational overprinting during the Damaran orogeny (Brandt, 1987). Brandt (1987) suggests a sedimentary genesis for the unit.

Table 2.1: Comparison between stratigraphy schemes for the Abbabis Complex (modified after Brandt, 1987).

	Smith (1965) Abbabis Inlier	**Sawyer (1981) Area SE of Walvis Bay**	**Marlow (1981) Abbabis Inlier**	**Brandt (1987) Abbabis Inlier**	**Thickness** proposed by Brandt (1987)
(Pre-Damaran)	Ortho-amphibolite		Amphibolite dykes	Amphibolite Dykes	
Narubis granitoid Complex		(Augen) gneiss	Gneisses (several of granitic composition)	Ortho (augen) gneisses	
Naob Formation	Biotite schist and para-amphibolite	Gneiss, schist, glassy quartzite	Metasediments (quartzite, schist, conglomerate, marble, calc-silicate) and interbedded metabasaltic and pyroclastic rock	Metavolcanic rocks (M6) Alternating (feldspathic) quartzite, marble, calc-silicate (M4)	±400m Average: 150m Maximum: 650m
	Dolomitic marble, calc-silicate	Calc-silicate, marble		Schist (dark) and meta-basite (M2)	300-750m
Tsawisis Formation	Abbabis gneiss, phyllitic quartzite, conglomerate	Quartz-feldspar gneiss, quartzite, micaceous quartzite, schist		Schist- (para-) gneiss meta-arkose, subordinate marble, calc-silicate, conglomerate	Undeterminable thickness (No floor present and Damara deformation overprint makes it difficult to determine minimum thickness)

(Horizontal lines do not always represent correlations)

Naob Formation

Overlying the Tsawisis Formation is the Naob Formation. This formation comprises three members, namely M2, M4 and M6 (Brandt, 1987). At the base of the Naob Formation, schists and metabasites (M2) are overlain by a coarse-grained feldspathic quartzite with locally developed crossbedding, thin marble and calcsilicate rocks (M4) succeeded by amygdaloidal metabasalts (M6) (Brandt, 1987). M4 and M6 comprise predominantly metasediments and metavolcanics. The basaltic metavolcanics suggest a tholeiitic continental basalt signature, and a limited number of rocks show komatiitic affinities (Marlow, 1981; Brandt, 1987). The contact between the Naob Formation and the overlying rocks is not well exposed (Brandt, 1987).

Narubis Granitoid Complex

Multiple phases of granitic intrusive rocks of the Narubis Granitoid Complex occur in the Abbabis rocks, however, their relative ages and correlations are uncertain (Brandt, 1987). These granitic intrusions have been deformed into augen gneisses, characteristic of the Abbabis Complex in other cores of the zone, where the Tsawisis and Naob formations are not present (or not yet described) (Miller, 2008). The augen gneisses are texturally, mineralogically and compositionally variable (Brandt, 1987). Correlation between augen gneiss varieties requires geochemical data (Marlow, 1981). Initially, Smith (1965) described the gneisses as underlying the Naob Formation as he did not observe intrusive relationships. However, after a reinvestigation of the crosscutting relationships, Marlow (1981) identified xenoliths of Tsawisis and Naob formations within the gneisses. These various granites and gneisses are grouped as they occur as relatively small bodies, such as veins, which makes the age determination of various intrusive phases challenging (Brandt, 1987).

2.3 Damara Supergroup in the southern Central Zone

Within the sCZ the Damara Supergroup is subdivivded into the lower Nosib and upper Swakop Groups (Fig. 2.3) (SACS, 1980). The Damara Supergroup unconformably overlies the Abbabis Complex basement (Fig. 2.2) (Gevers, 1931; Smith, 1965). However, within the Palmenhorst Dome this unconformity is less readily recognisable due to a higher degree of migmatisation (Miller, 2008). Figure 2.3 summarises the main rock types expected within the Damara Supergroup and underlying Abbabis Complex.

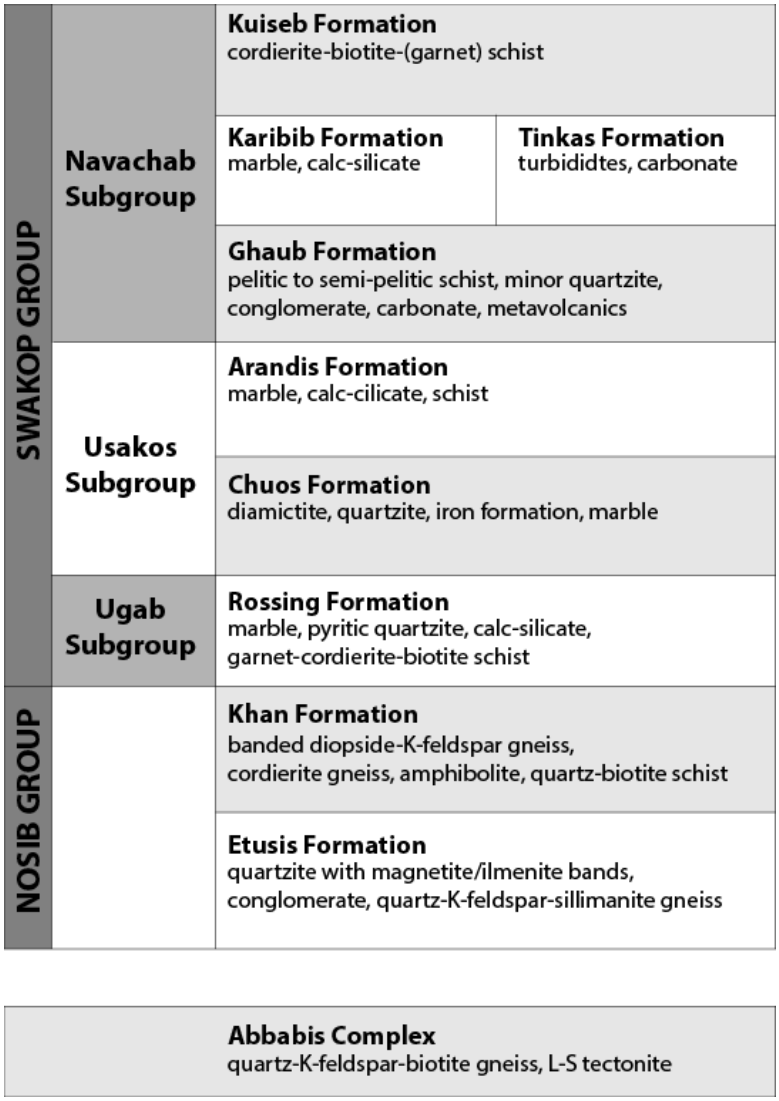


Figure 2.3: Simplified stratigraphic column of the sCZ with the main lithological differences for each Formation of the Damara Supergroup (Nosib and Swakop Groups) and the Abbabis Complex (modified after Hoffman *et al.*, 2004; Miller, 2008).

2.3.1 Nosib Group

The Nosib Group (Fig. 2.3), the base of the Damara Supergroup, unconformably overlies the Abbabis Complex and comprises the Etusis and Khan formations (Smith, 1965). A mainly arkosic metasedimentary succession, the Etusis Formation, comprises quartzites, conglomerates and quartzofeldspathic gneisses with characteristic heavy mineral concentrations of ilmenite and magnetite (Miller, 2008). These heavy minerals often mark the foresets of crossbeds. The Etusis Formation contains rift-associated sedimentary rocks and is interpreted as a (sandy) braided fluvial system (Henry, 1992) sourced from the Abbabis Complex, as shown by basal conglomerates displaying clasts of Abbabis composition (Gevers, 1931; Smith, 1965), along with Rb/Sr isotopic data and Nd/Sm model ages (McDermott *et al.*, 1989; McDermott and Hawkesworth, 1990). Additionally, tectonised Etusis Formation is often similar to, and indistinguishable from, the augen gneisses of

the Abbabis Complex (Sawyer, 1981). Overlying the Etusis Formation is the Khan Formation (Fig. 2.3) (Sawyer, 1981). In contrast, the Khan Formation displays a fine-grained succession of semi-pelites to meta-arkoses, which are characterised by ferromagnesian and calcareous minerals (Sawyer, 1981). Henry (1992) proposed a distal fluvial depositional setting with prevalent diagenetic carbonates.

2.3.2 Swakop Group

This group is subdivided into the Ugab (Rössing Formation), Usakos (Chuos and Arandis formations) and the Navachab (Karibib or Tinkas and Kuiseb formations) subgroups (Fig. 2.3) (SACS, 1980; Miller, 2008). At the base of the Swakop Group, the Rössing Formation is highly varied with its base marked by the first carbonate above the Khan Formation (Henry, 1992). This stratigraphic unit comprises marble, pyritic quartzite, calcsilicates and garnet-cordierite-biotite schist (Miller, 2008) originally deposited within a shallow marine environment (Henry, 1992). The Rössing Formation displays large lateral variations and is often missing in stratigraphy due to higher degrees of strain and attenuation (Nex, 1997). In this instance, the Chuos Formation directly overlies the Etusis or Khan formations along a tectonic contact. However, in less deformed areas the Chuos Formation unconformably overlies the Rössing Formation. The glaciomarine rocks of the Chuos Formation are massive tillites, which have been deformed into L-tectonites, along with iron formations, quartzites and marbles (Hoffmann *et al.*, 2004). This succession is often correlated with the Cryogenian Sturtian glaciation (ca. 710 Ma) (Hoffmann, 2005). The Arandis Formation represents the overlying cap carbonate with associated calcsilicates, schists and metagreywackes (Lehtonen *et al.*, 1995).

The Ghaub Formation represents the Marinoan glacial event (ca. 635 Ma) and a change in depositional environment to a passive continental margin (Hoffmann *et al.*, 2004; Miller, 2008). This stratigraphic unit is characterised by a diamictite, with isolated dropstones and mafic volcanics and also contains minor quartzites and pelitic to semi-pelitic schists (Hoffmann *et al.*, 2004). Thick successions of carbonates, marble and dolomite are characteristic of the Karibib Formation, although interbeds of breccia, calcsilicates, schists and meta-greywackes are present (Kisters, 2005). The Tinkas Formation is considered to be a lateral equivalent of the Karibib Formation along the southeast margin of the sCZ and comprises metamorphosed carbonates and turbidites (Miller, 2008). At the top of the Damara Supergroup, the Kuiseb Formation is identified as a thick metapelitic schist (Miller, 1983). This cordierite-biotite-(garnet) schist comprises most of the Okahandja Lineament and has been tectonically thickened (Kukla, 1993).

2.4 Metamorphism

The Abbabis Complex and supracrustal Damara Supergroup of the sCZ have undergone metamorphism associated with voluminous granitoid emplacement during the collision of the Congo and Kalahari cratons (Goscombe *et al.*, 2004; Longridge *et al.,* 2017; Goscombe *et al.,* 2017b). The sCZ represents the high-temperature, low-pressure metamorphic zone of the Damara Belt where temperatures typically increase towards the southwest (Fig. 2.4) (Hoffmann, 1976; Blaine, 1977; Sawyer, 1981; Bühn *et al.*, 1995; Masberg, 2000; Goscombe *et al.,* 2005; Goscombe *et al.,* 2017a; Longridge *et al.,* 2017). Debate remains on whether the Central Zone was affected by a single phase of metamorphism (Hawkesworth *et al.*, 1983; Hartman *et al.*, 1983; Puhan, 1983; Haack and Martin, 1983; Longridge, 2012) or by multiphase metamorphism (Nash, 1971; Barnes and Sawyer, 1980; Kröner, 1982; Ahrendt *et al.*, 1983; Oliver, 1995; Nex *et al.*, 2001a; Goscombe *et al.,* 2017a; Goscombe *et al.,* 2017b).

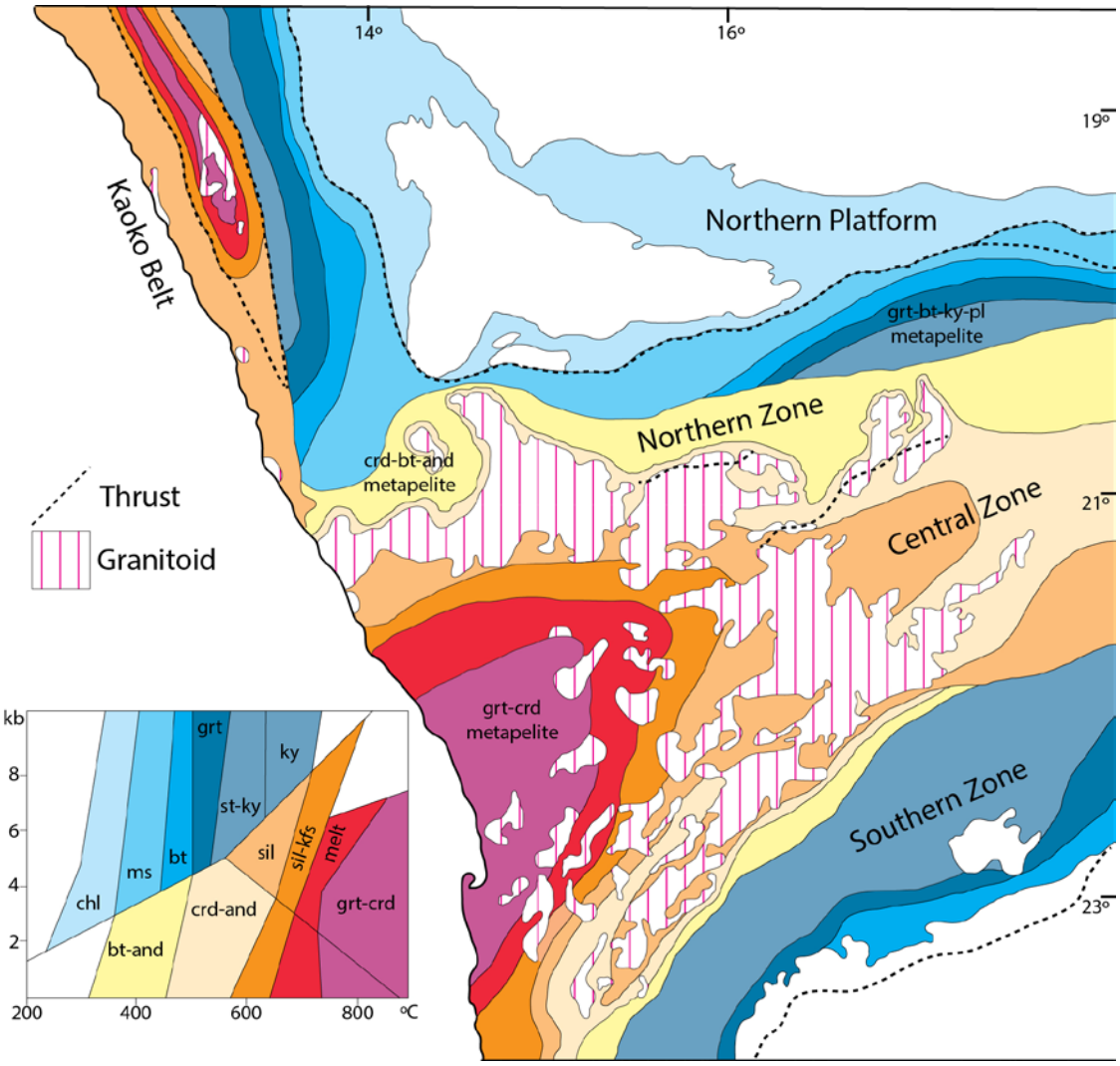


Figure 2.4: Simplified representation of peak metamorphic assemblages in the Damara Orogen (modified after Goscombe *et al.*, 2004).

Poli (1997) proposed the possibility of a metamorphic gap between the Damara Supergroup and the Abbabis Complex. He suggests that the Abbabis Complex basement exhibits higher-grade (800 °C and 6-7 kbar) metamorphic conditions in comparison to the supracrustal Damara Supergroup (660-690 °C and 3.3-4 kbar), and the basement lithologies appear to have experienced higher degrees of partial melting. This difference in metamorphic grade is proposed to be a result of a zone of constrictional deformation between the two units. However, recent studies on Damara Supergroup orthopyroxene-bearing pelitic migmatites suggest peak pressure and temperatures of the sCZ (Palmenhorst Dome) of 4.9 kbar and 835 °C (Longridge *et al.*, 2017), which are higher than previous estimates. Longridge *et al.* (2017) have also suggested that the orogen had undergone two different tectonometamorphic events along strike at different times, suggesting that the evolution of the Damara Belt is more complex than previously understood.

2.5 Structure and Deformation

2.5.1 Damaran deformation

Polyphase deformation of the Damara Sequence began with the closing of the Khomas Sea and resultant continent-continent collision (*ca.* 560 Ma) (Miller, 2008; Goscombe *et al.,* 2017b). Debate exists as to the number of deformational events that occurred during the Damara Orogen. This varies between two deformational events (Smith, 1965; Jacob *et al.*, 1983) to nine (Sawyer, 1981; Goscombe *et al.,* 2017b) deformational events. Alternatively, a single progressive deformational event has been proposed by Poli (1997). However, it is generally accepted that there are two intense Damaran events, commonly referred to as D2 and D3 (Smith, 1965; Nash, 1971; Blaine, 1977; Coward, 1983; Longridge, 2012; Lehmann *et al.,* 2016) with an early regional fabric forming event (Smith, 1965; Barnes, 1981; Coward, 1983; Blaine, 1977; Longridge, 2012). Although previous authors (Table 2.3) identified varying deformational histories in the Central Zone, that can be correlated and linked to the two main deformational events (D2 and D3), with D2 dated between *ca.* 530 Ma to 510 Ma and D3 occurring from *ca.* 510 Ma to 500 Ma (Lehmann *et al.,* 2016; Goscombe *et al.,* 2017b). Table 2.3 highlights the variations in deformational features from different localities in the Central Zone.

Table 2.2: Summary of deformation from early workers in the Central Zone (modified after Longridge, 2012; authors indicated by *) and a recent detailed study on the Palmenhorst Dome after Longridge, 2012.

	Smith (1965)*	Nash (1971)*	Blaine (1977)*	Barnes (1981)*	Sawyer (1981)*	Coward (1983)*	Jacob et al. (1983)*	Poli (1997)*	Longridge (2012)
					DC6- Small-scale open concentric folds, plunging N to NE				
			D5- Dextral movement along the northern margin of the Okahandja Lineament		DC5- Close to tight small to medium-scale folds, plunging NNE				
			D4- Zone of metamorphic banding cleavage along the Okahandja Lineament	F4- Weak deformation producing upright N- or NW-trending, gentle folds. Postdates metamoprhism and igneous activity	DC4- Close to tight folds, plunging moderately N or NNE	F4- Local N-verging folds			Post D3- Minor brittle faults, fractures and tension gashes
D3	Slightly bent D2 folds indicate a possible weak D3	F3- E-W trending minor mesoscopic folds	D3- Large open, upright concentric folds	F3- Upright folds, plunging NE. Upright faults in high strain areas, highly variable strain intensity	DC3- Tight to isoclinal upright folds, plunging gently to N. Subvertical axial planar cleavage or crenulation cleavage	F3- Upright to SE-verging large folds. Local sheat folds		Stage3- strain is partitioned into mylonites at the basement-cover interface	D3- Inteference upright open to gentle folds associated with dome formation
D2	D2- Refolding of NW-trending folds by NE-SW trending folds and associated dome formation with domes elongate NE-SW	F2- NE-SW trending upright folds, formation of the main Damaran structural trend	D2- Recumbent folding, low angle thrusting, transposition of earlier fabrics and development of a macroscopically penetrative cleavage	F2- Intense fabric, infolding of the pre-Damaran and Damaran rocks. Development of the regional fabric. Development of recumbent folds and thrusts	DC2- Gently inclined folds with W-dipping axial planes, N-S trending hinges. Thrusting with N-S trending hinges. Thrusting with N-S strike	F2- Recumbent, SW-verging sheath folds. Syn-tectonic high-grade metamorphism. Early granites and migmatites	DBD2- Upright folds with N-trending axes, formation of some ductile shear zones	Stage 2- main dome formation and formation of L- and S-tectonites. Local progressive tightening of structure	D2- Non-coaxial S to SE verging folds, NE-SW extension and high strain zones along N-dipping fold limbs
D1	Folds with NW-SE trending axes. Boudinage associated with this event	F1- NE-SW trending tight recumbent folds. Development of a penetrative cleavage	D1- Intrafolial, isoclinal folds with angular hinges. Biotite or biotite-fibrolite foliation	F1- Very rare, minor tight (often rootless and isoclinal) folds. Largely obliterated by F2. Preserved as inclusion trails in M1 porphyroblasts	DC1- Moderately inclined folds with W-dipping axial planes and NW-trending hinges. Axial planar schistosity	F1- Early thrusts and folds, probably SW-verging	DBD1- Tight, recumbent, S-verging folds. Folding of the basement-cover interface. Formation of 'ductile shear zones' (extensional shear bands)	Stage 1- Unequal constrictional shortening begins gentle dome formation. Formation of S1 by mimetic growth	D1- Rootless isoclinal intrafolial folds parallel to S0/1 lithological layering or foliation
Pre-Damaran	Pre-Damaran deformation noted but not characterised						DB- Foliation developed (augen gneisses), ductile shears with steeply dipping shear planes		Pre-Damaran deformation- S/L tectonites, refolded E-W linear fabrics

2.5.1 Pre-Damaran deformation

Smith (1965) was the first to recognize pre-Damaran deformation in the Abbabis Complex at the type locality but the deformation was not properly characterised (Table 2.3). Poli (1997) described pre-Damaran deformation in the basement lithologies in the Nose structure and Namibfontein-Vergenoeg Dome (Fig. 2.2) but noted that it was largely overprinted by Damaran fabrics. While Damaran deformation has been well documented, pre-Damaran deformational history is not well understood. Longridge (2012), based on work in the Ida and Palmenhorst domes, documented a pre-Damaran linear fabric which has been refolded by Damaran structures. These fabrics display an east-west trend, which is in contrast to the northeast plunging lineation commonly recognised in the Damara Supergroup (Downing and Coward, 1981). This fabric is truncated by Damaran amphibolites (Longridge, 2012), which represent the earliest phase of the Damara event, dated at 557 Ma (Longridge, 2012).

2.5.2 Dome formation

A characteristic physiogeologic feature of the Central Zone is the presence of basement-cored domes which are typically recognised as anticlines (Smith, 1965; Miller, 2008). Models for the formations of these domes are debated. Broadly, two mechanisms for dome formation in the Central Zone have been proposed, which include models involving voluminous granitoid emplacement (Barnes, 1981; Sawyer, 1981) or various styles of structural deformation leading to dome formation (Smith, 1965; Jacob *et al.,* 1983; Oliver, 1995; Longridge, 2012), the latter of which is most favoured (Goscombe *et al.,* 2017b). A detailed description of several dome formation models is given in Chapter 4.3. Structural deformation models for dome formation in the Central Zone purport that interference folding may have been responsible from two orthogonal deformational events (described below) (Smith, 1965; Longridge, 2012). A recent study has identified infolded Damaran metasediments in the Palmenhorst Dome providing further evidence for interference folding mechanisms (Longridge, 2012). The Nose Structure forms a series of km-scale isoclinal anticlines and synclines with infolded Damara Supergroup and Abbabis Complex (Longridge, 2012). Poli and Oliver (2001) described the Nose Structure being the result of single ductile flow episode at mid-crustal levels in the axial zone of the Damara Belt and proposed a basement-cover detachment zone known as the Khan -River detachment. The integration of dome formation mechanisms, into a structural history, has no consensus between authors which is why it is considered in this study.

2.6 Associated magmatism

The Central Zone is characterised by large volumes of syn- and post-orogenic granitoids (Miller, 2008). Numerous workers (e.g. Smith, 1965; Jacob, 1974; Brigueu *et al.,* 1980; Barnes, 1981; Marlow,

1981; Sawyer, 1981; Miller, 1983; Brandt, 1985; McDermott, 1986; Nex and Kinnaird., 1995; McDermott *et al.,* 1996; Jung *et al.,* 1998; Jung *et al.,* 2000; Jung *et al.,* 2002; Kinnaird and Nex, 2007) have classified the granitoids into a number of groups based on their mineralogy and relative timing within the tectonic history. A comparison of some of the different groups of granitoids is given in Table 2.2, but a subdivision of the multiple generations of sheeted leucogranites (SLGs) also exists (Nex and Kinnaird, 1995). The SLG nomenclature classifies the granites into six types, so named types A to F, ranging from oldest to youngest (Nex and Kinnaird, 1995). These various leucogranites are typically defined as post-tectonic leucogranites, alaskites or pegmatites (Marlow, 1981; Nex and Kinnaird, 1995; Nex, 1997; Basson and Greenway, 2004; Kinnaird and Nex, 2007; Longridge *et al.,* 2011).

Table 2.3: A comparison of various granite classification schemes by various authors (modified after Longridge, 2012).

Smith (1965)	Jacob (1974)	Marlow (1981)	Brandt (1985)	
Pegmatite and aplite of various ages with regard to structural and metamorphic events		Alaskites, fine-grained to pegmatitic, highly leucocratic anastomosing or vein-style of intrusion and may host uranium mineralisation	Alaskites and leucogranites, which occur as sheets at various stratigraphic levels, and are syn- to post-tectonic	youngest ↑
Itrusive granite and pegmatitic granite, homogeneous unfoliated leucocratic granite, or very coarse-grained pegmatitic granite	Post tectonic granites (Gawib, Achas, Bloodkoppie, Horebis and Donkerhuk granites. Alaskitic pegmatites are also included	Leucogranites, which are late- to post-tectonic, typified by the Bloodkoppie and Donkerhuk granites	Post-tectonic granites, which occur as stocks or plutons (the Gawib, Achas, Bloodkoppie and Kubas intrusives). The large Donkerhuk Granite is the most important of these	
			Red and grey homogenous syntectonic granites	
Red gneissic granite- red, homogenous banded gneisses with metasedimentary xenoliths, occur in domes and anticlines	Red granite-gneiss, an inhomogeneous, foliated red granite with metasedimentary xenoliths, occurs in anticlinal structures below the level of the Karibib Formation	Red granites, characterised by large amounts of K-feldspar and small amounts of ferromagnesian minerals. Occur as dykes, domes or lit-par-lit intrusions	Red inhomogeneous syntectonic granites, occuring at the stratigraphic level of the Nosib Group or Abbabis Complex rocks	
Salem gneiss and granite-porphyritic biotite granite, may be leucocratic in places and confined to synclines	Salem Granite Suite, comprising non-porphyritic gneissic granite, porphyritic biotite granite (youngest) and leucogranite (oldest)	Salem-type granites, a suite of different generations of granites, granodiorites and adamellites which may be porphyritic	The Salem granites. These grey, porphyritic granites may be pre-, syn- or post-tectonic	
quartz diorite and diorite gneiss (Goas Intrusive Suite), found locally in synclinal structures occupied by Kuiseb Formation schists		Gabbros within foliated diorites and granodiorites (Goas Intrusive Suite)		oldest ↓

2.7 Field mapping of the Palmenhorst Dome

Early work on the Abbabis Complex in the Palmenhorst Dome did not differentiate between lithologies (Fig. 2.5.A) present in the migmatised cores of domes. Often, these cores are referred to as "undifferentiated granite-gneisses" (eg. Smith, 1965; Miller, 2008; Lehtonen *et al.,* 1995). Jacob (1974) and Sawyer (1976) made refinements to the lithological mapping of the Tumas and lower

Swakop River region, however, the Palmenhorst Dome remained mapped largely as undifferentiated metasediments, paragneisses and Palaeoproterozoic and Mesoproterozoic orthogneisses. The discovery of an attenuated succession of Damaran supracrustals adjacent to the basement (Nex, 1997) differed from the interpretation of the sequence representing pre-Damaran basement in earlier works by Marlow (1981).

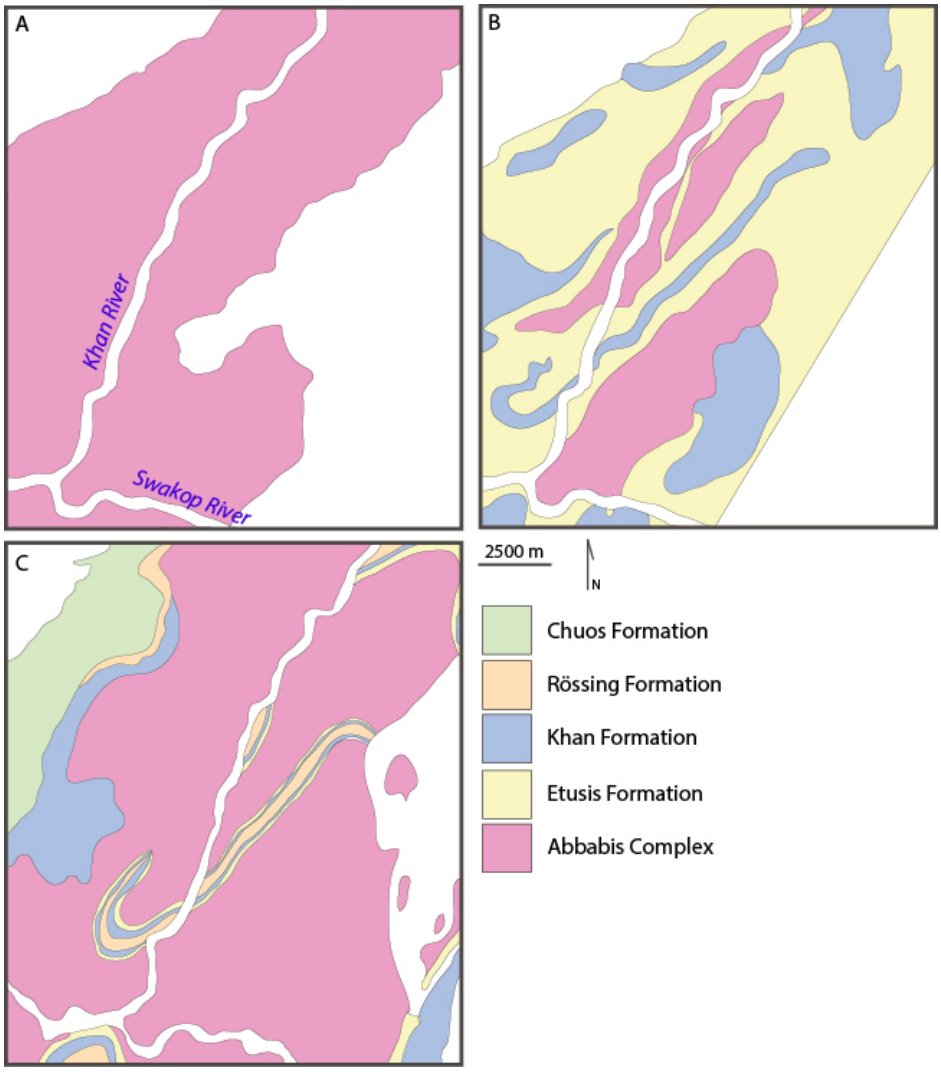


Figure 2.5: Distribution and comparison of the Abbabis Complex and Damara Supergroup (Rössing, Khan and Etusis formations) in the Khan-River Dome (or Palmenhorst Dome). Maps after (A) Smith (1965), (B) Barnes (1981) and (C) Longridge (2012) show considerable differences in the distribution of the Abbabis Complex and Damara Supergroup from undifferentiated basement cores to complex patterns of crustal elements within the basement. Modified after Longridge (2012).

Previous research documented certain domes within the Central Zone to be cored by Damaran-aged rocks, such as the Vergenoeg-Namibfontein (Poli and Oliver, 2001) and Rössing domes (Oliver and Kinnaird, 1996). Additionally, after mapping undertaken by Barnes (1981), Nex (1997), and Longridge (2012), the Palmenhorst Dome has been shown to contain infolded lower Damaran metasediments and Abbabis Complex gneisses. (Fig. 2.5). Barnes (1981) originally identified the

infolding of the Damara Supergroup within the Abbabis Complex, and predominantly mapped the basement as the underlying Etusis Formation (Fig. 2.5) with slivers of Khan Formation. Longridge (2012), in contrast, identified the Palmenhorst Dome to be underlain by the gneisses of the Abbabis Complex with infolded slices of Damara Supergroup present within isoclinal synclines. This infolding most likely occurred as a result of recumbent S- verging folds formed during D2 deformation (Longridge, 2012).

Longridge (2012) produced further revisions to Poli's (1997) map (Fig. 2.6), which included rafted amphibolites and metasediments within migmatised granitoids along the northern end of the Palmenhorst Dome near the Nose Structure. Poli (1997) proposed that these rafts could be correlated with the Tsawisis Formation (section 2.2.1). These rafts were traced along strike (eastward), where they were correlated with a complete lower Damara sequence and therefore were identified as Damaran metasediments rather than Tsawisis Formation (Longridge, 2012). As a result, it is suggested that the stratigraphy for the Abbabis Complex in the Palmenhorst Dome is far simpler than that in its type locality as there are no known metasedimentary or metavolcanic successions (Longridge, 2012). The Palmenhorst Dome is thus comprised solely of the Narubis Granitoid Complex of the Abbabis Complex (Longridge, 2012).

Toe *et al.* (2013) made additional refinements to Valois and Walgenwitz's (1979) work on the classification of the migmatitic basement in the Goanikontes to Ida Dome area. Valois and Walgenwitz (1979) initially classified metatexites, diatexites and gneisses. Toe *et al.* (2013), however, placed this initial classification into three tectonic units based on the proportion and distribution of the granitic fraction (Toe *et al.*, 2013). The three tectonic units include: (1) the lower unit, dominated by diatexites and plutons of homogeneous granites, (2) a middle unit which displays a predominantly sedimentary protolith and is characterised by metatexites, and (3) an upper unit that corresponds to the Damaran metasedimentary rocks with associated intrusive leucogranites (Toe *et al.*, 2013). Although the Abbabis Complex is still recognised amongst intense partial melt, this study highlights the importance of understanding the distribution of migmatites and how they aid in the evolution of the Damara Orogen.

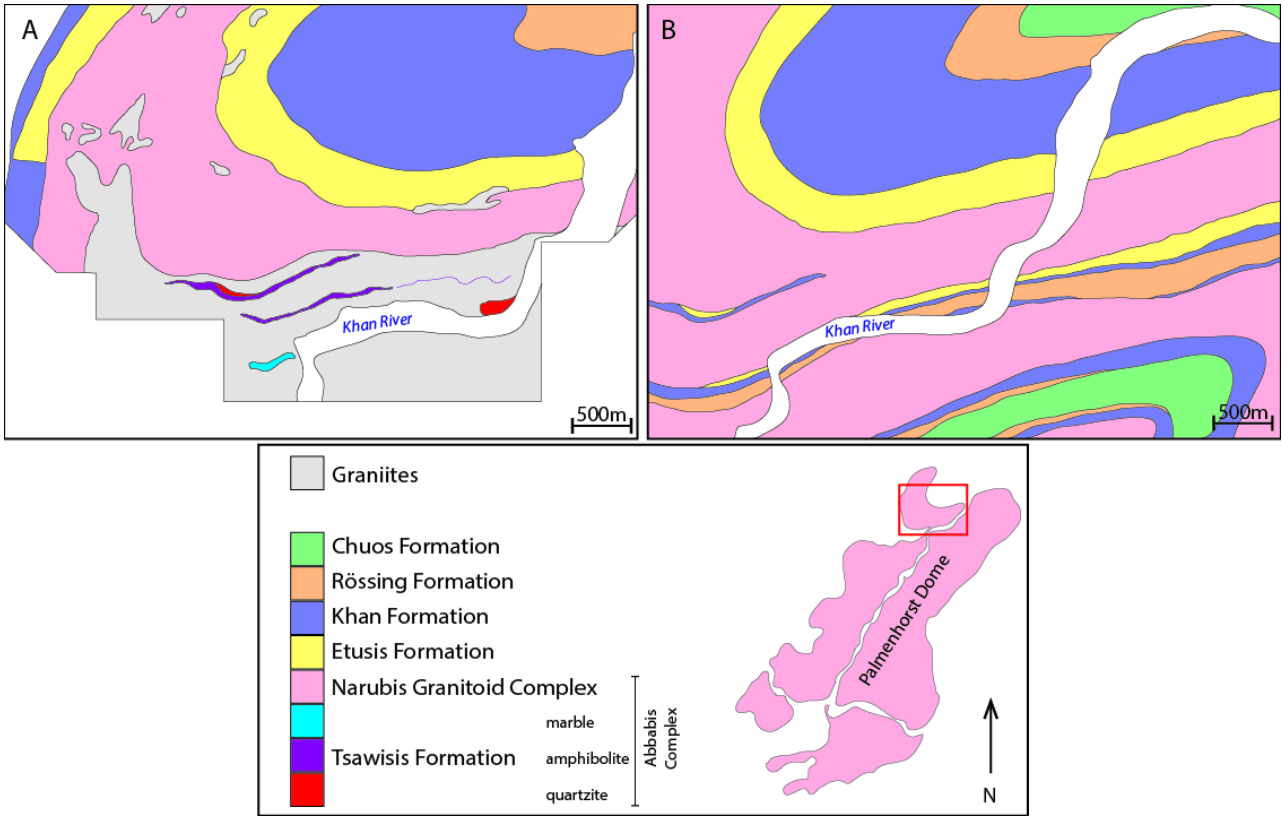


Figure 2.6: A map of the northern extent of the Palmenhorst Dome illustrating (A) Poli's (1997) proposed Tsawisis Formation of the Abbabis Complex showing rafted quartzites, amphibolite, conglomerate and marble within granites, and (B) a revised lithological map (Longridge, 2012) indicating a complete lower Damara Supergroup sequence correlated with the proposed rafts by Poli (1997). Damaran-aged granites (as indicated in grey) are omitted in illustration B (modified after Longridge; 2012). The inset shows an overview of the Palmenhorst Dome and where maps A and B are approximately located in terms of the larger Palmenhorst Dome.

The identification of Damaran lithologies within the so-called basement or the possibility of the migmatised (so-called) basement representing a remnant magmatic layer from the root of the Damaran orogeny has implications for the geological history of the orogen, source(s) of granitic rocks, and forms the basis for this study. In particular, sediments of the Etusis, Khan and Rössing formations have been mapped out in the previously undifferentiated Abbabis Complex gneisses, metasediments and metavolcanics (Barnes, 1981; Nex, 1997; Longridge, 2012). This recognition requires a more detailed and adequate differentiation of Abbabis type lithologies and younger Damara Supergroup supracrustals within the Khan River Dome.

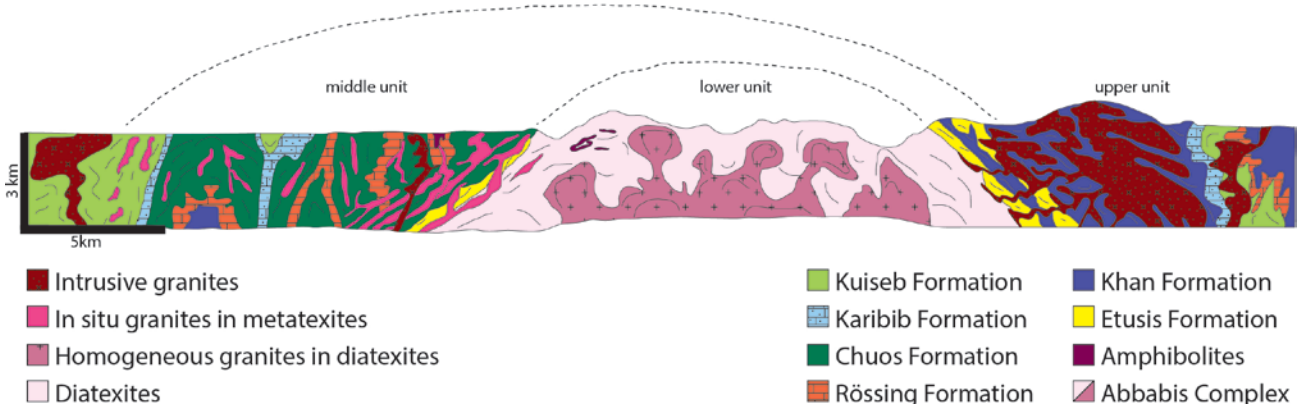


Figure 2.7: A geological cross section along the southern extent of the Palmenhorst Dome from Goanikontes to the Ida Dome. The geological cross section indicates "lower, middle and upper units" (after Toe *et al.*; 2013).

2.8 Geochronology of the Abbabis Complex

Jacob *et al.* (1978) performed the first age determination for the Abbabis Complex by dating the strongly foliated tonalities and gneissic granites from the Abbabis Inlier. A zircon discordia age of 1925 ±300 Ma was obtained and was considered a mean age of the Abbabis Complex, which allowed for the authors' comparison and possible link to the Franzfontein Granite Suite (Rehoboth Inlier), 230 km north-northwest of the Abbabis Inlier. As a result, Jacob *et al.* (1978) proposed that the host rocks of the Abbabis Complex are probably older than 2 Ga. Additionally, Nd model ages of Damaran-aged granites that formed from pre-existing Damaran and pre-Damaran rocks during the Damaran Orogeny display clusters around 2.0-2.5 Ga (Hawkesworth and Marlow, 1983), which supports the proposed Palaeoproterozoic age of the Abbabis Complex.

Kröner *et al.* (1991) reported zircon U-Pb discordia ages of 571 ±64 Ma, 1038 ±58 Ma and 2014 ±39 Ma from migmatised quartzofeldspathic gneisses from the lower Khan River. These ages represent a Damaran-aged overprint (571 Ma), the crystallisation age (1038 Ma) of the gneissic protolith and the ultimate source age (inherited) of the gneiss to be of Abbabis Complex affinity (2014 Ma) (Kröner *et al.*, 1991). Additionally, the authors interpreted the 1038 ±58 Ma age of the zircons to represent a pre-Damaran basement younger than the Abbabis Complex, which formed a possible northwest extension to the Rehoboth Inlier of the Kalahari Craton. Alternatively, these younger ages have been thought to represent a 1 Ga Kibaran overprint on *ca.* 2 Ga Eburnean basement from the Congo Craton (Rumvegeri, 1991; Longridge, 2012). Furthermore, the Abbabis Complex has been dated at *ca.* 2 Ga by using inherited zircons from Damaran-aged granitoids and the dating of Abbabis Complex gneisses confirming the Palaeoproterozoic age for the basement complex. The inherited zircons yielded ages of 2164 ±6 Ma (Jacob *et al.*, 2000) and 2038 ±5 Ma (Tack *et al.*, 2002) while the Abbabis Complex gneisses yielded ages of 2056 $^{+11}/_{-10}$ Ma, 2044 $^{+32}/_{-27}$ Ma and 2044 $^{+17}/_{-14}$ Ma (Longridge, 2012).

Amphibolitic dykes have often been used as a characteristic identifier for the Abbabis Complex, as they are often considered to be associated intrusives of pre-Damaran in age (Smith, 1965; Marlow, 1981). However, ortho-amphibolite dykes cross-cut Damaran metasediments at Rössing Mine (Nex, 2009 pers. comm. in Longridge, 2012). Longridge (2012) reported U-Pb zircon crystallisation ages of 2027 ± 2.3 Ma and 1820 ± 9.8 Ma for two generations of amphibolite dykes (Palaeoproterozoic and Damaran in age). These ages suggest these pre-Damaran dykes were emplaced within 20 Ma of the granitoid rocks of the Abbabis Complex (according to Longridge's zircon ages) and a pre-Damaran metamorphic event may have altered the basement rocks (evidence is limited), respectively. Conversely, magmatic zircons from amphibolites with ages of 557 Ma (Longridge, 2012) indicating that not all amphibolites are pre-Damaran in age and cannot be used as a basement identifying tool.

Lu-Hf isotopic studies are limited for the sCZ of the Damara Belt with εHf values for the Goas Suite (Milani *et al.,* 2015), Damaran supracrustals (Foster *et al.,* 2015) along with the Abbabis Complex and grey granites (Longridge *et al.,* 2018). All these studies show unradiogenic εHf values, and suggest crustal growth was limited to the Archaean to Mesoproterozoic and no new curst was generated during the Pan-African. A more detailed review of U-Pb age constraints and Lu-Hf isotopic work is outlined in Chapter 7. A comprehensive review on the age data for the Damara is provided in Milani *et al.* (2015).

3. Remote Sensing

3.1 Introduction

Although the Abbabis Complex has been recognised since the 1930s (Gevers, 1931), the lithological maps of the basement-cored domes are still being refined. Recent studies have located supracrustal components within the previously undifferentiated granite-gneiss complex. For instance, Longridge (2012) indicated that these crustal components were visible from Google Earth images and therefore remote sensing is a good first order discrimination tool in order to delineate additional supracrustal components within the "Nose" structure. The use of multi- and hyperspectral imagery is a further step to identify possible supracrustal components within the Abbabis Complex. A stratigraphic succession for the Abbabis Complex was identified at the type locality (Smith, 1965; Marlow, 1981; Brandt, 1987) and in the Palmenhorst Dome (Poli, 1997). Subsequent research disagreed with this proposal, suggesting that the units may represent portions of the lower Damara Sequence (Longridge, 2012). Therefore, detailed remote sensing on the northern extent of the dome may help to re-define the stratigraphy, variations in compositions of the Abbabis Complex and the presence of possible infolded Damaran metasediments allowing for targeted areas to be located from desktop studies. Remote sensing, particularly hyperspectral imagery, has the potential and capability to detect these compositional changes among as well as within different rock types (Lillesand *et al.*, 2004). Therefore, it is a suitable tool to detect crustal components within the basement. Additionally, remote sensing may be able to redefine the basement-supracrustal contact as well as contacts between the individual formations within the Damara Supergroup.

3.2 Methods and Materials

Both multispectral and hyperspectral datasets were used (Fig. 3.1). Multispectral imagery, namely Landsat 8 OLI (Operational Land Imager), was obtained from the United States Geological Survey website (https://earthexplorer.usgs.gov/) on 12 March 2017 and resized to a region corresponding to the northern Palmenhorst Dome (Fig 3.2). Landsat 8 data was pre-processed, processed and interpreted to delineate spectral domains of the region. Hyperspectral images, imaged by Hymap hyperspectral sensor, were obtained and had already been processed. Therefore, these data were utilised for interpretation and to compliment the Landsat 8 images. Hymap images were used to increase the validity of, and refine, the lithological domains in order to assign them to previously mapped Damara formations when combined with Landsat 8. Due to the complex nature of the sCZ, a lower resolution data set is useful to initially group domains, and subsequently refinements can be made using a higher resolution data set for increased accuracy.

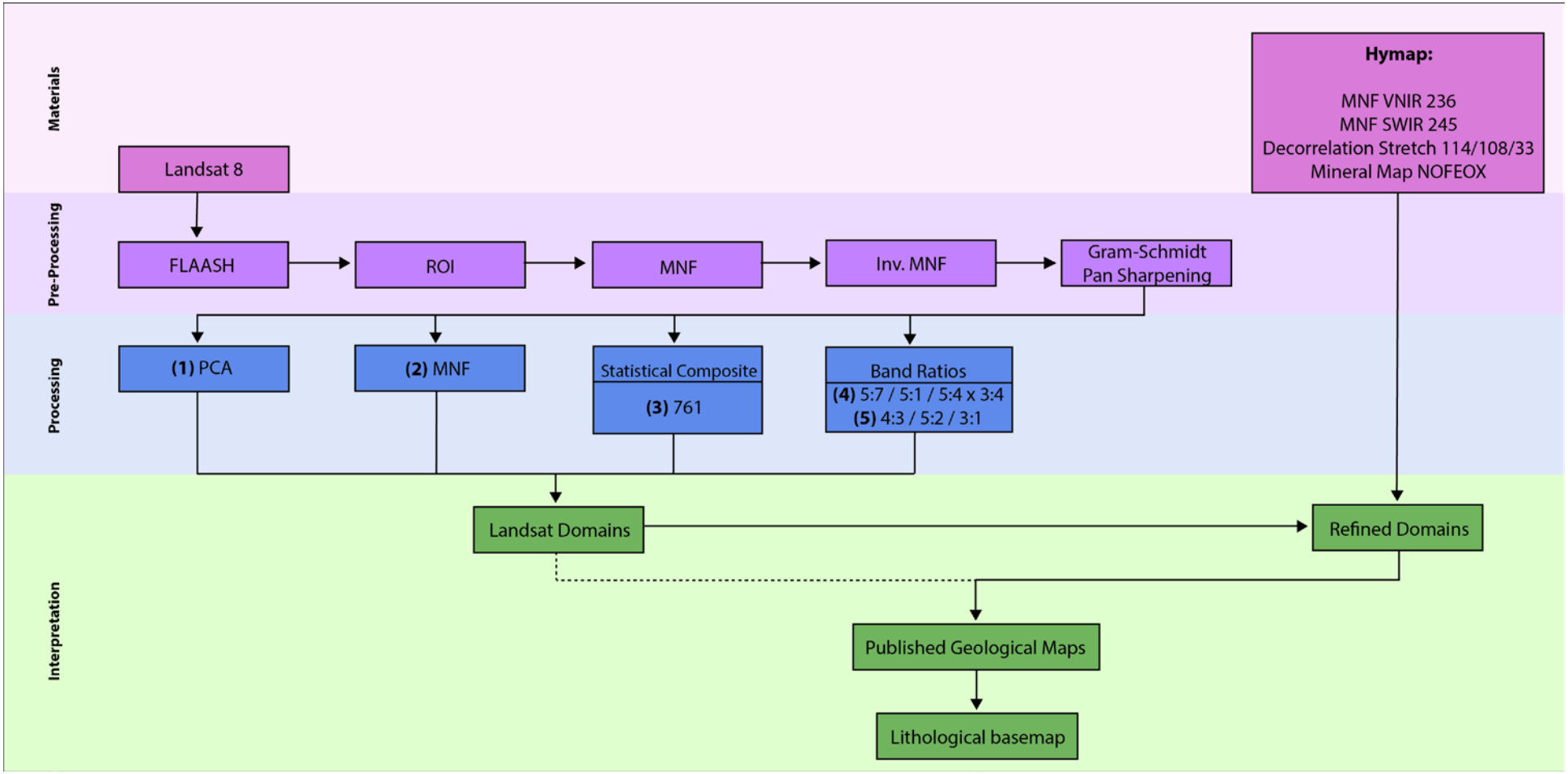


Figure 3.1: Schematic of the workflow used on Landsat 8 and Hymap hyperspectral imagery. The five images used for interpretation include the (1) Principal Component Analysis (PCA), (2) Maximum Noise Fraction (MNF), (3) statistical composite 761, and (4 and 5) two band ratio (5:7/5:1/5:4*3:4 and 4:3/5:2/3:1) images MNF= Maximum Noise Fraction; Inv. MNF= Inverse MNF; VNIR= Visible and Near-infrared; SWIR= Short-wave Infrared; FLAASH= Fast Line-of-sight Atmospheric Analysis of Hypercubes; ROI= Region of Interest; PCA= Principal Component Analysis; NOFEOX= no iron oxides.

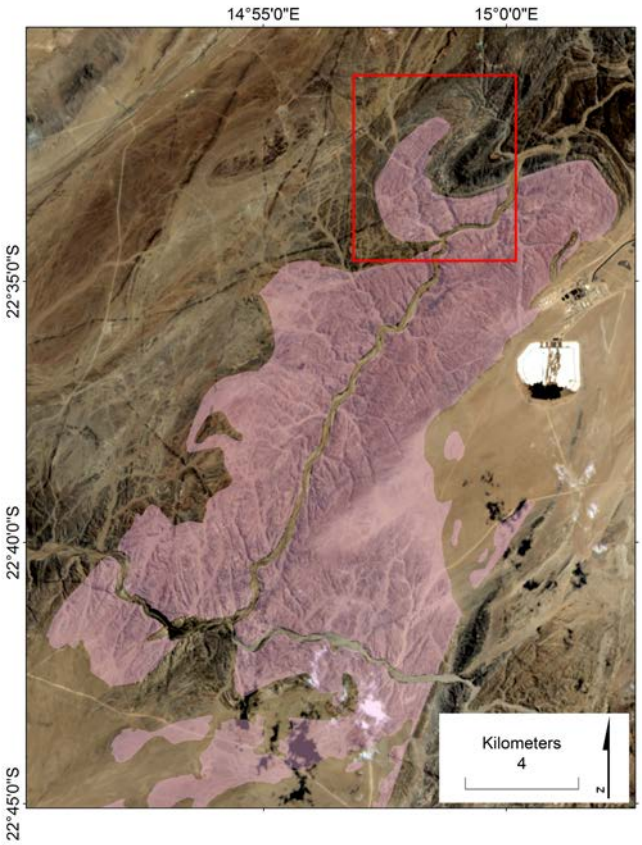


Figure 3.2: Landsat 8 Image of the Palmenhorst Dome. The pink colour highlights the Palmenhorst Dome and the red box indicates the northern extent of the dome, which is subject of this study. (Area is approximately 38 km^2).

3.2.1 Pre-processing of Landsat 8 data

The Landsat 8 image was pre-processed using ENVI software in a five-step process, with each corrected image result being the source for the next correction in the process. A radiometric correction, FLAASH (Fast Line-of-sight Atmospheric Analysis of Hypercubes), was performed (Fig. 3.1) to correct for variations in weather conditions or changes in sun illumination (Lillesand *et al.*, 2004), followed by a region of interest (ROI), a selected sample of a raster image, which enhances contrasts due to the smaller portion of the histogram selected. Following the ROI, a Maximum Noise Fraction (MNF) routine was performed to isolate and reduce noise in the data, which further prepares the data for easier processing (Boardman and Kruse, 1994). Subsequently, an Inverse MNF (Inv. MNF) procedure was undertaken, which returns data back to the original data format. Lastly, in order to increase the resolution of the data, Gram Panchromatic pan sharpening was used to simulate a higher spatial resolution. This method, which is considered more accurate than other pan sharpening methods, utilises higher resolution bands, namely the panchromatic band 8 (15 m spatial resolution) to increase the spatial resolution of the remaining bands (30 m resolution) (Laben and Brower, 2000). The final pre-processing product, namely the pan sharpened image, was then used to produce processed images.

3.2.2 Processing of Landsat 8 data

Processing of the pan-sharpened image was performed, using ENVI software, to produce the five images used for interpretation (Fig. 3.1). These five images include the (1) Principal Component Analysis (PCA), (2) Maximum Noise Fraction (MNF), (3) statistical composite 761, and (4 ad 5) two band ratio images (Fig. 3.1). Multiple images were created during processing; however, these images were chosen as they highlighted the greatest differences and displayed the most useful information.

Two spectral enhancement techniques were utilised: PCA and MNF transformations. The PCA image was chosen as it enhances the spectral response of an image. This is possible as the transformation compresses the repetition of values between the spectral bands producing uncorrelated bands that show the greatest variance for interpretation (Richards, 1999). Additionally, this spectral enhancement technique further reduces the noise fractions within the data set. Another spectral enhancement technique was utilised, namely the MNF transformation, as it reduces the noise within the spectral responses (Boardman and Kruze, 1994). This method is often used in both pre-processing and processing stages as it further identifies the coherent portions of the data, ultimately improving the spectral responses with the resultant image (Green *et al.*, 1988). This technique is favourable over PCA as the latter does not always produce images that are ordered from increasing to decreasing image quality. In contrast, the former transformation always produces this image quality order by means of the signal-to-noise ratio (Green *et al.*, 1988).

Band combinations and ratios, alternative approaches to spectral enhancements, were also used. Firstly, a simple band combination was selected to display the image, the RGB (red-green-blue) composite 761 (Fig. 3.1). Simply, Landsat 8 bands 7, 6 and 1 were assigned RGB, known as a colour composite. However, due to the problems associated with visual determination of colour composite assignment, a statistical analysis was performed to determine the most informative colour composite combination (Chavez *et al.*, 1982). This statistical method, the Optimum Index Factor (OIF), uses standard deviations and correlation coefficients to determine the OIF value for each of the Landsat 8 bands and their combinations (Chavez *et al.*, 1982). Therefore, this process determines the colour combination which provides the most informative image with the least amount of repetition between bands (Chavez *et al.*, 1982). With the use of the program ILWIS, the combination 761 was statistically determined to display the most informative Landsat 8 image.

Additionally, Chavez *et al.* (1982) outlines the importance of band ratios as these various combinations can enhance the image. These ratio images display spectral characteristics regardless

of the variations in brightness and contrast created from different scene illumination conditions resulting in enhanced differences between spectral signals and a reduction of the effects of topography (Lillesand *et al.*, 2004). In simple terms, various Landsat 8 bands (images) are divided or multiplied by one another to produce a new image. These new ratio images are then assigned to RGB for display.

Band ratios were chosen from previously published literature based on two broad criteria: (i) similar lithological units and (ii) discrimination between pelites, mafic rocks and non-mafic rocks. Simon *et al.* (2016) compared 35 band ratio combinations of the Dayang Bunting and Tuba Islands, Malaysia, which is comprised of similar lithologies when compared to the northern extent of the Palmenhorst Dome. These include granites, pelites, marbles and quartzites. In the study, three combinations were found to provide the greatest difference in spectral signatures: 4/3:5/2:3/1, 5/3:4/3:4/1 and 4/2:5/3:4/3 (Simon *et al.*, 2016). However, a visual inspection of band ratios (Fig. 3.3) suggests that the three combinations are redundant as they show minimal variability when considering the various rock types, and the ratios are merely varying colours of one another. Therefore, only band ratio 4/3:5/2:3/1 was used for interpretation in order to simplify interpretation. The band ratio combination 5/7:5/1:5/4*3/4 was selected due to the propensity for the composite to discriminate between pelitic schists (ratio 5/7), mafic rocks (ratio 5:1) and mafic versus non-mafic rocks (ratio 5/4*3/4) (Inzana *et al.*, 2003).

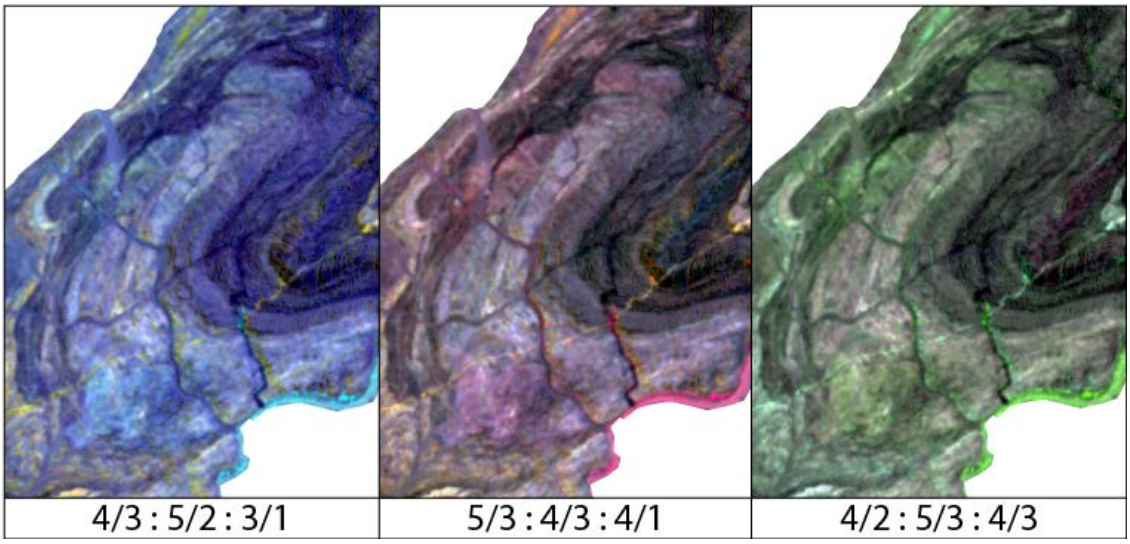


Figure 3.3: Images of multiple band ratios used for discriminating between different rock types showing minimal variability in their discrimination potential (from Simon *et al.*, 2016).

3.2.3 Selection of Hymap images

Hymap images were used to validate the lithological domains, refine these domains and fingerprint particular minerals and general rock types in each domain. This was justified by the greater spatial resolution of the Hymap images, with a resolution of 5 m x 5 m when compared to the significantly lower spatial resolution of the Landsat 8 data (30 m x 30 m). Additionally, hyperspectral scanners have higher spectral resolutions than Landsat 8 and acquire images in numerous and very narrow spectral bands, which span the entire visible and near to thermal infrared spectrum (Lillesand *et al.*, 2004). Processed maps include MNF VNIR 236 (Maximum Noise Fraction; Visible-Near Infrared), MNF SWIR 245 (Shortwave Infrared), Decorrelation Stretch 114/108/33 (DCS) and Multi-Mineral Rule Classified Map NOFEOX (no iron oxide included). Refined domains were established using the MNF VNIR 236, MNF SWIR and DCS 114/108/33.

Hyperspectral imagery is useful in determining the composition of lithologies (Lillesand *et al.*, 2004). Therefore, using the DCS 114/108/33 image, which has known compositions for each band, along with the multi-mineral map, a general classification of compositions can be determined for each domain. The RGB assigned bands each have a composition they are able to delineate (R= mafic MgOH minerals and carbonates, G= felsic minerals, AlOH-clays and micas and B= ferrous Fe minerals, including oxides). A RGB ternary plot showing the mixing of colours can aid in the determination of these compositions (see section 3.4.2). In contrast, the multi-mineral map determines the spatial extent of a plethora of minerals, due to the continuous collection of spectral responses within the VNIR range (Lillesand *et al.,* 2004*).*

3.2.4 Maps and image creation

Spectral domains were established using processed Landsat 8 images and Hymap images. Spectral domains in this study are defined as areas grouped due to similarities in texture and spectral reflectance assumed to represent similar lithologies or formations. Generally, these domains display homogeneous spectral responses with occasional highlights of another colour. However, this is usually consistent across the domain. In cases where these highlights are anomalous within the domain and yield a unique spectral response the term ”raft” is given to those features. These are often thin and faint but are the anomalies targeted for the presence of supracrustals, within the Abbabis Complex, during field mapping. First order discrimination of spectral domains was established with the use of Landsat 8 images, and then the Hymap images were used to refine these zones due to their increased spatial and spectral resolutions. A geological base map was established with the use of previously published geological maps (Lehtonen *et al.*, 1995; Longridge, 2012) and the known minerals within each formation assigning each domain to a Damara Supergroup

Formation or lithological unit within the Abbabis Complex. Software used for the base map creation include ArcMap and Global Mapper. Area is recorded as aerial area on the surface of the map and map thicknesses are recorded by measuring the approximate perpendicular thickness from contact of domain to opposite contact of domain.

3.3 Landsat 8 Results

From the processed Landsat 8 images produced (Fig. 3.4), namely the PCA, MNF, statistical composite 761, and multiple band ratios, spectral domains were established based on varying and distinct spectral signatures. Eight Landsat 8 domains were determined (Fig. 3.4), with each processed image clearly illustrating differences in responses from domain to domain. Each of these responses, within a single domain, has a characteristic colour as well as texture. The spectral responses are summarised and described in table 3.1 based on the eight Landsat 8 domains outlined (Fig. 3.4).

While each of these processed images show distinct differences within a domain, certain images highlight different features more effectively than others. For example, compositional differences between domain 4 and 5 are readily distinguished in the PCA and the band ratio 5:7/5:1/5:4x3:4, however, at the same time, if the PCA was only used, then domain 1 and 4 would show different boundaries. Another example includes variations, possibly reflecting lithological (or compositional) variations within the basement, which is the target for the study. The band ratios and the MNF highlight these anomalies in the basement best.

3.3.1 Landsat 8 Domains

The spectral response in each domain (Table 3.1) correlates to domains outlined in figure 3.4. The overall structural shape and outcrop pattern of the northern extent of the Palmenhorst Dome displays a folded geometry which can be seen in the remotely sensed images. For example, the ability to continuously trace folded domains around the central domains (1 to 3) as domes and folded axial trace has previously been identified in the sCZ (Smith, 1965) and the Nose Structure (Poli, 1997). Figure 3.4 inset, in the bottom right corner, shows the general orientation of the fold axial trace in the mapped area.

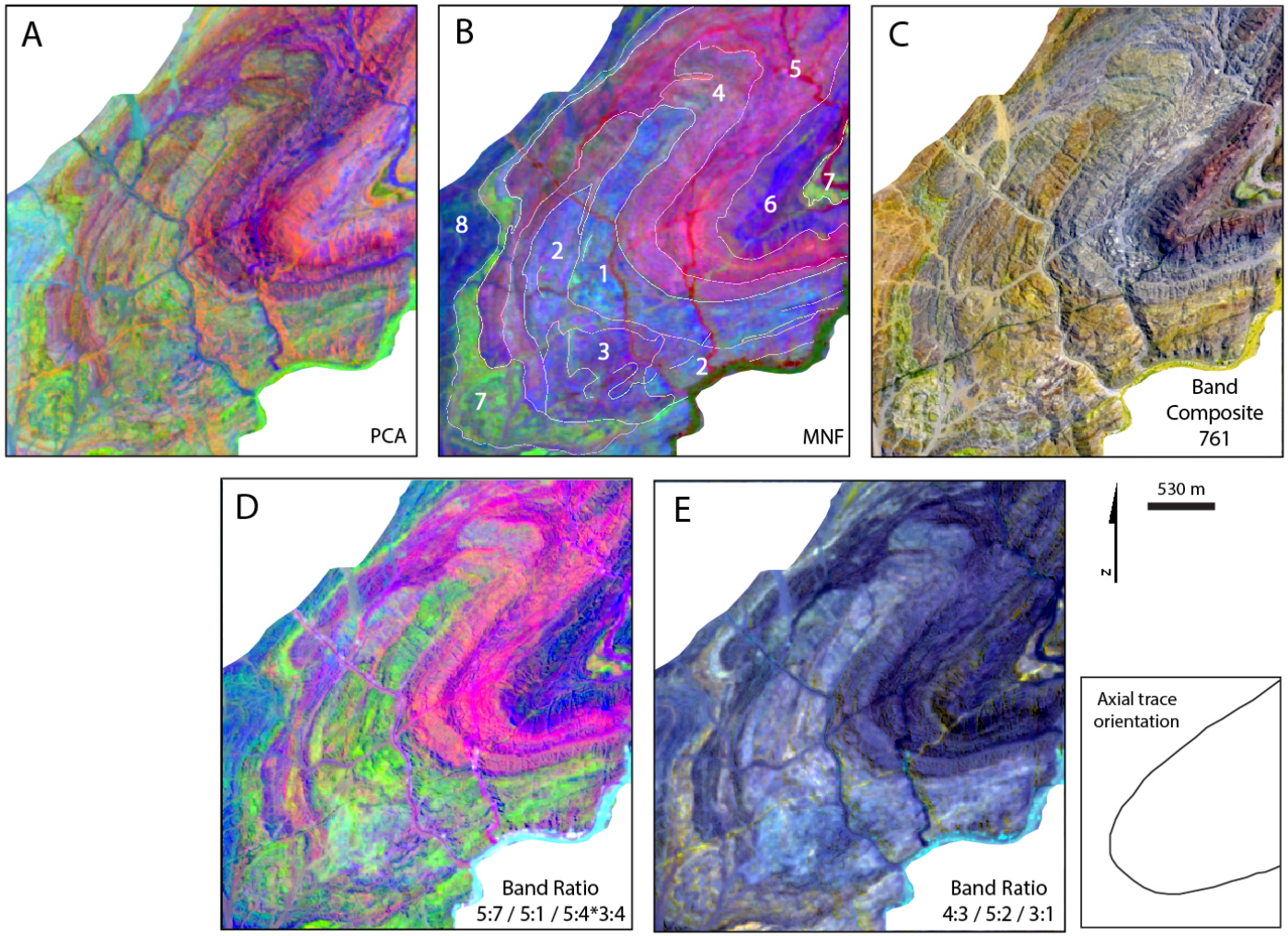


Figure 3.4: Processed Landsat 8 images used in the interpretation of the spectral domains and geological base map. Image (B) indicates the boundaries (white) for the spectral domains labelled from 1 to 8. These domains apply to all images. The inset, in the bottom right hand corner, illustrates the general orientation of the fold axial trace within the mapped area. Rafts are traced in white within domains 2 and 3 with the rafts in domain 3 displaying a folded geometry. Note the extension of thin slivers of domain 4 into domain 1 and 2 along the contact in the northern extent of domain 2.

Table 3.1: Table summarising the spectral colour responses from each spectral domain for all Landsat 8 processed images, namely the PCA, MNF, statistical composite, band ratio 5/7:5/1:5:4x3:4, and band ratio 4/3:5:2/3:1, as well as alluvium and cross-cutting dykes. Standardised RGB colours were used. A reference table can be accessed for comparison of the colours from https://www.rapidtables.com/web/color/RGB_Color.html.

Domain	PCA 123	MNF 123	Statistical Composite 761	Band Ratio 5:7 / 5:1 / 5:4 x 3:4	Band Ratio 4:3 / 5:2 / 3:1
1	Lime green with predominant traces of orange. Dark green rafts with orientation parallel to direction of contact.	Royal blue with undertones of cyan with minor dark violet. Traces of lime and indigo in isolated rafts.	Orange and sandy brown with highlights of beige and khaki. Isolated rafts of white and maroon are present.	Lime to lawn green with minor blue and purple. Isolated ratfs of yellow and medium blue are present.	Royal blue to medium slate blue with highlights of yellow. Isolated rafts of white and purple are present.
2	Sandy brown to lime green signals with isolated rafts of orange and purple.	Royal blue with undertones of blue violet. Lime rafts are present.	Sandy brown with plum highlights. Isolated rafts of white.	Sea green and orange with yellow. Isolated rafts of purple.	Slate blue with purple highlights. Rafts of sandy brown.
3	Sea green with isolated rafts of pink and blue.	A mixture of medium blue and purple with minor rafts of magenta and lime.	Sandy brown with maroon rafts.	Light sea green to violet with minor cyan in weathered areas. Isolated rafts of lime and purple are present.	Sky blue to royal blue with isolated rafts of white and navy.
4	Orange to deep pink which grades to a orange and sea green. Grades from domain 1 (green) to domain 4 (pink) in the north.	Variations of deep pink and purple with minor royal blue especially in weathered zone.	Medium purple with gradation to rosey brown.	Magenta and orange with minor purple along the edge of domain 1 and 4. Cyan and lime variations are present in the domain.	Dark slate blue with highlights of sky blue.
5	Magenta and purple with traces of blue that follow the direction of the domain contact.	Magenta with rafts of blue bands orientated parallel to domain contact direction. Grades to blue and purple when associated with weathered regions in the south.	Medium slate blue with dark blue and beige highlights.	Deep pink to magenta and purple with minor orange. Blue violet, purple and blue is more abundant in the south.	Dark blue to purple with highlights of royal blue.
6	Grades from domain 5 marked by orange to a medium purple and steel blue. Medium blue associated with weathered surfaces.	Medium blue and purple. Gradational with domain 5 which is marked by a gradation of magenta into purple.	Purple with variations of maroon along prominent v-shaped ridge.	Blue with minor highlights of purple.	Dark blue to purple with highlights of yellow and sandy brown.
7	Heterogeneous with a mix of lime to orange which grades along the domain contact direction.	Lime with royal blue and medium purple associated with weathered regions.	Sea green to lime green with dark green highlights. Variations of saddle brown along the domain contact.	Lime with minor blue variations.	Medium purple with yellow and sky blue (minor) highlights.
8	Cyan with rafts of lime and royal blue following the domain contact.	Navy blue with thin rafts of lime orientated parallel to domain contact direction.	Chocolate to orange with highlights of rosey brown in weathered areas.	Dodger blue to blue with variations of lawn green following domain contact.	Royal blue and blue with sea green and sky blue highlights.
Alluvium/ Tracks	Purple, medium blue and turquoise.	Appear deep pink to red with ocassional dark blue to purple in domain 5, 7 and 8	Yellow, violet and grey.	Purple to magenta and cyan.	Turquoise, yellow and navy.
Cross cutting dykes	Orange.	Lime.	Dark green.	Blue to lime.	Yellow.

Domain 1, approximately 3 km^2 in size (Fig. 3.4), is elongate and folded displaying a fairly homogenous spectral signature. However, anomalous signatures are present, best seen in the MNF image (Fig. 3.4.B) with lime and indigo rafts within the domain, which follow the general trend of the fold trace. This domain exhibits a constant mapped thickness of ± 680 m and is bound by domains 2, 3 and 4, which all display sharp and distinct contacts between domains. In the PCA image (Fig. 3.4.A), however, the northern extent of domain 4 and domain 1 display similar spectral signatures but are clearly distinct domains when compared with the other images.

Distinguishable from domain 1 by the lack of lime undertones, as seen in band ratio 5:7/5:1/5:4x3:4 (Fig. 3.4.D), domain 2 is compartmentalised into two portions. Domain 2 consists of northern and southern portions separated by domain 3, with spatial extents of 1.5 km^2 and 1.3 km^2, respectively, and is in contact with domains 1 and 4. Unlike domain 1, which only exhibits sharp contacts, domain 2 has a gradational contact with domain 3 and is characterised by two separate subdomains with faint spectral responses in most images. However, in band ratio 4:3/5:2/3:1 (Fig. 3.4.D) a marked spectral response of sky blue distinguishes domain 3. Significant isolated rafts occur within the domain and follow the general orientation of the fold and the orientation of the unit. The domain shows a mapped thickness of 690 m.

Domain 3 is most discernible in band ratio 4:3/5:2/3:1 (Fig. 3.4.E) and has an irregular contact and oval shape with an area of 2 km^2. This domain is discordant to the main fold shape as it does not follow the general orientation of the other domains. It is enveloped within domain 2 and displays sharp contacts with domains 4 and 7. Domain 4 displays the most noticeable and prominent rafts, which are discordant to the trace of the main fold, best seen in the MNF image (Fig. 3.4.B) as magenta and lime signatures. Additionally, a distinguishable feature of the rafts is the appearance of a folded geometry at a macro-scale.

Domain 4 (Fig. 3.4) envelopes the previous mentioned domains and has an area of approximately 5 km^2 and a map thickness of 590 m. The domain is distinct as the domain displays a varying thickness along the mean orientation of the fold, with the thinnest map extent along the western extent of the domain and fold. Another unique feature of the domain is the extension of slivers, approximately 90 m in map thickness, into domain 1 and 2 along the contact between these. Minor gradational changes within the zone are present in the PCA (Fig. 3.4.A), although the combination of various images show the mean spectral response does not change. Sharp contacts are observed between domains 1, 2, 3 and 5.

Similarly to domain 4, domain 5 extends into the former domain as thin slivers (Fig. 3.4). The size is approximately 4 km^2, with a relatively constant map thickness (700 m) thickening northwards. However, it terminates abruptly in domain 7 in the south-western corner of the map zone. Contacts with domain 6 and 7 are sharp and regular (north) to irregular (south) following the general geometry of the fold, whereas the contact with domain 4 is gradational. Spectral responses grade from magenta, in the north-east, to blue and purple along the edge of the fold, as displayed most clearly by the MNF image (Fig. 3.4.B) in the form of banding, which follows the orientation of the fold axial trace.

The contrast between domain 5 and 6 is distinct in most of the Landsat 8 images (Fig. 3.4), with a sharp contact. However, in band ratio 4:3/5:2/3:1 domain 5 and 6 display the same spectral signature (Fig. 3.4.E). Domain 6 is only present in the eastern portion of the map zone and does not enclose and envelop all the previous domains, unlike the preceding domains. The area is approximately 4 km^2, with an approximate thickness of 900 m. The domain displays internal spectral changes that are perpendicular to the mean trace orientation of the fold. A constant map thickness is maintained along the fold.

Domain 7 shows a mottled and mingled texture (Fig. 3.4). Noticeably, the domain is heterogeneous, has an irregular contact, which is sharp, and is thinner than the other domains, with thickening in the south creating a rounded bulbous shape. The approximate thickness is 1 km and an area of 4.5 km^2. Spectral changes occur along the edge of the fold trace.

In contrast, domain 8 is distinctly homogeneous throughout the domain. The contact is sharp between domain 7 and 8 and only occurs in the south-western extent of the map zone, but still follows the general trace of the fold. The domain has a thickness and area of approximately 290 m and 5 km^2, respectively.

Alluvium and the thin and prominent northeast-southwest trending cross-cutting dykes' spectral response are summarised in table 3.1.

3.4 Hyperspectral Imagery

The Landsat 8 domains, from the previous section, were improved and refined with the use of hyperspectral images (Fig. 3.5). The overall domain morphologies and areas did not change significantly. A detailed description of each domain's shape and morphology can be seen in the previous section (3.2.2) as they have not altered drastically from Landsat 8 results to the

hyperspectral results. The spectral response (Fig. 3.5) for each corresponding Landsat 8 domain is summarised in table 3.2. In addition to refinements of the domains due to better spatial and spectral resolution, these spectral maps are useful in attempting to correlate with previous geological maps due to their mineralogical and compositional information. Minerals were assigned to each domain using the mineral map. A brief description of refinements and minerals pertinent to each domain are explained below.

3.4.1 Domain refinements and anomalies

The hyperspectral images (Fig. 3.5) aided in the refinement of the contacts, such as between domain 7 and 8, which extend from the southwestern corner to the southeast following the overall geometry of the large fold in the map zone. This resulted in a change in shape of the domains, especially domain 4. In general, the domain contacts show greater resolution due to the ideal spatial resolution of the dataset.

Notably, the hyperspectral images (Fig. 3.5) show significant compositional changes within the domains themselves. The MNF VNIR image (Fig. 3.5.A) shows the true compositional complexity and intermingling within domain 7. Within domain 4 two zones of composition can be distinguished, accompanied by a gradation from mottled orange to lawn green (from south to north, respectively). Domain 2 demonstrates compositional differences within the domain with a complex signal in the northern portion of the domain. The MNF SWIR image (Fig. 3.5.B) introduces more complexities as it demonstrates the compositional and textural similarities between domain 2, 4 and 5 which were all separate in the Landsat domain analysis. Domain 2 displays a similarity to domain 1 in all three Hymap images (Fig. 3.5). Domain 8 displays significant heterogeneity, which was not visible from the distinctly homogeneous signal in the Landsat 8 images.

More delicate differences in composition are detectable with the Hymap sensors, making it possible for hyperspectral images to resolve isolated rafts within the domains. The MNF SWIR image (Fig. 3.5.B) shows the greatest potential for raft delineation. Domains 1, 3, 4, 5 and 7 contain rafts that run parallel to the contact of the domains, with domain 4 and 5 exhibiting alternating semi-continuous banding. A unique and distinct feature of domain 3 is the presence of purple rafts which display a folded geometry. The DCS image (Fig. 3.5.C) illustrates 3 groups of average spectral response. Domains 1 to 3 show blue to purple responses, while domains 4 and 5 are distinctly lime to lawn green in spectral response colours and, lastly, domains 6 to 8 are markedly blue to magenta in colour.

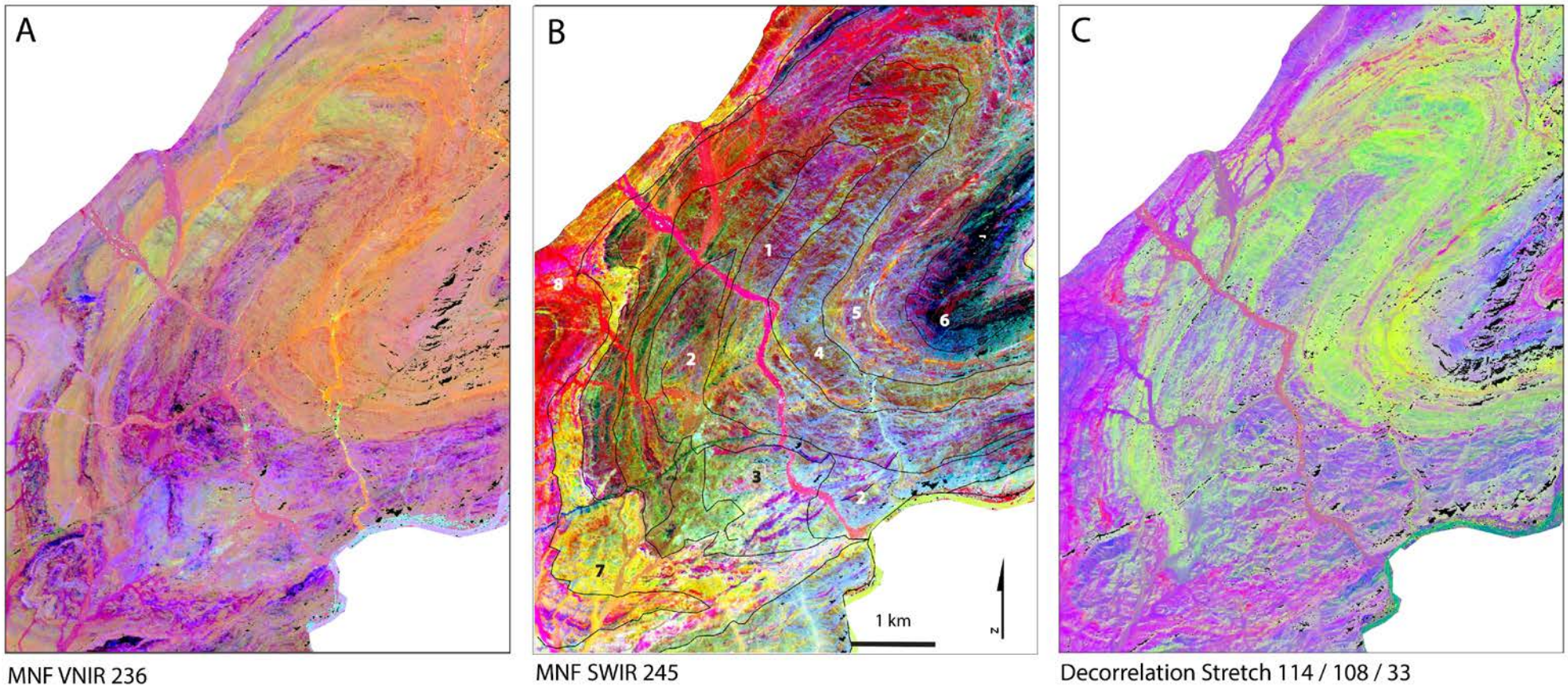


Figure 3.5: The three hyperspectral images used for the refinement of Landsat 8 domains: (A) MNF VNIR 236, (B) MNF SWIR 245 and (C) Decorrelation Stretch 114/108/33. Landsat domains 1 to 8 are also indicated on image B.

Table 3.2: Detailed summary of the spectral colour responses from the eight spectral domains for the three hyperspectral composites MNF VNIR 236, MNF SWIR 245 and the Decorrelation Stretch 114/108/33, as well as alluvium and cross-cutting dykes. A reference table can be accessed from https://www.rapidtables.com/web/color/RGB_Color.html for comparison of standardised RGB colours used as descriptors.

Domain	MNF VNIR 236	MNF SWIR 245	Decorrelation Stretch 114 /108 / 33
1	Purple and deep pink with notable linear NE-SW trending pattern in the northern extent of the domain. The southern extent shows mottled pink and purple texture. Purple rafts are present.	Mottled purple and royal blue grading to a green and yellow. Rafts of magenta to purple.	Mottled purple and green with thin blue bands that run parallel to the domain contact. Purple > green.
2	Mottled deep pink and violet texture with highlights of sandy brown. Magenta pink isolated rafts.	Mottled green to lime green with highlights of magenta and dark green.	Mottled green and purple. Green > purple.
3	Grades from royal blue to light pink from north to south, respectively. Rafts of dark blue to purple and salmon to yellow.	Grades from mottled green to yellow and cyan from north to south, respectively. Isolated and folded purple thin rafts are present.	Mottled green and purple with pink highlights and rafts.
4	Mottled orange and lawn green. Pink variations within the domain.	Mottled purple, cyan, magenta and yellow. Yellow is prominent parallel to the domain boundary. Red and green variations are present within the domain and grades from domain 2.	Mottled lime to lawn green with minor highlights of magneta and blue.
5	Mottled orange with faint lime and lime green bands parallel to the domain contact.	Alternating yellow, purple, orange and cyan bands that run parallel to the domain contact. Red variations are present in weathered zones and green banding which grades from domain 2 and 4.	Mottled yellow, lawn green with thin bands of magenta and violet that are parallel to the domain contact.
6	Salmon to coral with a prominent pink band.	Noticably dark domain with black , navy blue and purple which grades into light yellow and pink variations towards domain 7.	Violet with blue and magenta bands that are parallel to the contact of the domain. Minor highlights of yellow are present.
7	Noticeably heterogeneous. The domain displays a convoluted texture with colours ranging from pink, orange, purple, violet to green.	Yellow with highlights of magenta and lawn green. Displays a convoluted texture.	Mottled magenta and lawn green with minor highlights of blue and red. Pink > yellow.
8	Violet with variations of orange. Crimson bands can be seen parallel to the domains contact.	Red and orange with thin yellow bands parallel to the domain contact.	Alternating purple, magenta and blue banding parallel to the domain of the contact.
Alluvium/ Tracks	Violet, orange and magenta.	Lawn green, magenta and red.	Sea green, red, magenta, yellow and black.
Cross cutting dykes	Yellow to green.	Blue to green.	Black.

3.4.2 Domain compositions from Mineral Maps

Each domain's average composition can be approximately determined by the use of the DCS 118/104/33 composite image (Fig. 3.6.A) as well as the Multi-Mineral Rule Classified Map NOFEOX (Fig. 3.7).

The hyperspectral composite of bands 108/114/33 (Fig. 3.6.A) approximate signatures of (R) mafic MgOH minerals and carbonates, (G) felsic minerals, AlOH clays and micas, and (B) iron oxides and ferrous Fe minerals, respectively (Fig. 3.6.B). A summary of the RGB normalised values in each domain, calculated as a percentage that corresponds to the RGB ternary plot in figure 3.6.B, can be found in table 3.3. Additionally, the average compositions of each domain are summarised in table 3.3, with the use of the most abundant compositions used as the quoted average compositions.

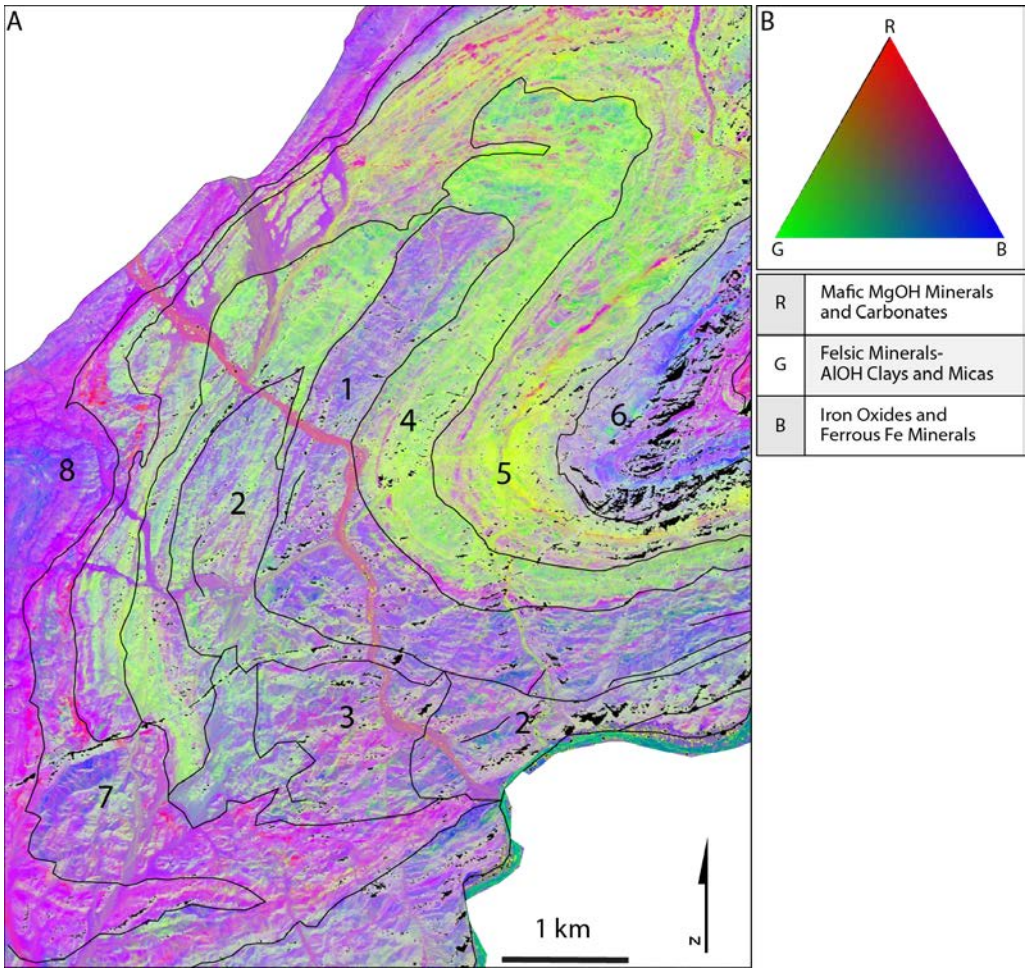


Figure 3.6: Decorrelation Stretch 114/108/33 (A) with the interpretive RGB ternary plot (B) showing mafic MgOH minerals and carbonates, felsic minerals, AlOH clays and micas as well as iron oxides and ferrous Fe minerals using RGB colours.

As previously mentioned, there are several domains that can be grouped, which result in 3 groupings based on a pair of observations, namely compositional (Table 3.3) and colour (Fig. 3.6.A) similarities.

Domains 1, 2 (southern portion) and 3 display mafic/carbonate-rich and iron-rich compositions and mottled purple and green colours. A second grouping includes domains 2 (northern), 4 and 5 with largely felsic/iron-rich compositions and clays with a marked lime to lawn green colour. Lastly, a more heterogeneous grouping includes domains 6 and 7, showing a predominance of mafic or carbonate-rich and iron-rich compositions and colours ranging from purple to magenta to blue.

Table 3.3: Table showing the RGB normalised values (quoted in percentages), established from the mean colour within each domain and then plotted on the RGB ternary plot in figure 3.6.A. Using the RGB normalised values, the average composition was determined with the greatest percentage compositions constituting the most likely composition of the domain. Most abundant spectral responses are listed in the mean composition row with brackets around the next most abundant spectral signature.

	1	2	3	4	5	6	7	8
RGB Normalised	30, 10, 60	10, 50, 40	50, 10, 40	30, 60, 10	40, 50, 10	10, 20, 70	55, 10, 35	40, 10, 50
Mean composition	(Mafic minerals and carbonates) + Iron oxides and ferrous minerals	Felsic minerals, clays and micas + (Iron oxides and ferrous minerals)	Mafic minerals and carbonates + (Iron oxides and ferrous minerals)	(Mafic minerals and carbonates) + Felsic minerals, clays and micas	(Mafic minerals and carbonates) + Felsic minerals, clays and micas	Iron oxides and ferrous minerals	Mafic minerals and carbonates + (Iron oxides and ferrous minerals)	(Mafic minerals and carbonates) + Iron oxides and ferrous minerals

The Multi-Mineral Rule Classified map (Fig. 3.7) shows the distribution of the minerals listed in the legend of figure 3.7. A summary of the minerals possibly encountered within each domain (Fig. 3.7) is provided in table 3.4. Generally, the spatial distribution of the minerals appears consistent with the refined domains showing varying assemblages of minerals in the respective domains (Table 3.4).

Domains 1, 2 and 3 display few mineral signatures. However, due to this feature the isolated rafts, previously mentioned within these domains, are highlighted. Compositions of muscovite-calcite, talc, phlogopite, calcite and biotite are most prevalent. The raft (muscovite-calcite) within domain 3 is emphasised, along with the fold geometry that was previously recognised. Figure 3.8 illustrates the rafts found within domain 1 to 3. The other rafts within the domains follow the general fold orientation. Markedly, the contact between domain 1 to 3 and domain 4 indicates an increase in the number of minerals detected with a wider range of minerals within an assemblage, typically 3 to 8 minerals within the subsequent domains (4 to 8) (Table 3.4). In terms of mineral content and diversity domain 7 is the most heterogeneous domain.

Tracks and alluvium, apparent as a southeast-northwest trending linear feature on the image, are marked by the presence of muscovite-calcite mix.

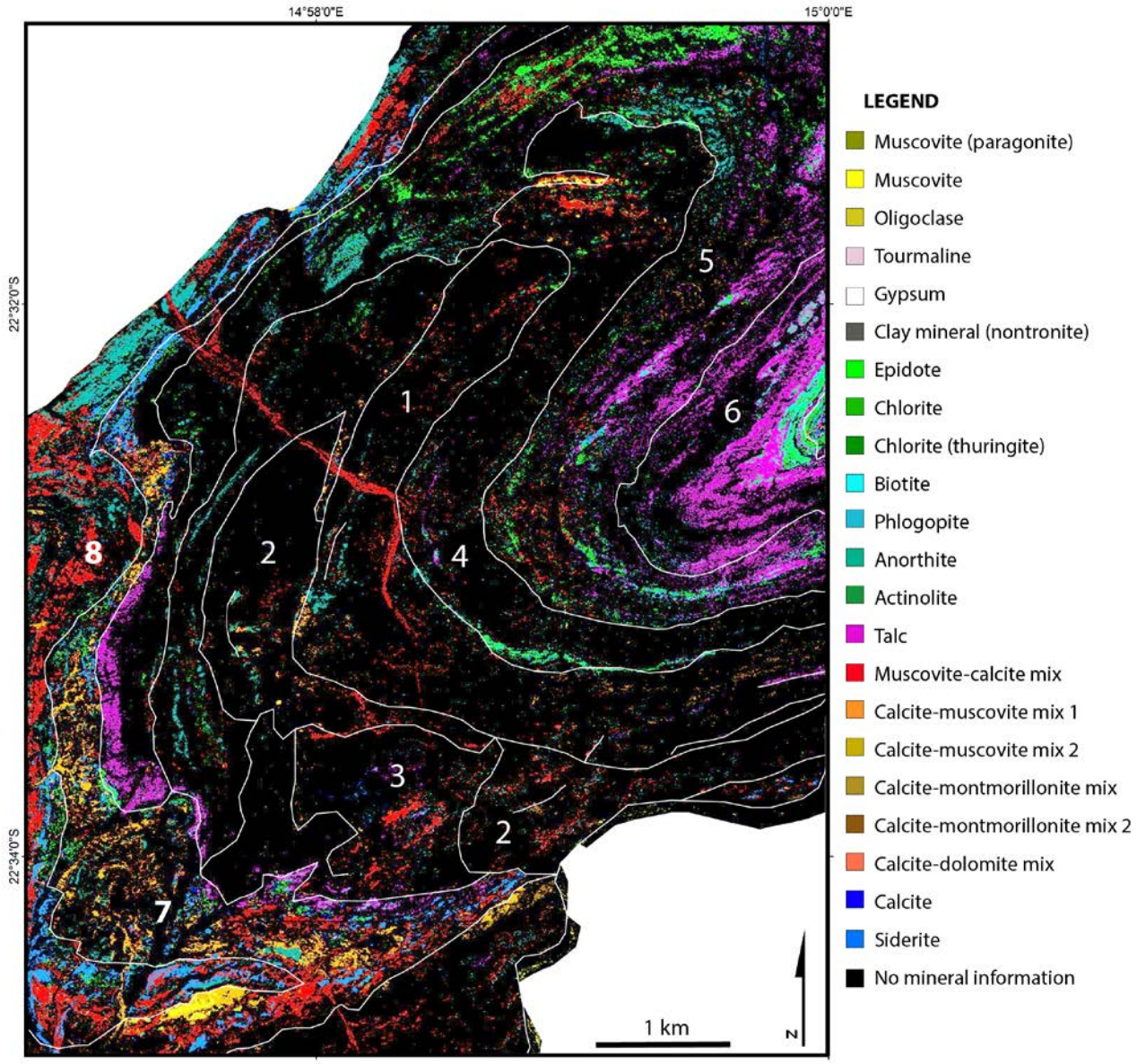


Figure 3.7: Multi-mineral Rule Classified Map NOFEOX (No Iron Oxide included) image of the northern extent of the Palmenhorst Dome. Mineral varieties that were noted from previous Hymap processing are indicated in brackets, but more common equivalents are noted. The spectral signatures are estimates and mineral identification was not performed in this study. Hyperspectral imagery was already processed. Montmorillonite is a type of clay mineral.

Table 3.4: Table summarising the minerals found in each domain in the Multi-Mineral Rule Classified Map of figure 3.7.

	1	2	3	4	5	6	7	8
Prominent Minerals	Muscovite-calcite, anorthite, calcite-muscovite	Muscovite-calcite, muscovite, biotite	Muscovite-calcite	Anorthite, muscovite-calcite	Talc, anorthite, epidote, muscovite-calcite	Talc, epidote, biotite	Muscovite-calcite, phlogopite, epidote, muscovite	Muscovite-calcite, anorthite, siderite
Other Minerals	Chlorite	Calcite, anorthite	Talc, siderite, calcite-muscovite, chlorite (thuringite), calcite, biotite	Talc, muscovite, epidote, calcite-muscovite	Chlorite (thuringite), calcite-muscovite, calcite-montmorillonite (clay mineral)	Calcite-muscovite, phologopite, thuringite (chlorite)	Talc, biotite, calcite, siderite, calcite-muscovite	Calcite-muscovite

3.5 Delineation of Rafts

Figure 3.8 highlights the isolated rafts documented in tables 3.1 and 3.2 in the Landsat 8 (Fig. 3.8.A and B) and Hymap (Fig. 3.8.C and D) images, respectively. The colours of each spectral signature of the rafts are explained in tables 3.1 and 3.2. Most of the rafts follow the same orientation as the trace of the fold and display a range of spectral signatures. The two rafts in the southwestern corner display a folded geometry and differ in colour from one another in each remote sensed image.

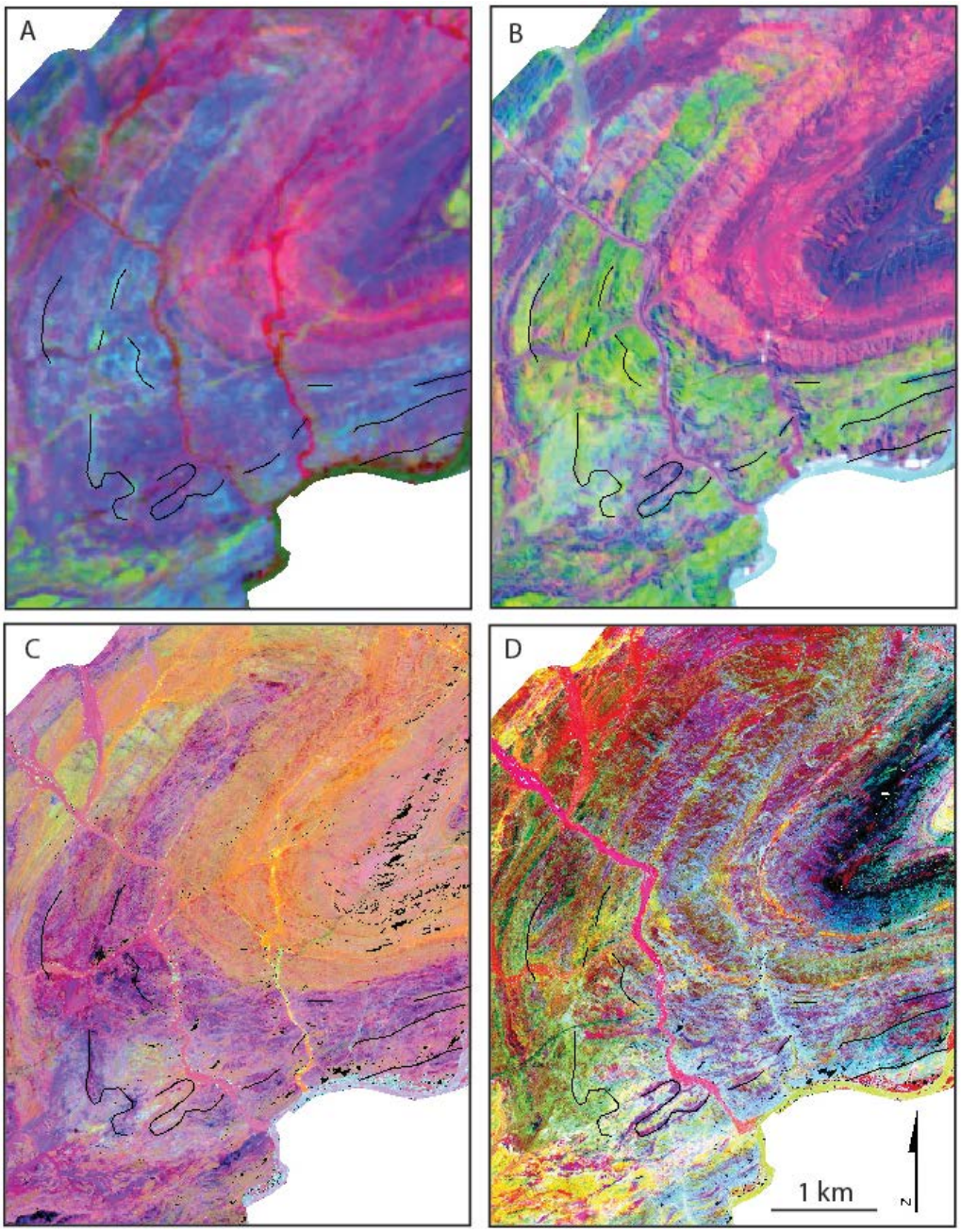


Figure 3.8: Landsat 8 images and Hymap images illustrating the isolated rafts within domains 1 to 3. (A) Landsat 8 MNF, (B) Landsat 8 band ratio 5/7:5/1:5/4x3/4, (C) Hymap MNF VNIR 236 and (D) Hymap MNF SWIR 245. Rafts shown as black lines in all images.

A greater extent of the Palmenhorst Dome is shown in the MNF VNIR Hymap image in figure 3.9. This image documents the presence of significantly larger rafts within the dome south of the mapping area. Additionally, when comparing the rafts within the mapping area and to the south, MNF VNIR images display similar colours of orange to pink and magenta (outlined in blue in Fig. 3.8). Likewise, the rafts in the south show a folded geometry, which is consistent with the shape of the rafts in the south.



Figure 3.9: The Hymap MNF VNIR image of the greater Palmenhorst Dome illustrates the presence of rafts within the dome – outlined by white lines for the greater extent of the dome and traced by black lines within the field area.

3.6 Discussion

Remote sensing is useful for mapping areas, in particular for selecting target points for more detailed lithological and structural mapping. Comparing the spectral domains with published geological maps (Fig. 3.10) helps to construct a base map prior to field studies. Most noticeably, the geometry of the spectral domains is consistent with the distribution of stratigraphic units documented in published maps and reports. The characteristic interference folding within the sCZ is documented in many instances (Gevers, 1963; Smith, 1965; Jacob *et al.*, 1983). These authors have noted structural patterns of refolded axial traces, whether their argument for deformation style proposed discreet (Gevers, 1963; Smith, 1965; Jacob *et al.*, 1983) or continuous deformation (Veenhof and Stel, 1991; Oliver 1994).

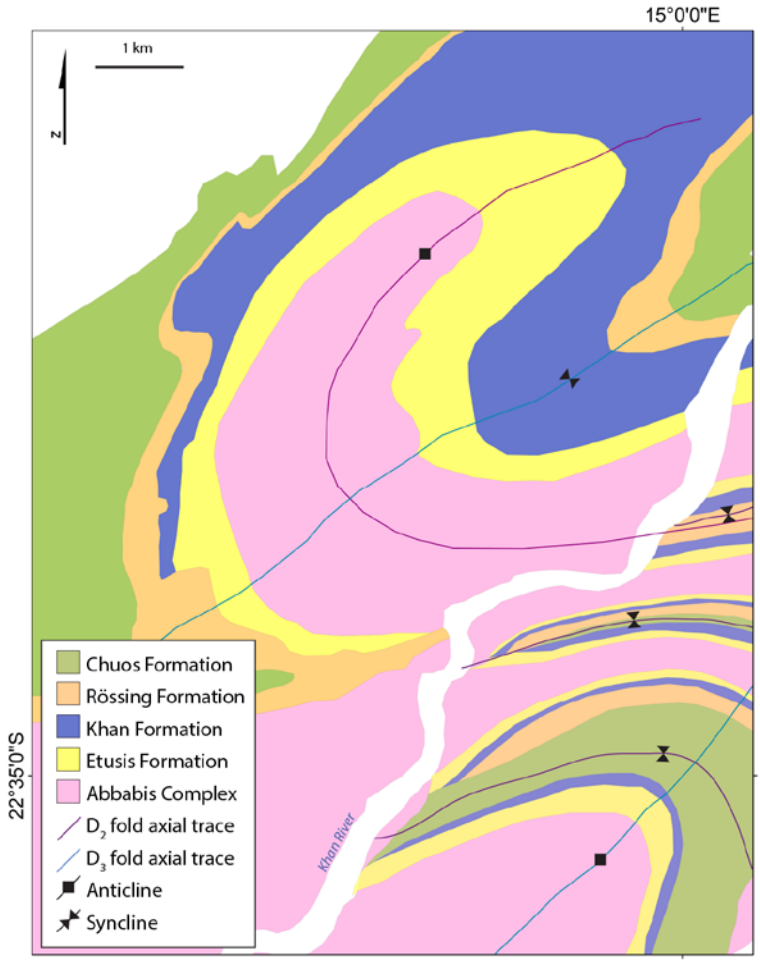


Figure 3.10: Geological map of the Nose Structure (modified after Lehtonen *et al.*, 1995 and Longridge *et al.*, 2011).

The D2 anticline is refolded by the northeast-southwest trending (fold axial plane) D3 event to produce the folding pattern seen in the map area (Fig. 3.11; Smith, 1965; Longridge, 2012). The spectral domains identified using remote sensing reproduce this shape within the Nose Structure as documented by published maps (Fig. 3.10). Based on the same structural pattern of the region (established from literature) that can be identified from the spectral domains identified, the general geology of the Nose Structure can be inferred, and domains can be correlated to existing geological units. Previous geological maps commonly show the presence of the Abbabis Complex occurring as cores to the Damaran Supracrustals and are therefore, dubbed as the characteristic basement-cored domes that define the sCZ (Smith, 1965; Oliver and Poli, 2001; Miller, 2008). Given that the domains display a similar structural trend to previous maps and that the domains follow pre-existing trends of the Damara metasediments and the Abbabis Complex, the presence of these characteristic basement-core domes can be correlated, and the aerial extent of the Abbabis Complex can be mapped out.

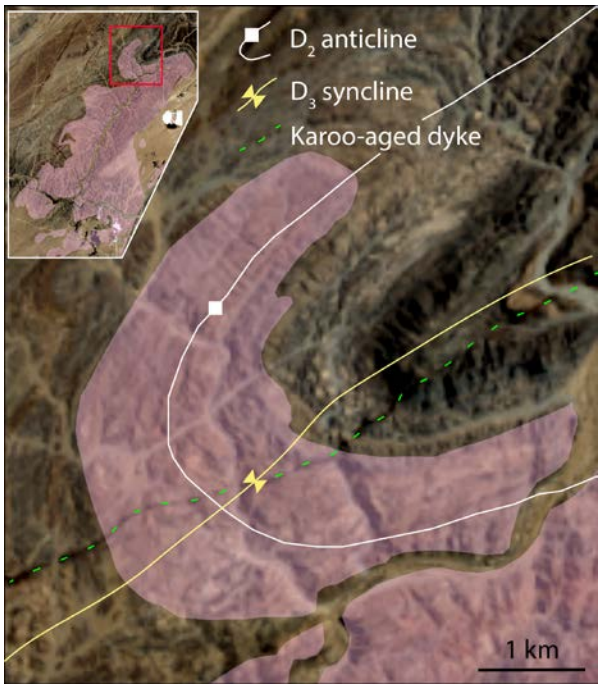


Figure 3.11: A Landsat image of the Nose Structure (in pink), showing the axial traces of the D2 and D3 folds. The inset, top left corner, shows the location of the Nose Structure as part of the greater Palmenhorst Dome (also shown in pink). A Karoo-aged dyke has been traced (green) from synthesis between the Landsat image and previous geological maps (Smith, 1965; Lehtonen *et al.,* 1995).

The extent of the Abbabis Complex can be inferred from the presence of the lower Damara Sequence identified in domains 4 to 8, due to the characteristic basement-cored domes of the sCZ (Poli and Oliver, 2001). Domains 1 to 3 are enveloped by the supracrustal rocks of the Damara Supergroup and most likely form the Abbabis Complex within the mapping area. The domains show a distinct felsic and mafic/iron component (Fig. 3.6), with alternating green (felsic) and purple (mafic/iron) bands. The Abbabis Complex is typically a mix of felsic granites and gneisses as well as more quartz-K-feldspar-biotite gneisses (Fig. 3.12; Smith, 1965). These alternating bands and a mottled texture, which shows faint northeast-southwest lineaments (Fig. 3.5.A and Fig. 3.6) in the northern extent of domain 1 and 2, may represent the described biotite and amphibole foliation or alignment of the gneissic basement (Miller, 2008). The mineral assemblage discernible in the images is defined by anorthite, muscovite and minor biotite, but is distinct from the supracrustals as the signatures in domains 1 to 3 yield less mineral information than the Damara metasediments (domains 4 to 8).

Hyperspectral compositions (from mineral map and DCS image 114/108/33), domain outcrop extents and pre-existing maps can aid in assigning the Damaran and the basement lithologies to particular spectral domains and a geological base map. The DCS image (114/108/33) and mineral maps provide approximations of diagnostic compositions for each domain. A well-informed assignment of each domain to a formation is possible based on documented mineral assemblages and lithological compositions of stratigraphic units within the lower Damaran sequence (Fig. 3.10).

Mineral assemblages and rock types within the lower Damara Supergroup and the Abbabis Complex are summarised in the stratigraphic column of Figure 3.12. Paired with the inferred hyperspectral compositions it is possible to assign each domain to a formation or the basement rocks.

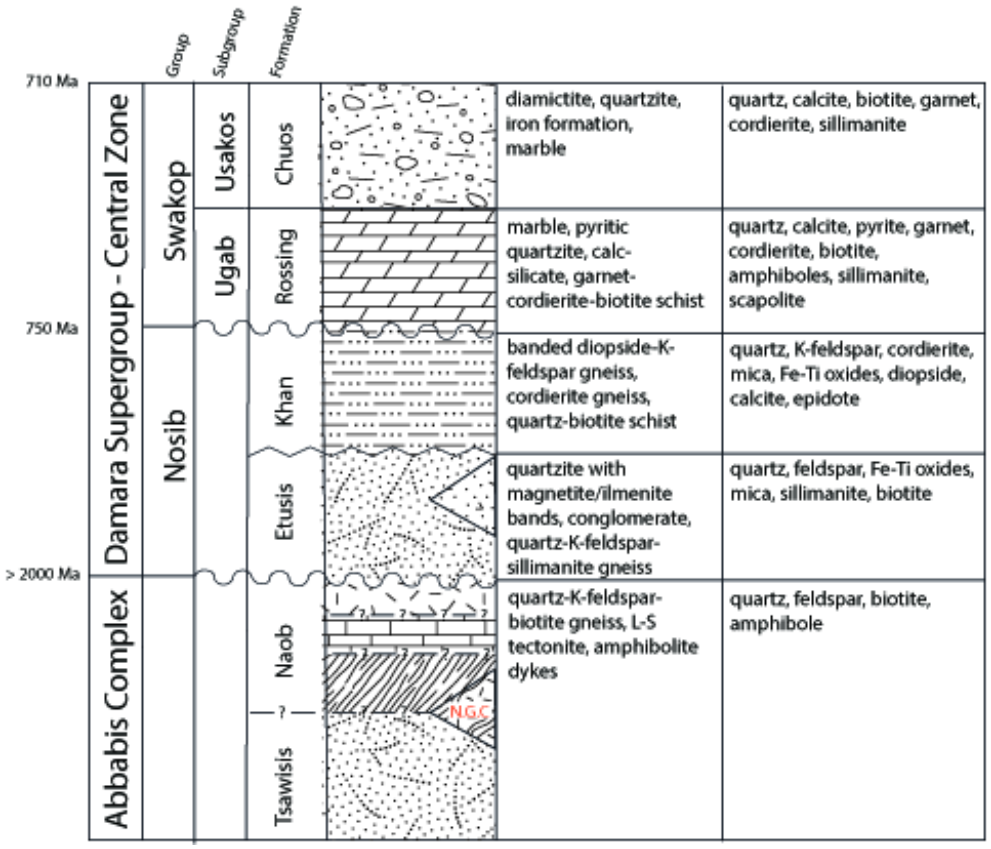


Figure 3.12: Stratigraphic column summarising rock types and associated mineral assemblages of the Abbabis Complex and Damara Supergroup (modified from Brandt, 1987; Badenhorst, 1992; Hoffman *et al.*, 2004; Miller, 2008; Longridge *et al.*, 2011; Rankin, 2015). N.G.C - Narubis Granitoid Complex.

Given the abundant felsic mineral signature from the DCS image (Fig. 3.6; Table 3.3), and the anorthite and muscovite signatures from the mineral map (Fig. 3.7), domain 4 may be best assigned to the Etusis Formation (Miller, 2008), with rock types that are characterised by high abundances of feldspar and mica (Fig. 3.12). The Etusis Formation has characteristically been noted as an arkosic quartzite (Smith, 1965; Henry, 1992; Miller, 2008), and therefore the abundance of feldspar is the most indicative mineral that can be used as the mineral distribution of quartz was not provided. The absence of a mafic component is consistent with published field observations (Miller, 2008). Henry (1992) described a gradational contact separating the Etusis and the Khan Formation, which likewise is consistent with the spectral domain signatures in the Landsat 8 images (Fig. 3.4) and the hyperspectral images (Fig. 3.5) that also display a gradational contact between 4 and 5. Additionally, the domain encloses domains 1 to 3, which is inferred to be the Abbabis Complex and therefore matches previous geological map outcrop extents.

Domain 5 exhibits a predominantly felsic/clay component (Table 3.3) and rafts consisting of a mix of mafic/carbonate minerals to iron oxide-rich compositions (Fig. 3.6) from the hyperspectral images. Considering that domain 5 has a gradational contact with domain 4 (assumed to represent the Etusis Formation) and the fact that the Khan Formation characteristically contains pelites and calcsilicates, domain 5 could represent the Khan Formation. The bulk composition of domain 5 is made of clays/felsic compositions (Table 3.3) and the clay mineral (montmorillonite; Table 3.4, Fig. 3.7) which could indicate a pelitic composition. While the pink rafts observed within the domain (Fig. 3.6) show mixed signatures of carbonates/mafics and iron-rich compositions which could suggest a calcsilicate assemblage, such as epidote (Ca, Fe), anorthite, talc (Mg), diopside (Ca, Mg) and calcite (Ca). All of these minerals could account for the mafic, carbonate- and iron-rich compositions. The felsic compositions (Fig. 3.6) could represent the presence of the banded K-feldspar gneisses observed in the Khan Formation (Fig. 3.12). Thus, the abundant calcsilicate, iron and pelitic signature correlates well with the known calcareous and ferromagnesian minerals documented for the Khan Formation lithologies (Fig. 3.12) (Sawyer, 1981). Similarly, domain 6 shows mineralogical similarities with the Khan Formation, although the mafic and iron signature is more prevalent (Table 3.3), possibly reflecting the abundance of ferromagnesium minerals (diopside and hornblende) within the Khan Formation (Sawyer, 1981; Hoffman *et al.*, 2004). The grouping of domains 5 and 6 is due to the compositional similarity, deduced from the DCS image (Fig. 3.6), the mineral map (Fig. 3.7) and spectral signatures in band ration 4:3/5:2/3:1 (Fig. 3.4.E), as well as the previous outcrop extent of the Khan Formation from previous maps.

The Rössing Formation is the most heterogeneous unit within the lower Damara Sequence (Longridge, 2012). This formation is therefore assigned to domain 7, which shows variable signatures in the Landsat 8 spectral responses (Fig. 3.4) and a marble-cake texture in MNF VNIR 236 image (Fig. 3.5.A). The compositional heterogeneity is also reflected by variable mineral assemblages (Table 3.4) of the mineral maps (Fig. 3.7). Domain 7 shows a calcareous nature (Fig 3.6 and Table 3.3), including calcium-rich minerals (calcite and epidote) which are characteristic of the marbles and calcsilicates of the Rössing Formation (Fig. 3.12) (Longridge, 2012). Additional diagnostic minerals of the Rössing Formation include siderite and talc (Longridge, 2012; Hoffman *et al.*, 2004) which correlates with the mineral map which located talc and siderite within domain 7. Lastly, domain 7 is noticeably thin, which is consistent with the estimated stratigraphic thickness of the Rössing Formation, especially in the Palmenhorst Dome region where the formation is typically attenuated (Nex, 1997; Longridge, 2012).

Domain 8 is homogeneous and shows calcareous/mafic and iron-rich compositions in the DCS image (Fig. 3.5.C). Seeing as the assigned band to red (in the RGB) for the DCS image represents either mafic or carbonate compositions, the red band could represent a mafic component. This would indicate that domain 8 had a mixed dominant composition of mafic and iron-rich lithologies and may represent the pelitic matrix of the Chuos diamictites that are typically biotite-amphibole schists (Fig. 3.12; Badenhorst, 1992; Hoffman *et al.*, 2004). The domain displays a distinctly calcium-rich mineral assemblage (Table 3.4), namely calcite and anorthite with minor iron minerals (siderite), determined from the mineral map (Fig. 3.7). This is consistent with reported minerals within the lithologies of the Chuos Formation, which comprises diamictites, iron formations and marbles (Fig. 3.12).

The northeast-southwest trending dyke (Fig. 3.11) that is straight, narrow and undeformed cross-cutting the other lithologies is considered to be similar in age to the Karoo Supergroup (Smith, 1965; Lehtonen *et al.,* 1995; Miller, 2008) and is not discussed in this study.

From the general fold geometry, the correlation of formations with domains, the recognition of the characteristic basement-cored domes enveloped by lower Damara Supergroup metasediments, and previous geological maps (Fig. 3.10) provides sufficient information to create a geological base map to assist in further field studies. However, there are numerous iterations of geological maps for the northern extent of the domain of the Palmenhorst Dome (Fig. 3.13) that can be used for comparison, but the geological map after Lehtonen *et al.* (1995) is most similar to the spectral domains determined by remote sensing. The domains have a similar geometry, distribution of lithologies and structural trend to this map and therefore, this map was used to serve as a guide for the examination of the distribution of lithologies and confirmation of spectral domain characterisation resulting in the geological base map (Fig. 3.14).

The Etusis and Khan formations display changes in spectral response both along and perpendicular to the D3 axial trace (domains 4, 5 and 6 in Fig. 3.4.D and Fig. 3.5.B). In particular, the Etusis Formation is documented to show pronounced lateral lithological heterogeneity (Henry, 1992), including arkoses, quartzites and conglomerates, but in certain areas the formation does not show the complete stratigraphy (Henry, 1992). Therefore, based on the above observations, the heterogeneous spectral response of domain 4, particularly in the Hymap MNF VNIR and SWIR images (Fig. 3.5.A and B), may represent lateral changes in facies as the spectral response changes along the axial trace of the D2 fold. However, this could also represent a structural or metamorphic overprint due to the high grade metamorphism and deformation experienced in the Damara Belt (Miller, 2008).

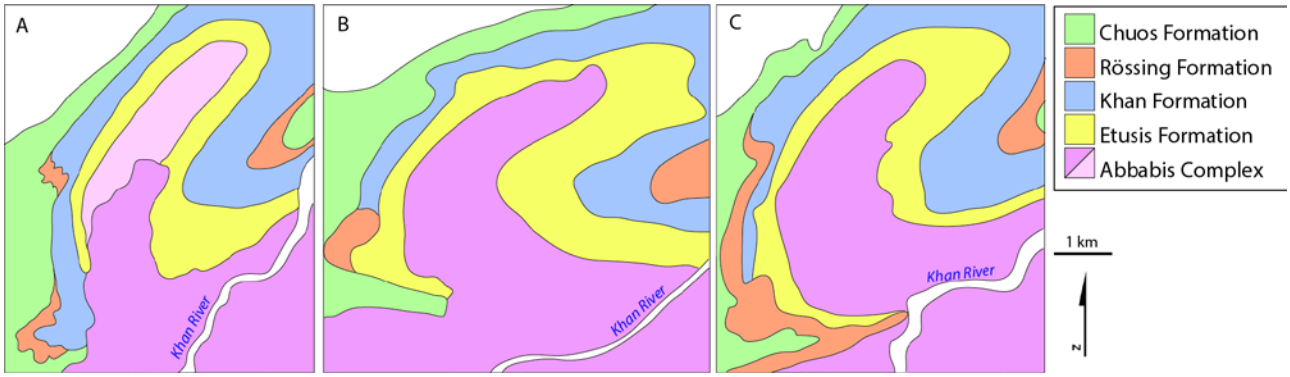


Figure 3.13: Different maps produced by (a) Smith (1965), (b) Volkman *et al.* (1988) and (c) Lehtonen *et al.* (1995) of the northern extent of the Palmenhorst Dome showing the evolution of mapping. These maps have been traced and do not necessarily indicate a migrating Khan River but rather highlights how there are varying outcrop patterns according to different authors.

Similarly, domain 5 is interpreted as the Khan Formation and displays spectral response heterogeneity. These spectral changes are manifested perpendicular to the orientation of the trace of the D3 fold between the Khan and the Etusis formations. Interfingering between the Khan and the Etusis formations has been reported (Jacob, 1974) and may account for the transitional domain boundary seen in the Landsat 8 PCA and band composite 761 (Fig. 3.4.A and Fig. 3.4.C, respectively). Based on spectral characteristics, domains 5 and 6 are grouped together and interpreted as the Khan Formation. The Khan Formation has compositional differences across the upper to lower units (Barnes, 1981; Nash, 1971; Longridge, 2012), showing distinct units ranging from pyroxene-amphibole-feldspar-banded gneiss to diopside-feldspar gneiss, although this differs from locality to locality. Thus, domains 5 and 6 could possibly be split into the lower and upper units of the Khan Formation, respectively. Similar lithological changes can be seen in other formations, due to alternate and cyclic banding reflecting cyclical changes in environmental conditions and provenance during deposition (Henry, 1992). Evidence of this is shown in the domains 4, 5 and 8 in the Landsat 8 PCA (Fig. 3.4.A), the Hymap MNF SWIR (Fig. 3.5.B) DCS (Fig. 3.5.C) with alternating colours in the spectral response.

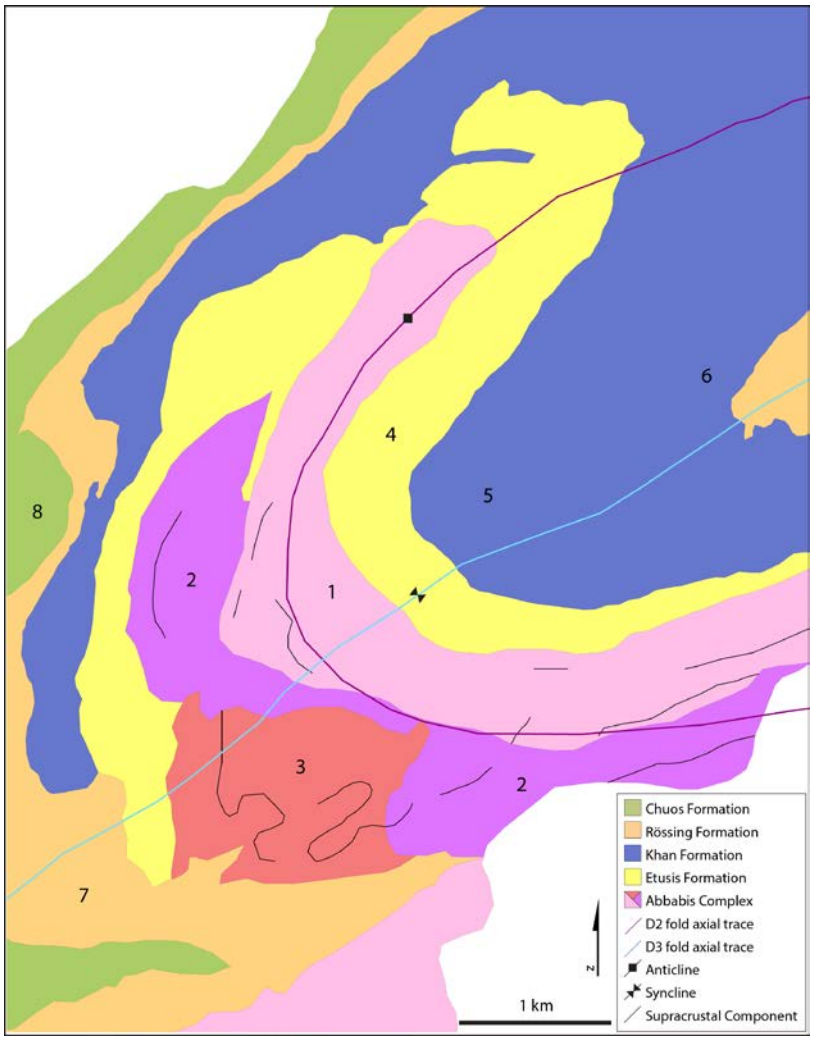


Figure 3.14: Proposed geological base map integrating spectral domain interpretation and stratigraphic subdivision from published geological maps (Lehtonen *et al.*, 1995 and Longridge, 2012). Domains are numbered from 1 to 8.

The distribution of lithologies and assignment to stratigraphic units within the Palmenhorst Dome was recently revised. Lower Damara Supergroup metasediments have been identified within the previously mapped undifferentiated granite-gneiss basement rocks of the Abbabis Complex southeast of the Khan River (Fig. 3.10; Barnes, 1981; Longridge, 2012). Longridge (2012) demonstrated multiple D2 synclinal rafts of Damaran sequence within the highly migmatised dome, which had not been previously identified. Considering the plausible presence of the rafts within the Abbabis Complex, domains 1,2 and 3, of the northern Palmenhorst Dome might represent supracrustal components (Fig. 3.14). The mineral map (Fig. 3.7) documents the presence of rafts extremely well due to the lack of mineral signatures in domains 1 to 3, in comparison to the supracrustal rocks. The geometry of most of the rafts, with the exception of those in domain 3, are simple linear rafts, which follow the general orientation of limbs or D2 axial trace. This is consistent with the interpreted structural pattern proposed by Longridge (2012) as D2 synclines that were refolded by large scale D3 event folds.

Using the supracrustal infolds identified by Longridge (2012) as a comparison, a distinction can be made between the mapped basement dome and the supracrustal infolds within the larger region of the Palmenhorst Dome (Fig. 3.9) southeast of the Nose Structure. As seen in figure 3.15, the rafts and supracrustal components (from the greater Palmenhorst Dome), initially outlined in figure 3.9, overlap considerably with the lower Damara sequence mapped by Longridge (2012). The spectral response (Fig. 3.15) for these larger rafts are markedly homogeneous (see Fig. 3.9 for a version of the image without superimposed geology) despite the synclines mapped as the Etusis, Khan, Rössing and Chuos formations (Longridge, 2012). This spectral response colour is similar to the spectral response colours for the possible smaller supracrustal components seen in domains 1 to 3 (Fig. 3.8). In addition, these larger rafts, south of the Khan River, display spectral responses that are not similar to any of the spectral responses observed in the other domains (1 to 8) within the mapping area. Therefore, based on the comparison between known Damaran infolds and spectral responses, the presence of these rafts (that are not folded) in domains 1 to 3 (Fig. 3.8) most likely represents infolded Damaran metasediments.

Alternatively, the rafts could represent folded amphibolite dykes, particularly the folded rafts in domain 3 (Fig. 3.8 and Fig. 3.15) due to their geometry. Amphibolite dykes within the sCZ have typically been associated with the basement rocks and are Palaeoproterozoic in age (Smith, 1965). However, some amphibolites have been found to cross-cut Damaran sediments, and recent U-Pb zircon dating by SHRIMP indicates Pan African ages (557.2 ± 7.4 Ma) for the emplacement of these dykes (Longridge, 2012; Longridge *et al.*, 2014). Nevertheless, amphibolites are well documented within the basement rocks. It is argued here that some rafts represent Palaeoproterozoic amphibolite dykes because their deca-meter scale folded geometry show a similar orientation as the Abbabis Complex with northeast-southwest trending fold axial traces (Fig. 3.15). Additionally, the spectral response of the folded rafts is consistent with mafic to iron-rich compositions (Fig. 3.6) and the presence of the calcite (Fig. 3.7). Hornblende as major constituent of amphibolites can account for the mafic and iron components as well as elevated Ca contents resembling calcite. Therefore, the folded rafts are most likely amphibolitic in nature, while the remaining rafts could represent a supra-crustal component. These (and other) mafic rafts (Fig. 3.6) may, in fact, represent the Khan Formation as the pelitic schists. These schists commonly contain abundant diopside, hornblende and biotite, could also account for the mafic composition and elevated Ca, and therefore the spectral responses cannot delineate between the rafts representing Khan Formation or amphibolite dykes. Therefore, ground truthing is required to truly evaluate this, although the general geometry and aspect of these

rafts do not follow the trends observed by Longridge (2012), which is useful in predicting the general orientation of these possible infolds.

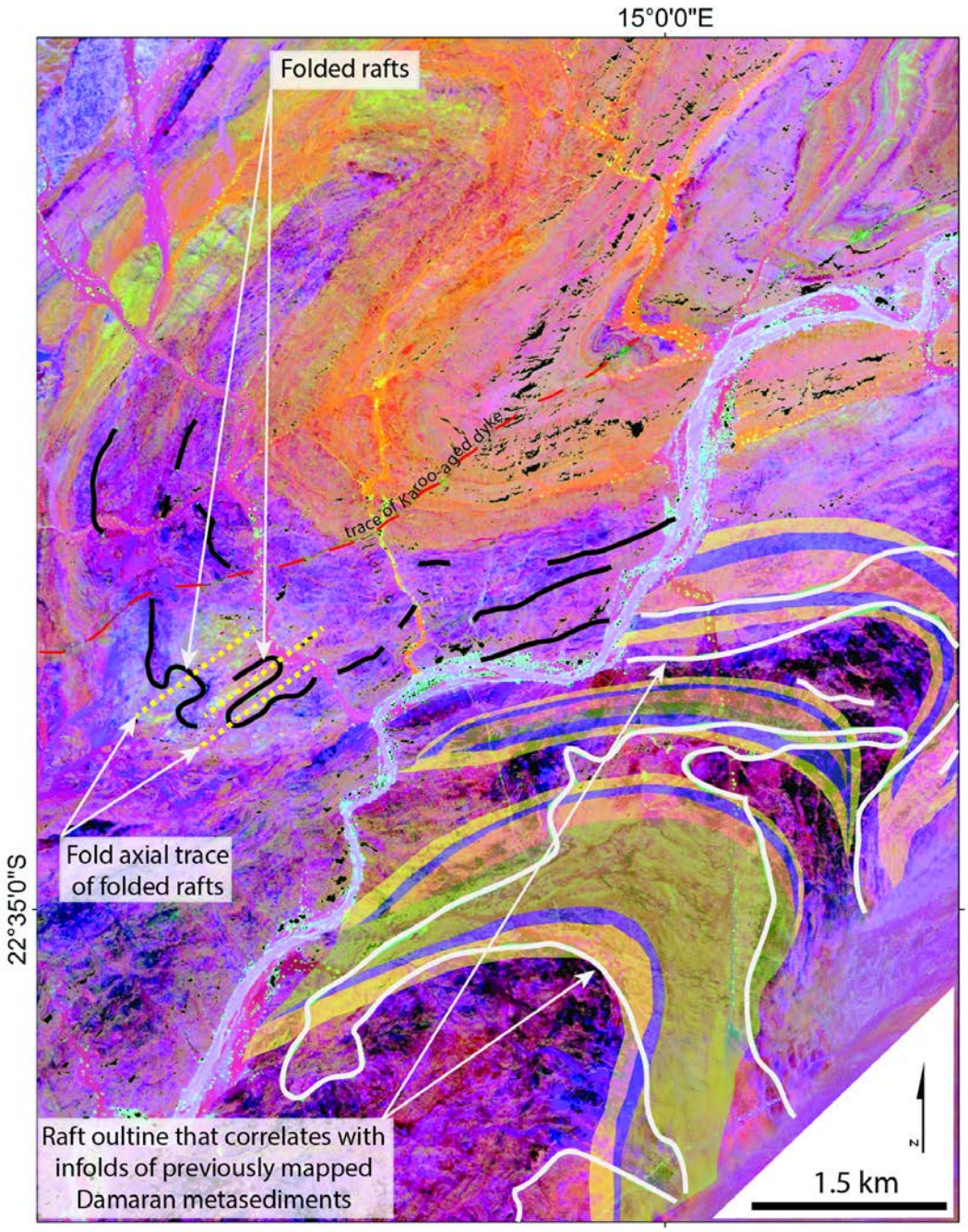


Figure 3.15: MNF VNIR image showing the Nose structure as part of the larger Palmenhorst Dome with proposed supracrustal components found in this study (outlined in black and white). The white rafts correlate with infolded lower Damaran sequences proposed by Longridge (2012). Overlain geology: Yellow= Etusis Formation, Blue= Khan Formation, Orange= Rössing Formation and Green= Chuos Formation. Proposed axial traces of the folded rafts are indicated (yellow) and a trace of the Karoo-aged dyke (red) is also shown.

Smith (1965) suggested a stratigraphy for the Abbabis Complex in the type locality of the Abbabis Farm 70, north of the mapping area, comprising the Narubis Granitoid Complex, the Tsawisis Formation and the Naob Formation. Poli (1997) later suggested possible lithologies of the typical

Abbabis Complex stratigraphy within the Palmenhorst Dome. Therefore, the distinct domains 1 to 3 seen within the Landsat 8 (Fig. 3.4) and hyperspectral images (Fig. 3.5) could represent the various stratigraphic units of the Palaeoproterozoic Abbabis Complex. From the DCS image (Fig. 3.6) domain 1 shows a distinct repetitive linear fabric, which could possibly represent the augen gneiss of the Narubis Granitoid Complex (Smith, 1965; Marlow, 1981). On the other hand, the higher proportion of a felsic component within domain 2 (Fig. 3.6), especially in the northwest portion, is most consistent with the quartz-feldspar gneisses of the Tsawisis Formation (Sawyer, 1981). Lastly, domain 3 shows calcareous, mafic and iron-rich components that are consistent with the calcsilicates and marbles as well as the biotite- and hornblende-bearing schists of the Naob Formation (Smith, 1965; Marlow, 1981; Sawyer, 1981). However, these domains are less distinct from one another when analysing different Landsat and hyperspectral images and may not truly represent the stratigraphy. For example, the south-eastern extent of domain 2 is most distinct from domain 1 in the Landsat 8 band composite image 761 (Fig. 3.4.C), whereas the other Landsat 8 images show very little difference between the two (Fig. 3.4) and would require careful consideration in the field.

Alternatively, these varying spectral responses within the domain could represent varying quantities of felsic anatectic melt that crystallised to form varying volumes of granitic material. In the past, many of the basement-cored domes were mapped as undifferentiated granite-gneisses and a stratigraphy for the Abbabis Complex was not established (Smith, 1965; Miller, 2008). The Palmenhorst Dome was no exception and was mapped as various Abbabis Complex granites and gneisses (Smith, 1965). However, recent studies have begun to unravel the complexities of this dome, such as the synclinal infolds of Damaran metasediments (Longridge; 2012). Toe *et al.* (2013) documented increasing partial melt intensities towards the core of the Palmenhorst Dome in the southern margin proposing three domains of partial melting intensities, which gave rise to a stratification of the crust within the sCZ. Given this, the three domains within the basement rocks could represent the varying degrees of high-grade metamorphism and anatexis and may confirm the subdivision into metatexites to diatexites (Toe *et al*., 2013). Given that domain 3 is towards the core of the Palmenhorst Dome and has a discordant morphology this domain could represent an intense zone of partial melting in order to produce a (diatexite) intrusive body.

Determining the difference between the Etusis Formation and gneisses and granites of the Abbabis Complex is inherently difficult due to the similar quartzofeldspathic compositions (Longridge, 2012). However, despite this difficulty there are still distinct differences between domain 4, interpreted as Etusis Formation and those domains (1 to 3) interpreted as basement. Domains 1 to 3 show a distinct mafic component (Fig. 3.6), and are quite similar, whereas domain 4 interpreted as Etusis Formation

shows a stark contrast with almost completely felsic compositions. Evidently, the Abbabis Complex fabric, which is mainly defined by biotite and hornblende (Smith, 1965), has a strong spectral response which creates a strong mafic undertone in the DCS image (Fig. 3.6) and allows for the distinction between the Etusis Formation and Abbabis Complex at a megascopic scale. Additionally, in the mineral map (Fig. 3.7), the Abbabis basement rocks show a drastic and noticeable lack of mineral spectral responses, creating an additional discernible feature for the basement compared to the Etusis Formation. This could possibly be attributed to the basement-cover detachment ("Khan River detachment" of Poli and Oliver, 2001), although remote sensing cannot validate its existence.

Lastly, the linear hatching in domain 1 and 2 (Fig. 3.4 and Fig. 3.5), which occasionally extend into domain 4 and 5, depending on the remote sensed image, represent the late stage pegmatites that trend northeast-southwest. This trend is consistent with the general orientation of the D3 pegmatites from literature (Fuchsloch *et al.*, 2018). These features are thin, appear to cross-cut all the units and are not folded. Based on previous accounts, these pegmatites are relatively undeformed in comparison to the other Damaran rocks and show cross-cutting relationships, which suggests that these pegmatites are related to post-tectonic extension (Nex and Kinnaird, 1995; Fuchsloch *et al.*, 2018).

3.7 Conclusions

Remote sensing was useful for constructing a base map for the northern extent of the Palmenhorst Dome. The domains were assigned formations and basement lithologies with the use of Landsat 8, hyperspectral (mineral maps) imagery and previous geological maps. Domains 1 to 3 form the core to the surrounding domains and is considered to be the Abbabis Complex, whereas domains 4 to 8 are considered to be Damaran supracrustals.

The Abbabis Complex represented by domains 1 to 3, displays a distinct felsic mineral combined with a mafic signature and shows compositional differences within the basement-cored domes themselves. This may represent a simplified stratigraphy as identified at the type locality (Smith, 1965) or variations in concentrations of crystallised partial melt. Domain 4 most likely represents the Etusis Formation due to the high abundance of anorthite in the mineral maps and the fact that it shares a contact with the basement lithologies. Differences are apparent between the Abbabis Complex domains and Etusis Formation domains, such as the mafic signature and lack of an abundant mineral signature in the mineral maps in the basement domains. The contact between the Etusis Formation and the Khan Formation (domain 5 and 6) is gradational and grades into a more carbonate-rich signature, consistent with the Ca in calcsilicates and diopside-rich semi-pelites of the

Khan Formation. The Khan Formation is divided into the upper (domain 6) and lower (domain 5) Khan Formation. The heterogeneous nature of the Rössing Formation (domain 7) makes this formation an ideal marker horizon as it has a distinct varied spectral signature, which is in contrast to the Chuos Formation (domain 8). Domain 8 shows a homogenous signature that is mafic in composition and therefore possibly resembling the pelitic matrix of the characteristic meta-diamictite of the Chuos Formation. Lateral facies, metamorphic or structural changes can possibly be identified from remote sensing too.

Landsat 8 and hyperspectral mineral maps can be utilised to delineate anomalies (rafts) within the basement lithologies. This is based on previous studies that suggest a possible stratigraphy for the basement rocks (Smith, 1965) or D2 synclinal infolds of Damaran metasediments within the basement (Longridge, 2012). These rafts are proposed to represent either infolds of Damaran metasediments or amphibolite dykes.

Possible late-stage northeast-southwest pegmatites are observed to cross-cut the basement and supracrustal domains.

4. Field studies

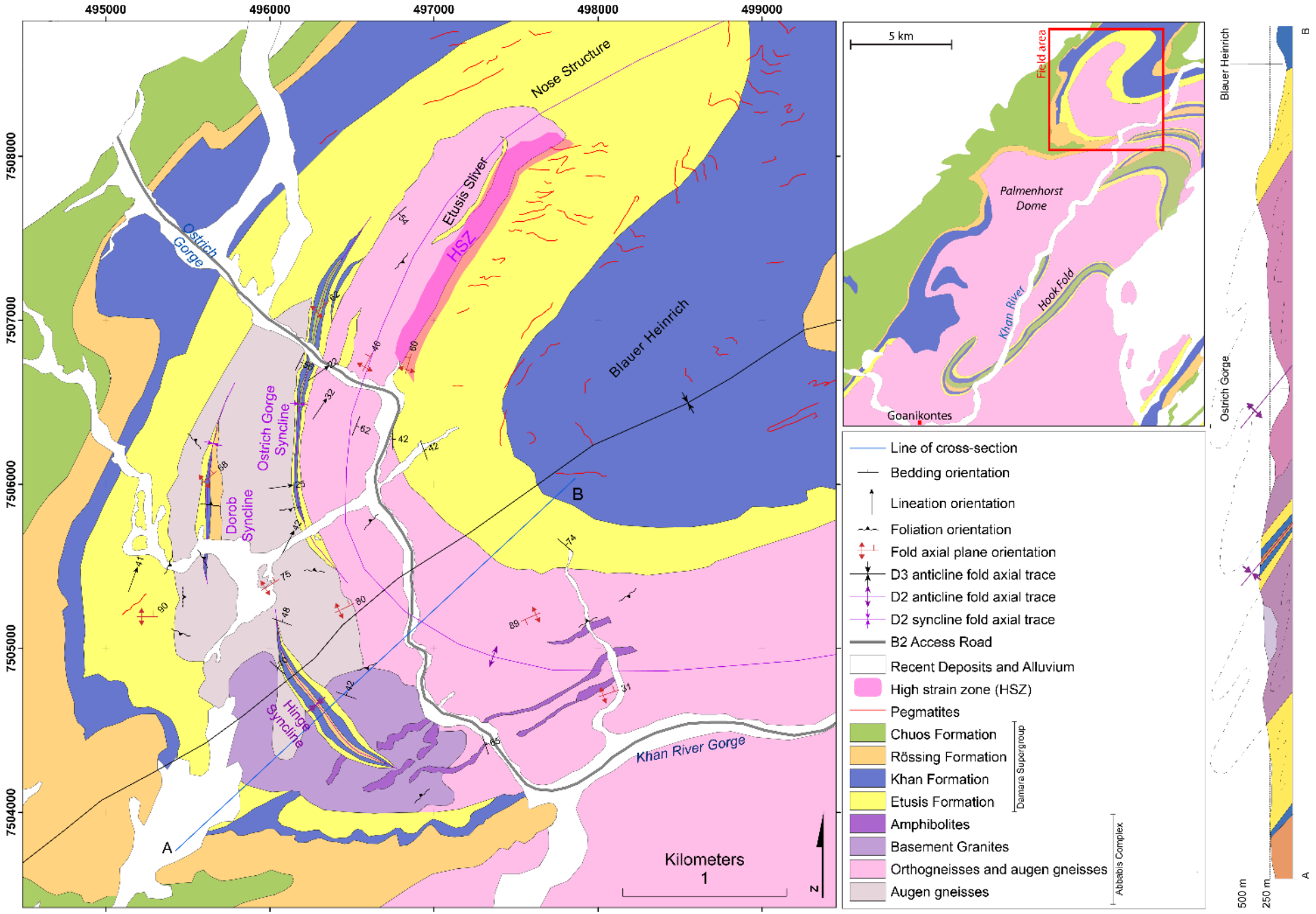
4.1 Introduction

Field mapping took place during two field seasons within the Palmenhorst Dome concentrating on the Nose Structure, an area of approximately 25 km^2. These field seasons focused on identifying possible Damaran Sequences within the Abbabis Complex, based on supracrustals identified within basement-cored domes by Longridge (2012), and their distribution. Additionally, a focus was placed on evaluating the basement-cover contact, history of deformation and intrusive relationships of the igneous rocks, with attention to characterisation of migmatites to determine varying partial melt intensities. Field-based studies included lithological and structural mapping, both at a (~ 1:15,000) map scale and large-scale pavement maps within the basement. The results for this chapter are subdivided into the stratigraphy, intrusive rocks, structure, and migmatites of the area. A geological map (Fig. 4.1) was produced showing the megascale interference (D2 and D3) folding, synclinal infolds, and the distribution of the lithologies and mappable intrusions.

4.2 Stratigraphy

Within the Nose Structure of the Palmenhorst Dome, the *ca.* 2 Ga Abbabis Complex basement rocks (Jacob *et al.,* 1978; De Kock *et al.,* 2000; Longridge *et al.,* 2014) are surrounded by a sequence of Damara Supergroup lithologies (Smith, 1965). The Abbabis Complex, at the type locality, displays a varied stratigraphy (Smith, 1965), and is identified in various domes across the sCZ (Marlow, 1981; Sawyer, 1981; Brandt, 1987). However, in the Palmenhorst Dome, this same stratigraphy is not seen, with only quartzofeldspathic gneisses of the Narubis Granitoid Complex identified (Brandt, 1987). However, Longridge (2012) noted minor paragneisses present within the Palmenhorst Dome. Previous work (Smith, 1965; Longridge, 2012) notes the similar quartzofeldspathic composition of the rocks of the Abbabis Complex and the Etusis Formation of the Damara Supergroup. Gevers (1931), Smith (1965) and later works (Hawkesworth *et al.,* 1983) proposed that the Etusis Formation was derived from the Abbabis Complex.

Figure 4.1 (on following page): Geological map produced from this study of the Nose Structure at the northeast end of the Palmenhorst Dome. Geological map with inset of the Palmenhorst Dome showing only the Abbabis Complex (as undifferentiated), the lower Damara Supergroup (Etusis, Khan, Rössing and Chuos Formation) and the field area within context of the greater Palmenhorst Dome on the top right and a cross section from A to B (indicated by the blue line on main geological map) along the right-hand margin.


495000
496000
497000
498000
499000
7508000
7507000
7506000
7505000
7504000
Nose Structure
Etusis Sliver
HSZ
Ostrich Gorge
Blauer Heinrich
Ostrich Gorge Syncline
Dorob Syncline
Hinge Syncline
Khan River Gorge
A
B
Kilometers
1
N
5 km
Field area
Palmenhorst Dome
Khan River
Hook Fold
Goanikontes
Line of cross-section
Bedding orientation
Lineation orientation
Foliation orientation
Fold axial plane orientation
D3 anticline fold axial trace
D2 anticline fold axial trace
D2 syncline fold axial trace
B2 Access Road
Recent Deposits and Alluvium
High strain zone (HSZ)
Pegmatites
Chuos Formation
Rössing Formation
Khan Formation
Etusis Formation
Damara Supergroup
Amphibolites
Basement Granites
Orthogneisses and augen gneisses
Augen gneisses
Abbabis Complex
Blauer Heinrich
Ostrich Gorge
500 m
250 m
B
A

The Neoproterozoic Damara Supergroup is subdivided into Nosib and Swakop Groups (SACS, 1980), both of which surround the characteristic basement-cored domes (Smith, 1965). These domes, initially identified as undifferentiated homogenous granite-gneisses (Smith, 1965), have been shown to contain lower Damaran sediments, namely the Etusis, Khan, Rössing and Chuos formations (Oliver and Kinnaird, 1996; Longridge, 2012). The sequence yielded depositional ages of 756 ±2 Ma (minimum age; Hoffmann *et al.,* 1996) and 635 ±1.2 Ma (maximum age; Hoffmann *et al.,* 1996) for the Etusis and Chuos formations, respectively, by means of U-Pb age dating of rift associated felsic magmatism. In addition, the Chuos Formation is correlated to the Sturtian (750 Ma to 720 Ma) glacial event (Kauffman *et al.,* 1997; Hofmann *et al.,* 2004).

Recognising the various lithologies of the Palmenhorst Dome is important in distinguishing between various granitoids, Damaran metasediments and the basement rocks to establish whether there are younger crustal components within the undifferentiated basement. Similarly, there have been multiple iterations of maps showing the distribution of various lithologies within the Dome (Smith, 1965; Barnes, 1981; Longridge, 2012) and, therefore, distinguishing between the Damaran metasediments and the migmatised gneissic basement was a key objective. Lateral facies variation of the Damara lithologies, upper amphibolite to granulite-facies metamorphism, deformation and voluminous granitoid emplacement present challenges when attempting to identify these formations in the domes of the sCZ (Masberg *et al.,* 1992; Poli, 1997). As a result, a set of criteria was established using published data:

- Based on previous work, the lower Damaran metasediments (the Etusis, Khan, Rössing and Chuos formations) were most commonly identified as synclines within the Palmenhorst Dome (Longridge, 2012). Therefore, if Damaran metasediments can be identified within the basement lithologies, the structural geometry is an useful initial criterion.
- These formations include a variety of lithologies and mineral assemblages with characteristic features (Table 4.1) for each of the formations, which can be used to establish the presence of Damaran metasediments within the basement when identified in an appropriate sequence.

Therefore, the ability to distinguish key characteristics, identify a package of lower Damaran metasediments and understanding the structural geometry can lead to an informed identification of crustal components within the basement (Longridge, 2012).

Figure 4.1 shows the results of field mapping with newly identified Damaran-cored synclines, namely the Ostrich Gorge, High strain zone (HSZ) Etusis raft, Hinge and Dorob synclines (Fig. 4.1), within the Abbabis complex rocks, guided by remote sensing and later field mapping.

Table 4.1: Table showing the characteristic features of the lower Damara Supergroup formations with the pitfalls associated with these characteristics (modified after Martin, 1965; Smith, 1965; Nash, 1971; Jacob, 1974; Sawyer, 1981; Henry, 1992; De Kock, 2001; Miller, 2008; Longridge, 2012).

Formation	Characteristic features	Complications
Chuos	Clasts of a variety of lithologies in quartz-biotite schist matrix, Thin iron formations, Garnet-bearing matrix to L-tectonite	Boudinage or transposition of granitic veins may ressemble pebbles
Rössing	Associated marbles, calc-silicates, quartzites and pelites, Heterogeneous and cyclic lithologies, scapolite associated with marbles and calc-silicates, Characteristic red colour- pyrite oxidation, Garnetiferous schists	Thick carbonates of the Karibib Formation however not the same variety as the Rössing Formation, Similar assemblages to other formations
Khan	Layers enriched in clinopyroxene, amphibole, apatite, epidote and scapolite, Clinopyroxene is not seen in other Damaran sediments, Chunky cordierite	
Etusis	Cross-bedded quartzites, Heavy-mineral (illmenite) concentrates along cross-beds, Quartzofeldspathic compositions, Sillianite-rich layers in quartzofeldspathic rock, Pebble lags at base of formation,	Sillimanite is present in aluminous granites, Abbabis Complex has similar quartzofeldspathic compositions

4.2.1 Abbabis Complex (AC)

The Abbabis Metamorphic Complex constitutes the basement rocks of the study area, and these are developed as cores (Fig. 4.1) to the megascale interference folding (Smith, 1965). These rocks are mainly quartzofeldspathic orthogneisses and augen gneisses (Fig. 4.2) that display variable intensities in deformation and partial melting. Limited examples of possible paragneisses (or grey orthogneisses) are observed, but where they do occur they are mostly observed in the northern part of the area. The establishment of paragneisses were named according to previous examples of paragneisses in the Abbabis Complex, both in the type locality in the Palmenhorst Dome (Smith, 1965; Longridge, 2012), but this needs to be assessed. These rocks display a prominent gneissic fabric that has been cross-cut and modified by numerous granitoids and structural components. These basement rocks show a distinct weathering profile as they are elevated in comparison to the supracrustal rocks and exhibit deeply incised valleys.

The banded quartzofeldspathic orthogneisses (Fig. 4.2.A) and augen gneisses (Fig. 4.2.B) are medium to fine-grained comprising quartz, K-feldspar, biotite and minor plagioclase. They occur as a continuum between one another and transitions can be seen between bands where augens may or may not be present. Additionally, the orthogneisses show more well-developed granitic textures with biotite foliations less prevalent in some cases. Gneissic banding (Fig. 4.2.C) is prevalent with

alternating layers of melanocratic, mainly biotite-rich, and leucocratic layers which differ in composition from plagioclase-rich to K-feldspar-rich. The augens comprise quartz, plagioclase and K-feldspar and are typically 1-2 cm in length (Fig. 4.2.B) with an alignment of all minerals. However, biotite forms the dominant foliation. The biotite foliation wraps around the augens and in many cases two foliations form the distinct pencil cleavage of the Abbabis Complex. The pencil cleavage results in distinct elongate, mostly leucocratic shards where the gneisses are less granitic and intruded by various Damaran Granitoids (Fig. 4.2.B). Minor chlorite and epidote alteration is present within the basement rocks and is most commonly associated with the augen and late stage faulting which cross-cuts basement rocks and associated granites within the study area.

The banded orthogneisses are highly strained (Fig. 4.2.D, E, F and G) along the contact between the Damara cover sequence and the basement rocks. A prominent HSZ trends northeast-southwest along the basement-cover contact and is located in the northeast region of the mapping area (Fig. 4.1). HSZ gneisses (Fig. 4.2. A, C, F and G) show alternating biotite-plagioclase and K-feldspar-rich layers with widths ranging from >1 mm to 10 cm thick bands. However, most commonly the biotite-rich layers are thickest and resemble paragneisses. These rocks are distinguished due to their crystalline type of weathering, which contrasts with the friable nature of the typical pencil cleavage weathering style of the ortho and augen gneisses. Additionally, the thin bands of leucocratic and melanocratic segregations, concentration of continuous cleavage and decrease of grain size are other distinguishing factors. The gneissic banding is commonly folded (both ptygmatic and tectonically controlled), boudinaged and sheared (Fig. 4.2. E, F and G, respectively), creating the appearance of convoluted blebs of leucocratic segregations (Fig. 4.2.E) within a distinctly foliated melanocratic rock. Commonly associated with boudinage and shearing is the localisation of plagioclase and quartz-rich leucosomes within the cores of boudin necks and the shear zones, respectively (Fig. 4.2.F and G). The melanocratic bands are dominated by a platy mineral foliation, defined by biotite, which appears as a parallel continuous cleavage that is zonal and relatively discreet. However, a parallel foliation formed by compositional layering is expressed by the separation of melanocratic and leucocratic layers. This HSZ has cross-cutting SLGs (see section 4.4) that have been deformed into parallelism with the gneissic fabric of the basement rocks.

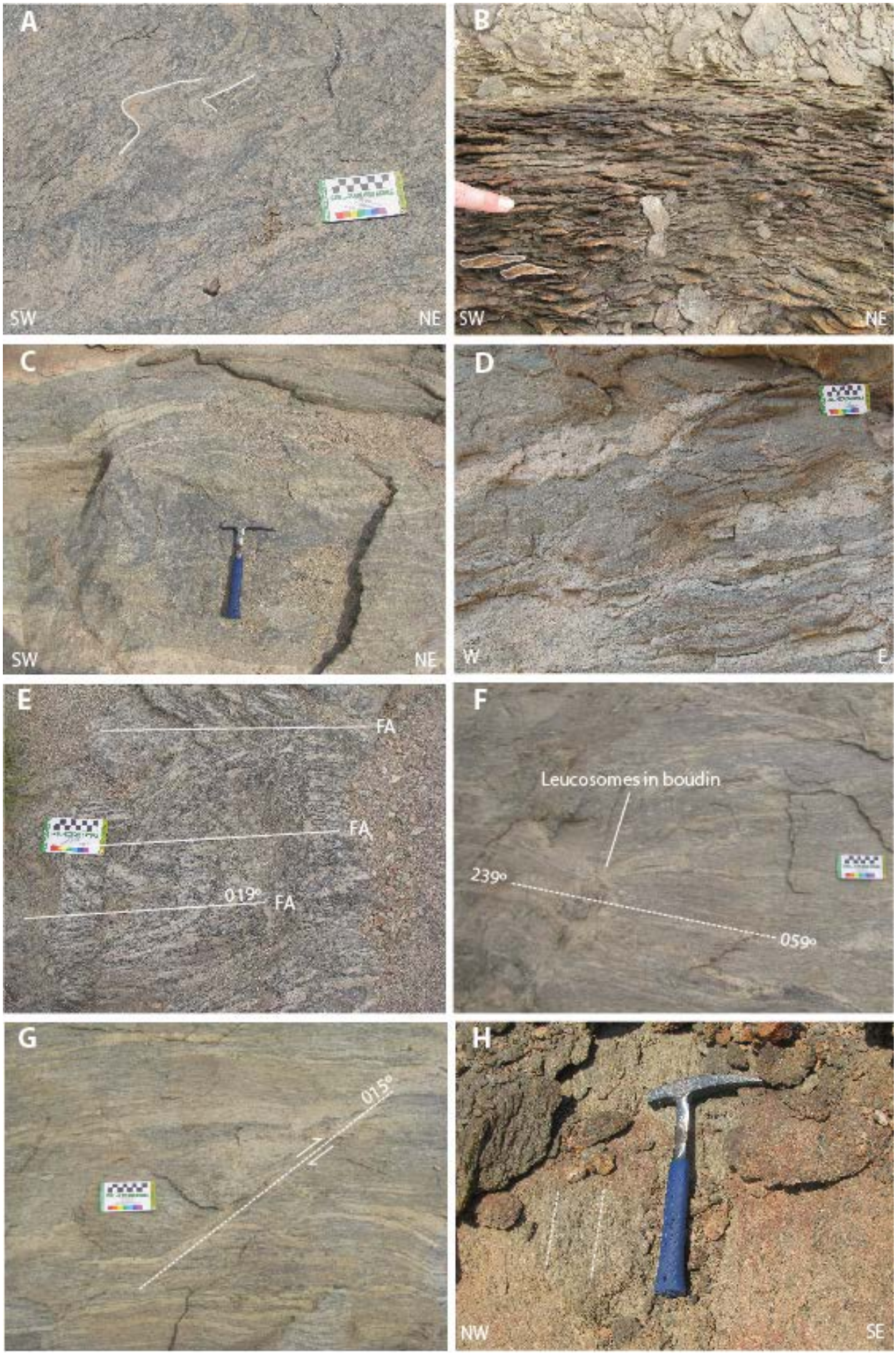

A
SW
NE
B
SW
NE
C
SW
NE
D
W
E
E
FA
FA
019°
FA
F
Leucosomes in boudin
239°
059°
G
015°
H
NW
SE

Figure 4.2 (on previous page): Outcrop field photographs of the various gneisses of the Abbabis Complex. (A) Banded orthogneiss within the HSZ displaying folding of foliation and strained K-feldspar-rich leucocratic segregations. Examples of folded leucocratic segregations traced in white. (B) Characteristic pencil cleavage of the augen gneiss. Examples of augen, comprising quartz, plagioclase and K-feldspar, are outlined in white in the bottom left hand corner. Sheets of augens are seen as weathered fragments in the picture. (C) A fine-grained banded orthogneiss in the HSZ. Alternating bands of biotite-rich and plagioclase -rich bands (< 1 – 2 mm thick) are convoluted and folded, but still maintain the general banded orientation. (D) Banded paragneiss/grey orthogneisses with SLGs intruding parallel to banding orientation. These feldspar-rich SLGs are convoluted and often nebulitic. (E) Folded HSZ paragneiss/grey orthogneisses with strained SLGs folded and extended into isolated leucocratic blebs. FA= fold axis indicating the axial trace orientation. (F) Boudinaged gneiss within leucosomes of fine-grained white migmatites in the core of the boudin (indicated in photograph). Main extension direction is indicated by the dashed line. (G) orthogneiss with SLG (type A) associated with a cross-cutting dextral shear zone. (H) Granite-gneiss with a defined biotite foliation (indicated with the white dashed line). Red K-feldspar, plagioclase and quartz are weakly aligned.

Some of these L-tectonised (HSZ) gneisses resemble paragneisses (Fig. 4.2.D, E and F) due to their melanocratic and quartz-rich compositions. These so-called paragneisses/grey orthogneisses display intense shearing and strain with thinned out alternating leucocratic, which vary in composition, and melanocratic bands, commonly only preserving the melanocratic bands. The foliation is well developed in these rocks and is continuous and parallel. These rocks show thinner bands than the augen gneisses, orthogneisses and granite-gneisses and occur most commonly in the HSZ of the mapping area. The nature of a possible sedimentary origin needs to be assessed.

The basement also displays less deformed granite-gneisses (Fig. 4.2.H), which show minor alignment of biotite, plagioclase and quartz in a groundmass of K-feldspar giving the rock a pink to red colour. No distinct banding is present in these granite-gneisses and the main biotite foliation is spaced, parallel and gradational. This is in contrast to orthogneisses, which generally have a more developed compositional and platy mineral foliation. These granite-gneisses are more abundant to the south and show a complex mingling between numerous granite types and are cross-cut by red granites, grey granites and various SLGs (see section 4.4).

There is a clear spatial variation in the distribution of rocks within the study area. Orthogneisses and augen gneisses are seen in the northern extent of the dome, while the granite-gneisses are concentrated in the south but not distinctly mappable (Fig. 4.1). Paragneisses/grey orthogneisses are seen in the north, however, these are mostly concentrated in HSZs. Within the basement rocks of the Nose Structure, lower Damaran metasediments are observed as synclinal rafts.

4.2.2 The Damara Supergroup

The Damara Supergroup comprises the Nosib and Swakop Groups that unconformably overlie the Abbabis Complex. Within the field area these supracrustals are seen as synclinal infolds, in the Ostrich Gorge, Hinge and Dorob synclines and also surrounding the basement rocks (Fig. 4.1). The

Etusis and Khan formations of the Nosib Group are most abundant in the field area, while the Rössing and Chuos formations are the only lithologies from the Swakop Group that were observed and identified. Due to the deformation in the sCZ the individual formations often display gradational contacts in the field area and are frequently fragmented by intruded partial melts or associated migmatisation. Therefore, complete, undeformed and relatively less intruded stratigraphic sections were not found within the mapping area itself, and as a result the full range of documented lithologies within the formations may not be observed. All lithologies of the Damara Supergroup identified in the field are metamorphosed and therefore metasedimentary in nature.

Etusis Formation

The Etusis Formation forms the base of the Nosib Group and unconformably overlies the Abbabis Complex. This contact, in the field (Fig. 4.3), is difficult to identify due to the similar quartzofeldspathic compositions that the basement and Etusis lithologies share and the often tectonised and intruded contact between them. In addition, the rocks are similar in colour (Fig. 4.3) and exhibit similar textures. Therefore, the criteria in table 4.1 were utilised. The main lithologies (Fig. 4.4) observed in the field area include cross-bedded quartzites (Fig. 4.5.A and B) to quartzofeldspathic arkoses (Fig. 4.5.D and E) and sillimanite- (± biotite) schists. These rocks are generally in contact with the Abbabis Complex around the megascale fold, although they do appear as attenuated slivers of infolds within and extending into the basement (Fig. 4.1).

The most common unit associated with the Etusis Formation is a banded quartzite (Fig. 4.5.A and B), which occasionally displays faint cross bedding with associated heavy mineralisation along foresets. Grain size ranges from meta-sandstones to gritstones, and in some places, they may be conglomeratic. They comprise mainly subrounded to angular quartz grains with fine amorphous feldspars. Ilmenite is a common accessory mineral and is concentrated along the cross beds, when they are present, and bedding of the quartzites (Fig. 4.5.A). Sheeted granites cross-cut the Etusis Formation and commonly contain noted concentrations of ilmenite (aggregates 2-4 cm in diameter) along intrusive boundaries and occasionally associated with pegmatitic quartz and K-feldspar-rich cores. Interbeds, between 2-30 cm thick, of quartz-rich to K-feldspar-rich layers are present with conglomeratic pebble lags (Fig. 4.5.B), often occurring at the base of the Etusis Formation. These pebbles are highly flattened, with a thin layer of Etusis in the attenuated synclinal extensions into the basement, such as observed at the contact with the basement and Etusis of the Ostrich Gorge Syncline. Bedding parallel SLGs are commonly observed in this formation. There are isolated incidences of carbonate, possibly calcsilicate layers (Fig. 4.5.C) within the Etusis Formation. These layers are mostly made up of fibrous calcite that have weathered to a grey creamy colour with red

stained quartzite-rich interbeds. A similar layer occurs within the Khan Formation however, it contains diopside. These quartzites are most commonly seen along the basement-cover contact, in the Ostrich Gorge and Hinge Synclines.

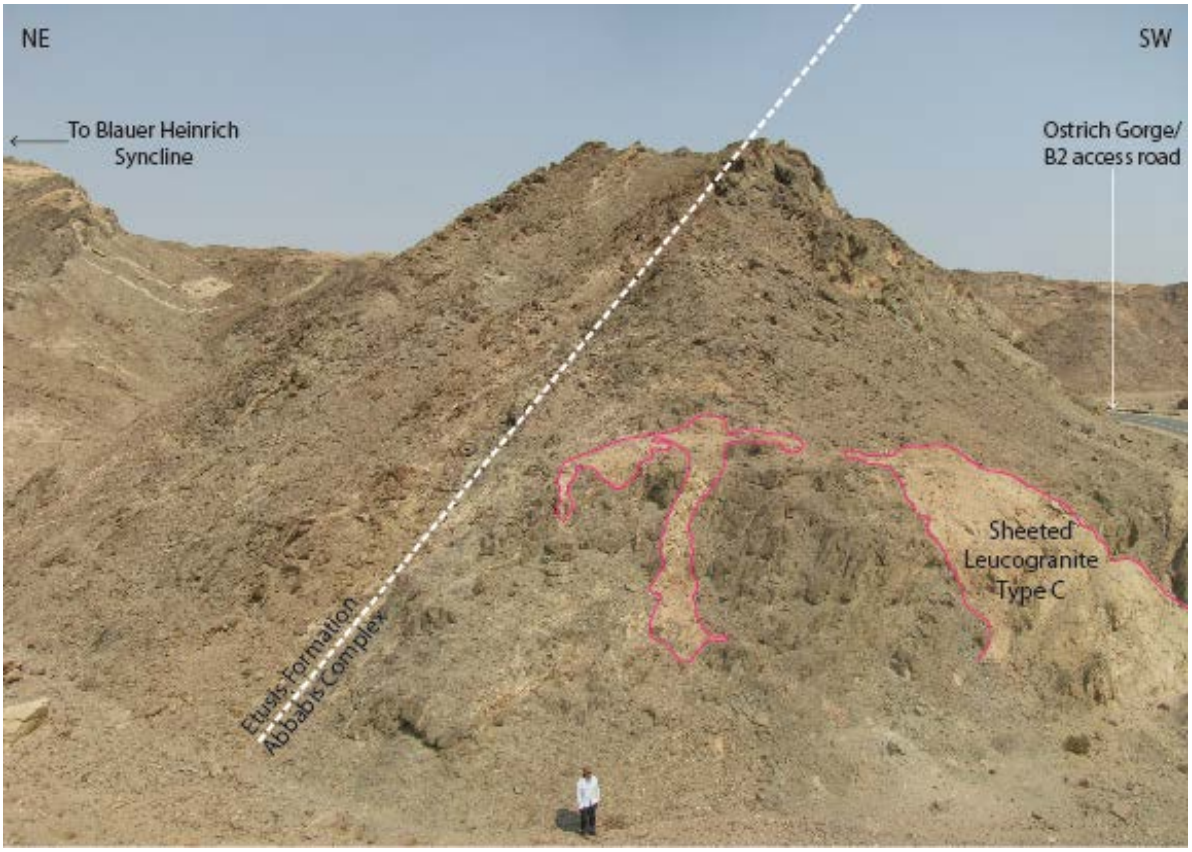


Figure 4.3: Field photograph illustrating the difficulty in identifying the contact between the Abbabis Complex and the Etusis Formation due to their similar compositional and textural characteristics.

Beds dominated by arkosic compositions are similar to the quartzites, although this unit contains more feldspar-rich interbeds (Fig. 4.5.D), has a crumbly and gritty nature and a pink colour (Fig. 4.5.D and E). This colour creates confusion between the arkoses with the red granites and the basement granites (Section 4.5). Another common feature of the Etusis arkoses and the red granites is the presence of sillimanite porphyroblasts, which typically form a mineral lineation (0.5 cm x 2 cm) (Fig. 4.5.E). Partially melted rocks of the Etusis Formation show porphyroblasts of sillimanite lineations that have the same orientation as other Etusis Formation lineations. Banding is a distinguishing feature of the arkosic Etusis rocks, although heavy mineral accumulations are not as commonly seen in these lithologies as they are in the banded quartzites. However, the arkoses appear to grade into the semi-pelitic Khan Formation and interbeds between the biotite-cordierite semi-pelites and banded arkoses are common. This unit is seen along the southwest basement-cover contact and in

the Hinge Syncline, which makes distinguishing the Etusis from the intrusives and basement in that area challenging.

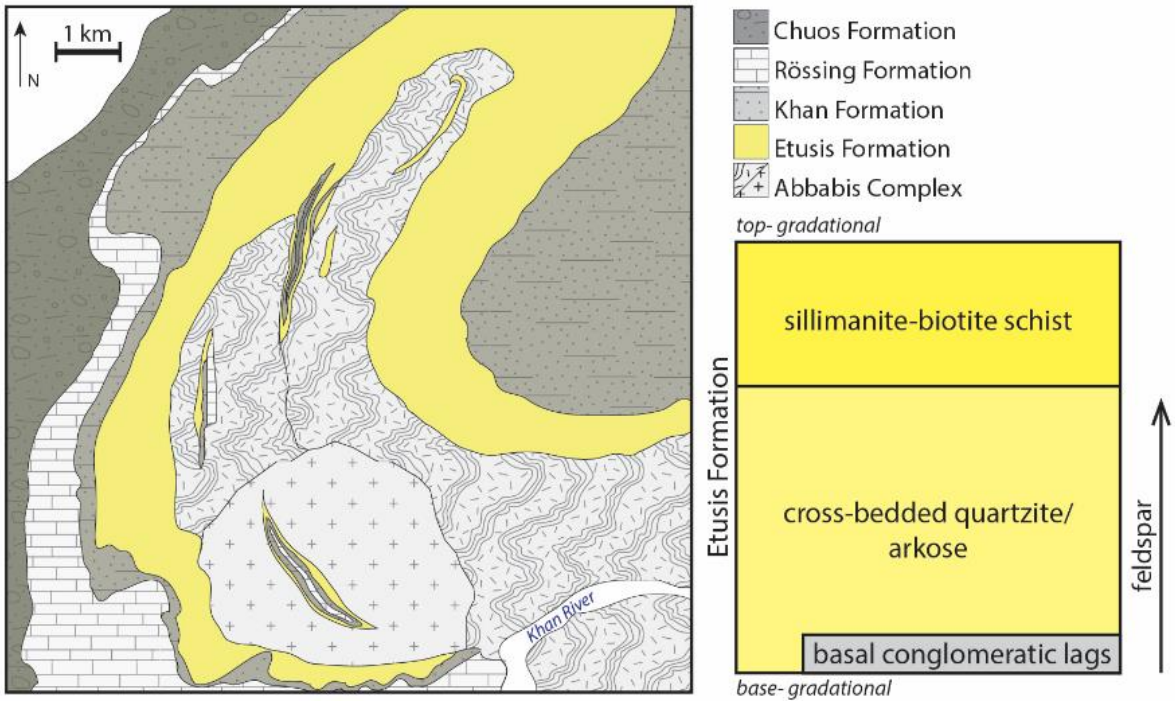


Figure 4.4: A simplified geological map of the field area highlighting the distribution of the Etusis Formation with a summary of the lithologies identified (lower right) for the Etusis Formation in the field area. The column height is not drawn to scale, but the quartzite is more common in the field area and therefore has an increased representation. Colours in the column do not correspond to those shown in the alongside map.

A less common lithology of the Etusis Formation are pelitic schists. These include assemblages containing sillimanite and biotite (Fig. 4.5.F). This rock type is most commonly found in the northeast region of the mapping area at the contact of the Abbabis Complex and the Etusis Formation, particularly in the HSZ. Additionally, the HSZ Etusis Sliver (Fig. 4.1) is comprised of sillimanite-quartz-biotite schist. This is largely the reason for its ease of identification in comparison to the quartzofeldspathic basement rocks. Sillimanite porphyroblasts form lineations, ranging from 1 mm to 1 cm in length, in a quartz-biotite schist matrix. Biotite forms a continuous foliation that is parallel and discrete. Both the lineation and foliation are commonly folded at outcrop scale These schists form interbeds between quartzofeldspathic layers which are often convolute and folded (Fig. 4.5.F).

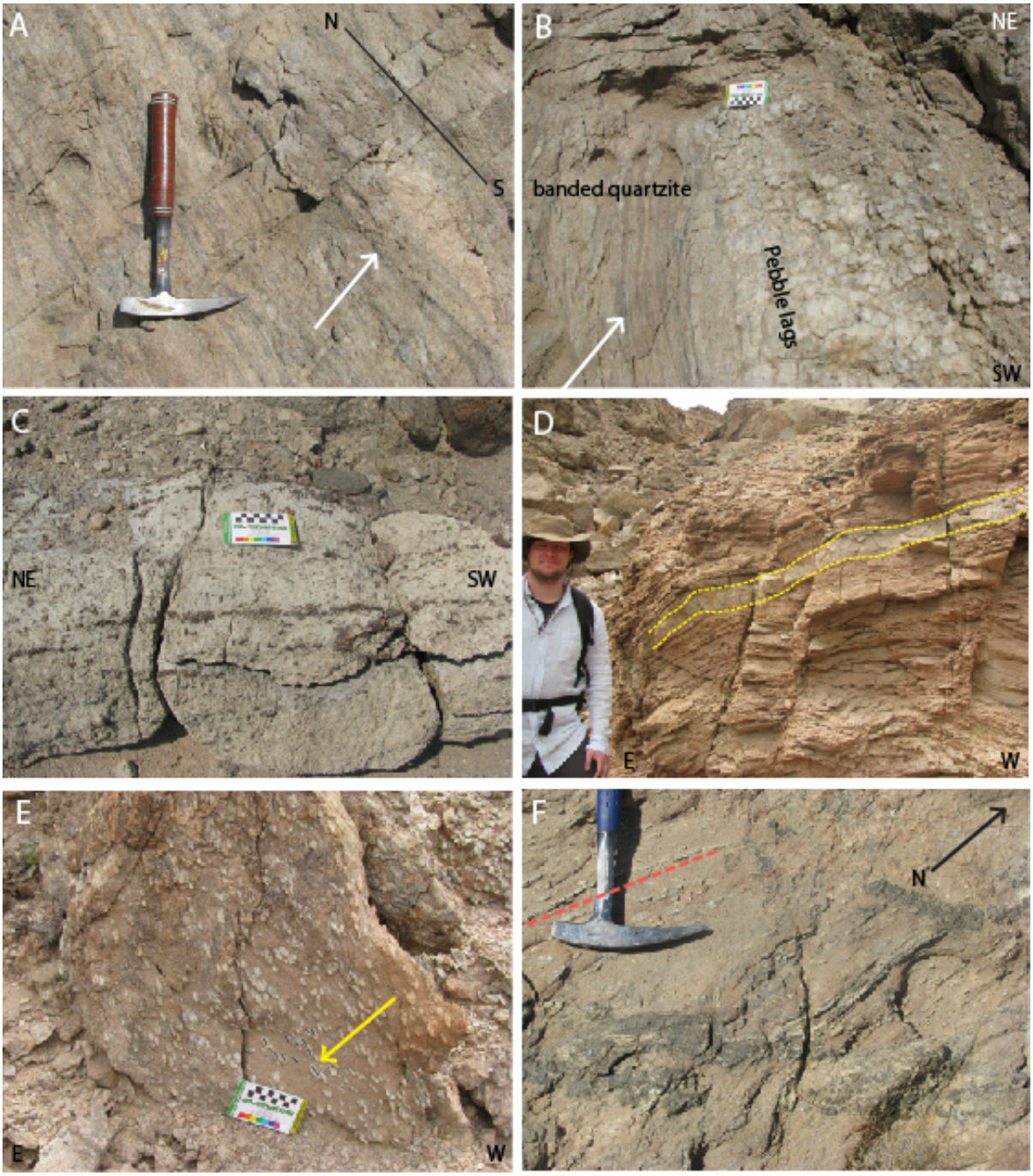


Figure 4.5: Outcrop field photographs of the Etusis Formation. (A) A banded quartzite with heavy mineralisation (white arrow). (B) A banded quartzite with heavy mineralisation (white arrow) and pebble lags. Pebbles comprise flattened quartz grains 1-2 cm in length. (C) Isolated carbonate layer in banded quartzite to gritstone. Calcite (grey) and quartz-rich (red-brown) interbeds are present. (D) A banded arkose showing interbeds of quartz-rich (light brown to tan - indicated in yellow) and K-feldspar-rich layers (pink). Cross-cutting brittle joints are present. (E) An arkose with sillimanite teeth forming a lineation. Teeth are traced in fine black dashes indicated by the yellow arrow. (F) Sillimanite-quartz-biotite schist interlayered with meta-arkose. Sillimanite lineation is defined by the dashed red line.

Khan Formation

The Khan Formation is the uppermost unit of the Nosib Group and has a gradational contact with the underlying Etusis Formation. While the Etusis Formation is dominated by siliciclastic rocks the Khan Formation contains semi-pelitic schists, banded gneisses and associated calcsilicates (Fig. 4.6).

Common assemblages include diopside, amphiboles, K-feldspar, scapolite, epidote, cordierite and biotite. The Khan Formation surrounds the Etusis Formation in the case of the megascale fold, the Nose Structure, and is enclosed by the Etusis in the synclines within the basement (Fig.4.1 and Fig. 4.6).

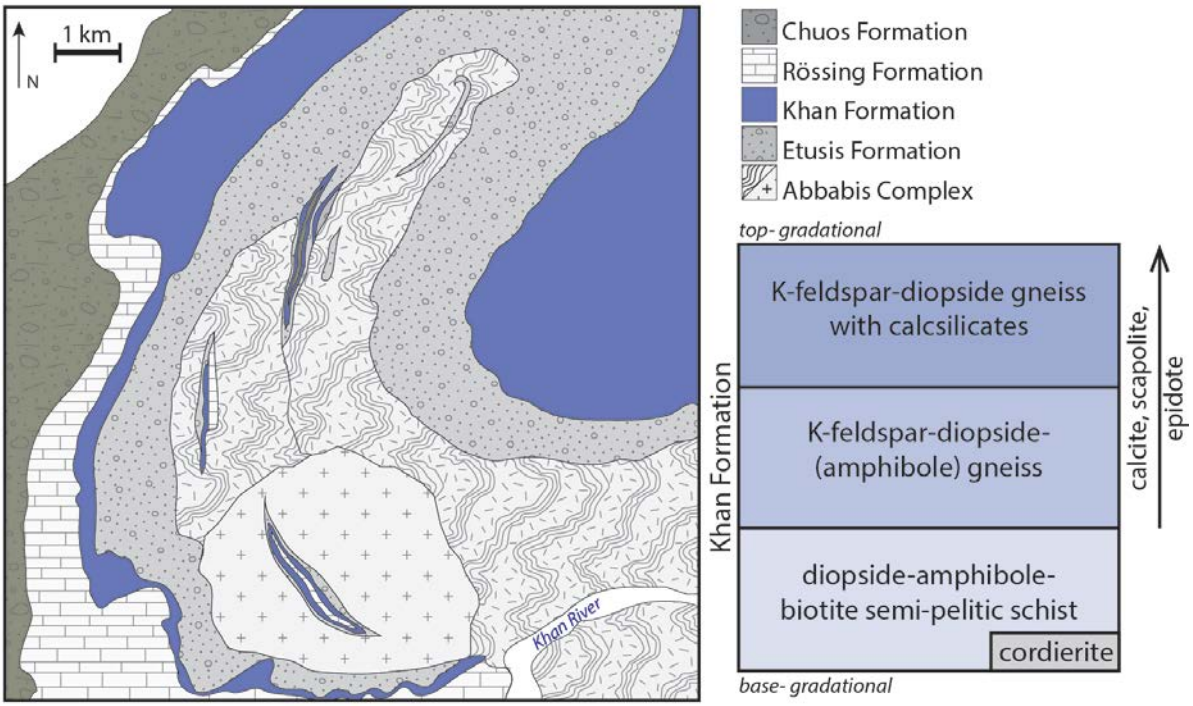


Figure 4.6: A simplified geological map of the field area highlighting the distribution of the Khan Formation with a summary of the lithologies identified (lower right) for the Khan Formation in the field area. The column height is not drawn to scale and the colours in the column do not correspond to those shown in the alongside map.

Semi-pelitic diopside-amphibole-(cordierite-biotite) schists are fine-grained and finely-foliated. The foliation is continuous and largely defined by amphibole and biotite. They appear finely-laminated (Fig. 4.7.A) or chunky and nodular (Fig. 4.7.B) when abundant porphyroblasts of cordierite are present. The dark grey to dark green semi-pelites contain leucosomes that are white and have stromatic and net-textured leucosome morphologies (Fig. 4.7.A). Individual beds are boudinaged and separated along bedding planes by plagioclase-rich leucosomes resulting in distinct dismembered melanosomes (dark green) and leucosome (white) net effect. In situ partial melts and intrusive sheeted granites are easily distinguished due to the contrast in colour. Radial and fibrous scapolite can be seen when carbonate-rich layers are present. Nodular cordierite porphyroblasts give the outcrop a bluish colour and these porphyroblasts are surrounded by plagioclase-rich leucosomes. Cordierite is seen near the base of the Khan Formation, while the presence of diopside, scapolite and epidote appear to increase towards the top of the semi-pelitic units when associated

with the calcsilicates and near the contact with the Rössing Formation, which contains abundant carbonate-rich beds. Attenuated carbonate-rich interbeds near the Rössing Formation are common.

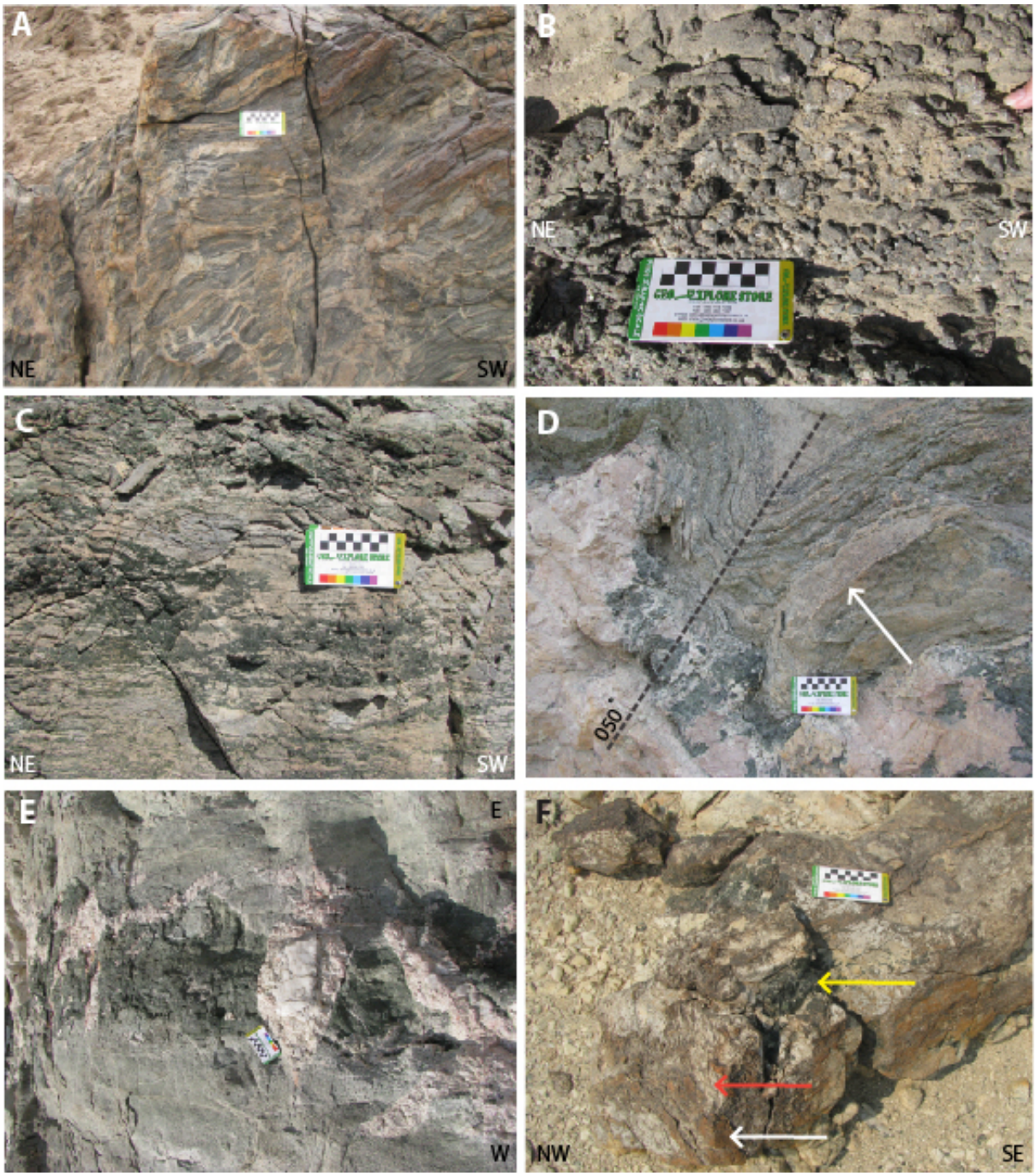


Figure 4.7: Outcrop field photographs of the Khan Formation. (A) A stromatic and net-textured diopside-amphibole-(biotite-cordierite) schist. This semi-pelitic schist contains migmatitic bands of leucosomes and palaeosomes giving it the distinctive white and dark green-grey colour, respectively. (B) A diopside-amphibole-(biotite-cordierite) schist is present with nodular cordierite in a biotite-amphibole matrix. (C) A banded gneiss showing gneissic bands of diopside and K-feldspar. Attenuated diopside layers are present. (D) Folded banded diopside-K-feldspar gneiss with orange calcite (white arrow) and associated (folded) type C′ SLGs. Dashed black line indicates fold axis orientation (strike of plane= 050˚). (E) Green calcsilicate with accumulations of cross-cutting diopside-amphibole vein-like feature with cross-cutting parallel K-feldspar and plagioclase-rich boudin controlled SLG. (F) Weathered calcsilicate with interbeds of calcite-rich (red arrow) and quartzite (white arrow) layers with replacement of calcite with diopside (yellow arrow). These layers are convolute and show a positive-negative weathering relief.

The medium- to coarse-grained banded diopside-K-feldspar gneisses are distinct due to their alternating pink-green bands (Fig. 4.7.C). These lithologies contain alternating K-feldspar-rich (pink) and diopside-rich (green) stromatic gneissic banding. The latter bands, which are semi-pelitic in nature, contain minor amphibole, in addition to the diopside. This banding is constant and relatively thin, approximately 0.5 cm in thickness, with the diopside-rich layers often dismembered and appearing as elongate augen. Alternating pelitic schists and banded gneisses are seen in the field. Accumulations of large (up to 4 cm) orange calcite grains are commonly associated with both the structural features (within boudins) and along the edge of granitic intrusions (Fig. 4.7.D). These banded gneisses are commonly located near the Etusis-Khan contact within the field area.

Similarly, the coarse-grained calcsilicate units are rich in diopside and show the characteristic green (and pink when intrusives are present) colour of the Khan Formation (Fig. 4.7.E). They typically comprise diopside-sphene-garnet-amphibole assemblages. Coarse diopside, garnet and amphibole are distinctive. SLGs commonly cross-cut these layers in parallel sheets with sharp contacts to the host rock (Fig. 4.7.E). These rocks occur within the Khan units that surround the Nose Structure fold (Fig. 4.1). However, other calcsilicates are seen in the Hinge Synclinal raft as fibrous calcitic layers with interbeds of quartzite (Fig. 4.7.F). The fibrous calcite is grey in colour with radial patterns on the weathered surface. The unweathered surface is white and chalky in the calcite-rich layers. The quartzite interbeds are convolute and red-brown in colour with diopside, and minor amphibole, associated with the calcite layers. Diopside replaces the calcite as patchy and massive accumulations. A distinct characteristic of these interbeds are the cross-hatched negative and positive weathering profiles of the calcite-rich and quartzite interbeds, respectively. This unit is laterally extensive, varies in thickness and has a distinct metallic hollow sound when hit with a geological hammer.

Rössing Formation

The Rössing Formation is the lowermost formation of the Swakop Group and displays a gradational contact with the Khan Formation. Calcsilicates, marbles and pyritic-garnetiferous quartzites gradational into pelites (Fig. 4.8) are observed within the Rössing Formation and constitutes the most varied package of rocks within the cover sequence. These units have a characteristic red colour, are typically the thinnest, of the Damara Supergroup and are dismembered quite significantly by granitic intrusions and leucosomes. In addition, these units are gradational and are interbedded with one another in many cases. Within the field area, the Rössing Formation is best observed along

the southwest area of the field area, where the unit is thickest, and in the core of the Dorob and Hinge Synclines. This formation is missing in the Ostrich Gorge Syncline (Fig. 4.8).

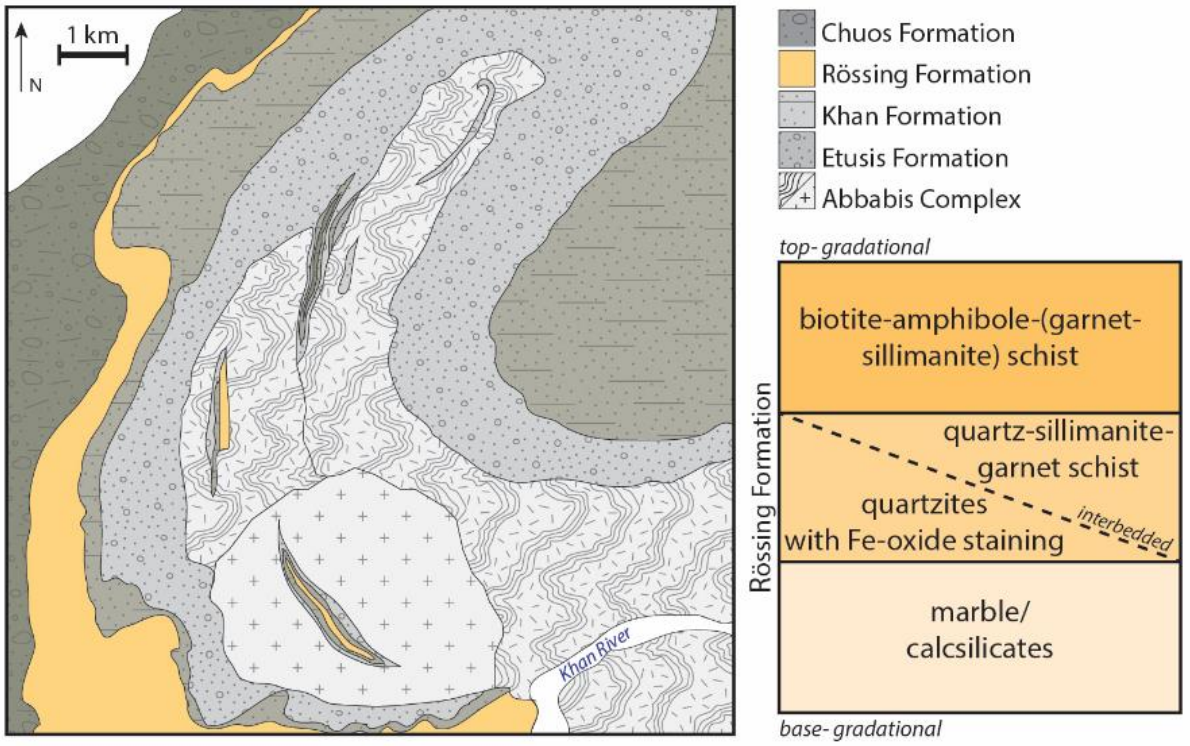


Figure 4.8: A simplified geological map of the field area highlighting the distribution of the Rössing Formation with a summary of the lithologies identified (lower right) for the Rössing Formation in the field area. The column height is not drawn to scale and the colours in the column do not correspond to those shown in the alongside map.

The Rössing Formation comprises fine- to medium-grained marbles (Fig. 4.9.A) and calcsilicates (Fig. 4.9.B). The marbles are characteristically white and an ideal marker horizon for the base of the Rössing Formation. They contain homogeneous calcite and are often interbedded with the red quartzites (Fig. 4.9.C, D and E) and semi-pelitic schists (Fig. 4.9.C). These interbed thicknesses commonly range from 15 cm (Fig. 4.9.C and E) to less than 1 cm (Fig. 4.9.D), depending on how deformed and attenuated the units are (Fig. 4.9.D and F). The calcsilicates and, occasionally, the marbles, contain associated scapolite as radial green to yellow laths (Fig. 4.9.B) and minor diopside at the base of the formation.

The quartz-rich layers are fine- to medium-grained with a distinctive colour possibly due to oxidation of iron-rich minerals not visible in hand sample or at outcrop scale. These quartzites are occasionally arkosic due to a feldspathic component. Calcite is also present in the matrix of the lithology possibly due to the proximity of marble interbeds. The quartzite ranges from interbedded quartzite/arkosic quartzite to a quartz-sillimanite-garnet schist (red quartzite - Fig. 4.9.C). Porphyroblasts of sillimanite and garnet are often present within the quartzite layers, particularly in

layers that are deeper red to maroon (Fig. 4.9.C, E and F) and when the quartzites grade into semi-pelites.

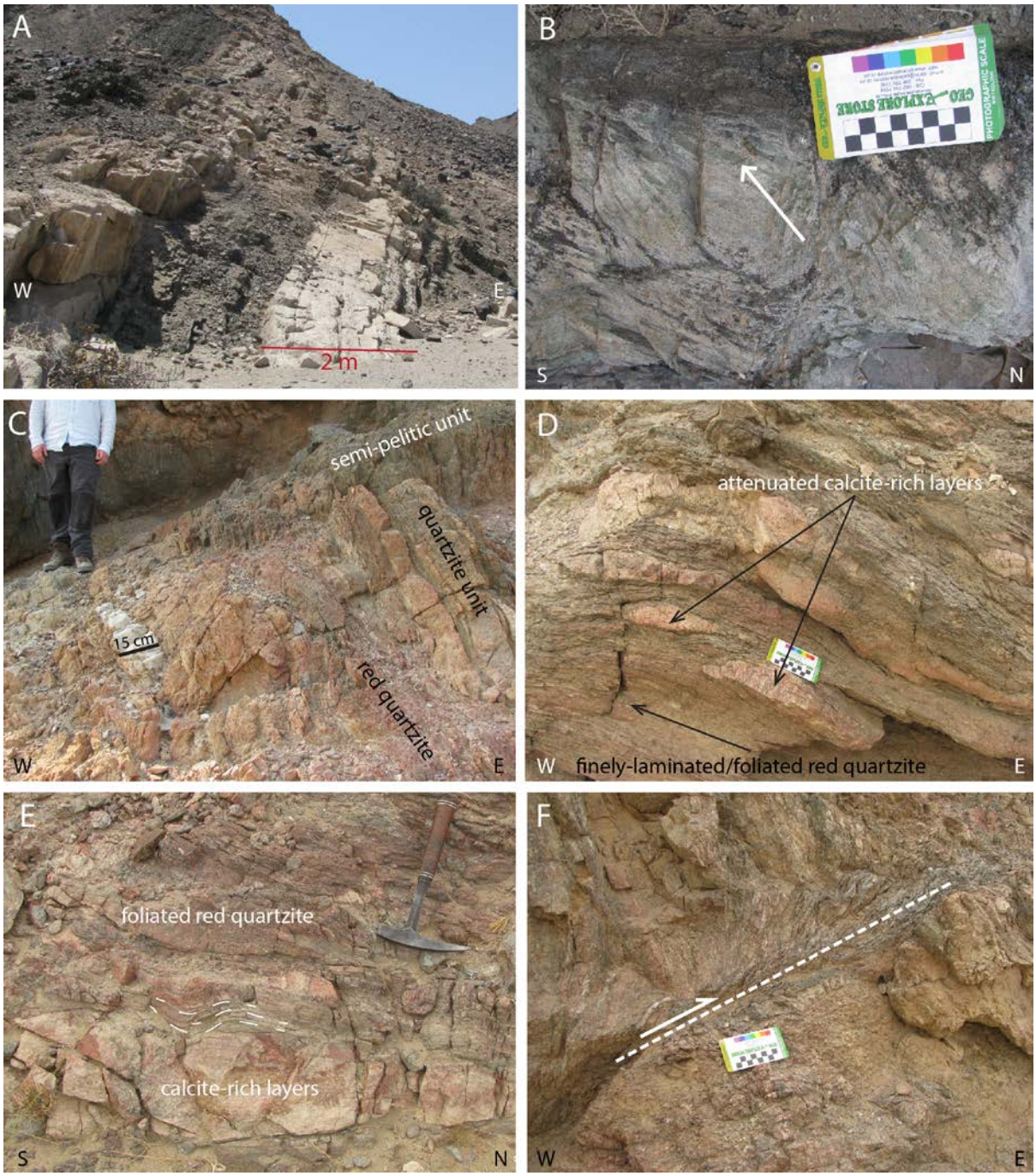


Figure 4.9: Outcrop photographs of the Rössing Formation. (A) Two white to tan marble units of the Rössing Formation interbedded with the pelitic schists of the Khan Formation. This highlights the gradational contact. (B) A calcsilicate with calcite (grey), biotite (dark brown to black) and radial laths of green-blue scapolite (white arrow). (C) Interbedded marble (white lithology with scale on it), quartzite, semi-pelitic schists and garnet-sillimanite-quartz schist (red quartzite). Red quartzite is highly foliated. Lateral facies change along strike. (D) Interbedded marble layers and foliated sillimanite-garnet schist (red quartzite). Marble is attenuated, and foliation is continuous indicating increased deformation. (E) Interbeds of quartzite- and calcite-rich layers that are folded (dashed white lines). Calcite-rich layer is thicker. (F) A shear zone cross-cutting and bending the foliation of the maroon pelitic schist with sillimanite and garnet porphyroblasts. Deflection of the foliation is only on one side of the shear.

Green to grey coloured semi-pelitic units (biotite-amphibole schists) (Fig. 4.9.C) are sometimes flecked with lineations of white sillimanite and rounded red garnets (pelitic schist), although these are not always visible at outcrop scale. The semi-pelitic to pelitic schists are also interbedded with the variations of quartzite, however, this lithology approximates the top of the Rössing Formation in the field area as it grades into the Chuos Formation.

Chuos Formation

The Chuos Formation represents the highest stratigraphic level of the Damara Supergroup that is encountered in the field area and is part of the Swakop Group (SACS, 1980). There is a gradational contact from the underlying Rössing Formation into the Chuos Formation with pelitic schists and a notable increase in biotite and amphibole from the Rössing to the Chuos formations. However, in other areas the contact between these two is unconformable (Miller, 2008). Additionally, in the southern part of the field area (Fig. 4.10), a dismembered Khan Formation calcsilicate layer is present and grades into the Chuos Formation semi-pelitic schist matrix of the characteristic diamictites, where the Chuos Formation overlies the Khan Formation. Diamictites and garnet-cordierite-biotite schists are the two Chuos lithologies encountered in the field area, however minor thin iron-formations are present (Fig. 4.11.A). The Chuos Formation forms the core to the Ostrich Gorge Syncline and is missing in the Hinge Syncline (Fig. 4.10). The most abundant outcrop of Chuos Formation is in contact with the Rössing Formation around the megascale fold (Fig. 4.10).

The diamictites, forming L-tectonites, comprise a semi-pelitic schist matrix with polymict clast compositions that have been strained and flattened (Fig 4.11. B and C). The semi-pelitic schist matrix is a biotite-amphibole-quartz schist that has a continuous tectonic foliation, which is bedding parallel. The platy minerals, biotite and amphibole, define the foliation and wrap around the clasts in the same elongation direction. The clasts are primarily granular quartz in composition with some quartzofeldspathic compositions. Clasts vary from 0.5 to 3 cm in length and show flattening and elongation with no rotation of the clasts. Clast trails are usually extended in one direction from the clast (Fig. 4.11.B). Cross sectional views of the clasts (Fig. 4.11.C) show that the clasts have been elongated and strained parallel to bedding. There are interbeds of thin boudinaged marble units (Fig. 4.11.C) that may represent the gradation between the Rössing and Chuos formations. The diamictites contain beds that are both matrix and clast supported. The Chuos diamictites are found in the core of the Ostrich Gorge Syncline and the foliation and clasts are folded as near upright open folds (Fig. 4.11.D), although the clasts are seen to be folded twice with rootless isoclinal folding also present. This unit is seen in the Ostrich Gorge syncline and around the basement-cored domes in contact with the Rössing Formation. The iron-rich formations are interbedded with calcite-rich and

quartzite-rich layers where the quartzites are iron-rich and red in colour (Fig. 4.11.A). This lithology was identified as Chuos Formation as it was thinly interbedded with the matrix supported diamictites.

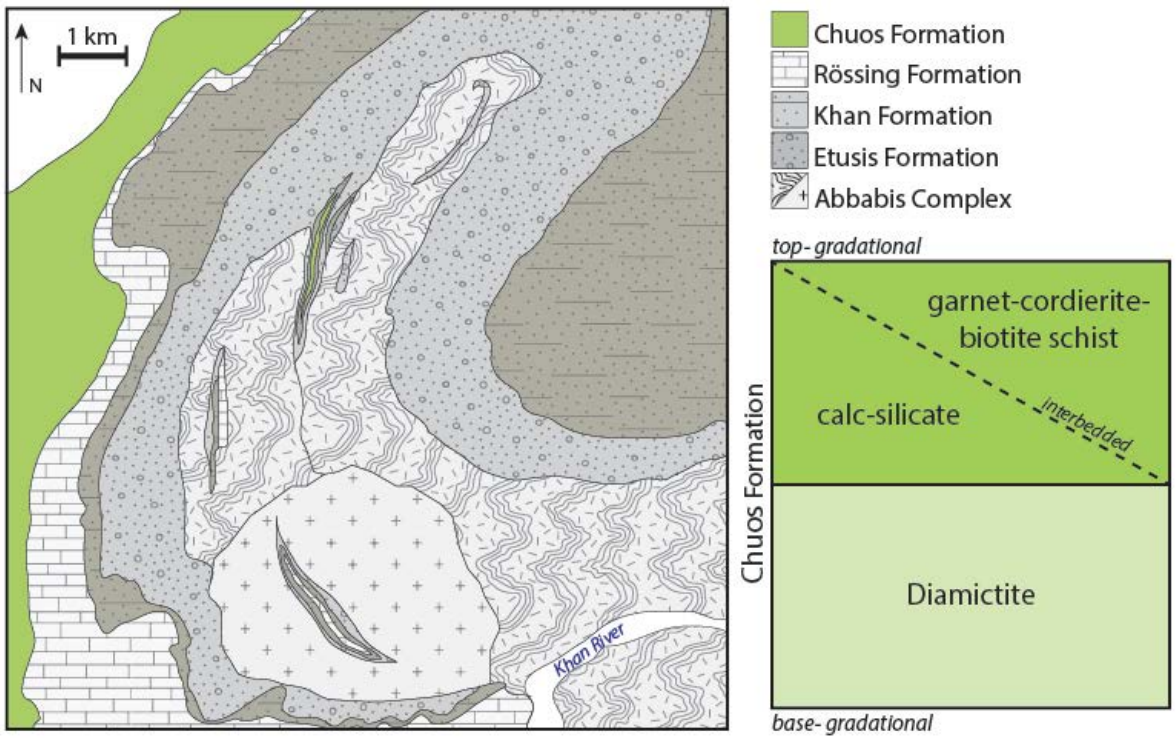


Figure 4.10: A simplified geological map of the field area highlighting the distribution of the Chuos Formation with a summary of the lithologies identified (lower right) for the Chuos Formation in the field area. The column height is not drawn to scale and the colours in the column do not correspond to those shown in the alongside map.

Stratigraphically, the garnetiferous schists occur above the diamictites (Fig. 4.10). This contact is gradational and appears as if the clasts gradually disappear to form pelitic schists. Therefore, the garnet-biotite-amphibole-(quartz) schist is more homogeneous (Fig. 4.11.E) than the diamictites. Rounded red garnets are seen at outcrop scale, ranging between 1 and 2 mm in diameter. The foliation is continuous and is formed by biotite and amphibole with elongate flecks of plagioclase or sillimanite accumulations. These accumulations have diffuse contacts with the pink-purple pelitic schist, are approximately 4 – 8 mm in size and have blebby to amorphous shapes. This unit is only seen in the large Nose Structure fold and not in the synclines within the basement.

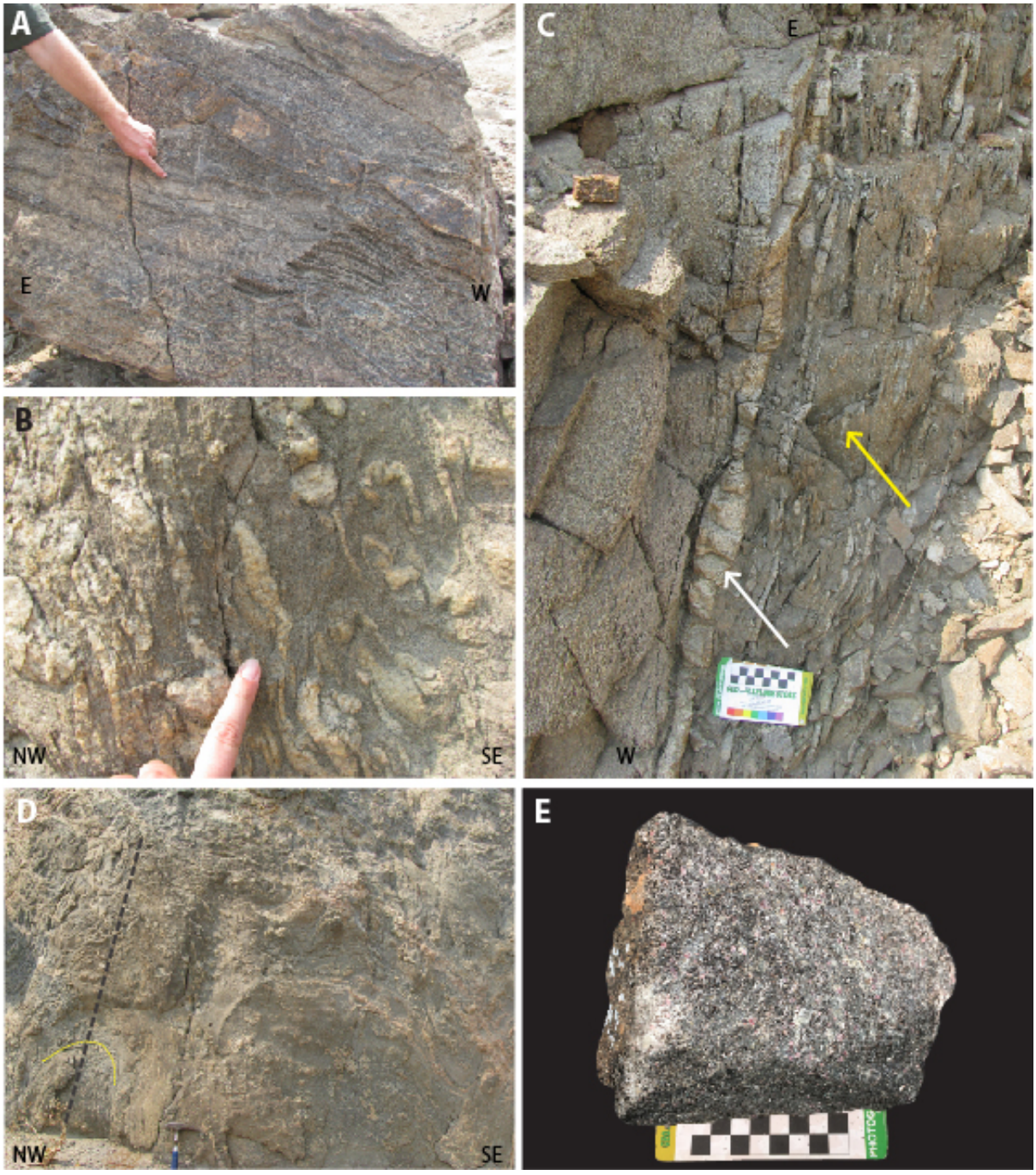


Figure 4.11: Outcrop field (A to D) and hand sample (E) photographs of the Chuos Formation. (A) Iron-rich interbeds of calcite-rich layers (grey) and iron-rich quartzite in a thin iron-formation. (B) Cross sectional view of strained clasts from the Chuos diamictites. Flattened clasts that are folded and granular quartz in composition. (C) Down dip view of the Chuos Formation showing flattened clasts (yellow arrow) in a semi-pelitic matrix and interbeds of marble layers (white arrow). (D) Cross sectional view of an upright open fold. The diamictite is folded with both the foliation and clasts folded. Black dashed line is approximate fold axis with the yellow trace highlighting the folded layers. (E) A garnet-biotite-amphibole-quartz schist with white sillimanite or plagioclase blebs.

4.2.3 Lithological mapping of the synclinal infolds

Three synclinal infolds were observed in the field containing various units of the lower Damaran stratigraphy (Fig. 4.12). The Rössing and Khan formations are useful marker horizons to establish the presence of Damaran sequences within the Abbabis Complex basement. This is especially useful in

the case of the Hinge Syncline where the basement granites and the Etusis Formation are remarkably similar. Both lithologies are homogeneous and quartzofeldspathic in composition and therefore, in the instance of the Hinge Syncline, the contact between the Abbabis Complex and Etusis Formation is largely inferred. However, the Etusis Formation displays faint cross-bedding in some areas, which is useful in distinguishing between the two. In addition, the Hinge Syncline is largely made up of calcsilicates of the Khan Formation that is rich in diopside and garnetiferous Rössing Formation lithologies and distinctive marble units (Fig. 4.12).

In the Dorob syncline, the Rössing Formation shows sheared marble units with scapolite, which is also a distinctive metamorphic mineral within this formation, and sillimanite (Fig. 4.12). This syncline exhibits partial melting of the Rössing Formation lithologies and granitoid intrusions are common. However, the most distinctive feature in this syncline is the sillimanite-biotite schist (Fig. 4.12) that shows a distinct contact with the basement gneisses. In both synclines, the Chuos Formation is not identified possibly due to erosion.

Lastly, the Ostrich Gorge Syncline shows distinctive L-tectonites, or diamictites, from the Chuos Formation within a semi-pelitic schist (Fig. 4.12). The Rössing Formation is missing from this syncline, although there is a distinctive diopside-rich semi-pelitic schist present, which is diagnostic of the Khan Formation. The Etusis Formation is once again, similar in composition, to the Abbabis Complex and granites, however, due to the sequence of these in contact with one another and the repetition of the units, a synclinal raft could be identified.

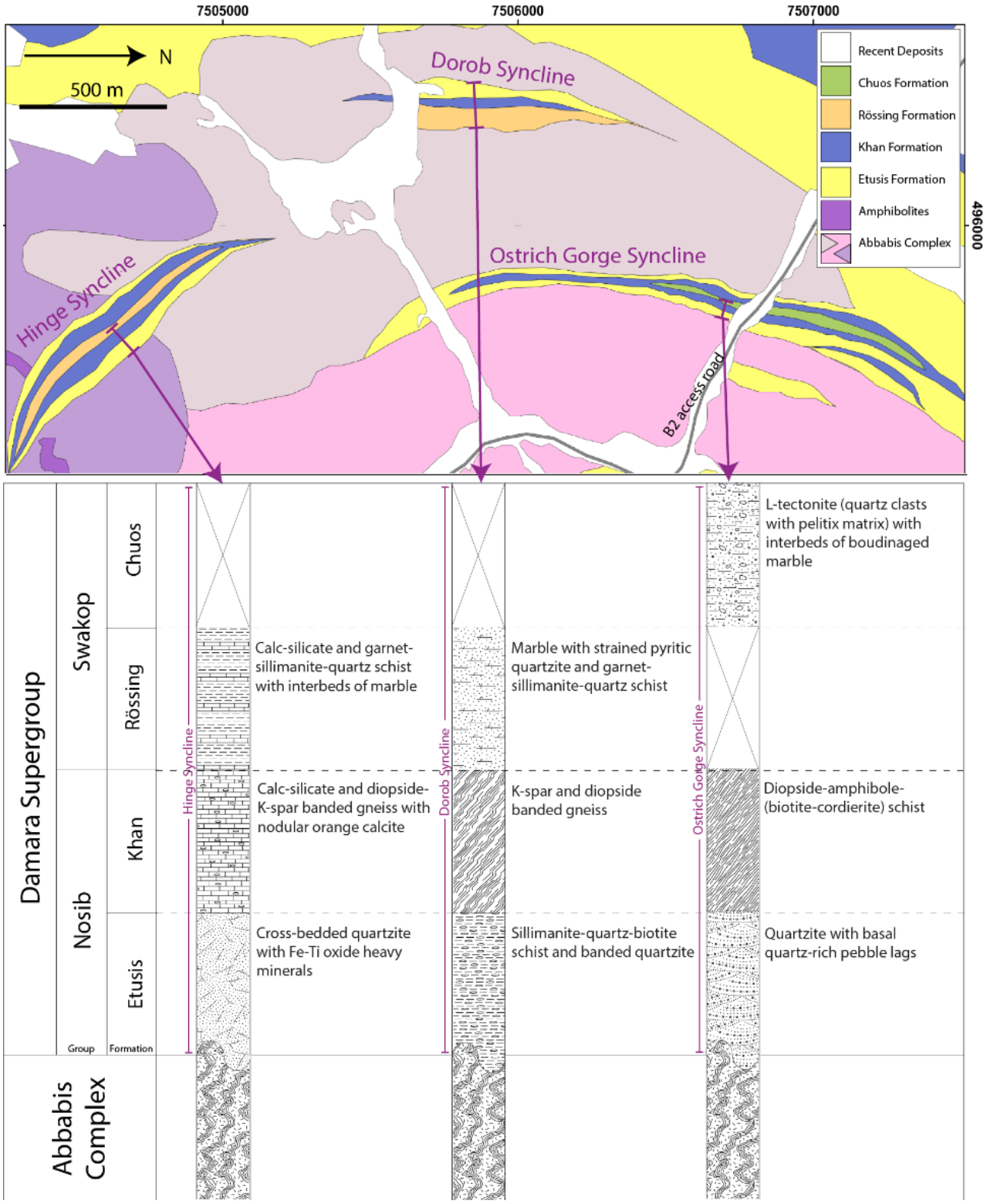


Figure 4.12: Geological map showing the synclinal infolds and their associated lower Damaran stratigraphic units in each syncline. The Hinge, Dorob and Ostrich Gorge Synclines are illustrated in the stratigraphic sections. Thicknesses are not representative. X indicates missing formations in the stratigraphic sections.

4.3 Structure

Structural observations in the Nose Structure were considered in order to establish relative temporal relationships with the intrusive types and general geological history within the field area. Structural measurements, descriptions, and cross-cutting relationships of several structural components were noted. These components included various fold generations, shear zones, HSZs, brittle deformation features, and associated foliations and lineations. Understanding the structural geometry of the megascale interference fold and the several synclinal infolds is key to understanding the processes in the formation of the characteristic basement-cored domes in the sCZ. Several models for dome formation are proposed and outlined in table 4.2 below, and each of these have characteristic features. Several debates surrounds the number of deformational events present in the Damara Belt, with two (Jacob *et al.,* 1983) to six (Sawyer, 1981) deformational events proposed. Likewise, the debate around continuous and progressive deformation (Poli, 1997) is a factor to consider. Five main deformational events were established, each with associated structural components. A pre-Damaran fabric was seen within the Abbabis Complex, with four events associated with the Damaran metasediments and the basement rocks.

Table 4.2: Table detailing the different dome formation arguments presented by various authors with their respective characteristics.

Dome formation mechanisms	Characteristics and comments	
Inteference Folding	orthogonal constriction or superposition of two phases on folding	Smith (1965) Jacob *et al* (1983)
Single phase of constrictional deformation	contraction perpendicular to extension progressive deformation with early phase of horizontal fabric= gentle domes to SW vergent increased strain at basement-cover contact extension and linear fabrics	Poli (1997) Poli & Oliver (2001)
Metamorphic core complex development	brittle upper crust is seperated from deep exhumed crust by a zone of high-T mylonites extensional shear bands and stretching lineations	Oliver (1994) Oliver (1995)
Diapiric remobilisation of basement into Damara Supergroup rocks	radial stretching lineations and tangential flattening foliations in the domes diapiric rise of lower density material (Damara metasediments)	Barnes & Downing (1979) Barnes (1981) Sawyer (1981)
Magmatic deformation by ballooning granites	radial lineations and flattening foliation around the domes diapiric rise in lower density material flattened strains and folded veins around the margins of the dome	Barnes & Downing (1979) Kröner (1984)
Mega-scale sheath folds	major, gently, dipping shear zone that are modified by diapirism owing to the intrusion of late granites	Coward (1981)
Tip-line folds located above blind thrusts	fold-thrust style tectonics tip line blind thrusts above thrust duplexes	Kisters *et al* (2004)

4.3.1 Pre-Damaran Deformation in the Abbabis Complex

The Abbabis Complex lithologies and associated magmatism, namely the basement granites and amphibolites, display an early fabric (S_{AB}), and augen that is cross-cut and folded by the Damaran foliation (S_0/S_1), intrusives and folding events. No other units show two cross-cutting foliations as observed for the Abbabis Complex gneisses (Fig. 4.13). The Abbabis Complex displays a pencil cleavage prominent in the western part of the field area and has a characteristic weathering style with jagged features protruding from the outcrop (Fig. 4.13). The early Abbabis Complex fabric is

primarily a gneissic fabric (S_{AB}), which is aligned with the augens and compositional layering of the gneisses. However, this gneissosity has largely been reoriented into parallelism with the Damaran folding events. In some instances the later Damaran foliation (S_0/S_1) cross-cuts the gneissic fabric at a low angle and is often sub-parallel forming the characteristic weathering profile and pencil cleavage. However, these foliations are reoriented by later folding events and appear as axial planar to the open and upright folds or to the compositional layering of the Damaran metasediments. The gneissic foliation is also folded by recumbent isoclinal to tight and upright open folds. In addition, the fabric is stretched in the HSZ, which preserves thinner gneissic bands. Pre-Damaran deformation in the Palmenhorst Dome is largely overprinted due to the high-grade metamorphism associated with the Damara Belt (Longridge, 2012). The basement granites, amphibolites and granite-gneisses do not show this same gneissosity as the basement gneisses but rather show a prominent mineral aligned foliation.



Figure 4.13: Field photograph of the Abbabis Complex augen and/or orthogneiss displaying an early fabric and later Damaran fabric cross-cutting one another resulting in the characteristic pencil cleavage that creates the jagged weathering profile of the gneisses. The yellow line indicates the Abbabis Complex gneissic fabric, while the white line indicates an axial planar foliation from the open folding event.

4.3.2 Damaran Deformation

The Damaran deformation shows the most intense deformation within the field area and overprints many of the pre-existing fabrics and structures in the Abbabis Complex. It contains three main events with a late stage brittle deformational phase, which post-dates all the other structures. The

first Damaran event (D1) is preserved as a regional fabric, which is associated with a bedding-parallel foliation. D2 and D3 events are the most pronounced deformational structures associated with the preceding events. Tight to isoclinal folds, shear zones and HSZs are associated with D2, while D3 reorients these folds into open and upright folds with associated fold-axis parallel extension. Lastly, brittle faulting (D4) is observed although relative temporal relationships are not sufficient to determine whether this is part of the Damara orogenic event or not.

Early fabric forming deformation (D1)

An early fabric is developed throughout the field area and is developed parallel to compositional layering as a bedding parallel foliation (S_0/S_1). This foliation is commonly defined by platy mineral alignment, such as biotite and amphiboles, although it is also frequently observed as compositional banding. D1 foliation is mainly seen in the metamorphosed Damaran sediments. This foliation is an early development and typically reoriented or affected by later folds, shears and strain zones (Fig. 4.14). Most notable is the presence of this foliation within the HSZs, which are typically parallel to bedding that have been attenuated in later D2 events. Interestingly, there are rootless intrafolial folds that are attenuated and extended parallel to the foliation (Fig. 4.15.B- see section on D2 deformation) and show no bending of foliation. These have a similar geometry to the D2 recumbent folds and no refolding of these folds or cross-cutting relationships are observed. This event is not clearly discernible in the Abbabis Complex due to the Pre-Damaran gneissic banding.



Figure 4.14: An example of the early regional fabric, identified in the field, that is reoriented by later D2 and D3 events. The foliation is traced in a solid black line and the orientation, of the undeformed and bedding parallel portion, is given alongside.

Southwest to west verging recumbent folds, high strain zones and limb parallel extension (D2)

The southwest to west verging recumbent folds and associated HSZs (and shears) constitutes the second deformational (D2) event associated with the Damaran Orogeny and is the most intense in terms of deformation and metamorphism. The deformational event is characterised by recumbent tight to isoclinal folding (Fig. 4.15.A and B), shear zones (Fig. 4.15.C) and zones of higher strain (Fig. 4.16), particularly at the basement-cover contact. A gently dipping northeast trending lineation (often developed as sillimanite porphyroblasts) that mainly occurs in the cover sequence and migmatisation of the basement-cover lithologies is also associated with D2. Based on lithological mapping, map-scale refolded D2 synclinal Damaran metasediments were observed, although most of the evidence for these folds is found in small-scale parasitic folds at outcrop scale. Both the basement and cover sequences were subjected to this folding event, and these lithologies can be observed within folds, as well as earlier granites and SLGs (types A, B and C') are folded by the tight folding event. D2 is preserved as large-scale folds for the Damaran and Basement lithologies, with a gneissic fabric developed especially in the Abbabis Complex, Khan Formation and Rössing Formation.

Generally, these folds are tight to isoclinal, with typical interlimb angles ranging from 5° to 25°. A strong southwest (to west) vergence, resulting in gently inclined to recumbent (Fleuty, 1964; average fold axial plane dip is 10°) geometries, is seen in the folds that are not reoriented by later deformation (Fig. 4.15.B). From outcrop scale parasitic folds axial plane measurements were taken and most fold limbs display a gentle dip towards the northeast (Fig. 4.15.A and D). The average fold axial plane orientation is northwest-southeast striking, with an average gentle dip of 10° to the northeast (Fig. 4.15.D). An axial planar foliation is present in small outcrop scale in the HSZ and the rest of the field area, although this is typically reoriented by later deformation. This can be seen in figure 4.15.D where the measured fold axial planes for the D2 folds have an overlapping conical projected average with the foliation planes (plotted as poles). The early regional D1 foliation is generally folded into isoclinal folds and types A, B and C' SLGs (see section 4.5.5) cross-cut the D1 foliation (S_0/S_1) when they are folded into D2 folds. This D1 foliation is predominantly seen in the Damaran metasediments and is refolded at a large scale. However, in the HSZs the fold limbs are attenuated, rootless and run parallel to the dominant foliation in the Abbabis Complex gneisses at an outcrop scale. Fine platy minerals, such as biotite, are seen within the folds as cleavage.

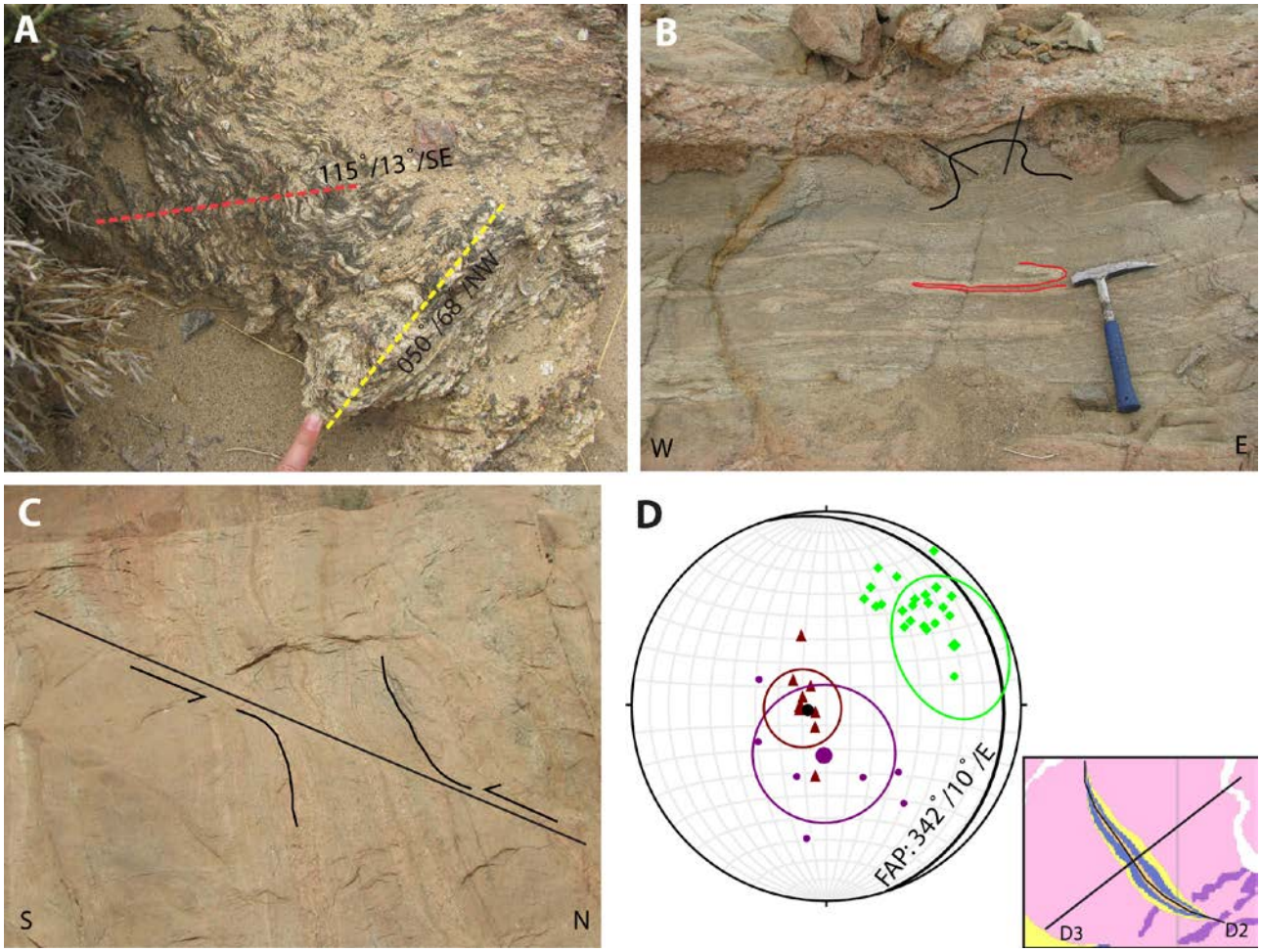


Figure 4.15: Field photographs (A to C), equal area stereonet plot of the D2 folds (D) and geological map of the Hinge Syncline. (A) Folded sillimanite-biotite schist, of the Etusis Formation, with two fold generations. D2 (red) is recumbent and tight meanwhile D3 (yellow) has reoriented the axial planes but is open and more upright. (B) Intrafolial isoclinal and recumbent D2 folds (red) of SLG. A D3 open fold (black) that has folded the foliation and displays two fold axial planes. (C) Discordant sinistral shear zone that has cross-cut basement granites. (D) An equal area stereoplot of the poles of fold axial planes (maroon triangles) measured from parasitic isoclinal folds, axial planar foliation (purple circle) and northeast gently dipping lineation (green diamonds). The circles, and their colours correspond to conical best fit projections of each data set with the centre and enlarged points indicating the average. The average fold axial plane (FAP) shows a northeast dipping and north-south striking fold axial plane. The black filled circle shows the pole to the FAP. The in-set in the bottom right shows the Hinge Syncline where there is a large scale D2 syncline refolded by the D3 folding event. Pink= Abbabis Complex; purple= amphibolites; yellow= Etusis Formation; blue=Khan Formation; orange= Rössing Formation; white= recent deposits.

The development of the northeast plunging lineation is related to D2 as it is parallel to the main D2 anticline in the Nose Structure. Plotted on the stereonet, they lie on the average axial plane of the D2 fold (Fig. 4.15.D). Individual sillimanite porphyroblasts are folded into D2 recumbent tight folds and then refolded by D3 upright open folds and therefore must have developed prior to D2 folding was complete (see D3 section). These porphyroblasts are mainly seen in the Etusis Formation. Due to reorientation of the D2 fold by D3, the lineation direction is also reoriented to align with the axial plane of the main D3 folds in the field area. However, the gentle northeast plunge of these lineations more closely approximates the fold axial plane of D2 and the individual sillimanite porphyroblasts show interference folding patterns, therefore the lineation is attributed to the D2 folding event. The

Etusis and Chuos formations also contain attenuated pebbles, which extend in the northeast-southwest direction. Amphibolites with the pre-Damaran foliation were folded into tight, rootless and isoclinal dykes that verge to the southwest (Fig. 4.1). Both the foliation and the amphibolites are folded. Migmatised basement gneisses preserve isoclinal folded leucosomes, although these are often cross-folded.

From lithological mapping in the field area, synclines of lower Damaran metasediments are located within the basement rocks (Fig. 4.1 and 4.15.D). These synclines displayed a southwest vergence and had been refolded by later D3 deformation, resulting in slightly steeper dips for the fold plane. The synclines, generally cored by Rössing or Chuos formations, showed attenuated sequences (as previously described Fig 4.12) of Rössing Formation to the point that it was missing within the lower Damaran Sequence in the Ostrich Gorge Syncline and Dorob Infold. These infolded synclines, the Ostrich and Dorob Synclines (Fig. 4.1), are developed as remnant parasitic recumbent D2 S-folds. In contrast, the Hinge Syncline is developed as a complete syncline within the hinge of D3 syncline.

Discordant shear zones (Fig. 4.15. C) are often associated with D2 deformation. This relationship was established from cross-cutting relationships between the shear zones and the SLGs. SLGs with established relative age relationships (with respect to the other SLGs and deformational features) were also useful in determining the relative timing of the shear zones. Types A, B and C' SLGs are all sheared by these approximately coaxial (parallel) shears, however, they are then intruded by younger SLGs, such as type E. Type E SLGs occur in coaxial shears that post-date the HSZ indicating two generations of shear zones: the discordant shears and straight gneisses of the HSZ. The shear zones related to the D2 event show zones intruded by types A, B and C', that share the general trend of the shear zones, are sheared by D2 shears and are discordant to the main stretching direction of the HSZ. However, the syn-shear intrusives have diffuse contacts along the edges between the intrusives and the strained basement rocks and extend into the northeast-southwest direction of strain as well as the foliation (Section 4.4- pavement map) indicating that the shearing and strain are related. This results in blebs of SLGs that are dismembered in the HSZ. The trends of these shear zones generally show approximate northeast-southwest to north-south directions and are extensional, as the extension direction (northwest-southeast) is perpendicular to the main compressive direction for this folding event (northeast-southwest). These shear zones occur throughout the field area with the D2 shear zones most commonly associated with SLGs in the Abbabis Complex and then as foliated and friable zones with bent foliations in the schists of the Damara Supergroup.

The HSZs are common in the D2 event with strain increased along the basement-cover contact and along the Rössing Formation when located in the infolds and synclines. The HSZ does not show rotational features but rather stretching that is manifested as straight gneisses (Fig. 4.16). The basement-cover strain zone (Section 4.4- Pavement map) is oriented northeast-southwest and is defined by a closely spaced foliation and thinned gneissic banding in the Abbabis Complex and intensely foliated schistose lithologies in the cover sequence in the same direction. These HSZs are parallel to the fold limbs and appear to be attenuated limbs of the folds as this extension direction is parallel to the main (folding) compressive direction (northeast-southwest). The HSZs most likely occur along the long limb that has not been overturned from southwest vergence.

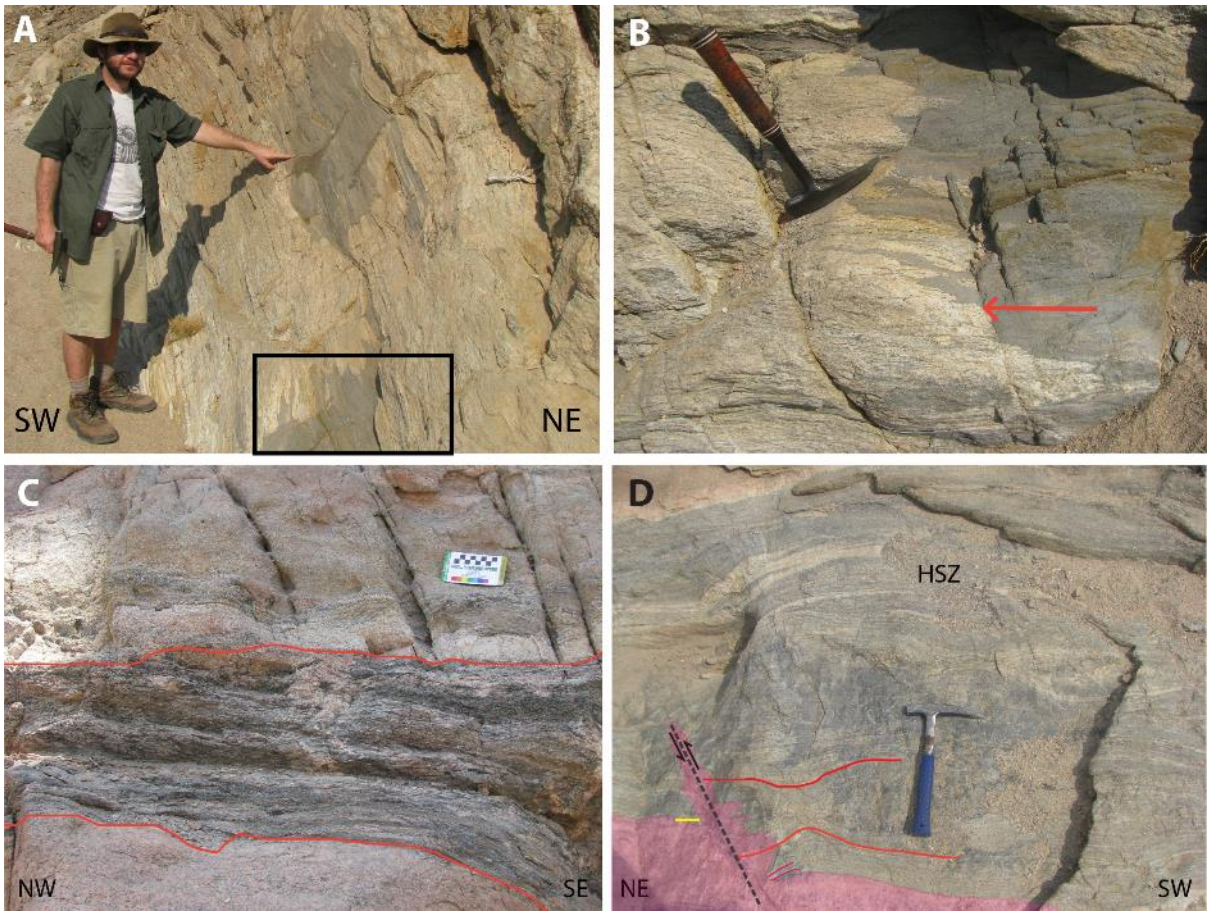


Figure 4.16: Field photographs of the D2 HSZ. (A) A grey granite being extended into the strain direction as zig-zag edges attenuate the granite into the basement gneiss. (B) The area in image A indicated by the black box, showing a more detailed image of the of the strain extending the granite into the gneiss. (C) Bedding parallel foliation within a HSZ. Foliation spacing is thinned and now continuous. (D) HSZ gneisses (HSZ) with foliation parallel and cross-cutting type A SLG (pink) being extended into the gneissic fabric by the strain. Discordant sinistral shear zone intruded by the SLG. Stretching and boudinage (red) are in a northeast-southwest direction parallel to compressive direction.

Typically, the HSZ shows types A, B and C' SLGs, the red and grey granites being extended into parallelism of the stretching direction (Fig. 4.16.A and B). The grey granites in particular show attenuation and straining into the gneissic fabric of the basement rocks (Fig 4.16.A and B). The

foliations in each rock are parallel and generally show a concentration and alignment of biotite and amphibole (Fig. 4.16.C) along with typical bedding parallel foliation orientations when housed in the Damaran metasediments and the basement rocks. In figure 4.16.D the HSZ rocks are highly attenuated but they show discordant shearing. The Rössing Formation shows increased partitioning of strain and shear, and often thins out or is not present in the lower Damaran sequence.

Additionally, northeast-southwest extension is also identified where foliation and bedding has been boudinaged (Fig. 4.17) parallel to the HSZ. Boudinage of bedding parallel foliation of the Etusis, Khan and Rössing formations with associated SLGs within the core of extension sites (Fig. 4.17.A), Etusis Formation sillimanite porphyroblasts (Fig. 4.17.B), northeast-southwest stretched clasts within the Etusis and Chuos formations, and the thinning of the foliation or gneissic banding within the basement rocks and associated granites (Fig. 4.17.C) all occur within the HSZ.

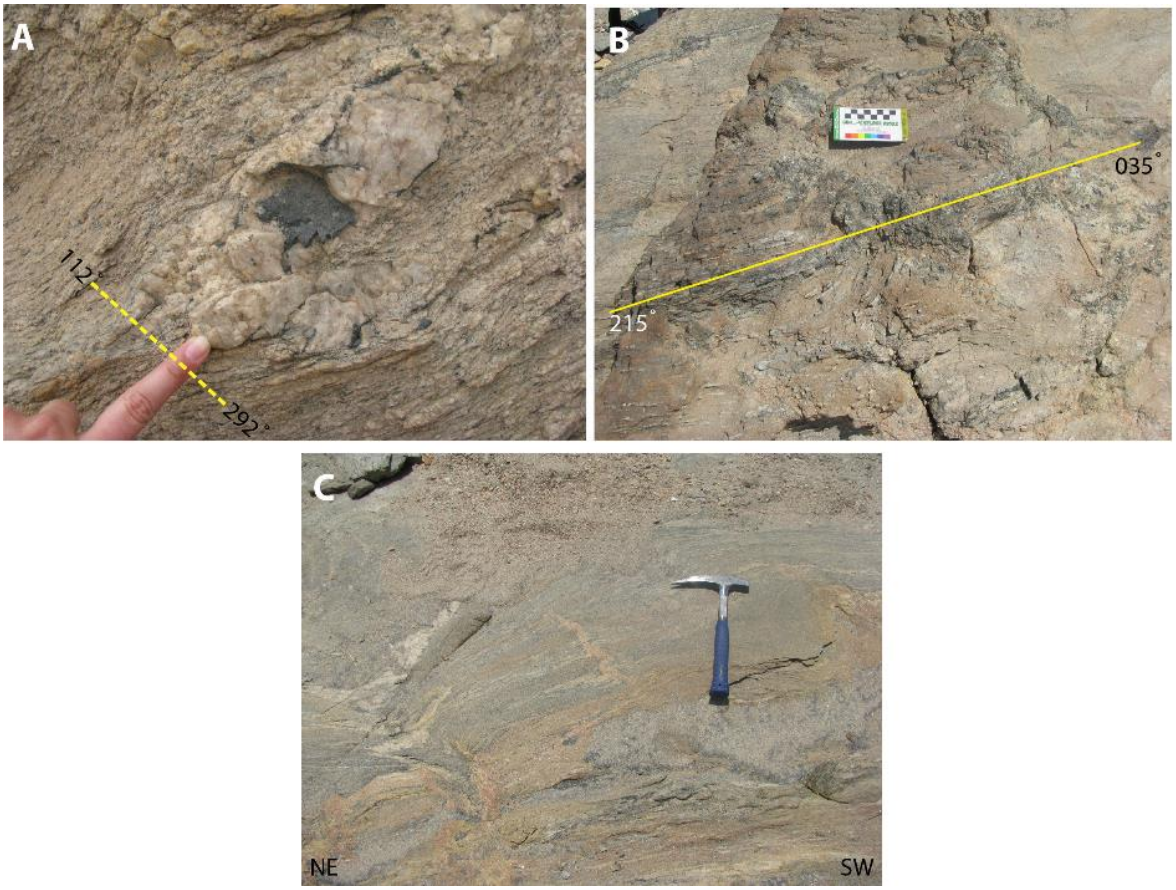


Figure 4.17: Field photographs of boudinage parallel to the northeast-southwest trending HSZ. (A) Strained Rössing Formation showing bedding parallel foliation with boudinage. SLG present in the core of the extension site. (B) Sillimanite porphyroblasts, in the Etusis Formation, are boudinaged and extened into the HSZ extension direction. (C) Basement rocks within the HSZ, and associated SLG boudinaged and extended into the direction of stretching.

Interference upright and open folds with northeast-southwest extension parallel to the fold axial plane (D3)

The upright open folding transposes the deformational features developed during the D2 event and creates a typical interference fold pattern. This deformational event is also associated with a northeast-southwest extensional phase that is perpendicular to the northwest-southeast compressional direction. These folds show bent fold axial planes in outcrop due to cross-folds and are more abundant than the parasitic outcrop folds of D2. They too, are most commonly seen as parasitic folds in outcrop with large scale folding of the basement and cover rocks. This large-scale folding is identified quite easily by the use of satellite imagery, where the Nose Structure and Blauer Heinrich Mountain form the limbs of the main D3 syncline of the field area (Fig. 4.1). These folds generally deform most of the components described in this chapter in the field area including the basement lithologies, the Damaran metasediments, the early granites and all the SLG types except for type F. D3 folds are most commonly seen in the gneissic banding of the Abbabis Complex where leucocratic and melanocratic alternating banding shows the abundant folding. Likewise, the Damara Supergroup preserves these folds as larger scale folds that are not always readily seen in outcrop. Some exceptions are present and show schistose folded lithologies and sillimanite porphyroblasts in the Etusis Formation. Types A, B, C' and E SLGs are also folded, but only the last is not refolded by the previous D2 event.

The D3 event is characterised by open and upright to near upright folds that generally dip to the northwest or southeast in outcrop scale (Fig. 4.18.A and B). The interlimb angles range from 75° to 100°, although closed folds are present where interference exists with D2 tight folds (Fig. 4.18.B). These interference patterns form domal structures at an outcrop scale (Fig. 4.18.C), which mimics the map-scale interference fold patterns. General orientation of the open folds are northeast-southwest trending axial planes that are steeply dipping to the northwest or southeast (Fig. 4.18.D). The equal area stereoplot shows the D3 fold axial plane data that is more scattered than the data displayed in D2 plots and this is probably due to interference patterns as the units were already deformed (Longridge, 2012). Two near vertical clusters are present, with associated axial planar cleavages that plot in the same conical average best fit areas. Axial planar cleavages show two dip directions and may be due to the refolding of the D2 fold axial plane. The stretching lineation cluster also falls on the average axial plane, however, this is probably due to the reorientation of D2 components as the average lineation measurement does not fall onto the D3 average axial plane. In some instances, two foliations can be seen (Fig. 4.18.A), one which is folded (S_0/S_1) and one that is parallel to the fold axial plane (S_2). This folding event typically folds the surrounding foliation (Fig 4.18.B) and cross-cuts the foliation in places where it is preserved in SLGs (unlike D2 folding).

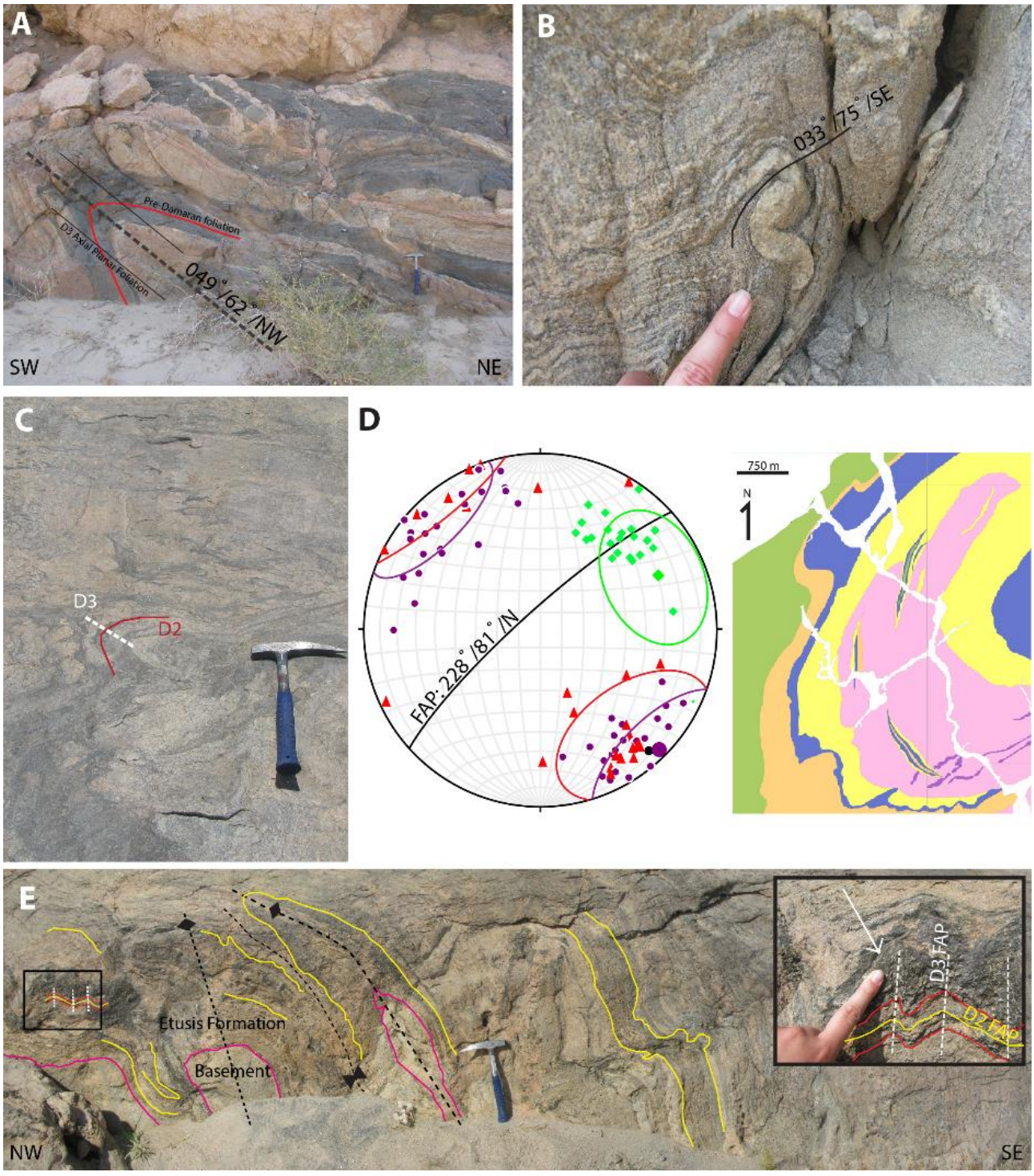

A
Pre-Damaran foliation
D3 Axial Planar Foliation
049°/62°/NW
SW
NE
B
033°/75°/SE
C
D3
D2
D
FAP: 228°/81°/N
750 m
N
1
E
Etusis Formation
Basement
NW
SE
D3 FAP
D2 FAP

Figure 4.18 (on previous page): Field photographs of the D3 interference folds (A to C and E), stereoplots (D) and geological map of the field area. (A) Open and steeply dipping folds of amphibolite dykes and SLGs cross-cutting basement rocks. Two foliations are present: axial planar foliation (black dashed line) and one folded (red line). (B) A parasitic open fold with a bent fold axial plane (plane line) due to interference patterns in the Chuos Formation. Surrounding biotite and amphibole foliation folded too. (C) Dome-like interference patterns from outcrop scale folds in a HSZ gneiss. Red fold axial plane (D2) is refolded by D3 (white) fold to form a basement-cored fold. (D) Equal area stereoplot showing measured poles of fold axial planes (red triangles), axial planar foliation (purple circles) and stretching lineation (green diamonds) with the fold average fold axial plane (FAP; black) derived from the conical best fit average of the fold axial plane pole measurements. average pole indicated by the black circle. Circles, in the same colours as the datasets, are conical best fit projections with the average poles indicated in slightly enlarged symbols. (E) Cross section of a folded outcrop. Basement-cored domes (pink) with surrounding Etusis Formation (yellow) is a result of fold interference patterns between D2 and D3 at the outcrop scale. Top right inset: interference fold pattern of recumbent D2 (yellow= limbs; red= fold axial plane) folds being refolded by D3 open and vertical folds (white). Inset is enlargement of black box outlined on the left.

In figure 4.18.E, the overall interference pattern in outcrop scale replicates the large-scale interference pattern and forms a summary cross section representation of the field area's structure. Open and upright folds are present, which show the basement gneisses in the core of the Etusis Formation in a series of anticlines and synclines. The fold axial planes are generally bent and dip to the southwest. A bedding parallel foliation is present that has been refolded by two folding events. The inset of Fig. 4.18.E shows recumbent tight fold (D2) limbs (in red) and the proposed D2 fold axial plane (yellow) refolded by upright open D3 folds (white). In addition, individual sillimanite porphyroblasts show signs of being folded by both of these events. The porphyroblasts are elongate and show parasitic folds parallel to the recumbent fold as well as the upright fold. This indicates sillimanite porphyroblast growth was probably developed during D2 deformation.

A second event of approximate northwest-southeast trending fold axis parallel extensional shearing is associated with D3 and is generally associated with a series of parallel shears cross-cutting the HSZ with associated type E SLG intruding into the shears as conduits. S-C fabrics have developed between parallel shear surfaces (see section 4.5.5, Fig. 4.31). These do not appear to be extended into the strain zone and visibly cross-cut the shear. These shears are more rotational as they show more pronounced deflections of the foliation and granites, in which they cross-cut (types A, B and C' SLGs). However, as in the previous deformation, rotation of clasts and granites are not observed. Stretching of the Etusis clasts (northeast-southwest) and folding of tectonised Chuos Formation clasts are only seen. In the case of the Chuos clasts (see section 4.2.2) the clasts were extended in the D2 stretching lineation direction first, and then folded. The northwest-southeast extension in this zone is closely linked to the shears as they are orthogonal.

Late stage brittle deformation

The last stage of deformation visible in the area is brittle in nature and is associated with a series of joints and faults, which generally form low angles to the horizontal (Fig. 4.19.A and B). These joints strike approximately east-west and dip towards the south, although conjugate sets are occasionally

observed (Fig. 4.19.B). These joints cross-cut the basement rocks, metasediments and all granites except for type F SLGs (Fig. 4.19.A and B). Type C' SLGs are cross-cut by two fault zones and displaced (Fig. 4.19.A). The faults are sharp, often bifurcate and have a predominantly sinistral movement. This brittle deformation is associated with chlorite along fractures (Fig. 4.19.C). Brittle deformation is also associated with type F SLGs as they intruded brittle structures and trend east-west and occasionally northeast-southwest. These granites are tabular, undeformed with no shearing along the edges of the intrusion.

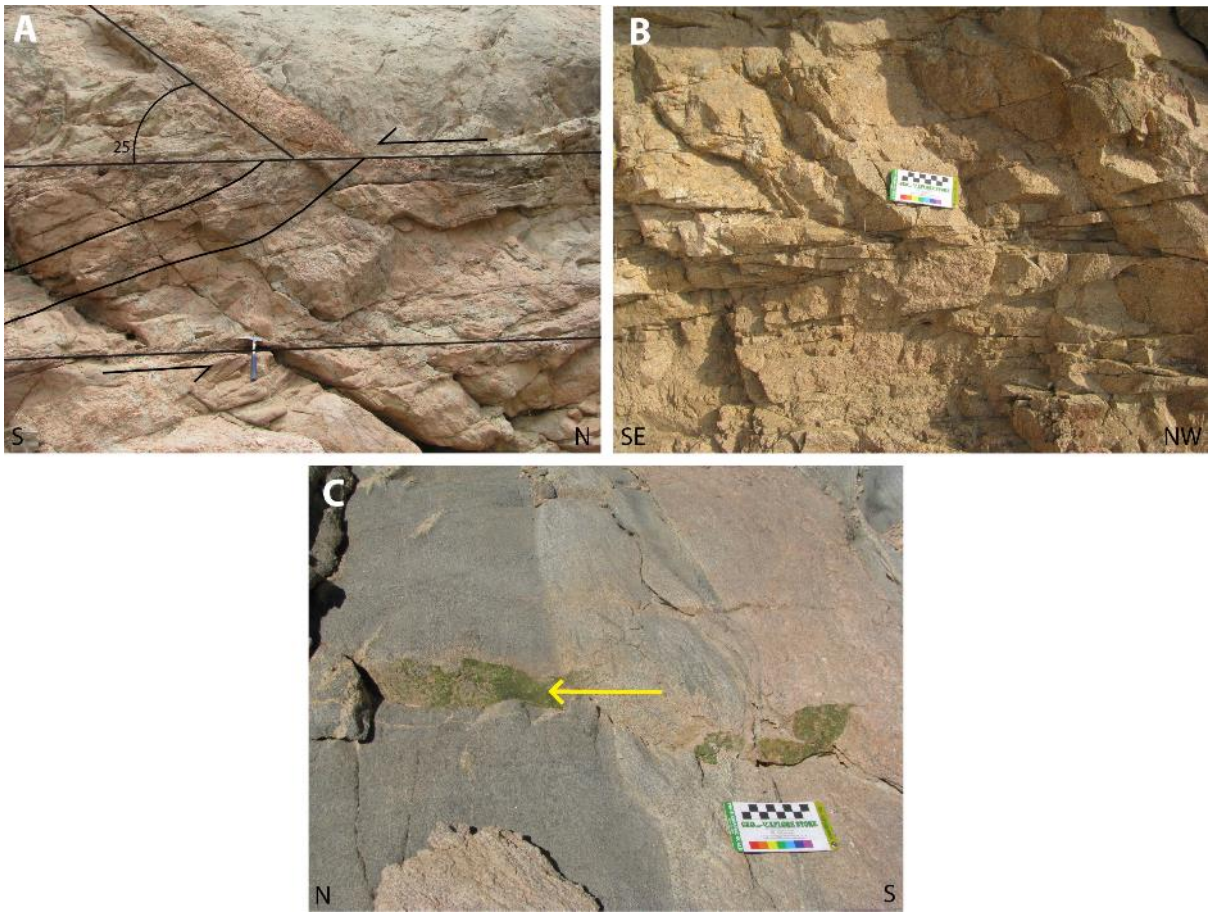


Figure 4.19: Field photographs of the brittle deformation associated with D4. (A) Brittle sinistral faulting displacing various SLGs. The zone has cleavage within the displacement zone. (B) Low angle conjugate joints within the Rössing Formation. (C) Brittle joints associated with chlorite and/or epidote alteration along the joint planes (indicated by the yellow arrow). This joint cross-cuts basement rocks and a SLG in this picture.

4.4 Pavement map: synthesis of cross-cutting deformational and intrusive relationships

The pavement map in figure 4.20 shows a summary of the cross-cutting relationships between the Abbabis Complex, Damara Supergroup, granites and deformational features in the HSZ described in the previous sections. The HSZ in figure 4.20 has a northeast-southwest extensional direction and is associated with D2.

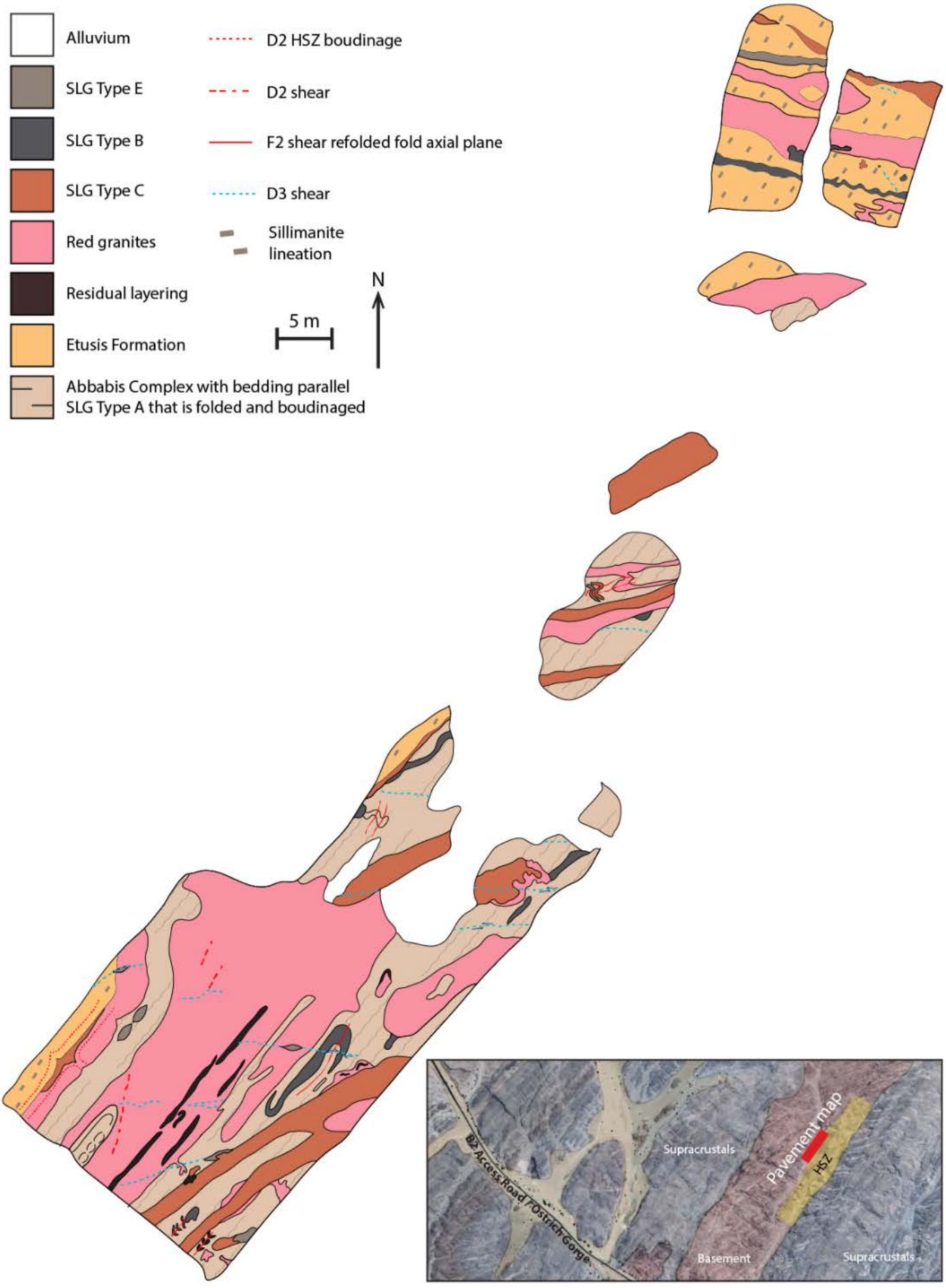


Figure 4.20: Pavement outcrop map of the HSZ, summarising the cross-cutting relationships between the supracrustals, basement rocks, granites and deformational features. The lower right inset shows the locality of the pavement map in the northern extent of the field area. Residual layering is present within xenoliths of palaeosomes.

4.5 Intrusive Rocks

The Central Zone was affected by widespread magmatism, which is characteristic of the zone within the belt (Miller, 2008). Numerous authors have subdivided and classified these intrusions (Table 4.3) based on their morphologies, mineralogy and relative timing in context of the deformational history (Smith, 1965, Jacob, 1974; Marlow, 1981; Brandt, 1985; McDermott, 1986; Kinnaird and Nex; 2007). In addition, several smaller subdivisions exist to distinguish between the various SLGs within the Central Zone (Nex and Kinnaird, 1995; Nex, 1997; Freemantle, 2017). In this study, intrusions were classified, in the field and petrographically, and placed into the various intrusive types outlined by Miller (2008). In terms of the SLGs, classification of Nex and Kinnaird (1995) scheme was used.

Table 4.3: Classification of granites based on field characteristics in the study area using the nomenclature of Smith (1965), Marlow (1983), Brandt (1985), McDermott (1986) and Nex (1997) with the table modified after Freemantle (2017).

Suite	Type	Description
Pegmatite	White	White pematitic, clear quartz, no accessories visible in hand-specimen. Intrudes most other granites,accessory quartz-tourmaline segregations
Sheeted leucogranites	A-type	Thin, very light pink to white, bedding parallel, very few accesories, often folded and boudinaged within Damaran metasediments
	B-type	White to light pink, medium-grained, homogeneous, bedding parallel, folded and boudinaged, variable width. Disseminated accessory garnet (< 1 cm) with poikiblastic garnet porphyroblasts at Valencia, accessory tourmaline, biotite, apatite and allanite
	C-type	Extensive sheets or coalescenced sheets, sometimes parallel, predominantly cross cuts Nosib and Swakop Group, white to light pink in colour, medium to coarse-grained, sometimes pegmatitic, accessory entrained biotite, magnetite (clusters and disseminated), tourmaline (5 to 6 cm), dark green amphibole and epidote. Often structurally controlled
	D-type	White, medium to coarse-grained, granular texture, with smoky quartz and minimal biotite although biotite often hosts U, yellow uranium secondary phases may be exposed on exposed joint surfaces, irregular and anastamosing (1 - 7 m)
	E-type	Deep pink amorphous veins and fingers of granite, commonly oxidised, intrudes pelitic sediments and earlier granites, high biotite content and smoky quartz. Often considered to be from autohyrdation-derived alteration during emplacement of D-types
	F-type	Deep pink, pegamtitic, milky quartz, cross cuts most features, basement and granites, sharp contacts, tabular and parallel sides
Grey Granites	Type 1	Dark grey, fine to medium-grained, homogenous texture, biotite-rich, white feldspar, prominent biotite foliation
	Type 2	Lighter shade of grey than type 1, has distinctive porphyroblasts of white/pink feldspar (< 1 cm)
	Type 3	Lighter grey than both type 1 and 2, often intrudes type 2, often contains white pegmatites in the form of thin veins which intrude into the host lithologies
Red Granites	Red Th granite	Red to light pink, fine to medium-grained, anomalous Th content, intrudes Basement and parts of the Nosib Group, heterogenous and homogeneous textures, accessory sillimanite
Salem Granites	Salem 1	Dark grey, high % biotite, High Ca (An35) foliated, quartz-plagioclase dominant
	Salem 2	Lighter grey, subtle foliation, less Ca (An25) large megacrysts of white and pink K-feldspar (up to 5 cm), high % biotite
Basement Granites and Gneisses	Granite	Larger bodies, many tens of metres across, constituets a large portion of the basement lithologies, white to light pink, fine-grained, minimal accessories except for biotite
	Porphyritic Granite Gneiss	Dark grey with distinctive white feldspar porphyroblasts (2 cm long), characterised by pink partial-melt
	Basement Gneiss	Light grey, coarsely nanded gneiss, distinctive leucocratic and mafic segregations and pink partial melt

Granitic intrusions observed in the field area include basement granites, red granites, grey granites and various SLGs. The SLGs are named according to the nomenclature of Nex and Kinnaird (1995) primarily based on size, morphology and mineralogy, however, cross-cutting relationships are not always consistent with Nex and Kinnard's (1995) field relationships, and this is discussed in section

4.7. Amphibolites are also observed within the field area. These intrusions are described below from oldest to youngest based on field criteria. Observations regarding cross-cutting relationships with other intrusions, metamorphic indicators and deformation were recorded to determine relative timing of events.

4.5.1 Basement granites

The basement granites are the oldest granitic intrusives and formally they belong to the Abbabis Complex (Smith, 1965). However, this lithology shows intrusive contacts with the basement gneisses and forms an approximate 1.5 km body, termed the Ostrich Gorge basement granites, within the Abbabis Complex lithologies (Fig. 4.21). The basement granites do not cross-cut the Damara cover rocks but surround them in the Hinge Syncline, with no intrusive relationships observed. This intrusion type forms large bodies that sometimes appear amorphous (because the contact is inferred from remote sensing and field mapping) and has a relatively homogenous texture (Fig. 4.22.A) that only shows faint banding of alternating quartzofeldspathic bands that vary in modal quartz abundances and grain size.

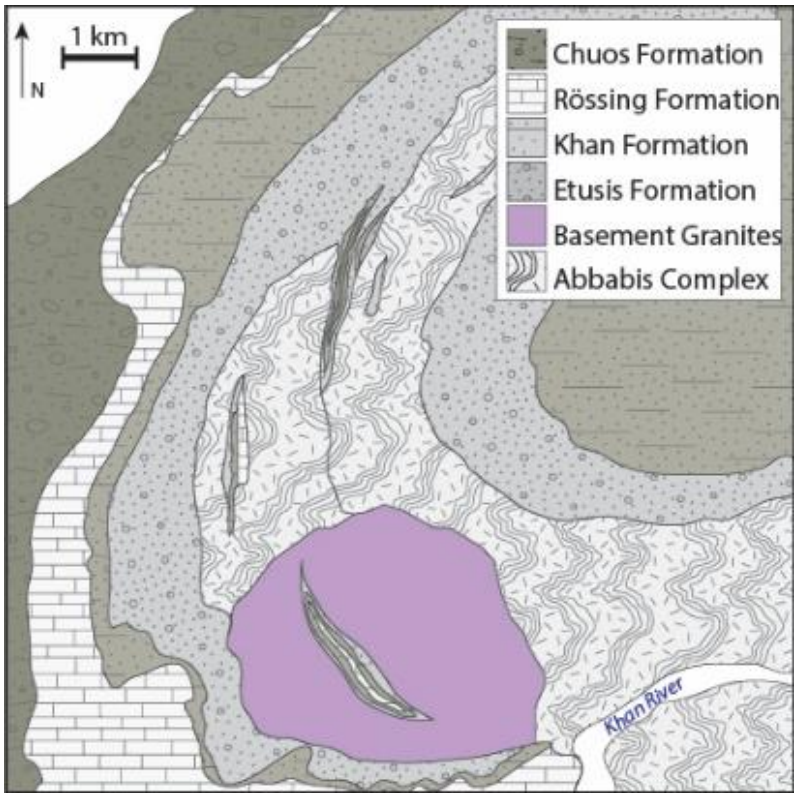


Figure 4.21: Simplified geological map of the field area, modified from figure 4.1, highlighting the estimated extent of the basement granites.

The various granitic-gneisses of the Abbabis Complex show a distinct biotite foliation, while the basement granites only show a faint alignment of plagioclase and quartz within a K-feldspar-rich granite at outcrop scale. This granite type has a musky to light pink colour (Fig. 4.22) with flecks of aligned white quartz or plagioclase, especially in the Khan River Gorge. This foliation is weakly defined and not gneissic like the Abbabis Complex gneisses. In the Ostrich Gorge Intrusion, the granite is more weathered with a granular and fragmented appearance (Fig. 4.22.A). This granite type is fine-grained, K-feldspar-rich with minor plagioclase, while the foliation (S_1) defining quartz and plagioclase crystals are typically 3 – 5 mm in length. This foliation is spaced and parallel. The microgranite displays no accessory minerals and is notably homogeneous.

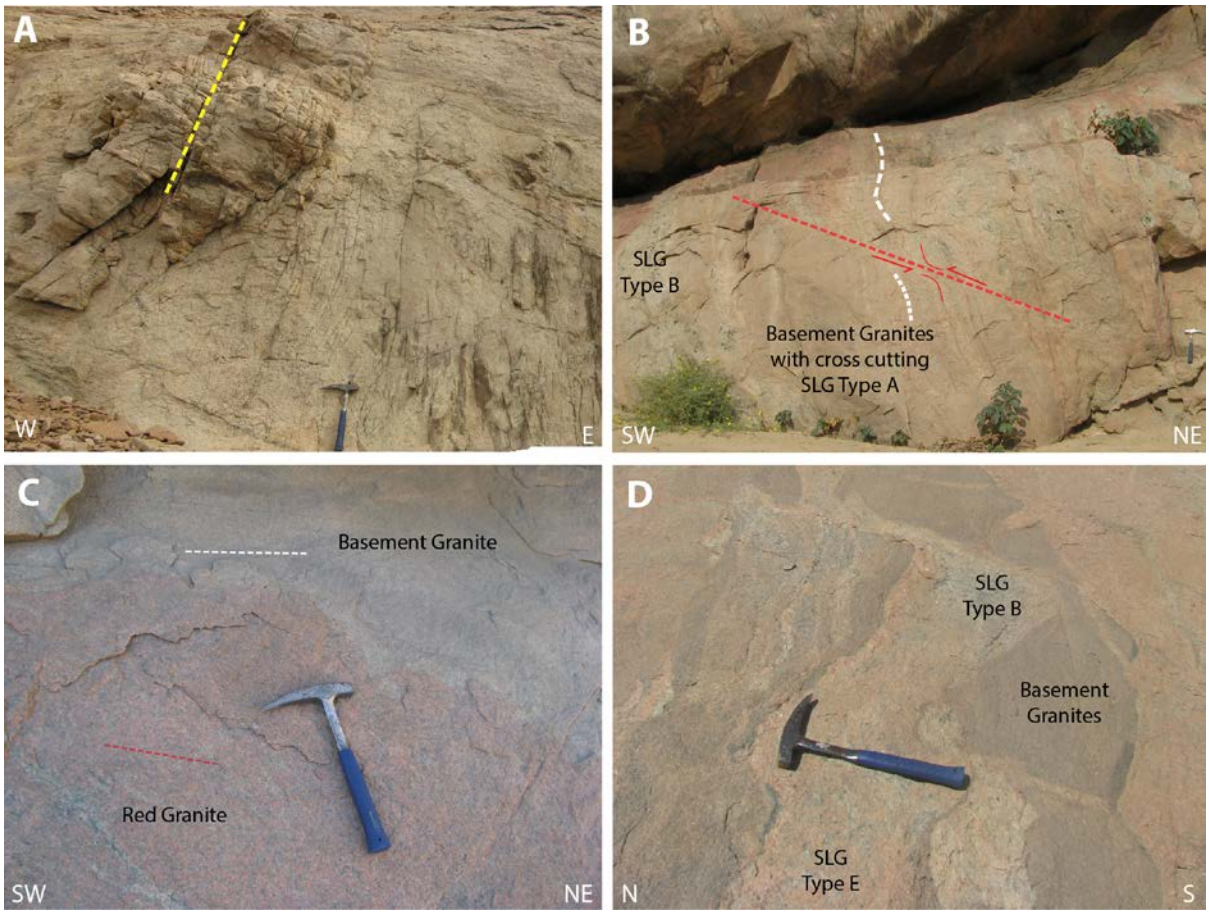


Figure 4.22: Outcrop photographs of the basement granites. (A) Weathered outcrop of a basement granite, in the Ostrich Gorge Intrusion, showing the distinct light pink to musky pink colour of the microgranite. Late stage joints (dashed yellow line) cross-cut the granite. (B) Polished basement granites cross-cut by type A SLGs (white dashed line) and B, with type B cross-cutting type A SLGs. All granites are sheared by a sinistral shear (red dashed line and arrows= shear; red solid line= sense of movement). (C) basement granite cross-cut by red granite. Foliations within both granites (white dashed line= basement granite foliation; red dashed line= red granite foliation) are sub-parallel. (D) basement granite cross-cut by two generations of SLGs, namely type B and then by type E.

These granites are frequently intruded by other granites and have complicated intrusive relationships (Fig. 4.22.B). The basement granites are cross-cut by red granites (Fig. 4.22.C), amphibolite dykes, grey granites and types A (Fig. 4.22.B), B (Fig. 4.22.D) and E (Fig. 4.22.D) SLGs. The

contact between the Etusis and the basement granites is difficult to locate in the south west quadrant of the mapping area due to the similar appearance and also recent alluvial deposits, although remote sensing was useful in delineating the contact. Additionally, the Hinge Syncline has an unclear contact with the surrounding basement granites for the same reasons. These granites do not appear to be structurally controlled, but they are deformed by D2 sinistral shears as well as D2 and D3 folds. The basement granites are cross-cut by late stage brittle and parallel joints that have associated chlorite in the cracks of the joints (Fig 4.22A).

4.5.2 Amphibolites

The amphibolite dykes are distinctive within the basement rocks due to their black colour and can be easily seen from remotely sensed images. The dykes are not seen to cross-cut the Damaran cover sequence and occur only in the basement rocks of the study area. These foliated dykes are generally tabular, anastomosing, attenuated and folded. The length of the dykes ranges from a few meters to a kilometre but are commonly intruded by other Damaran granitoids, which obscures the original shape and size. Compositionally, the fine-grained amphibolite dykes contain biotite and amphibole, with minor quartz, and are intensely foliated (Fig. 4.23.A). They are dark brown to black in colour, although the colour lightens to a dark grey and rusted red colour where abundant intrusions cross-cut the dykes (Fig. 4.23.B).

The amphibolites are mainly cross-cut by anastomosing SLGs. Type C′ SLGs (Fig. 4.23.D) most commonly cross-cut these dykes, but types E and F are also observed to cross-cut the dykes and the foliation within them. Intrusive contacts with the basement gneisses are obscured by the voluminous granitoid emplacement. The dykes show distinctive contrasts to the pink and white granitic melts and display preserved structural information, such as southwest verging folding (at outcrop and map scale) and northeast-southwest trending boudinage. The foliation in the amphibolites is folded as well as truncated by cross-cutting SLGs (Fig. 4.23.A). The foliation can extend into the partial melt neosomes as melanosomes along the boundary between the SLG and the proposed palaeosome of the amphibolite dykes (Fig. 4.23.C and D). Melanosomes show a concentration of intensely foliated amphibole and biotite whereas the palaeosome retains the amphibole, biotite and quartz compositions of less intruded amphibolite dyke examples with a less continuous foliation (see section 4.6).

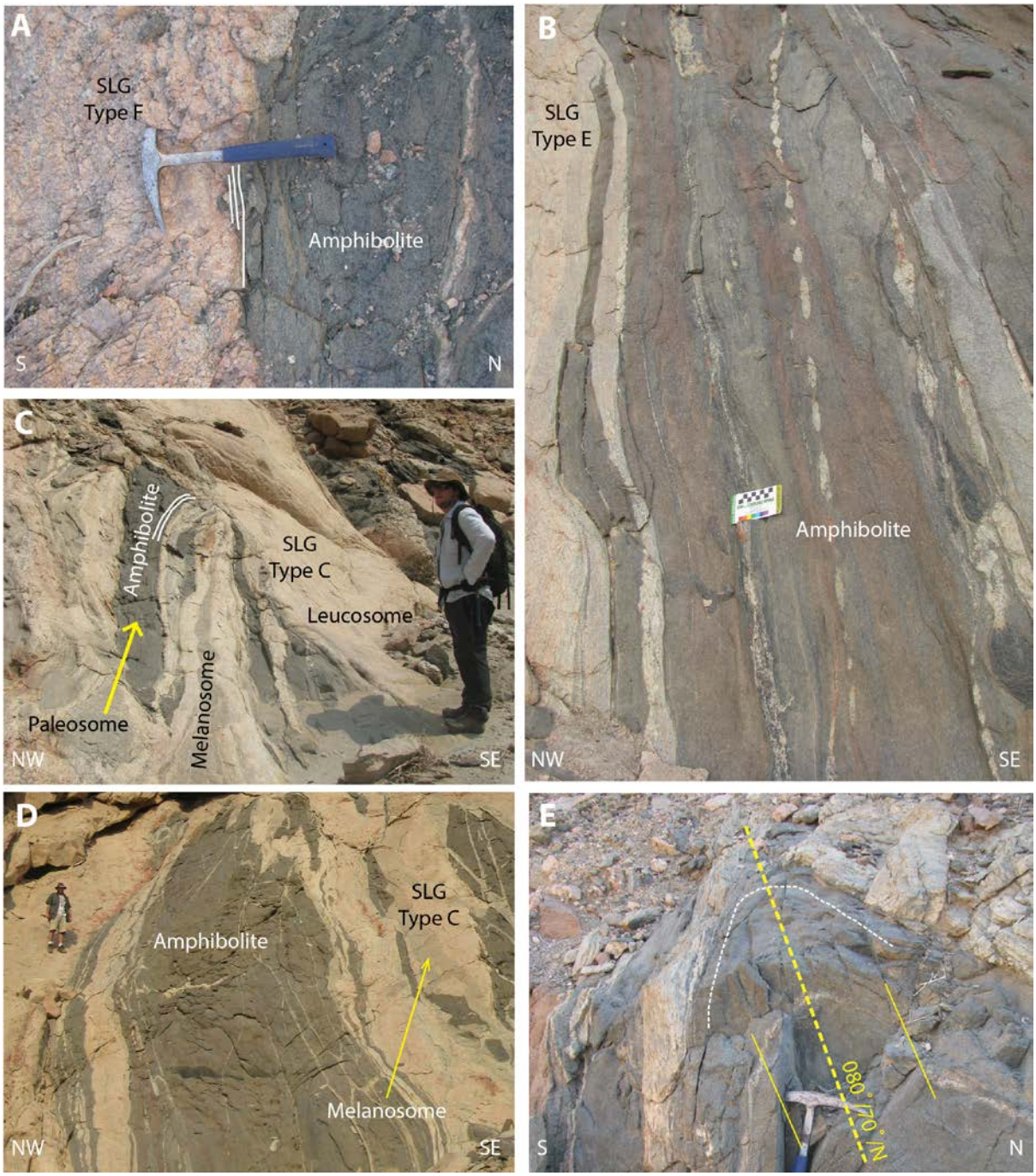


Figure 4.23: Outcrop photographs of the amphibolite dykes. (A) Foliated amphibolite dyke with cross-cutting tabular type C′ SLGs. (B) Red stained and lighter grey amphibolite dyke with intruding type E SLGs. Both lithologies have been boudinaged. (C) Folded amphibolite dyke with associated intruded type C′ SLGs. Leucosome, melanosome and palaeosome are all identified. (D) Large outcrop (10 m across) of amphibolite dyke intruded by type C′ SLGs. The type C′ SLGs have an anastomosing and sheeted morphology with rafts of melanosomes and palaeosomes within the granitic intrusion. (E) Near upright open folded amphibolite dyke with parallel type B SLGs. Approximate fold axial plane (dashed yellow line) with parallel axial planar foliation (solid yellow line) associated with folded amphibolite foliation (white dashed line).

4.5.3 Red granites

The red granites are the oldest of the Damaran Granites in the study area, based on cross-cutting field relationships, and show a distinct red to pink colour with a foliation. These granites are

generally (up to 10 m across) amorphous in shape and occur most commonly in the southern region of the field area and mostly intrude into the Abbabis lithologies, although they do intrude into the Nosib and Swakop Groups. In outcrop the red granites are fine- to medium-grained with a characteristic red to medium pink colour (Fig. 4.24.A and B). In addition, these granites show polished surfaces (Fig. 4.24.A) to granular textures (Fig. 4.24.B). The granites comprise mainly K-feldspar with minor quartz and biotite and display a moderate foliation (Fig. 4.24.C). The foliation, which is folded and sheared, is most intense in these rocks in comparison with the other Damaran granites and SLGs.

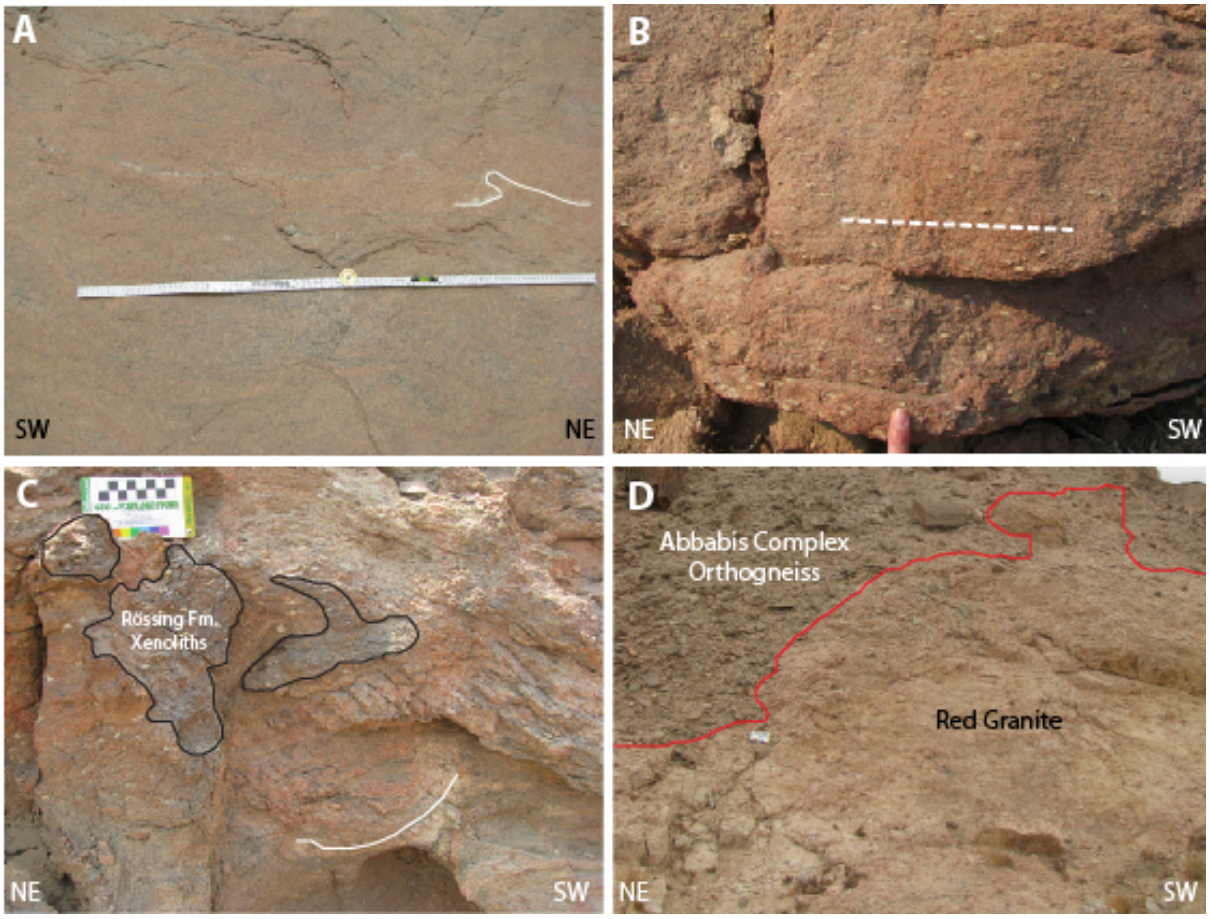


Figure 4.24: Field photographs of the red granites. (A) Polished red granite showing the distinctive deep red colour with a quartz pod (traced in white) that is refolded by tight to isoclinal folds. (B) Granular red granites with sillimanite knots (white dashed line). (C) A foliation (white line) that is folded. Xenoliths of proposed Rössing Formation are present that contain a sillimanite lineation that extend to the granite. The lineation remains parallel and are at an angle to the foliation. (D) A photo illustrating the homogeneous texture of the red granite intruding into the orthogneisses of the Abbabis Complex. Contact indicated in red.

Typically, the red granites are homogeneous (Fig. 4.24.D), although they do contain contaminated fibrous sillimanite knots that range from 0.5 to 2 cm in length (Fig. 4.24.B and C) and xenoliths of supracrustals (Fig. 4.24.C). These sillimanite knots are contained within crystalline quartz and feldspar of a typical granitic composition. In contrast, the sillimanite porphyroblasts of the Etusis

Formation are observed in a semi-pelitic biotite-rich matrix. In addition, the red granites typically cross-cut the Damaran metasediments (Fig. 4.24.C) indicating an intrusive origin with contaminated sillimanite rather than the sillimanite bearing Etusis Formation. The sillimanite lineation in the granite and the elongation of the supracrustals are parallel although it is at an angle to the foliation.

The red granites cross-cut the basement granites and the various granite-gneisses of the Abbabis Complex (Fig. 4.24.C) and are cross-cut by types C' and E (Fig. 4.20) SLGs. The basement granites and the red granites have parallel foliations but the biotite foliation in the red granites are commonly bent at the intrusive contact. Quartz pods cross-cut the red granite and are folded in tight to isoclinal folds, and in some cases are refolded (Fig. 4.24.A). Generally, the contact between the red granite and other lithologies are diffuse and gradational.

4.5.4 Grey granites

The grey granites are voluminous in outcrop throughout the field area and cross-cut both the basement gneisses and Damara metasediments. The largest outcrop was identified along the B2 access route, in the southern region of the Abbabis Complex. In general, the grey granites are amorphous and extend up to 10 m across in outcrop. The grey granites are the most variable intrusive rocks with three closely related types, defined here as types 1 to 3 and can be distinguished based on colour, mineralogy and cross-cutting relationships. Generally, the grey granites contain amphibole, biotite, plagioclase and quartz and exhibit a continuous and moderate foliation. Typically, these intrusions are granodiorites to quartz diorites, although they are named grey granites for simplicity, to conform with the nomenclature of previous workers.

Type 1 is the darkest grey in colour and is the oldest (Fig. 4.25.A and B). Mineralogically, type 1 contains the largest proportion of mafic minerals with granular quartz and plagioclase at outcrop scale. The granite is homogeneous and the most intensely foliated (Fig. 4.25.B). Type 2 has distinctive plagioclase phenocrysts and is lighter grey in colour (Fig. 4.25.C) than type 1. These phenocrysts, which range from 0.3 to 0.8 cm in length, form a lineation parallel to the mafic mineral defined foliation (Fig. 4.25.C). However, the lineation is not always very pronounced, and some sections of the intrusion are more porphyritic than aligned. Both types are cross-cut by type 3 (Fig. 4.25.A), which ranges from light grey, white to pink with a distinct foliation (Fig. 4.25.A) and has associated plagioclase veins. The type 3 grey granites tend to be darker grey when associated with the plagioclase veins (Fig. 4.25.D and E). These veins are typically thin, approximately 1 – 3 cm in width, and most commonly form parallel sheets to occasional erratic networks (Fig. 4.25.D and E). Similarly, these type 3 grey granites are amorphous to sheeted and finger into type 1 and 2 as cross-

cutting bodies (Fig. 4.25.A) and are far richer in plagioclase and quartz than the other types of grey granites.

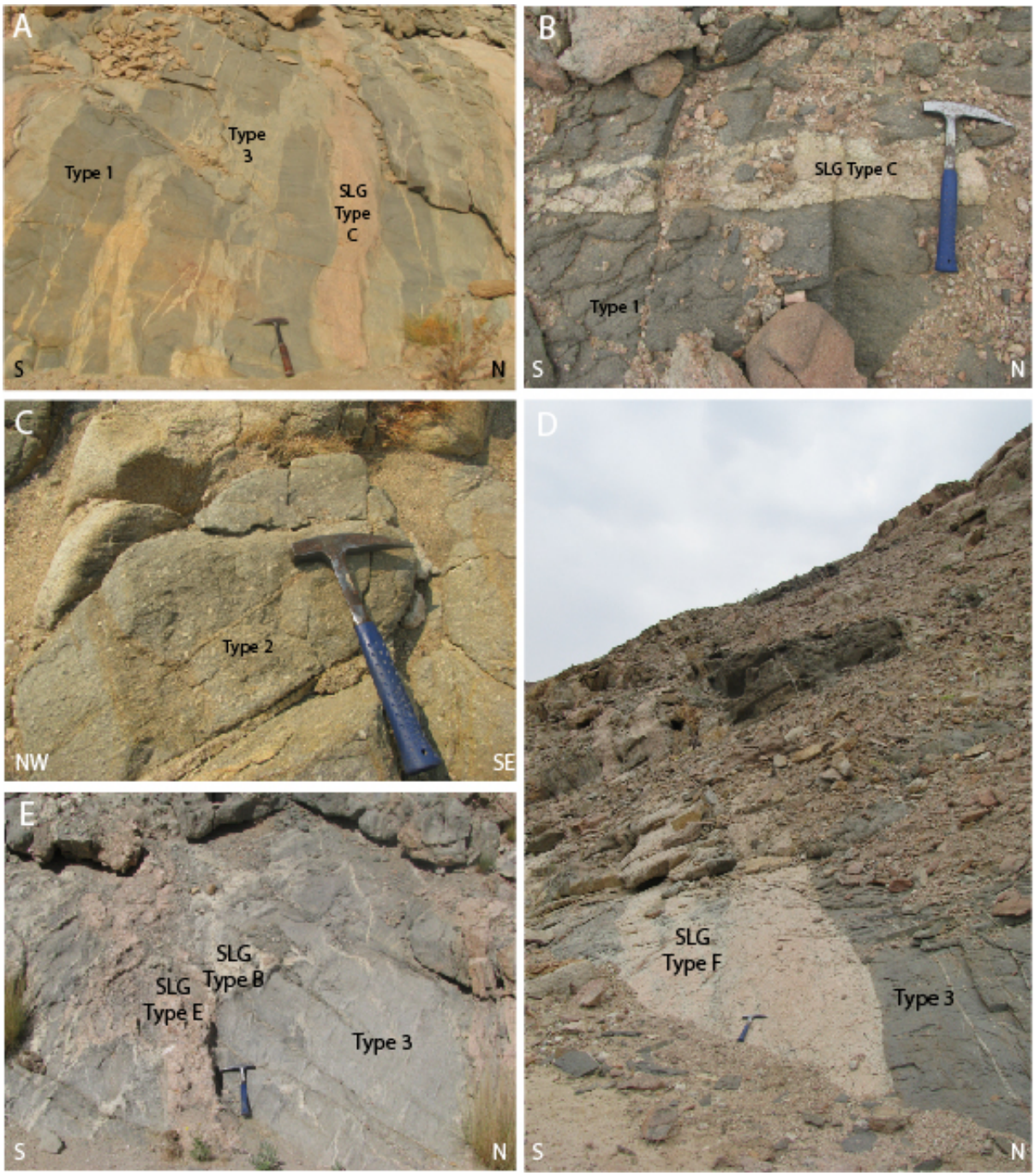


Figure 4.25: Outcrop photographs of the grey granites. (A) Melanocratic type 1 grey granite with cross-cutting more felsic type 3 grey granites and type C' SLGs. (B) Melanocratic type 1 grey granite with a moderate foliation cross-cut by tabular type B SLGs. The sheeted body has rafts of the grey granite. (C) Porphyritic type 2 grey granite with a plagioclase lineation and a defined foliation. (D) Light type 3 grey granite with associated sheeted plagioclase veins. Tabular cross-cutting type F SLG is present. (E) Type 3 grey granite with associated plagioclase veins. Cross-cutting type B SLG, which is cross-cut by type E SLG.

Types B, C', E and F SLGs, that do not contain a foliation, cross-cut these grey granites (Fig. 4.25.A, B, D and E). Types B and C' cross-cut grey granites types 1 and 3 and type E and F are seen to cross-cut the grey granites type 3. In addition, the grey granites are attenuated into D2 shears with the contacts of these granites commonly intruded by various SLGs.

4.5.5 Sheeted leucogranites

The various SLGs cross-cut the earlier granite types, the Damaran supracrustals, the basement granite-gneisses and associated basement intrusives. These sheeted intrusives have varying rock forming mineralogies, accessory mineral types and abundances, contact types, morphologies and relative temporal relationships. The SLGs are so named using the terminology of Nex and Kinnaird (1995) based on their mineralogy and geometries, for simplicity, however they do not necessarily follow the relative chronology established by the previous works (Nex, 1997; Basson and Greenway, 2004; Fremantle, 2017). Described below are the SLG types seen within the field area, which include types C', A, B, E and F, ranging from oldest to youngest.

Type C': K-feldspar-quartz-(magnetite and biotite)

The type C' SLGs are the oldest of the SLGs and are cross-cut by other SLGs and include younger deformational features. These bodies are seen throughout the field area but are most common in zones of concentrated deformation, where they cross-cut the Damaran supracrustals and also along the basement-cover contact. They typically intrude parallel to bedding (Fig. 4.20.A) when intruding the Nosib and Swakop Groups and occasionally display a weak foliation. However, these intrusives can be discordant to bedding where the sheets intrude the Abbabis Complex lithologies (Fig.4.20.B). Their contacts range from tabular to anastomosing, thicknesses range from less than 1 to 15 m across and are sometimes amorphous with individual coalesced sheets joining together. These sheets can be traced for considerable distances across the field area in excess of 100 m.

The type C' SLGs are medium- to coarse-grained, although pegmatitic cores are seen, typically light pink to cream in colour and exhibit a homogeneous texture in outcrop (Fig. 4.26.A and B). At outcrop scale, they comprise K-feldspar, quartz and minor plagioclase. Euhedral K-feldspar and blebby quartz are typically preserved in the pegmatitic patches. In most cases, the sheeted bodies do not display abundant accessory minerals, although accumulations of magnetite and biotite melanosomes can occur concentrated at the edges of the intrusions. However, these accessory minerals are typically concentrated in pegmatitic patches. These biotite accumulations show an alignment of biotite developed as a weak foliation. Type C' SLGs are typically cross-cut by all of the SLGs, namely A, B, E and F, and cross-cut the earlier granites (Fig. 4.26.C and D). Generally, the granitic

sheets have sharp contacts with the country rocks although, gradational and diffuse contacts between other sheeted granites are seen in the HSZ, especially with type A and B SLGs and are often seen intruding D2 fold axial planes and shears.

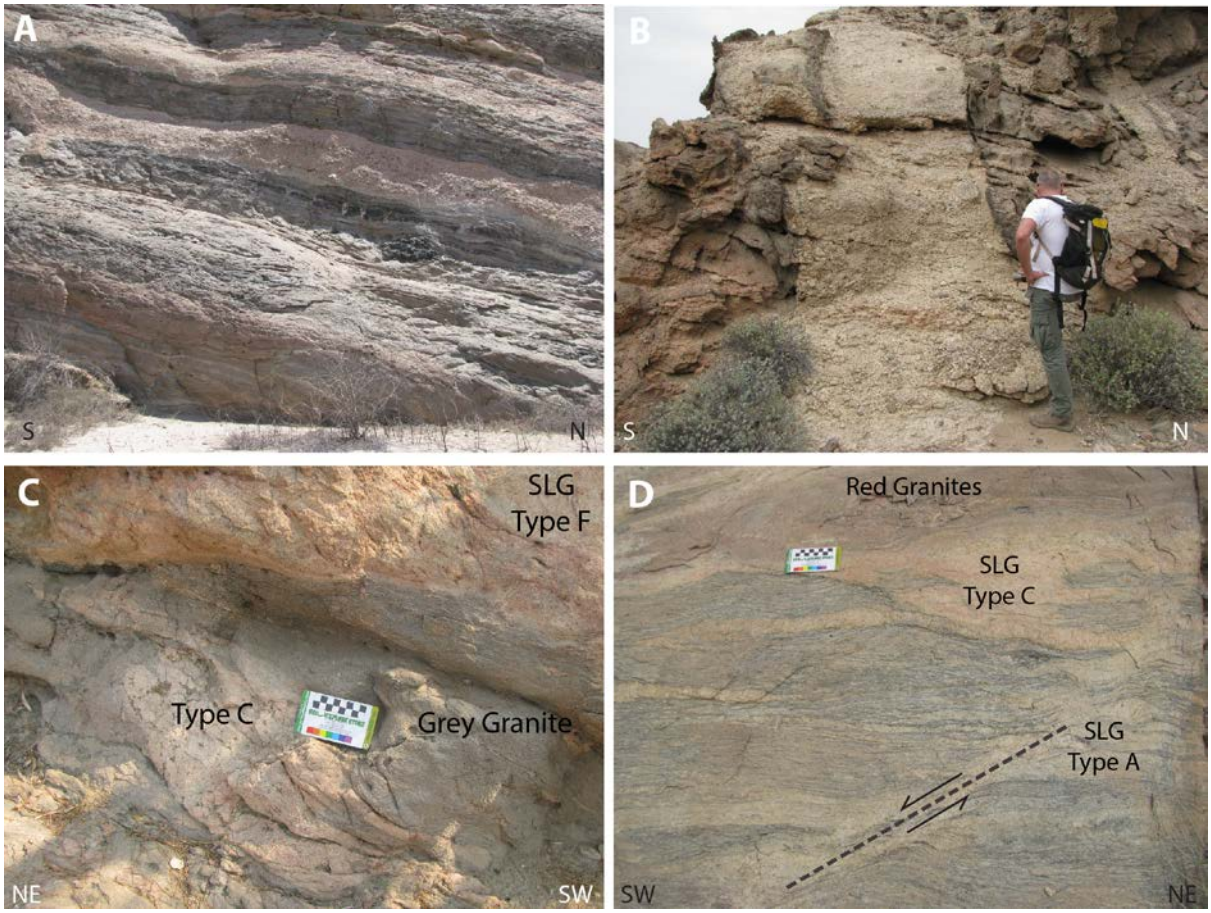


Figure 4.26: Outcrop field photographs of the type C' SLGs. (A) Homogeneous and tabular type C' SLG intruded bedding parallel. (B) Near vertical and tabular type C' SLG highlighting the homogeneous nature. (C) Amorphous and deformed type C' SLG cross-cutting the grey granites and cross-cut by type F SLG. (D) Type C' SLG cross-cutting red granites, and cross-cut by type A SLG. Type A and C are both sheared, strained and cross-cutting relationships are not always apparent.

Type A: Feldspar-quartz-biotite

The type A SLGs are common in the HSZ, cross-cutting the Abbabis Complex, Nosib Group metasediments, red granites and type C' SLG, as dismembered and blebby pink and white segregations running parallel to the stretching direction and foliation (Fig. 4.20), although bedding parallel sheets are seen most commonly within the Damaran cover sequence and Abbabis Complex Gneisses. These SLGs are commonly thin, 1 – 40 cm in thickness and are bedding parallel (Fig. 4.27.A), and are typically seen as dismembered, convolute and chaotically folded where the host rock is deformed (Fig. 4.27.A and B). The type A SLG are fine- to medium-grained (Fig. 4.27.B) and contain varying amounts of K-feldspar and plagioclase with quartz, which determines the range in light pink to white colours (Fig. 4.27). The quartz is often granular with no accessory minerals noted.

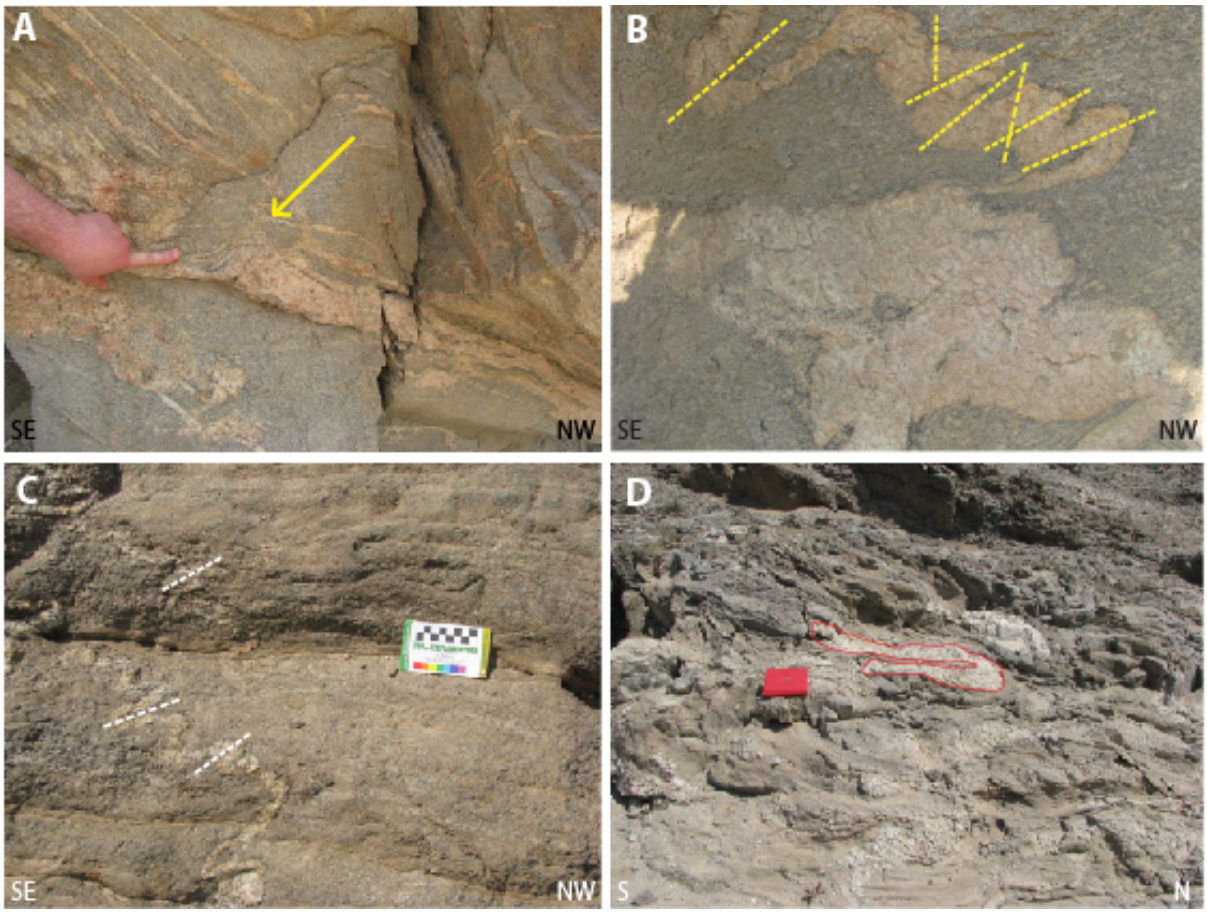


Figure 4.27: Outcrop field photographs of the type A SLGs. (A) Bedding parallel and thin type A SLGs cross-cutting Damaran metasediments. The intrusion is associated with boudinage and occurs within the dilation features (yellow arrow). (B) Convoluted and folded type A intrusion cross-cutting Abbabis Complex gneisses. The SLGs are folded by two folding events because there are two-fold axial planes (yellow dashed line). (C) Continuous and discordant type A intrusions folded into gently inclined tight folds (fold axial planes= white dashed lines). (D) Rootless isoclinal and gently inclined folds, indicated by the red outline, of type A SLG.

These SLGs are cross-cut by types B, E and F SLGs and have sharp contacts with the host lithologies even when attenuated and blebby in nature. Outcrop scale folding of the intrusions are common as tight to isoclinal recumbent and sometimes rootless folds (Fig. 4.27.B, C and D) that are commonly refolded. Convoluted and more amorphous intrusions are present, but usually related to or extend from (folded) bedding parallel intrusives (Fig. 4.27.B). In addition, the type A SLG occur in D2 dilational features and intrude into shears indicating that this intrusion type is related to deformation.

Type B: Plagioclase-quartz-(biotite-garnet)

Type B SLGs are present most commonly in the Damaran cover sequence and in the HSZ at the basement-cover contact cross-cutting other SLGs, other earlier granites, the Abbabis Complex and the Nosib Group. They range from sharp tabular bedding parallel (Fig. 4.28.A) to diffuse and

convolute (Fig. 4.28.B) morphologies with a weak to moderate foliation. Thicknesses of these intrusives range from a few centimetres (Fig. 4.28.C and D) to several meters (Fig. 4.28.A) and they exhibit a homogeneous texture when accessory minerals are not observed. Typically, they are fine- to medium-grained and characteristically white with a weakly developed biotite foliation that is bedding parallel. They comprise mostly plagioclase with quartz and biotite. Garnet and amphibole accumulations are seen in outcrop that generally have a diameter of 1 – 4 cm (Fig. 4.28.C).

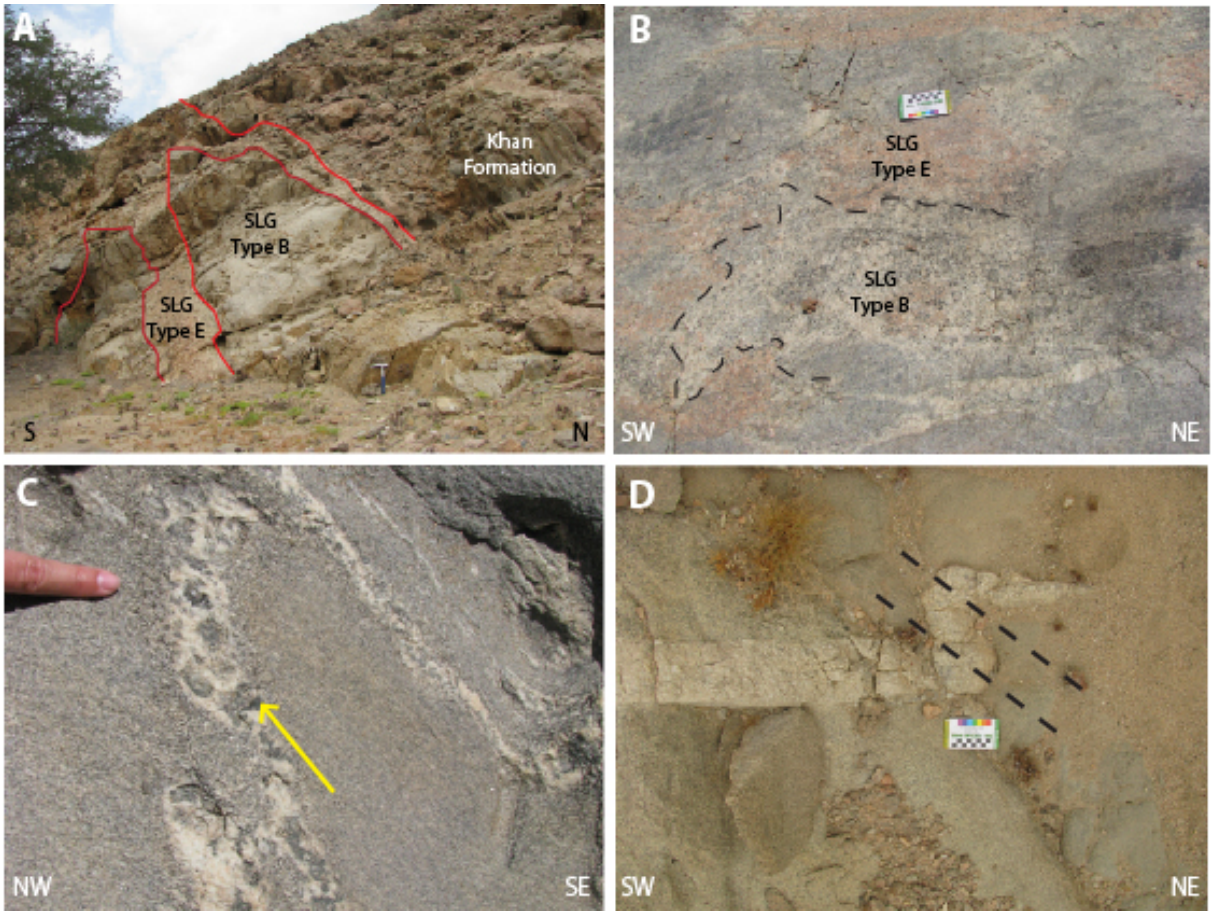


Figure 4.28: Field photographs of type B SLGs. (A) Homogeneous white type B SLGs which cross-cut Khan Formation semi-pelitic schists. type E SLG cross-cuts both the Khan Formation and type B SLGs. Sharp intrusive contact between the two SLGs are indicated in red. (B) Diffuse contact (black dashed line) between type B SLGs and E, in the HSZ, with type E cross-cutting type B. (C) Type B SLG leucosome cross-cutting grey granites type 1. Yellow arrow indicates the porphyroblastic garnet and amphibole. The SLG is openly folded. (D) A sharp intrusive contact between basement granites and type B SLG. The SLG is an openly folded Z-fold (fold axial trace= black dashed lines).

Type B SLGs are cross-cut by types E and F SLGs and generally have tabular and sharp intrusive contacts (Fig. 4.28.A), although occasionally show patchy, amorphous and diffuse contacts (Fig. 4.28.B) with the country rock and other SLGs. The diffuse contacts are most prevalent in the HSZ (Fig. 4.28.B). These intrusives are folded in D3 open folds (Fig. 4.28.D) with the spaced biotite foliation also folded. Very few examples of tight to isoclinal folds are observed in the type B SLGs.

Type E: Feldspar-quartz-(biotite)

The type E SLG occurs mainly in the cover sequence and in the HSZ and are seldomly seen in the Abbabis Complex. These granites are younger and generally less deformed than the other intrusives. Type E granites appear as chunky folded tabular sheets (Fig. 4.29.A) or amorphous bodies that scatter the surfaces of outcrops of other intrusives and the country rocks as granular K-feldspar and quartz (Fig. 4.29.B). The size of these intrusives vary between 10 cm to several meters. These intrusives comprise coarse-grained to pegmatitic abundant tabular K-feldspar and quartz (Fig. 4.29.A) with flecks of white plagioclase. Accessory minerals are present, with biotite books and minor ilmenite present in outcrop. Granophyric textures between K-feldspar and quartz are seen in hand sample with blebs of quartz set within pegmatitic K-feldspar crystals. The SLGs are characteristically granular in texture and lack a foliation.

Type E SLGs cross-cut the Damara Supergroup, the Abbabis Complex as well as the gneissic foliation in the HSZ with no extension of the intrusive type into the strain direction (Fig. 4.29.A and Fig. 4.20). This SLG type is cross-cut by type F SLGs, are only seen to be folded by D3 open folds (Fig. 4.29.A) and occurs within D3 shear zones (Fig. 4.20). These granites have varied contact types from sharp to diffuse more amorphous with the country rocks and other intrusives (Fig. 4.29).

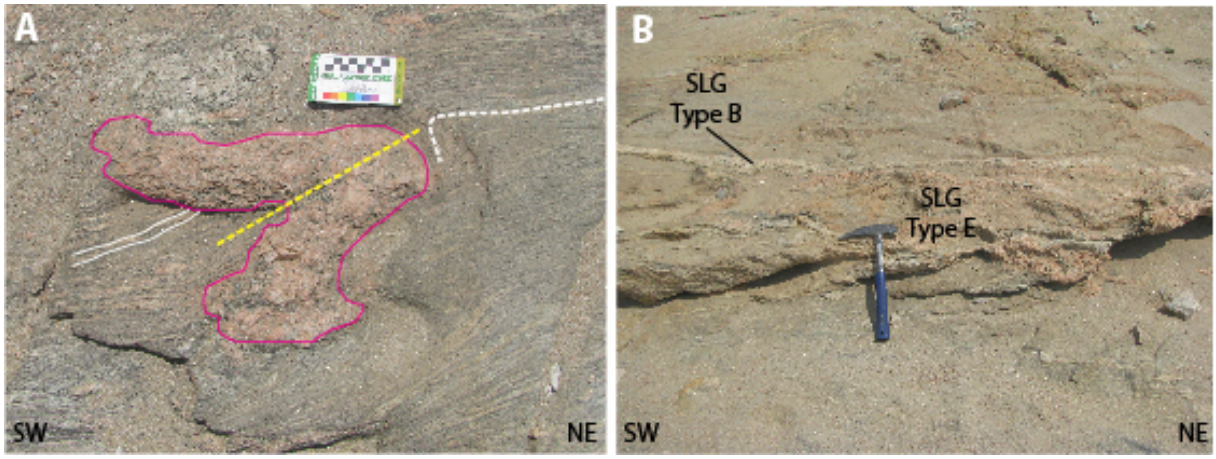


Figure 4.29: Field photographs of the type E SLGs. (A) Rootless openly folded type E SLGs (outlined in pink) cross-cut the foliation in the HSZ. The foliation (white dashed line) is bent and folded as well as truncated by the type E intrusion. Fold axial trace= yellow dashed line. (B) Granular pegmatitic K-feldspar and quartz appear to be scattered over the basement rocks and cross-cut the type B SLG.

Type F: K-feldspar-quartz-(biotite-magnetite) Pegmatite

The type F SLG are the youngest of the granites and generally trend northeast-southwest (Fig. 4.30) and cross-cut the basement and cover sequence lithologies. They are relatively undeformed and have tabular and parallel margins (Fig. 4.31.A and B). These intrusions are arranged in en-echelon

sets of intrusions as dilational features (Fig. 4.30). These SLGs cross-cut all shear zones and foliations. Type F SLGs can be traced in the field and from remotely sensed images for approximately 50m to 100m.

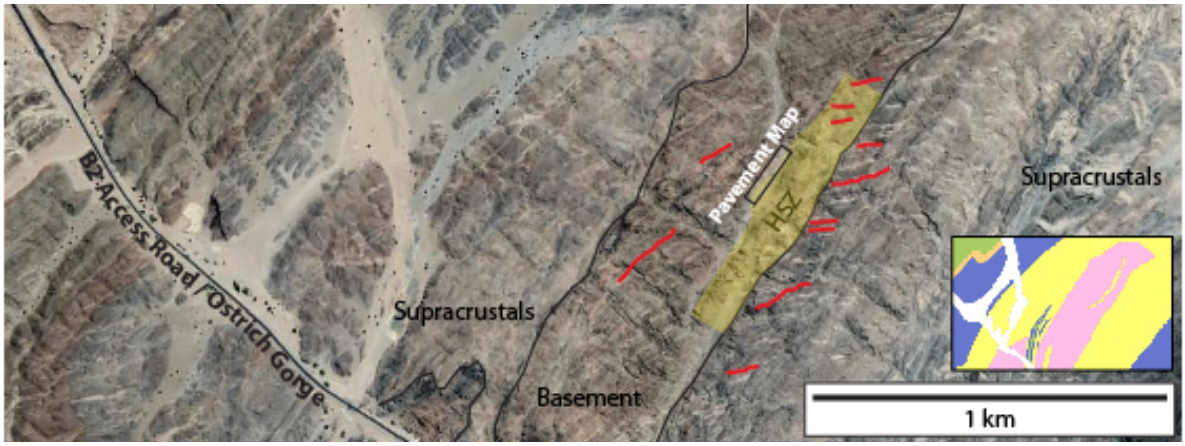


Figure 4.30: Satellite image of the northern extent of the field area showing a portion of the basement and Damara cover sequence. Some examples of type F SLG pegmatites are indicated by the red lines. Other SLGs observed may be Type F SLGs, however only a few examples have been traced so not all the examples were obscured by the traced lines. The yellow shaded area indicates the HSZ and the location of the pavement map (Fig 4.20) in the black box. The in-set (bottom right) shows a geological map of the area in the satellite image (pink= Abbabis Complex; yellow= Etusis Formation; blue= Khan Formation; orange= Rössing Formation; green= Chuos Formation).

The intrusives are coarse-grained to pegmatitic with a distinctive deep red to pink colour (Fig. 4.31.A). In addition, these pegmatites are granular comprising K-feldspar and smoky quartz that is often blebby in appearance and occurs as inclusions within the K-feldspar. The accessory minerals are mainly biotite and magnetite or ilmenite that occur in pockets where grain size is pegmatitic and quartz is generally concentrated. The intrusive is often shiny due to the exposed cleavage planes of the euhedral K-feldspar, so it is distinctive to identify in the field. type F SLG cross-cut all other granitic intrusions. These intrusive contacts are sharp with the cover sequence, Abbabis Complex and the granites. They are not folded, nor do they contain a foliation. The intrusion cross-cuts all foliations and shears present in the HSZ, and in the surrounding field area.

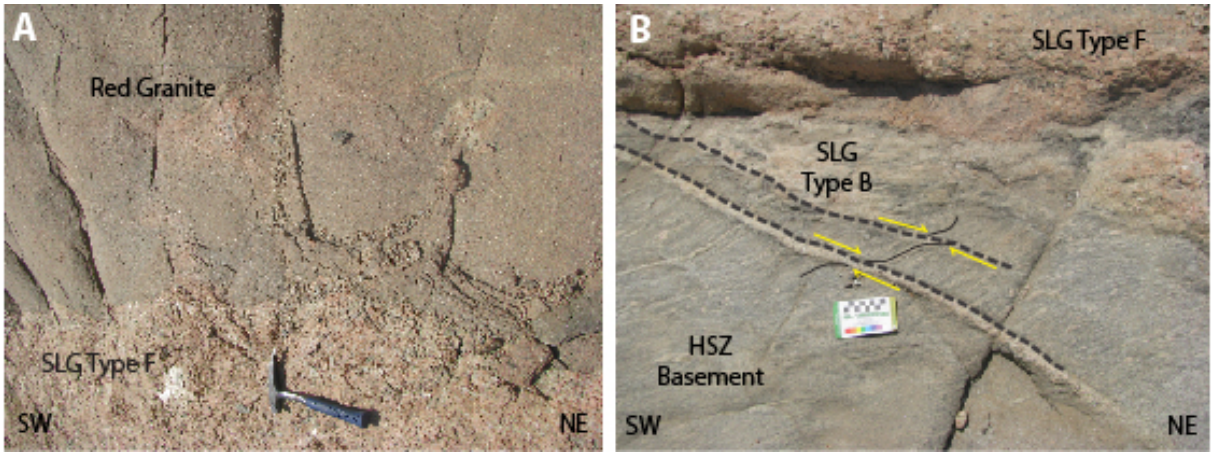


Figure 4.31: Field photographs of the type F SLGs. (A) A sharp contact of the type F SLG and the red granite. Pegmatitic SLGs with shiny cleavage plane of K-feldspar. (B) Cross-cutting type F SLGs with shears, foliation and type B SLG. The shear is a set of two dextral shears (dashed black lines; kinematics indicated by yellow arrow) with S-C fabric in between the shears (solid black line). Foliation is bent by shears. Type B SLG in the shear and sheared by the deformational feature.

Certain SLGs are difficult to distinguish between due to similarities in mineralogy, emplacement styles and structure. For example, figure 4.28.D is a type B SLG which could be confused with type F SLGs. However, Type F SLGs are tabular, not folded, typically thicker, are typically pink, K-feldspar-rich and pegmatitic. Whereas the SLG in figure 4.28.D is fine- to medium-grained, more homogenous and plagioclase-rich. However, it is also noted that these SLGs can be variable and the type is not always easily distinguishable and cannot always be correlated across the southern Central Zone.

4.6 Migmatites of the Palmenhorst Dome

Migmatites are mixed rocks found in medium- to high-grade metamorphic areas that are heterogenous, composed of two (or more) parts with one part having formed as a result of partial melting (Mehnert, 1968; Ashworth, 1985; Sawyer, 2008). A detailed description of the nomenclature used to describe the migmatites can be found in Appendix 1. In the study area the migmatites have been sub-divided into four types based on the classification and terminology outlined in section 1.6 after Sawyer (2008). These types include intrusive bedding and foliation parallel metatexites (Fig. 4.32.A), intrusive sheeted granites (Fig. 4.32.B), sheeted granites with rafted palaeosomes (Fig. 4.32.C) and homogeneous granite diatexites and plutons (Fig. 4.32.D).

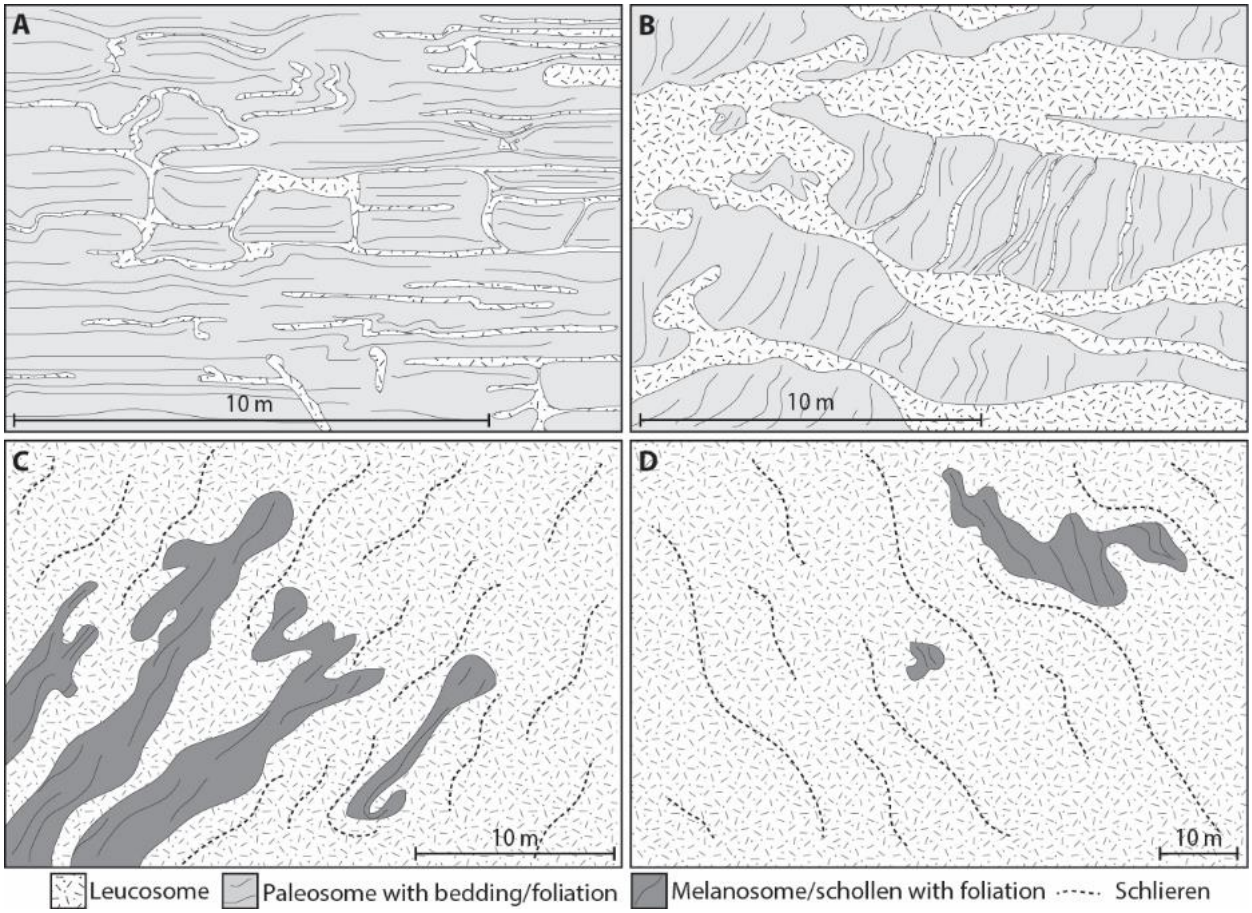


Figure 4.32: Schematic illustration of the 4 groups of migmatites identified in the Palmenhorst Dome. These types include (A) intrusive bedding and foliation parallel metatexites, (B) intrusive sheeted granites, (C) sheeted granites with rafted palaeosomes and (D) homogeneous granite diatexites and plutons.

These types are broadly divided into metatexites and diatexites, as a first order classification, and their locations are shown in figure 4.33. Metatexites are heterogenous, comprise more preserved palaeosome than neosome and therefore pre-partial melting textures are largely preserved (Sawyer, 2008). In contrast, diatexite migmatites constitute more neosome than palaeosome and the partial melting is more pervasive, resulting in replacement of pre-partial melt features by melt structures (Sawyer, 2008). See section 1.6 for a full description.

Metatexites

The metatexites mainly occur in the Damaran supracrustals and within the northern extent of the Abbabis Complex. Generally, the remnant and crystallised melt fraction increases towards the southern extent of the field area and along the contact between the supracrustals and the basement rocks, where more stromatic (Fig. 4.34) and net-textured (Fig. 4.35) migmatites are observed. There is an increase in crystallised partial melt fraction from intrusive bedding and foliation parallel metatexites to the intrusive sheeted granites.

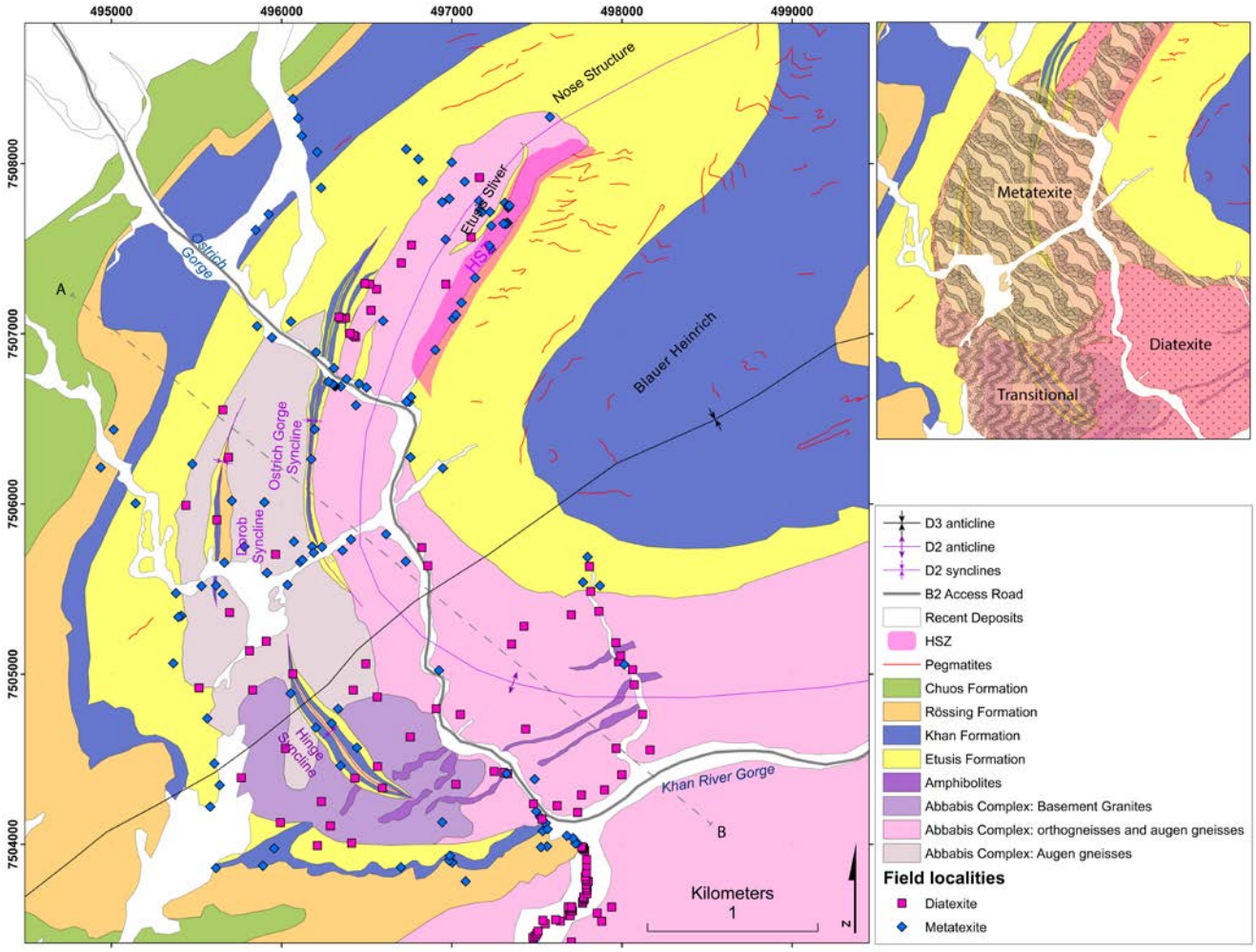


Figure 4.33: Geological map of the field area showing localities of metatexite and diatexite outcrops. Metatexites are largely concentrated in the north of the field area and along the basement-cover contact. In contrast, the diatexites are concentrated in the south of the field area, although similarly, transitional diatexites are seen at the basement-cover contact. Proposed zones of metatexite, transitional and diatexite migmatites are outlined in the top left inset (metatexite= pale orange with blank and solid banding; transitional= peach with hatched and lined banding; diatexite= pink with crosses; banding orientations do not represent a preferred orientation but is used for distinction between the domains). Section A-B is indicated on the map which correlates to the cross section in section 4.7.5.

Intrusive bedding and foliation parallel metatexites

These migmatites show a continuum, and increase in crystallised partial melt fraction, between the different morphologies of metatexites. The intrusive bedding and foliation parallel metatexites include patch (Fig. 4.34.A), dilation (Fig. 4.34.B), net (Fig. 4.34.C) and stromatic (Fig. 4.34.D) migmatites. In general, remnant partial melts intrude along bedding or foliation planes and concentrate in extensional dilation features such as boudin necks. The patch metatexites have diffuse contacts and are generally concordant to the foliation, although in some instances where there are developed dilation structures and increased leucosomes, the patch migmatites are discordant to compositional change (bedding) and foliation (Fig. 3.34.A). These leucosomes, commonly not more than 10 – 15 cm in diameter, do not have developed melanosomes. These

migmatites, rounded to amorphous in shape, preserve the palaeosome and the pre-anatectic partial melt features.

Dilation migmatites are larger and more developed in the cores of dilation structures, such as boudinage features and these units are commonly extended parallel to the compositional change and foliation. These leucosome types are larger and more pervasive into the palaeosome (Fig. 4.34.B). In most cases, there is a melanosome present, usually constituting biotite, amphiboles, garnet and cordierite, and the partial melt shows intrusive and diffuse contacts. Most commonly the dilation metatexites are sill and laccolith shaped and the palaeosomes are deformed by the same deformation, i.e. boudins and folds. Size ranges from outcrop to outcrop, although the proportion of leucosomes are similar.

Partial melt that intrudes along the bedding and discordant to bedding dismembering the palaeosome are considered net-textured metatexites. These net-textured migmatites (Fig. 4.34.C) show elongate rafts of palaeosome, generally ranging from 2 – 3 cm in thickness and 5 – 15 cm in length, are surrounded by intruded and in situ leucosome. These leucosomes commonly show sharp contacts into dilation features and along bedding parallel directions. In some instances, the palaeosome is pelitic and the white and pink leucosomes contrast with the protolith. Residuum and melanosomes are common within these migmatite types and are developed as aligned biotite (sometimes amphiboles depending on the protolith), which mimics the palaeosome foliation direction. Net-textured migmatites are common textures developed by the type A SLG intrusions (Fig. 4.7.A), as seen in the Khan Formation (Section 4.2).

Lastly, when crystallised partial melting is most pervasive for this subgroup, stromatic migmatites are developed that generally dismember the palaeosome and form bedding parallel partial melt bands (Fig. 4.34.D). These are developed mostly in the basement gneisses, metasediments located near the basement-cover contact and within fold hinges. Strained palaeosomes are banded with alternating neosomes. The neosome is segregated into the leucosomes with one sided melanosomes of biotite and amphibole. Banding of the leucosomes appear as rhythmic sills parallel to the compositional layering and axial planar foliation.

These four morphologies of metatexites are structurally controlled by dilational structures, strain and folding. In fact, many leucosomes are closely related to the folding and therefore, they can also be classified as fold-structured migmatites. Most of the sheeted granites make up the leucosomes

to the migmatite, although the most prolific SLGs observed in the subgroup are the types A, B, C' and E.

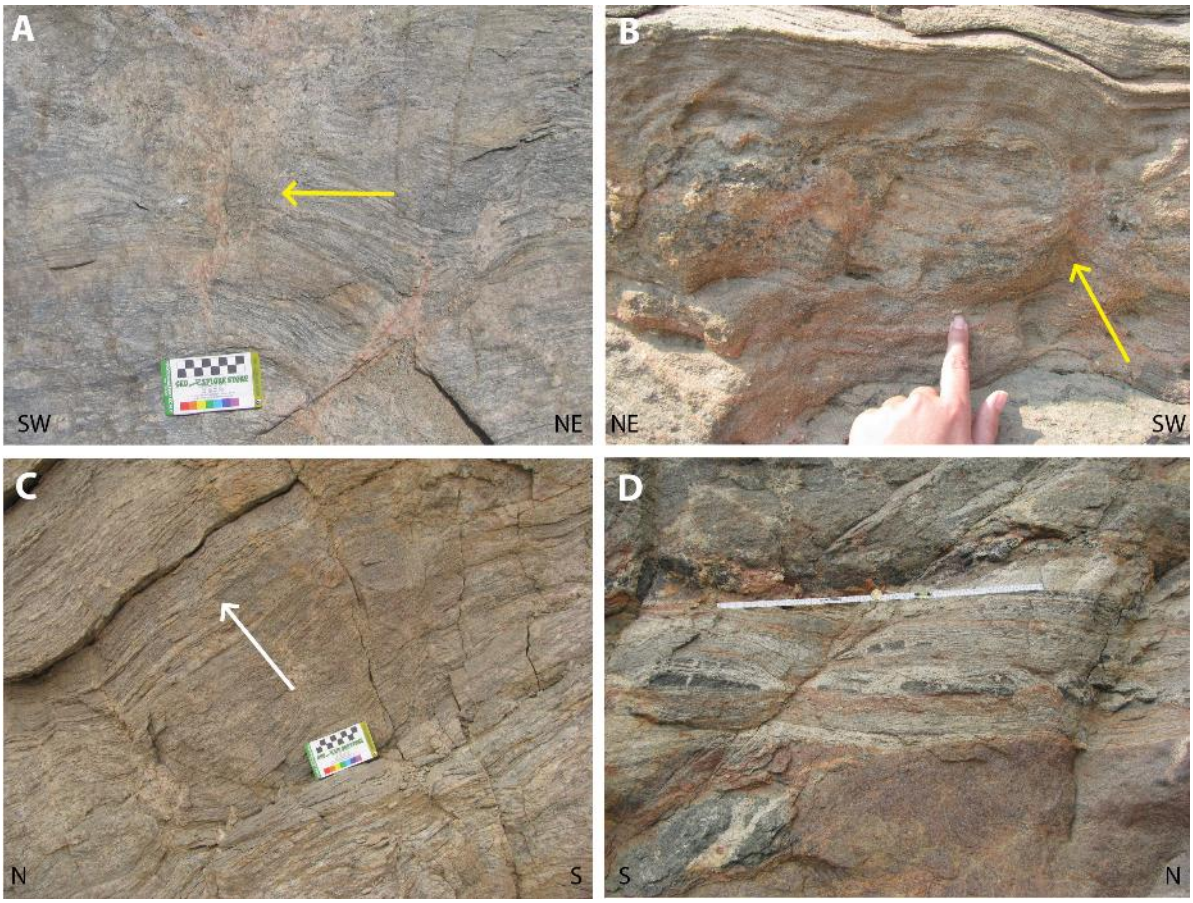


Figure 4.34: Field photographs of the intrusive bedding and foliation parallel metatexites. (A) In situ patch neosome (yellow arrow) weakly developed in a dilational structure cross-cutting the HSZ basement. (B) Dilation to net-textured leucosomes (yellow arrow) with a biotite melanosome. Both in-source leucosome and palaeosome has been boudinaged. (C) Net-textured migmatite showing elongate palaeosome blocks with two directions of intrusive leucosomes (white arrow). (D) Stromatic migmatite with dismembered boudins of palaeosome, Khan Formation. Meter-rule for scale.

Intrusive sheeted granites

These intrusive sheeted granites are generally discordant to bedding and foliation, although bedding-parallel examples do exist, and almost exclusively show in-source and leucocratic veined migmatites as illustrated by Sawyer (2008). The in-source migmatites occur within the same lithology as other metatexites and commonly have a leucosome and melanosome. In addition, they are the most variable. Leucosomes are preserved as intrusive crystallised melts and are commonly seen throughout the field area. Likewise, this type intrudes the sheeted granites with rafted palaeosomes as well as the homogeneous granite diatexites and plutons subgroups while cross-cutting some elements of the previously discussed migmatite subgroup. The most common form of the intrusive sheeted granites migmatite subgroup is pegmatitic, tabular to anastomosing, but they can also be observed as irregular granitic bodies (Fig. 4.35.A) and are usually less deformed and non-

foliated than the other migmatite subgroups. Palaeosomes are still discernible (Fig. 4.35.B, C and D) and appear as rafts inbetween the multiple intrusions of leucosomes. The leucosomes can be divided into three main groups: leucocratic veins, stromatic and nebulitic migmatites.

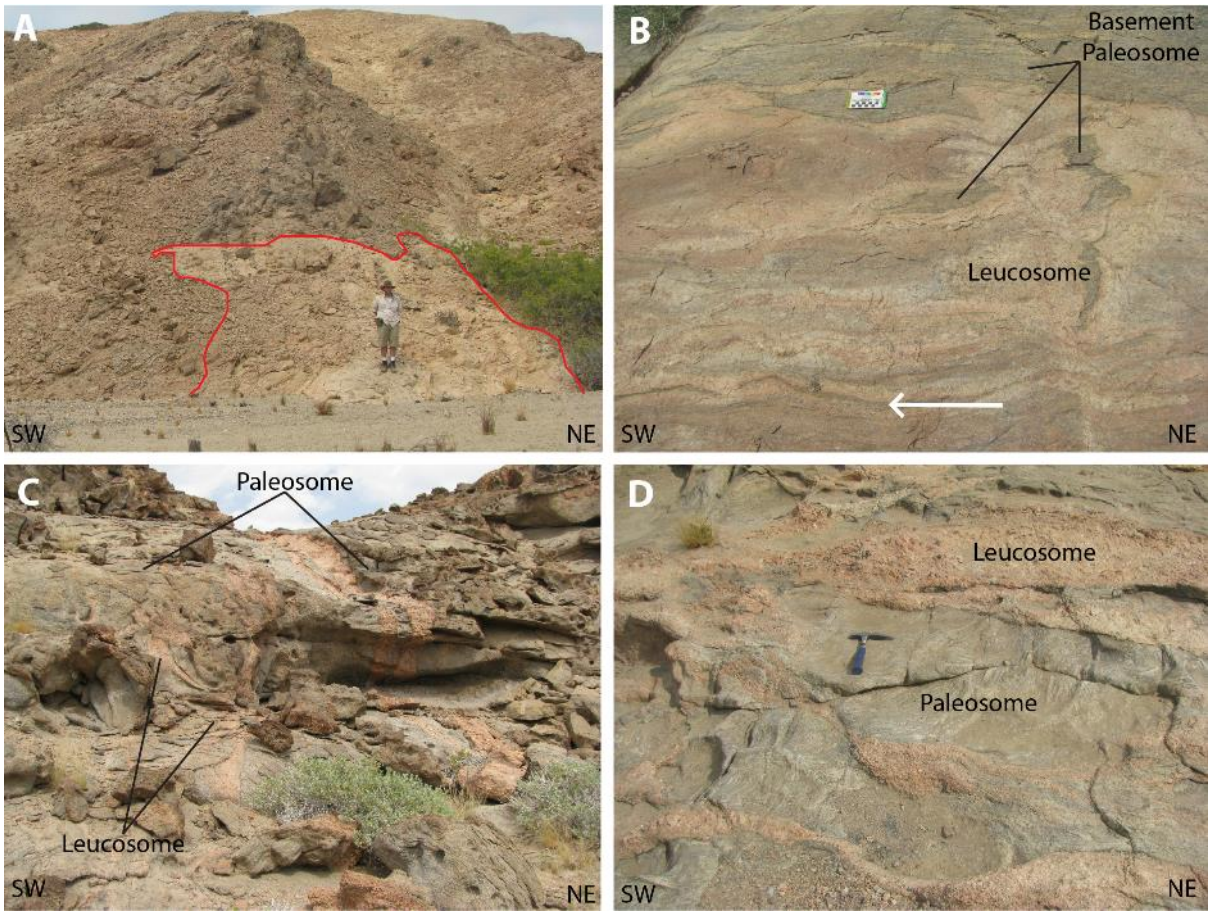


Figure 4.35: Field photographs of the intrusive sheeted granites metatexites. (A) Amorphous leucocratic vein structured migmatite, outlined in red, in contact with the basement gneisses. (B) Two generations of migmatites forming a stromatic texture (white arrow). Palaeosome is present as Abbabis Complex gneisses. (C) Anastomosing vein-structured migmatite, which has still preserved the palaeosome. Contacts are sharp. (D) Anastomosing vein-structured migmatite showing the intrusive nature yet the contacts are diffuse in some instances.

The veins show tabular sides with sharp contacts with the protolith (Fig. 4.35.C and D). They are generally intrusive leucocratic veins as extensive dykes can be traced, for sometimes several meters. Generally, no melanosomes are present at the edges of the intrusion and the leucosomes cross-cut the foliation and sometimes bedding parallel intrusions. Additionally, these leucosomes cross-cut earlier migmatitic partial melts. Some of the leucocratic dykes are irregular and have offshoots into and around palaeosome rafts, and therefore are transitional between metatexites and diatexites. These SLGs are typically the youngest and are most commonly made up of types E and F SLGs, although type C' SLG are also observed in this subgroup.

Stromatic migmatite types are generally bedding or foliation parallel (Fig. 4.35.B) and cross-cut earlier migmatite partial melt generations. The stromatic partial melts in this subgroup are more voluminous, anastomosing and do not display the rhythmic banding as regularly as the intrusive bedding and foliation parallel metatexites nor is the neosome segregated into melanosomes and leucosomes. The contacts between the leucosomes are generally sharp, although they appear as in-source crystallised melts as there are not connected to dykes that can be traced extensively. These are generally type A and C' SLGs.

The nebulitic to intrusive migmatites (Fig. 4.35.D) are most commonly type E SLGs and show intrusive natures but generally have diffuse contacts that resemble amalgamated patch migmatites. These leucosomes have intrusive relationships as they are discordant to layering and foliations, although the contacts, in some areas of the SLG, grade into more dispersive and gradational contacts with the palaeosome. There are variable melanosomes, specifically consisting of biotite, present but they are not aligned to the foliation, however they are sometimes aligned to the walls of the intrusion.

Diatexites

The diatexites are seen most commonly in the southern extent of the field area where the early granites are present as voluminous intrusions into basement gneisses and supracrustals. These diatexites increase in volume towards the main extent of the Palmenhorst Dome and are commonly referred to as undifferentiated basement rocks (Smith, 1965). These migmatites are generally pervasive and preserve very little to none of the palaeosomes. Palaeosomes are only seen as rafts of resister lithologies/protoliths, which are generally the dark and distinctive amphibolite dykes. The contacts are sharp, and the outcrop types show distinctive walls, particularly in the Khan River Gorge, of crystallised granitic melts coalesced to near continuous to continuous granitic plutons in the extreme cases. These diatexites, especially the vein- or dyke-structured migmatites, are similar to injection complexes described along the Swakop River by Hall and Kisters (2012) and in the Holland's Dome by Kruger and Kisters (2016).

Sheeted granites with rafted palaeosomes

These diatexites comprise mainly schollen migmatites with schlieren, or flow structures, present within those associated crystallised melts (Fig. 4.36.A and B). The schlieren are defined by entrained biotite. These are typically homogeneous and extensive leucosomes that anastomose and coalesce to form SLGs that stretch up to several meters in width. The intrusions are sharp sided and typically cross-cut the foliation in the schollen (rafts of palaeosome) at low angles (Fig. 4.36.B) and the

schollen themselves. The amphibolite dykes are typically intruded and sometimes experience partial melting themselves (presence of melanosome). The amphibolite dykes (palaeosome) are typically seen as schollen (palaeosome) and preserve melanosomes or residuum along the contacts between the contact of the leucosome and palaeosome (Fig. 4.36.A and C). These schollen are darker (in colour) than the crystallised partial melt and lighter than the amphibolites forming a mix between the two components. The schollen are lozenge shaped when they are smaller, 50 cm in length, but also appear as elongate 10 to 20 m long rafts that are parallel to the sheeted (sides) morphology of the diatexite (Fig. 4.36.B and Fig. 4.36.A, respectively). Melanosomes are distinctive along the leucosome-palaeosome interface as an alignment of platy minerals, namely biotite and amphibole (Fig. 4.36.B), although it is not always easy to detect in the case of the amphibolites due to the protolith mineralogy being predominantly mafic.

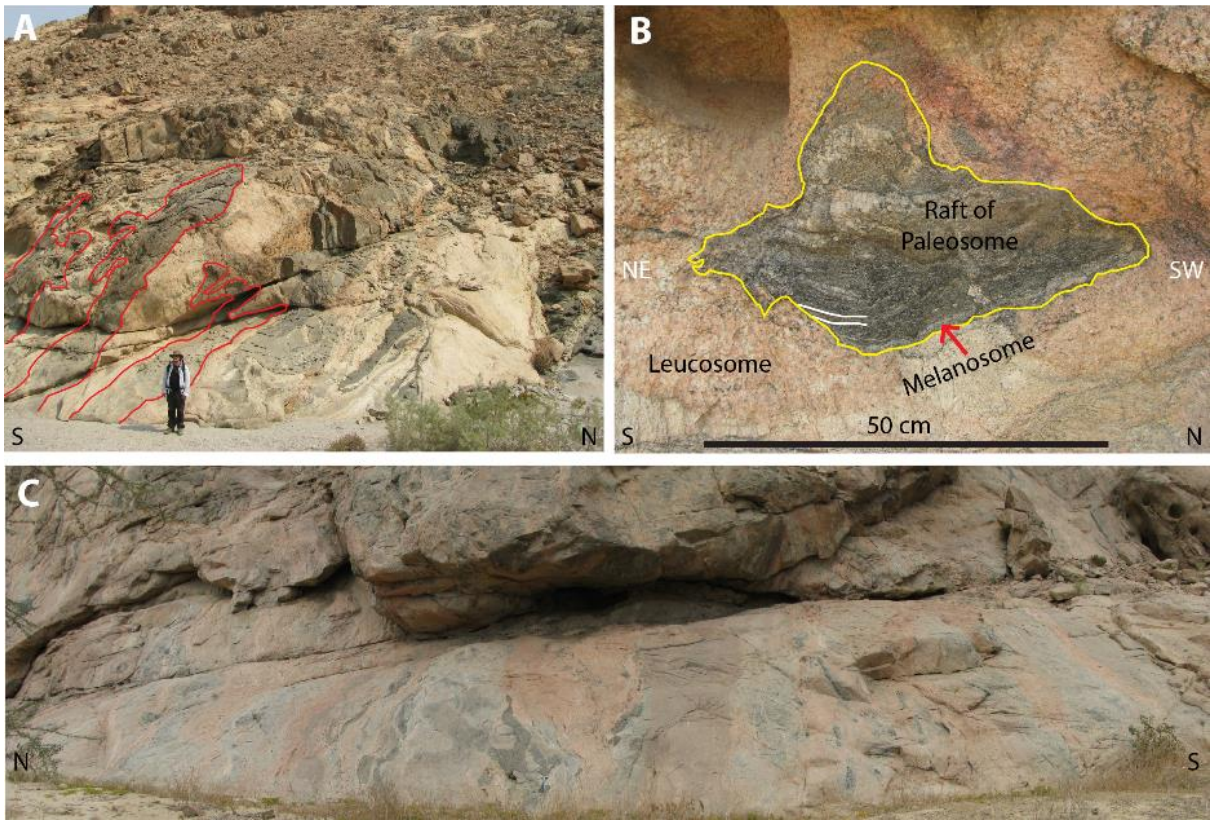


Figure 4.36: Field photographs of the sheeted granites with rafted palaeosome diatexites. (A) Schollen of amphibolite dykes (examples outlined in red) as the palaeosome within a schlieren dominated leucosome. (B) An example of a smaller raft (outlined in yellow) that is a lozenge shaped. The foliation in the palaeosome truncates the leucosome at a low angle (white lines truncated by the yellow outline of the raft). Melanosomes are present at the contact between the palaeosome and leucosomes and is developed as a concentration of biotite and amphibole platy dark minerals (red arrow) and in this case is similar to the palaeosome due to the protolith mineralogy. (C) A wall of multiple partial melt generations with schollen of dark palaeosomes.

Amalgamated sheeted granites and earlier granites coalesce to form these diatexite types (Fig. 4.36.C) and are in-source to intrusive melts. Generally, these granites are formed by the types C' and

E SLGs with the red granites also showing pervasive melt intrusions. These granites constitute the abundant lithology in outcrop and only rafts of palaeosomes are seen. These diatexites form the transition between the metatexites and the diatexites as they still preserve some pre-melting features but are comprised of mostly leucosome components and occur in the transitional zone between the true diatexites of the south and the metatexites migmatites of the north.

Homogeneous granite diatexites and plutons

This diatexite subgroup displays the most pervasive natures and comprise primarily continuous granitic intrusions (Fig. 4.37). These are true diatexites and show minimal schollen of palaeosomes (Fig. 4.37.A). They are generally homogeneous and represent the basement granites and red granites. In addition, the granites show intrusive and ballooning shapes into the country rock (Fig. 4.37.A).



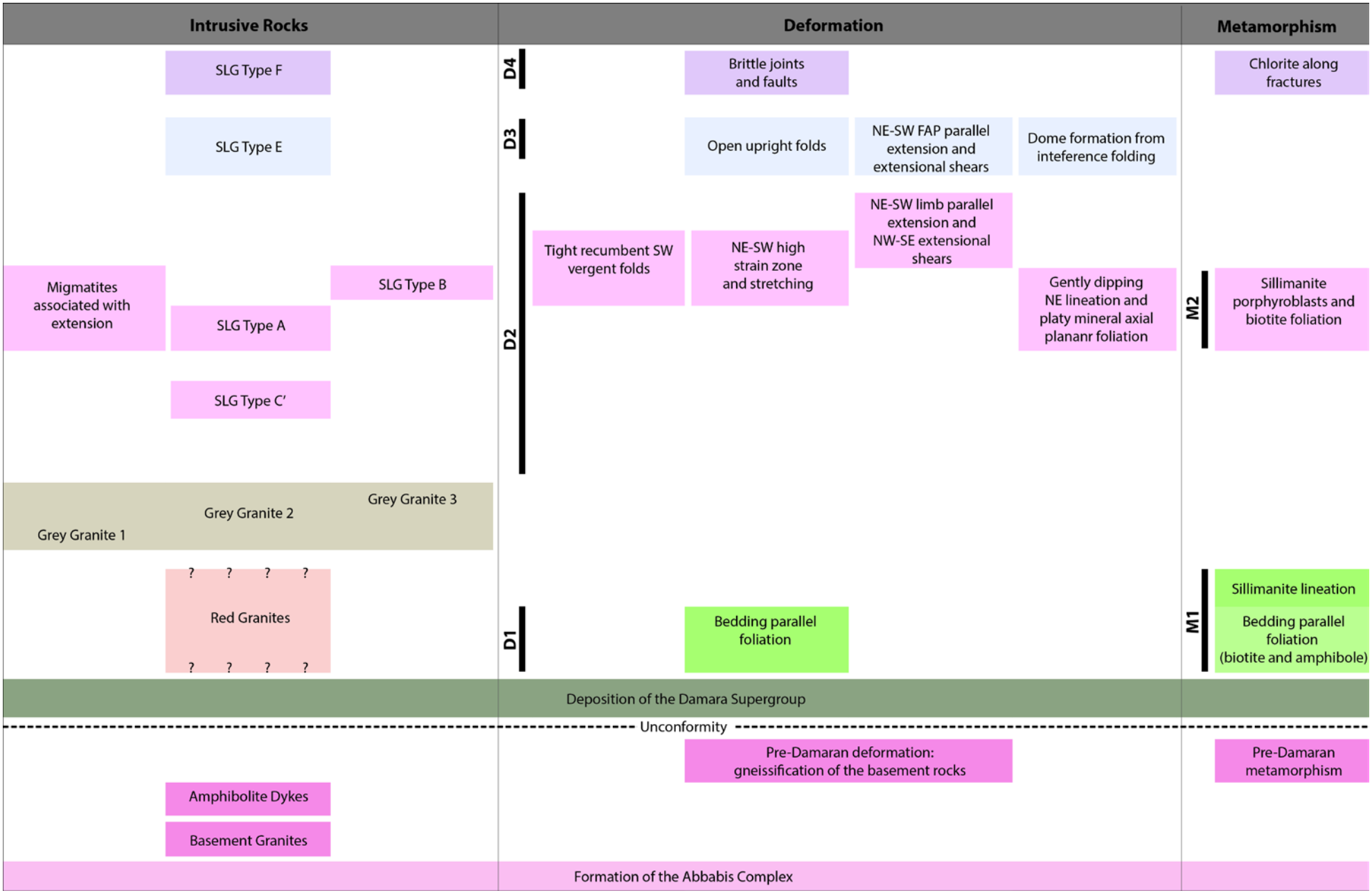
Figure 4.37: Field photographs of the homogeneous granite diatexites and pluton migmatites. (A) A gorge wall of a diatexite intruding into the basement gneisses. Homogeneous red granites are observed. (B) Khan River Gorge outcrop of multiple generations of migmatites or SLGs coalesced to form diatexites. Resister lithologies are present and examples are outlined in white.

Coalesced SLGs are also observed to form these diatexite migmatites (Fig. 4.37.B), which give the granitic fractions a more heterogeneous nature. Resister lithologies are also observed, although since they are so heavily intruded and not associated with known lithologies it is difficult to determine the exact protolith nature of these schollen (Fig. 4.37.B). These granites occur primarily in the south of the mapping area and form large plutons of basement granites (Fig. 4.1). Multiple intrusions cross-cut one another to form coalesced migmatites of different generations. Quartzofeldspathic segregations are present in these homogeneous granites, and appear as grain size changes, which are mainly coarse-grained to pegmatitic. These outcrops are generally preserved as walls in the deep river gorges, such as the Khan River Gorge, and undulating hilly terranes in the basement granites in the hinge of the D3 fold.

4.7 Discussion

From field mapping, various cross-cutting relationships between lithological units, numerous intrusives, deformational features and metamorphism were observed resulting in a synthesised relative geological history for the Nose Structure (Table 4.4). Two main deformational divisions were observed, the Damaran and Pre-Damaran deformational histories. Although, the Pre-Damaran signature is not as obvious, the remnant deformational history is still identifiable. Four main events of Damaran deformation were identified, with the second and third events representing the most prominent and visible. The geological history of the mapping area can be correlated with the entire sCZ and broader studies that have suggested there are two main events D2 and D3 (Smith, 1965; Jacob *et al.,* 1983; Longridge, 2012).

Table 4.4: Table showing the relative timing of the multiple intrusions, deformational and metamorphic events based on cross-cutting relationships from field observations.



4.7.1 The Abbabis Complex and associated magmatism

The Abbabis Complex consists primarily of quartzofeldspathic orthogneisses, augen gneisses, with the associated intrusive basement granites, the latter of which constitute a large intrusive body in the south of the field area (Fig. 4.1). The Abbabis Complex shows compositional variations as predicted by remote sensing. The stratigraphy of the Abbabis in the type locality includes the Tsawisis Formation (quartzite to phyllitic schists and gneisses), Naob Formation (calcsilicates, marbles and biotite schists) and the Narubis Granitoid Complex (Smith, 1965), although the Abbabis Complex has varying stratigraphies documented in various domes across the zone (Sawyer, 1981; Marlow, 1981; Brandt, 1987; Oliver and Kinnaird, 1996). The presence of possible paragneisses in the Abbabis Complex raises the possibility of the Tsawisis or Naob formations being present. However, due to the homogenous nature and no identified mesoscopic layering (Passchier *et al.,* 1990) the gneisses are most likely orthogneisses. Additionally, these paragneisses/grey orthogneisses are locally seen in the HSZ and are probably highly strained end members of the orthogneisses. Fine-banding and a decrease in grain size are commonly associated with strain partitioning (Platt and Behr, 2011). Straight gneisses in the Grenville Orogen have also been identified as highly strained gneisses at mid-crustal levels (Hanmer and McEachern, 1992; Nadeau and Hanmer, 1992) and coincidentally were also initially interpreted as paragneisses. Thus, the lithologies are similar to and most likely represent the Narubis Granitoid Complex although the stratigraphic succession differs.

This study has identified three areas of Damaran stratigraphy infolded within the Abbabis Complex in the mapping area based on distinctive lithologies, lithological sequences and structural relationships. Although Poli (1997) suggested that remnants of the Tsawisis Formation were present these have been re-interpreted as part of Damaran Sequence lithologies which is consistent with synclines identified by Longridge (2012) in the northern Palmenhorst Dome.

Magmatic rocks in the area include basement granites and amphibolites. The basement granites contain foliations that are truncated by Damaran structures. However, this foliation has generally been reoriented into parallelism with Damaran deformational features. The amphibolites in the sCZ have been interpreted to have formed as part of the Abbabis Complex (Smith, 1965; Marlow, 1981; Barnes, 1981), however, Damaran equivalents have been identified (Longridge *et al.,* 2014), with their mafic compositions linked to the Goas Suite (Longridge *et al.,* 2014). Two different ages have been found for these Damaran amphibolite dykes and the Abbabis Complex amphibolite dykes, at 557 Ma (Damaran amphibolite Dykes) and 2026 Ma (Abbabis Complex amphibolite dykes), respectively (Longridge *et al.*, 2014). The amphibolites in the study area are foliated, sometimes

folded, cross-cut the basement lithologies and are all Palaeoproterozoic with presumed ages of *ca.* 2.0 Ga, in agreement with Longridge *et al.* (2014).

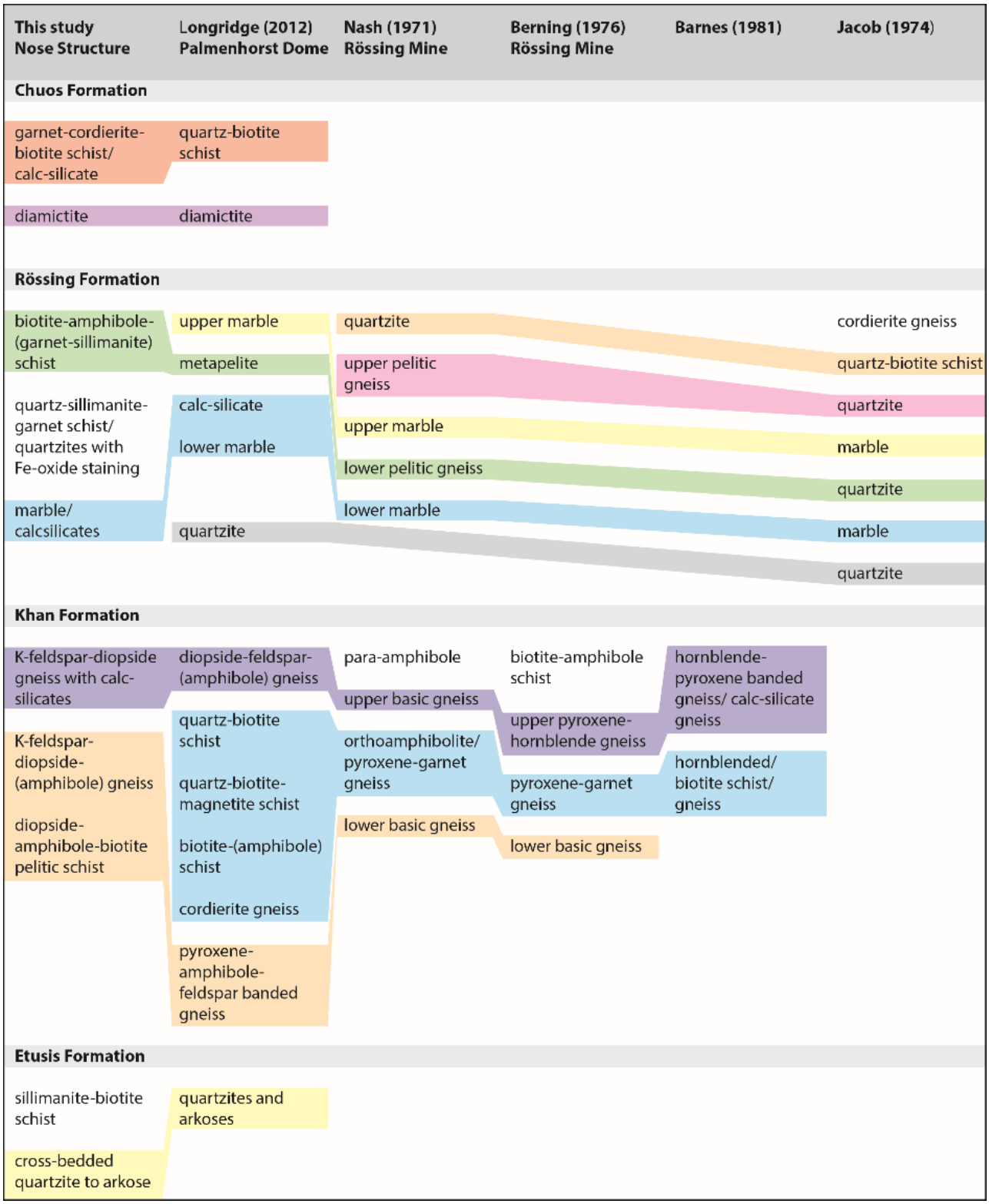
The Pre-Damaran structural and metamorphic indicators are not well developed in the area although previous studies have shown well developed L- and S-tectonites in the basement rocks (Jacob *et al.,* 1978; Kröner *et al.,* 1991). These tectonic features are seen but they have been largely overprinted by, and also attributed to, Damaran deformation in HSZs. Pre-Damaran folds have been located in the basement rocks in the past (Smith, 1965; Poli, 1997), however, no visible pre-Damara folds were observed in the field area. It is not possible to know conclusively, based purely on field relationships, whether the foliations within the basement granites and amphibolites are of Pre-Damaran or Damaran origin, although the truncation of foliations by Damaran granitoids within the basement granites suggests a Pre-Damaran origin, at least for this foliation.

4.7.2 The Damara Supergroup

The identification of Damara Supergroup lithologies within the Palmenhorst Dome is aided by identifying coherent sequences of the lower Damaran formations; specifically sequences of Etusis, Khan, Rössing, and Chuos formations. The Nosib lithologies and general stratigraphy, from the Etusis and Khan formations, can be correlated with the quartzites, gneisses, semi-pelitic schists and calcsilicates of previous studies (Table 4.5).

On an individual basis it is difficult to distinguish between the Etusis Formation and the Abbabis Complex, as they are both quartzofeldspathic, deformed and intruded by granitic rocks. This also means that the unconformity between them is obscured, apart from where basal conglomerates are present. The contact between the Etusis and Khan formations is gradational and shows lateral changes in composition, which could represent the interfingering and switching between the sandy braided fluvial system and distal fluvial setting proposed (Jacob, 1974; Henry, 1992).

Table 4.5: Summary table of previous workers' stratigraphies correlated by Longridge (2012), and this study's stratigraphy correlated with previous work.



The Swakop Group lithologies and general stratigraphy of the Rössing and Chuos formations can be correlated with the marbles, iron-rich quartzites, diamictites and semi-pelitic to pelitic schists identified in previous studies (Table 4.5). However, the heterogenous nature and carbonate-rich nature of the Rössing Formation and the identification of the Chuos Formation diamictites are ideal marker lithologies. The Rössing Formation is sometimes missing from the stratigraphic sequence of the infolds of the Damara Supergroup, where the Chuos Formation directly overlies the Khan Formation. This may be due to considerable attenuation as it is more easily deformed, a situation which is has been described by Nex (1997) for Goanikontes in a high strain zone along the basement-cover contact. In this study, there is a gradational contact between the Rössing and the Chuos formations, however it is normally recognised as an unconformity (Hofmann *et al.,* 2004; Miller, 2008). This may be due to depositional features that have not been identified or may be due to overprinting of the regional Damaran fabric which obscured primary sedimentary processes. The Chuos Formation, originally recognised as a tillite/diamictite by Gevers (1931), is a particularly distinctive lithology and where present helps to confirm the Damaran Sequence within the Palmenhorst Dome.

The distribution of the Damaran metasediments from this study is similar to other studies (Fig. 4.38) in the sense that the supracrustals surround the basement-cored domes (Smith, 1965; Volkman *et al.,* 1988; Lehtonen *et al.,* 1995). Refinements of the basement-cover contact in the area and the distribution of basement lithologies with three distinct domains are an improvement on previous work. Recognition and detailed mapping of the synclines of Damaran sediments within the basement (Hinge Syncline, Dorob Infolds and Ostrich Gorge Syncline) reveals additional structural complexity when compared to the existing models for the evolution of the Damara Belt.

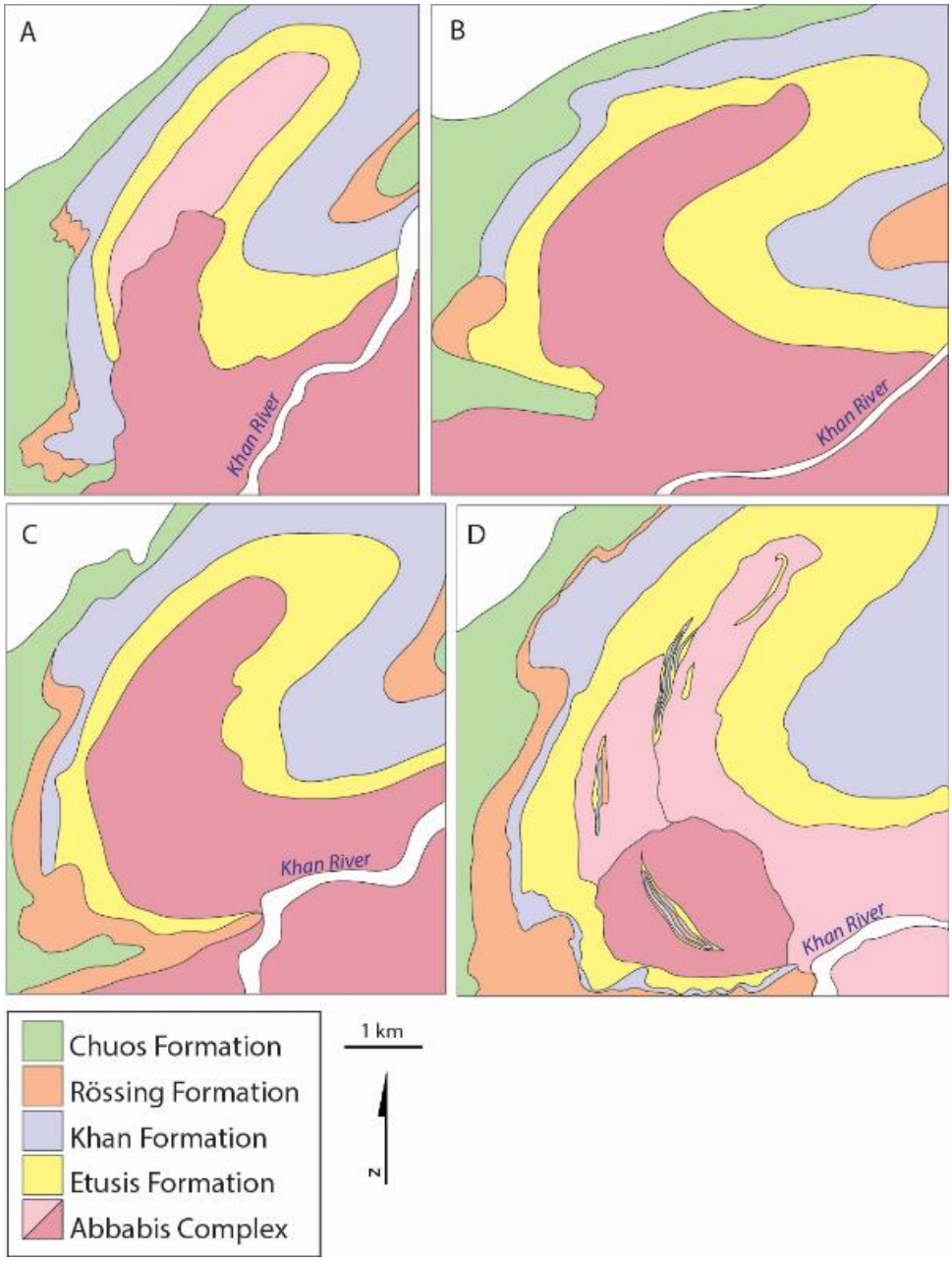


Figure 4.38: Lithological distributions in the Nose Structure from various authors and this study. (A) Smith (1965); (B) Volkman *et al.* (1988); (C) Lehtonen *et al.* (1995) and (D) lithological distributions from this study showing the new distribution of Damara metasediment-cored synclines within the basement rocks.

4.7.3 Structure and Metamorphism

Relative timing of structural and metamorphic events identified in this study are similar to the sequence observed by previous workers (Smith, 1965; Nash, 1971; Blaine, 1977; Coward, 1981; Jacob *et al.*, 1983; Barnes, 1981; Oliver, 1995; Nex, 1997; Longridge, 2012), with an early D1 and M1 regional fabric, D2 tight to isoclinal west to southwest verging nappe-like folds and D3 interference open upright northeast-southwest trending folds. These fold geometries and compressive events approximate the proposed larger evolution of the Damara Belt whereby (D2) orogen parallel east-

west shortening occurred due to the closure of the Adamastor Ocean and (D3) north-south shortening was a result of the Congo-Kalahari collision (Lehmann *et al.,* 2016).

From the literature, the preservation of D1 and M1 is debatable (Blaine, 1977; Barnes, 1981; Oliver, 1995; Goscombe *et al.,* 2017b), although according to Longridge *et al.* (2017) the thermal source of the M1 metamorphism is related to early Damaran granites such as the Goas Suite, Salem Granites and possibly the red granites. Likewise, studies have suggested that the presence of granites within the fold structures and lower crustal levels may have provided the heat required to weaken the crust and create these large refolded nappe-like structures created by interference folding (Anthonissen, 2009).

The D2 folding event is the most complex deformational event observed in the field area and displays numerous features associated with the event (Fig. 4.39). Southwest vergence and gently plunging folds form elongate sheet-like bodies that are interpreted to be basement-cored nappe-like structures. Outcrop scale nappe-like folds are observed as recumbent folds which are extended to the southwest as a sheet-like body with younger "layers" surrounding older "layers". The outcrop scale is proposed to refelect a larger scale nappe-like fold. These D2 nappe-like folds are a common feature observed in the Central Zone (Downing and Coward, 1981; Coward, 1983), which have exposed Palaeoproterozoic basement-cored domes surrounded by Damaran metasediments, resulting in a tectonic window. Northeast plunging prolate pebbles/lineations and high strain zones are also associated with D2 and are concentrated along the basement-cover contact. These prolate lineations were also observed in the Nose Structure by Poli (1997) and indicated a detachment zone between the basement-cover rocks. This is consistent with the structural features and geometries identified in this study and highlight the presence of extension during D2 associated with the verging folding.

Northeast-southwest HSZs have been identified and interpreted to occur along the top limb of anticlines (not overturned) of D2 folds. Limb parallel extension in the HSZs are proposed to accommodate the lengthening of the limbs (Fig. 4.39) due to the verging geometry possibly created by pure shear during a dominant northeast compressive direction (Davis and Reynolds, 1996; Platt and Behr, 2011). Additionally, there are other basement-cover contact high strain zones identified in the Palmenhorst Dome (Nex, 1997; Goanikontes area) and shear zones associated with the overturned limb of D2 synclinal infolds in the Palmenhorst Dome (Longridge, 2012). The latter shears may be associated with equivalent deformational events but are not associated with the same limbs that have undergone extension in this instance.

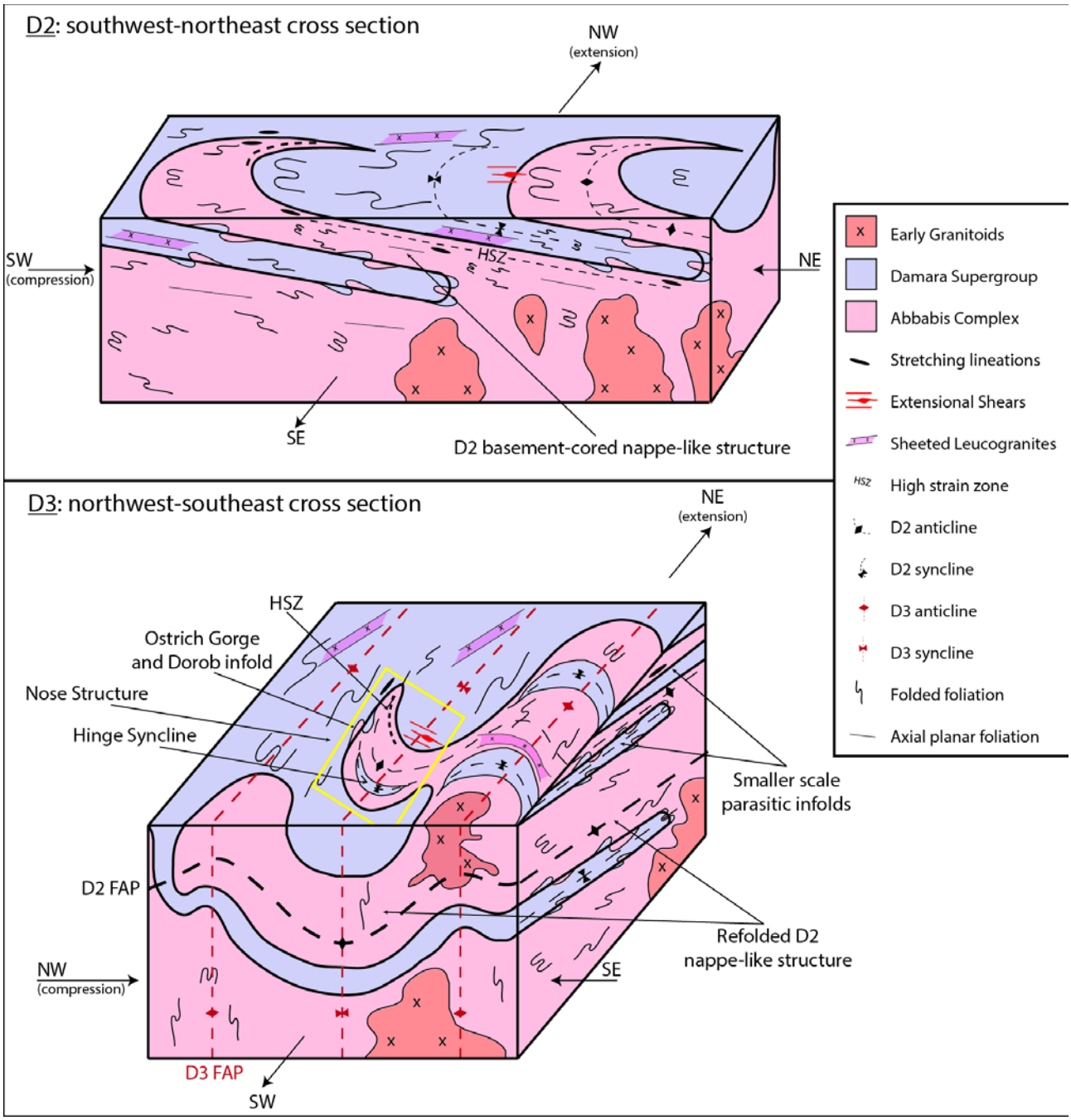


Figure 4.39: Schematic block diagrams of cross-sections of D2 and D3 deformational events. Folding and associated fabrics and intrusions are noted. (D2) Southwest verging northeast plunging to recumbent folds resulting in basement-cored nappes, high strain zones (HSZ) on the attenuated and upright limb of the folds. Southwest-northeast compression and northwest-southeast extension. (D3) Northwest-southeast compression and northeast-southwest extension is orthogonal to D2 with open upright folds (D3 FAP= red dashed line). D2 nappe-like structures are refolded (D2 FAP= black dashed line) by D3 folds resulting in dome formation. The interference fold pattern and parasitic folds yield similar outcrop extents seen in the geological map produced for the Nose Structure (yellow rectangle) and the northern extent of the Palmenhorst Dome from other studies (plan view of northern margin folds after Longridge, 2012).

Folding and extension associated with the upright northeast-southwest trending D3 fold axial planes and D3 compression is orthogonal to the D2 nappe-like structures and are seen to refold the

fold axes and limbs of gently northeast plunging to recumbent D2 folds (Fig. 4.39). Both outcrop (Fig. 4.18.E) and mapscale (Fig. 4.1, Damaran synclines within the basement with folded axial traces) examples are identified. This orthogonal change is thought to represent progressive kinematic changes during collision (Kisters *et al.,* 2004; Longridge *et al.*, 2017; Lehmann *et al.,* 2016). Inteference folding has been previously identified in the sCZ, with it often being attributed to the cause of the characteristic dome formation in the zone (Smith, 1965; Jacob *et al.,* 1983; Longridge *et al.*, 2007).

A nappe-like structure can be used to explain the basement-cored domes to a point. However, the folded geometries of the basement and infolded Damaran metasediments with folded axial traces as well as the northeast-southwest trending anticlines (defined by basement-cored domes) requires an additional interference folding event. The schematic block diagram (Fig. 4.39) demonstrates the outcrop pattern for the Nose Structure and part of the Palmenhorst Dome, which can be explained by a D2 nappe-like structure refolded by upright and open D3 folds. This accounts for both the folded axial planes as well as the folded outcrop extent of the Nose Structure (and associated synclinal infolds) and is consistent with a similar model proposing that the Palmenhorst Dome was a result of interference folding (Longridge *et al.,* 2012). D2 km-scale parasitic folds are used to interpret the presence of D2 synclines within the basement-cored domes (Fig. 4.39). The outcrop extents of the Hinge, Dorob and Ostrich Gorge synclines as well as the Nose Structure can be explained by parasitic folding which is exposed due to the current level of erosion. Present levels of exposure could also account for the limited Damaran sequence observed in these synclines. These basement-cored refolded nappe structures have been identified across the Damara Belt (Downing & Coward, 1981; Anthonissen, 2009) and similar structural styles were observed in the associated Kaoko Belt (Stanistreet and Charlesworth, 2001).

4.7.4 Early Damaran Intrusives

Field relationships of the red and grey granites from this study are similar to those reported in previous studies (Nex, 1997; Basson and Greenway, 2004; Longridge, 2012; Fremantle, 2017) and therefore are likely to be equivalent in age and intrude earlier in during the Damara Orogen. These granites are younger than the SLGs and most likely intruded prior to the onset of D2 based on the foliated nature of these granites.

The red granites represent the oldest Damaran Granitoids from this study and have been dated at 539 to 536 Ma previously (Longridge, 2012). They contain a D2 foliation and are proposed to be an early phase of magmatism related to middle crustal processes during D2 (Longridge, 2012). The grey granites are the most strongly foliated intrusions and within the D2-related HSZs they tend to

exhibit sharp contacts. Previous work suggests that they are either Damaran syn-tectonic granites (Nex and Kinnaird, 1995; Kinnaird and Nex, 2007) or are associated with various sheeted post-tectonic leucogranites (Longridge, 2012) indicating that their relative timing remains contentious.

4.7.5 Damaran sheeted leucogranites

Based on field relationships and mineralogy, the SLGs noted in this study can be correlated to those described by other workers (Nex, 1997; Basson and Greenway, 2004; Fremantle, 2017). However, type C' SLGs are problematic as in this study they appear to be the oldest. They are cross-cut by purportedly older SLGs (types A and B; Nex, 1997) and so may not be directly correlated with other type C SLGs. Longridge (2012) described type C SLGs that were similar to those of Nex and Kinnaird (1995), but the relative timing differed. He concluded that these SLGs had local variability and comparisons across the sCZ are not always possible. Conversely, these SLGs may be different and the descriptions need to be revisited or the original descriptions were not precise enough to account for the variability with in the Central Zone. Alternatively, SLGs may produce more than one generation of a very similar granite at different times in varying locations.

Types A, B and C' SLGs are synchronous to D2 deformation and are commonly seen folded by both D2 and D3 folds, whereas type E SLGs appear to be synchronous to D3 and are only folded during D3. Type F SLGs are correlated with the late-stage pegmatites that are associated with end-orogeny crustal relaxation (Fuchsloch *et al.,* 2018). Fuchsloch *et al.* (2018) proposed that the late stage pegmatites were most likely intruded along crustal weaknesses, such as fold axial planes. Earlier stages of upright open folds (D3), as defined in this study, also produced northeast-southwest trending fold axial planes that could have accommodated the northeast-southwest trending Type F SLGs during the end-orogeny relaxation.

4.7.6 Migmatites

The migmatite subgroups established in this study are based on the spatial distribution, textures and sources for the migmatites, SLGs and earlier granites of the northern extent of the Palmenhorst Dome. The present study is one of few thorough textural assessments of the various types from the Damara Belt.

Toe *et al.* (2013) observed a spatial distribution of different migmatite types, with metatexites mainly occurring in the supracrustals, while the earlier granites and basement granites were primarily identified in the cores of the Palmenhorst Dome (Abbabis Complex) as pervasively crystallised

partial melts and diatexites. This resulted in a stratified tectonic model for the migmatites based on granite emplacement and partial melt pervasiveness. This is also identified in the Palmenhorst field area, where the metatexite subgroups are mainly located in the supracrustals surrounding the main fold and in the northern extent of the basement gneisses. This is in contrast to the diatexites, which appear to increase towards the south of the mapping area, which represents the larger extent of the Palmenhorst Dome. However, there is a transitional zone between the two where both metatexites and diatexites co-exist. This appears to correlate with the tectonic zones proposed where remnant partial melt increases towards the core of the dome (Toe *et al.,* 2013).

A simplistic idea of how much melt was theoretically present is achieved from melt fraction models (Fig. 4.40). These models are based on the textural classification of a migmatite, which is considered to represent a theoretical melt proportion and idealised increase in strain (Renner *et al.*, 2000; Sawyer, 2008; Pawley *et al.,* 2015). Essentially, it is proposed that there is a progressive increase in melt fraction from bedding/foliation parallel metatexites through intrusive sheeted granites and sheeted leucogranites with rafted palaeosomes to diatexites/plutons (Fig. 4.40), and as a result strain partitioning into the melt is possible making it easier to fold the basement and supracrustal rocks into nappe-like structures. Especially so, because these diatexites are associated with earlier granites (red granites), which would have provided heat prior to D2 folding. This also means that the migmatites in the core of the dome were able to develop into more pervasive melts that possibly fed some of the SLGs that intruded higher stratigraphic (and tectonic levels). This is the case noted in the southern Palmenhorst Dome near Goanikontes (Toe *et al.,* 2013).

Dilation to net-textured metatexites are generally structurally controlled and emplaced at higher crustal levels (that are possibly colder) than the diatexites, which have progressed into more amorphous ballooning granites, implying that these more amorphous granites are further from their source rocks. In contrast, the metatexites contain more in-source to in situ melts that have not migrated far. This is consistent with net-textured migmatites from Karibib (Hall and Kisters, 2012), where localised dilational to net-textured melts developed into self-stabilizing systems with increasingly far-reaching and more pervasive melts. Additionally, stratification of the crust has been previously recognised in the sCZ (Toe *et al.,* 2013; Longridge *et al.,* 2017).

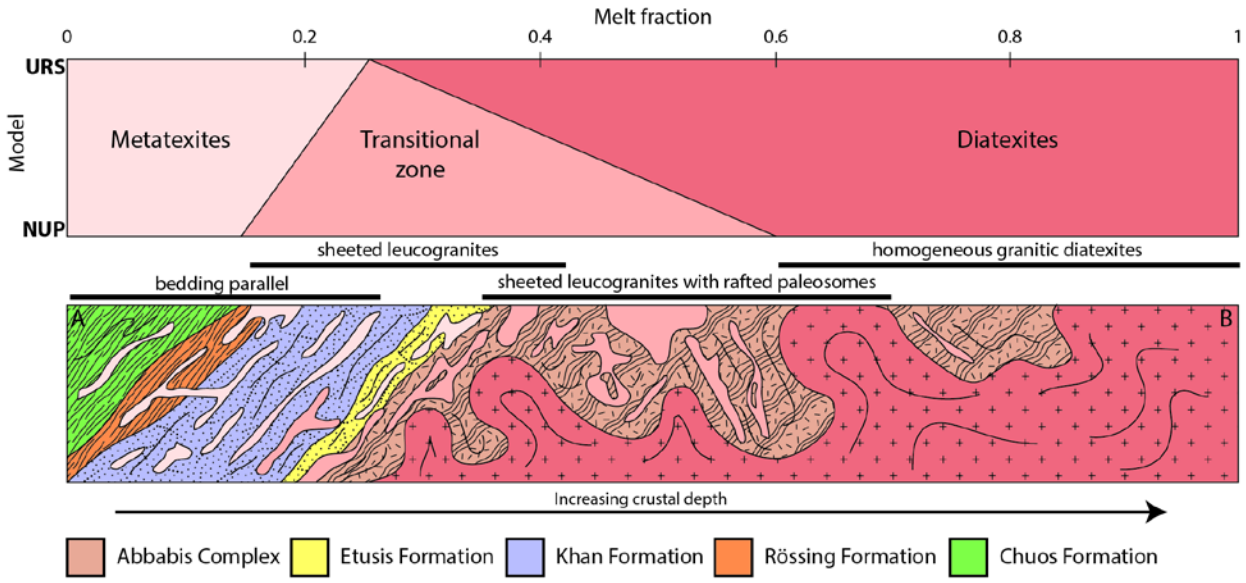


Figure 4.40: Northwest-southeast schematic cross section of the field area showing the stratification of the intrusions based on the distribution of the migmatites in the field area. First order classification of the migmatites are shown, based on a function of the fraction of melt present, in the top diagram. The uniform, rigid spheres (URS) and non-uniform in size and shape (NUP) models are illustrated after Renner *et al.* (2000) and Sawyer (2008). The distribution of the four different groups of migmatites, described in section 4.4, within the crust is indicated in the middle by the black distribution bars. Cross section from A-B (see figure 4.35) is showing the basement and cover lithologies and the types of partial melt associated with each.

The type A and B SLGs (sometimes type C') are generally associated with metatexites and in situ to in-source melting (Pawley *et al.,* 2015). This suggests that they were sourced from either the host lithologies or lithologies not far from the crystallised melt (Hall and Kisters, 2012) and therefore, their compositions may be controlled by host lithologies. Ward *et al.* (2008) suggested that the presence of new garnet and cordierite in the leucosome could be identified as features of in situ melting in the palaeosome. Garnet is only associated with type B SLGs, suggesting that possibly these melts are from in situ sources. Types C', E and F SLGs are intrusive and most likely represent SLGs that have migrated, most likely up stratigraphy (Hall and Kisters, 2012) and can no longer be linked to their sources. Hall and Kisters (2012) did suggest that these far-reaching SLGs were possibly initiated as net-textured migmatites that eventually develop into more intrusive and extensive morphologies, but no conclusions can be made from this study. The diatexites, such as coalesced type C' SLGs and the earlier granites probably had sources in the basement lithologies/cores of anticlines and lower Nosib Group due to their locality. The sheeted leucogranites with rafted palaeosomes have melanosomes present and therefore may represent to some extent in-source melting (Sawyer, 2008; Pawley *et al.,* 2015).

4.8 Conclusions

From field mapping a synthesised relative geological history for the Nose Structure was established (Table 4.4). A pre-Damaran fabric was identified but the second and third Damaran episodes overprinted previous fabrics.

The Abbabis Complex in the Nose Structure is primarily made up of various orthogneisses and granite-gneisses that are variably strained, which may be correlated to the Narubis Granitoid Complex. The paragneisses identified in the field do not have a sedimentary origin and most likely represent highly strained orthogneisses. However, this study has identified textural and compositional variations in the basement lithologies.

The basement granites are part of the Abbabis Complex and constitute a different component present in the basement core. In addition, the amphibolite dykes are also interpreted to be Palaeoproterozoic in age and therefore associated with the Abbabis Complex. Structural fabrics present in theses magmatic rocks do not show clear relationships as they are often deformed into parallelism during Damaran deformation.

Additionally, Damaran metasediments have been infolded into the basement lithologies and were identified from detailed lithological and structural mapping. The synclinal infolds generally contain a sequence of lower Damaran lithologies: The Etusis, Khan, Rössing and Chuos formations. The general stratigraphy identified in the field area can be correlated with other Nosib and Swakop Group lithologies, however, the contacts between all the Damaran formations are gradational which is contrary to the literature. This is attributed to possible deformational effects and anatexis.

It is difficult to distinguish between the Etusis Formation and Abbabis Complex as the unconformity is tectonised and obscured unless basal conglomeratic layers are identified. Lateral facies changes are identified within the Etusis and Khan formations, which is most likely due to sedimentary processes. The Rössing and Chuos formations are ideal marker horizons, although the Rössing is commonly missing in stratigraphy due to attenuation in the study area.

Refinements to existing lithological maps have been made in the northern extent of the Palmenhorst Dome. These include the recognition of various compositions in the Abbabis Complex, synclines (Hinge Syncline, Dorob Infolds and Ostrich Gorge Syncline) infolded into the basement lithologies and a refinement of the basement-cover contact.

Relative timing of structural and metamorphic events identified in this study are similar to the sequence of events observed by previous workers, with an early D1 and M1 regional fabric, D2 tight to isoclinal west to southwest verging nappe-like folds and D3 interference, open and upright northeast-southwest trending folds. Recumbent D2 folding initially creates the nappe-like structures of basement-cored anticlines that are refolded by D3 folds. Interference folding of these nappe-like structures is proposed to be the mechanism for dome formation prcesses. Gneissic thinning and elongate prolate pebbles are attributed to HSZs and stretching as a result of attenuation of the top upright limb of the D2 anticline of recumbent D2 folds.

Field relationships of the red and grey granites from this study are similar to those in previous works; these granites were emplaced prior to the SLGs. The red granites are the oldest Damaran Granites from this study followed by the grey granites. Cross-cutting relationships with other structural features were tenuous and the relative timing with regards to D2 and metamorphism cannot be easily established for the red granites.

Based on field relationships and mineralogy the SLGs can be correlated with SLGs of previous workers. However, type C' SLGs are problematic as they show different emplacement chronologies developed by previous studies and may not be directly correlatable. As a result, the nomenclature may need future revisions.

The migmatite subgroups established in this study takes into account the spatial distribution, textures and sources for the migmatites, SLGs and earlier granites of the northern extent of the Palmenhorst Dome. The spatial distribution of different migmatites is similar to what was established in other studies, where crystallised partial melt increases in intensity away from the surrounding Damaran metasediments and towards the basement-cored domes. Metatexites and SLGs are mainly observed in the supracrustals and the coalesced SLGs, with rafted palaeosomes and diatexites increasing in abundance and extent towards the core of the dome. Therefore, from melt fraction models, partial melt intensity increased towards the cores of these domes (at the time of partial melting) providing sufficient heat to accommodate folding. Migmatites in the basement cores developed more pervasive melts and possibly fed the intrusive SLGs that were emplaced at higher tectonic levels.

Dilation to net-textured migmatites (types A and B SLGs) possibly represent in situ to in-source melts with compositions possibly controlled by host lithologies, whereas the SLGs (typically type B and C') are typically intrusive resulting in migrated partial melts. The diatexites (type C' SLGs, red and

granites) are typically too pervasive to allow further characterisation of their source. However, due to their position in the basement and lower Nosib Groups, they most likely were sourced from the lithologies within the cores of the anticlines.

5. Petrology

5.1 Introduction

The various lithologies encountered in the field area (from Chapter 4) are examined petrographically, with a focus on the modal abundances of minerals, textures, deformational features and the presence of crystallised partial melt. Mineral assemblages and petrographic descriptions are used to confirm the nature of the lithologies and their affinities, such as the Abbabis Complex, Damara Supergroup and the intrusions described in previous chapters, and to make comparison with findings from published studies. The deformational features are examined within the context of the larger tectonic setting. Partial melt textures are not placed in the migmatite classification scheme proposed in Chapter 4, as crystallised partial melt preserved at a thin section scale may not represent the overall structure or migmatites developed during anatexis (Sawyer, 2008). Partial melt features are identified using the criteria outlined in Sawyer (2008), which include cuspate-lobate and tetrahedral grain boundaries with pockets of smaller grains that extend into larger "host' grains, rounded minerals as a result of corroded edges into possible remnant melt, narrow microcrystalline rims or films of minerals along cuspate grain boundaries and pockets, cracks or pockets showing smaller quartzofeldspathic material adjacent to larger grains, narrow trains of blebby inclusions of quartz within larger feldspars along grain boundaries indicating enlargement of grains due to crystallisation of melt (crystals are commonly euhedral), and lastly granophyric textures within coarser grains (Simpson and Wintsch, 1989; Sawyer, 2008). Individually these lines of evidence are not concrete evidence for crystallisation of partial melt in residual rocks, however, when they paired together they may suggest the presence of partial melt. Even though the early granites and SLGs are products of partial melt, there are multiple generations of granitoids that cross-cut one another and occur throughout the belt. Therefore, remnant partial melt textures were also considered in these intrusions as a possibility. Point counting was performed on all the intrusive rocks for classification purposes. Additionally, the modal abundances of the quartzofeldspathic Etusis Formation and Abbabis Complex was established in order to compare the lithologies compositionally. Thin sections were cut perpendicular to foliation and parallel to lineation when these features were present.

5.2 Basement and Damaran Lithologies

The various Abbabis Complex and Damaran lithologies are described below and all of which are metamorphic in nature.

5.2.1 Abbabis Complex

The Abbabis Complex consists of various gneisses that show a granoblastic polygonal texture and comprise quartz, microcline, minor plagioclase and biotite (Fig. 5.1). The overall texture is of a mosaic of equigranular quartzofeldspathic minerals and a foliation defined by biotite (Fig. 5.1). Gneissic banding and quartzofeldspathic augens are also present with varying grain sizes in the orthogneisses, grey orthogneisses and granite-gneisses.

The orthogneisses contain primarily euhedral to subhedral (1 - 2 mm) quartz (50%), plagioclase (31%), microcline (15%) with accessory minerals (less than 5%) of biotite, chlorite and minor opaque minerals, most commonly ilmenite and magnetite (Fig. 5.1.A and B). Compositional banding and alignment of all minerals is present with concentrations of dusty microcline and strained quartz-rich bands and quartz with minor plagioclase banding (Fig. 5.1.A). The microcline and strained quartz banding is thinnest (1 to 2 mm thick) and is made up of three to four (larger) microcline crystals. Polycrystalline augen containing mainly altered microcline and quartz show an increase in grain size from the surrounding matrix. However, this relationship is a gradational one with the biotite foliation concentrating along and wrapping around the edges of augens. Brown biotite defines a foliation (Fig. 5.1.A and Fig. 5.2.A). The biotite laths have accumulated along the margins between the gneiss and SLGs as a melanosome (Fig. 5.1.A and B). The laths are parallel to gneissic banding. Quartz and microcline are commonly altered, resorbed and annealed, seritised and remnant plagioclase twinning may be present (Fig. 5.1.B). Green chlorite replaces biotite along the grain boundaries (Fig. 5.2.A). Inclusions of rounded chlorite, biotite and quartz are present within altered plagioclase, although in some cases this may be cordierite rather than plagioclase (Fig. 5.2.C).

The granite-gneiss is more homogeneous than the orthogneiss and are less deformed than the orthogneisses (Fig. 5.1.C and D). The mineralogy includes (1 -3 mm) microcline (53%), quartz (35%), plagioclase (11%), with biotite and ilmenite as accessory minerals (< 5%). This sample does not show gneissic banding. Alteration by sillimanite and sericite of the feldspars (Fig. 5.2.D) is common along with inclusions of quartz and biotite within ilmenite. The granite-gneisses are less altered than the orthogneisses. Some quartz grains are poikiloblastic and elongate, approximately 3 mm in length, and parallel to the platy minerals, namely biotite, and form a foliation. Biotite is concentrated in zonal and discrete accumulations (Fig. 5.1.C).

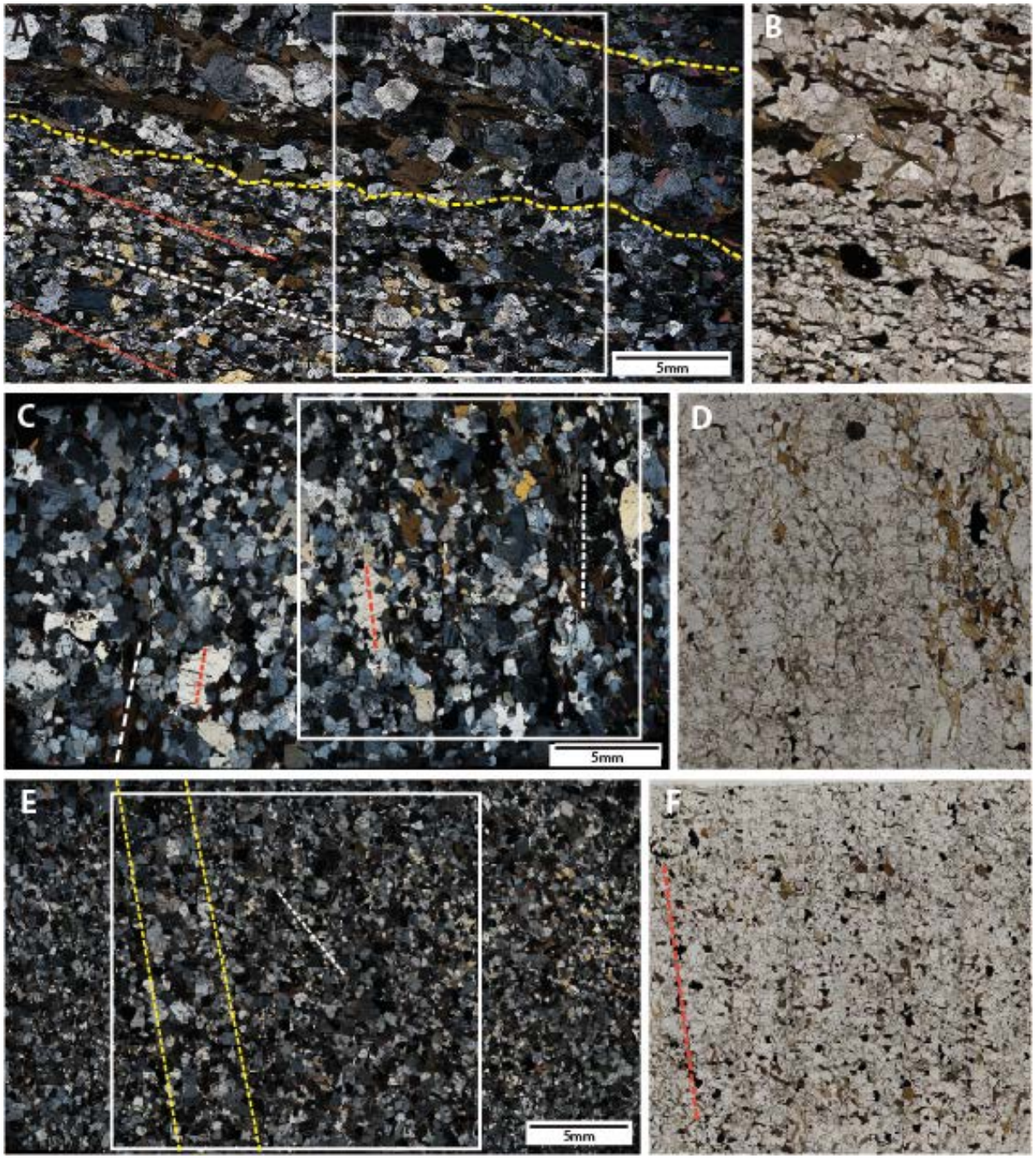


Figure 5.1: Overview photomicrographs of thin sections from the Abbabis Complex. (A) Cross-polarised light (XPL) photomicrograph showing overall rock texture of an orthogneiss with an associated sheeted leucogranite outlined with dashed yellow lines. Biotite foliation= white dashed lines. Two foliations are present - one is parallel to the yellow dashed line and younger than the foliation at an angle. Red dashed line indicates microcline compositional layering direction and distribution. (B) A plane polarised light (PPL) photomicrograph showing biotite foliation, mineral alignment and opaque mineral distribution in the area indicated by the white box in image (A). (C) Overview photomicrograph showing a granite-gneiss with elongate, poikiloblastic quartz indicated by the dashed red lines. Biotite accumulations and foliations are indicated with the white dashed line (XPL). (D) Biotite accumulations in the area indicated by the white box in image (C) (PPL). (E) Overall rock texture of a grey orthogneiss with grain size banding. Increase in grain size, with respect to the other grains= yellow dashed line; Biotite foliation= white dashed line (XPL). (F) Opaque and biotite alignment (red dashed line) in the area indicated by the white box in image (E) (PPL).

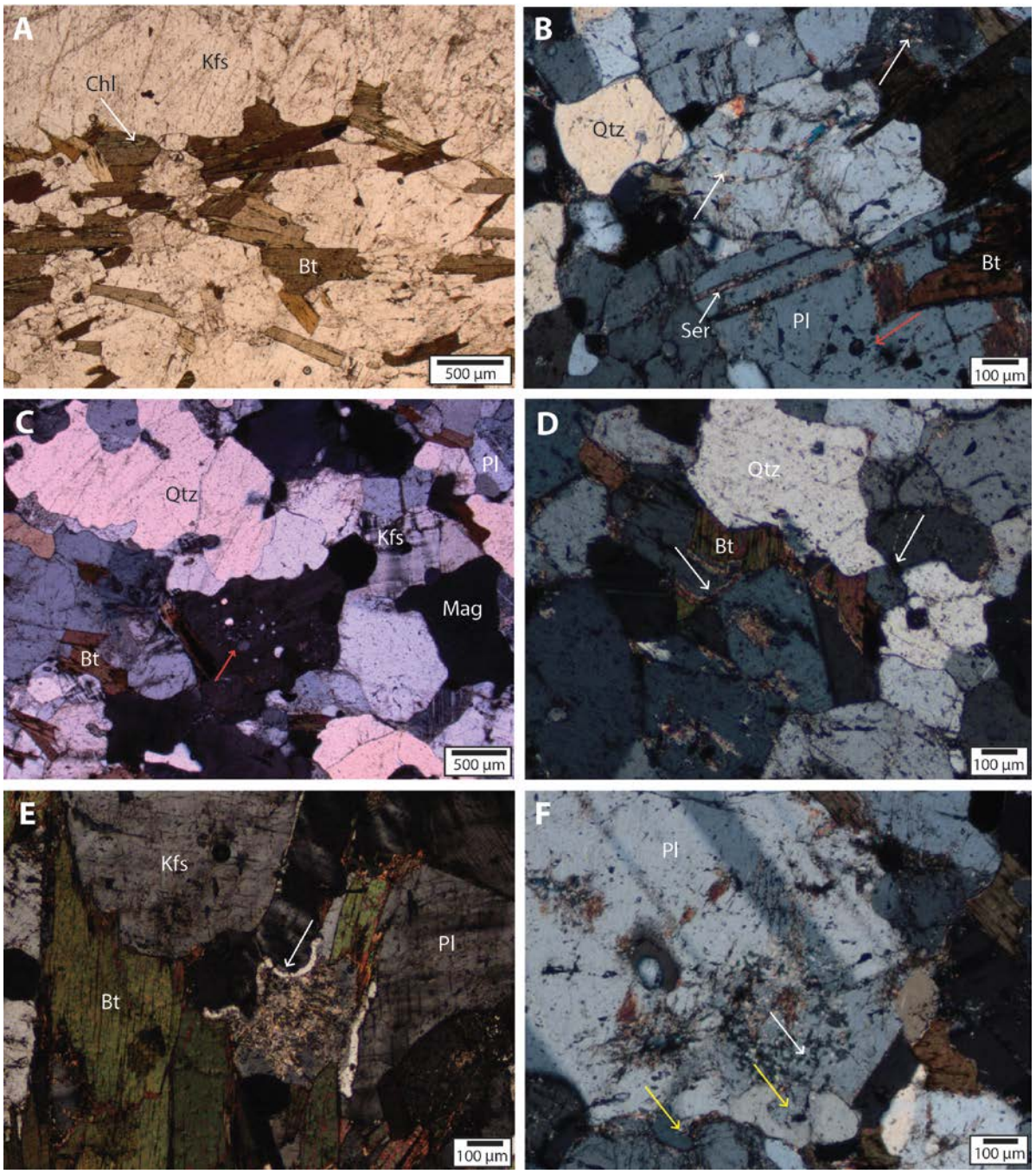


Figure 5.2: Photomicrographs of the Abbabis Complex gneisses. (A) Dusty and altered microcline, foliated biotite being replaced by chlorite (white arrow) and cuspate lobate grain boundaries (PPL). (B) Altered quartz and plagioclase. Seritisation replacing remnant plagioclase twinning, along with alteration along cracks within quartz (white arrows). Rounded inclusions within plagioclase (red arrow). (C) Cream quartz, microcline, biotite, plagioclase and magnetite. Rounded inclusions of quartz within altered plagioclase (red arrow). Poikiloblastic and elongate quartz is also present (XPL). (D) Granoblastic quartz and biotite. Biotite has altered and replaced remnant plagioclase (white arrow), which then has undergone seritisation. (XPL) (E) Microcline and plagioclase replaced by biotite as microcline remnants are present within biotite laths. Microcrystalline rims along cuspate grain boundaries (white arrow). Plagioclase is altered to sericite. (XPL) (F) Large plagioclase grain with cuspate lobate grain boundaries (yellow arrow). Granophyric intergrowths within the plagioclase grain (white arrow) (XPL). Mineral abbreviations are after Kretz (1983).

The grey orthogneisses contain a higher proportion of mafic minerals than other Abbabis Complex lithologies. Minerals include microcline (39%), biotite (36%), quartz (24%) and plagioclase (1%) (Fig.

5.1.E and F). Notably, the grey orthogneisses are finer-grained with banding defined by a variable grain size banding (Fig. 5.1.E). Grain size ranges from 1 mm to 2 – 3 mm grains. Additionally, quartz shows two main grain size categories; one that is similar to the average grain size (approximately 1 mm) and a small subset (approximately 0.2 mm in size) of rounded quartz that is most commonly displayed as inclusions distributed throughout the sample. Biotite forms a foliation and replaces plagioclase and pinnitised and seritised plagioclase (Fig. 5.2.E and F).

Micro-structures

Two foliations are present in these basement rocks. Both of these foliations are defined by biotite however, the younger foliation is also defined by compositional and grain size gneissic banding. The earliest foliation is a spaced foliation and is less well developed. This foliation is crenulated, reoriented by the younger dominant foliation as deflected laths of subhedral biotite, is truncated by the younger biotite foliation and is discordant to the gneissic banding and parallel sheeted leucogranites. The dominant younger foliation is more continuous and developed preserving gneissic banding. Certain leucosomes are foliation and banding parallel. In the orthogneiss the younger brown biotite foliation (Fig. 5.1.A and Fig. 5.2.A), most easily seen in plane polarised light (PPL) (Fig. 5.1.A and Fig. 5.2.A), has a spaced foliation in thin section. The foliation is concentrated as zonal and discrete accumulations. Poikiloblastic quartz and laths of biotite form the spaced foliation, the younger foliation, in the granite-gneisses. The granite-gneisses also show an earlier biotite foliation that is discordant to the younger foliation and defined by older biotite laths. In the grey orthogneiss, there is also gneissic banding as the younger foliation that is discordant to the first biotite foliation.

5.2.2 The Damara Supergroup

Etusis Formation

The arkosic quartzites of the Etusis Formation are generally quartz- and feldspar-rich. Textures vary and include granoblastic polygonal (Fig. 5.3.A and B), aligned schistose and porphyroblastic (Fig. 5.3.C and D). Both the quartzite and sillimanite-quartz-biotite schist show an alignment of minerals to varying degrees. In addition, the Etusis samples show a distinct lack of microcline (K-feldspar) when compared to the Abbabis Complex lithologies.

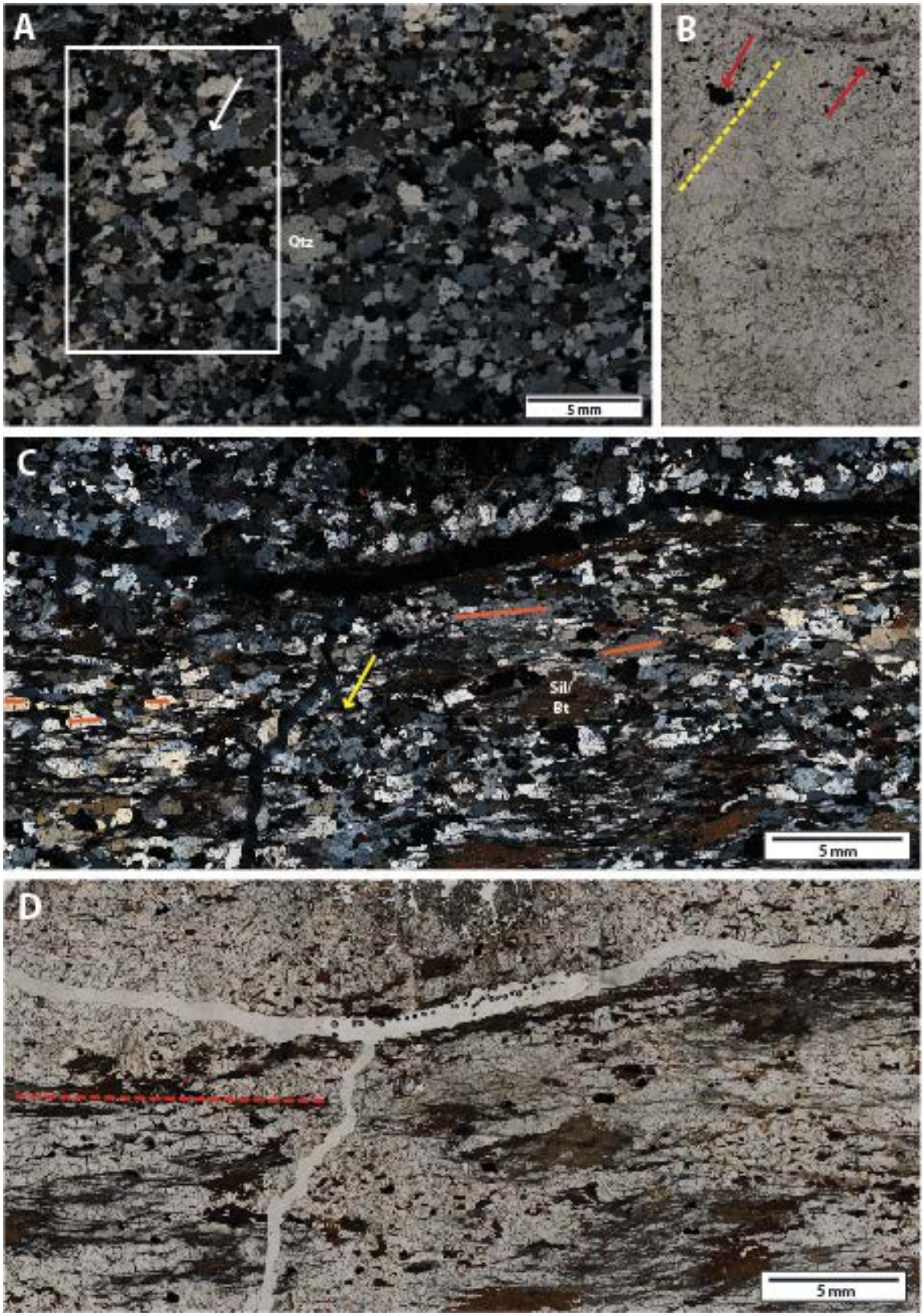


Figure 5.3: Overview photomicrographs of thin sections from the Etusis Formation meta-siliciclastic rocks. (A) Banded quartzite showing a granoblastic polygonal texture, comprising mainly quartz and feldspar (white arrow). Large quartz are aligned with banding (XPL). (B) Ilmenite banding is indicated by the yellow dashed line in the PPL image of area indicated by white box in image (A). Ilmenite is indicated by the red arrows. (C) Sillimanite-quartz-biotite schist showing the sillimanite-biotite lineation and foliation within a quartz and minor feldspar matrix. Quartz elongation direction (red lines) is parallel to the foliation; microcline= yellow arrow (XPL). (D) Sillimanite knots (grey fibrous texture) and distinct biotite foliation (red arrow) in PPL image of area in (C). Mineral abbreviations are after Kretz (1983).

The banded quartzites show a homogeneous and distinct granoblastic recrystallisation texture (Fig. 5.4.A). They comprise quartz (90%), plagioclase (20%), ilmenite and minor biotite (Fig. 5.4.A), the quartzite shows an alignment of larger poikiloblastic quartz grains (1 mm) (Fig. 5.3.A). Quartz and plagioclase contain rounded inclusions of smaller quartz, plagioclase and ilmenite, although sometimes ilmenite surrounds quartz and plagioclase grains (Fig. 5.4.A). Faint banding is present in thin section with alternating layers of quartz-rich, quartz- and plagioclase-rich layers. Ilmenite (100 – 300 μm) shows a blebby texture and is faintly aligned.

In contrast, the sillimanite-quartz-biotite schists show a more complex texture and are mineralogically more heterogenous. These consist of fibrous sillimanite, biotite and quartz with minor ilmenite and feldspars (Fig. 5.4. B). Grain size is variable; with composite biotite-sillimanite knots up to 5 mm in length with elongate quartz and ilmenite commonly between 1 and 2 mm in size. Elongate quartz grains are parallel to the sillimanite-biotite foliation (Fig. 5.3.C). The biotite forms the major part of the foliation while sillimanite replacing biotite forms a lineation (Fig. 5.4.D and E). The composite foliation anastomoses around the quartz grains (Fig. 5.4.C and D). Fibrous sillimanite also occurs within quartz grains, although the age relationships between these minerals are not equivocal. Poikiloblastic textures are present, with quartz and ilmenite enclosing and semi-enclosing biotite, quartz and ilmenite inclusions and smaller grains.

Micro-structures

The metasediments of the Etusis Formation preserve variable deformational features with the quartzite showing less evidence for deformation than the sillimanite-quartz-biotite schist. The former only displays compositional banding. While in contrast, the sillimanite-quartz-biotite schist contains a well-developed biotite foliation and a sillimanite lineation, which is developed as a S-C fabric (Fig. 5.4.F). This closely related composite foliation and lineation (Fig. 5.4.E and F) is a spaced foliation in thin section, with an anastomosing and discrete morphology that may represent a S-C fabric (Fig. 5.3.D and Fig. 5.4.C and D). In addition, the foliation is also defined by poikiloblastic quartz,- which is parallel to the well-developed biotite foliation.

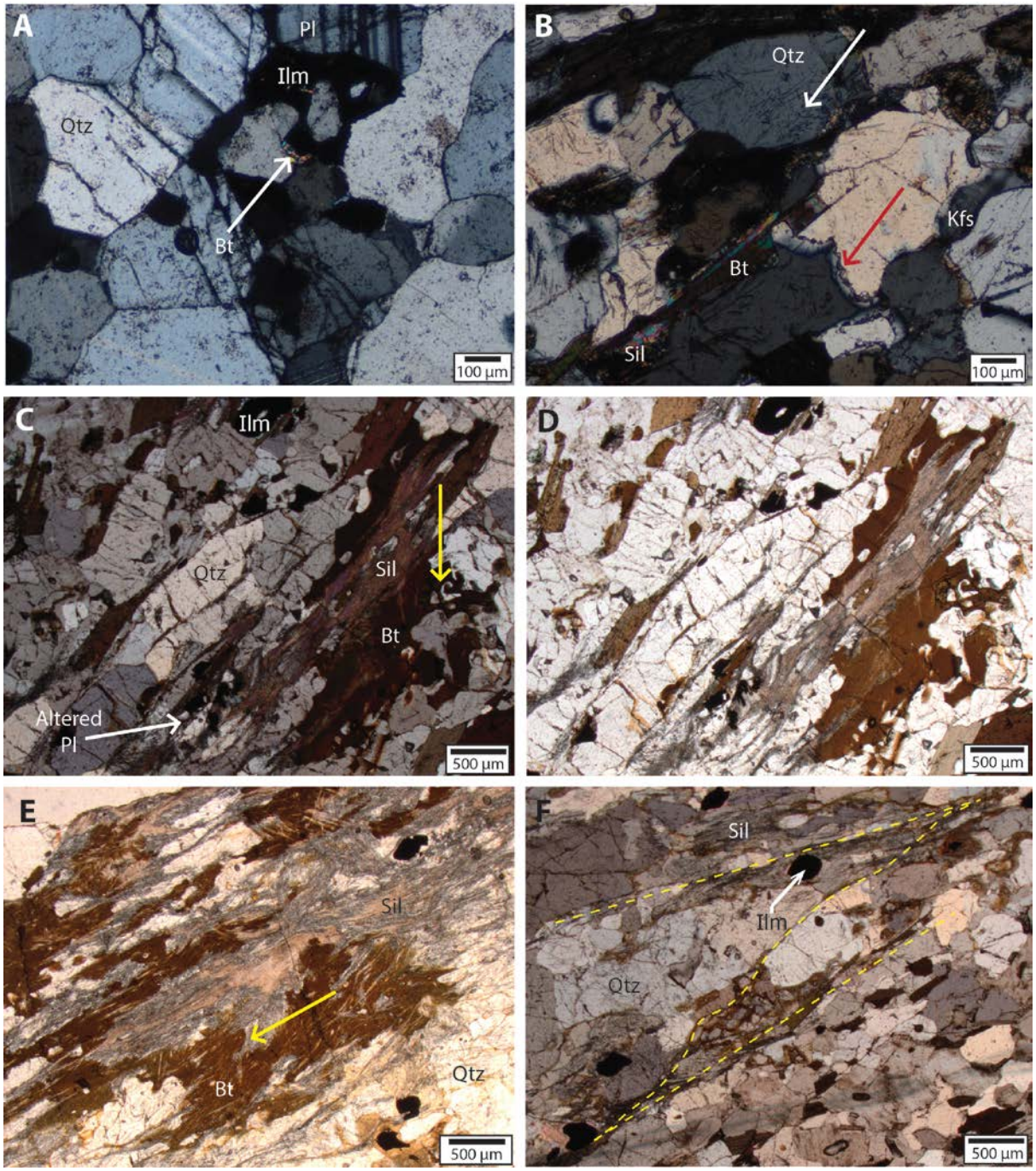


Figure 5.4: Photomicrographs of the Etusis Formation meta-siliciclastic rocks. (A) Granoblastic quartzite with quartz, plagioclase and ilmenite and minor biotite (XPL). (B) Sillimanite-quartz-biotite schist with quartz, microcline, sillimanite and biotite (XPL). Microcrystalline rims around quartzofeldspathic minerals (red arrow). (C) Sillimanite-quartz-biotite schist with elongate quartz laths, as well as biotite and sillimanite knots. Altered and replaced plagioclase (XPL). (D) Biotite-sillimanite porphyroblast as red-brown and pink-grey, respectively. The bright quartz shows the anastomosing nature of the sillimanite-biotite lineation (PPL). (E) Sillimanite-quartz-biotite schist showing the fibrous nature of the sillimanite and how it replaces the biotite. Intergrowth and alignment of quartz with the sillimanite and biotite (PPL). (F) Sillimanite-quartz-biotite schist with elongate poikiloblastic quartz and alignment of ilmenite with a S-C fabric (yellow dashed line). Mineral abbreviations are after Kretz (1983).

Khan Formation

The Khan Formation contains variable lithologies including schists, gneisses and calcsilicates (Fig. 5.5). All samples contain variable amounts of poikiloblastic diopside and the general texture of the

lithologies are typically granoblastic polygonal, although this texture it is not as well developed as in the rock types of the Abbabis Complex or the Etusis Formation.

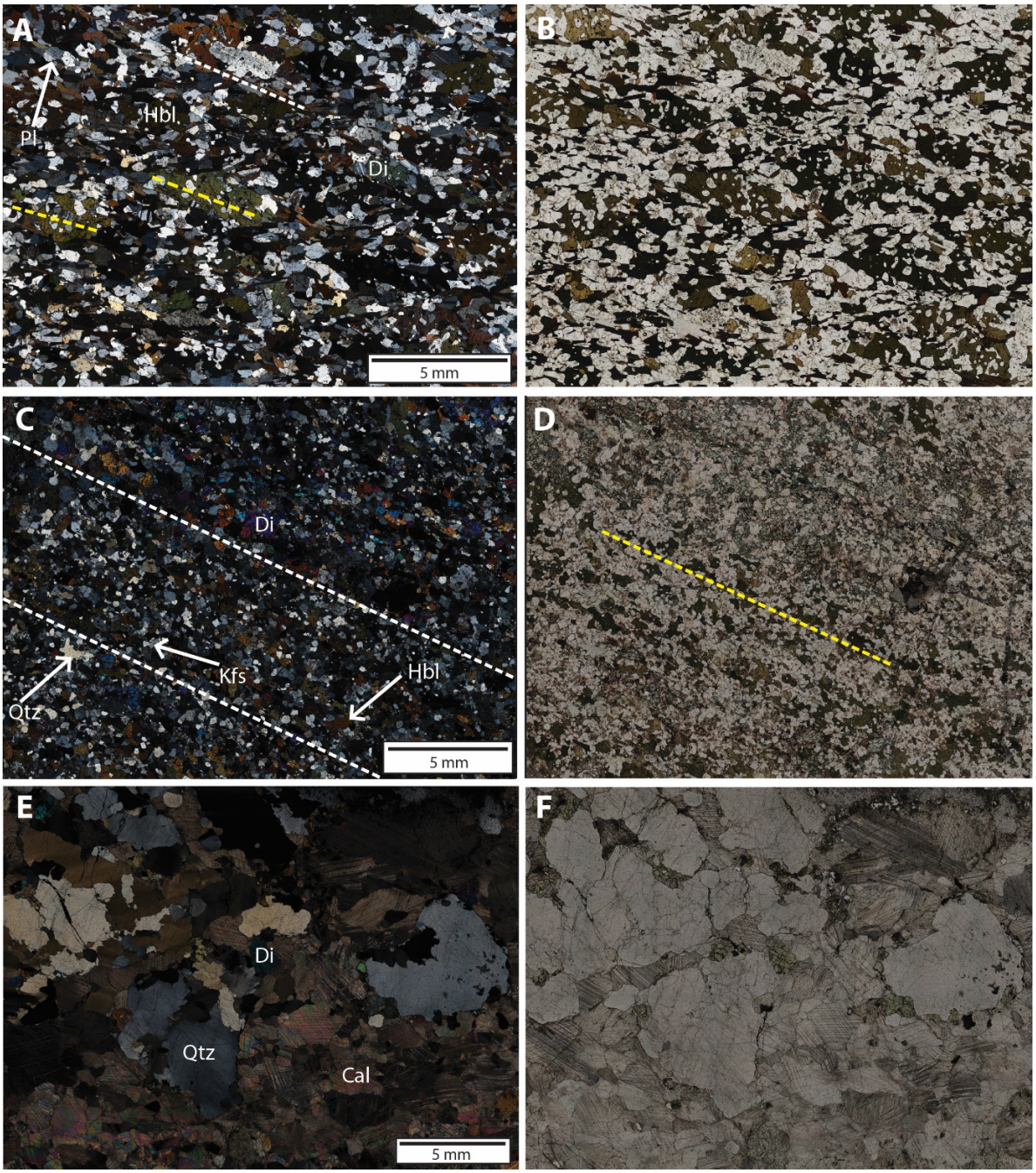


Figure 5.5: Overview photomicrographs of thin sections from the Khan Formation. (A) Hornblende-diopside-plagioclase-quartz-biotite schist showing an alignment of poikiloblastic hornblende and diopside (yellow dashed lines) and biotite laths (white dashed line). Quartz is also faintly aligned (XPL). (B) Poikiloblastic nature and distribution of hornblende (dark green) and diopside (tan) is best illustrated in PPL. (C) Banded diopside-hornblende-microcline-(quartz) gneiss. The gneiss shows compositional banding (white dashed line) with alternating banding of diopside + microcline + quartz-rich and hornblende + microcline + quartz + minor diopside banding. Alignment of diopside and hornblende is present (XPL). (D) Poikiloblastic and aligned (yellow dashed line) diopside and hornblende is best illustrated in PPL. (E) Calcsilicate unit comprising calcite, quartz and diopside. The quartz is polycrystalline with undulose extinction. The calcite and diopside are interstitial to the quartz (XPL). (F) PPL photomicrograph of the area in (E) The green diopside appears along quartz grain boundaries and as interstitial minerals to quartz. Calcite is grey and shows faint cross-hatching from calcite twinning (PPL). Mineral abbreviations are after Kretz (1983).

The hornblende-diopside-plagioclase-quartz-biotite schists comprise hornblende, diopside, biotite, plagioclase, quartz, minor microcline and magnetite (Fig. 5.5.A and Fig. 5.6.A). There is an alignment of poikiloblastic porphyroblasts of tan diopside and poikiloblastic green hornblende approximately 1 mm in length, that contain rounded inclusions of plagioclase, quartz and magnetite (Fig. 5.5.A and B; Fig. 5.6.B). The poikiloblastic porphyroblasts are generally the largest and are surrounded by smaller (100 - 500 µm), slightly aligned, subhedral to anhedral grains of predominantly plagioclase, quartz and biotite (Fig. 5.5.A). Grain boundaries are sharp, suggesting that the minerals are in equilibrium (Fig. 5.6.A). Alteration of plagioclase in the form of seritisation and / or pinnitisation is common. Plagioclase contains inclusions of biotite, diopside, magnetite and quartz, however, in some cases the plagioclase may in fact be cordierite indicated by the presence of the mineral inclusions and pinnitisation.

The banded gneisses comprise diopside, hornblende, microcline, quartz, cordierite and biotite. There is a defined compositional banding of diopside and hornblende-(diopside) assemblages with both of them including quartz, microcline, cordierite and biotite (Fig. 5.5.C and D). The granoblastic polygonal recrystallisation is more developed in the banded gneisses than in the schists. Diopside and hornblende show poikiloblastic textures in alternating layers. Both minerals are larger (500 – 700 µm) than the surrounding grains (100 µm) of anhedral quartz and microcline (Fig. 5.6.C and D). Seritised microcline (Fig. 5.6.D) is present with minor sillimanite replacement.

The calcsilicates consist of calcite, quartz, diopside and minor titanite. Mineral grains are larger in the calcsilicates than in the other Khan lithologies with quartz up to 5 mm in diameter (Fig. 5.5.E and F). Quartz is polycrystalline and shows undulose extinction (Fig. 5.5.E and Fig. 5.6.E). and show irregular grain contacts (Fig. 5.6.E). The other minerals range from 1 – 2 mm in size. Diopside and calcite commonly are interstitial to quartz (Fig. 5.6.F).

Micro-structures

A spaced foliation is defined by biotite and hornblende and is present in the schists and gneisses (Fig. 5.5.A, B, C and D), however, a foliation is not present within the coarse-grained calcsilicates (Fig. 5.5.E and F). Most minerals are aligned in the schists and gneisses, with the gneisses displaying compositional banding as a composite foliation. The pelitic schists have a well-developed foliation defined by laths of biotite, poikiloblastic biotite and hornblende. In addition, epidote is commonly associated with veins and may represent late stage hydrothermal processes. The banded gneiss displays a spaced and parallel foliation defined by compositional banding as well as aligned platy

and poikiloblastic minerals, namely biotite, hornblende and diopside. The compositional foliation has alternating diopside- and hornblende-rich zones.

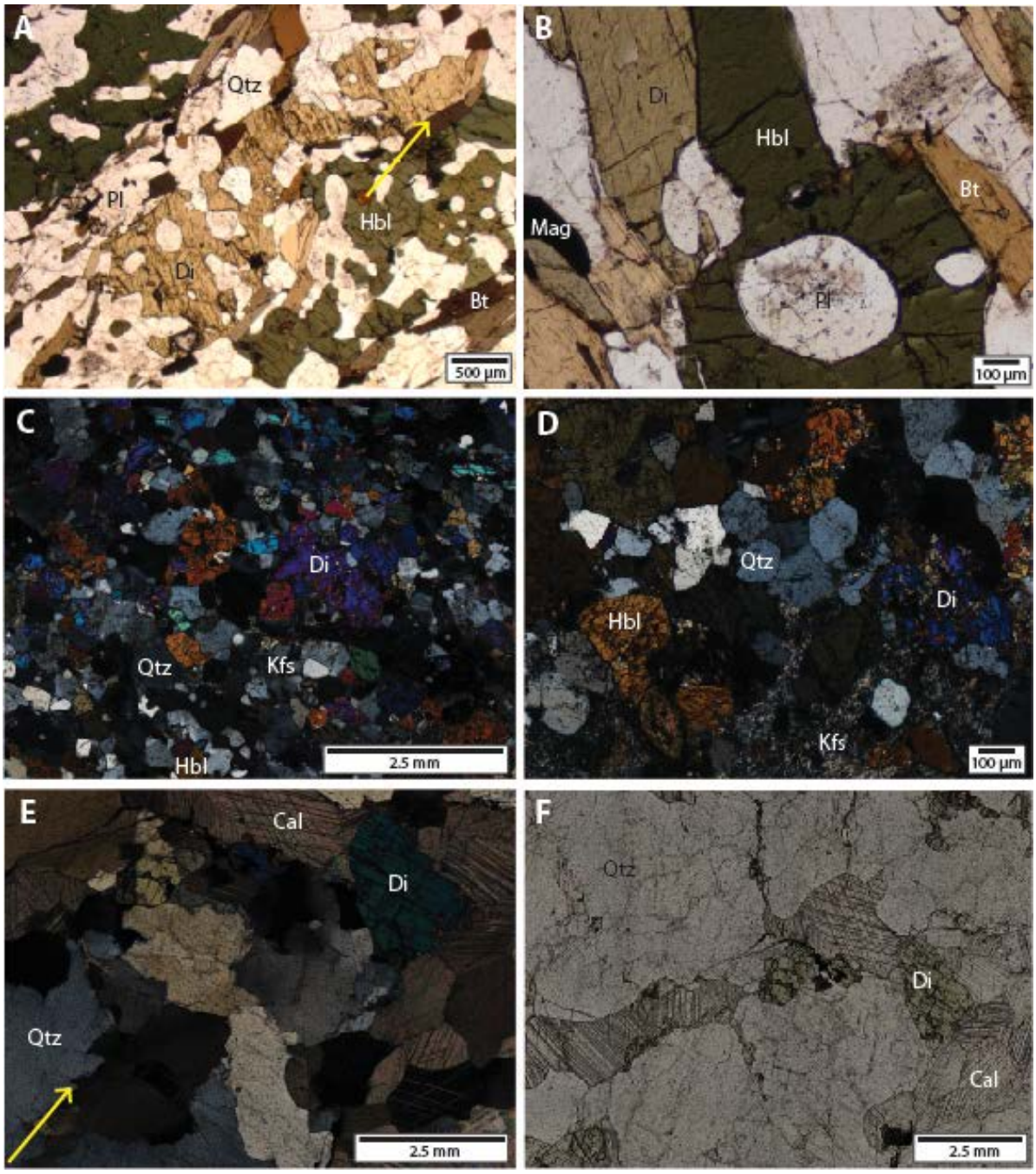


Figure 5.6: Photomicrographs of the Khan Formation lithologies. (A) The pelitic schist comprising diopside, hornblende, biotite, plagioclase and quartz. Poikiloblastic diopside and hornblende are aligned with rounded inclusions of quartz and plagioclase. Biotite cross-cuts the diopside and hornblende (yellow arrow) (PPL). (B) The pelitic schist with inclusions of plagioclase within hornblende and diopside. Aligned biotite truncates hornblende and diopside. Magnetite is present in minor amounts (PPL). (C) The banded gneiss showing diopside + microcline + quartz-rich bands in the top right corner, and a small portion of the hornblende + quartz + microcline band in the bottom left corner. Amalgamated diopside encloses microcline and quartz (XPL). (D) Granoblastic polygonal quartz with hornblende and diopside in a banded gneiss. Altered microcline is present (XPL). (E) Polycrystalline quartz (yellow arrow) with undulose extinction. Calcite and diopside are interstitial to quartz (XPL). (F) Quartz, diopside, and calcite in a calcsilicate. Quartz grains are largest with interstitial calcite and diopside (PPL). Mineral abbreviations are after Kretz (1983).

Rössing Formation

One garnet-cordierite-sillimanite-biotite-pyrite schist of the Rössing Formation was examined petrographically (Fig. 5.7). This lithology grades from a quartz-rich granoblastic polygonal-textured rock to a schistose rock containing pyrite (Fig. 5.7.A and B), sillimanite (Fig. 5.7.C), porphyroblastic garnet (Fig. 5.7.D), cordierite (Fig. 5.7.A and B) and biotite (Fig. 5.7). These minerals are all aligned except for garnet and cordierite. Quartz is elongate and poikiloblastic containing biotite inclusions close to the grain boundaries between garnet and quartz (Fig. 5.7.D). Pyrite is associated with biotite (Fig. 5.7.A and B) and fibrous sillimanite. It overgrows cordierite, which has rounded inclusions of biotite (Fig. 5.7.A and B). Quartz and biotite are replaced by fibrous sillimanite (Fig. 5.7.C). Garnet porphyroblasts (Fig. 5.7.D) contain inclusions of rounded biotite and close to the grain boundaries garnet encloses subhedral biotite laths.

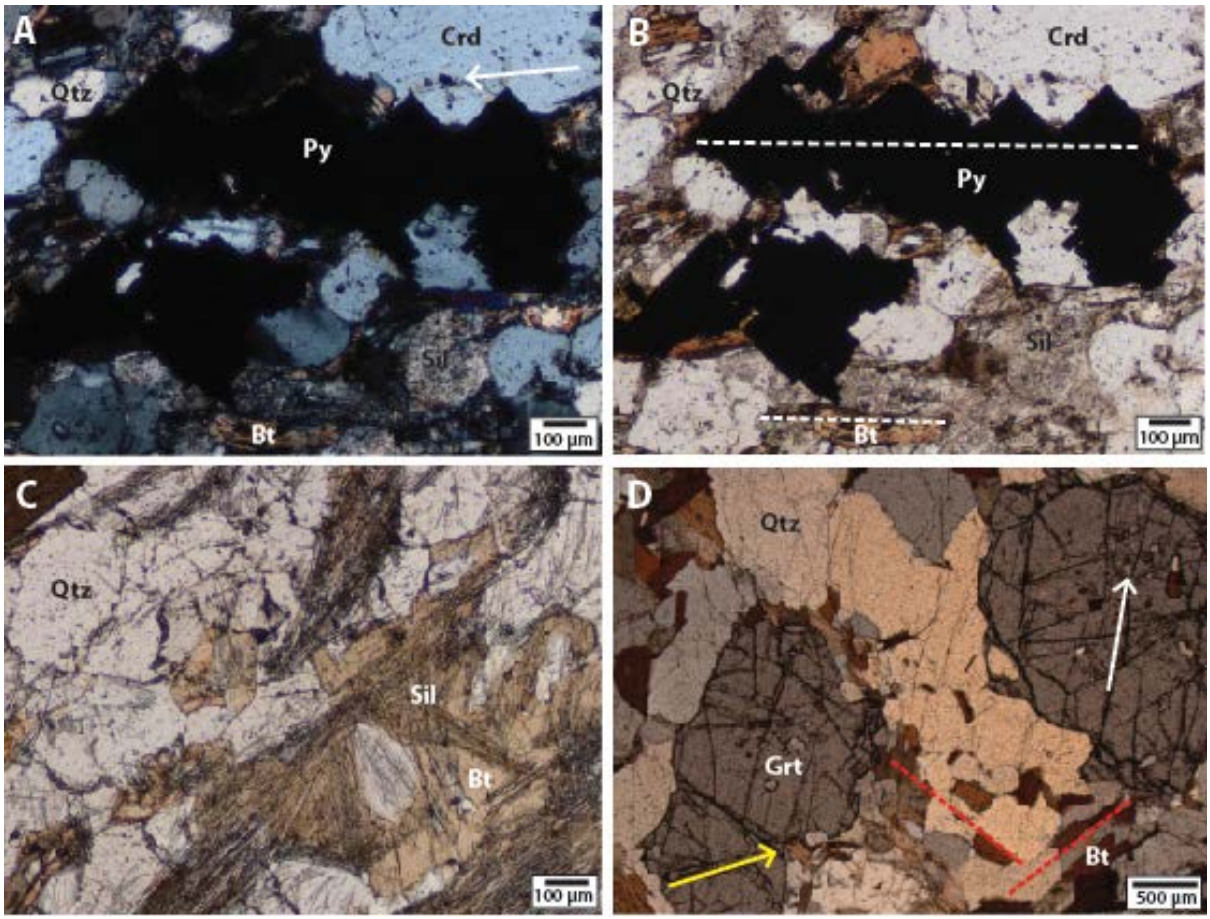


Figure 5.7: Photomicrographs of the Rössing Formation. (A) Garnet-cordierite-sillimanite-pyrite-biotite schist with aligned cubic pyrite and biotite with cordierite, quartz and fibrous sillimanite (XPL). (B) Aligned pyrite and biotite is highlighted (dashed white lines) (PPL). (C) Garnet-cordierite-sillimanite-pyrite-biotite schist with acicular sillimanite replacing biotite. Quartz matrix is present (PPL). (D) Garnet-cordierite-sillimanite-pyrite-biotite schist showing porphyroblastic garnet enclosing biotite laths (yellow arrow) and rounded biotite inclusions (white arrow). Quartz is poikiloblastic and elongate with biotite inclusions. Biotite is concentrated along grain boundaries of quartz and garnet with two foliations (red dashed line) directions (PPL). Mineral abbreviations are after Kretz (1983).

Micro-structures

A well-developed foliation is present in the schist with most of the minerals aligned. Platy biotite, poikiloblastic quartz, elongate pyrite and fibrous sillimanite are all aligned parallel to one another in a spaced and parallel foliation. Inclusions in the garnet porphyroblasts are rounded and not aligned with the foliation. An older foliation is present that is approximately orthogonal to the main foliation, although this foliation is not well developed and largely overprinted. Small acicular biotite is aligned in two directions (Fig. 5.7.D).

Chuos Formation

Both the Chuos Formation units described; diamictites and pelites, contain abundant garnet, cordierite, quartz and biotite. They are fine- to medium-grained with a distinct granoblastic polygonal texture.

The diamictites contain distinct quartz clasts within a pelitic matrix. The flattened clasts comprise coarse-grained (2 – 5 mm) polycrystalline quartz (Fig. 5.8.A and B) embedded within finer rounded grains of quartz and cordierite (~100 μm) concentrated around the clast boundaries (Fig. 5.9.A). The polycrystalline quartz in the clasts shows seriate textures along grain boundaries, while the quartz grains at the clast boundaries contain rounded inclusions of biotite and quartz (Fig. 5.9.B). The clast's shape is asymmetrical with one end that is rounded while the other end shows an elongate trail of finer-grained quartz (Fig. 5.8.A and B). Biotite is also concentrated along the boundary of the clast and is typically aligned in the same direction as the clast (Fig. 5.9.A). Some biotite wraps around the rounded end. The matrix is a biotite-hornblende-quartz-(microcline) schist and the distinction between matrix and clast is very distinct due to the drastic change in grain size (grains up to 5 mm in the clast and grains typically 100 μm in the matrix). Within the matrix poikiloblastic hornblende encloses quartz and microcline with the poikiloblasts stretching up to 5 mm in diameter (Fig 5.8.B and Fig. 5.9.C). Minor ilmenite is present as inclusions along the clast-matrix boundary. Subrounded garnet is present within the matrix (Fig. 5.9.D) that are fractured and vary greatly in size. The garnet porphyroblasts are commonly associated with biotite.

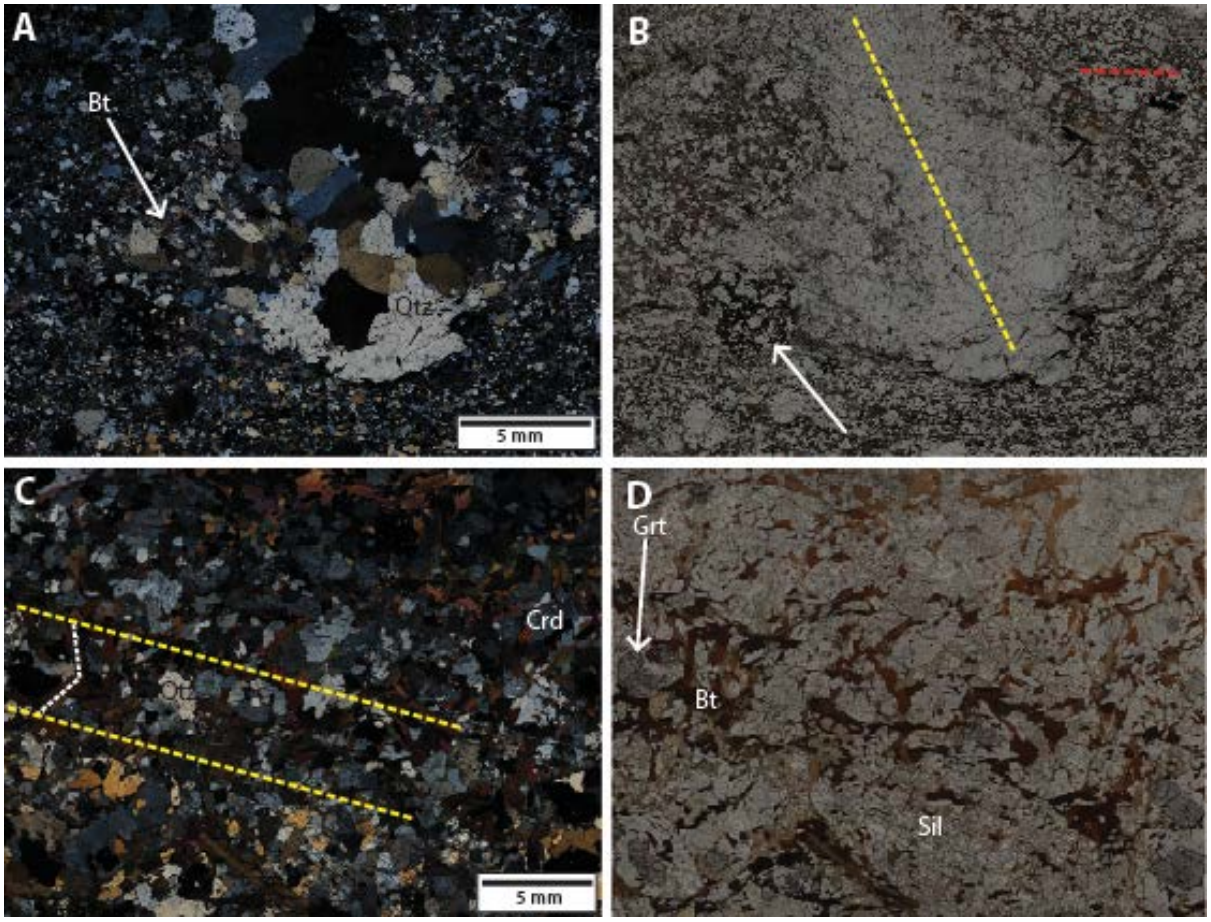


Figure 5.8: Overview photomicrographs of thin sections from the Chuos Formation. (A) Diamictite clasts showing the asymmetrical morphology of the quartz clast. Biotite and quartz make up most the matrix (XPL). (B) PPL image of the same area shown in (A) highlighting the clast elongation direction (younger foliation; yellow dashed line) and the biotite foliation (red dashed line) at an angle to the older foliation direction (PPL). (C) Biotite-garnet-hornblende-quartz-sillimanite-(cordierite) schist. A younger biotite foliation (dashed yellow line) and an older crenulation cleavage (white dashed line), which is kinked, is present (XPL). (D) PPL image of the same area in image (C). Mineral abbreviations are after Kretz (1983).

The biotite-garnet-hornblende-quartz-sillimanite-(cordierite) schist has a foliation defined by brown-red biotite and tan hornblende (Fig. 5.8.C and D). There are two different generations of biotite distinguished by varying shades of brown. The lighter brown biotite shows alteration to sillimanite. Biotite is commonly associated with and surrounds garnet porphyroblasts. Garnet is porphyroblastic (~1 mm in size), rounded to subrounded and contains rounded inclusions of quartz and biotite and replaces both generations of biotite. Grain boundaries of the porphyroblast are sharp and suggest that the minerals are in equilibrium. Minor microcline is present with quartz and cuspate-lobate grain boundaries. Microcline is also replaced by fibrolitic sillimanite. Cordierite contains inclusions of ilmenite and is up to 1 mm in length.

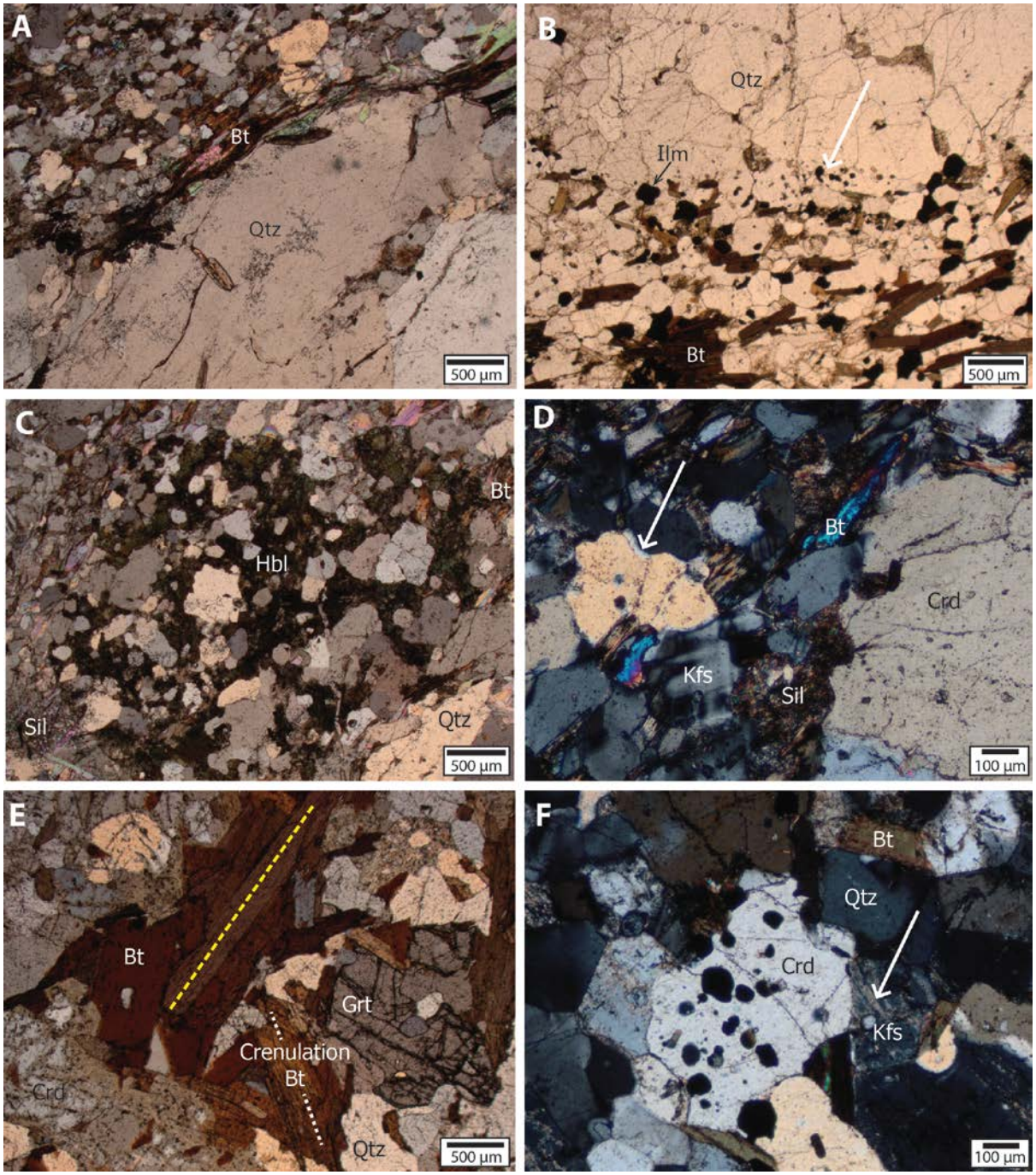


Figure 5.9: Photomicrographs of the Chuos Formation. (A) A diamictite showing the edge of the quartz clasts and biotite accumulations along the clast boundary. Biotite defines the main foliation. Rounded quartz grains (100 µm in diameter) are concentrated adjacent to the the larger grains of the clast (XPL). (B) Diamictite showing a quartz clast with inclusions of biotite and ilmenite along the clast boundary (white arrow) (XPL). (C) Poikiloblastic hornblende in a diamictite. The poikiloblasts have inclusions of quartz, biotite and occasionally sillimanite (XPL). (D) Biotite-garnet-hornblende-quartz-sillimanite-(cordierite) schist. Cordierite, aligned biotite, microcline and sillimanite are present. Microcline is replaced by sillimanite and the cordierite shows small inclusions within the grain. Cuspate-lobate grain boundaries are present (white arrow) (XPL). (E) Biotite-garnet-hornblende-quartz-sillimanite-(cordierite) schist highlighting the two biotite foliations: younger deep red-brown biotite (dashed yellow line) and younger tan-brown biotite (white dashed line). Garnet porphyroblasts contain rounded inclusions of quartz (XPL). (F) Ilmenite inclusions in cordierite. Other minerals include microcline altered to sillimanite (white arrow), quartz and biotite (XPL). Mineral abbreviations are after Kretz (1983).

Micro-structures

In thin section, the Chuos Formation shows two foliations that are spaced and anastomosing (Fig. 5.8.B and C). The foliations are largely defined by biotite, although aligned quartz also defines the most prominent and youngest foliation. In the diamictite the older foliation is defined by biotite, crenulated and truncated by the elongate clasts of the younger cross-cutting foliation. This kinked foliation is approximately orthogonal to the main spaced foliation (Fig. 5.8.B), more faintly aligned and anastomosing. The youngest and most pervasive foliation is defined by flattened asymmetrical clasts, platy biotite and poikiloblastic hornblende that are elongate parallel to one another in the diamictite. This foliation truncates the older foliation and crenulates the older biotite laths. The garnet-hornblende-quartz-sillimanite-(cordierite) schist also has two discordant foliations (Fig. 5.8.C and D). There appears to be two generations of biotite laths (1 – 2 mm in length), one which is predominantly brown and lighter in colour (PPL) and defines the older crenulation cleavage, which is kinked (Fig. 5.8.C and D) and a younger second foliation, which is more developed and defined by the deep red-brown (PPL) biotite and poikiloblastic hornblende (Fig. 5.8.C and D). These are not completely exclusive to either foliation however, the crenulation biotite is truncated by the deep red-brown parallel foliation.

5.3 Intrusions related to the Abbabis Complex and the Damara Belt

5.3.1 Basement granites

Petrographically, the basement granites have a fairly homogeneous, granoblastic polygonal texture of microcline and plagioclase with elongate quartz crystals (Fig. 5.10.A). Quartz (45%; 5 – 20 mm) usually appears as monocrystalline elongate grains (Fig. 5.10.A) with a preferred orientation. The quartz grain boundaries are irregular to the microcline (25%) and plagioclase (20%) (Fig. 5.10.B and C). The microcline and plagioclase are occasionally altered by seritisation (Fig. 5.10.D) with minor biotite (10%) laths also observed.

Micro-structures

The basement granites show aligned elongate quartz that is distinct from the granoblastic polygonal texture of the plagioclase and microcline. The most prominent deformational features are the parallel brittle fractures that commonly anastomose and bifurcate cross-cutting the quartz, microcline and plagioclase. Chlorite is commonly observed within these fractures, although biotite and fine-grained micas are also present (Fig. 5.10.D). Other than the aligned quartz there is a lack of the common biotite foliation that is seen in the other samples.

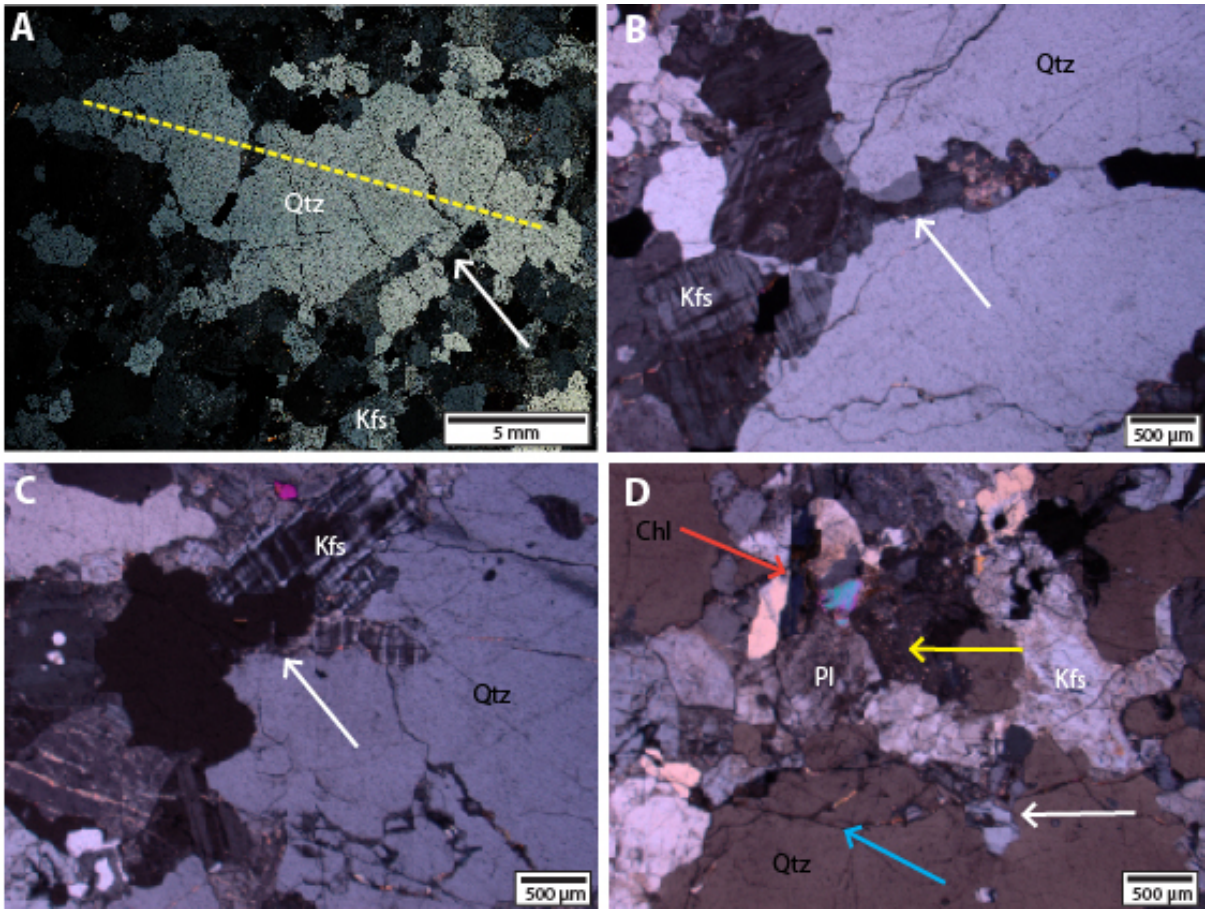


Figure 5.10: Photomicrographs of the basement granites. (A) XPL Alignment of quartz (dashed yellow line) and surrounding finer-grained granoblastic polygonal microcline (XPL). (B) Irregular elongate quartz (Qtz) grain boundary with cuspate-lobate features (white arrow) between microcline. Thin rims of quartz are present (XPL). (C) Large quartz grain boundary with microcline that is cuspate-lobate (white arrow). Fractures with sericite are present (XPL). (D) Altered quartz, plagioclase and microcline. Granite is affected by sericitic alteration (yellow arrow). Chlorite (red arrow) is present within fractures (blue arrow). Quartz phenocrysts and microcline have cuspate-lobate boundaries (white arrow) (XPL). Mineral abbreviations are after Kretz (1983).

5.3.2 Amphibolites

The amphibolites comprise biotite (35%), hornblende (25%), plagioclase (20%) and quartz (20%) (Fig. 5.11.A and B). Accessory minerals are present, such as chlorite (Fig. 5.11.C), epidote (Fig. 5.11.D) and ilmenite (Fig. 5.11.B). Plagioclase, tan and deep brown biotite, green hornblende, quartz and blue chlorite are all aligned. Poikiloblastic hornblende encloses rounded inclusions of plagioclase and quartz (Fig. 5.11.A) and occurs occasionally as elongate interstitial minerals within plagioclase (Fig. 5.11.B). Biotite and chlorite appear as euhedral to subhedral tabular laths and are aligned parallel to hornblende. Biotite has inclusions of plagioclase and quartz. Hornblende and biotite truncate against one another with chlorite enveloped within biotite (Fig. 5.11.C). Epidote is present and is partially enclosed in biotite. Both chlorite and epidote share sharp contacts with biotite suggesting textural equilibrium. Sericitised plagioclase is aligned with biotite.

Micro-structures

The well-developed foliation is spaced to continuous and defined by aligned plagioclase, elongate quartz, biotite laths and poikiloblastic hornblende with minor chlorite. Biotite and hornblende are the most continuous and prominent with individual laths continuously touching. As a result, quartz and plagioclase occur in between these poikiloblasts and laths as faintly developed compositional banding.

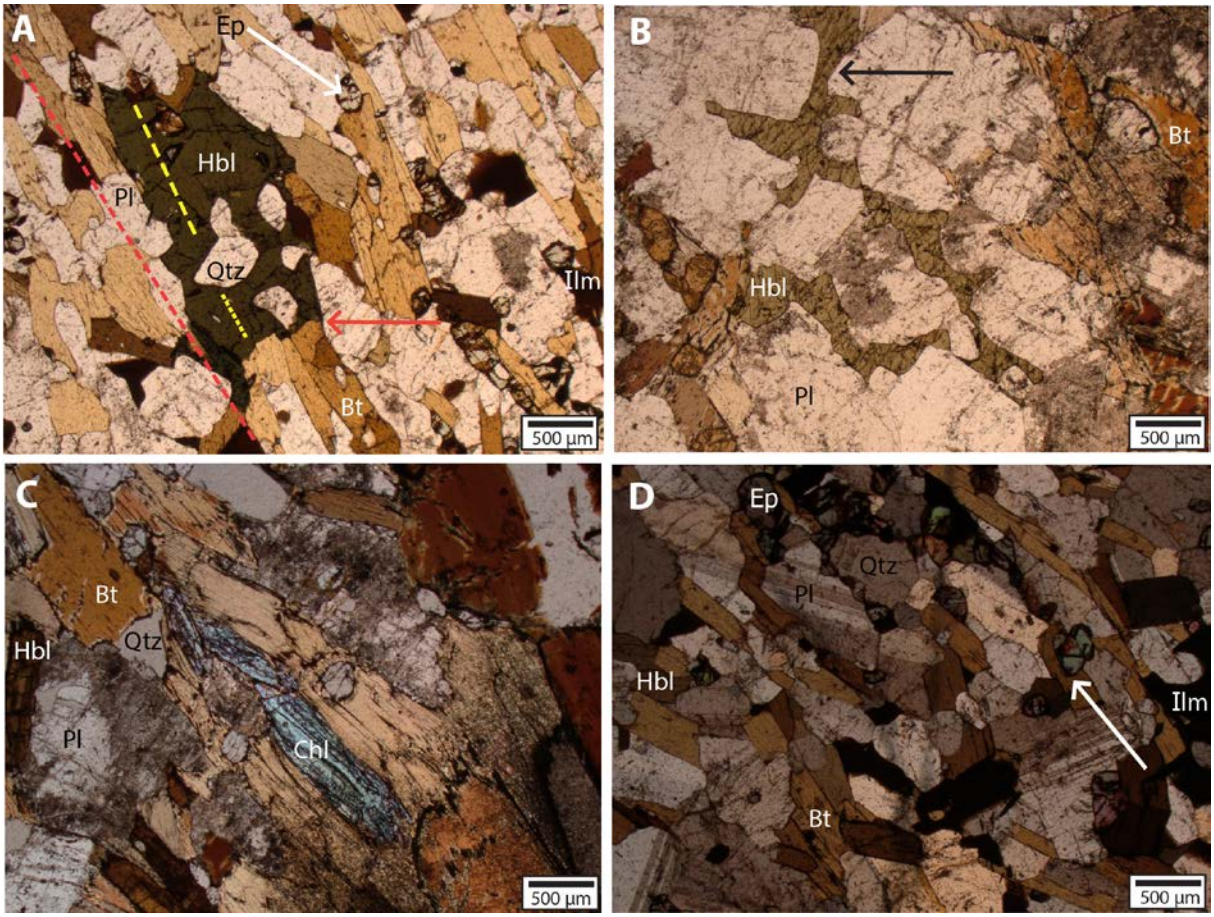


Figure 5.11: Photomicrograph of the amphibolite dykes. (A) Overall rock texture and aligned poikiloblastic hornblende (yellow dashed line), biotite (red dashed line), plagioclase and quartz. Accessory ilmenite and epidote are present (PPL). (B) Interstitial hornblende to plagioclase (black arrow). Biotite is present, along with altered plagioclase (PPL). (C) Aligned chlorite, biotite and hornblende with altered plagioclase. Inclusions of rounded quartz in biotite. Chlorite enclosed in biotite (PPL). (D) Overall rock texture comprising plagioclase, quartz, biotite and hornblende. Alignment of main rock forming minerals. Accessory epidote and ilmenite Epidote is enclosed in biotite (white arrow) (XPL). Mineral abbreviations are after Kretz (1983).

5.3.3 Red granites

In thin section, the red granites are distinctly granoblastic polygonal comprising mainly microcline (52%), quartz (36%), plagioclase (6%) and minor accessory minerals (6%), including cordierite, sillimanite, magnetite, biotite and chlorite (Fig. 5.12). Quartz is monocrystalline and larger (1 mm in diameter) than most of the grains (± 500 µm). Green chlorite is aligned in accumulations of euhedral

to subhedral tabular laths (Fig. 5.12.C). Highly altered microcline and plagioclase is observed along with possible cordierite altering from plagioclase (Fig. 5.12.B). Sillimanite overgrows quartz or plagioclase with fibrous sillimanite extending into the overgrown mineral (Fig. 5.12.D).

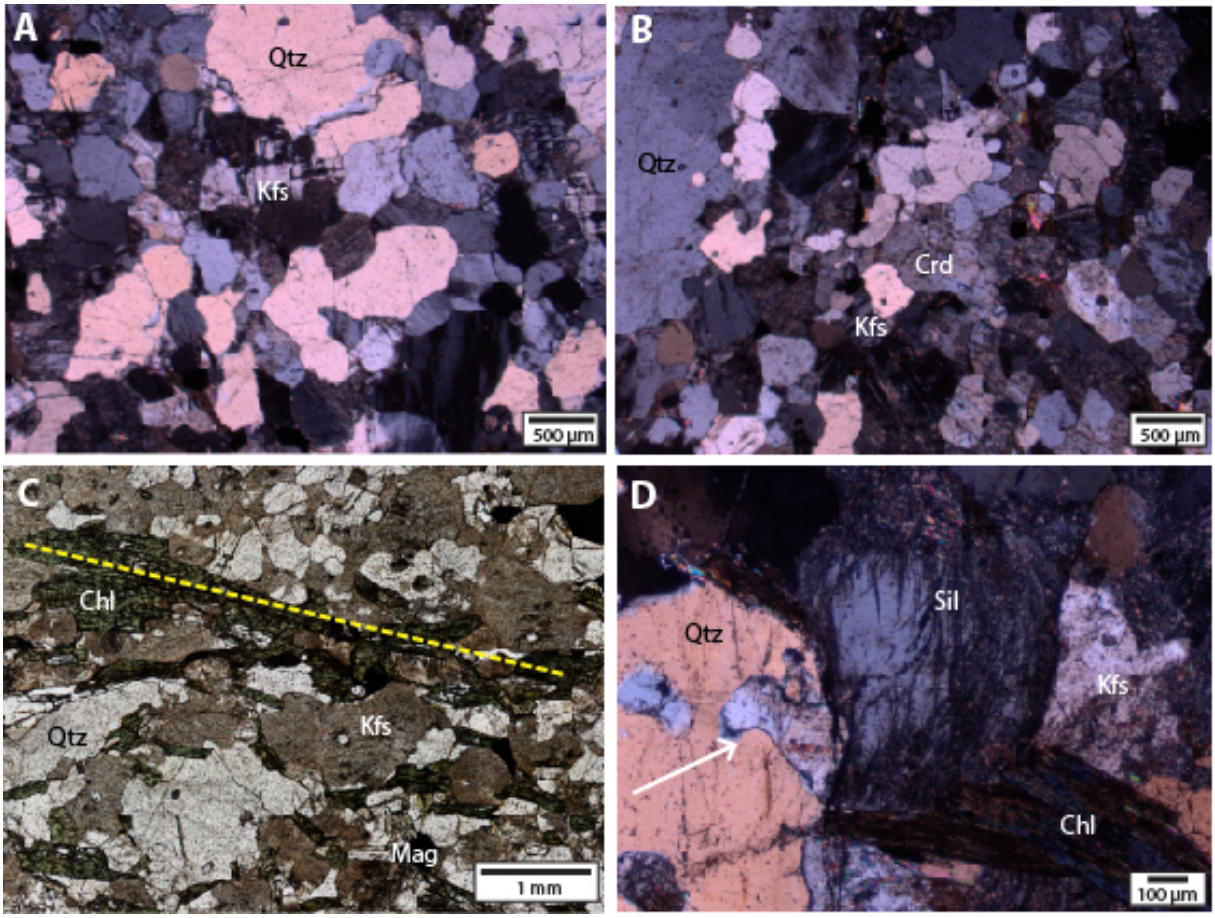


Figure 5.12: Photomicrographs of the red granites. (A) Larger quartz with anhedral microcline. Cuspate-lobate grain boundaries are prevalent in quartz (XPL). (B) Monocrystalline quartz overgrowing rounded quartz. Microcline and cordierite surround the quartz grains. Minor altered biotite is present. (C) Aligned chlorite as tabular laths of amorphous accumulations. Altered microcline, large anhedral quartz and accessory magnetite is present. (D) Quartz displays cuspate-lobate grain boundaries. Overgrown quartz or plagioclase by sillimanite, with tabular subhedral chlorite and altered microcline. Mineral abbreviations are after Kretz (1983).

Micro-structures

The red granites contain two spaced and faint foliations defined by chlorite laths as well as fibrous sillimanite. The fibrous sillimanite is not aligned with the foliation developed by chlorite (Fig. 5.12.D) and is less defining than the chlorite. Chlorite occurs in accumulations that are typically elongate and parallel to one another. Additionally, individual tabular chlorite shows an alignment in the accumulations (Fig. 5.12.C). In the field, the red granites show an occasional alignment of quartz or plagioclase and a gneissosity, however this is not apparent in thin section.

5.3.4 Grey granites

Petrographically, the grey granites comprise plagioclase (45%), quartz (27%), biotite, hornblende, minor cordierite and magnetite (Fig. 5.13.A and B). Biotite and hornblende constitute approximately 28% of the minerals. The grey granites display a granoblastic polygonal texture, which is best displayed by the quartz crystals. Microcline is also present although it is commonly associated with granophyric intergrowths with quartz (Fig. 5.13.C and D). Biotite appears as subhedral laths, while anhedral hornblende is developed as elongate crystals that surround plagioclase and quartz, but do not generally enclose these as inclusions. Plagioclase crystals are elongate and anhedral (Fig. 5.13.A and B), possibly altered to cordierite as remnant plagioclase twinning and mineral inclusions are present within cordierite (Fig. 5.13.A). Cordierite grains contain distinctive, rounded and anhedral grains of biotite and magnetite (Fig. 5.13.A), respectively. Plagioclase and microcline are commonly seritised.

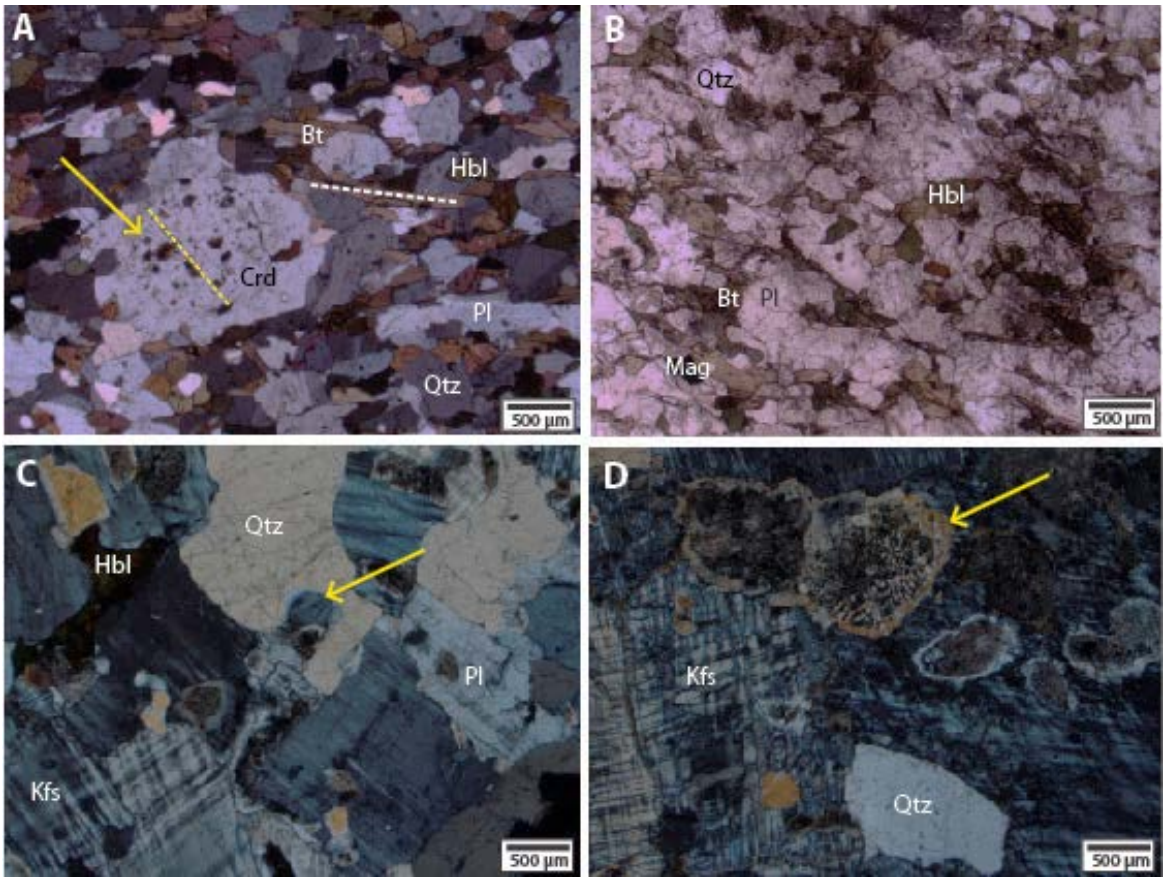


Figure 5.13: Photomicrographs of the grey granites. (A) XPL image of biotite, hornblende, plagioclase, quartz and cordierite. Biotite and hornblende are aligned and form a foliation (white dashed line). A second foliation is present, indicated by the yellow dashed line, within the cordierite and is defined by the biotite inclusions. Rounded magnetite inclusions (yellow arrow) are also present within the cordierite porphyroblast. (B) PPL image of quartz, plagioclase, biotite, hornblende and magnetite. The PPL image shows the biotite, hornblende and plagioclase foliation best. Plagioclase shows seritisation in PPL. (C) Cuspate-lobate textures between quartz and microcline in a XPL image. Hornblende and plagioclase also show minor anatexis. (D) XPL image of poikiloblastic microcline with granophyric intergrowths between microcline and quartz (Qtz; yellow arrow). Microcrystalline rims, around granophyric textures, occur within the microcline grain. Mineral abbreviations are after Kretz (1983).

Micro-structures

The grey granites have a well-developed, spaced foliation defined by biotite laths, elongate hornblende and elongate plagioclase crystals (Fig. 5.13.A and B). However, the biotite inclusions within the cordierite porphyroblasts appear as laths that are aligned at an angle to the biotite-hornblende foliation (Fig. 5.13.A) and may preserve an older foliation.

5.3.5 Sheeted Leucogranites

Type C': K-feldspar-quartz-(magnetite and biotite)

The type C' SLG comprise medium- to coarse-grained microcline (43%) and quartz (22%), both ranging from 0.5 mm to 15 mm, with minor biotite and magnetite (Fig 5.14.A). In addition, plagioclase (34%) (Fig. 5.14.B) is also present in samples that are lighter pink in hand sample. The quartz and microcline form large anhedral crystals that are commonly cracked and altered. Plagioclase (up to 500 µm) shows little to no fractures and alteration (Fig. 5.14.B). Magnetite and biotite are interstitial and appear as chadacrysts in the oikocrysts of quartz and microcline. Biotite is occasionally aligned or forms as accumulations. When the contact between the SLG and the host rock is seen in thin section it is sharp and truncates the minerals of the host lithology (Fig. 5.14.B). This is illustrated particularly well when the SLG cross-cuts and truncates the biotite laths or feldspar twinning.

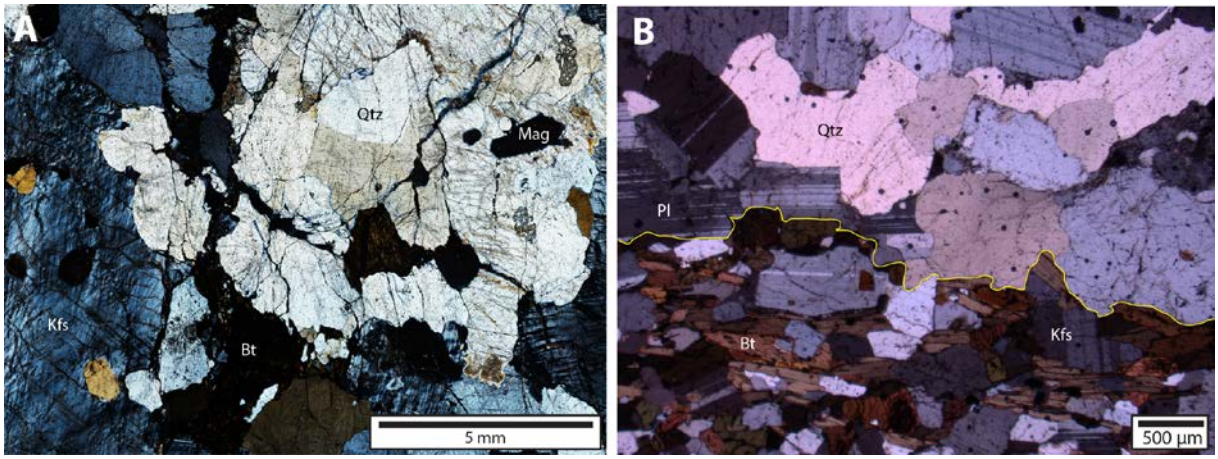


Figure 5.14: Photomicrographs of the type C' SLGs. (A) Large monocrystalline quartz and microcline with interstitial biotite and magnetite. Fractures and joints cross-cut the quartz and microcline (XPL). (B) The sharp and intrusive contact between the basement orthogneisses (bottom) and the type C' SLG (top), which is indicated by the yellow line. Quartz and plagioclase truncate the biotite foliation and microcline, quartz and plagioclase of the orthogneiss (XPL). Mineral abbreviations are after Kretz (1983).

Micro-structures

These SLGs only show a faintly defined biotite foliation. Due to the coarse-grained nature and minimal amount of biotite within the type C' SLG, the foliation is not as recognisable. Brittle fractures cross-cut the quartz and microcline in conjugate sets (Fig. 5.14.A).

Type A: Feldspar-quartz-biotite

In thin section, the type A SLG comprise microcline (45%), quartz (20%) and plagioclase (5%), with a developed biotite (30%) foliation (Fig. 5.15.A). Biotite is anhedral to euhedral with brown to tan laths truncating against quartz. The anhedral feldspars are the most abundant minerals with microcline most abundant in light pink SLGs, and plagioclase in the white SLGs. Microcline contains inclusions of biotite. Sericite alteration of the feldspars is common. Elongate quartz is often aligned with the biotite foliation. A sharp and intrusive jagged contact is present between host lithologies and SLGs.

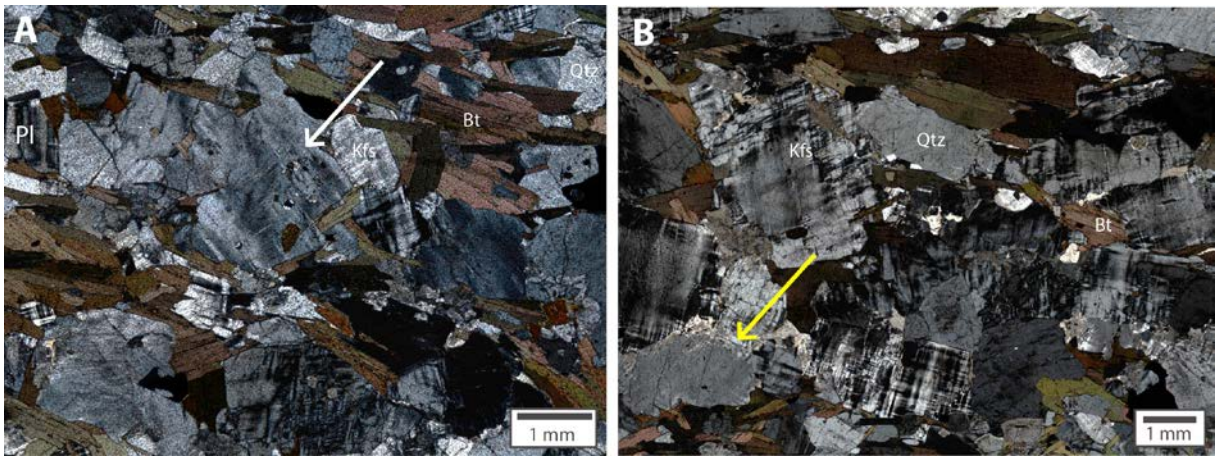


Figure 5.15: Photomicrographs of the type A SLGs. (A) Quartz, microcline and plagioclase, all of which are compartmentalised by the spaced biotite foliation (XPL). (B) Microcline, quartz and biotite. Sericite alteration microcline along grain boundaries (yellow arrow) (XPL). Mineral abbreviations are after Kretz (1983).

Micro-structures

The type A SLGs contains a well-developed biotite foliation, which is typically parallel to the host rock foliation. The foliation occasionally compartmentalises microcline, quartz and plagioclase between the spaced foliation (Fig. 5.1.A). Elongate quartz is parallel to the biotite foliation.

Type B: Plagioclase-quartz-(biotite-garnet)

Petrographically, the type B SLG are medium-grained and comprise predominantly of plagioclase (40%), microcline (30%) quartz (28%) and biotite (<5%) with a preferred orientation (Fig. 5.16). Biotite laths are subhedral to euhedral, with quartz generally enveloping the ends of the laths (Fig. 5.16.A). In addition, the biotite also occurs as interstitial anhedral grains to quartz and plagioclase

(Fig. 5.16.B). Quartz, microcline and plagioclase are generally anhedral. Microcline is overgrown by rims of plagioclase and quartz (Fig. 5.16.B).

Micro-structures

These SLGs show a spaced biotite foliation that is not as pervasive as the previous SLGs. The quartz and feldspars are randomly oriented.

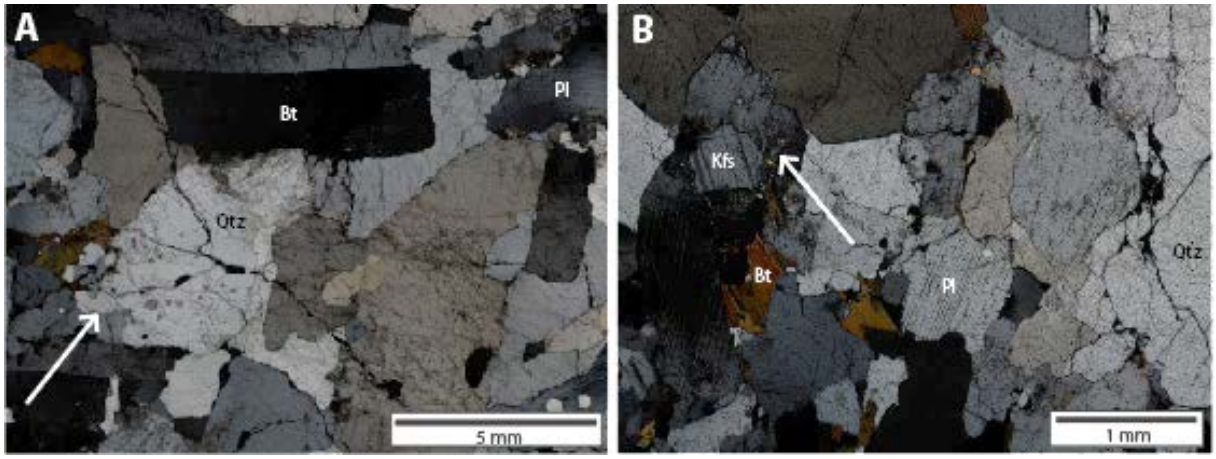


Figure 5.16: Photomicrographs of the type B SLGs. (A) Quartz and plagioclase sheeted granite, with associated aligned biotite (XPL). Cuspate-lobate grain boundaries are sometimes present (white arrow). (B) Quartz and plagioclase with minor microcline. Interstitial biotite to plagioclase and quartz. Plagioclase and quartz surround microcline (white arrow) (XPL). Mineral abbreviations are after Kretz (1983).

5.4 Possible indicators for the presence of remnant partial melt

Due to the well-established high temperature metamorphism of amphibolite to granulite grade in the sCZ (Hoffmann, 1976; Blaine, 1977; Sawyer, 1981; Bühn *et al.*, 1995; Masberg, 2000; Goscombe *et al.,* 2005; Goscombe *et al.,* 2017a; Longridge *et al.,* 2017) remnant partial melt textures should be well-preserved in the lithologies found within the Damara Belt. Possible crystallised partial melt textures are outlined in Table 5.1. Partial melt remnants are more likely when more than one feature is observed, however, when just cuspate-lobate boundaries, or a single other texture are present, then it is not used for evidence of anatexis.

Table 5.1: Summary of possible indicators for the presence of crystallised partial melt or intrusive features for each lithology examined under thin section. Textures indicating the presence of partial melt are adopted from Sawyer (2008). The table describes the oldest to youngest lithologies as outlined in previous sections (5.2 – 5.3).

		Features suggesting the presence of remnant partial melt
Abbabis Complex	Orthogneiss	Remnant partial melt pockets of accumulations of finer-grained crystals of quartz and plagioclase that are commonly rounded. Granophyric intergrowths of quartz and plagioclase or quartz and microcline. SLGs that are foliation parallel are present which display intrusive and sharp contacts.
	Granite gneiss	Cuspate-lobate grain boundaries associated with thin and extremely fine-grained rims along the boundaries of plagioclase and microcline (Fig. 5.2.C). Rounded inclusions (Fig. 5.2.C) of quartz grains and isolations of fine-grained crystals of quartz and plagioclase within larger grains.
	Grey orthogneiss	Cuspate-lobate grain boundaries associated with thin microcrystalline rims along the boundaries of plagioclase and microcline (Fig. 5.2.E and F). Cuspate triangular intergrowths and annealment textures with associated granophyric intergrowths of quartz and plagioclase along the boundaries between the gneisses and the sheeted leucogranite as well as within the gneisses (Fig. 5.2.F). Pockets of rounded circular quartz in the paragneiss are present.
Etusis Formation	Arkosic quartzite	Less developed remnant partial melt textures. Cuspate-lobate grain boundaries of quartz and feldspars associated with thin microcrystalline rims.
	Pelitic schist	None pervasive triangular annealing features, cuspate-lobate grain boundaries as well as microcrystalline rims around plagioclase, microcline and quartz (Fig. 5.4.D). Partial melt textures are more pervasive in the sillimanite schist than the quartzite, however, it is not as pervasive as partial melt textures in the Abbabis Complex.
Khan Formation	Semi-peltic schist; Banded gneiss	Cuspate-lobate grain boundaries and microcrystalline rims are abundant along plagioclase and quartz grain boundaries of the Khan Formation lithologies however, these textures are not pervasive.
Rössing Formation	Pyritic schist	Cuspate-lobate grain boundaries occur along quartz and garnet grain boundaries and the elimination of smaller grains indicate the presence of remnant partial melting but these textures are not pervasive.
Chuos Formation	Diamictite	Minor cuspate-lobate boundaries, annealing textures, small inclusions within poikioblastic quartz however, these textures are not pervasive in this unit.
	Pelitic schist	Pockets of small grains of quartz and plagioclase along with trails of blebby quartz and feldspars within larger quartz and feldspar grains. Cuspate-lobate grain boundaries are present along quartz and plagioclase boundaries.
Basement Granites		Grain boundaries are commonly jagged in this granite and show cuspate-lobate boundaries (Fig. 5.10.B, C and D) associated with fine-grained (less than 100 µm) quartz and microcline along these boundaries. Thin microcrystalline rims surround quartz along grain boundaries (Fig. 5.10.B).
Amphibolites		Cuspate-lobate grain boundaries are present particularly along biotite laths where quartz and plagioclase have extended and cross-cut into the lath (Fig. 5.11.A) but these textures are not pervasive.
Red Granites		Cuspate-lobate grain boundaries, inclusions of smaller circular quartz grains within large quartz grains, blebby trails of circular feldspar and thin microcrystalline rims surrounding quartz and feldspar grains (Fig. 5.12) are present.
Grey Granites		Plagioclase, quartz and microcline commonly preserve cuspate-lobate grain boundaries which display microcrystalline rims (Fig. 5.13.C). Microcline and quartz commonly show granophyric intergrowths that have additional microcline rims surrounding this texture (Fig. 5.13.D).
SLGs (Types A, B and C)		Cuspate-lobate textures observed but not in association with any other textures.

5.5 Discussion

Modal abundances of felsic rock forming minerals for various gneisses and granitoids (Abbabis Complex, Damara granites; this study and published studies) are summarised in a Streckeisen diagram (Fig. 5.17). The Abbabis Complex and the Etusis Formation are compared with one another, despite being gneissic and metasedimentary in nature, as a manner to distinguish between the two lithological groups. This could present a possible thin section technique to distinguish between these lithologies despite their similar quartzofeldspathic nature.

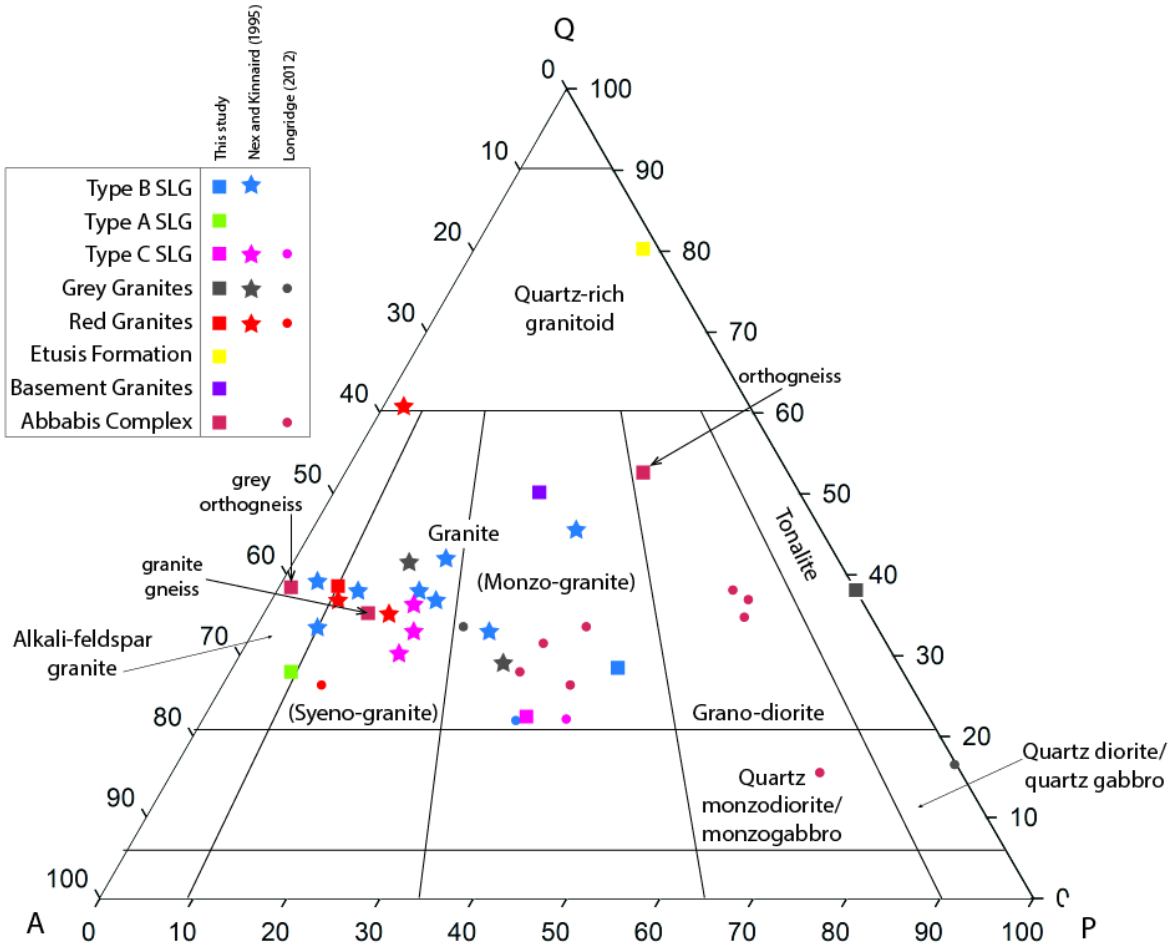


Figure 5.17: Streckeisen diagram showing modal mineral abundances for of the Abbabis Complex, red granites, grey granites and SLGs. The various gneisses of the Abbabis Complex and quartzofeldspathic Etusis Formation sample are compared to establish modal mineralogy differences. Intrusions reported by Nex and Kinnaird (1995) and Longridge (2012) from the Palmenhorst Dome are also shown.

5.5.1 The Abbabis Complex

The Abbabis Complex orthogneisses, grey orthogneisses and granite-gneisses all contain a gneissic fabric and show comparable modal abundances to other studies (Fig. 5.17). The orthogneisses and grey orthogneisses show similar compositions with varying plagioclase compositions. The grey (ortho?)gneisses, however, do show a textural variance (Fig. 5.17) and a considerable decrease in

grain-size in comparison to the other gneisses. The presence of increased biotite may suggest a sedimentary origin (Passchier *et al.,* 1990), although the modal abundances do not suggest elevated abundances that are anomalous for common igneous rocks (Passchier *et al.,* 1990) as well as the fact that the composition is similar to the composition of the orthogneiss. The higher strains in the grey orthogneiss (established in chapter 4: grain-size decrease and thinning of gneissic banding; Passchier *et al.,* 1990; Platt and Behr, 2011), and the similar compositions to the orthogneiss therefore indicates that gneisses may represent high strain equivalents of the orthogneisses rather than a type of paragneiss.

However, the orthogneisses show a compositional difference to the granite-gneisses (Fig. 5.17), suggesting that there are varying compositions for the basement lithologies. Varying modal abundances were observed by Longridge, (2012). However, the spatial distribution was not noted. However, the identification of various gneisses in the field is also based on textural distinction, with varying degrees in foliation intensity evident in thin section. This confirms a lithologically more diverse basement than previously established for the Abbabis Complex of the northern Palmenhorst Dome (Smith, 1965; Miller, 2008). Despite being lithologically diverse, the various gneisses most likely only represent the Narubis Granitoid equivalents of the Abbabis Complex (Smith, 1965), as their average compositions are similar to those of common igneous rocks and do not contain anomalous abundances of quartz or alumina-rich minerals (Passchier *et al.,* 1990).

Magmatism associated with the Abbabis Complex includes the basement granites and amphibolite dykes, both of which show granoblastic polygonal textures, are foliated and show possible partial melting features, possibly indicating their emplacement prior to Damaran deformation and peak metamorphism. The basement granites are less foliated than the basement gneisses but are comparable in composition and (*sensu stricto*) are meta-granites (Fig. 5.17). Therefore, adding considerable lithological variability to the previously mapped undifferentiated granite-gneisses of the Palmenhorst Dome (Smith, 1965; Miller, 2008), which represents the Abbabis Complex.

The amphibolite dykes of the Abbabis Complex have been described as ortho-amphibolites (Smith, 1965; Jacob, 1974; Barnes, 1981; Marlow, 1981), commonly contain hornblende and plagioclase with biotite (Longridge, 2012; Longridge *et al.*, 2014) and are foliated. Therefore, the amphibolite dykes from this study are correlated with the Palaeoproterozoic Abbabis Complex amphibolite dykes rather than the typically unfoliated Damaran amphibolites (Longridge *et al.,* 2014).

Due to the dark colour (mafic compositions) of the amphibolites these dykes may be confused with the semi-pelitic schists of the Khan Formation, especially when these dykes occur as rafts within extensive coalesced SLGs. However, a diagnostic mineral of the Khan Formation is diopside, which is distinctly lacking in the amphibolite dykes therefore are unlikely to represent infolded Damaran metasediments, more specifically the Khan Formation, in the basement rocks.

5.5.2 The Damaran metasediments

The Damaran metasediments display lithologies which show similarities with previously noted units within the sequence (Miller, 2008), and therefore the recognition of these metasediments within the synclines is possible.

The Etusis Formation quartzite differs from the Abbabis Complex gneisses and granites as it displays higher abundances of quartz and distinctly lacks microcline (Fig. 5.17), which may be a distinguishing feature. The modal abundances also eliminate the possibility of the paragneisses/grey orthogneisses being strained Etusis Formation as the compositions are not comparable. Additionally, the quartzite contains ilmenite which is a distinguishing accessory mineral for the Etusis Formation (Smith, 1965; Henry, 1992; Miller, 2008). Jacob (1974) describes various schists occurring in the Abbabis Complex, but specifically identified biotite-sillimanite schists in the Etusis Formation, similar to metapelitic schists recognised in this study. These medium- to coarse-grained rocks with a quartz-rich composition indicate a high energy depositional environment, such as a sand-dominated fan (de Kock and Botha, 1988) or a distal braided fluvial system (Henry, 1992). The Khan Formation is characterised by K-feldspar, clinopyroxene-, and amphibole-rich schists to gneisses (with variable amounts of biotite, carbonate and epidote) and calcsilicates (Smith, 1965; Henry, 1992; Miller, 2008; Longridge, 2012), which are similar to the lithologies identified in the Khan Formation in the study area. These semi-pelitic schists are fine-grained, which indicates deposition under lower energy conditions consistent with sediments that were originally feldspathic sands to muds in a distal fluvial or flood plain environment (Henry, 1992).

The Rössing Formation is compositionally and mineralogically variable, in particular along strike, and includes quartzites and pelitic schists (Smith, 1965; Nash, 1971; Jacob, 1974, Henry, 1992; Miller, 2008; Longridge, 2012). The Rössing Formation quartzites comprise garnet, sillimanite, biotite and pyrite, all of which are common minerals associated with the quarzitic schists of this unit (Nash, 1971; Jacob, 1974, Henry, 1992; Longridge, 2012). The diamictites of the Chuos Formation are ideal marker horizons and easy to identify. Based on the presence of clasts within a pelitic matrix the diamictite

is correlatable to the previously identified diamictites from other studies (Gevers, 1931; Henry, 1992; Hoffman *et al.,* 2004; Longridge, 2012).

5.5.3 Early Damaran Granites

The red and grey granites of this study show compositions and fabrics similar to those noted in previous work (Fig. 5.17; Smith, 1965; Jacob, 1974; Brandt, 1985; Nex and Kinnaird, 1995; Longridge, 2012). Red granites from this study show high abundances of K-feldspar and sillimanite, which has been used as a defining feature of these granites (Smith, 1965; Longridge, 2012). The modal abundances of the grey granites may differ from other studies (Fig. 5.17) but the mineralogy, foliation and field relationships are all comparable to other voluminous emplacement of grey granites in the Palmenhorst Dome (Nex, 1997; Longridge, 2012). This modal abundance differences may be due to the variations seen by the grey granites even at an outcrop scale.

From field relationships, the red and grey granites are proposed to have been emplaced before D2 metamorphism. The strongly developed granoblastic polygonal overprint of these granites and a clearly defined foliation suggest these granites were subject to deformation, which is not typically seen in the SLGs. However, detailed petrological work has not resolved the timing of the emplacement of the red granites. Previous workers (Smith, 1965; Jacob, 1974; Brandt, 1985; Nex and Kinnaird, 1995) have noted that these granites represent early Damaran granitoids and noted the defining fabric. However, other studies in the Palmenhorst Dome propose that the red granites in the Palmenhorst Dome may be a mid-crustal response during the first generation of metamorphism associated with D2, whereas the grey granites are emplaced later during D2 (Longridge, 2012; Longridge *et al.,* 2017). Thus, highlighting the different opinions regarding the relative timing of these granitoids.

5.5.4 Damaran sheeted leucogranites

The SLGs were named after their similarities to the nomenclature established by Nex and Kinnaird (1995), and therefore at an outcrop scale are similar in mineralogy and exhibit similar field relationships. Generally, the modal mineralogy of the SLGs agrees with classifications from previous studies (Fig. 5.17; Nex and Kinnaird, 1995; Nex, 1997; Longridge, 2012; Freemantle, 2017), and are possibly equivalent to the SLGs they are named after. The SLGs in this study typically lack a granoblastic polygonal overprint and are therefore possibly associated with, and are a result of, the high-temperature metamorphic event (Hoffmann, 1976; Blaine, 1977; Sawyer, 1981; Bühn *et al.*,

1995; Masberg, 2000; Jung and Mezger, 2003; Goscombe *et al.,* 2005; Goscombe *et al.,* 2017 a; Longridge *et al.,* 2017).

5.5.5 Structure and metamorphism

Deformation and metamorphism are closely linked in the Nose Structure as the metamorphic minerals largely define the foliations. From detailed petrological work, a dominant foliation (the younger and second foliation) is preserved in most the examined lithologies, with very little evidence for a Pre-Damaran or early Damaran metamorphic episode. The pervasive younger foliation and metamorphic porphyroblasts preserve D2 deformation and M2 metamorphism, where recent metamorphic studies propose that peak metamorphism was coeval with D2 for the sCZ (Goscombe *et al.,* 2017b; Longridge *et al.,* 2017). In the Abbabis Complex, some of the Damaran metasediments and limited granites contain an older foliation which is cross-cut by the dominant foliation and may represent a pre-Damaran event (in the case of the basement lithologies) or the well documented early Damaran D1 fabric. Longridge (2012) also noted a second foliation, but the main foliation was dominantly recognised as D2. The red granites contain chlorite and sillimanite foliations which are interpreted as possible hydrothermal minerals, such as sillimanite observed along shear surfaces in the Rössing dome (Kinnaird, pers. comms.) and chlorite observed along fractures of the D4 deformation of this study.

The identification of possible partial melt textures, the amphibole-diopside-biotite assemblages, granoblastic polygonal recrystallisation and obliteration of previous deformational features suggests a high temperature metamorphic event of amphibolite facies, with sillimanite growing after biotite indicating an increase in temperature (Winter, 2001). This metamorphic grade is well documented in the sCZ (Hoffmann, 1976; Blaine, 1977; Sawyer, 1981; Bühn *et al.*, 1995; Masberg, 2000; Goscombe *et al.,* 2005; Goscombe *et al.,* 2014; Goscombe *et al.,* 2017 a; Longridge *et al.,* 2017). The fact that most of the lithologies, except for the SLGs, exhibit granoblastic polygonal textures indicates that the metamorphic episode outlasted structural deformation of D2, however, given that the lack of granoblastic polygonal recrystallisation in the SLGs, these granites may have been emplaced as a partial melt phase of M2 during D2 deformation.

5.5.6 Evidence for partial melting

This study attempted to identify remnant partial melt textures in all the lithologies and not just the pelitic rocks, which generally constitute fertile rocks for partial melting (Sawyer, 2008; Pawley *et al.,* 2015). Possible indicators for the presence of partial melt were observed in most of the lithologies

except for the SLGs, but alone do not constitute signs of crystallised melt (Sawyer, 2008). A combination of these indicators are used to propose possible signs of anatexis in the Abbabis Complex and Damaran metasedimentary rocks. Most of the basement and supracrustal rocks are seen to exhibit varying signs of partial melt and high temperature metamorphism (Poli, 1997). To some extent it may indicate that the Abbabis Complex (granites to gneisses), Etusis Formation (quartzofeldspathic to pelitic compositions) and limited semi-pelitic to pelitic schists could represent a source for the Damaran Granitoids, which is consistent with studies that have proposed that the Abbabis Complex and the Etusis Formation may be sources for these granites (Miller, 2008; Jung *et al.,* 2003). Additionally, it has been noted that the Abbabis Complex showed higher degrees of partial melting than the cover sequence (Poli, 1997; Miller, 2008). Biotite melanosomes are seen in contact between the leucosome and Abbabis Complex suggesting in situ melt generation (Sawyer, 2008; Pawley *et al.,* 2015). Some crystallised partial melt textures cross-cut metamorphic porphyroblasts, which may indicate an episode of metamorphism prior to partial melting. This is consistent with a previous study which highlights that peak metamorphism occurred at between 525 Ma and 504 Ma, from Sm-Nd garnet ages, as a second episode of metamorphism (Jung and Mezger, 2003). This previous study also provided evidence that migmatisation was related to the intrusion of granites (Jung and Mezger, 2003), therefore verifying the lack of partial melt textures in the SLGs.

5.6 Conclusions

The Abbabis Complex in the Palmenhorst Dome orthogneisses, grey orthogneisses and granite-gneisses are comparable to other lithologies from the Abbabis Complex in the type area. The paragneisses are confirmed as strained grey orthogneisses. Petrographic studies confirm the varying lithologies in the basement rocks with the distinction based on both compositional and textural differences. This results in a lithologically more diverse Abbabis Complex in the northern extent of the Palmenhorst Dome than previously identified. The Abbabis Complex basement granites and amphibolite dykes are considered to be basement-aged intrusives. The presence of amphibolite dykes is confirmed to not represent synclinal infolds of Khan Formation.

Petrologically, the Damaran metasediments are comparable to lithologies identified in other studies, and therefore the presence of identified synclinal infolds can be confirmed. A distinction between the quartzofeldspathic Etusis Formation and Abbabis Complex is also possible due to the increased abundance of quartz in the Etusis Formation. The Rössing and Chuos formations are also distinctive petrographically as they contain unique mineral assemblages and clasts, respectively.

The red and grey granites of this study show compositions and fabrics similar to those of previous work. Modal mineralogy is slightly different to what has been reported by other studies for the grey granites, however, this is possibly due to the large varieties of grey granites observed in this study and others. These early Damaran Granitoids are metamorphosed, subject to partial melting and contain a fabric which suggests that these granites were emplaced prior to the onset of D2 deformation, however, uncertainty about the timing of emplacement still exists.

There are similarities between the SLGs and the previously outlined SLGs based on the nomenclature of Nex and Kinnaird (1995). The SLGs do not show typical metamorphic indicators and therefore were not exposed to the metamorphic event as the other lithologies examined.
Rather, the SLGs are considered to be a result of anatexis during high-temperature metamorphic episode that also affected the other lithologies.

Deformation and metamorphism are closely linked in the Nose Structure as the metamorphic minerals largely define the foliations. A pervasive D2 foliation cross-cuts an older possible pre-Damaran fabric (in the basement lithologies) or an earlier Damaran fabric (D1). However, this metamorphic and deformational (D2) event obliterated most evidence for earlier deformation. Peak metamorphic events are coeval with D2 deformation and the thermal effects outlasted the deformation. Amphibolite to granulite facies grade metamorphism is inferred from possible partial melt textures, the amphibole-diopside-biotite assemblages, granoblastic polygonal recrystallisation and consequent obliteration of previous deformational features. This high-temperature metamorphism is well-documented in the sCZ.

This study examined remnant partial melt textures in all the lithologies and not just the pelitic rocks which generally constitute fertile rocks for partial melting. Most of the basement and supracrustal rocks are seen to exhibit varying signs of partial melt and high temperature metamorphism, which may represent the propensity of these lithologies being sources for the Damaran Granitoids. The Abbabis Complex shows higher degrees of partial melt than the supracrustals.

6. Geochemistry

6.1 Introduction

Geochemical analysis was performed on Abbabis Complex gneisses, amphibolites, Damaran metasediments, Damaran granitoids (Red, Grey and sheeted leucogranites) by means of X-ray fluorescence (XRF) for major oxides and inductively coupled plasma mass spectrometry (ICP-MS) for trace element data. Geochemical data are used in order to classify rock types, assess possible links between the Damaran metasediments and supracrustals as well as evaluate crystallisation and emplacement systematics. Commonly used classification methods (Streckeisen, 1976; Barker, 1979; Le Maitre *et al.,* 1989) were employed to define lithological types based on whole-rock geochemical data and to compare the Abbabis Complex gneisses with the quartzofeldspathic Etusis Formation. Additionally, an assessment of the likely sedimentary or magmatic origin of the Abbabis Complex gneisses and granites was done. Field mapping identified two principal granite types, namely the red and grey granites along with various sheeted leucogranites, where all were assessed for crystallisation processes. Whole rock geochemical information is used to determine any significant geochemical differences between these various intrusions.

6.2 Laboratory Methods

Localities where rock samples were collected are shown on the geological map (Fig. 6.1) and a list of sample descriptions and GPS coordinates is provided in Appendix 2. Samples were coarsely crushed into aggregates using a carbide-steel jaw crusher. Migmatitic samples with associated sheeted leucogranites were separated into chips of melanocratic/melanosomes and leucocratic/leucosome phases with appropriate suffixes added to sample numbers. Coarse aggregates were then milled into a powder using a carbide-steel swing mill. Whole-rock major element XRF data (Appendix 3.A) were obtained from the milled products using a PANalytical PW2404 WD XRF spectrometer (Earth Lab, University of the Witwatersrand) using the procedures outlined in Wilson (2012), and results are reported in wt.%. Specific analytical procedures are outlined in Appendix 3.B. Certified reference materials (CRMs) BHV02, GSP2, NIM-D, NIM-P and DTS1 were also analysed, and all major oxide wt.% analytical results were within 0.44 % agreement of reference standard values. Precision and accuracy testing is presented in Appendix 3.C. ICP-MS was used to analyse the milled products for trace elements using an ELAN DRC-e quadrupole ICPMS (Earth Lab, University of the Witwatersrand) following analytical procedures outlined in Appendix 3.B. Trace element data are reported in ppm (Appendix 3.A). Certified reference materials BHV02 and GSP2 were used for precision and accuracy assessment with precision evaluation documented in Appendix 3.C. Five internal calibration standards were analysed inbetween every nine unknowns.

Major and trace element data are utilised in various classification, normalised rare earth element (REE) plots and Harker diagrams in order to classify the lithologies and characterise them with respect to their likely geodynamic regime.

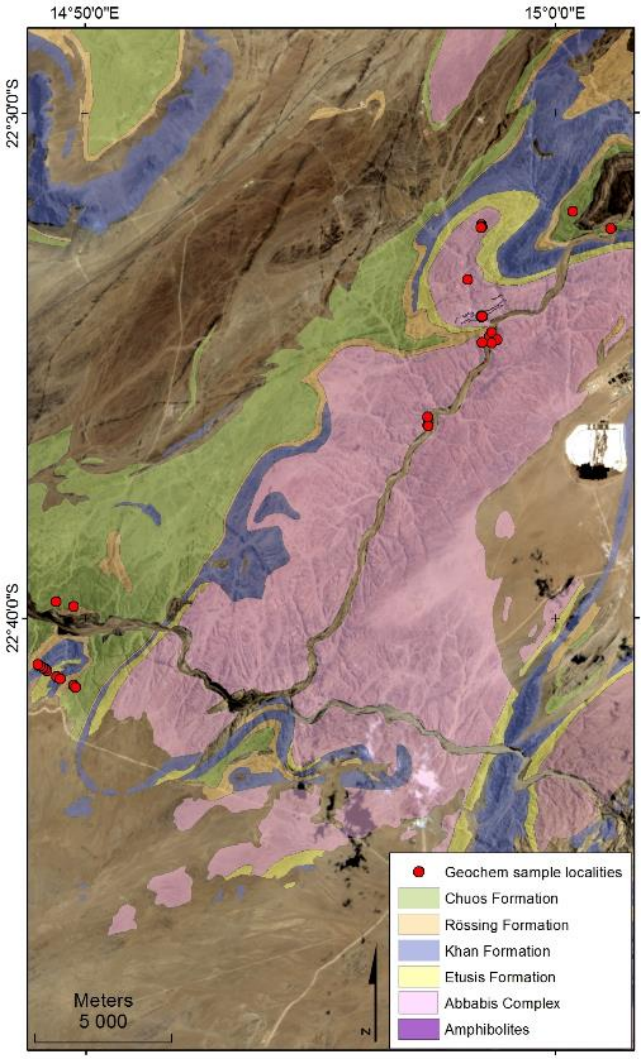


Figure 6.1: Localities of the samples collected in the field and surrounding areas. Sample localities are indicated by red circles. Geology (modified after Lehtonen *et al.*, 1995 with additions from this study) of the Palmenhorst Dome (Abbabis Complex) and enveloping Damara Supergroup (Etusis, Khan, Chuos and Rössing formations) superimposed over a Landsat 8 satellite image.

6.3 Whole-rock geochemistry

In addition to petrographic classification of the various igneous rocks, namely granites, gneisses and amphibolites, whole rock geochemistry is also used to compare lithologies of the Etusis Formation, the Abbabis Complex and various intrusions. Trace element geochemistry, specifically the Rare Earth Elements (REE) and Large ion lithophile elements (LILE) were used to further assess the Damaran Granitoids, which comprise the sheeted leucogranites, the red granites and the grey granites. Lastly, whole rock geochemical data were used to further classify granitoids according to the scheme set

out by McDermott *et al.* (1996), which is specific to the granitoids of the Damara Belt with respect to assessing the role of biotite-dehydration melting. The dataset of the present study is compared to other datasets for Damara rocks in the discussion.

6.3.1 Major oxide geochemical classification of field lithologies

Major oxides are used to classify the various igneous rocks. Classification schemes included the Q-A-P (Streckeisen, 1976), TAS (Le Maitre *et al.,* 1989), An-Ab-Or (Barker, 1979), and the Shand Index (Shand, 1927). Major oxide wt.% data are used in cation normative calculations, such as the CIPW normative calculation, and recalculated molecular normative compositions for the Streckeisen (1976) and An-Ab-Or (Barker, 1979) classifications, respectively. In addition, the molar values of Al_2O_3, CaO, Na_2O and K_2O were used to calculate the Shand Index for the classification of granites (Shand, 1927). The Abbabis Complex meta-igneous lithologies and Damaran granitoids are geochemically classified below. The Streckeisen (1976) and TAS (Le Maitre *et al.,* 1989) are widely used and particularly useful when combined with one another to assign rock names (Rollinson, 1993), or used in conjunction with petrographic classification.

The Abbabis Complex lithologies include the grey orthogneisses (or paragneisses), orthogneisses and basement granites as well as the amphibolites. Geochemically, the basement gneisses and granitoids are classified as monzo-granites, granodiorites, monzonites and quartz monzodiorites, defining a wide spread on the Streckeisen diagram (Fig. 6.2.A) and significant compositional heterogeneity within the Abbabis Complex. The grey orthogneisses show less cation normative quartz and alkali feldspar, which is not consistent with the petrographic classification as granites. These grey orthogneisses contain more biotite in thin section and show grain-size reduction in comparison with the orthogneisses and basement granites, which may account for the discrepancy. The orthogneisses contain higher cation normalised percentages of quartz and alkali-feldspar and plot in the monzogranite field, consistent with the petrographic classification as granites. Lastly, the basement granites form an array of varying amounts of quartz and alkali-feldspar at approximately constant quantities of plagioclase, resulting in classification as granodiorites, quartz monzodiorites and monzodiorites. which is not consistent with the petrographic classification of the basement granites as true granites. The wide spread of data for the basement lithologies is mirrored in the TAS diagram (Fig. 6.2.B) and is variably consistent with petrographic classifications. The grey orthogneisses (monzonites), the orthogneisses (granites to syenites) and basement granites (trachy-diorites to granodiorites) compositions differ more from the petrographic classifications in the TAS classification. There is an increase in silica content from the basement granites, grey orthogneisses to the orthogneisses, although their alkali ratios remain relatively constant. Similarly, the An-Ab-Or

(Fig. 6.2.C) classification diagram indicates that most lithologies can be classified as granitic in composition. Granodiorite to tonalite compositions are also observed, which is consistent with more intermediate to basic compositions (SiO_2 wt.% of 48 - 65) relative to the granitic extremes for the basement granites. According to the Shand Index all lithologies are peraluminous (Fig. 6.2.D).

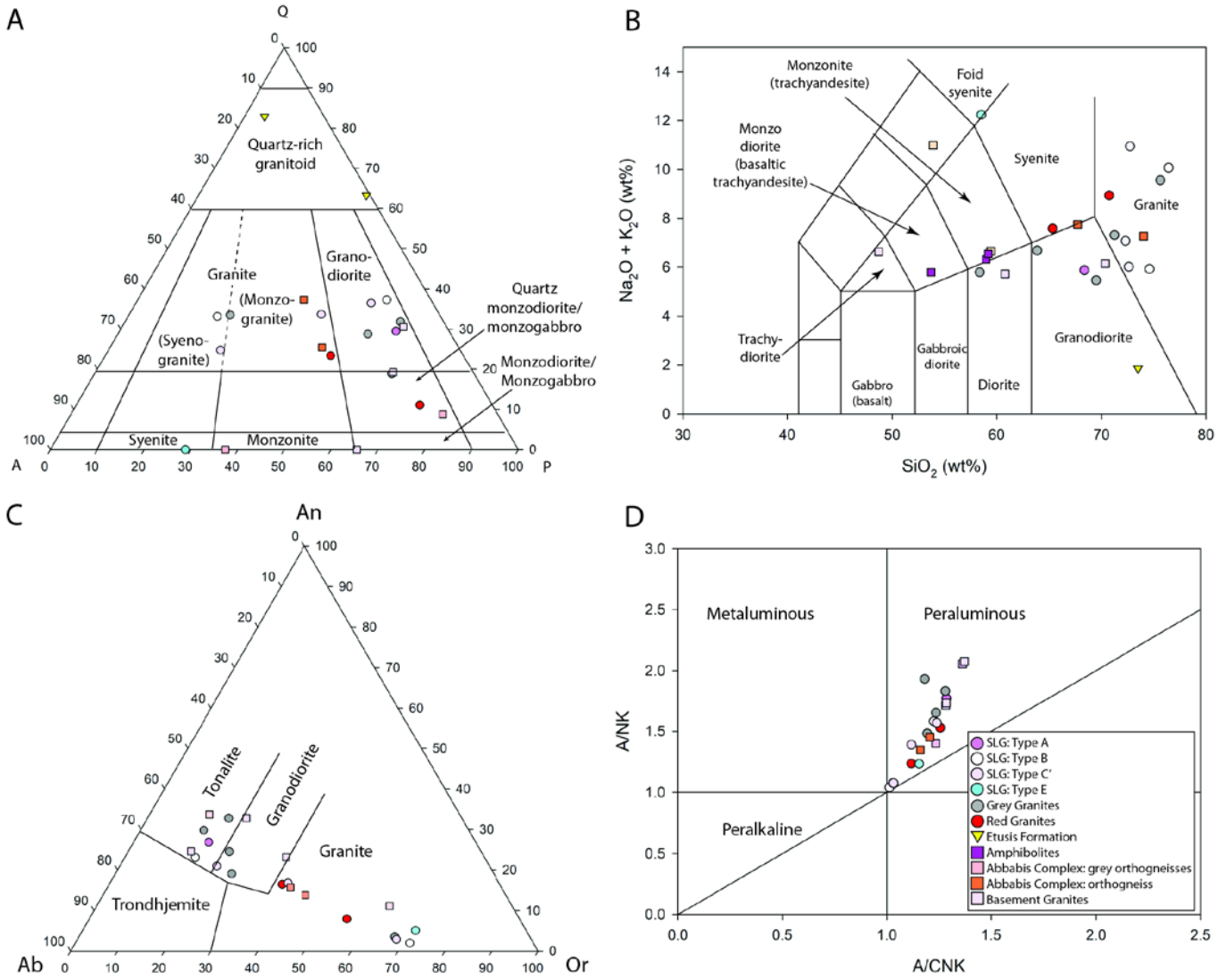


Figure 6.2: Whole rock geochemical plots of the Abbabis Complex gneisses and migmatites, amphibolites, Etusis Formation, red granites, grey granites and sheeted leucogranites (SLGs) from the study area. (A) QAP diagram of the CIPW normalised Abbabis Complex gneisses and granites, amphibolites and Damaran Granites (Streckeisen, 1976). Metasedimentary rocks of the Etusis Formation are shown for comparison, but a classification is not applied. (B) TAS classification diagram (Le Maitre *et al.*, 1989). (C) Molecular normative values plotted on the An-Ab-Or diagram (Barker, 1979). (D) Shand index (Shand, 1927) classification showing the peraluminous nature of the lithologies. A/CNK= $Al_2O_3/(CaO+Na_2O+K_2O)$ molar and A/NK= $Al_2O_3/(Na_2O+K_2O)$ molar.

The quartzofeldspathic Etusis Formation (sample 1.1) is plotted on the Streckeisen classification diagram despite being metasedimentary in nature because it provides a means of comparison with the Abbabis Complex gneisses. The Etusis Formation shows a composition corresponding to quartz-rich granitoids (Fig. 6.2.A). This is consistent with petrographic observations as the Etusis Formation

shows elevated quartz in comparison to the Abbabis Complex lithologies, and also highlights the differences between the Etusis Formation and the Abbabis Complex.

Geochemically, the amphibolites show less spread (Fig. 6.2.B) with more basic compositions (SiO_2 wt.% between 55 and 60) with relatively constant total alkali compositions. The amphibolites are geochemically characterised as trachyandesites and basaltic trachyandesites. The amphibolites observed in the field have been intruded by coalesced sheeted leucogranites and display melanosomes along the variably sharp to diffuse contacts. As a result, these amphibolite dyke compositions most likely do not represent the original mafic composition.

All the lithologies which have been assigned to the Abbabis Complex (gneisses, granites and amphibolite dykes) typically display higher P_2O_5/TiO_2 and low MgO/CaO ratios indicating more of a magmatic signature (Fig. 6.3; Werner, 1987). Two samples (grey orthogneisses and basement granites) show a sedimentary affinity based on major element discrimination. This finding is in conflict with field characterisation, and therefore and these are considered outliers.

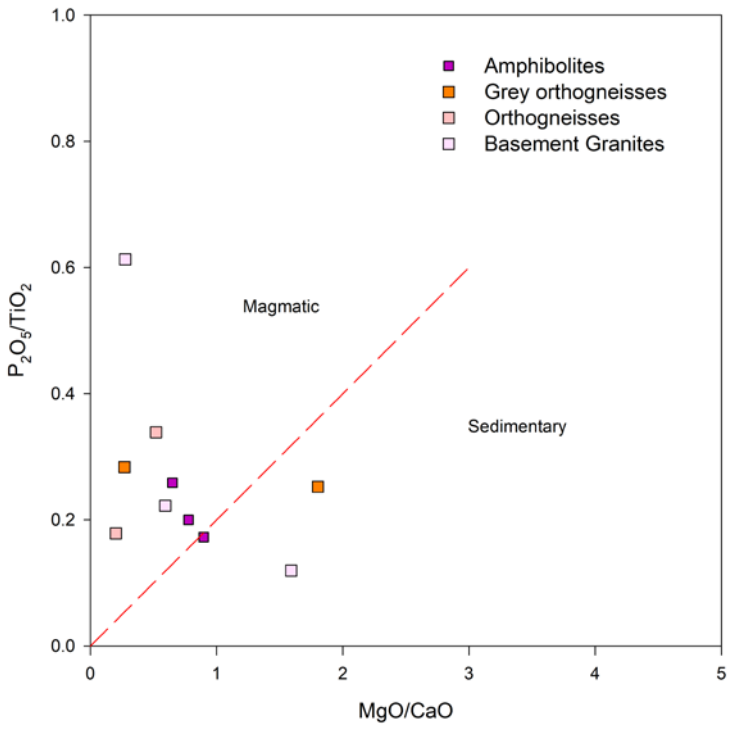


Figure 6.3: Major element discrimination diagram distinguishing between paragneisses or orthogneisses of the Abbabis Complex lithologies (Werner, 1987; Passchier *et al.,* 1990).

The Damaran granitoids, namely the red, grey and sheeted granites, show a wide range in compositions from the QAP, TAS and An-Ab-Or classification schemes (Fig. 6.2.A, B and C), but all show peraluminous affinities (Fig. 6.2.D) with A/CNK ranging from 1 to 1.4 and A/NK from 1 to 2.

Similarly, the major element oxides tend to decrease with increasing SiO_2 compositions (Fig. 6.4) within different granite types and for the Damaran granitoids as a whole. CaO and MgO versus SiO_2 typically show more dispersion than the other major element oxides (Fig. 6.4).

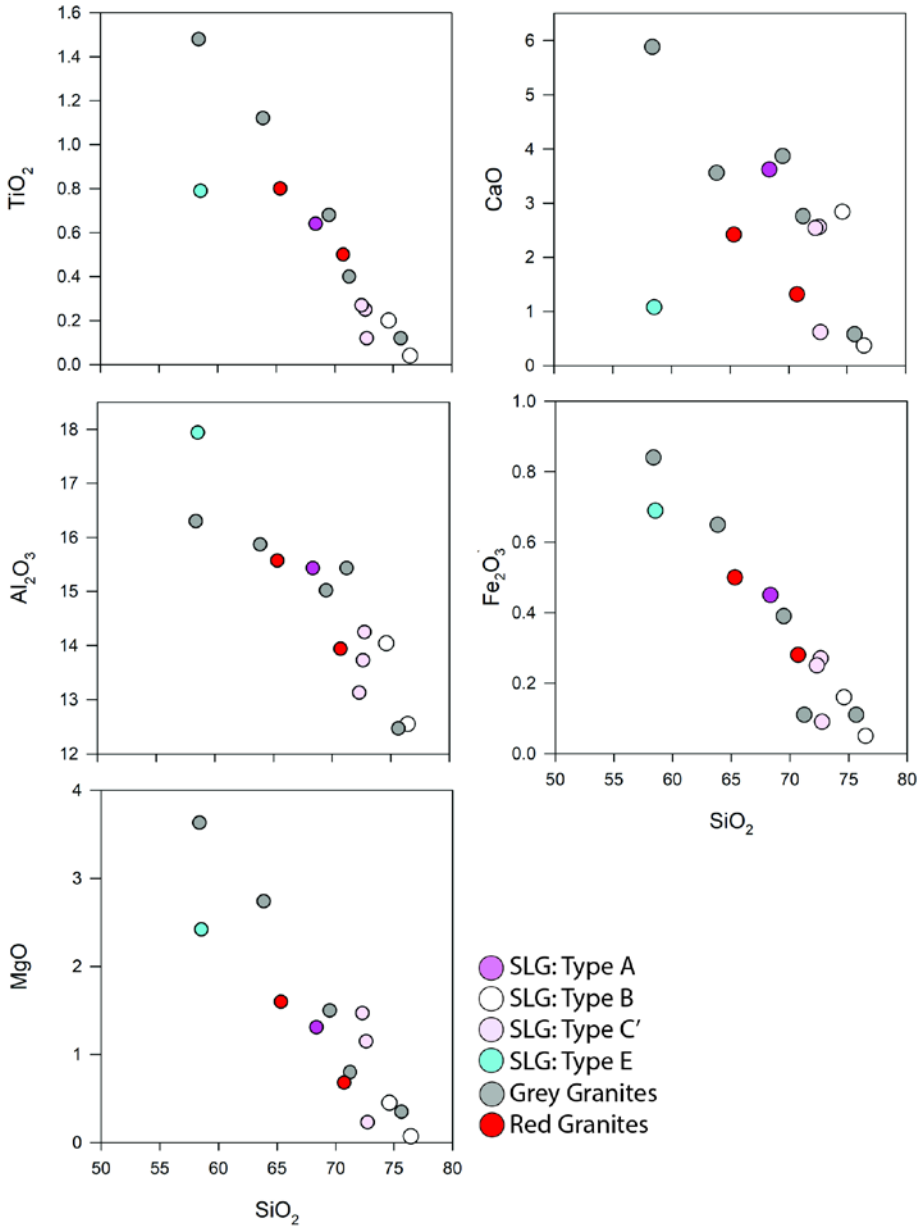


Figure 6.4: Stacked major element oxides versus SiO_2 for the Damaran Granitoids.

The red granites have SiO_2 of 65 – 71 wt.%, Na_2O >4 wt.% and K_2O >8 wt.%, respectively, with low Fe_2O_3 >5 wt.% and Al_2O_3 of 13 - 15 wt.% (Fig. 6.4). The red granites are classified as monzo-granites and quartz monzodiorite using the Streckeisen diagram (Fig. 6.2.A) and granites to syenites using the TAS diagram (Fig. 6.2.B). The TAS classification agrees with the petrographic classification of the red granites as syenites to granites, whereas the Streckeisen classification is somewhat inconsistent. This granite type has a relatively small range in total alkali compositions (Fig. 6.2.B). In addition, the

red granites plot as granites using the An-Ab-Or classification but tend towards the granodiorite field.

Similarly, the grey granites define a mineralogical range from granites to granodiorites and diorites (or quartz monzodiorites) (Fig. 6.2.A and B). Total alkali compositions are between 5 - 10 wt %, while the SiO_2 content shows a range from 58 -78 wt.%. Al_2O_3 compositions are 12 - 17 wt.% with generally higher Fe_2O_3 (2 – 7 wt.%) values than the red granites (Fig. 6.4). The grey granites plot as tonalities to granites in the An-Ab-Or plot (Fig. 6.2.C), which is consistent with the petrographic classification as tonalities.

The sheeted leucogranites show the widest compositional spread among the Damaran granitoids with SiO_2 58 - 77 wt.%, Na_2O+K_2O > 15 wt.%, and low, but variable Fe_2O_3 of 1 – 7 wt.%. Al_2O_3 compositions are >20 wt.% (Fig. 6.4). Based on normative calculations, the sheeted leucogranites plot in several fields using the Streckeisen, TAS and An-Ab-Or classifications (Fig. 6.2.A.B and C). The type A SLGs are classified as granodiorites (Fig. 6.2.A and B) in the Streckeisen and TAS schemes, and plot in the tonalite field in the An-Ab-Or plot (Fig. 6.2.C). They do not match the petrographic classification as a syeno-granite. Type B SLGs are classified as granites to granodiorites in the Streckeisen classification scheme, however, classify as granites using the TAS scheme (Fig. 6.2.B), which is consistent with the petrographic classification of monzo-granites. Similarly, the type B SLGs plot as two extremes in the granite and tonalite fields on the An-Ab-Or plot (Fig. 6.2.C). Type C' SLGs are classified as granites to granodiorites (Fig. 6.2.A. B and C) in the Streckeisen, TAS and An-Ab-Or classification plots consistent with petrographic classification. Lastly, type E SLGs is the outlier of the SLG and plots in the syenite field in the Streckeisen diagram (Fig. 6.2.A), straddling the foid syenite and syenite fields in the TAS plot (Fig. 6.2.B). These SLGs are considered granites in the An-Ab-Or plot (Fig. 6.2.C).

6.3.2 Trace Element Geochemistry

Chondrite-normalised REE compositions for the Abbabis Complex gneisses and granites are enriched in the LREE over the HREE (Fig. 6.5.A). Light REE are more strongly fractionated (La_N/Sm_N = 1.9 - 4.9), than the HREE (Gd_N/Lu_N = 2 – 4). Moderate to slight Eu anomalies are mostly negative (Eu/Eu* = 0.5 - 0.9), with the exception of one single positive anomaly (1.6) from the basement granites. The basement granites show the most enriched and least enriched REE patterns. The grey orthogneisses and the orthogneisses display similar enrichment patterns, although the grey orthogneisses are typically more enriched.

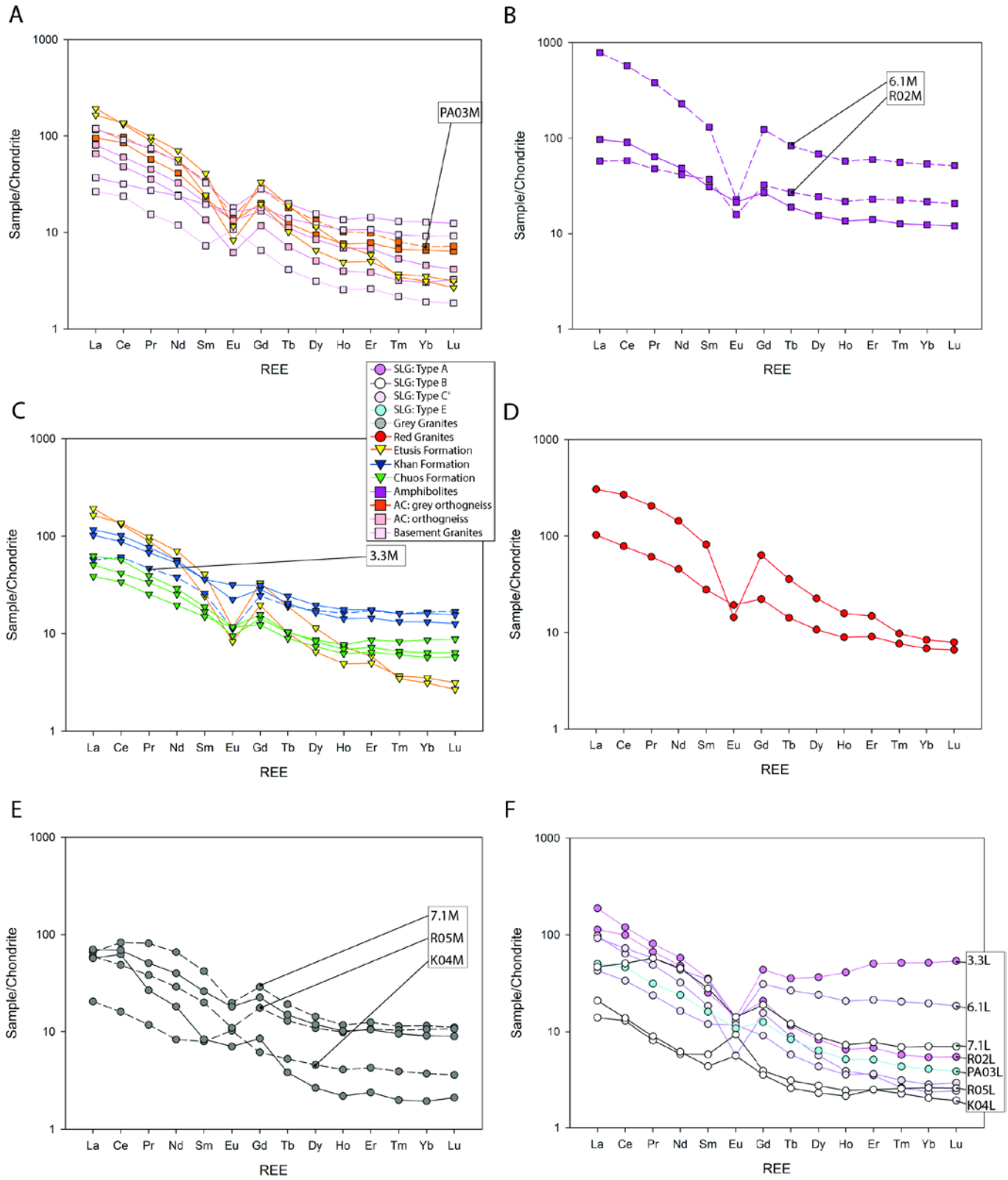


Figure 6.5: REE chondrite-normalised diagrams (Anders and Grevesse, 1989): (A) Abbabis Complex granite-gneisses, (B) amphibolites, (C) Damaran metasediments, (D) red granites, (E) grey granites and (F) the SLGs. Samples that contained both leucosomes (L) and melanosomes (M; dashed lines) are indicated by the sample number and suffix.

The amphibolites show higher overall REE concentrations compared with the Abbabis Complex lithologies (Fig. 6.5.B) and show gentle slopes (La_N/Lu_N= 5.8 – 8) with a single outlier with a steeper REE pattern (La_N/Lu_N= 15.3). The LREE (La_N/Sm_N= 1.6 – 3.1) are generally less enriched over the HREE (Gd_N/Lu_N= 1.6 – 2.5), although one sample shows stronger LREE enrichment relative to the HREE (La_N/Sm_N= 6, Gd_N/Lu_N= 2.4). Eu anomalies are moderately negative (Eu/Eu*= 0.2 – 0.8).

Supracrustal rocks of the Damara Supergroup display similar REE patterns when compared to the Abbabis Complex (Fig. 6.5.C) with gentle to moderate slopes and similar enrichment patterns, and consistently negative Eu anomalies. LREEs are less enriched up stratigraphy. The Etusis Formation shows steeper slopes (La_N/Lu_N = 49) than the other Damaran supracrustals (La_N/Lu_N = 5.1 – 7.5). In addition, this formation shows the most pronounced negative Eu anomalies (Eu/Eu* = 0.3 - 0.4) when compared to compositions of Khan and Chuos formations (Eu/Eu* = 0.7), respectively. The Khan Formation shows less enrichment of the LREE (La_N/Lu_N= 2.7 – 7.3) and stronger enrichment of the HREE (Gd_N/Lu_N= 1.3 – 2) in comparison to the Etusis Formation (Fig. 6.5.C). Europium is variably depleted (Eu/Eu*= 0.68 – 0.92, one outlier with 0.4). The Chuos Formation display gentle slopes (La_N/Lu_N= 5.8 – 9.8) (Fig. 6.5.C). La_N/Sm_N values of 2.6 - 3.3 indicate enrichment of LREE over MREE. Gd_N/Lu_N values range from 1.6 to 2.5. Negative Eu anomalies are consistently most weakly developed in comparison to the other metasediments (Eu/Eu* = 0.6 - 0.9).

The REE patterns of the red granites (Fig. 6.5.D) show variable enrichment of the LREE relative to MREE and HREE (La_N/Sm_N= 2.6 - 3.7; Gd_N/Lu_N= 1.6 - 8.0). Europium is variably depleted (Eu/Eu*= 0.2, 0.8). REE patterns for the grey granites are variable, and total REE are well above chondrite values (Fig. 6.5.E). LREE are enriched relative to MREE and HREE (La_N/Sm_N= 1.6 - 6.8, Gd_N/Lu_N= 1.6 – 4.1), although some samples have flatter slopes throughout the LREE and HREE. Eu anomalies (Eu/Eu*= 0.6) are negative or absent. The REE patterns for these samples are more variable than patterns for other lithologies.

In general, the Damaran granitoids are peraluminous, have relatively low HFSE and variable but high Rb/Sr ratios. These are characteristics of the Group I Damaran granites (McDermott *et al.,* 1996) where fractional crystallisation was proposed for the mechanism of crystallisation and therefore the use of LILEs are useful in assessing plagioclase crystallisation (McDermott *et al.,* 1996). The large ion lithophile elements (LILE) for the Damaran granitoids generally decrease with increasing SiO_2, however they display considerable spread (Fig. 6.6). Additionally, LILEs typically decrease within different granite groups, especially the red granites, with increasing SiO_2 too. Rb/Sr ratios decrease with an increase in Sr but increase slightly with an increase in Ba (Fig. 6.7). This LILE relationship

approximates the plagioclase and biotite fractional crystallisation vectors from McDermott *et al.* (1996) and references within.

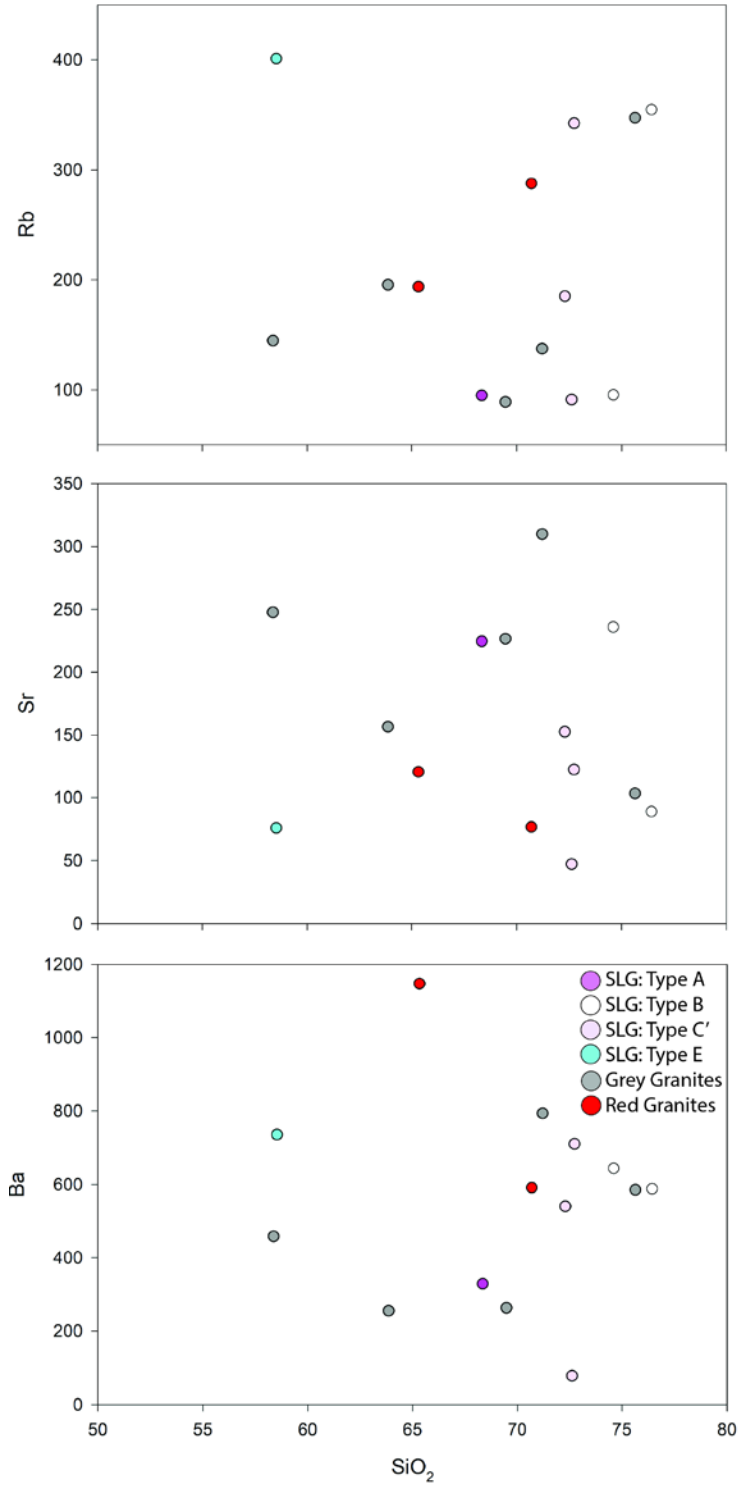


Figure 6.6: Stacked large ion lithophile element versus SiO_2 plots for the Damaran granitoids.

The SLGs also show variable REE patterns (Fig. 6.4.F). Ratios of La_N/Sm_N (1.6 - 5.3) and Gd_N/Lu_N (0.8 - 6.4) are variable and indicate LREE enrichment. Eu anomalies also vary from positive to negative (0.3 - 0.8 and 1.2 – 2.0), respectively. The SLGs intrude one another along with the basement and supracrustal lithologies, and therefore in some cases were sampled with other lithologies. These leucosomes (suffix: L) and melanosomes (suffix: M) were separated and the samples which are related are indicated (Fig. 6.5).

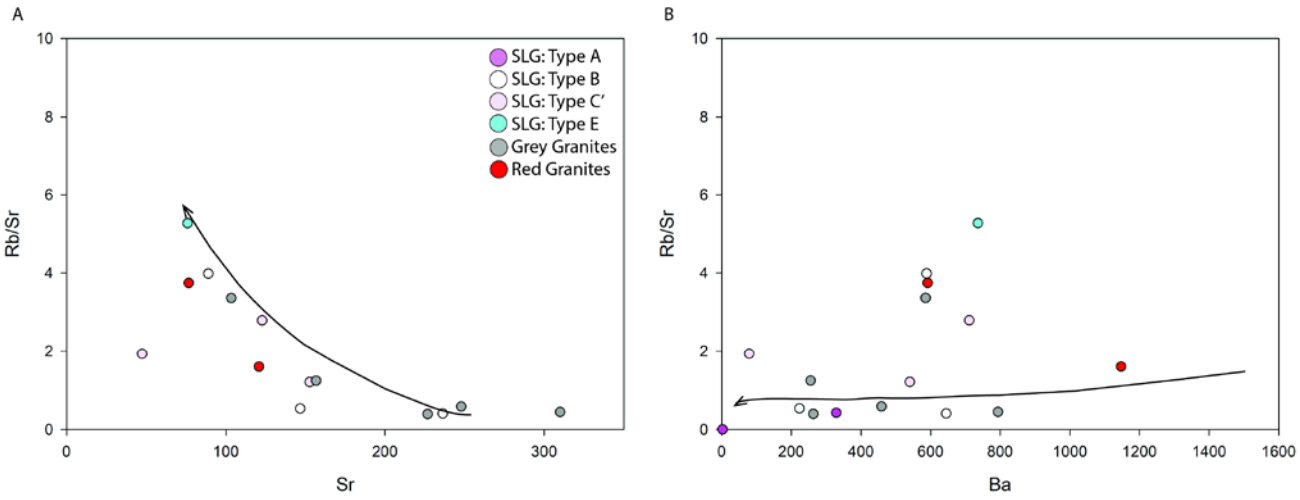


Figure 6.7: Rb/Sr versus (A) Sr and (A) Ba with plagioclase fractionation (A) and biotite fractionation trends (B) (after McDermott *et al.,* 1996 and references within) of the SLGs.

In multi-element normalised diagrams, the Abbabis Complex gneisses, amphibolite dykes and Damaran granitoids show LILE enrichment relative to the HFSE as well as HREE flattened depletion (Fig. 6.8). Notable depletions of Ba, Nb, Ta and Sr and enrichment of Th and Pb. The amphibolite dykes show more enriched signatures when compared to the Abbabis Complex gneisses and granites. The Damaran granitoids show a relatively consistent enrichment pattern, although the red granites and the type C' SLGs show the most and least enriched signatures.

Trace elements such as Th, Nb and Yb (Fig. 6.9) can act as geochemical fingerprints for mafic rocks derived from either MORB or OIB (Pearce, 2008). A recent study on amphibolite dykes from Naxos (Bolhar *et al.,* 2016) used Th/Yb versus Nb/Th to fingerprint crustal interaction with the magma. The amphibolite dykes from this study show elevated Th/Yb ratios that are enriched above the OIB-MORB array (Fig. 6.9).

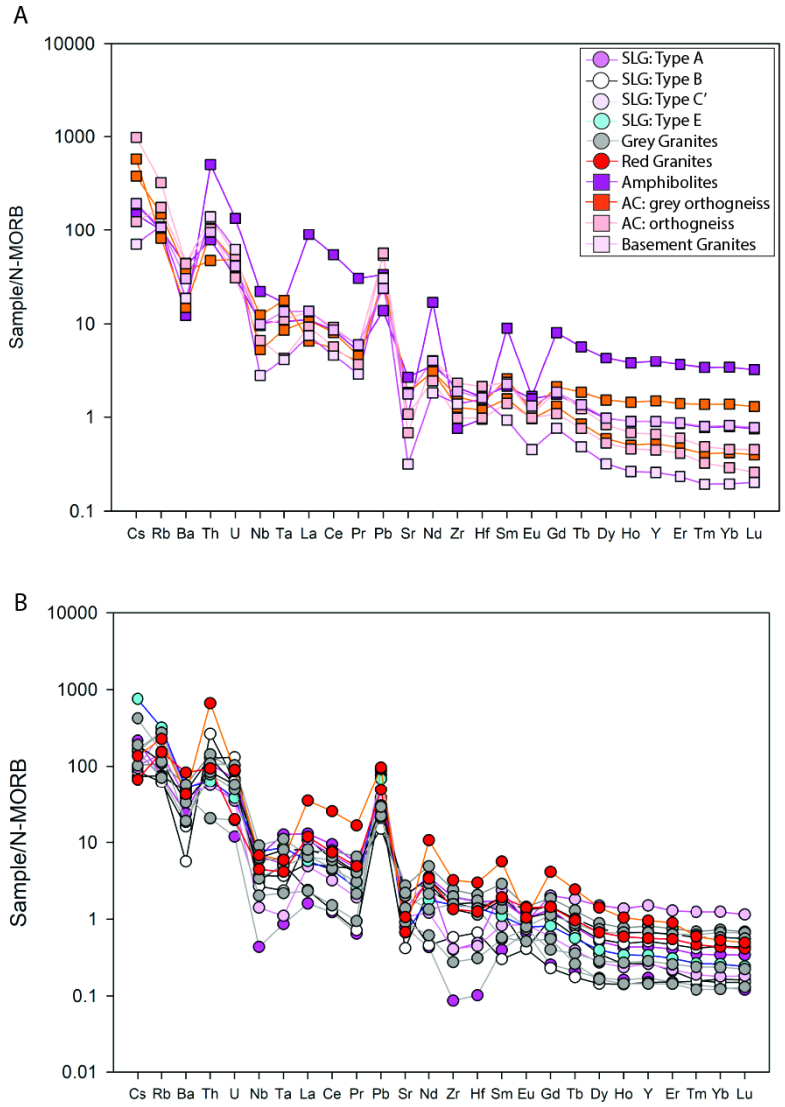


Figure 6.8: N-MORB normalised multi-element plots of the (A) amphibolite dykes, Abbabis Complex gneisses (and granites) and (B) the Damaran Granitoids. Elemental array after Kamber *et al.* (2002) and normalisation values after Hofmann (1988).

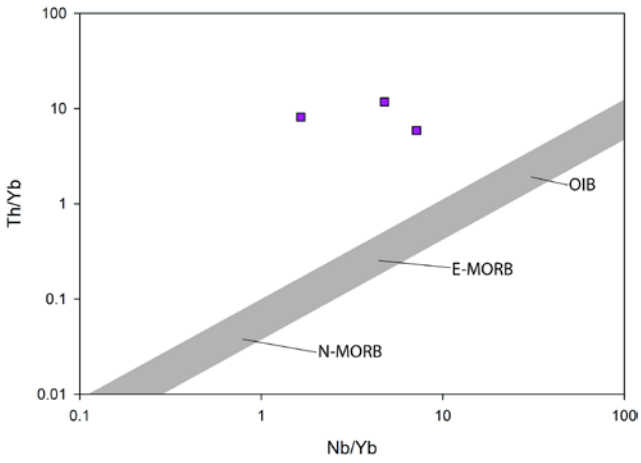


Figure 6.9: Th/Yb versus Nb/Yb plot of the amphibolite dykes to show crustal contamination. OIB-MORB array after Pearce (2008).

6.3.3 Provenance links between the Abbabis Complex and Damaran metasediments

Both Abbabis Complex lithologies and Damaran metasediments have under gone high-temperature metamorphism (Longridge *et al.,* 2017) and therefore likely experienced element mobility (Taylor and McLennan, 1985; Rollinson, 1993). Immobile elements, such as high field strength elements (Th, Zr) and REEs, were utilised due to their immobility during metamorphism (Taylor and McLennan, 1985) and weathering (Humphris, 1984; Rollinson, 1993). Th, Zr and La are typically more enriched, in felsic rocks, than Sc because of preferential fractionation during magma differentiation (Taylor and McLennan, 1985). Therefore, higher Th/Sc and La/Sc ratios may be indicative of more felsic sources and lower ratios most likely represent mafic sources. In addition to trace element geochemical data (CaO + MgO) – SiO_2 – (Na_2O + K_2O) diagrams (Taylor and McLennan, 1985) were used to assess similarities between the basement lithologies and Damaran metasediments. It is recognised that combined Na_2O and K_2O may be mobile during partial melting and weathering and therefore is merely used as a comparison between the metasediments and basement lithologies.

The Damaran metasediments show variable Na_2O + K_2O, CaO + MgO and SiO_2 compositions (Fig. 6.10). The Etusis Formation quartzofeldspathic and pelitic samples have variable Na_2O + K_2O values, but show constant low CaO + MgO and elevated SiO_2 values. This may reflect the sediment maturity (Taylor and McLennan, 1985). In contrast, the Khan Formation semi-pelitic schists and various banded gneisses display more variable Na_2O + K_2O, SiO_2 and CaO + MgO compositions, which range from more felsic in nature to more mafic (Taylor and McLennan, 1985) sediments, away from the Abbabis Complex gneisses to the amphibolite dykes. The Chuos Formation is comparable to the Khan Formation however it typically has Na_2O + K_2O, SiO_2 and CaO + MgO compositions which range between the Etusis and Khan formations. These metasediments (Khan and Chuos formations) display ratios that range from the Abbabis Complex gneisses and amphibolites after Longridge (2012). The Abbabis Complex lithologies show significant compositional heterogeneity and variable Na_2O + K_2O compositions, which most likely reflects variable partial melting, therefore a more representative sample set (Longridge, 2012) was chosen that appeared to have been less affected by element mobility during migmatisation.

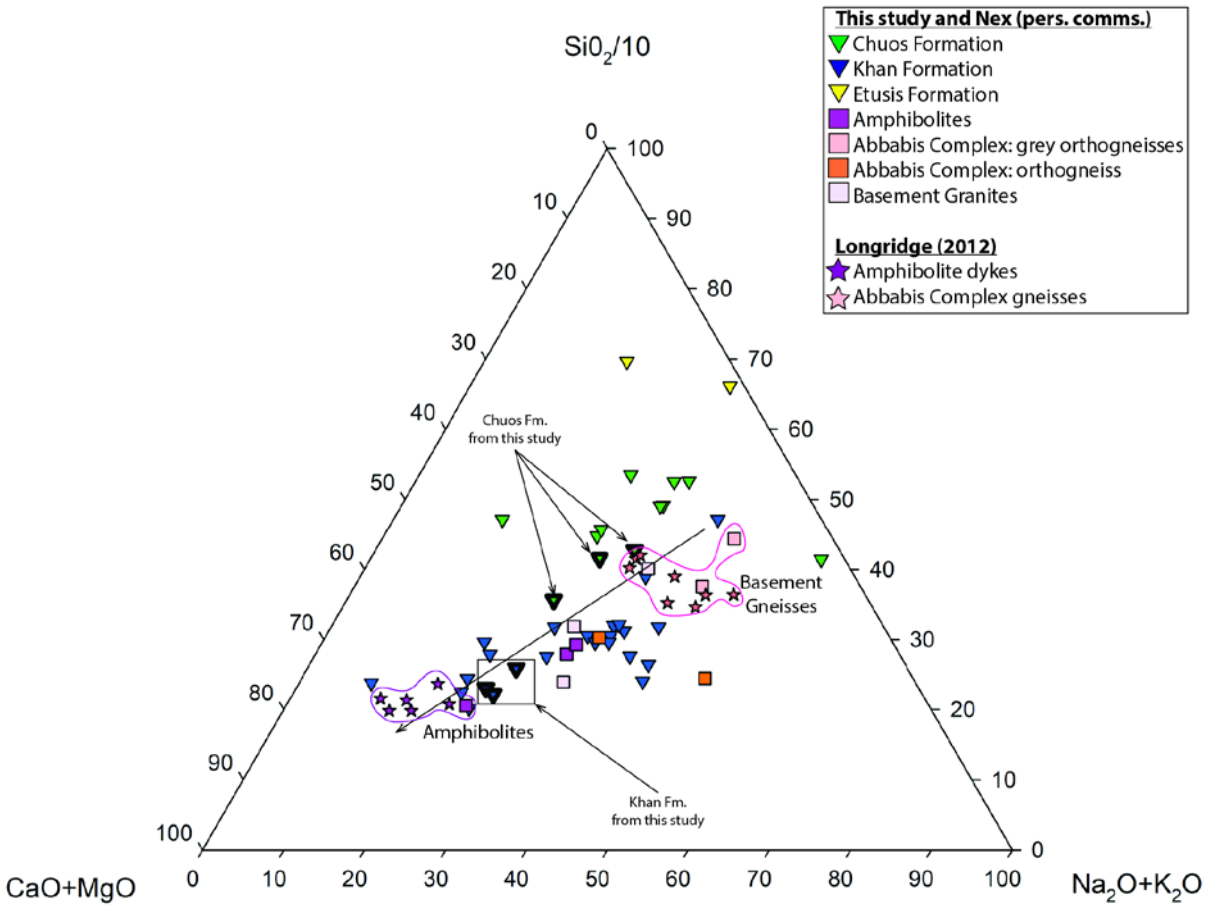


Figure 6.10: SiO_2/10, CaO + MgO and Na2O + K2O plot (Taylor and McLennan, 1985) showing the Abbabis Complex lithologies and amphibolite dykes, which represent possible felsic to mafic end members. An array, of the Damaran metasediments, is observed from the basement gneisses to the amphibolite dykes. Abbabis Complex gneisses and amphibolite dykes are plotted from Longridge (2012) to use a more homogenous representation. Most the whole rock data for the Khan and Chuos formations (not bolded) are from Nex (pers. comm.) and data collected from this study (bolded) can be seen in Appendix 3.A.

The trace element concentrations samples from this study are given in Appendix 3.A, however a more robust dataset for the Khan and Chuos formations were supplied by Nex (pers. comm.) from the Goanikontes area (Fig. 6.11). The metasediments show a relationship of Th/Sc and La/Sc versus Zr/Sc ratios (Fig. 7.11) which is consistent with a provenance-dependent trend (Taylor and McLennan, 1985). The Etusis Formation (Th/Sc= 6 – 11; La/Sc= 12 – 26) has higher La/Sc and Th/Sc ratios than the other metasediments. The Khan (Th/Sc= 0.5 – 2.4; La/Sc= 1.4 – 4.6; from this study and Nex, pers. comms.) and Chuos (Th/Sc= 0.5 – 3.3; La/Sc= 1 – 8.1; from this study and Nex, pers. comms.) formations have a range from higher to lower Th/Sc and La/Sc ratios, which may suggest a mixing pattern (Taylor and McLennan, 1985) and compositional variation from more felsic (higher Th/Sc and La/Sc ratios) to more mafic (lower Th/Sc and La/Sc ratios) sources. The Chuos Formation shows an array of ratios between the Etusis and Khan formations with a single outlier with the lowest Th/Sc and La/Sc ratios. The felsic (Abbabis Complex orthogneisses) and mafic (amphibolite dykes) components that were sampled from the Abbabis Complex (Th/Sc= 1 – 8; La/Sc= 3 – 9) were used

as end-member comparisons as the Nosib Group is proposed to be derived locally from the basement lithologies. The Khan Formation shows mixing between the felsic and mafic end members.

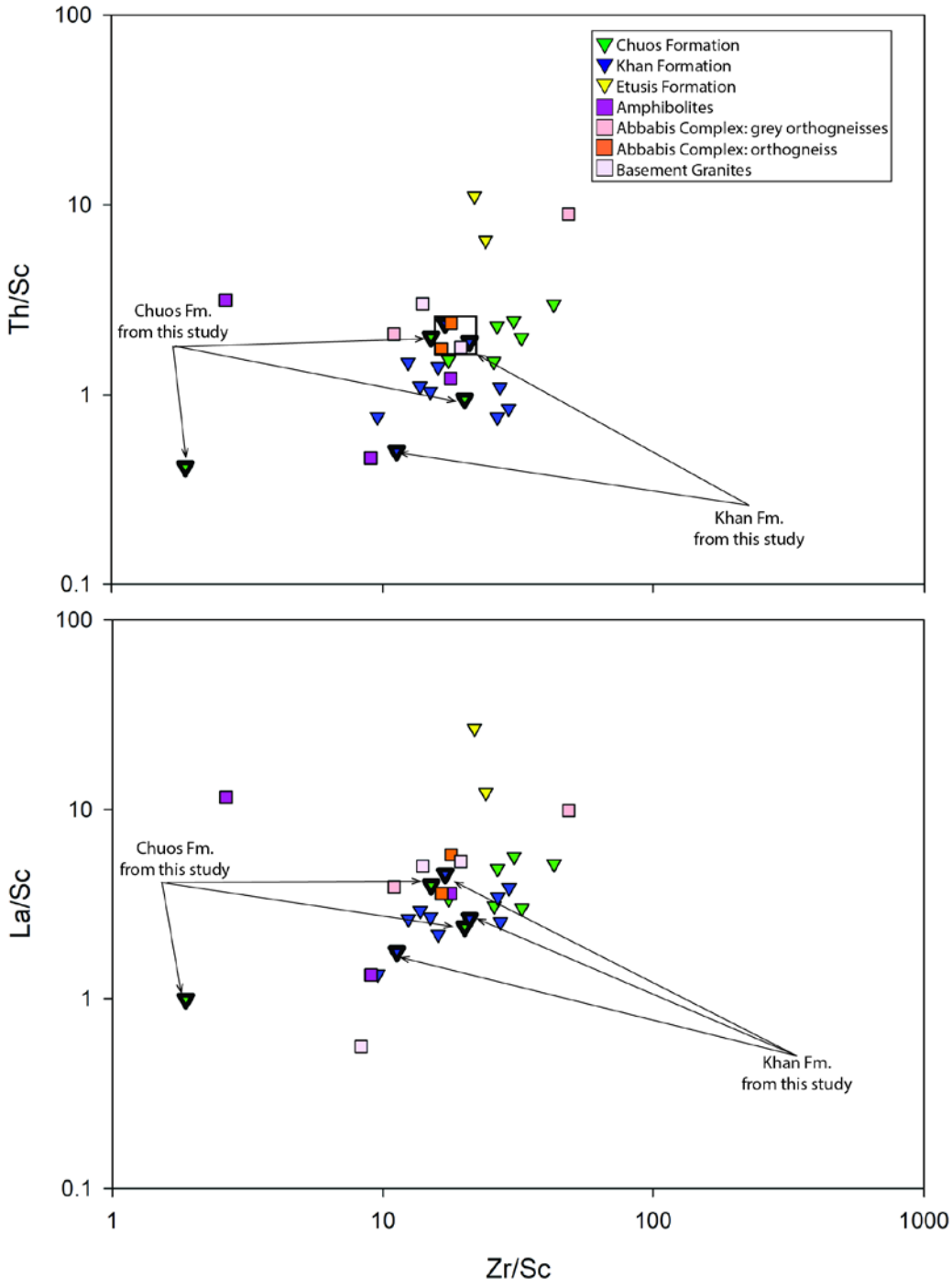


Figure 6.11: Stacked Th/Sc and La/Sc versus Zr/Sc binary plots after Taylor and McLennan (1985). Most the trace element data for the Khan and Chuos formations are from Nex (pers. comm.) and data collected from this study (bolded) can be seen in Appendix 3.A.

6.4 Discussion

The Abbabis Complex gneisses and granites, amphibolite dykes and Damaran Granitoids show comparable compositions to those noted by previous workers (Fig. 6.12), with similar compositional and mineralogical variability. The amphibolite dykes, however, have compositions different to those reported in previous studies (Fig. 6.12) as they have most likely been affected by partial melting during the emplacement of SLGs associated with the Damara Belt.

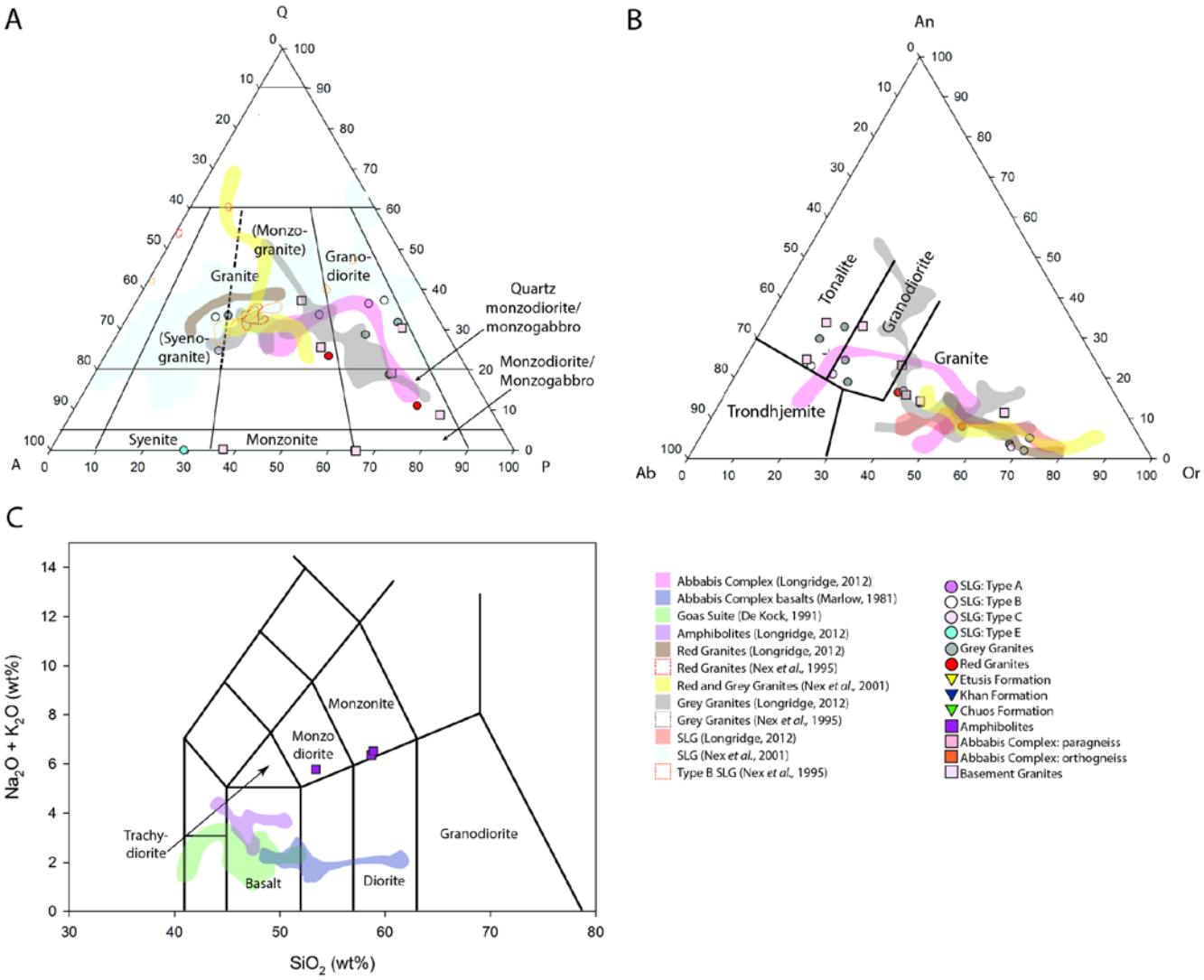


Figure 6.12: Diagrams comparing geochemical data for whole rock samples from this study and published studies. Classification schemes include (A) QAP, (B) An-Ab-Or, (C) TAS plots.

6.4.1 The Abbabis Complex

Geochemically, the various granites and gneisses of the Abbabis Complex show compositional heterogeneity as previously identified based on remote sensing domains, field and petrological classifications. However, the petrographic and geochemical classifications are not always consistent,

which could be attributed to element mobility of K and Na due to high grade metamorphism and partial melting (Sawyer, 2008). From major element plots the Abbabis Complex lithologies, including the amphibolite dykes, most likely have magmatic origins. The grey orthogneiss outlier, with a higher MgO/CaO ratio, is not considered to have a sedimentary affinity due to previously established field and petrological determinations. This classification is used as a guideline and a tool to corroborate field and petrographic observations (Werner, 1987; Passchier *et al.,* 1990). Considering that the Mg/CaO ratio is not much higher than ratios in other samples a magmatic origin appears most plausible. Therefore, the presence of a paragneiss is discounted again confirming that the Abbabis Complex of the Palmenhorst Dome most likely consists of the Narubis Granitoid Complex (Smith, 1965). The Etusis Formation is seen to have higher compositions of normalised quartz than the Abbabis Complex lithologies, which allows for the discrimination between the quartzofeldspathic counterparts of the Abbabis Complex and the Etusis Formation, probably reflecting sediment maturity (Taylor and McLennan, 1985).

The amphibolites do not have basaltic compositions which may be due to a possible crustal contamination signature. The multi-element plots (Nb and Ta enrichment), elevated Th/Yb ratios (Fig. 6.9) and enriched REE patterns may indicate that these dykes may not preserve the original melt compositions and have a component of crustal assimilation (Bolhar *et al.,* 2016). Therefore, a comparison between the Goas Suite (de Kock 1991) or Abbabis Complex metabasalts (Marlow, 1981) is not meaningful (Fig. 6.12) and U-Pb dating needs to be used to confirm the age relationship of the amphibolite dykes. Highly depleted HREE over LREE and a negative Eu anomaly indicates possibly melting in the presence of garnet and plagioclase (Rollinson, 1993) and the flattening of the HREE in multi-element plots may indicate previous partial melt extraction (Williams *et al.,* 2004).

6.4.2 The Damaran metasediments

Selected trace element ratios and major element plots (Taylor and McLennan, 1985) hint at a mix of compositions and relationship between the Etusis and the Khan formations (Fig. 6.10), while the Chuos Formation may be a mix in composition between these two formations (Etusis and Chuos Formation). Th/ and La/Sc ratios also suggest a mix in compositions between the three formations, with the more felsic compositions (higher Th and La/Sc ratios) of the lower Nosib Group and the more mafic compositions (lower Th and La/Sc ratios) of the lower Swakop Group.

The Etusis Formation is largely made up of quartzofeldspathic units and minor pelitic schists (Smith, 1965; Henry, 1992) with both of these units showing increased Th and La/Sc ratios and resultant more felsic sources (Taylor and McLennan, 1985; Tran *et al.,* 2003). However, these sediments show

elevated ratios and are not as similar to the Abbabis Complex gneisses as the Khan Formation lithologies. A possible reason may be the role of sorting, sediment maturity and presence of heavy minerals (Taylor McLennan, 1985; Taylor and McLennan, 1993) as the Etusis Formation is a mature rift sediment (Henry, 1992), which would have higher SiO_2 compositions reflecting the high quartz abundances and coarser grain-size accumulations. Both the Etusis Formation metasediments show comparable REE patterns that have a typical magmatic pattern (Taylor and McLennan, 1985) and compositions similar those of the orthogneisses of the Palaeoproterozoic Abbabis Complex, which may represent the source. This conclusion is consistent with many field-based, trace element and isotopic studies (Smith, 1965; Hawkesworth and Marlow, 1983; McDermott *et al.*, 1989; McDermott and Hawkesworth, 1990) that propose that the Etusis Formation was locally derived from the basement lithologies of the Abbabis Complex. This is further augmented by U-Pb studies identifying Palaeoproterozoic detrital U-Pb ages for the Nosib Group (Foster *et al.,* 2015; Nascimento *et al.,* 2017) as well as comparative Lu-Hf isotopic work that shows similarities between the Nosib Group and basement lithologies (Foster *et al.,* 2015).

The semi-pelitic schists and gneisses of the Khan Formation show similar trace element ratios to the Abbabis Complex gneisses and granites from this study, and the tightly clustered compositions of the Abbabis Complex gneisses (Longridge, 2012) suggest that the Khan Formation rocks were most likely sourced from more felsic sources of the Abbabis Complex. Nascimento *et al.* (2017) found that the Nosib Group (Etusis and Khan formations) and the Swakop Group (Chuos Formation) were most likely sourced from local Palaeoproterozoic basement sources based on regional detrital U-Pb studies, highlighting the likelihood of the Khan Formation may have been derived from Abbabis Complex rocks. However, the Khan and Chuos formations have less enriched REEs as well as Th and La/Sc ratios and show a mixing trend with the Abbabis Complex gneisses and the amphibolite dykes (with increasing mafic affinities) as possible endmembers. There is insufficient evidence to suggest that the Khan and Chuos formations were sourced from the amphibolite dykes but given that U-Pb and L-Hf isotopic studies suggest that these sediments were locally derived in the sCZ and that their source was less evolved and possibly mafic (Foster *et al.,* 2015). Therefore, the amphibolite dykes cannot be eliminated as a possible contributor. Other studies suggested that the provenance for these sediments was not local and may have included a wider range of lithologies from the East African Orogen (Foster *et al.,* 2015). The application of major and trace elements, to establish sediment mixing patterns, was also utilised on granulite facies rocks of the Palaeoproterozoic metasediments along the margin of the Archaean Hearne Craton (Tran *et al.,* 2003) highlighting that these provenance mixing trends (Taylor and McLennan, 1985) have been applicable to high grade metasediments.

6.4.3 The Damaran Granitoids and their petrogenesis

Geochemically the Damaran granites show similarities to those analysed by previous workers (Fig. 6.12). The red granites from this study can be most reliably compared with the early red and grey granites examined in previous studies (Nex *et al.*, 2001a; Longridge, 2012). Grey granites and SLGs show considerable variation but are comparable to other documented grey granites (Longridge, 2012; Nex *et al.*, 2001a). Given the highly heterogeneous compositions among the SLGs, distinguishing among lithological varieties is better accomplished in the field, using cross-cutting relationships, grain size distribution, the presence of accessory minerals and modes of emplacement.

The Damaran Granitoids show fractional crystallisation trends from decreasing major element compositions with increasing SiO_2 and Rb/Sr ratios versus Ba and Sr, which show plagioclase and biotite fractional crystallisation trends (McDermott *et al.,* 1996) within and among granite types and as a whole. This is consistent with the proposed mode of crystallisation of Damaran granitoids by McDermott *et al.* (1996). McDermott *et al.* (1996) proposed that the variations between various granites represent different sources or varying degrees of partial melting and the lowest SiO_2 wt% represents the initial melt compositions (McDermott *et al.,* 1996). The grey granites are the least fractionated and possibly represent earlier compositions of melt, which is consistent with the more mafic compositions and their proposed equivalence to the Goas Suite (Miller, 2008).

Previous work suggested and modelled that the Damaran granitoids were a result of biotite-dehydration melting that was either limited by the presence of plagioclase or biotite (McDermott *et al.,* 1996). The geochemical constraints developed for this model were used as the granitoids were correlatable to their Group I Damaran granitoids, and fractional crystallisation trends (from major and trace elements) were observed in this study similar those of McDermott *et al.* (1996). Diagrams using Rb/Sr and Ba/Sr versus Fe_2O_3 + MgO (Fig. 6.13) can be used to determine biotite- and plagioclase-limited melting (McDermott *et al.,* 1996). Variable Rb/Sr and Ba/Sr ratios indicate that the Damaran granitoids formed under biotite- and plagioclase-limited melting (McDermott *et al.,* 1996), however these conditions do not appear to change when Rb/Sr to Ba/Sr ratios are considered for the different granites. Additionally, Lu/Tb versus combined Fe_2O_3 and MgO consistently fingerprints the role of biotite-dehydration melting for the Damaran granitoids (Fig. 6.13; McDermott *et al.,* 1996) along with variable HREE depletions, indicating melting in the presence of garnet (Rollinson, 1993; McDermott *et al.,* 1996).

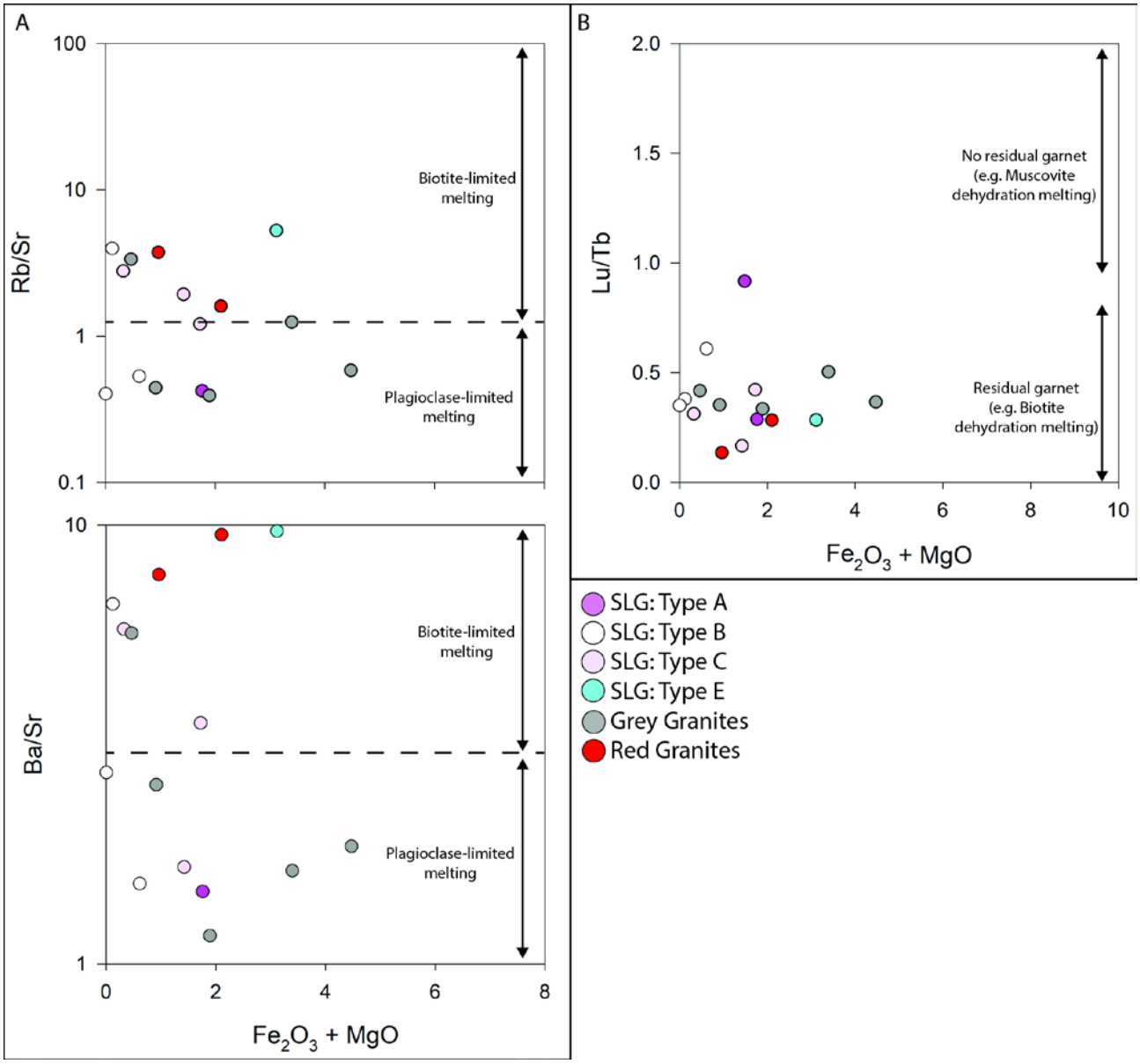


Figure 6.13: (A) Stacked Rb/Sr and Ba/Sr versus combined Fe_2O_3 and MgO after McDermott *at al.* (1996) for the Damaran granitoids determining plagioclase- and biotite-limited melting regimes. Lu/Th versus combined Fe_2O_3 and MgO (McDermott *et al.,* 1996) used to established biotite- or muscovite-dehydration melting.

Johannes *et al.* (2003) proposed that dehydration melting lead to partial melt development of migmatites in the Turku area in southern Finland and that the leucosomes that often develop into more extensive leucogranites formed by a two stage processes: partial melt that crystallises as cumulates and then residual melt migrates to form granites. The preferential enrichment of LREE and a negative Eu anomaly suggests fractional crystallisation of final melts (Johannes *et al.,* 2003), whereas the variable REE patterns (and positive Eu anomalies) were interpreted as cumulates of plagioclase. The red granites have REE patterns that are consistent with final melt compositions (Johannes *et al.,* 2003), from which plagioclase segregated (Rollinson, 1993). On the other hand, the grey granites and the SLGs display variable REE patterns indicative of both partial melting and

fractional crystallisation (Rollinson, 1993; Johannes *et al.,* 2003). Eu anomalies fingerprint plagioclase crystallisation as a cumulate (positive Eu) and during fractional crystallisation (negative Eu) that may have migrated. This suggests that the grey granites and SLGs may represent melts that contributed to different generations of grey granites from successive migratory melts.

Leucosomes that are adjacent to palaeosomes occasionally show positive Eu anomalies with enriched LREE in the crystallised melt (leucosome) and negative Eu anomalies with less enriched LREE in the corresponding country rock. This may represent partial melts where plagioclase crystallised in the newly formed melt, possibly extracting Eu from the surrounding host lithologies and may provide evidence for in situ to in-source partial melts. This is due to the fact that these partial melts developed as cumulates and had not yet developed into migratory or intrusive melts. No interaction between the palaeosome and leucosome occurred in the instances where both the leucosomes and country rock have negative Eu anomalies as these leucosomes tend to be more intrusive (from cross-cutting relationships). Therefore, fractional crystallisation most likely occurred in the leucogranites suggesting more intrusive migratory melts that formed from fractional crystallisation (Johannes *et al.,* 2003).

6.4.4 Tectonic setting and petrogenesis of the Palaeoproterozoic amphibolite dykes and the Damaran granitoids

LILE enrichment relative to HFSE coupled with a depletion of HREE, an enrichment of incompatible elements (Th) with a depletion of Nb and Ta is considered diagnostic of subduction-related metasomatism or continental intraplate magmatism (e.g. Kamber *et al.,* 2002; Williams *et al.,* 2004) with magma crust interaction inferred from the negative Nb and Ta anomalies (Bolhar *et al.,* 2016). The Abbabis Complex, the amphibolite dykes and Damaran granitoids all show this subduction or intraplate magmatism-related or crustal assimilation signatures, which suggests that there may have been a Palaeoproterozoic and Pan-African related intraplate magmatism event or crustal assimilation during emplacement related to the amphibolite dyke emplacement and Damaran granitoids, respectively.

Subduction/arc magmatism or crustal assimilation of the proposed Palaeoproterozoic amphibolite dykes has not been previously discussed and would require detailed geochemical constraints and fingerprinting which is beyond the scope of this study. From Th/Yb and Nb/Yb ratios the amphibolite dykes show possible crustal contamination signatures of the OIB-MORB array (Pearce, 2008), but based on geochemistry it is impossible to say whether it was conclusively arc magmatism or crustal contamination. However, the fact that the amphibolite dykes display higher

concentrations of incompatible elements compared to the Abbabis Complex gneisses and granites suggests that the latter were not involved in crustal assimilation by these dykes.

Subduction of the leading edge of the Kalahari Craton beneath the Congo Craton during continent-continent collision and arc magmatism (Goas Suite and matchless amphibolite) has been established during the Pan-African Orogeny (Kennedy, 1964; McDermott, 1986; Miller, 2008), with associated voluminous granitoid emplacement (Miller, 2008). Therefore, based on the geological evidence, from previous studies, either crustal assimilation or subduction geochemical signatures are probable, and a combination of the two is likely based on the felsic compositions of the granitoids.

6.5 Conclusions

The Abbabis Complex gneisses and granites, amphibolite dykes and Damaran Granitoids show comparable compositions to those describe by previous workers (Fig. 6.12) with similar heterogeneity in composition. However, the amphibolites cannot be compared with other metabasalt compositions as they have been contaminated by granitic melts as the amphibolites have been intruded by voluminous granitoids during the Damara Orogen. The amphibolite dykes appear to have a crustal assimilation signature inferred from depletion of Nb and Ta, elevated Th/Yb ratios and enriched REE patterns. U-Pb relationships are required to confirm whether these dykes are related the Goas Suite (Damaran amphibolites) or the basement metabasalts (Abbabis Complex amphibolites). Given the highly heterogeneous compositions among the SLGs, distinguishing among lithological varieties is better accomplished in the field, using cross-cutting relationships on the outcrop scale, grain size distribution, the presence of accessory minerals and modes of emplacement.

The Abbabis Complex granites and gneisses show compositional heterogeneity, but the geochemical classifications have most likely been affected by element mobility (K and Na), so combined field and petrological evidence is used. Various lithologies, including the gneisses, granites and amphibolites of the Abbabis Complex, are found to have a magmatic origin and are, therefore, orthogneisses and ortho-amphibolites, thus confirming a Narubis Granitoid Complex affinity. The Etusis Formation quartzofeldspathic units have higher cation normalised quartz than the Abbabis Complex, which allows for a distinction between the two.

Trace element ratios (Th/Sc and La/Sc) for the Damaran metasediments show mixing between the more felsic Abbabis Complex and mafic amphibolite dykes from this study and others. The Etusis

Formation shows elevated Th/Sc and La/Sc, which may reflect sediment maturity and heavy mineral concentrations. In contrast, the Khan and Chuos formation display a range of ratios comparable with Abbabis Complex and amphibolite dykes as well as a spread inbetween the two. These Damaran metasediments appear to be sourced from more felsic affinities at the base, such as the Abbabis Complex to more mafic affinities in the Khan and Chuos formations.

The Damaran Granitoids can be considered group I granitoids after McDermott *et al.* (1996). The various granitoids show fractional crystallisation trends with decreasing major element compositions with increasing SiO_2 and Rb/Sr ratios versus Ba and Sr, consistent with plagioclase and biotite fractional crystallisation (McDermott *et al.,* 1996). In addition, Rb/Sr, Ba/Sr and La/Tb versus combined Fe_2O_3 + MgO plots indicate that these granites were a product of biotite dehydration melting that was limited by either the presence of plagioclase or biotite. Additionally, the granites appear to have crystallised under varying conditions during anatexis. SLGs typically crystallised plagioclase to form cumulates (positive Eu anomaly), while the red granites represent more final melts (as termed by Johannes *et al.,* 2003; negative Eu anomaly) that most likely migrated from the original anatexis site to form under typical fractional crystallisation processes. The grey granites as well as the SLGs show variations in cumulate to fractional crystallisation and, therefore, do not always show the same style of crystallisation. These grey granites and SLGs do not always show host rock and leucosome interaction (both palaeosome and leucosome show negative Eu anomalies) with a preferential enrichment of Eu into cumulate plagioclase (leucosome) and depletion in the host lithology (palaeosome).

LILE enrichment relative to HFSE coupled with a depletion of HREE, an enrichment of incompatible elements (Th) with a depletion of Nb and Ta is considered diagnostic of a subduction related metasomatism or continental intraplate magmatism or crustal assimilation. The Abbabis Complex, amphibolite dykes and Damaran granites have this subduction/intra-plate or crustal assimilation signature. Therefore, indicating a Palaeoproterozoic intraplate magmatic arc or crustal assimilation during the emplacement of the amphibolite dykes. Based on geochemistry neither scenario can be concluded. Damaran-aged subduction of the Kalahari Craton beneath the leading edge of the Congo Craton or crustal assimilation during the Pan-African is inferred for the Damaran granitoids. Given these intrusives are granites, both are likely but impossible to distinguish between based on geochemical constraints.

7. Geochronology

7.1 Introduction

Relative timing of geological events, such as intrusive emplacements and metamorphism, was established by means of detailed field work and petrography. Cathodoluminescence (CL) image-guided U-Pb zircon geochronology was used to establish absolute age relationships of magmatic and metamorphic events, which affected the Abbabis Complex, including amphibolites and Damaran granites. Hafnium isotope systematics were additionally employed to provide information about source materials and timing of melt extraction from a hypothetical mantle reservoir. U-Pb geochronology, coupled with Hf isotope geochemistry, provides a more holistic understanding of the evolution of the Damara Belt.

Numerous crystallisation ages have been published for intrusions and various metamorphic events, and a well constrained temporal framework for the formation of granites and basement rocks has been established (see Table 7.1). The amphibolite dykes are less well constrained geochronologically, in comparison to the Damaran granitoids (Longridge *et al.,* 2014). The first chronometric ages for the amphibolite dykes were reported by Longridge *et al.* (2014) who discovered two generations of amphibolite dykes: Palaeoproterozoic dykes associated with the basement lithologies and Pan-African amphibolites thought to be related to the Goas Suite, which is proposed to represent the first magmatic event during the Damara Orogen during the collision of the Congo and Kalahari cratons in a subduction setting (Barnes and Sawyer, 1980). Although, detailed studies exist for the Goas Suite (e.g. Milani *et al.,* 2015), only one study (Longridge *et al.*, 2014), determined U-Pb age constraints for the amphibolite dykes. Considering the scarcity of available U-Pb ages, amphibolite dykes from this study were chosen for age dating. U-Pb zircon ages were used to corroborate previous studies to constrain the relative age relationships of granitoids identified in this study.

Table 7.1 (on following page): Summary of published crystallisation and metamorphic ages for various lithologies of the Damara Belt. Table modified after Longridge (2012), with recent age dates included. Reported ages are magmatic ages except for the metamorphic ages at the bottom of the table. U-Pb "discordia zircon" ages are from upper intercepts between regression and concordia curve. A more extensive summary on geochronological work in the Damara is provided by Milani *et al.* (2015).

Rock Type	Age (Ma)	Method	Reference
Abbabis Complex gneisses and related rocks			
Abbabis Complex gneisses	2056-2044	U-Pb discordia zircon	Longridge (2012)
Abbabis Complex amphibolite	2026.9 ± 2.3	U-Pb titanite	Longridge *et al.* (2014)
Naauwpoort rhyolite	2031-2005	U-Pb inherited zircon cores	De Kock *et al.* (2000)
Abbabis Complex granite gneiss	1925 +330/-280	U-Pb zircon	Jacob *et al.* (1978)
Khan River orthogneiss	1038 ± 58	U-Pb discordia zircon	Kröner *et al.* (1991)
Goas Intrusive Suite diorites and related rocks			
Goas granite	580 ± 30	U-Pb discordia zircon	Allsop *et al.* (1983)
audawib metagabbro	573-570	U-Pb zircon	Milani *et al.* (2015)
Gamikaub diorite	569 ± 8	U-Pb zircon	Milani *et al.* (2015)
Okatuwo diorite	568 ± 3	U-Pb zircon	Milani *et al.* (2015)
Neikhoes metagabbro	567 ± 7	U-Pb zircon	Milani *et al.* (2015)
Oamikaub granodiorite	564 ± 12	U-Pb zircon	Milani *et al.* (2015)
Mon Repos quartz diorite	564 ± 5	U-Pb zircon	Jacob *et al.* (2000)
Palmental diorite	564 ± 55	Rb-Sr whole rock	Mc Dermott (1986)
Okongava diorite	562 ± 6	U-Pb zircon	Milani *et al.* (2015)
Palmental monzonite	558 ± 13	U-Pb zircon	Milani *et al.* (2015)
Okangava diorite	558 ± 8	U-Pb zircon	De Kock *et al.* (2000)
Mon Repos quartz monzonite	558 ± 8	U-Pb zircon	Milani *et al.* (2015)
Oamikaub granite	556 ± 10	U-Pb zircon	Milani *et al.* (2015)
Mon Repos quartz diorite	546 ± 6	U-Pb zircon	Jacob *et al.* (2000)
Rotekuppe granite	543 ± 5	U-Pb zircon	Jacob *et al.* (2000)
Damara amphibolite	557.2 ± 7.4	U-Pb titanite	Longridge *et al.* (2014)
Rotekuppe granite	539 ± 6	U-Pb zircon	Jacob *et al.* (2000)
Okangava diorite	539 ± 10	U-Pb titanite	Jung *et al.* (2002)
Goas granites	535 ± 2	U-Pb discordia zircon	Allsop *et al.* (1983)
Salem-type granites			
Salem-type granite	601 ± 79	Rb-Sr whole rock	Marlow (1983)
Salem-type granite	563 ± 63	Rb-Sr whole rock	Hawkesworth *et al.* (1983)
Salem-type granite	554 ± 17	Rb-Sr whole rock	Kröner (1982)
Salem-type granite	554 ± 33	Rb-Sr whole rock	Downing (1982)
Red granites			
Goanikontes red granite	534 ± 7	U-Pb monazite	Briquet *et al.* (1980)
Palmenhorst Dome red granite	539-536	U-Pb zircon and monazite	Longridge *et al.* (2011)
Leucogranites and grey granites			
Stinkbank leucogranite	549 ± 11	U-Pb zircon	Johnson *et al.* (2006)
Ida Dome grey granite	542 ± 6	U-Pb zircon	Tack *et al.* (2002)
Ida Dome grey granite	526 ± 17	U-Pb zircon	Tack *et al.* (2002)
Palmenhorst Dome leucogranite	526 ± 34	U-Pb discordia zircon	Longridge (2012)
Baukwab leucogranite	525.5 ± 1	Pb-Pb zircon evaporation	Jung *et al.* (1998)
Oetmoed granite	526-516	U-Pb monazite and titanite	Jung *et al.* (2000)
Palmenhorst Dome leucogranite	520-510	U-Pb discordia zircon, monazite	Longridge (2012)
Palmenhorst Dome grey granites	519.1 ± 4.2	U-Pb discordia zircon	Longridge *et al.* (2011)
Palmenhorst Dome leucogranite	434.4 ± 2	U-Pb discordia zircon	Longridge (2012)
Alaskites and mineralised veins			
Goanikontes uraniferous alaskite	508 ± 2	Concordant monazite	Briquet *et al.* (1980)
Goanikontes uraniferous alaskite	509 ± 1	Concordant uraninite	Briquet *et al.* (1980)
Palmenhorst Dome anatectic leucosome	506-508	U-Pb discordia zircon, monazite	Longridge (2012)
Navachab lamprophyre	496 ± 6	U-Pb titanites	Jacob *et al.* (2000)
Navachab Au veins	500 ± 10	U-Pb titanites	Jacob *et al.* (2000)
Navachab Au veins	494 ± 8	U-Pb titanites	Jacob *et al.* (2000)
Metamorphic ages			
Khan River orthogneiss	571 ± 64	U-Pb zircon overgrowth	Kröner *et al.* (1991)
Anatectic granites	540-535	U-Pb zircon, monazite	Longridge *et al.* (2011)
Migmatites and granites	540-530	Sm-Nd garnet whole rock	Jung and Mezger (2003)
Unmigmatised metapelite	525-504	U-Pb monazite, Sm-Nd garnet	Jung and Mezger (2003)
Damara amphibolites	520 ± 6.9	U-Pb zircon overgrowth	Longridge *et al.* (2014)
Anatectic granites	520-510	Sm-Nd garnet	Jung and Mezger (2003)
Migmatite	518 ± 3	U-Pb monazite, Sm-Nd garnet	Jung and Mezger (2003)
Anatectic granites	509-515	U-Pb zircon, monazite	Longridge *et al.* (2011)
Damara amphibolites	493.4 ± 6.4	U-Pb titanite	Longridge *et al.* (2014)

The Abbabis Complex is widely accepted to have a crystallisation age between 2056 and 1925 Ma (Jacob *et al.*, 1978; De Kock *et al.,* 2000; Longridge, 2012; Longridge *et al*., 2014). However, Kröner *et al.* (1991) reported U-Pb discordia upper intercept ages of 1038 ± 58 Ma for migmatised quartzofeldspathic gneisses, which were proposed to represent the gneissic generation age and a northwest extension of the Rehoboth Inlier (Kröner *et al.*, 1991). Recent U-Pb zircon ages of 2056 Ma to 2044 Ma (Longridge, 2012; Longridge *et al*., 2018) confirm a *ca.* 2.05 Ga crystallisation age for the Abbabis Complex and suggest that the *ca.* 1 Ga (Kröner *et al.*, 1991) may represent remnants of the Abbabis Complex crust generated during the 1 to 1.4 Ga Kibaran event (Longridge, 2012). More dating is presented for the Abbabis Complex to supplement existing studies and to add Hf systematics with a focus on distinguishing between metamorphic and magmatic events in order to understand the respective roles of crust formation and reworking.

Several studies suggested that the Etusis Formation was sourced from the Palaeoproterozoic Abbabis Complex (Smith, 1965; Hawkesworth and Marlow, 1983; McDermott *et al.*, 1989; McDermott and Hawkesworth, 1990). Furthermore, a maximum depositional detrital age of *ca.* 2 Ga and a minimum depositional age of 756 ± 2 Ma from zircon dating of the rift-related Oas quartz syenite intrusion were obtained (Hoffman *et al.,* 1996). Whole rock Nd model ages and trace element geochemistry also suggest that source material for the Etusis (and Khan) formations is older than the source material for the upper stratigraphic units of the Swakop Group. An Abbabis Complex provenance for the Etusis Formation is also consistent with similar (*ca.* 2 Ga) model ages for both the Abbabis Complex (Hawkesworth and Marlow, 1983; McDermott *et al.*, 1989; McDermott and Hawkesworth, 1990) and the basal clasts of Abbabis gneisses within the Etusis Formation at the type locality (Smith, 1965). Limited detrital Lu-Hf work (Foster *et al.,* 2015) indicate that the Etusis and Khan formations were both products of recycling of pre-existing crustal components with a Congo Craton affinity and negative εHf values similar to values for inherited zircons proposed to be from the Abbabis Complex. Previously, it has been proposed that the Abbabis Complex has a Congo Craton affinity (Longridge, 2012), further highlighting the genetic link between the Etusis Formation and the Abbabis Complex. Therefore, the distinction between the Etusis Formation and Abbabis Complex is not straightforward due to their similarities in mineralogy, composition, isotopic and age characteristics (Smith, 1965; Hawkesworth and Marlow, 1983; McDermott *et al.*, 1989; McDermott and Hawkesworth, 1990; Kinnaird and Nex, 2007; Miller, 2008; Longridge, 2012; Foster *et al.,* 2015). While U-Pb geochronology in this thesis is expected to yield age results for the Abbabis Complex ages similar to published ages, detrital ages will be used to further evaluate a genetic relationship between Etusis Formation and Abbabis Complex. Lu-Hf isotope systematics will provide additional

insights into the source of the Etusis Formation as a fingerprint of different sources through comparison with existing studies of the Abbabis Complex (Milani *et al.,* 2015; Longridge *et al.,* 2018).

In this study, crystallisation ages were determined from magmatic zircons, and metamorphic overgrowths or overprinted zircons were used to resolve metamorphic events (established in previous Chapters 4 and 5) on ten samples representative of key lithologies within the study area. Samples include various migmatitic gneiss types from the Abbabis Complex, amphibolites, red granite and sheeted leucogranites (SLG; types A and C), in addition to metasediments of the Etusis Formation. U-Pb-Hf isotopic data of samples and standards are provided in Appendix 4. A list of samples, their localities and a description of rock types are provided in figure 7.1 and table 7.2. U-Pb ages are coupled to CL imagery, so that dates can be linked to geologically meaningful events based on specific micro-structures (Corfu *et al.*, 2003). As discussed in previous chapters, red granites were emplaced earlier than the SLGs based on cross-cutting relationships. In addition, since emplacement of the SLGs are closely related to the D2 and D3 events, U-Pb geochronology is used to further explore these temporal relationships.

While a relatively large body of whole-rock Sm-Nd isotope data are available for the Damara Orogen (McDermott; 1986; Seth, 1999; Jung *et al.,* 2001, Jung *et al.,* 2002; Jung and Mezger, 2003; Jung *et al.,* 2004; Ostendorf *et al.,* 2014; Osterhus *et al.,* 2014; Jung *et al.,* 2015; Stammeier *et al.,* 2015; Clemens *et al.,* 2017), zircon Lu-Hf isotopic data are relatively limited. A compilation of Nd isotopic data (Longridge *et al.*, 2018) suggests that there was little generation of new crust during the orogeny. Instead, crustal recycling appears to have played a major role during the collision of the Congo and Kalahari Cratons. Sr-Nd-Sm and trace element whole rock studies on the Abbabis Complex and the overlying Damaran metasediments (McDermott *et al.,* 1989; McDermott and Hawkesworth, 1990) further document that significant crustal growth occurred before 2.5 Ga and after 1 Ga, and that crustal reworking was not accompanied by an increase in crustal mass during the Pan-African Damara Orogen from *ca.* 560 Ma to *ca.* 400 Ma.

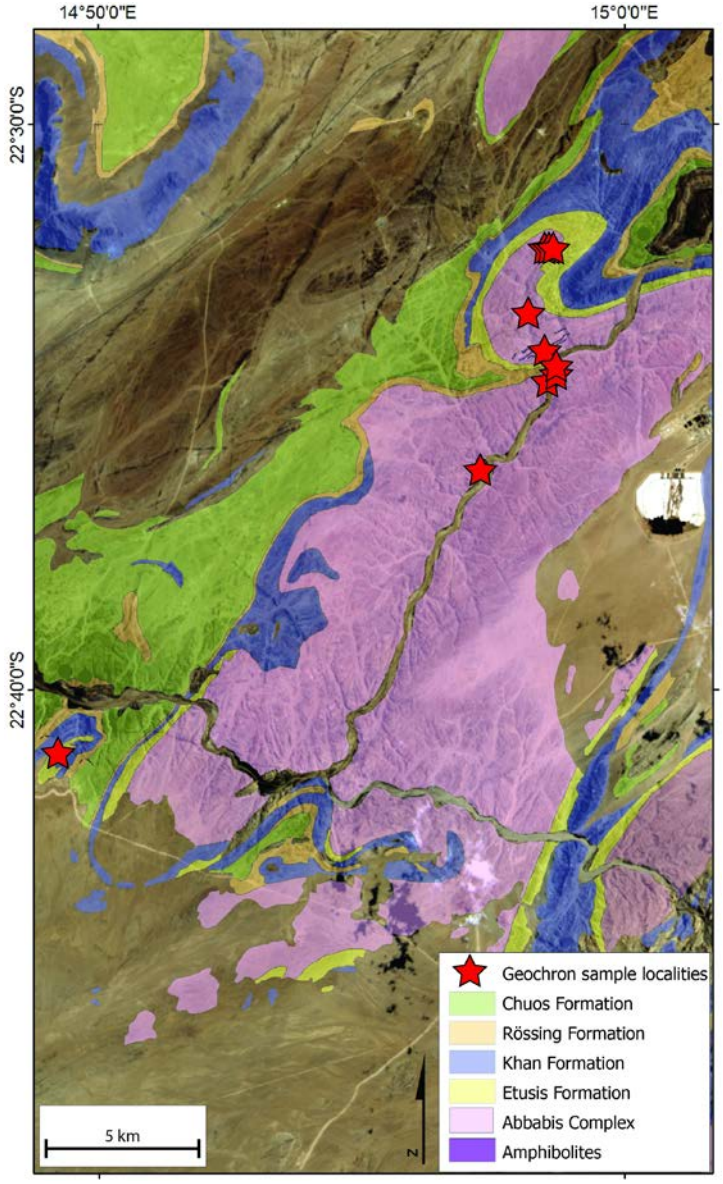


Figure 7.1: Landsat 8 image with overlain simplified geology of the Palmenhorst Dome showing locations of samples selected for geochronology (geology modified after Lehtonen *et al.*, 1995 and Longridge *et al.*, 2011).

Few existing Lu-Hf studies (Milani *et al.,* 2015; Longridge *et al.,* 2018) are consistent with the Sm-Nd isotope data, suggesting that no new crust was generated during the Pan-African Orogeny. A comprehensive zircon Lu-Hf study of the Goas Suite (Milani *et al.*, 2015) yielded consistently negative εHf values, suggesting long-term crustal reworking of the central-western African Orogeny, involving multiple and mixed components. This previous study also could not add to the debate on the involvement of subduction during collision and therefore as a mechanism of magmatism (Milani *et al.,* 2015). However, recent zircon Lu-Hf systematics of the grey granites and Abbabis Complex gneisses (Longridge *et al.,* 2018) suggest that there was no oceanic subduction during collision but rather reworking of the Congo Craton and leading edge of the Kalahari Craton during continent-continent collision. The basement lithologies, often proposed to be an extension of the Rehoboth

Inlier (Miller, 2008), show Congo Craton affinities with Archaean model ages, whereas the Damaran Granitoids showed an invariable Kalahari Craton affinity with model ages younger than 1 Ga (Longridge *et al.*¸ 2018). Furthermore, due to unradiogenic εHf values and Kalahari affinity model ages, it has been proposed that the Goas Suite and the grey granite magmatism was a result of heating and remobilisation of the mafic lower crust of the Kalahari Craton (Longridge *et al.,* 2018). This contrasts with previous assumptions that proposed that the calc-alkaline to tholeiitic Goas Suite was a result of subduction-related magmatism during the collision between the Congo and Kalahari cratons (Barnes and Sawyer, 1980; Miller, 1983; De Kock, 1991). However, unradiogenic εHf values preclude a juvenile magma source (Milani *et al.,* 2018; Longridge *et al.,* 2018).

Table 7.2: A list of samples chosen for for U-Pb geochronology. Sample numbers correspond to the localities in figure 7.1. Samples from outside the field area (Nose Structure, Northern Palmenhorst Dome) are indicated in the table. SLG= sheeted leucogranite.

ID	Lithology Type	Sample description
K05	Abbabis Complex	Musky pink basement microgranite with foliated plagioclase laths that are aligned with a discontinuos biotite foliation. Sample from the Khan River Gorge.
R06		Moderately banded orthogneiss with high contents of K-feldspar and quartz. Fine grained with a discontinuous biotite foliation. Sample resembles arkosic quartzites of the Etusis Formation and contains mafic selvages, or melanosomes, adjacent to orthogneiss in outcrop.
PA02		Fine grained banded grey orthogneiss in the high strain zone. Alternating bands of foliated biotite-rich and plagioclase-rich gneissic layers are convoluted and folded with cross cutting and bedding parallel SLGs and migmatisation.
7.3	Amphibolite dykes	Intensely foliated amphibolite dyke comprising predominantly biotite and amphibole. Forms pronounced mafic selvages within anastamosing SLGs. Cross cut by SLGs and dyke manifests as mafic schollen.
R02		Folded and continuously foliated amphibolite dyke comprising predominantly biotite and amphibole.
1.1	Etusis Formation	Arkosic quartzite with heavy mineralisation along cross bedding. Cross cut by SLG with illmenite accumulations along the boundaries between the Etusis Formation and SLGs. Sample collected from well defined Etusis Formation (no partial melt influence) in the Goanikontes area.
PA01		Sillimanite-quartz-biotite schist interlayered with meta-arkose. Teeth of sillimanite define a prominent NE plunging lineation within the pelitic schist. Is an isolated infolded raft of Etusis Formation within the Abbabis Complex.
K06	Red Granites	Homogeneous Red Granite with a discontinuous foliation defined by plagioclase and minor biotite. Sample taken from Khan River Gorge.
K07	Sheeted leucogranites	Homogeneous and tabular **type C'** SLG (after Nex and Kinnaird, 1995) intruding musky pink basement granites. SLG is granular comprising predominantly graphic quartz and K-feldpsar.
PA03		Coarse-grained pink to red pegmatite with equigranular quartz and granular K-feldspar. **Type E** SLG after Nex and Kinnaird (1995). Sample cross-cuts Abbabis Complex HSZ orthogneiss.

Lu-Hf isotope systematics are used to compare the Abbabis Complex and the Etusis Formation in order to examine a possible genetic link or to explore alternative sources for the Etusis Formation at the time of rifting and deposition *ca.* 1 Ga ago. In addition, this study aims to corroborate previous results of crustal reworking before 1 Ga and to further assess whether crustal reworking was solely responsible or if juvenile magma can be identified in the amphibolite dykes.

7.2 Methodology

Ten samples representing a variety of lithologies from the Palmenhorst Dome, surrounding Damaran metasediments and associated granitoids were selected for U-Pb-Hf isotope ratio analysis (Table 7.2). Samples were crushed into rock aggregates using a carbide-steel jaw crusher at the School of Geosciences (University of the Witwatersrand, Johannesburg). Aggregates were then handpicked to exclude highly weathered or altered aggregates and any aggregates that had visibly been affected by the rock saw. Leucosomes from anatectic granites (samples K06 and PA03) were only selected and their melanosome components discarded in order to date anatectic events. Rock aggregates (250 *ml*) were further processed using the SELFRAG Lab S2.1 at the University of Pretoria for (electrical) fragmentation into individual grains. This method is preferred over traditional mechanical fragmentation methods due to the production of less fines, general preservation of large clean grain sizes and the preservation of the original shape of the mineral (Spener *et al.,* 2014). The procedures carried out for electrical fragmentation were similar to those employed by Spener *et al*. (2014). A summary of the experimental parameters for each sample is given in Appendix 4.A.

After electrical fragmentation, conventional mineral separation methods were used at the Earth Lab in the School of Geosciences (University of the Witwatersrand). Final heavy mineral concentrates were obtained by standard density separation using bromoform and Frantz magnetic separation. Zircons were then handpicked from the heavy mineral separates using a binocular microscope. Picked zircons formed a spread of different morphologies representative of different populations within each sample. Any altered, metamict or cracked zircons were avoided to obtain the best quality zircon grains for dating. Up to 100 zircons per sample were picked, resin mounted and polished. Mounted zircons were imaged using the Cameca SX5-FE Electron microprobe analysis for back-scattered electron (BSE) images at the Microscopy and Microanalysis Unit (MMU) at the University of the Witwatersrand and, in addition, using the TESCAN VEGA3 Scanning Electron Microprobe (SEM) for cathodoluminescent (CL) images at Spectrum at the University of Johannesburg. Classification of zircon internal morphologies, using the guidelines of Corfu *et al.* (2003), into magmatic, metamorphic or inherited was done with the use of the BSE and CL images. For most zircons cores and rims were targeted for separate analysis. U-Pb-Th isotope ratio

measurements were carried out using a 197 nm excimer laser (ASI Resolution SE) coupled to a single collector, magnetic sector ICP-MS (Thermo Fisher Scientific Element XR) in the Earth Lab at the University of the Witwatersrand. A summary of the methods and instrument settings used for LA-IC-PMS are detailed in Appendix 4.B. Zircons from two samples (R02 and R06) were analysed using the same laser as above but coupled to a Nu Plasma II multicollector inductively coupled plasma mass spectrometry (MC-ICP-MS). U-Pb data were reduced using Iolite v. 3.6 and the VizualAge add-in, following guidelines by Petrus and Kamber (2012). Analytical results for the samples selected are presented in Appendix 4.C, analytical results for measured reference standards (91500, Plesovice, GJ-1, Temora 2 and QGNG) are listed in Appendix 4.D and a comparison between measured reference standards and accepted published ages are presented in concordia age plots (for each experiment run) in Appendix 4.E. Reduced data were graphically interpreted using IsoplotR of Vermeesch (2008), an update and extension of the software Isoplot of Ludwig (2003). Concordia ages and regression ages were calculated using IsoplotR and errors are reported as 2 standard errors. York (1969) regression ages were calculated using IsoplotR's built-in algorithms (Vermeesch, 2008). Only upper intercept ages were considered, following the recommendations of Mezger and Krogstad (1997).

Lu-Hf isotopic analysis was performed on all samples using the same zircon age-dated spots that displayed less than 10% discordance. Analysis of Lu-Hf isotopic ratios were performed at Spectrum at the University of Johannesburg using the LA-MC-ICP-MS (see above). Analytical procedures and results are given in Appendix 5.A and 5.B (respectively), along with the respective U-Pb ages. In addition, analytical results for the measured standards (Temora 2, Mud Tank and LV11) are listed in Appendix 5.C as well as accuracy and precision testing of these standards against accepted published $^{176}Hf/^{177}Hf$ ratios are illustrated in Appendix 5.D. Epsilon Hf (εHf) values at the time of crystallisation were calculated using the following formula (e.g. Kinny and Maas, 2003),

$$\varepsilon_{Hf(t)} = \left[\frac{\left(^{176}Hf/^{177}Hf\right)_{sample}}{\left(^{176}Hf/^{177}Hf\right)_{CHUR}} - 1\right] \times 10^4$$

$^{176}Hf/^{177}Hf$ ratios were calculated using

$$^{176}Hf/^{177}Hf_{(t)} = \left(^{176}Hf/^{177}Hf\right)_0 - \left(^{176}Lu/^{177}Hf\right)_0 * \left(e^{\lambda t} - 1\right)$$

Here, λ represents the ^{176}Lu decay constant of 1.86 x 10^{-11} y^{-1} (Scherer *et al.,* 2001; Söderlund *et al.,* 2004), *t* represents the elapsed time in Ma. Present day $^{176}Hf/^{177}Hf$ and $^{176}Lu/^{177}Hf$ values of 0.282785 and 0.0336 (Bouvier *et al.,* 2008) were used for Chondritic Uniform Reservoir (CHUR). Two-stage Depleted Mantle (DM) model ages were calculated using the following formula

$$Hf\ T_{DM} = \frac{1}{\lambda} \times ln\left[\frac{\left(^{176}Hf/^{177}Hf\right)_{T0} - \left(^{176}Hf/^{177}Hf\right)_{DM}}{\left(^{176}Lu/^{177}Hf\right)_{T0} - \left(^{176}Lu/^{177}Hf\right)_{DM}} + 1\right] + Age\ (Ma)$$

Here, DM $^{176}Hf/^{177}Hf$ values were determined by the $^{176}Hf/^{177}Hf(t)$ formula above using $^{176}Hf/^{177}Hf_{(0)}$ and $^{176}Lu/^{177}Hf$ values of 0.28325 and 0.0384 similar to those used in Longridge *et al.* (2018), respectively. An average crustal $^{176}Lu/^{177}Hf$ value of 0.0113 (for the mafic amphibolites; parameters used in Milani *et al.,* 2015) and 0.15 (for the felsic lithologies) after Rudnick and Gao (2003) and Griffin *et al.* (2002) was utilised for calculating the $^{176}Lu/^{177}Hf$ value of the rock hosting the zircons. Two stage DM model ages were calculated using the same standards utilised by Longridge *et al.* (2018) in order to compare the model ages.

7.3 U-Pb Geochronology Results

Descriptions of morphology and types of zircons from CL imagery and results from LA-ICP-MS U-Pb geochronology for the selected ten samples are outlined in this section. In general, the homogenous and convolute zircon types, classified here as metamorphic domains, typically show a higher degree of discordance.

7.3.1 Abbabis Complex

Three samples, K05, R06 and PA02, were chosen from the Abbabis Complex and include microgranite, banded paragneiss and foliated orthogneiss. Approximately 30 to 40 spots were analysed for each sample.

CL description and interpretation of zircon domains

Overall, the zircons in these samples are euhedral to subhedral and generally stubby in morphology (Fig. 7.2.A; Fig. 7.3.A; Fig. 7.4.A). The zircons show a degree of rounding and many tips have been corroded. Both magmatic and metamorphic zircons are present with few examples of inheritance. A bright rim of new zircon growth is present throughout most the samples. Sample R06 displays the most homogeneous internal morphologies (Fig. 7.3.A).

Sample K05, a basement granite, shows a range in zircon sizes from ± 100 µm to 350 µm with euhedral to subhedral morphologies (Fig. 7.2.A). Some grains show a great degree of rounding and appear as anhedral crystals. These grains, since they were extracted from a granite, may be inherited from a sedimentary source or the rounding may be due to chemical corrosion. CL imagery reveals a distinctly magmatic zircon type (Fig. 7.2.A, zircons 2, 3, 4 and 6) with varying widths of oscillatory zoning. Thin bands less than 20 µm and thicker bands of up to 50 µm are present. Zoning varies from symmetrical to asymmetrical. Generally, the cores display broader banding than the outer zones. Oscillatory zoning, however, is commonly disrupted by convolute banding due to metamorphism (Ashwal *et al.,* 1999; Hoskin and Black, 2000; Connelly, 2001; Schaltegger *et al.,* 2002;

Corfu *et al.*, 2003). Some zircons show distinct magmatic oscillatory zoning that has homogenised bulbous embayments, indicating metamorphism, in the core with an oscillatory zoned rim (Fig. 7.2.A, zircons 2, 4 and 7). Homogeneous metamorphic embayments cross-cut zoning and form characteristically darker and dull metamorphic rims around magmatic cores, which have corroded the edges of these cores, resulting in truncated ghost oscillatory zoning (Fig. 7.2.A, zircons 5 and 9). Metamorphic domains also appear as convolute zoning (Fig. 7.2.A, zircons 1, 5, 6 and 7) (Ashwal *et al.,* 1999; Hoskin and Black, 2000; Connelly, 2001; Schaltegger *et al.,* 2002; Corfu *et al.*, 2003) and show patchy and mosaic textures (Fig. 7.2.A, zircons 1, 5, 6 and 7) that are often homogenised in the core of zircon grains. Thin, bright overgrowths may represent the last geological event seen from CL imagery. These rims are less than 10 µm in thickness and seldomly enclose the entire zircon with just fractions along the edge, and sometimes cracks, representing new zircon growth.

Zircons from the foliated orthogneiss, sample R06, display euhedral to subhedral tabular morphologies. Zircons are more metamict and contain fractures appearing more commonly in the magmatic than in the metamorphic domains. The zircons display brittle and were easily fragmented during picking. These zircons range from ± 200 µm to 500 µm, have corroded tips and are typically more elongate than those from the previously described sample (Fig. 7.3.A). The internal make-up is typically less complicated and shows more homogeneous metamorphic domains with faint, remnant magmatic zoning. Metamorphic zircons constitute most of the zircons picked in this sample with a few examples of faintly oscillatory zoned magmatic zircons. Ghost textures of remnant magmatic zoning (Fig. 7.3.A, zircons 1 to 4 and 6 to 9) are observed in these metamorphic zircons. These textures are seen throughout, however, they are more common where there is less homogenisation. Zircons have faint alternating bands of light and dark that vary in shape and size. The zoning is relatively broad, which may be a result from the homogenisation during metamorphism (Ashwal *et al.,* 1999; Hoskin and Black, 2000; Connelly, 2001; Schaltegger *et al.,* 2002; Corfu *et al.*, 2003) and typically asymmetric. Homogeneous metamorphic zircons are dark and dull in comparison to the remnant magmatic zonation. When metamorphic embayments are present they truncate highly convoluted zonation creating a patchy texture, which could be the result of early stage recrystallisation (Rubatto, 2017). Most age dated spots in this sample show more than 10% discordance (Fig. 7.3.A). Different from sample K05, no bright rims are seen around these zircons, although a single example of a fracture being filled with bright new precipitation of zircon is present (Fig. 7.3.A, zircon 5).

Sample PA02, a banded paragneiss, yielded more subhedral grains (Fig. 7.4.A) with respect to other samples. The zircons are typically ± 150 µm to 200 µm in length and vary between elongate to

stubby with many showing fracturing and cracks in metamict zircons (Fig. 7.4.A, zircon 8). Both zircon types show magmatic cores with bright rims. This sample has a mix of magmatic and metamorphic grains and the internal microstructures are generally more complicated than what is observed for the previous Abbabis Complex samples. The magmatic cores show faint to distinct asymmetric oscillatory zoning (Fig. 7.4.A, zircons 1, 2, 6 and 11), which is mainly quite thin (10 – 20 μm), indicating possible recrystallisation (Rubatto, 2017). Zoning thickness is varied and typically more random when the zoning is broader (Fig. 7.4.A, zircon 7). The metamorphic zircons also show oscillatory zoning. However, theses zircons tend to show convoluted (Fig. 7.4.A, zircon 4), patchy (Fig. 7.4.A, zircons 1 and 3) mosaic and chaotic zoning and are more complicated. Another zircon type shows homogenisation of previous zoning (Fig. 7.4.A, zircon 10). Metamorphic bulbous embayments (Fig. 7.4.A, zircon 10) are common in these homogenous domains and truncate the remnant magmatic zoning with dark metamorphic overgrowths around the magmatic core (Ashwal *et al.,* 1999; Hoskin and Black, 2000; Connelly, 2001; Schaltegger *et al.,* 2002; Corfu *et al.,* 2003; Rubatto, 2017). Ghost textures are also present as faint zonation within homogenised zones. A bright rim is seen along the edges of zircons along both magmatic and metamorphic zircons.

U-Pb LA-ICP-MS geochronology

The Abbabis Complex samples yielded no concordia ages and upper intercept ages were used to determine crystallisation and metamorphic ages for each sample.

The Abbabis Complex basement granite, sample K05, yielded mostly discordant ages; these were used to construct regression lines intersecting the concordia curve. Magmatic and metamorphic ages were regressed separately. The regression of the data for the magmatic cores yielded an upper intercept age of 2071.39 ± 5.39 Ma and a lower intercept age of 815.2 ± 13.8 Ma (n= 12, MSWD= 7.5; Fig. 7.2.B). Obvious outliers were removed from the regression to improve errors. Less than 5 measurements were concordant and therefore a concordia age was not calculated. Metamorphic rims and convolute cores yielded an upper and lower intercept age of 2062.18 ± 5.75 Ma and 610.4 ± 12.1 Ma, respectively (n= 12; MSWD= 12; Fig. 7.2.C). The magmatic domains are typically more concordant than the metamorphic domains. Sample K05 has a dominant population of grains, from both the magmatic and metamorphic domains, with Th/U of 1 to 0.5, consistent with a magmatic origin (Fig. 7.5; Rubatto and Gebauer, 2000). Some outliers from metamorphic domains with Th/U <0.1 are likely metamorphic in origin.

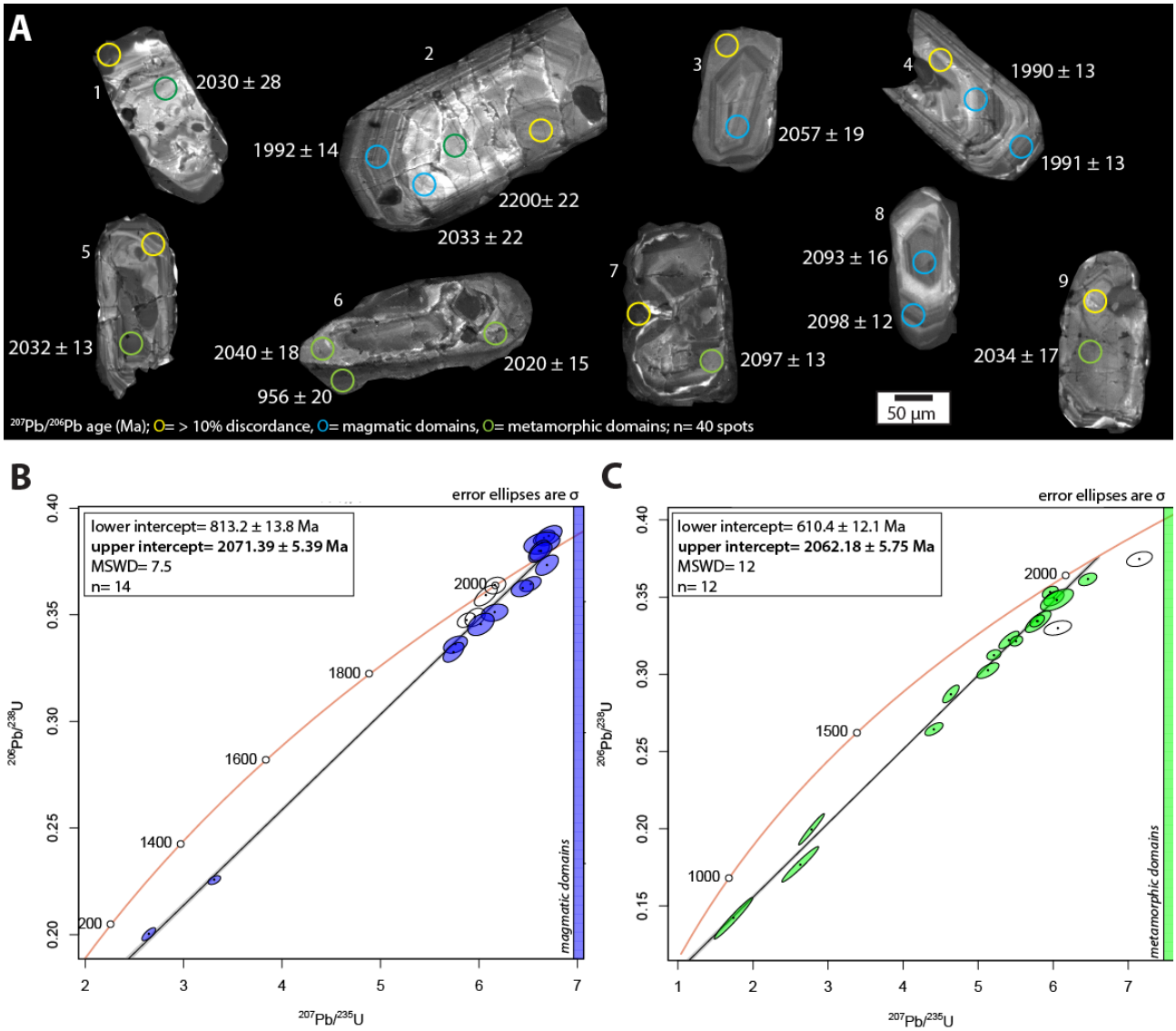


Figure 7.2: (A) CL images of selected zircons with spot placement and $^{207}Pb/^{206}Pb$ ages (only near-concordant data with < 10% discordance shown). Concordia age plots of (B) magmatic and (C) metamorphic domains for a basement granite sample (K05) from the Abbabis Complex. Colourless error ellipses were excluded from the regression calculations. MSWD= Mean Square of Weighted Deviates.

U-Pb measurements of zircon for sample R06, an Abbabis Complex banded orthogneiss, yielded discordant measurements for both the magmatic and metamorphic populations. Negatively discordant and highly discordant (> 30 to 35% discordance) ages that did not fit the obvious regression trends were not considered. A regression through the magmatic domains yielded an upper intercept age of 1998.6 ± 14.9 Ma and a lower intercept age of 726.5 ± 30 Ma (n= 8, MSWD= 8; Fig. 7.3.B). The regression showed more dispersed U-Pb data than the previous Abbabis Complex sample. Outliers were removed from the regression calculation. An upper intercept age of 1985.2 ± 12.8 Ma (Fig. 7.3.C) was established for the metamorphic rims with a lower intercept of 762.1 ± 15.8 Ma (n=16; MSWD= 3.3). Only one outlier was excluded from the regression as the magmatic data points were more tightly aligned along the regression curve. The majority of Th/U ratios, both from

magmatic and metamorphic domains, for sample R06 plot at or below values of 0.1. These ratios from magmatic and metamorphic populations are not distinct from one another despite the low Th/U ratios.

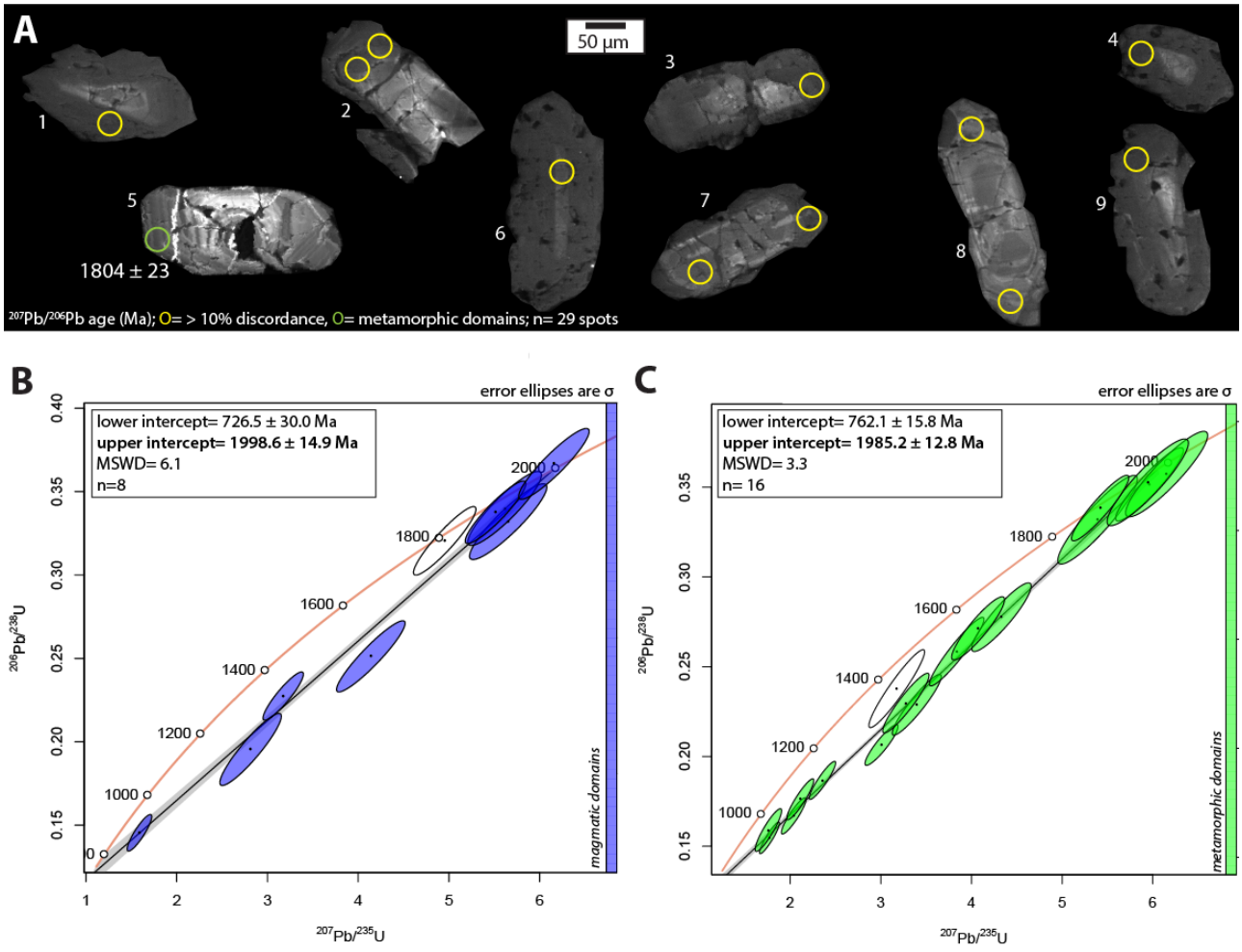


Figure 7.3: (A) CL images of selected zircons with spot placement and $^{207}Pb/^{206}Pb$ ages (only near-concordant data with < 10% discordance shown). Concordia age plots of (B) magmatic and (C) metamorphic domains for an orthogneiss sample (R06) from the Abbabis Complex. Colourless error ellipses were excluded from the regression calculations. MSWD= Mean Square of Weighted Deviates.

Sample PA02, a finely banded grey orthogneiss from the high strain zone, displays similar degrees of discordance as the other samples from the Abbabis Complex. Highly discordant measurements and negatively discordant measurements were not considered for age calculation for both magmatic and metamorphic domains. Upper and lower intercept ages for the magmatic cores are 2002.5 ± 13.9 Ma and 411 ± 214 Ma, respectively (n= 7, MSWD= 2.1; Fig. 7.4.B). Metamorphic ages form a regression with an upper intercept of 2044.25 ± 6.31 Ma and a lower intercept age of 550.4 ± 15.8 Ma (n= 14, MSWD= 4; Fig. 7.4.C). U-Pb isotopic ratios for metamorphic grains are generally more discordant and form a more reliable regression than the magmatic results.

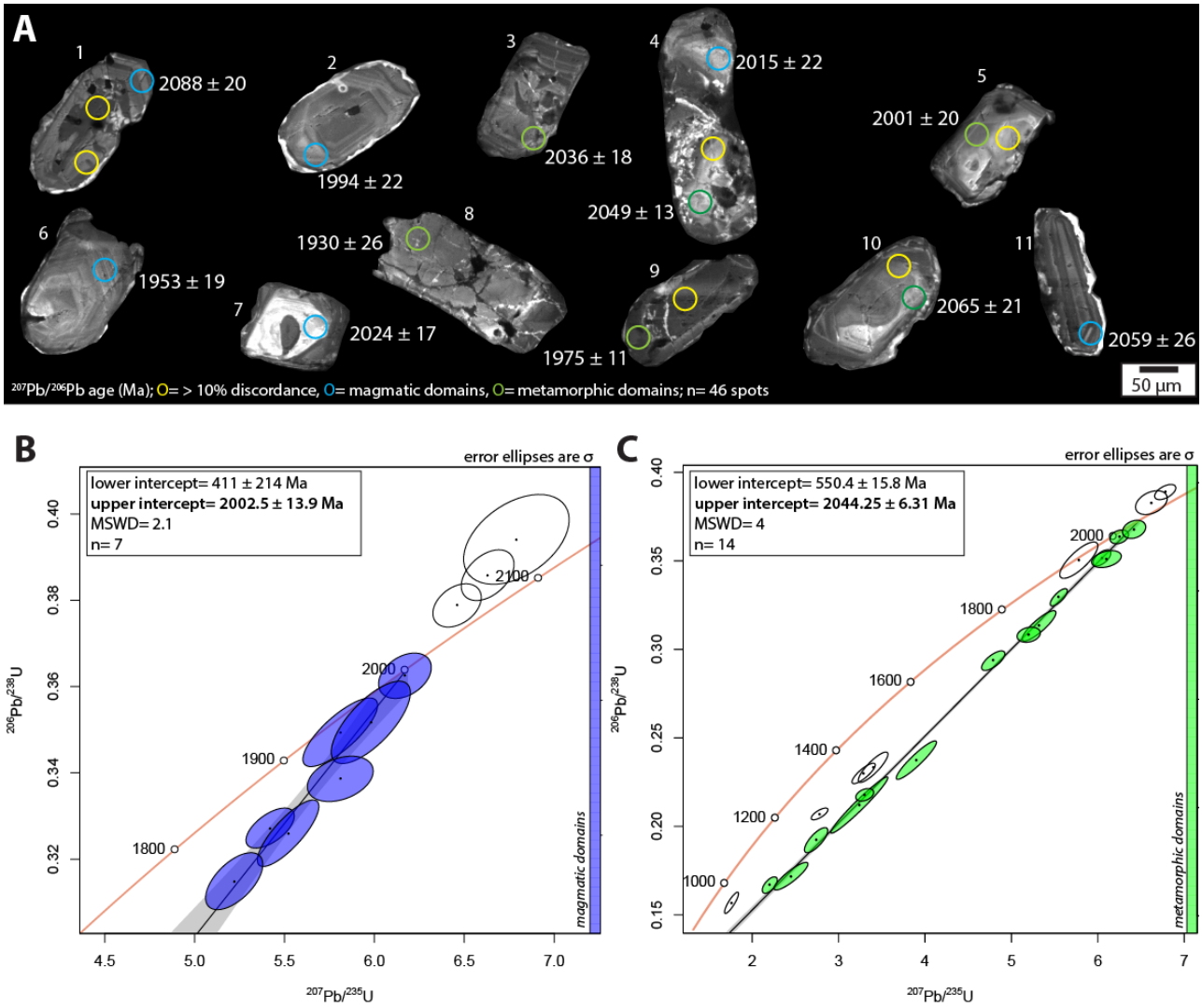


Figure 7.4: (A) CL images of selected zircons with spot placement and $^{207}Pb/^{206}Pb$ ages (only near-concordant data with < 10% discordance shown). Concordia age plots of (B) magmatic and (C) metamorphic domains for a grey orthogneiss sample (PA02) from the Abbabis Complex. Colourless error ellipses were excluded from the regression calculations. MSWD= Mean Square of Weighted Deviates.

The majority of Th/U ratios (>0.1) for zircons from the grey orthogneiss (sample PA02; Fig. 7.5) suggest a magmatic origin (Rubatto and Gebauer, 2000). The magmatic domains have higher Th/U ratios than the ratios from the metamorphic domains, but the populations are not distinct from one another. The Th/U ratios for the magmatic domains show a tighter cluster than the metamorphic domains. Some metamorphic domains have Th/U ratios below 0.1 however, most of the ratios are higher than 0.1.

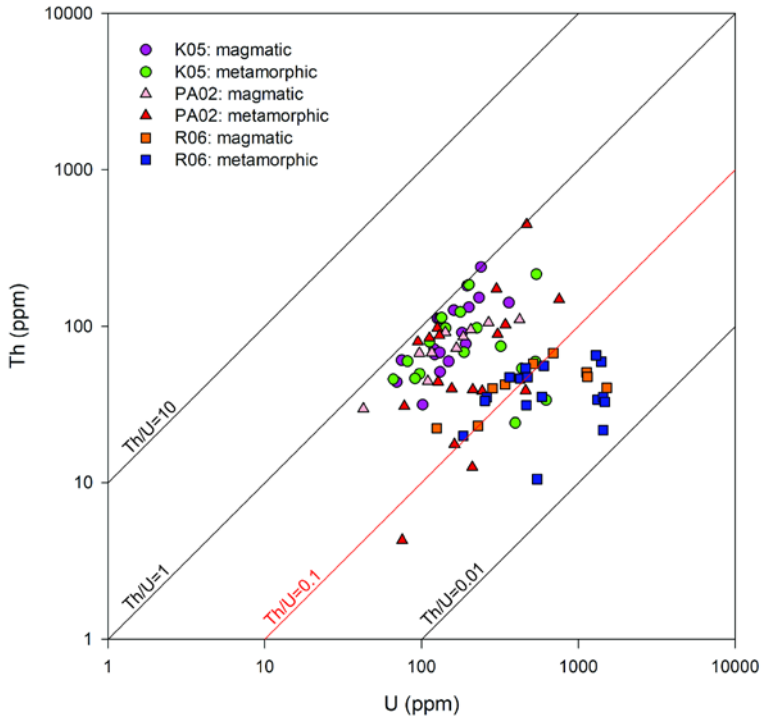


Figure 7.5: Th/U ratios for zircons from various lithologies of the Abbabis Complex. Line indicate constant Th/U ratios where Th/U ratios below 0.1 may be considered to indicate metamorphic zircon growth (Rubatto and Gebauer, 2000).

7.3.2 Amphibolites

The amphibolite samples produced less zircons and generally yielded highly discordant ages that were discarded. Two samples of amphibolite dykes were chosen for U-Pb analysis, namely 7.3 and R02, both of which had been subjected to partial melting. 20 to 35 spots were analysed for each sample.

CL description and interpretation of zircon domains

Samples 7.3 (Fig. 7.6.A) and R02 (Fig. 7.7.A) have distinctly homogeneous zircons that are generally dark and dull in reflectance. Zircons are generally euhedral to anhedral and are often acicular in shape. These elongate zircons are generally more friable and brittle than most other samples, and many broke in half when handled for picking. Therefore, rounding and fragmented zircons are expected and may not represent a sedimentary origin. Mainly metamorphic zircons appear to be present. However, faintly zoned magmatic zircons are also observed. Few examples of inheritance were found using CL imagery.

Amphibolite 7.3 underwent the most partial melt and in outcrop appears as rafted schollen within SLG partial melt. The zircons range in size between ±150 µm to 250 µm, with the long axis up to 6 or 7 times longer than the short axis (Fig. 7.6.A). Most zircons appear to be metamorphic based on homogenous domains and chaotic zoning, however, there are magmatic zircon types with faint

oscillatory zoning and ghost zoning. The oscillatory zoning is asymmetrical, and the thickness varies throughout the sample. These magmatic zircons are generally more euhedral than the metamorphic zircons, which commonly have corroded tips. Ghost zoning is seen as relicts of magmatic zoning of grains or as isolated rafts within and truncated by the homogenous metamorphic embayments. In high grade metamorphic rocks, faint oscillatory zoning can commonly be found in near-homogeneous metamorphic domains (Rubatto, 2017). Metamorphic domains yield concordant ages (Fig. 7.6.A). These metamorphic domains also contain bright inclusions. A single inherited grain was located with bright magmatic zoning and produces an older age than the rest of the population. The inherited grain (Fig. 7.6.A, zircon 8) shows oscillatory zoning. Minor bright partial rims are observed on select zircons and represents new zircon growth possibly associated with partial melt (Rubatto, 2017). Therefore, there are three geological events observed in CL imagery: crystallisation of zircon with subsequent metamorphic recrystallisation, and lastly new precipitation of zircon growth along the rim.

Zircons within sample R02 are similar in shape and size when compared to amphibolite 7.3, with euhedral to subhedral acicular zircons that range in size from ± 100 µm to 250 µm. These zircons are elongate and display more fragmented and stubbier morphologies than sample 7.3 (Fig. 7.7.A). Faint oscillatory zoning is present in magmatic zircons. However, magmatic zoning is less common. Zoning is variable in thickness, although predominantly these magmatic domains appear as cores that have been recrystalised by metamorphic zircon growth resulting in thinning and disturbed magmatic zoning. Magmatic zoning is truncated by bulbous embayments of homogeneous metamorphic zircon. This can be seen where homogeneous dark metamorphic domains disrupt and truncate primary zoning. Bright ghost textures are seen within homogenous metamorphic domains.

U-Pb LA-ICP-MS geochronology

The amphibolite dykes yielded mostly metamorphic zircons with concordant ages. The two samples have a wide spread of age clusters along the concordia plot.

Concordia U-Pb age dates, for sample 7.3, yielded a population between 600 Ma and 500 Ma of both magmatic and metamorphic ages with a single inherited zircon ($^{207}Pb/^{206}Pb$ age of 1053 Ma) (Fig. 7.6.A and B). A concordia age for magmatic cores was established to be 550.48 ± 0.85 Ma (n= 6, MSWD= 3.4; Fig. 7.6.C). Outliers defining a smearing towards younger ages were excluded from the concordia calculation.

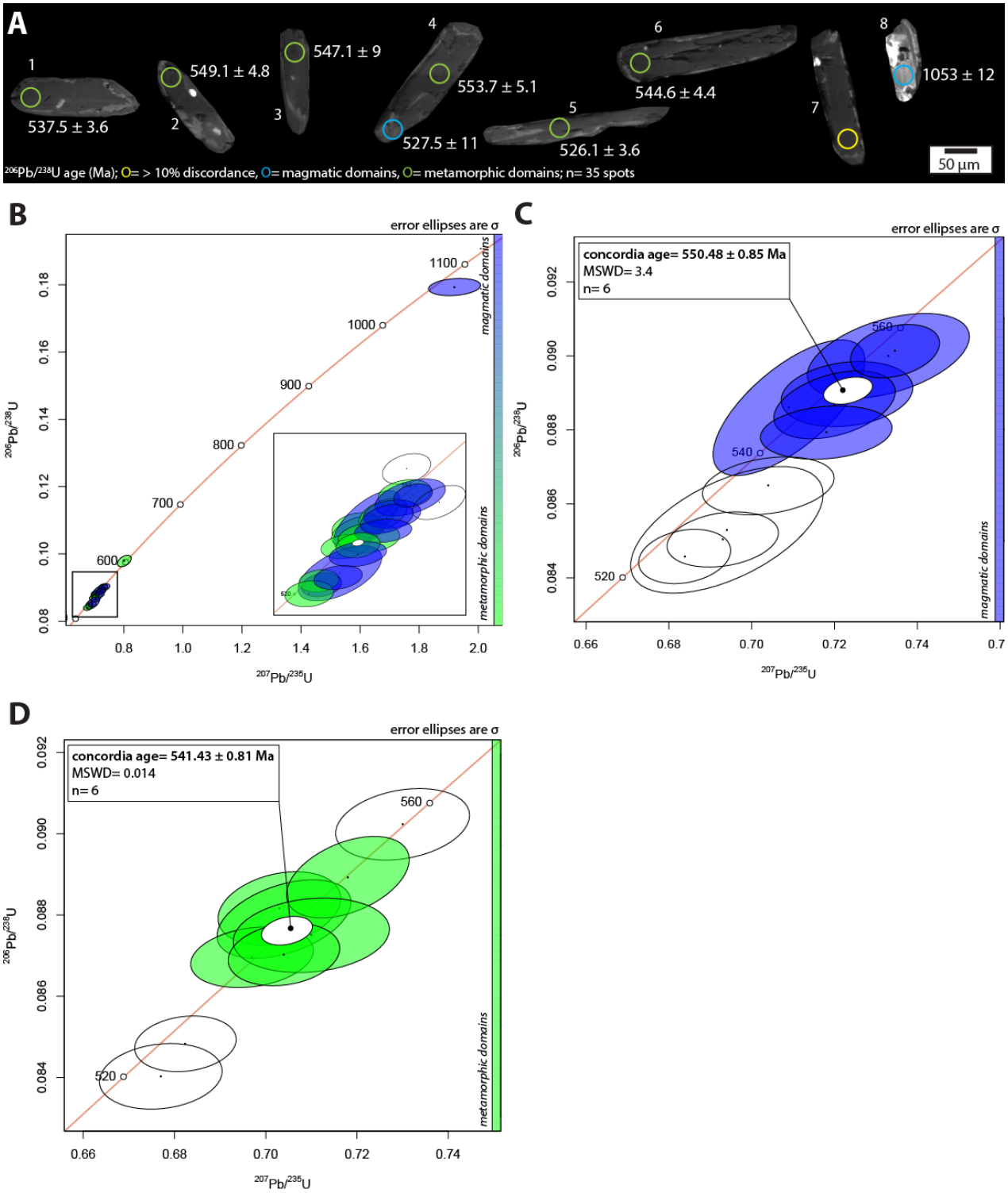


Figure 7.6: (A) CL images of selected zircons with spot placement and $^{206}Pb/^{238}U$ ages (only near-concordant data with < 10% discordance shown). Concordia age plots of (B) all domains (C) magmatic and (D) metamorphic domains for amphibolite sample 7.3 from the amphibolites. Colourless error ellipses were excluded from the concordia calculations as they represent outliers. MSWD= Mean Square of Weighted Deviates. Inset in lower right of figure (B) shows a detailed plot of the *ca.* 600 Ma to 500 Ma population of both magmatic and metamorphic ages.

A younger metamorphic concordia age of 541.43 ± 0.81 Ma (n= 6, MSWD= 9) was established for the metamorphic domains (Fig. 7.6.D). Obvious outliers were excluded from the calculation to

improve precision. The zircon Th/U ratios of >0.1 indicate a magmatic origin for sample 7.3. Both magmatic and metamorphic domains are clustered together and have Th/U ratios of approximately 10. Outlying metamorphic domain Th/U ratios tend towards Th/U= 1, which is not atypical of high-temperature metamorphism (Rubatto, 2017 and references within).

Amphibolite R02 yields near-identical metamorphic and magmatic ages, similar to what is observed for sample 7.3. Generally, individual dates are highly discordant (> 70 - 80%), and do not align along the major regression curve. In order to obtain precise pooled ages obvious outliers among the magmatic and metamorphic populations were excluded (Fig. 7.7.A and B).

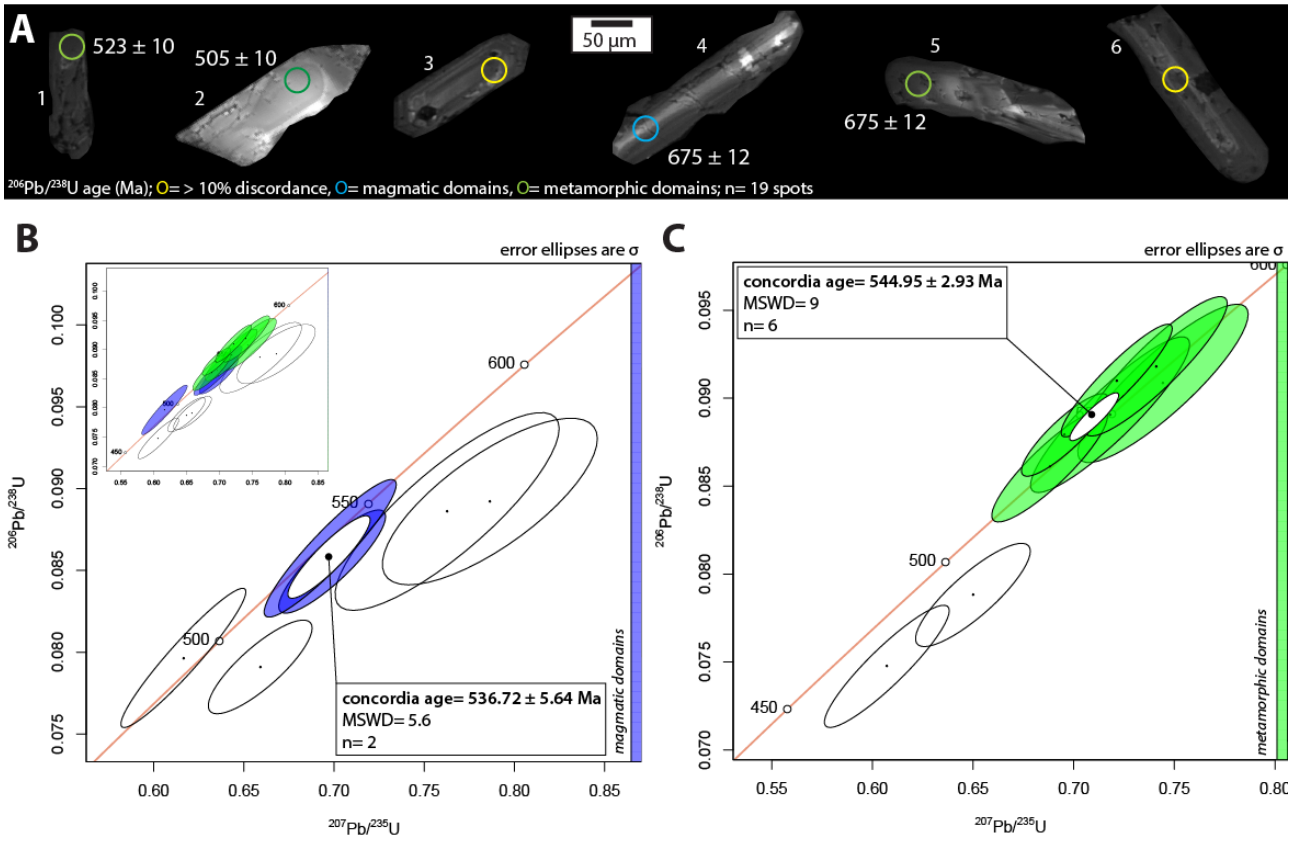


Figure 7.7: (A) CL images of selected zircons with spot placement and $^{206}Pb/^{238}U$ ages (only near-concordant data with < 10% discordance shown). Concordia age plots of (B) magmatic and (C) metamorphic domains for amphibolite sample R02. Colourless error ellipses were excluded from the concordia calculations. MSWD= Mean Square of Weighted Deviates. Inset in upper left of figure (B) shows closely related magmatic (blue) and metamorphic (green) events around 550 Ma.

The magmatic population comprises only two individual dates and therefore interpretation of the concordia age of 536.72 ± 5.64 Ma (n= 2, MSWD= 5.6) could be incorrect or may not represent a magmatic age as it is younger than the metamorphic age. Therefore, this concordia age is not considered. Six individual measurements from metamorphic domains combine to a concordia age of 544.95 ± 2.93 Ma (n= 6, MSWD= 9; Fig. 7.7.C). Considering analytical uncertainties metamorphic

and magmatic concordia ages are indistinguishable, however the magmatic age is less reliable in this instance.

Amphibolite sample R02 shows zircon Th/U ratios of 1 to 10 (Fig. 7.8) with a wide spread of Th/U measurements for both magmatic and metamorphic domains. These populations are not distinct from one another and show similar Th/U ratios.

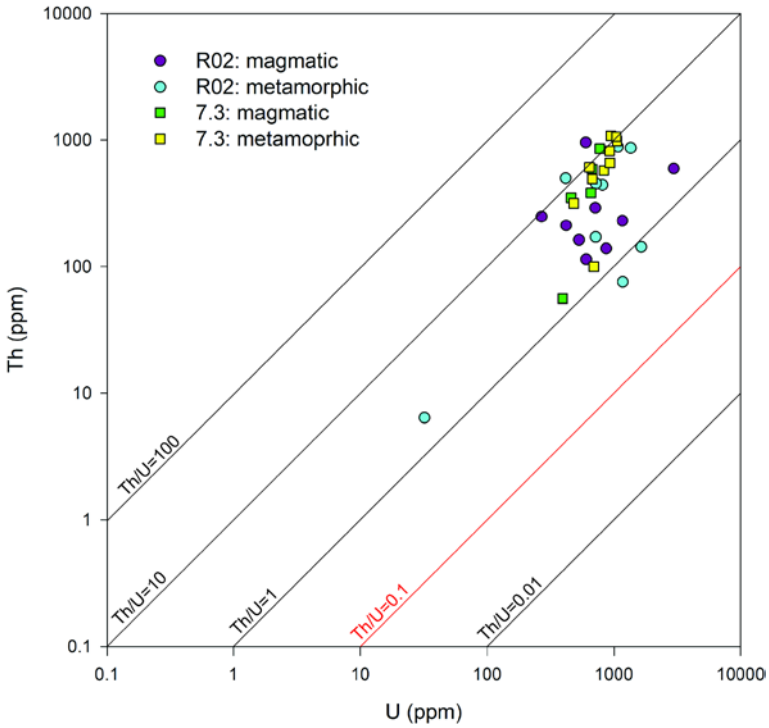


Figure 7.8: Th/U ratios for zircons from the amphibolites. Line indicate constant Th/U ratios where Th/U ratios below 0.1 may be considered to indicate metamorphic zircon growth (Rubatto and Gebauer, 2000).

7.3.3 Etusis Formation

Two samples, namely an arkosic quartzite (sample 1.1) and a pelitic schist with sillimanite porphyroblasts (PA01; Table 7.2), were selected for U-Pb geochronology from the Etusis Formation. Seventy-eight (sample 1.1) and 26 spots were targeted for U-Pb age determination (sample PA01).

CL description and interpretation of zircon domains

Detrital zircons form the Etusis Formation are typically subrounded. Some zircons still preserve their elongate shape and only display corroded tips. In general, zircon grains are stubby and show similarities in internal morphologies to zircons extracted from the Abbabis Complex. Both magmatic and metamorphic zircons are present, although magmatic zircons with early signs of homogenisation and convoluted zoning because of metamorphism, (Ashwal *et al.,* 1999; Hoskin and

Black, 2000; Connelly, 2001; Schaltegger *et al.,* 2002; Corfu *et al.*, 2003) appear more abundant. Under the binocular microscope zircons were clear and robust with very little signs of fragmentation. Inherited cores were seen to be surrounded by bright rims.

Sample 1.1, an arkosic quartzite, yields largely subangular to subrounded and elongate grains, with sizes ranging from 100 to 300 μm. CL imagery displays a distinctly magmatic population (Fig. 7.9.A, zircons 4, 7 and 8) with prominent oscillatory zoning. Zoning is variable in thickness, although it is most commonly thin (<10 μm) when primary magmatic zoning is preserved. Zoning can thicken when zircons show signs of homogenisation. Zoning is typically asymmetric. Fractures are seen in the magmatic domains predominantly. Metamorphic domains are present within sample 1.1 and they cross-cut and truncate secular zoning. Bulbous embayments of homogeneous zircon (Fig. 7.9.A zircons 1, 2, 3, 5 and 6) typically convolutes remnant magmatic zoning with patchy textures indicating subsolidus metamorphism and the early stages of recrystallisation (Rubatto, 2017). Ghost textures are common as rafts within the metamorphic domains (Fig. 7.9.A, zircon 9). Metamorphic overgrowths enclose the magmatic cores and are generally dark and dull. Irregular shapes of the domains are common, and the ages are typically discordant, although concordant metamorphic dates are present too. Whether rounding of zircon grains took place after metamorphism is difficult to ascertain, although new zircon formed after sedimentary deposition, as bright rims of new zircon coat the rounded edges (Fig. 7.9.A, zircon 1) enclosing dark metamorphic overgrowth domains and truncating previous magmatic zonation directions (Fig. 7.9.A, zircon 9).

The sillimanite-biotite pelitic schist (sample PA01) shows smaller zircon grains than sample 1.1 (Fig. 7.10.A), with grains ranging in size from 80 to 200 μm. Zircon grains from PA01 are subangular to subrounded, but typically more rounded than sample 1.1. Brecciation of smaller zircons is observed. Symmetric magmatic zoning (Fig. 7.9.A, zircons 4, 6 and 7) is present in the cores of zircons and is usually thin (<10 μm). Truncated oscillatory zoning is also present in and around metamorphic cores (Fig. 7.9.A, zircon 2 and 3). Internal morphologies for these metamorphic zircons are more complex with few grains showing just primary magmatic zoning. Most grains display chaotic (Fig. 7.9.A, zircons 1, 2, 3, 5 and 9) or homogeneous textures (Fig. 7.9.A, zircons 4 and 8) that are characteristic of metamorphic zircons (Corfu *et al.,* 2003). The mosaic texture is a possible result of earlier stages of homogenisation and recrystallisation of the zircon by metamorphism (Rubatto, 2017). Chaotic zoning appears as patchy rafts are surrounded by dark homogeneous recrystallised zircon growth as ghost textures. Contacts between the metamorphic and magmatic domains are irregular and truncate and dismember primary zonation leaving behind ghost textures of primary zoning. Fractures are filled with homogenous metamorphic zircon and cross-cut magmatic cores.

U-Pb LA-ICP-MS geochronology

Detrital zircon age spectra for the Etusis Formation display two distinct peaks, namely at *ca.* 1 Ga and 2 Ga. Concordia age plots show that zircons have discordant ages (Fig. 7.8.B and Fig. 7.9.B). Highly discordant ages (> 10%) were removed for the relative density probability plots and histograms.

A concordia plot (Fig. 7.8.B) of the arkosic quartzite (sample 1.1) confirms the two populations (1 and 2 Ga) that are prevalent in the Etusis Formation quartzites. Histogram and probability density plots of sample 1.1 (Fig. 7.11.A) further reveal that there are two peaks in the detrital signal around 1020 Ma and 2015 Ma with the *ca.* 1 Ga (1000 to 1020 Ma bin) population exhibiting the highest peak and the largest population. The *ca.* 2 Ga population shows a peak between 2000 to 2020 Ma. Most metamorphic domains yield $^{207}Pb/^{206}Pb$ ages of *ca.* 1 Ga, indicating metamorphic overprinting and/or new growth of zircon. $^{207}Pb/^{206}Pb$ ages of *ca.* 2 Ga are commonly found within remnant magmatic and primary zoned domains. Ages belonging to both populations are often observed within the same zircon, for example zircon 6 (Fig. 7.9.A). Th/U ratios (0.1-1.0) indicate a magmatic origin (Fig. 7.12). Magmatic and metamorphic domains are widespread and show distinction between the two, however, the magmatic domains show slightly elevated Th/U ratios in comparison to the metamorphic domains.

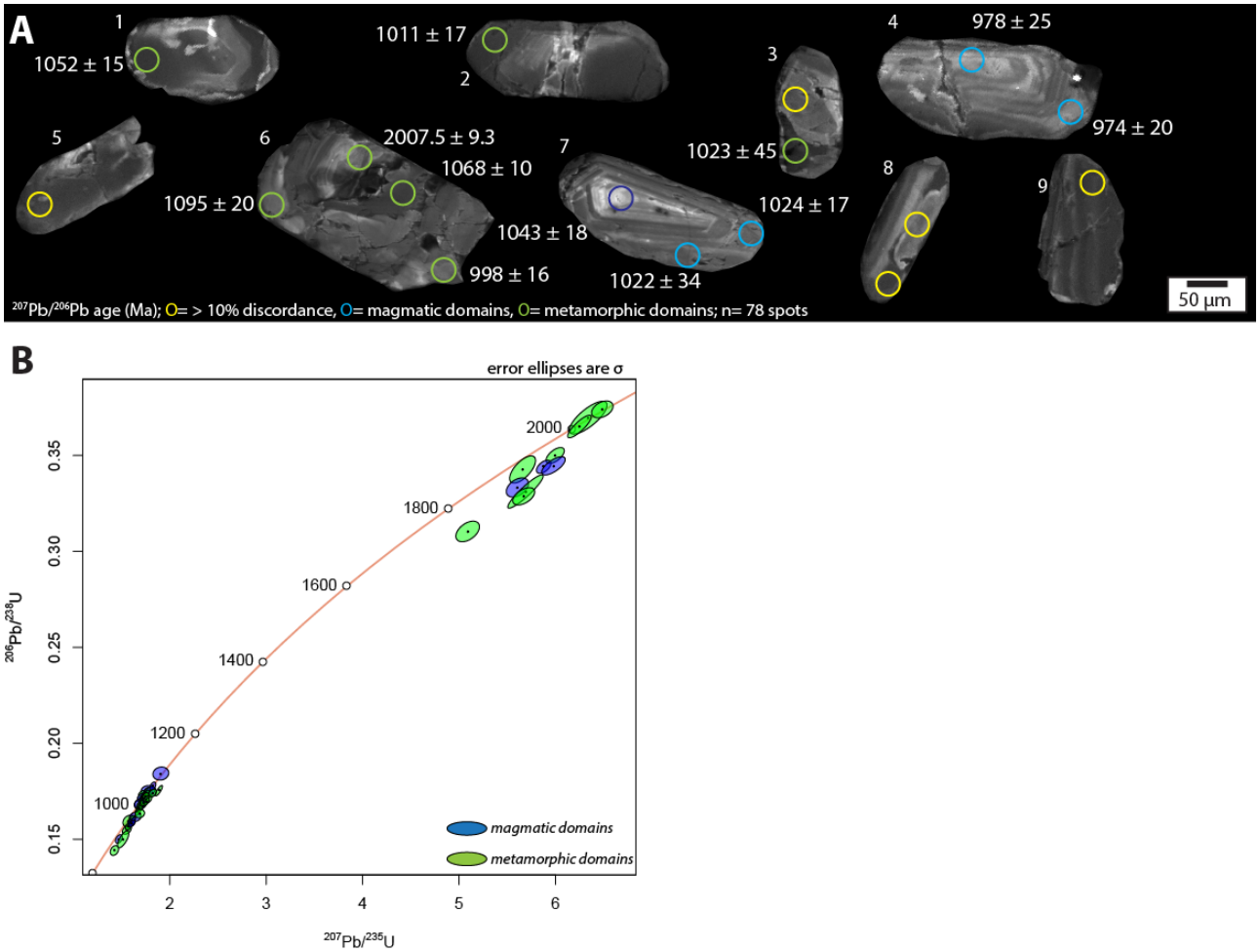


Figure 7.9: Detrital U-Pb geochronology results for arkosic quartzite sample 1.1 from the Etusis Formation. (A) CL images of selected zircons showing spot placement and $^{207}Pb/^{206}Pb$ age dates. (B) Wetherill diagrams showing two populations (1, 2 Ga) for magmatic and metamorphic domains. Ages with > 10% discordance are omitted in both diagrams.

Sample PA01 yields a major detrital age population of 2 Ga and highly discordant ages (Fig. 7.10.B). $^{207}Pb/^{206}Pb$ ages with <10% discordance are plotted in a relative probability density curve and a histogram (Fig. 7.11) yielding detrital signals from the pelitic schist that show multiple population peaks at 1860-1880 Ma, 1960 -1980 Ma and 2020 – 2040 Ma (Fig. 7.11.B) with the highest amplitude in the latter range. The most concordant ages cluster around *ca.* 2 Ga, while the younger ages at *ca.* 1860 to 1980 Ma are more discordant and do not plot along the concordia curve (Fig. 7.10.B). Zircon Th/U ratios indicate a predominantly magmatic origin (Fig. 7.12). Sample PA01 shows a cluster between Th/U= 0.1 – 1.0 for both magmatic and metamorphic samples. These domains are indistinct and cluster together, however the magmatic Th/U ratios are slightly higher than the metamorphic domains.

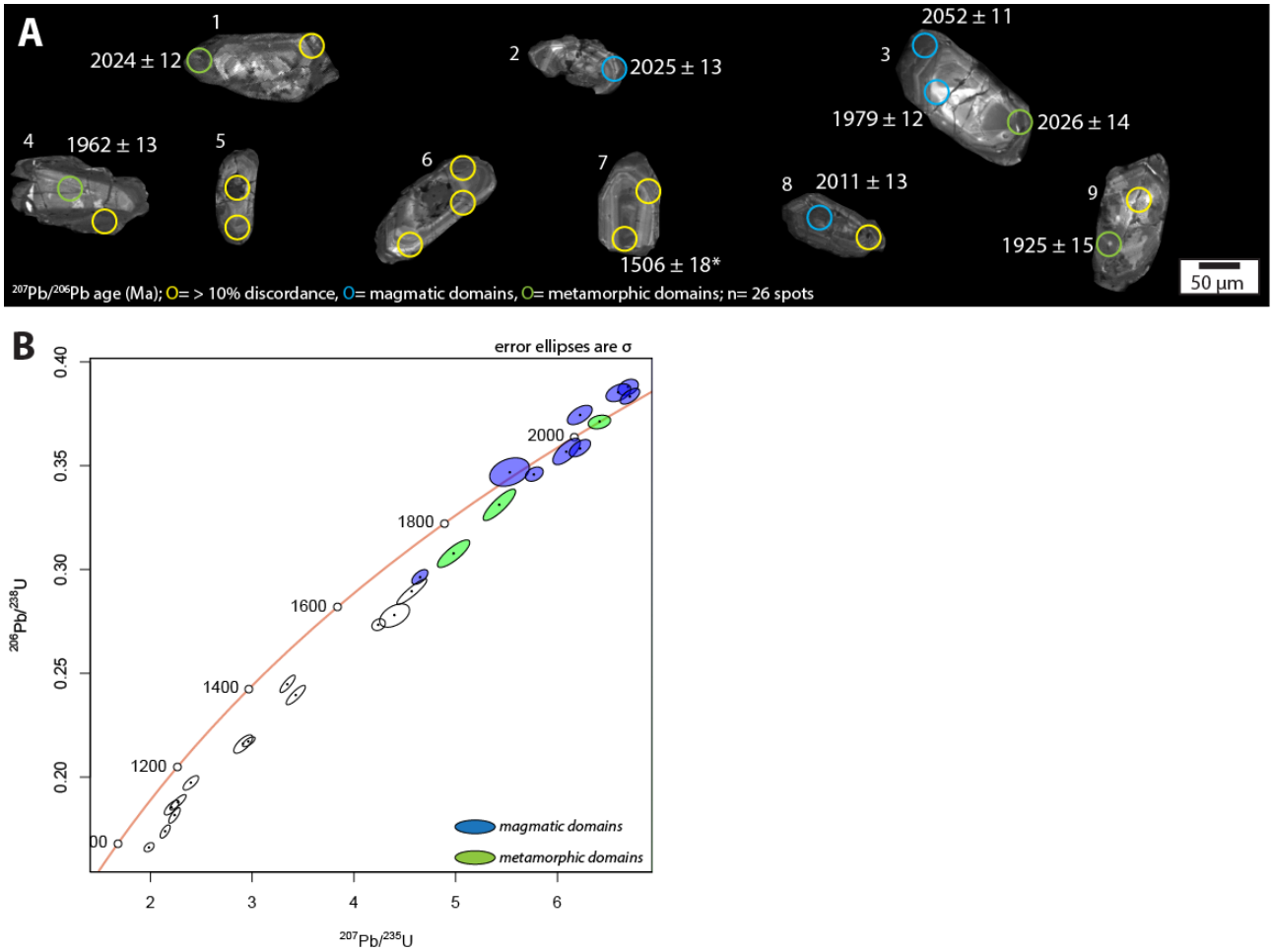


Figure 7.10: Detrital U-Pb geochronology results for sillimanite-biotite pelitic schist sample PA01 from the Etusis Formation. (A) CL images of selected zircons showing spot placement and $^{207}Pb/^{206}Pb$ age dates. (B) Wetherill diagrams showing a more concordant magmatic population (2 Ga) and younger discordant metamorphic domains. Ages with > 10% discordance are omitted in both diagrams.

The most relevant peak at 2020 Ma for sample PA01 is comparable to the signal produced by sample 1.1. Likewise, the younger signals at *ca.* 1860 and 1960 Ma for PA01 are comparable to smaller peaks seen in sample 1.1. These smaller peaks display a Gaussian distribution shape. When both datasets are combined they (Fig. 7.11.C) show overlapping *ca.* 2 Ga peaks.

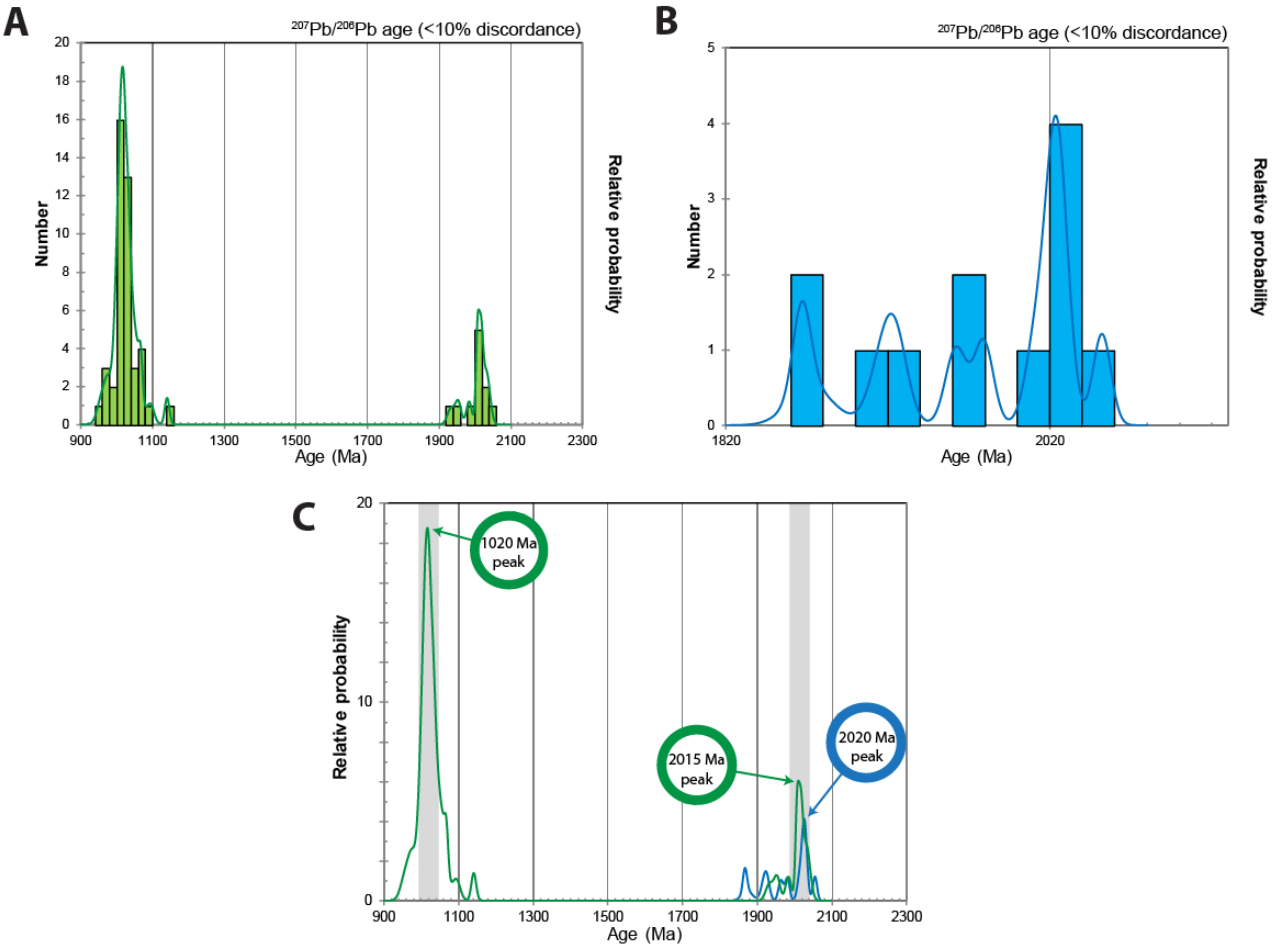


Figure 7.11: Detrital age spectra for the Etusis Formation displayed as histograms and relative density probability plots. $^{207}Pb/^{206}Pb$ ages with < 10% discordance were utilised with a bin size of 20 myr. (A) Histogram for sample 1.1 showing two populations of ages, at *ca.* 1 and *ca.* 2 Ga, and associated density curve (solid green line) highlighting these peaks. Bin 1000 - 1020 Ma displays the highest frequency of ages, with a second peak at 2000 - 2020 Ma. (B) Histogram for sample PA01 showing three populations at *ca.* 1860 to *ca.* 1960 Ma and *ca.* 2 Ga (density curve as solid blue line). The relative density curve shows a fourth peak at 1900 Ma. Bin 2020 - 2040 Ma displays the highest frequency of ages, with less significant peaks at 1860 - 1880 Ma and 1960 - 1980 Ma. (C) Comparison of relative density distributions for both samples (green solid line: sample 1.1, blue solid line: sample PA01).

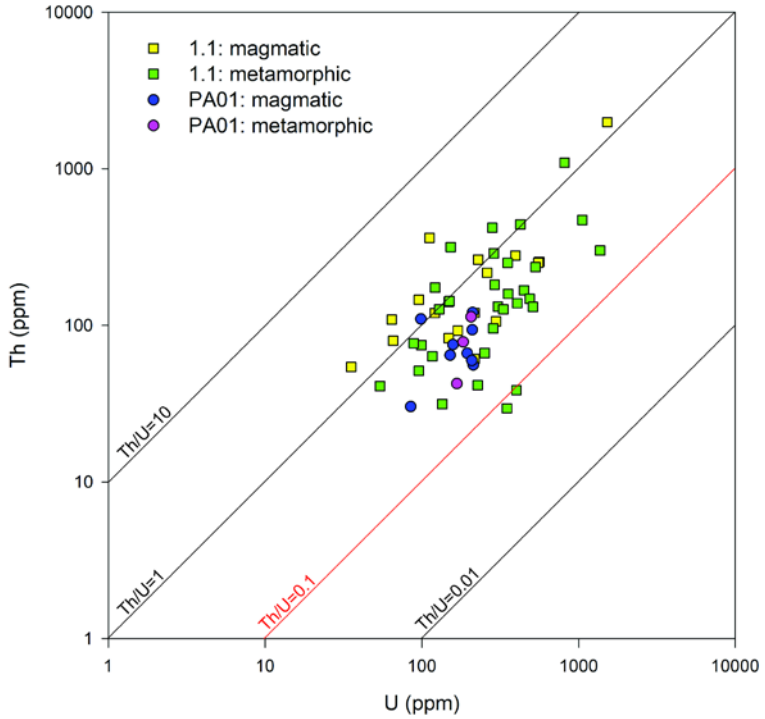


Figure 7.12: Th/U ratios for zircons from sillimanite-biotite pelitic schist and arkosic quartzite. Line indicate constant Th/U ratios where Th/U ratios below 0.1 may be considered to indicate metamorphic zircon growth (Rubatto and Gebauer, 2000).

7.3.4 Red granites

One red granite sample (K06) was selected for U-Pb zircon dating. Thirty-three spots were targeted on the most pristine grains with no cracks.

CL description and interpretation of zircon domains

Zircons extracted from the red granite are euhedral to subhedral and often display corroded tips, especially in the case of elongate zircons (Fig. 7.13.A). Inherited zircons show more irregular, rounded and anhedral morphologies (Fig. 7.13.A, zircon 6). The zircons are typically broken and fragmented requiring careful spot placement for laser ablation. Zircon crystals range from 50 to 400 µm along the c-axis with some grains stubbier or more elongate than others. Two populations can be discerned within K06 based using CL imagery: grains with magmatic cores enveloped by metamorphic overgrowths and inherited metamorphic cores overgrown by disturbed magmatic zonation and hat-like metamorphic zircon. The former population displays more pronounced and uninterrupted oscillatory zonation, although homogenisation and embayments of the zoning is present along the edges as metamorphic overgrowths (Fig. 7.13.A, zircons 1, 5, 7, 8, 9 and 10). These metamorphic embayments leave behind and truncate ghost structures of relatively symmetric zonation. Zonation is faint or homogenous and broad.

In some cases, metamorphic domains are present, which exhibit patchy and mosaic textures of previous oscillatory zoning (Fig. 7.13.A, zircons 4 and 6) as well as dark homogenous domains (Fig. 7.13.A, zircon 2). These domains occur as inherited homogeneous cores that show metamorphic textures (Fig. 7.13.A, zircon 6) and are surrounded by convoluted magmatic zoning. These grains are typically older in age and show mosaic textures of cores and metamorphic domains.

U-Pb LA-ICP-MS geochronology

The red granite, sample K06, yields a narrow spread of ages along the concordia between 560 Ma and 520 Ma (Fig. 7.13.B). Inherited zircons at *ca.* 1 Ga and 2 Ga (Fig. 7.13.B) were not considered in the concordia age calculation. Excluding the most discordant analyses a magmatic concordia age of 535.77 ± 0.96 Ma (n=7, MSWD= 0.0015) can be obtained (Fig. 7.13.C).

The metamorphic domains seemingly yield three populations (Fig. 7.13.C), with concordia ages of (1) 557.94 ± 1.80 Ma (n=3, MSWD= 1.9), (2) 540.74 ± 1.74 Ma (n= 2, MSWD= 1.2) and (3) 523.72 ± 1.02 Ma (n= 5, MSWD= 0.069). However, the metamorphic age domains are near continuous along the concordia from approximately 560 Ma to 520 Ma and therefore, were pooled to produce an age of 533.76 ± 1.65 (n= 10; MSWD= 1.7; Fig. 7.13.D) because Pb loss could not be excluded and individual ages were not defined by enough ages.

Zircon Th/U ratios, for sample K05 (Fig. 7.14), generally plot between 0.1 and 1 for both the magmatic and metamorphic domains. The magmatic domains show a tighter cluster and have higher ratios (< 0.1) than the metamorphic domains, which have a greater spread and typically tend towards lower ratios (> 0.5 to 0.1).

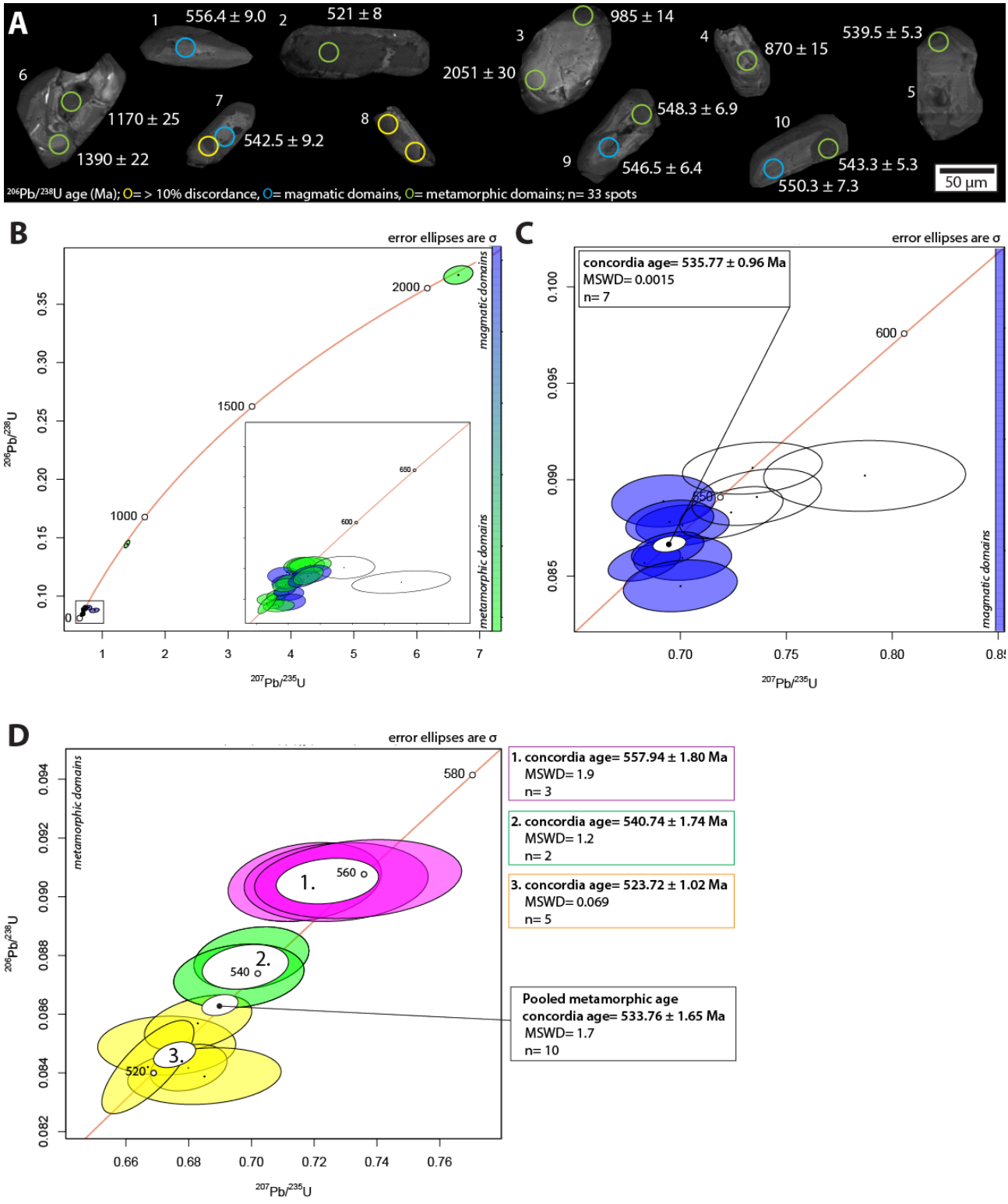


Figure 7.13: (A) CL images of selected zircons with spot placement and $^{206}Pb/^{238}U$ ages (only near-concordant data with < 10% discordance shown). Concordia age plots of (B) all data (including inheritance), (C) magmatic and (D) metamorphic domains for sample K06 from the red granites. Colourless error ellipses were excluded from the concordia calculations. MSWD= Mean Square of Weighted Deviates. Figure (D) highlights three possible metamorphic populations (1 to 3) and a final pooled metamorphic age.

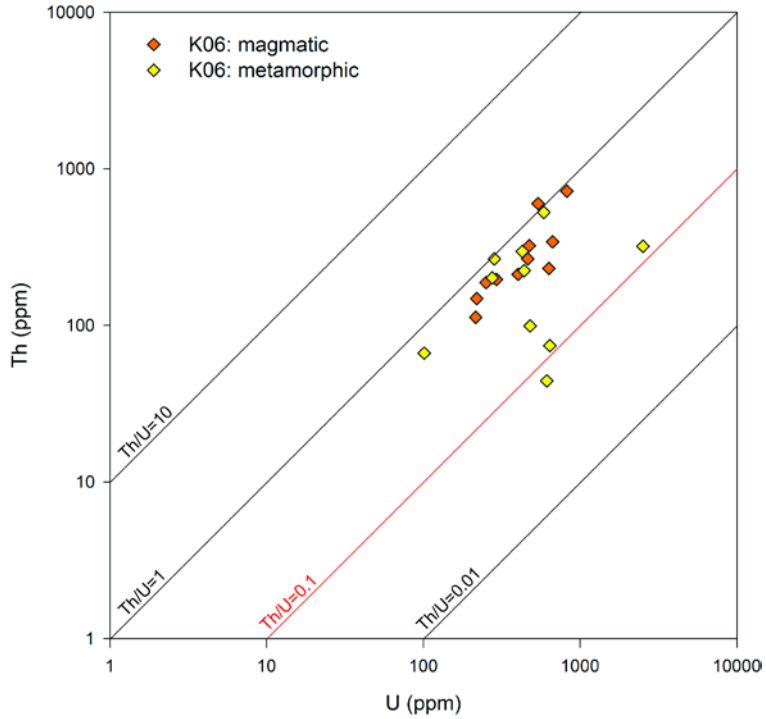


Figure 7.14: Th/U ratios for zircons from the red granite. Line indicate constant Th/U ratios where Th/U ratios below 0.1 may be considered to indicate metamorphic zircon growth (Rubatto and Gebauer, 2000).

7.3.5 Sheeted leucogranites

Two sheeted leucogranite types were dated including types C' and E. Sample K07, SLG type C, yielded few zircons of poor quality. The zircons are brittle and discoloured to grey, possibly metamict. Twenty-three spots were analysed on the most pristine zircons and domains. Similarly, sample PA02, SLG type E, yielded few zircons. Only 7 spots were U-Pb dated.

CL description and interpretation of zircon domains

Type C' SLG, sample K07, yielded zircons that were typically homogenous with a low CL response, indicating a metamorphic texture (Corfu *et al.,* 2003). These dull zircons are typically subhedral to anhedral in shape (Fig. 7.15.A), but some grain shapes may be attributed to electrical fragmentation. Some grains appear to be more rounded and the tips show corrosion. This may hint at a possible inherited sedimentary origin in this sample. Zircons range from 100 to 200 µm in size along the long axis, and are typically elongate, although many are broken so it is difficult to determine the true ratio. Magmatic zoning, albeit rare, is present (Fig. 7.15.A, zircon 1), with variable thickness and symmetry. Magmatic zircons produced concordant ages. Primary magmatic zoning is commonly convolute or dismembered (Fig. 7.15.A, zircons 2, 4, 6 and 7) by homogeneous metamorphic embayments or domains as metamorphic rims (Ashwal *et al.,* 1999; Hoskin and Black, 2000; Connelly, 2001; Schaltegger *et al.,* 2002; Corfu *et al.,* 2003). Most of the spots age dated show variable discordance usually > 10%. Most zircons show little to no remnant magmatic zonation and are

completely homogenous (Fig. 7.15.A, zircons, 3, 5 and 8) indicating that the zircon has been largely recrystallised (Rubatto, 2017). Age relationships with zoning and metamorphic domains are not simple, with younger ages appearing in the core, while older ages are located along the rim, however, in most instances these ages are discordant.

Sample PA03 contains stubby and tabular zircons showing cracks. Theses cracks have not been filled by new precipitation of zircon growth. The grains are approximately 300 μm long and have subhedral shapes. Two dated (Fig. 7.16.A) grains are significantly larger than other zircons that were picked but not dated. The tips have been corroded or eroded which indicates a possibility of a detrital inheritance of the SLGs. The zircons are metamorphic in nature and show remnant magmatic zonation that has been dismembered and convoluted by the homogenous domains (Ashwal *et al.,* 1999; Hoskin and Black, 2000; Connelly, 2001; Schaltegger *et al.,* 2002; Corfu *et al.,* 2003). These domains typically occur as rims to disrupted magmatic cores.

U-Pb LA-ICP-MS geochronology

The geochronology results for the SLG show a high degree of discordance. Sample K07 yields complicated age relationships, including magmatic and metamorphic concordia ages as well as two metamorphic regressions based on (discordant) inherited ages. The other SLG, sample PA03, yielded older ages that were largely discordant, and therefore did not represent the crystallisation age of the SLG.

The discordant ages, from sample K07, are interpreted to reflect inheritance. Magmatic and metamorphic concordia ages were determined using the most concordant ages at *ca.* 500 Ma (Fig. 7.15.B). Inherited ages plotting along concordia are also observed (Fig. 7.15.C). The magmatic concordia age of 525.72 ± 1.91 (MSWD= 6.6; Fig. 7.15.B) is calculated from only two concordant ages and is therefore not considered to be reliable. However, this age is resolvably older than a metamorphic age and is therefore used an estimate for the crystallisation age. A metamorphic concordia age of 510.74 ± 1.18 Ma (MSWD= 0.94; Fig. 7.15.B) was established from 3 concordant grains.

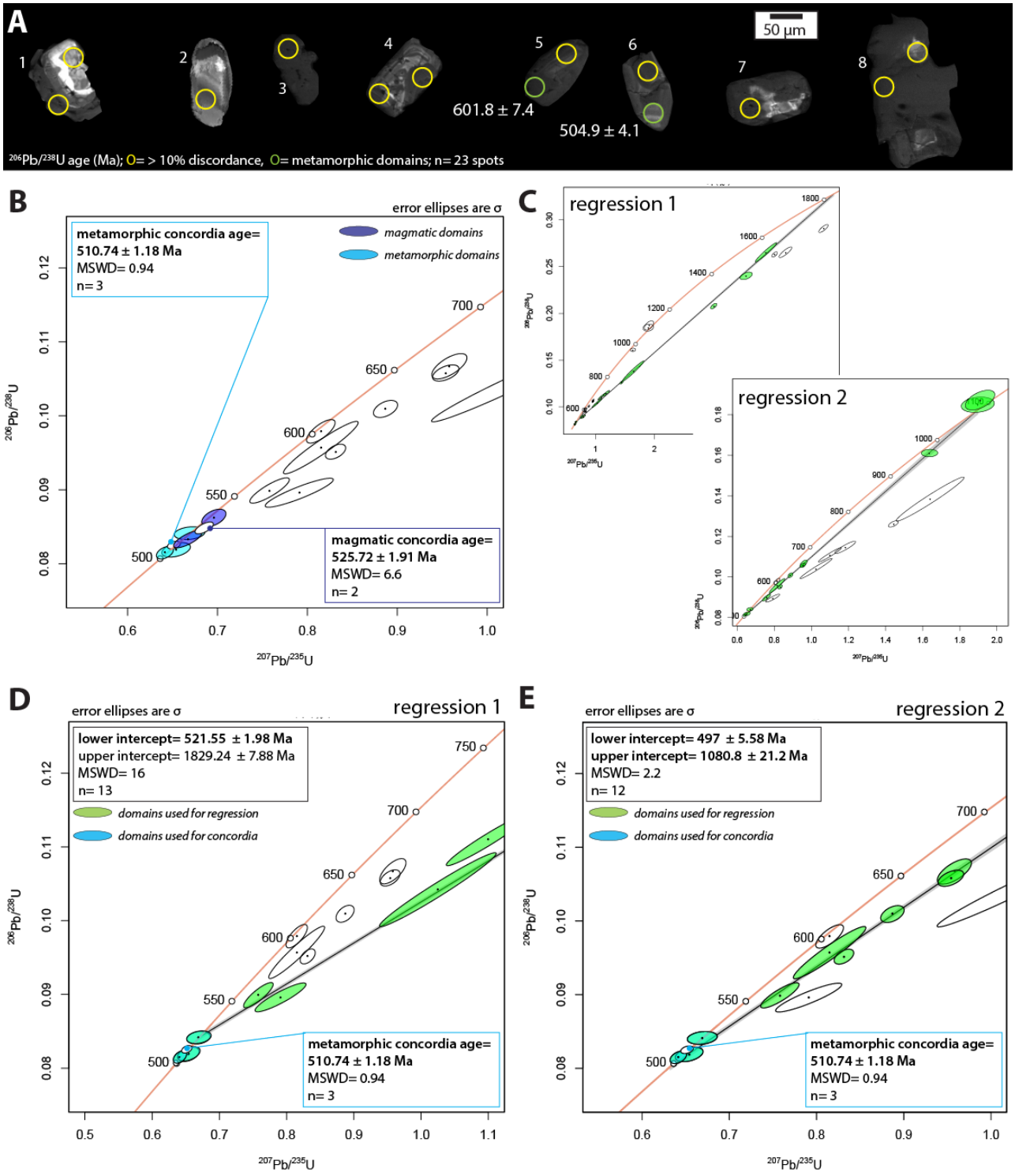


Figure 7.15: (A) CL images of selected zircons with spot placement and $^{206}Pb/^{238}U$ ages (only near-concordant data with < 10% discordance shown). Concordia age plots of (B) magmatic and metamorphic domains for sample K07 from the type C' SLGs. (C) Regression of two metamorphic populations with detailed concordia age plots of (D) regression 1 and (E) regression 2. Colourless error ellipses were excluded from the concordia calculations. MSWD= Mean Square of Weighted Deviates.

Two regressions are possible using the discordant data (Fig. 7.15.C). Both regressions seem to be related to crystallisation or metamorphism as the lower intercepts coincide with the concordia ages within error, whereas, the upper intercept age is possibly an inherited crystallisation age. Regression

1 (Fig. 7.15.D) has an upper and lower intercept of 1829.24 ± 7.88 Ma and 521.55 ± 1.98 Ma (n= 13, MSWD= 16), respectively. Discordant ages that appear to define a separate population were disregarded from the regression calculations. The second regression (Fig. 7.15.E) provides an upper intercept of 1080.8 ± 21.2 Ma (n= 12; MSWD= 2.2), which coincides with concordant inherited grains at *ca.* 1 Ga and may represent inherited crystallisation ages. The lower intercept age of 497 ± 5.58 Ma coincides with the metamorphic concordia age and is considered more reliable than regression 1 when taking into account the MSWDs (Fig. 7.15.D).

Th/U ratios for the type C' SLGs cluster along the Th/U= 0.1 gradient, however the magmatic and metamorphic domains do not show distinct populations (Fig. 7.17). The metamorphic domains show a greater spread of ratios. These gradients show mixed metamorphic and magmatic origins and do not discern between magmatic and metamorphic domains effectively. Additionally, Th/U systematics are in conflict with CL imagery classification.

Sample PA03 yields only one *ca.* 2 Ga concordant age that forms part of a linear array of negatively and positively discordant ages (Fig. 7.16.B). The metamorphic zircons are discordant and yield a regression with upper and lower intercept ages of 1906.73 ± 8.46 Ma and 587.7 ± 31.1 Ma (n= 7, MSWD= 7), respectively, with the upper intercept possibly indicating an inherited crystallisation age. Based on the field relationships, these zircons are probably inherited as the SLG cross-cut basement gneisses. Due to the small number of analysed zircons the ages only serve as an age estimate of the material that was assimilated during emplacement, and no crystallisation age could be determined. Based on field relationships (chapter 4) type E SLG cross-cuts type C' SLG and, therefore, the former SLG cannot yield older ages.

The zircon Th/U ratios for sample PA03 range from 0.1 to 1.0, indicative of a magmatic origin (Fig. 7.17; Rubatto and Gebauer, 2000). Again, this contrasts with the characterisation by CL imagery. Exceptions do exist, however, where high-temperature metamorphism can result in elevated zircon Th/U ratios (Rubatto, 2017).

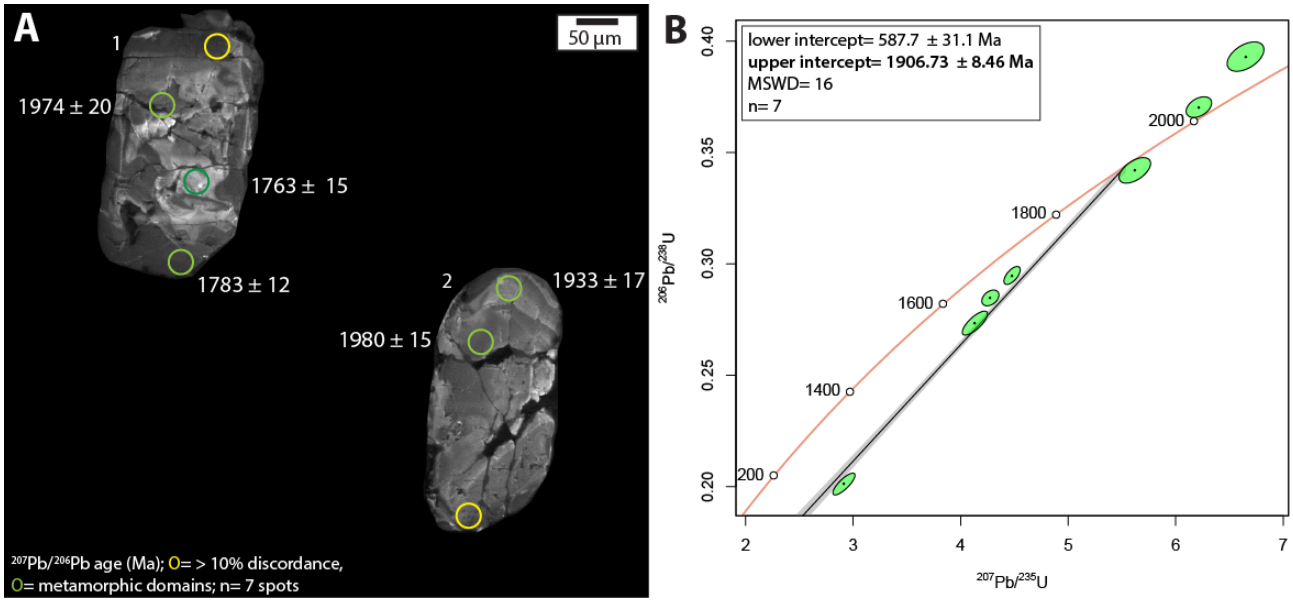


Figure 7.16: (A) CL images of selected zircons with spot placement and $^{207}Pb/^{206}Pb$ ages (only near-concordant data with < 10% discordance shown). Concordia age plots of (B) metamorphic domains for sample PA03 from the type E SLGs. MSWD= Mean Square of Weighted Deviates.

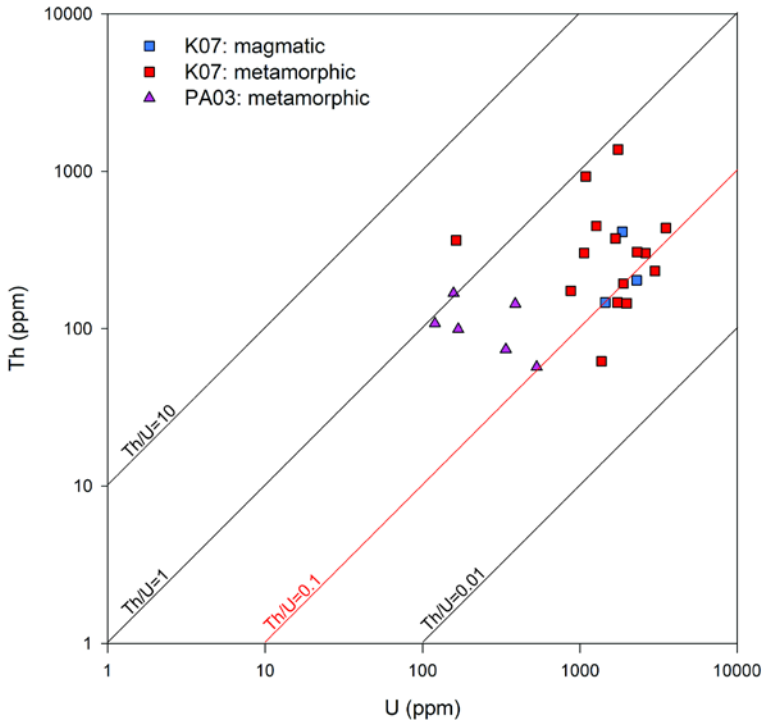


Figure 7.17: Th/U ratios for zircons from various SLGs. Line indicate constant Th/U ratios where Th/U ratios below 0.1 may be considered to indicate metamorphic zircon growth (Rubatto and Gebauer, 2000).

7.4 Lu-Hf isotope analysis

Lu-Hf isotope ratio analysis was performed on all rock types dated with the U-Pb chronometer, namely gneisses of the Abbabis Complex, amphibolites, metasediments of the Etusis Formation, red granite and the SLGs, using zircon with concordant to near-concordant ages (<10% discordance).

Due to insufficient concordant ages for the Etusis Formation and amphibolite dykes, only one Etusis sample (1.1) and amphibolite sample (7.3) were analysed for zircon Lu-Hf. Sample PA02 showed inheritance and therefore crystallisation ages were not available. U-Th-Pb-Hf results are listed in Appendix 5.B. $^{207}Pb/^{206}Pb$ ages were used for spots that yielded ages older than 1 Ga and $^{207}Pb/^{238}U$ ages were used for spots that yielded ages younger than 1 Ga.

Figure 7.18 shows the $\varepsilon Hf_{(t)}$ vs time plot of all samples. Values for εHf for Abbabis Complex lithologies (K05, R06 and PA02) plot below below CHUR (-2.8 to -8.8 at 2.1 to 1.8 Ga). Samples K05 and PA02 display a narrower range in εHf, although values for all three samples overlap within errors. A single spot from sample K05 plots above CHUR and is considered an outlier. Depleted Mantle (DM) model ages for the Abbabis Complex are approximately 2.8 – 3.1 Ga.

Values for εHf for amphibolite sample 7.3 display a range of -5 to -9.5 at *ca.* 500 Ma, well below CHUR. Model ages (T_{DM}) of *ca.* 1.6 – 1.9 Ga are distinctly younger than the 2 Ga to 2.8 Ga model ages of the other samples.

The Etusis Formation shows three distinct detrital εHf populations with a single outlier that plots with the Abbabis Complex populations. Two populations (Et1 and Et2) with crystallisation ages of *ca.* 1 Ga show variable εHf values below CHUR. Population Et1 yields the most unradiogenic εHf values (-25 to -28) with a DM model age of *ca.* 3.5 to 3.6 Ga. Population Et2 shows less unradiogenic εHf values, ranging from -11 to -17, translating into a younger DM model age of 2.6 - 2.9 Ga. Values for εHf are distinctly more radiogenic (+ 4 to +9) for Et3 translating into DM model ages of 2.2 to 2.4 Ga.

Similarly, the εHf values for the red granites (K06) plot along the Eburnean crustal εHf evolution trend, corresponding to DM model ages of 2.7 - 3 Ga. These granites show distinctly unradiogenic εHf values of -21 to -24 (excluding one outlier with -19). The red granites, Abbabis Complex and Etusis Formation fall along the same evolution (Fig. 7.18).

The SLG samples did not produce reliable U-Pb ages, with both samples showing highly discordant ages and sample PA03 producing inherited ages. Therefore, this resulted in only 1 (K07) and 3 (PA03) spots being analysed for both samples. Sample K07 yields εHf = -25 and overlaps the red granite, although these SLGs are younger (*ca.* 515 Ma). In contrast, sample PA03 shows similar εHf vs age values as the Abbabis Complex samples with εHf values of -3 to -5. Despite these differences, both samples show similar DM model ages of *ca.* 3 Ga.

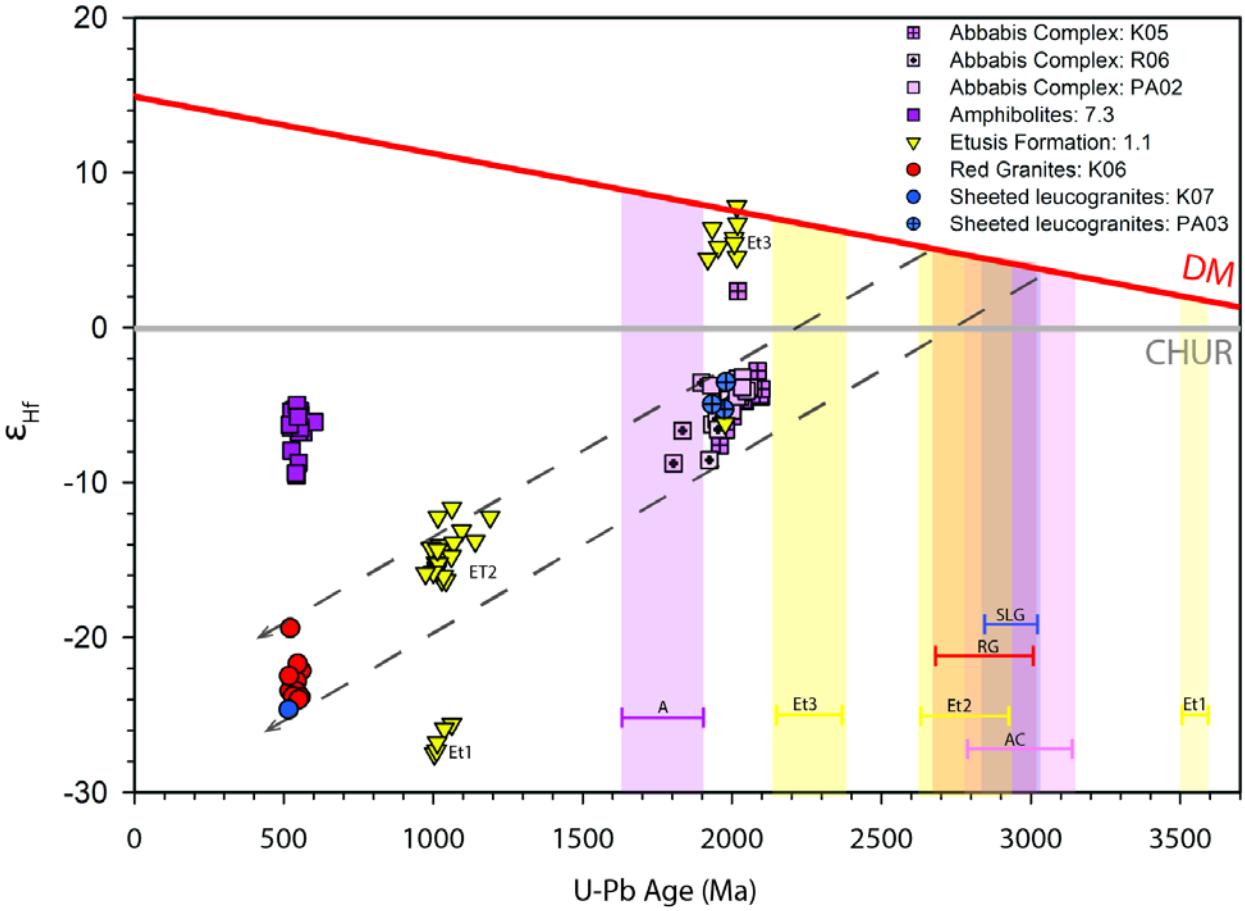


Figure 7.18: εHf vs U-Pb ages (Ma) plot showing all samples. $^{207}Pb/^{206}Pb$ ages were used for spots that yielded ages older than 1 Ga and $^{207}Pb/^{238}U$ ages were used for spots that yielded ages younger than 1 Ga. Evolution curves for Chondrite Uniform Reservoir (CHUR) (after Bouvier *et al.*, 2008) and Depleted Mantle (DM) (after Gerdes and Zeh, 2006) are shown in grey and red, respectively. Ranges for DM model ages are indicated by different coloured and labelled bars. Dots below bars indicate individual model ages calculated. These are plotted to show clusters and breaks within the ranges. AC= Abbabis Complex, A= amphibolites, Et= Etusis Formation, RG= red granites, SLG= sheeted leucogranites. The Etusis Formation defines three populations translating into three distinct ranges of model ages.

7.5 Discussion

U-Pb geochronology and Lu-Hf isotopic results are used to develop a chronological framework for the lithologies dated in this study. A simplified interpretation of these ages and a summary of the ages can be seen in figure 7.19, however they are discussed in more detail in later sections. A comparison of U-Pb geochronology paired with εHf values yielded genetic links and differences among certain lithologies, which are compared with existing age constraints and Lu-Hf studies (Fig. 7.20).

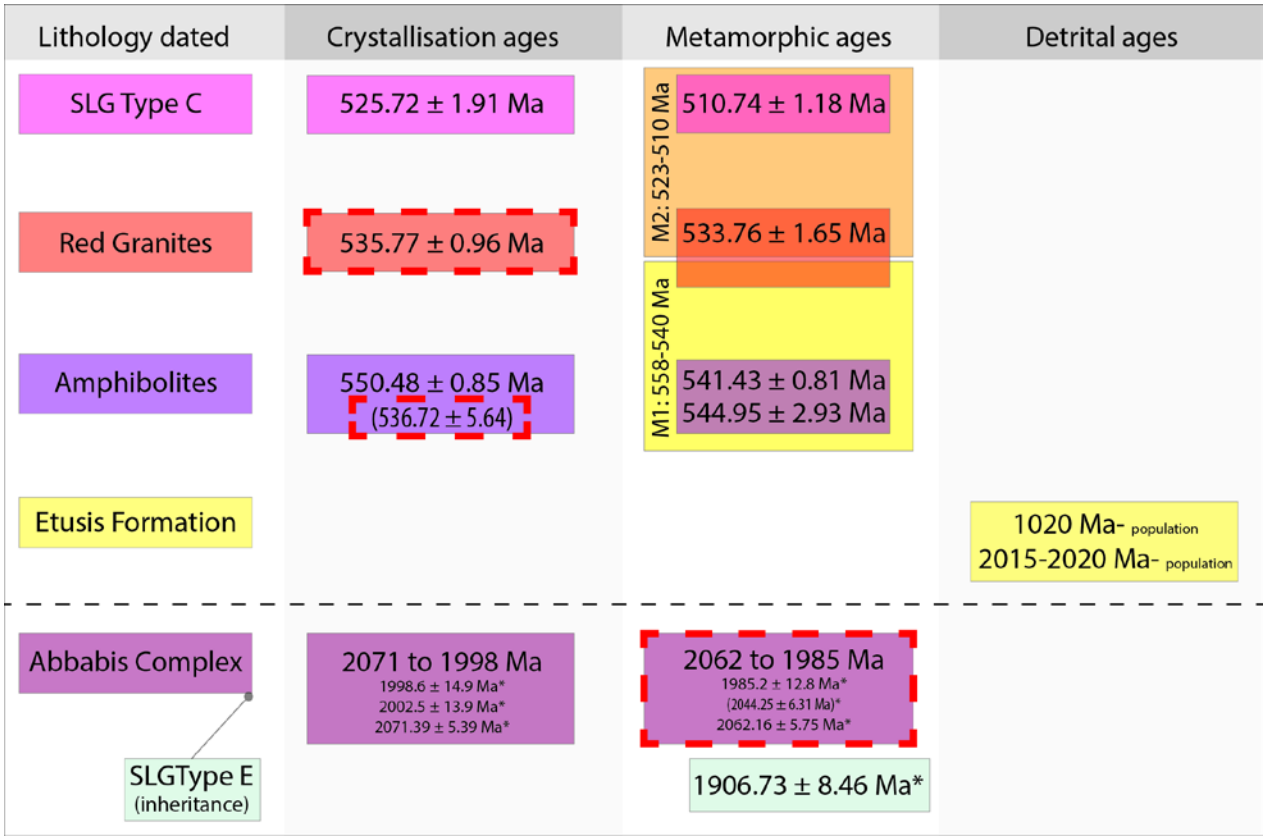


Figure 7.19: Summary of the U-Pb age data for the lithologies in chronological order. Ages are concordia or regression ages (latter indicated by the symbol *). Ages in brackets are less reliable. Type E SLG U-Pb ages show inheritance (see discussion text) and not a true crystallisation age. Red dashed lines indicate unreliable ages, which have been considered in the text.

7.5.1 The Abbabis Complex

Selected lithologies of the Abbabis Complex yielded crystallisation ages of 1998.6 ± 14.9 Ma, 2002.5 ± 13.9 Ma and 2071.39 ± 5.39 Ma (discordia intercept ages) indicating a major magmatic event at *ca.* 2 Ga. The 2002.5 ± 13.9 Ma age is less reliable because metamorphic rims yield an older upper intercept age of 2044.25 ± 6.31 from the same sample (PA02). The *ca.* 2 Ga crystallisation ages agree with studies by Jacob *et al.* (1978), De Kock *et al.* (2000), Tack *et al.* (2002), Longridge (2012) and Longridge *et al.* (2018). Some workers (Longridge *et al.,* 2011; Longridge, 2012; Longridge *et al.,* 2018) propose that the Abbabis Complex may represent extensions of, or show affinities to, the Congo Craton due to the similarity in *ca.* 2 Ga ages (which is generally older than the expected ages for the Kalahari Craton) (Hoal *et al.*, 2000; Singletary *et al.,* 2003) and oxygen-hafnium isotopic compositions (Longridge *et al.,* 2018). The 2 Ga ages from this study are older than age estimates proposed by Jacob *et al.* (1978) for migmatised gneisses near the Khan River (upper intercept age of 1038 ±58 Ma). Ages ($^{207}Pb/^{238}U$ individual ages) of 1 Ga in this study were obtained from homogeneous or convolute metamorphic domains that yielded generally discordant ages which could possibly be

attributed to either a Damaran metamorphic overprint (Longridge, 2012), a possible older Kibaran orogeny overprint (Longridge, 2012), or metamictisation and associated Pb loss.

Metamorphic upper intercept ages 1985.2 ± 12.8 Ma, 2044.25 ± 6.31 Ma and 2062.18 ± 5.75 Ma for selected lithologies of the Abbabis Complex are variable and similar to crystallisation ages. A *ca.* 2 Ga age for metamorphism of the Abbabis Complex has not been previously established and could possibly be a product of crustal reworking during the central-western African Palaeoproterozoic Eburnean Orogeny as the age dates are not consistent with the ages for the two dominant Damaran tectono-thermal events at 560 - 540 Ma and 520 - 510 Ma (Longridge, 2012). The Abbabis Complex may preserve evidence for pre-Damaran deformation (and metamorphism) in the type locality (Smith, 1965) and a higher grade of metamorphism than the cover rocks (Poli, 1997), therefore a record of an older metamorphic event preserved within the Abbabis Complex is possible.

Abbabis Complex metamorphic ages are derived from domains that display convolute and homogenous (CL imagery) textures that are typical of metamorphic textures (Ashwal *et al.,* 1999; Hoskin and Black, 2000; Connelly, 2001; Schaltegger *et al.,* 2002; Corfu *et al*., 2003; Rubatto, 2017) and were interpreted as metamorphic rims or domains. However, the interpretation of convolute and mosaic textures can also be interpreted as late stage magmatic recrystallisation textures (Corfu *et al.,* 2013 and references within). Ratios of Th/U, for the various Abbabis Complex lithologies (especially samples PA02 and K05), are higher than typical ratios for metamorphic zircons which may suggest a magmatic origin (Rubatto, 2017). However, recrystallised magmatic domains in ultra-high temperature environments with non-metamorphic Th/U ratios have been reported (Rubatto, 2017 and references within). The Th/U ratios from the metamorphic and magmatic domains do not delineate distinct populations, even in the case of sample R06, where the majority of the ratios straddle the boundary (Th/U= 0.1) that typically divides magmatic and metamorphic origins, and therefore more than likely represent similar origins. In addition, these metamorphic domains yield ages within error of the magmatic ages or sometimes even older (sample PA02) and therefore these ages may be assigned to magmatic domains (with variable CL textures) that have undergone late stage recrystallisation.

The Abbabis Complex yielded unradiogenic εHf values and DM model ages of 2.8 Ga to 3.1 Ga substantially older than crystallisation ages (Fig. 7.20). These unradiogenic εHf values indicate a lack of juvenile crust (Kinny and Maas, 2003; Hawkesworth and Kemp, 2006), and hence large portions of the Abbabis Complex most likely represent the product of crustal reworking. Extraction from Depleted Mantle sources to generate juvenile crust occurred from 3 Ga to 2.8 Ga. This Archaean

crust was later reworked during the Eburnean orogeny to form the Abbabis Complex at 2 Ga (U-Pb crystallisation age) suggesting an older crustal source for the basement lithologies. Indicating that the Abbabis Complex has a complicated crustal history prior to the Pan African. However, extensive high-grade mobile belts commonly destroy the possibility of unravelling the complicated history prior to the assembly of Gondwana (Jacobs *et al.,* 2008 and references within) thus unravelling the exact nature of the Abbabis Complex, during Eburnean and Rodinian orogenesis, is difficult. The geometry of the Abbabis Complex (assumed to have a Congo Craton affinity), the Congo Craton and proto-Kalahari Craton may have been more complicated than proposed and may represent a continental fragment caught between the Congo and Kalahari cratons prior to or during the Pan-African collisional event.

The extent, location and rifting history of the proto-Kalahari Craton (Hartnady *et al.,* 1985; Dalziel, 1991; Jacob *et al.,* 2008) remains ambiguous due to the high-grade overprinting of the surrounding accreted mobile belts of the Congo (Goscombe *et al.,* 2017b) and Kalahari cratons (Jacob *et al.,* 2008). Some models also consider a northern and southern component of the Congo Craton and suggest only the southern Congo Craton was involved in the Pan-African event (Merdith *et al.,* 2017). In fact, the exact extent of the edge of the cratons remains unclear based on geophysical studies but is largely inferred from the extent of the outcropping basement-cored domes (Rankin, 2015) assuming that the Abbabis Complex has a Congo Craton affinity (Jacob *et al.,* 1978; Hawkesworth and Marlow, 1983; Tack *et al.,* 2002; Miller, 2008; Longridge, 2012). From magnetic geophysical data, the Abbabis Complex inliers are manifested as isolated anomalies that could not be directly correlated to the Congo or Kalahari cratons (Rankin, 2015), however, Khoza *et al.* (2013) have outlined that the southern extent of the Congo Craton is further south than previously inferred (possibly extending beneath the Central Zone). This continued uncertainty impedes palaeogeographic reconstructions of Rodinia and older continental configurations. The Congo and Kalahari cratons both have accreted mobile belts of various ages (including, but not limited to the Archaean to Palaeoproterozoic) (Hartnady *et al.,* 1985; Jacobs *et al.,* 2008; Goscombe *et al.,* 2017b; Merdith *et al.,* 2017). This opens up the possibility that 2 Ga aged material identified for the Abbabis Complex was sourced from a reworked Archaean to Palaeoproterozoic mobile belt accredited to the Kalahari Craton based on the premise that the Hf data indicates crustal reworking.

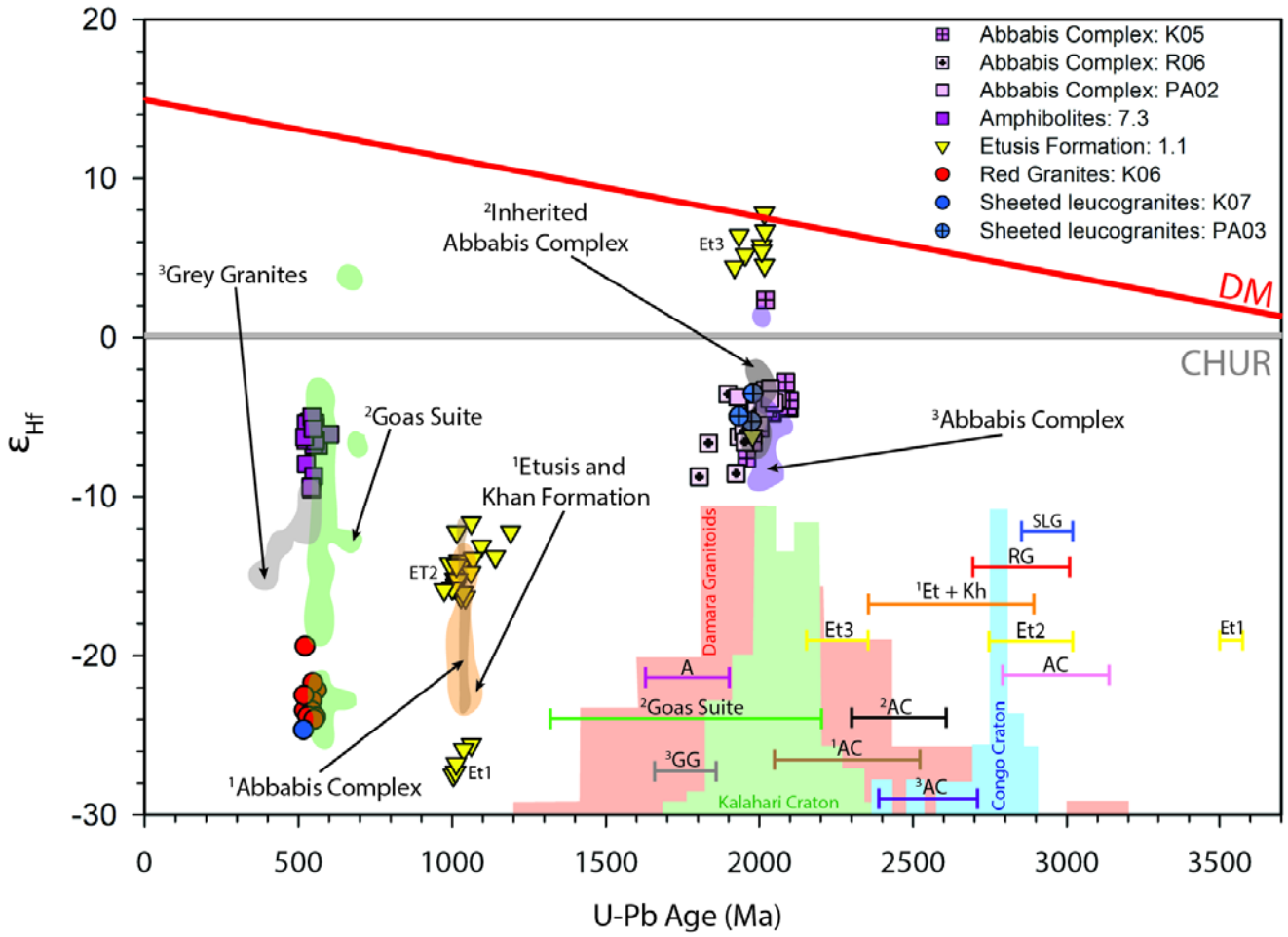


Figure 7.20: Comparison of U-Pb and Lu-Hf isotopic data from this and previous studies (both εHf and εNd). Superimposed fields for various εHf values from (1) Foster *et al.* (2015), (2) Milani *et al.* (2015) and (3) Longridge *et al.* (2018). Numbers (1 to 3) correspond to those in the diagram. DM model age histograms for the Damaran granitoids (red), Congo (blue) and Kalahari (green) Cratons are taken from compilation by Longridge *et al.* (2018; references therein). Histograms do not correspond to the y-axis scale. For original scaling see Longridge *et al.* (2018). Abbreviations: AC= Abbabis Complex; A= amphibolites; Et= Etusis Formation; Kh= Khan Formation; RG= red granites; GG= grey granites; SLG= sheeted leucogranites. Et1 to 3 populations of the Etusis Formation. Solid horizontal bars indicate DM model age ranges (colours correspond to model age range bars that correspond to the different lithology types). CHUR and DM evolution curves after Bouvier *et al.* (2008) and Gerdes and Zeh (2006), respectively.

However, recent work (Longridge *et al.,* 2018) suggest that the basement rocks consistently show new crustal generation during the Archaean, which is consistent with the DM model ages for this study, and consequently crustal growth in the Abbabis Complex was concurrent with the crustal growth of the Congo Craton during the period of 2.4 to 2.8 Ga (Fig. 7.20), implying that the Abbabis Complex is an extension of the Congo Craton (Longridge *et al.,* 2018). Both 2 Ga U-Pb crystallisation age data (Hoal *et al.*, 2000; Singletary *et al.,* 2003), similar DM model ages (Foster *et al.,* 2015; Milani *et al.,* 2015; Longridge *et al.,* 2018) and comparable oxygen isotope values (Longridge *et al.,* 2018) between the basement lithologies and the Congo Craton all favour the Abbabis Complex being an extension of the Congo Craton. In addition, magnetotelluric data also supports the presence of the Congo Craton beneath the Damara Belt (Khoza *et al.,* 2013), consistent with the notion that the

Abbabis Complex is most likely an extension of the Congo Craton. Given these multiple lines of evidence and the high-grade Damaran overprint limiting further reconstruction of the Abbabis Complex, this conclusion has well-documented evidence (Jacob *et al.,* 1978; Hawkesworth and Marlow, 1983; Tack *et al.,* 2002; Miller, 2008; Longridge, 2012; Longridge *et al.,* 2018) and is the most likely.

7.5.2 Amphibolite dykes

U-Pb age data for the amphibolite dykes indicate a long-lived event since metamorphic and magmatic ages are similar but resolvable within uncertainties. The amphibolite dykes yield magmatic age of 550.48 ± 0.85 Ma. The younger age of 536.72 ± 5.64 Ma is considered less reliable and was not considered (see results section 7.3.2). Additionally, these dykes show inheritance present as a 1 Ga population. A different origin of the older grains is also indicated by a stronger degree of magmatic zoning. The U-Pb age of these amphibolites corresponds to the zircon age of 557.2 ± 7.4 Ma obtained for the Damaran Amphibolites (Longridge *et al.,* 2014) proposed to be related to the 580 to 535 Ma (Jacob *et al.,* 2000; de Kock *et al.,* 2000, Jung *et al.*, 2002; Milani *et al.*, 2014; Milani *et al.*, 2015) mafic to dioritic Goas Suite of the Central Zone. The first age dates for the amphibolite dykes (Longridge *et al.,* 2014) highlighted the presence of two amphibolite dyke generations and therefore these dykes were not a distinguishing feature for the Abbabis Complex as previously thought. The more reliable zircon age obtained in this study agrees with the age reported by (Longridge *et al.* (2014) for Damaran amphibolites in the sCZ, and also matches within analytical uncertainty the age range published for the Goas Suite. This magmatic suite appears to have been formed during a continuous and relatively short-lived (zircon U-Pb age range of 580 to 545 Ma) magmatic event (Milani *et al.,* 2015).

Metamorphic concordia ages of 541.43 ± 0.81 Ma and 544.95 ± 2.93 Ma for the amphibolite dykes obtained for homogeneous and convolute metamorphic domains may represent the metamorphic overprint due to the onset of collision between the Congo and Kalahari cratons some 580 to 540 Ma, which lead the emplacement of the voluminous Goas Suite (Longridge *et al.,* 2014; Milani *et al.,* 2015), and which manifests as the early M1 event derived from field and petrographic studies. These metamorphic zircon ages for the amphibolites also overlap with the older tectonothermal event established in the Damara Belt at 560 - 540 Ma (Longridge, 2012). A protracted tectonothermal event may be responsible for the spread of ages along the concordia for the amphibolite dykes.

These metamorphic ages are determined from zircon domains that yielded Th/U ratios higher than typically observed in metamorphic zircons, although this is commonly noted in zircons exposed to

high-temperature metamorphism (Rubatto, 2017 and references within). Both the magmatic and metamorphic Th/U ratios are tightly clustered and not distinguishable from one another for both samples and therefore do not serve as reliable tool to distinguish between metamorphic and magmatic zircons in this case. However, typical metamorphic textures (Corfu *et al.,* 2003), such as the distinctly homogenous domains, are generally better preserved than the magmatic zircons in the amphibolites. Based on the above considerations the metamorphic ages are viewed as more reliable than the magmatic ages.

The distinctly negative εHf values for the amphibolites are similar to the εHf values derived from the Goas Suite (Milani *et al.*, 2015) which provides further evidence that the dykes and Goas Suite may be related. Milani *et al.* (2015) eliminated a juvenile source for the Goas Suite, based on the unradiogenic εHf values, and disagreed with a magmatic arc setting (McDermott, 1986; Miller, 2008). Various petrogenetic studies have suggested different emplacement settings for the Goas Suite and Damaran-aged amphibolites. Examples include, emplacement as a result of crustal reworking of variably aged lower mafic crust (Milani *et al.,* 2015), underplating of the pre-Pan-African crust by mantle derived magmas as a result of delamination of the mafic lower crust (Longridge *et al.,* 2014; Longridge *et al.*, 2018) or partial melting of the sub-continental lithospheric mantle (Jung *et al.,* 2015). This study does not preclude a juvenile source for these amphibolites which is in contrast to theories by Milani *et al.* (2015) and Longridge *et al.* (2018). Juvenile mafic crust can yield unradiogenic εHf values if crustal assimilation occurred at some point during emplacement (Kirkland *et al.,* 2013; Vervoort and Kemp, 2016), which is likely in this scenario as the dykes intruded into primarily quartzofeldspathic and granitic lithologies. From whole rock geochemical results, the amphibolites indicate a possible subduction or crustal assimilation signature (LILE enrichment relative to HFSE, depletion of HREE, enrichment of incompatible elements (Th) with a depletion of Nb and Ta) which could possibly account for the mafic compositions and assimilation of continental crust resulting in unradiogenic εHf values and a multi-element subduction/crustal assimilation signature. However, based on geochemical data and limited isotopic studies, distinguishing between the two scenarios is not possible. Crustal assimilation most likely occurred (Th/Yb and Nb/Yb ratios; section 6.4.4) during emplacement of the dykes as the dykes intruded into continental crust, and subduction may be possible due to geological evidence where arc magmatism is purported (McDermott, 1986). However, it is not possible to conclude between the two.

Longridge *et al.* (2018) purported that the Goas Suite and grey granites were a result of reworking of the Kalahari Craton due to younger crystallisation ages (< 1 Ga) and similar DM model ages (between 2.4 and 1.7 Ga) produced from Damaran intrusives. However, the amphibolites are not

considered to be a result of crustal reworking (this study) as previously suggested, but the DM model ages (1.6 to 1.9 Ga) for the dykes may indicate a possible contribution of variably aged crust from the Kalahari Craton (based on the characteristics of the Kalahari Craton established by Longridge *et al.* (2018).

7.5.3 The Etusis Formation

Several observations suggest that the metasediments of the Etusis Formation were derived from gneisses and granites of the Abbabis Complex (Smith, 1965; Hawkesworth and Marlow, 1983; McDermott *et al.*, 1989; McDermott and Hawkesworth, 1990). The Abbabis Complex in particular is a purported source owing to Abbabis clasts found within the basal conglomerate of the Etusis Formation at its type locality (Gevers, 1931; Smith, 1965). In addition, εNd values of -4 to-18 determined for the Etusis Formation are similar to the range in isotopic values for the Abbabis Complex basement rocks (McDermott and Hawkesworth, 1990). Increasing Sm/Nd and decreasing Th/Nd ratios with stratigraphic height through Damaran and Nama metasediments have been interpreted to indicate that the provenance switched from older and more granitic sources (Abbabis Complex) for lower Damaran sediments to younger and more mafic sources higher in stratigraphy (McDermott and Hawkesworth, 1990). εHf values for the Etusis Formation and inherited zircons assumed to be the Abbabis Complex appear to be similar (Foster *et al.,* 2015). However, two other recent studies (Milani *et al.,* 2015; Longridge *et al.,* 2018) did not yield the same results for the Abbabis Complex as Foster *et al.* (2015). In addition, U-Pb detrital ages for the Etusis Formation of *ca.* 1030 Ma and 2040 Ma are proposed to indicate an Abbabis Complex age signature and, more broadly, that of the Congo Craton (Forster *et al.,* 2015). Previous age dates for the Abbabis Complex are recorded at *ca.* 2 Ga (Jacob *et al.,* 1978; De Kock *et al.,* 2000; Longridge, 2012; Longridge *et al.,* 2014) as well as a *ca.* 1 Ga crystallisation age in some instances (Kröner *et al.,* 1991; Foster *et al.,* 2015) that is also thought to represent a Kibaran overprint of the Abbabis Complex (Longridge, 2012). However, the 1 Ga ages for the Abbabis Complex are not reliable and difficult to interpret. A minimum depositional age of 800 Ma for the lower Nosib Group was established from rift associated intrusions of the Oas quartz syenite (Hoffman *et al.,* 1996).

Based on detrital εHf values, from this study, the metasedimentary Etusis Formation shows three distinct populations, so named Et 1 to 3, and a single zircon age that has a similar U-Pb age and εHf value to the Abbabis Complex (Fig. 7.20). Therefore, this formation can be assigned to four different source areas, a recycled Archaean source with a DM extraction age between 3.5 and 3.6 Ga (Et1), another recycled Archaean source with a 2.6 to 2.9 Ga DM extraction age (Et2), a juvenile source crystallised at 2 Ga (Et3) and the Abbabis Complex. Therefore, the initial conclusion is that the Etusis

Formation was not entirely sourced from the Abbabis Complex based on Lu-Hf isotopic work from this study.

If detrital ages and εHf values are considered and compared with previous studies, a possible link between the southern Congo Craton and the Etusis Formation can be established. Detrital age spectra for the Etusis Formation obtained from this study displays two detrital age peaks at 1020 Ma and 2020 Ma. These detrital age peaks correspond well with prominent 1030 Ma and *ca.* 2 Ga detrital peaks for the Congo Craton Damaran Sequence over the Kalahari Craton Damaran Sequence (Fig. 7.21) reported by Foster *et al.* (2015). Highlighting the similarities of the Etusis Formation to the age spectra of the sediments along the Congo Craton's edge suggesting the southern Congo Craton as a possible source area. Unradiogenic εHf values for Et2 also correspond to the previous study for the Etusis and Khan formations showing similarities between the Nosib Group metasediments in the sCZ. However, the Abbabis Complex results from Foster *et al.* (2015) are not considered as these included U-Pb ages and Hf ratios that are derived from inherited zircons assumed to represent the basement lithologies and are not consistent with other Abbabis Complex results (Fig. 7.20).

Detrital zircon ages ranging from 1770 Ma to 1744 Ma for the Nabis-Nosib Group (Nascimento *et al.;* 2017) do not correlate with the major detrital ages obtained in this study. However, a less significant population at 1992 Ma was interpreted to have been sourced from the Abbabis Complex and multiple other Palaeoproterozoic sources, surrounding, or associated with, the Congo Craton (Nascimento *et al.;* 2017). Nascimento *et al.* (2017) has interpreted the Abbabis Complex to be of Kalahari Craton affinity, which is contrary to interpretation by other authors (Jacob *et al.,* 1978; Hawkesworth and Marlow, 1983; Tack *et al.,* 2002; Miller, 2008; Longridge, 2012; Longridge *et al.,* 2018) and this study favouring a Congo Craton affinity. This interpretation was concluded using data based on inherited Abbabis Complex ages of *ca.* 1 Ga from Foster *et al.* (2015), suggesting that the Abbabis Complex was a palaeo-high that extended from the Kalahari Craton (Nascimento *et al.,* 2017). However, the Abbabis Complex is *ca.* 2 Ga in age (see section 7.5.1). Therefore, the southern edge of the Congo Craton is still a more likely source for the Etusis Formation than the Kalahari Craton as the detrital signatures from Foster *et al.* (2015) provide a broader comparison.

The Palaeoproterozoic U-Pb ages, in the detrital signatures from this study, could be attributed to the Abbabis Complex due to the similarities in 2 Ga ages. In addition, the Abbabis Complex falls along the same evolution path as the Etusis Formation when comparing the εHf age trajectory of the Etusis Formation (Et2) (Fig. 7.18), which may indicate that Et2 and the Abbabis Complex are related. This is also supported by a single εHf value that is similar to those of the Abbabis Complex

and the same Archaean DM model ages produced by Et2 and the Abbabis Complex (Fig. 7.20), which consequently overlap with model ages for the Congo Craton.

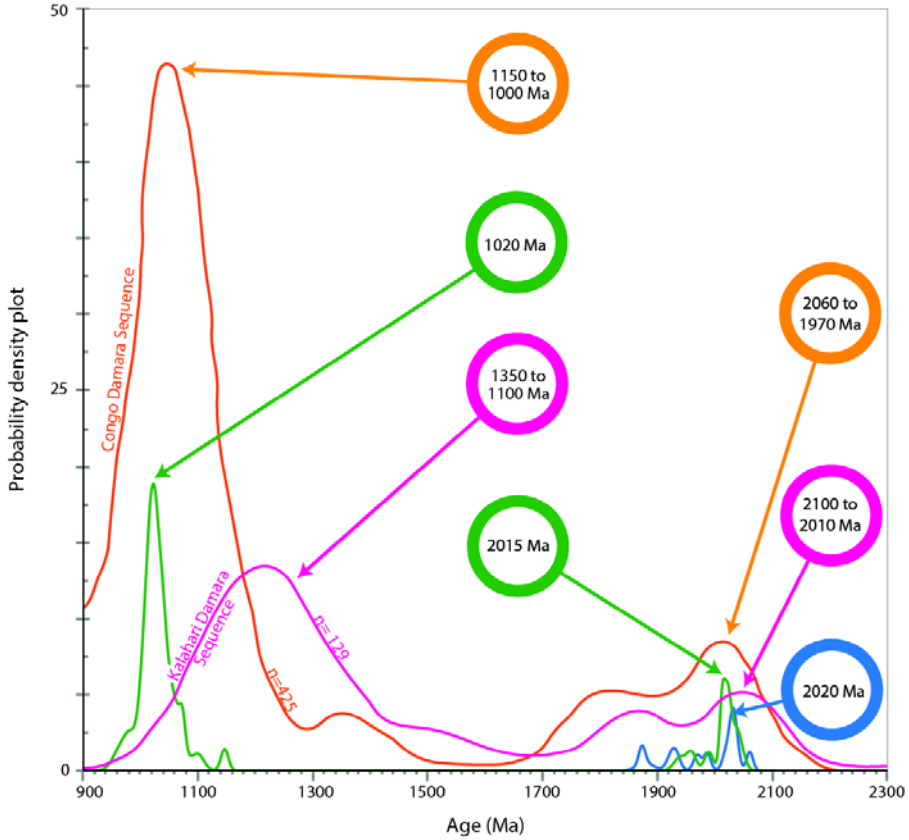


Figure 7.21: Comparison of detrital zircon age spectra of Damaran sediments from the Congo and Kalahari Craton edges (after Foster *et al.*, 2015) and of the Etusis Formation (this study). The signatures show that the Etusis Formation show similarities to the Congo Craton Damara Sequence as the peaks at *ca.* 2015 Ma and 1020 Ma overlap with the Congo Craton peaks at 2060 Ma to 1970 Ma and 1150 Ma and 1000 Ma, respectively. Blue and green curves correspond to samples 1.1 and PA01; orange curves and arrows correspond to the Congo Craton Damara Sequence; pink curves and arrows correspond to the Kalahari Craton Damara Sequence.

Therefore, it is possible that the Etusis Formation was sourced locally from a combination of either the Abbabis Complex, as recognised in the sCZ, or other portions of the Congo Craton not exposed or both. The local exposures of the Congo Craton in the sCZ (the Abbabis Complex) U-Pb ages cannot account for the Kibaran ages (*ca.* 1 Ga) found for the Etusis Formation. Previous data (see summary in Longridge *et al.,* 2018; Fig. 7.20) suggests that younger 1 Ga U-Pb detrital ages are characteristic of the Kalahari Craton but subsequently yield younger 2.5 – 1.7 Ga DM model ages which do not match any of the Etusis Formation populations (Et 1 to 3) that have 1 Ga detrital ages. Therefore, the Kalahari Craton is an unlikely source area but both the local Abbabis Complex and other unexposed portions of the Congo Craton may have provided a varied source area. Population Et2 may have an Abbabis Complex link based on an εHf age trajectory, however, the remaining populations do not show an overlap with εHf values for the Abbabis Complex (this study; Milani *et*

al., 2015; Longridge *et al.,* 2018). Therefore, the Congo Craton could provide the heterogeneity in sources for the Etusis Formation and show older DM model ages than expected for the Kalahari Craton (Fig. 7.20; Longridge *et al.,* 2018). The DM model ages for Et 1 are old enough to be Congo Craton affinity (Fig. 7.20) and with minor juvenile Palaeoproterozoic crust of the Congo Craton (Longridge *et al.,* 2018) which would account for the juvenile crust component (Et3). A wider source area is contrary to observations made by Foster *et al.* (2015) who proposed that the Nosib Group metasediments in the sCZ were locally sourced from the Abbabis Complex and not from the southern edge of the Congo Craton.

Nascimento *et al.* (2017) suggests that the Congo and Kalahari cratons were proximal during rifting, which contradicts Foster's *et al.* (2015) proposal that these continents were not proximal until their amalgamation during Gondwana. A proximal Congo-Kalahari craton is also supported by a recent palaeomagnetism study (Salminen *et al.,* 2018). The data from this study is not regional enough to make any conclusions as to which model is more plausible, but it does suggest that the Congo Craton/Abbabis Complex is more likely a significant contributor when compared to the Kalahari Craton in the sCZ. This prominent Congo Craton signature is present in several datasets (Foster *et al.,* 2015; Nascimento *et al.,* 2017; this study) and suggests that there must have been a division of the basin between largely Congo or Kalahari provenances. Whether this is due to an Abbabis palaeo-high (Nascimento *et al.,* 2017), or separation of Congo and Kalahari cratons during Rodinia, is questionable. However, the lack of extensive deep marine sediments associated with the Damara supracrustals (Henry, 1992) may indicate that they were more proximal during rifting.

The sediments of the Etusis Formation were sourced from a mix of reworked and juvenile crustal terrains given that the εHf values are so varied. This is a similar conclusion drawn for the upper Swakop Group (Foster *et al.,* 2015), which overlies the Nosib Group including the Etusis Formation. This variation in the Etusis Formation may provide further evidence that the Abbabis Complex may be more complicated and that models concerning the geodynamic setting of the Abbabis Complex prior to the assembly of Gondwana may require revision. Based on field and analytical studies, varied εHf values could be manifesting remnants of a more complex Abbabis Complex, similar to what is identified in the type locality described by Smith (1965). Smith (1965) identified and described these basement-cored domes across the sCZ and noted that a basic stratigraphy of the Abbabis Complex including the Tsawisis and, Naob formations and the intrusive Narubis Granitoid Complex (Brandt, 1987). This heterogenous lithological make up would provide a heterogenous source including juvenile material such as the Palaeoproterozoic amphibolite dykes commonly associated with the basement lithologies. Given that the Abbabis Complex lithologies that have been sampled and

analysed for Lu-Hf work are primarily gneissic (Longridge *et al.,* 2018) and therefore, cannot represent the basic stratigraphy identified by Smith (1965). As a result, an assessment of whether the provenance of the Etusis Formation is locally derived (from the Abbabis Complex) or not is limited.

7.5.4 Red granites

Crystallisation ages of 535.77 ± 0.96 Ma for the red granites are within analytical uncertainty of published dates of *ca.* 539-534 Ma for red granites from the northern extent of the Palmenhorst Dome and Goanikontes area (Longridge, 2012; Briqueu *et al.*, 1980). This granite type predates the D2 deformation and therefore marks the oldest limit of deformation in the sCZ between 536±1 Ma. Based on ages, field relationships, petrogenesis and compositions the granites studied here are considered to be the equivalents of red granites studied by Nex *et al.* (2001a). The red granite sample (K06) also contains apparent inherited cores with ages of *ca.* 1 and 2 Ga.

A pooled metamorphic age of 533.76 ± 1.65 Ma was established using individual ages that showed a spread along the concordia. Th/U ratios tend from ~ 0.9 towards 0.1 for these metamorphic domains. The individual ages ranged from *ca.* 560 to 520 Ma which may indicate a protracted metamorphic event similar to the two main tectonothermal events of 560 to 540 Ma and 540 to 520 Ma in the Damara Belt (Longridge, 2012). This metamorphic age is within error of the *ca.* 545 to 540 Ma metamorphic ages that were produced from the amphibolites in this study and could be equivalent to the end of the second and younger tectonothermal event of the Damara Belt between 540 and 520 Ma (Longridge *et al.,* 2011). From the concordia plots, it is clear that there is a range of metamorphic ages that are long-lived and near continuous metamorphic event rather than two discrete episodes, despite an apparent presence of three metamorphic populations.

The quartzofeldspathic Etusis Formation and basement lithologies are considered to be possible sources for the red granites (Nex *et al.*, 2001a). However, the distinction between these two possible sources is near impossible to unravel due to the similarities (mineralogically, geochemically and isotopically) between these lithologies (Kinnaird and Nex, 2007). Field observations indicate that both the Etusis Formation and the red granites contain sillimanite which may initially exclude the Abbabis Complex as a source. However, other studies have also indicated that the basement lithologies can sometimes contain sillimanite in various schists (Smith, 1965; Brandt, 1987). Zircons with U-Pb ages that match ages for the Abbabis Complex and the Etusis Formation are most likely inherited from these lithologies. Values of εHf for the red granites plot along an εHf-age trajectory (from DM εHf to εHf at *ca.* 550 Ma) defined by the Etusis Formation and Abbabis Complex (Fig. 7.18).

Therefore, the red granites may have been a product of melting of either the Abbabis Complex or the Etusis Formation. However, the U-Pb ages for the corresponding εHf values and DM model ages are younger (at *ca.* 1 Ga) and do not fit the dominant inherited ages for the red granite. This may suggest that the Abbabis Complex is a possible source which is similar to a study by Jung *et al.* (2003) who proposed the basement rocks as a source.

Unradiogenic εHf values for the red granites are similar to the unradiogenic εHf and εNd values from other studies (Fig. 7.20; Longridge *et al.,* 2018 and references within). These unradiogenic εHf values indicate crustal recycling of variably aged Archaean to Palaeoproterozoic crust (DM model ages of 2.7 to 3 Ga). However, DM model ages of 2.7 to 3 Ga are characteristically older than other Damaran granitoids from previous studies and the amphibolite dykes from this study (Fig. 7.20), but rather show similarities in model ages with the Congo Craton, Abbabis Complex and the Etusis Formation (Fig. 7.20). This study provides evidence that the red granites were derived from crustal material of the Congo Craton (DM model ages > 2 Ga) and suggests that the red granites were sourced from recycled older Archaean crust, without any net crustal growth during the Pan-African which agrees with previous studies for granitoids of the sCZ (McDermott *et al.,* 1989; Milani *et al.,* 2015; Longridge *et al.,* 2018).

7.5.5 Sheeted leucogranites

The type C′ SLG yields a concordia age of 525.72 ± 1.91 Ma interpreted to reflect igneous crystallisation. This 525.72 ± 1.91 Ma zircon age matches ages for other leucogranites in the sCZ (526 - 519 Ma: Jung *et al.,* 1998; Jung *et al.,* 2000; Longridge *et al.,* 2011; Longridge, 2012). Crystallisation of various SLGs and alaskites are considered contemporaneous with D2 deformation, and the second episode of metamorphism (550 to 520 Ma; Jung *et al.,* 1998; Jung *et al.,* 2000; Tack *et al.,* 2002; Johnson *et al.*, 2006; Longridge *et al.,* 2011; Longridge, 2012). In addition, field relationships from this study (Chapter 4) for type C′ SLGs document a link with D2 deformation supporting the notion that these SLGs can be used to date D2 deformation. Therefore, D2 deformational event can be constrained to have occurred contemporaneously at *ca.* 525 Ma, which is equivalent in age to other D2 syn-tectonic granites (520 – 510 Ma; Longridge *et al.,* 2011; Longridge, 2012) equivalent to those described in this study.

A concordia age of 510.74 ± 1.18 Ma from metamorphic rims for the type C′ SLG are equivalent to previously estimated dates for D3 deformation at *ca.* 515 Ma (Longridge, 2012) and *ca.* 508 Ma (Briquet *et al.*, 1980) using syn-tectonic (D3) uraniferous leucogranites. Petrographic observations also suggest that metamorphic rims may be associated with D3 or protracted M2 metamorphism.

However, this is in contrast to petrographic evidence that indicated no crystallised partial melt and metamorphic observations where the SLGs did not show evidence of metamorphism. Therefore, this metamorphic age may be related to the high-grade extensional event identified by Jung and Mezger (2003). Upper intercept ages reflect inheritance: the 1829.24 ± 7.88 Ma age represents magmatic grains from the Abbabis Complex and the 1080.8 ± 21.2 age may represent Kibaran metamorphic ages for the Etusis Formation. The lower intercepts at 521. 55 ± 1.98 and 497 ± 5.58 Ma loosely coincide with the metamorphic concordia age. A single unradiogenic εHf value was measured for the type C' SLGs (sample K07) and is similar to the εHf values for the red granites from this study (Fig. 7.20), which may indicate that these SLGs were sourced from the red granites. Zircon Hf isotope systematics for the two SLGs are indicative of recycled Archaean crust with a DM model age of *ca.* 3 Ga and, hence, showing affinity with the Congo Craton rather than the Kalahari Craton. This disagrees with findings from Longridge *et al.* (2018).

Type E of the SLGs (sample PA03) yielded zircons that cannot represent the timing of crystallisation. Field relationships suggest that this specific SLG cross-cuts type C' (525 Ma) and therefore cannot be older than type C' SLG. As a result, the U-Pb intercept ages of 1906.73 ± 8.46 Ma and 587.7 ± Ma represent inheritance, possibly from the 2 Ga Abbabis Complex. The εHf values match those of the Abbabis Complex (Fig. 7.20) confirming that the type E SLG assimilated Abbabis Complex zircons.

7.6 Conclusions

The Abbabis Complex yields *ca.* 2 Ga crystallisation ages from upper concordia intercept ages. These ages are equivalent to 2 Ga published ages but are older than the 1 Ga age produced by Jacob *et al.* (1978) of a Khan orthogneiss. The convolute and sometimes homogenous domains are interpreted as late stage magmatic textures rather than metamorphic growth. Unradiogenic zircon εHf values for the Abbabis Complex translate into DM model ages of 2.8 to 3 Ga, consistent with reworking of Archaean crust during Eburnean orogenesis. Since Hf DM model ages for the Abbabis Complex are similar to those from the Congo Craton the basement lithologies most likely represent an extension with the Congo Craton. Further reconstructions are speculative due to the intense high-grade metamorphic overprint during the Pan-African.

Concordant crystallisation and metamorphic ages for the amphibolite dykes of 550.48 ± 0.85 and *ca.* 540 Ma, respectively. On this basis, the dykes appear to be equivalent to the Damaran amphibolites and the Goas Suite. The metamorphic ages are attributed to a thermal event associated with voluminous magmatism and emplacement of the Goas Suite during the early onset of the first Damaran tectonothermal event (560 to 540 Ma). Whole rock subduction or crustal

assimilation signatures and trace element ratios suggest that the dykes may have had a juvenile source (possibly arc magmatism; McDermott, 1986) that assimilated variable continental crust during emplacement, resulting in the unradiogenic εHf values observed from the amphibolite dykes. One amphibolite shows DM model ages of *ca.* 1.6 to 1.9 Ga, similar to those reported for the Kalahari Craton (2.4 - 1.7 Ga), and possibly indicate assimilation of the Kalahari Craton (Longridge *et al.,* 2018).

Based on detrital εHf values three distinct populations are identified for the Etusis Formation, namely Et 1 to 3, and a single zircon age that has an affinity to the Abbabis Complex. The Etusis Formation received contributions from three distinct sources: recycled Archaean material with a crystallisation age of 1 Ga (model age: 3.5 – 3.6 Ga) (Et1), recycled Archaean material with a crystallisation age of 1 Ga (model age: 2.6 - 2.9 Ga) (Et2), and a juvenile source extracted from the DM and crystallised during the Eburnean orogeny at 2.2 to 2.4 Ga (Et3) and the Abbabis Complex. Indicating that the Etusis Formation was not entirely sourced from the Abbabis Complex based on Lu-Hf isotopic work from this study.

From U-Pb detrital spectra the Etusis Formation shows similarities to the Damaran metasediments along the edge of the Congo Craton as well as similar DM model ages for Et3 to the Congo Craton. Therefore, suggesting a Congo Craton provenance for the heterogenous sources established for the Etusis Formation. Unradiogenic εHf values of Et2 follow the εHf age trajectory which has a similar trend to the Abbabis Complex, and therefore Et2 was most likely sourced from the local Abbabis Complex. Suggesting that the provenance for the Etusis Formation comes from a combination of the Abbabis Complex and the Congo Craton. This heterogeneity may represent a more complex Abbabis Complex that has not been sampled and analysed for Lu-Hf yet, as most U-Pb-Hf results are derived from gneisses or inherited zircons and therefore, cannot represent the variability seen in the Abbabis Complex lithologies at the type locality (Naob and Tsawisis formation as well as the Narubis Granitoid Complex).

The red granites have a crystallisation age of 535 Ma and metamorphic age of 533 Ma. The crystallisation age is within error of other published dates and the 533 Ma metamorphic age is also within analytical error for the metamorphic ages established from the Damaran amphibolite dykes. Metamorphism appears to be near continuous rather than episodic. U-Pb and εHf data from this study cannot be used to resolve the debate on whether the source for the red granites is the Abbabis Complex or the Etusis Formation as both are possible from U-Pb-Hf studies. Unradiogenic εHf values for the red granites indicate crustal recycling and DM model ages (2.7 to 3 Ga) are resolvably older

than model ages reported in previous studies for other Damaran granitoids. Therefore, the red granites were sourced from older Archaean crust rather than the Kalahari Craton as proposed by Longridge *et al.* (2018). This study provides evidence that the red granites (a Damaran granitoid) shows reworking of the Congo Craton with a more variable reworking signature than Longridge *et al.* (2018) observed.

Type C' SLGs were emplaced at 525 Ma contemporaneously with D2 deformation. These SLG ages are consistent with ages for other syn-tectonic SLGs. A younger age of 510 Ma obtained from metamorphic rims are proposed to extend the constraints of the M2 metamorphic event. A single unradiogenic εHf value was measured for the type C' SLGs which is similar to the εHf values for the red granites and may indicate that these SLGs were sourced from the red granites. Unradiogenic εHf values indicate that no new crust grew during Damaran orogenesis. DM model ages of 2.7 to 3 Ga suggest crustal reworking of Congo Craton affinity rather the Kalahari Craton.

Zircons extracted from type E SLG are considered as inherited as these leucogranites are younger than the other SLGs and the Abbabis Complex lithologies from cross-cutting field relationships. Similarities in age and εHf values is best interpreted in terms of inherited material from the Abbabis Complex. No reliable information could be extracted regarding emplacement of this SLG type.

8. Synthesis and Conclusions

8.1 The evolution of the northern Palmenhorst Dome in the context of the southern Central Zone of the Damara Belt

Based on detailed remote sensing, lithological mapping, structural analysis, petrographic examination as well as the interpretation of geochemical and U-Pb-Hf geochronological data, a revised concept for the evolution of the northern extent of the Palmenhorst Dome is presented (Fig. 8.1). The evolution and timing of deposition, deformation, emplacement of intrusives and metamorphism is placed in context of the southern Central Zone and its evolution from ocean closure to orogenic collapse (Fig. 8.1). A recent synthesis of data available from the Damara Belt correlated deformational, metamorphic, intrusive and depositional relationships across the different zones of the belt (Goscombe *et al.,* 2017b). Three thermal events and nine deformational events were established within the sCZ. However, the authors do note that the sCZ is the most complex to interpret as it situated in the core of the orogen and therefore preserves the most intense deformation and metamorphic histories.

The several deformational events that Goscombe *et al.* (2017b) synthesised are comparable to the D1 to D4 deformational events identified in this study. A regional study enabled Goscombe *et al.* (2017b) to establish nine deformational events but they were not all identified individually in the field. The intrafolial folds and main foliation of D1 and D2 (Goscombe *et al.,* 2017b) are correlatable with D1 (this study) and early Kaokoan collisional phases (Goscombe *et al.,* 2017b) and closure of the Khomas Ocean (Lehmann *et al.,* 2016). D3 to D6 (Goscombe *et al.,* 2017b) are associated with recumbent folding with a high-grade thermal event and is comparable to D2 (from this study), formed during the closure of the Adamastor Ocean (Lehmann *et al.,* 2016) and the start of orogenic collapse due to increased crustal thickening and reaching a critical thickness (Longridge, 2012). Deformation events D7 to D9 (Goscombe *et al.,* 2017b) are proposed to be responsible for dome formation and upright east-west trending folds, and thus can be correlated to the events identified in D3 (this study) affecting the region during the collision between the Congo and Kalahari cratons (Lehmann *et al.,* 2016). The final phases of orogenic collapse are associated with extension and core exhumation and have been associated with the post-tectonic type F SLGs and D4 from this study. Ages reported by Goscombe *et al.* (2017b) for subduction and assigned to phases of the orogeny are used as it was beyond the scope of this study. Detailed synthesis and conclusions from this study are discussed below in terms of the Palaeoproterozoic basement, the supracrustals, structure, metamorphism and Damaran anatectic events.

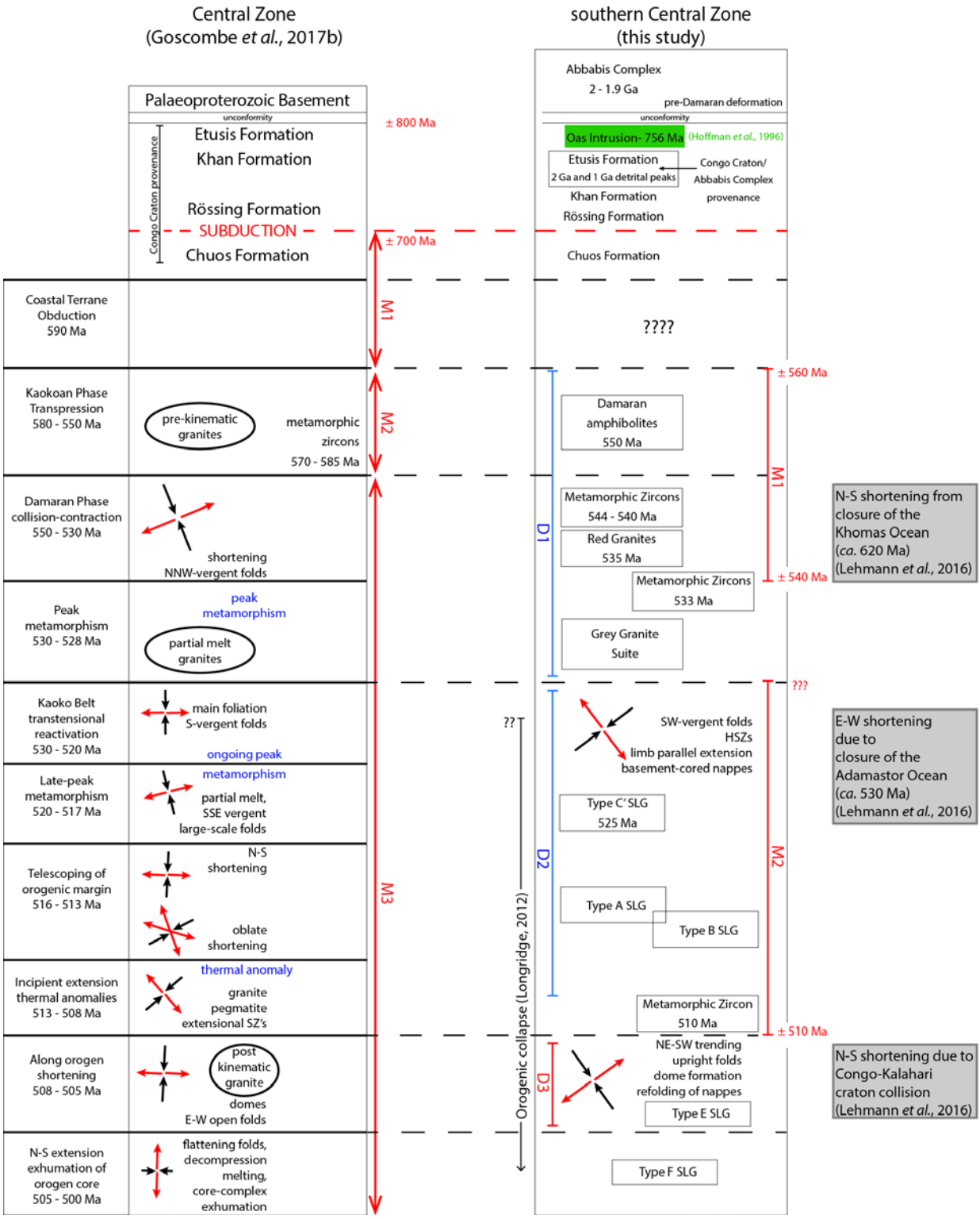


Figure 8.1: A summary of the deformational, metamorphic and emplacement events that took affected the sCZ as well as age constraints from other studies (modified after Goscombe *et al.*, 2017b and references within) and this one. Where there was no evidence found from this study correlations to the synthesis established from Goscombe *et al.* (2017b) were performed and other references were utilised (Hoffman *et al.*, 1996; Longridge, 2012; Lehmann *et al.*, 2016).

8.1.1 The Abbabis Complex and associated intrusives

Using remote sensing the extent of the Abbabis Complex was established from the compositional spectral fingerprint and the overall well-known structural trends of basement-cored domes from interference folding (Smith, 1965; Lehtonen *et al.,* 1995; Longridge, 2012), which was confirmed by field observations. Domains 1 to 3 were demonstrated to be basement lithologies and are mineralogically, texturally and compositionally heterogeneous. This provided evidence for a lithologically heterogenous makeup of the Abbabis Complex in the northern Palmenhorst Dome. However, despite this difference the various lithologies of the Abbabis Complex provide consistent crystallisation ages *ca.* 2 Ga, and unradiogenic εHf values with varied Archaean model ages. Domain 1 contains orthogneisses and augen gneisses, while domain 3 comprises basement granites. Based on lithological mapping, however, domain 2 could not be divided into the northern and southern extents identified from remote sensing, as the southern extent mainly comprises orthogneisses and augen gneisses (resembling domain 1) that had been more affected by melt infiltration. The northern extent of domain 2 (northern) predominantly comprises augen gneisses.

This heterogenous nature of the basement lithologies is based on both compositional differences and textural variations. The grey orthogneisses (initially proposed to be paragneisses) were not assigned to the Tsawisis or Naob formations, based on compositional and mineralogical characteristics, and therefore the Abbabis Complex is correlated with the Narubis Granitoid Complex. These paragneisses/grey orthogneisses represent highly strained equivalents of the orthogneisses due to grain-size reduction and thinning of gneissic banding (Passchier *et al.,* 1990; Platt and Behr, 2011), but also on the basis of igneous compositions (P_2O_5/TiO_2 versus MgO/CaO).

Pre-Damaran structural indicators are not readily identified in the field as they have been reoriented into parallelism with the Damaran fabric. However, a second foliation is identified in the basement lithologies, at both mesoscopic and microscopic scales. Due to the highly tectonised nature of these lithologies determination of whether these foliations in the basement granites and amphibolite dykes constitute a pre-Damaran or Damaran fabric is problematic. However, U-Pb age constraints and similar unradiogenic εHf values indicate that the basement granites are Palaeoproterozoic in age and therefore constitute a component of the Abbabis Complex. Additionally, the amphibolite dykes yield 550 Ma ages, which correspond to ages for the Damaran amphibolite dykes, and in fact, represent early Damaran magmatism. The overall structural trend of the Abbabis Complex foliations is northeast-southwest from field mapping and is commonly observed within the basement lithologies in Landsat 8 and hyperspectral imagery. This observation applies mainly to the gneisses but not to the basement granites. Therefore, highlighting that remote sensing may be a useful tool

for identify varying metamorphic rocks of the basement lithologies based on textural differences. This is due to the lack of a continuous foliation in the basement granites, whereas the gneisses had a well-developed foliation.

Metamorphic indicators of pre-Damaran age are not typically identified other than metamorphic minerals defining foliations and feldspar porphyroblasts (augen). The presence of extensive migmatites are also observed in the basement lithologies, but this partial melt episode has largely been attributed to the basement displaying increased metamorphic grades during the early phases of collision during the Pan-African (Poli, 1997; Goscombe *et al.,* 2017b). These partial melts are seen in thin section but are most identifiable in the field where they have been extended parallel to the foliation. However, these foliation parallel partial melts are also observed in the Damara Sequence and therefore most likely represent early Damaran partial melts (Goscombe *et al.,* 2017b and references within). This also applies to the granoblastic polygonal textures, observed in thin section, which overprints crystallised melts and gneissic rocks indicating a high-grade recrystallisation event associated with M1 metamorphism. The first metamorphic event identified in this study is most likely comparable to the second metamorphic event identified (Fig. 8.1) in the regional synthesis of the Damara Orogen of Goscombe *et al. (*2017b).

Basement-cored domes either contain a simple stratigraphy (Smith, 1965; Brandt, 1987 and references within), are cored by Damaran lithologies (Oliver and Kinnaird, 1996) or contain infolded Damaran metasediments (Longridge, 2012). The core of the northern extent of the Palmenhorst Dome is found to comprise basement lithologies that contain infolded Damaran supracrustals, which is consistent with the findings from studies in the greater extent of the Palmenhorst Dome (Longridge *et al.,* 2011; Longridge, 2012). Three synclinal infolds were identified, the Ostrich Gorge, Dorob and Hinge Synclines, in the northern extent of the Palmenhorst Dome, and may correlate with northern margin infolds identified by Longridge (2012). It can be ruled out that these represent the paragneisses of the Abbabis Complex (Poli, 1997). These synclines were identified based on a repetition of a sequence of lower Damaran lithologies with common and distinctive minerals. Infolds previously proposed by Longridge (2012) can be identified using a remote sensing approach, where similar spectral signatures were compared to infolds identified in this study. Therefore, remote sensing can be used as a tool to target anomalies in the basement-core domes.

Based on age and Lu-Hf isotopic data (this study), the various granites and gneisses of the Narubis Granitoid Complex yield similar *ca.* 2 Ga ages to one another. Therefore, these lithologies all formed during a similar event, involving recycled Archaean crust. U-Pb zircon ages of 2 Ga are consistent

with other published data (Jacob *et al.*, 1978; De Kock *et al.,* 2000; Tack *et al.,* 2002; Longridge, 2012; Longridge *et al.,* 2018) confirming a Palaeoproterozoic age for the basement (Fig. 8.1), and that this metamorphic complex consists of Archaean crust that was reworked during the Eburnean orogeny. The Abbabis Complex has been proposed to represent highly strained equivalents of the Congo Craton (Jacob *et al.,* 1978; Hawkesworth and Marlow, 1983; Tack *et al.,* 2002; Miller, 2008; Longridge, 2012; Longridge *et al.,* 2018) and the Archaean (2.8 – 3.1 Ga) DM model ages show overlap with DM model ages for the Congo Craton. Therefore, from this study the Abbabis Complex most likely represents an extension of the Congo Craton. The high-grade overprint of the Damara Orogen, and debates surrounding palaeogeographic reconstructions (Merdith *et al.,* 2017) impedes further conclusions on the reconstruction of the Abbabis Complex in context of the Eburnean and Rodinian events.

8.1.2 Comparison between the quartzofeldspathic Abbabis Complex and the Etusis Formation

The Abbabis Complex and the Etusis Formation are both quartzofeldspathic in composition and have similar mineralogical, geochemical, U-Pb detrital ages and Nd-Sm isotopic signatures and are commonly difficult to distinguish between (Smith, 1965; McDermott and Hawkesworth, 1990; Foster *et al.,* 2015; Nascimento *et al.,* 2017). However, hyperspectral imagery provided an effective tool in delineating the contact between the basement gneisses and feldspathic quartzites of the Etusis Formation and aided in the refinements of this contact. The remote sensing "contact" between domains 1 to 3 (basement lithologies) and domain 4 (the Etusis Formation) almost always yielded an effective estimate for the basement-cover contact in the field which is otherwise obscured by complex deformation and intrusive overprinting. Hyperspectral mineral maps lack abundant mineral signatures for the Abbabis Complex, whereas the Etusis Formation shows an increased spectral response (based on mineral maps provided). In addition, various Landsat 8 and hyperspectral images showed characteristic spectral signatures of mafic compositions for the Abbabis Complex, which possibly reflected the near continuous biotite foliation identified in the basement rocks (absent in the Etusis Formation). Additionally, the Abbabis Complex shows a distinct northeast-southwest trending fabric (at outcrop and remote sensing scales) that is typically not observed in the supracrustal rocks. These supracrustals commonly show megascopic and mesoscopic banding that is parallel to folding.

Mineralogically, the Etusis Formation contains more quartz than the Abbabis Complex and displays lower modal abundances of microcline than the basement lithologies. This distinction is possible both petrographically and geochemically. Rare Earth Element patterns for the Etusis Formation and

the Abbabis Complex are near identical. Trace element ratios (Th/Sc and La/Sc) of the quartzofeldspathic to pelitic schists of the Etusis Formation (Th/Sc= 6 – 11; La/Sc= 12 – 26) and the various gneisses and granites of the Abbabis Complex (Th/Sc= 1 – 8; La/Sc= 3 – 9) show, however, distinct variations. The Etusis Formation shows more elevated Th/Sc than the Abbabis Complex, possibly a result of the mineral sorting (e.g. enrichment of ilmenite) and sediment maturity (Taylor and McLennan, 1985). Trace element geochemistry suggests the Etusis Formation was derived from more felsic sources than the other Damaran metasediments studied, which is consistent with other isotopic and trace element studies (McDermott and Hawkesworth, 1990).

Unradiogenic εHf values for the Etusis Formation fingerprints a more complicated source than just the proposed Abbabis Complex (Smith, 1965; McDermott and Hawkesworth, 1990; Foster *et al.,* 2015; Nascimento *et al.,* 2017). A trajectory from εHf values at the time of separation from the DM and εHf values corresponding to detrital ages of population Et2 (Fig. 7.18) indicate that the Etusis Formation has one population (Et2) sourced from the Abbabis Complex. Archaean DM model ages for the Etusis Formation (Et2: 2.6 – 2.9 Ga) are similar to those calculated for the Abbabis Complex (2.8 – 3.1 Ga). However, populations Et1 and Et3 have εHf values that do not show a link or similarities to the Abbabis Complex and were most likely sourced from the southern edge of the Congo Craton. This is due to the similar U-Pb detrital age spectra for Damaran metasediments sampled along the Congo Craton and the detrital spectra for the Etusis Formation from this study (Fig. 7.21). The Congo Craton would also provide a wider source for the Etusis Formation resulting in the heterogenous unradiogenic and radiogenic Et1 and Et3 populations. Therefore, the Etusis Formation was most likely sourced from a wider source terrain that included the local Abbabis Complex and the southern edge of the unexposed Congo Craton, contrary to a previously proposed local source terrain (Smith, 1965; Foster *et al.,* 2015; Nascimento *et al.,* 2017).

Foster *et al.* (2015) states that the Congo and Kalahari cratons may not have been proximal during Rodinia but only during the Neoproterozoic when these cratons sutured in response to the Pan-African collisional event due to the distinct Congo and Kalahari provenances. Whereas Nascimento *et al.* (2017) prefers a proximal reconstruction during rifting with the Abbabis palaeo-high separating the basin into Congo and Kalahari provenances. These varied populations may not have been sourced from the Congo Craton during rifting but rather another unknown source comprising mixed juvenile and reworked components if Foster's *et al.* (2015) model is favoured. However, this also brings into question the nature of the Abbabis Complex during rifting and whether it could be a probable source as it has been documented to be an extension of the Congo Craton. The available U-Pb-Hf data from this study cannot resolve the question of an Abbabis palaeo-high (Nascimento *et*

al., 2017) or distal Congo-Kalahari craton reconstructions (Foster *et al.,* 2015), but the lack of deep marine sediments in the lower Damaran sediment record and the fact that the Abbabis Complex is proposed to be an extension of the Congo Craton does suggest a more proximal geometry during rifting. Further resolution for this paradox is limited due to the high-grade Damaran metamorphism and the lack of extensive Lu-Hf datasets for metasedimentary and metavolcanics of the Abbabis Complex.

8.1.3 The Damara Supergroup

A gradational contact was observed between the Etusis Formation and the Khan Formation, which has been noted before (Jacob, 1974; Henry, 1992). This gradational contact can be seen in various remote sensed images where domain 4 (Etusis Formation) and domain 5 (Khan Formation) display indistinct gradational domains. In addition, the interfingering and lateral facies changes often observed in the field could be identified at a megascopic scale from hyperspectral imagery and could be attributed to switches between fluvial and distal fluvial deposition (Jacob, 1974; Henry, 1992). Remote sensing provided a useful delineation tool for the outcropping extent of a formation and for a crude assignment of the main rock types. Domains 5 and 6 were assigned as Khan Formation from remote sensing and were later identified as semi-pelitic (domain 5) grading to more calcsilicate-rich (domain 6) metasediments of the lower and upper Khan Formation. This holds true for the heterogenous domain 7, which was identified as the Rössing Formation and domain 8 representing the Chuos Formation as expected by the base map.

The general lithologies were easily correlated with other studies and were therefore confirmed to represent the Damaran lithologies. The quartzites, semi-pelitic schists and banded gneisses belong to the Nosib Group, whereas the Swakop Group provided ideal marker horizons, such as the Chuos diamictite (Gevers, 1931) and heterogenous marbles and schists of the Rössing Formation, which proved useful for the identification of supracrustal infolds in the basement. The Khan and Chuos formations were identified to be in contact with one another, however this was more likely to be a result of tectonic attenuation rather than facies variation as the marble units of the Rössing Formation are more susceptible to deformation (Nex, 1997).

Trace element ratios and major element plots (Taylor and McLennan, 1985) show an array of more felsic affinities to more mafic affinities from the Etusis Formation to the Chuos Formation (Th/Sc= 0.4 – 2; La/Sc= 0.9 – 2). The Khan and Chuos formation (Th/Sc= 0.5 – 2.4; La/Sc= 1.4 – 4.6; Th/Sc= 0.5 – 3.3; La/Sc= 1 – 8.1, respectively) appears to have received contributions from both felsic and mafic source regions, including lithologies of the Abbabis Complex (Th/Sc= 1 – 8; La/Sc= 3 – 9) and

amphibolite dykes, respectively. However, these amphibolite dykes have been shown to be Pan-African in age, by U-Pb ages (Chapter 7), and therefore cannot represent a possible source. But it does demonstrate that the Damaran metasediments may have had contributions from a more mafic source. The juvenile populations (radiogenic εHf of Et3) identified in the Etusis Formation may have also fingerprinted a more mafic source component. Foster *et al.* (2015), Nascimento *et al.* (2017) and this study confirmed that the Nosib Group was most likely sourced from the local basement lithologies and the southern edge of the Congo Craton, therefore the fact that the Khan Formation has similar Th/Sc and La/Sc ratios to the Abbabis Complex is not surprising.

8.1.4 Structure and Metamorphism

The overall structural pattern was established by combining previous geological maps and remotely sensed images. This pattern indicated a folded axial plane (D2 refolded by D3), which is consistent with some dome formation models for the basement-cored domes (Smith, 1965; Poli, 1997; Longridge, 2012). The relative timing of structural and metamorphic events identified in this study are similar to those established by other authors (Smith, 1965; Nash, 1971; Blaine, 1977; Coward, 1981; Jacob *et al.*, 1983; Barnes, 1981; Oliver, 1995; Nex, 1997; Longridge, 2012) and are somewhat correlatable to the larger evolution of the Damara Orogen (Lehmann *et al.,* 2016). The early D1 and M1 regional fabrics and D2 isoclinal southwest verging nappe-like folds that are refolded by upright open northeast-southwest trending D3 folds are consistent with the orogen parallel east-west shortening and north-south shortening arising from collision between the Congo and Kalahari Craton (Lehmann *et al.,* 2016).

However, a recent synthesis of metamorphic, deformational and structural data for the sCZ (Goscombe *et al.,* 2017b) shows that the structural evolution for the sCZ is more complex. The authors identified up to nine deformational events and three metamorphic events (Fig. 8.1), documenting a progression from subduction to orogen collapse and core exhumation. The similarities between Goscombe *et al.* (2017b) and this study are discussed below, including age constraints on the absolute timing of various deformational and metamorphic events from U-Pb ages from this study.

Deformational event D1 and metamorphic event M1 (from this study) correspond to the Kaokoan phase to early Damaran collisional phase and M2 metamorphism from the regional study after Goscombe *et al.* (2017b). The earliest metamorphic event noted by Goscombe *et al.* (2017b; M1) was not identified in the field or through petrographic examination but may represent the bedding parallel partial melts described in Goscombe *et al.* (2017b). The timing of M1 (from this study) was

constrained by spread of metamorphic ages from the red granites ranging from 560 to 520 Ma and that are most likely linked to the emplacement of the Damaran amphibolites (550 Ma, this study; 557 Ma, Longridge *et al.,* 2014) and the Goas Suite (580 – 535 Ma; Milani *et al.,* 2015). Metamorphic zircons with ages of 585 to 570 Ma have been previously identified in the sCZ (Goscombe *et al.,* 2017b). D1 deformation appears to be related to M1 metamorphism, but this association is partly obscured due to the metamorphic overprint of M2. Replacement of biotite by sillimanite indicates a temperature increase from M1 to M2 (Winter, 2001). The red granites, Goas Suite and Salem Granites may be related to M1 metamorphism from field observations and metamorphic studies (this study, Longridge *et al.,* 2017). Therefore, the emplacement age of the red granites (535 Ma) and metamorphic age (533 Ma) constrain the end of the M1 metamorphic event to approximately 540 Ma. This is consistent with the first tectonothermal event of the Damara Belt, which was dated at 560 to 540 Ma (Longridge, 2012; Longridge *et al.,* 2017). The associated granitoid emplacement is thought to have provided the heat required to weaken the crust to facilitate the folding of the crust into nappe-like structures (D2) (Anthonissen, 2009).

The second deformational event (D2) and peak metamorphic event (M2) are most likely equivalent to several phases of deformation (D3 to D6; Goscombe *et al.,* 2017b), based on similar structural styles and the long-lived nature of M3 metamorphism (Goscombe *et al.,* 2017b). These events are associated with transtensional reactivation of the Kaoko Belt to incipient extension (Fig. 8.1). This is the most complex deformational event and therefore a separation into several shorter events is plausible as observed in Goscombe *et al.* (2017b). Certain structural features, from Goscombe *et al.* (2017b), resemble those observed for D2 in this study, such as high strain zones. The nappe-like structures are a defining feature of D2 and are a result of the recumbent to gently inclined folds (this study; Downing and Coward, 1981; Coward, 1983). Additionally, northeast plunging lineations and prolate pebbles as well as high strain zones are common features observed and described as separate events in Goscombe *et al.* (2017b). These northeast-southwest trending HSZs are interpreted to occur along the top limbs of the anticlines of D2 verging folds (i.e. at the top of the nappe-like structure). Longridge (2012) suggested that his southwest verging folds were formed during orogenic collapse (Fig. 8.1) where both extension that is parallel (HSZs) and perpendicular (D2 shears) to the orogen are possible during folding associated with orogenic collapse (Harris *et al.,* 2002). Therefore, recumbent folding was most likely due to ductile extension (equivalent to D2 HSZs) as a response to gravitational collapse after crustal thickening reached a point where it could not sustain the thickness (Harris *et al.,* 2002; Longridge, 2012). Gravitational collapse resulting in fold vergence may account for the apparent compressional asymmetry, but distinct lack of shear sense indicators observed within the HSZs rather than a dominant northeast compressive direction.

Crustal thickening and then associated orogenic collapse has been debated in the Damara Orogen due to the isobaric P-T-t paths established by Longridge et al. (2017), where the authors argue for extensional gravitational collapse as a result of crustal thinning with no decompression. Previous studies in other collisional belts with associated high-grade temperatures due to anatectic melt emplacement has highlighted that later high temperature thermal events can completely obliterate early prograde metamorphic histories (Cottle et al., 2015), therefore, preserving no evidence of crustal thickening. In addition, P-T-t studies in the Damara Orogen by Buhn et al. (1995) from Otjosondu and Nex et al. (2001b) near Goanikontes establish higher pressures and a decompression history (5-8 kbar to 4 kbar). This, coupled with the presence of abundant folding and thrusting, suggests early stages of crustal thickening that have been overprinted by high-grade thermal events.

The timing of D2 deformation and M2 metamorphism was constrained by the emplacement age of the type C' SLGs at 525 Ma and metamorphic zircons from type C' SLG dated at 510 Ma. These ages are consistent with the second tectonothermal event for the Damara Belt (540 - 520 Ma; Longridge, 2012). Metamorphism (M2) and deformation (D2) appear to have more or less overprinted earlier events, which suggests that M2 metamorphism was the peak metamorphic event. This event also out-lasted D2 deformation (Fig. 8.1) as a pervasive granoblastic polygonal texture is identified in all lithologies, except for the SLGs. Suggesting that these SLGs associated with D2 deformation were most likely partial melt products as a result of M2 high-temperature metamorphism. The M2 metamorphic grade is proposed to be amphibolite facies (amphibole, diopside, sillimanite and biotite assemblages) which is consistent with other grades established for the sCZ (Hoffmann, 1976; Blaine, 1977; Sawyer, 1981; Bühn *et al.,* 1995; Masberg, 2000; Goscombe *et al.,* 2005; Goscombe *et al.,* 2014; Goscombe *et al.,* 2017a; and Longridge *et al.,* 2017).

The third and final deformational event (D3) resulted in the open upright folds (this study) and orogen parallel shortening (Goscombe *et al.,* 2017b) correlated to N-S compression due to the collision of the Congo and Kalahari cratons (Lehmann *et al.,* 2016) and exhumation of the orogen core took place possibly due to crustal thinning. Possible evidence for this is a detachment fault identified between the the basement and Damara cover for evidence supporting core complex formation (Oliver, 1994 and 1995). The D3 deformational event could not be linked to any U-Pb zircon ages that were associated with deformation, but the type C' SLG metamorphic zircons most likely fingerprinted the end of the M2 event at 510 Ma. Therefore, D3 and the emplacement of the associated SLGs were most likely shortly thereafter given that the timing of open and upright folding was previously constrained between 508 and 505 Ma (Goscombe *et al.,* 2017b). D3 deformation has

an orthogonal compressional direction to D2 deformation (Lehmann *et al.*, 2016), where the orthogonal change is thought to preserve kinematic switches during collision (Kisters *et al.,* 2004; Longridge *et al.*, 2007; Lehmann *et al.,* 2016). D2 structures are refolded, such as the basement-cored nappe folds which resulted in the characteristic dome formation of the sCZ. Dome formation is also attributed to the D3 equivalents of the evolution of the Damara Orogen of Goscombe *et al.,* (2017b).

Refolded D2 folds are used to explain dome formation in this study and block diagrams show the outcrop patterns at the present level of exposure (Fig. 4.39). Upward-facing infolds of Damaran metasediments within the Abbabis Complex can be interpreted as km-scale parasitic folds, possibly as part of a D2 nappe structure similar to those inferred by Anthonissen (2009) for the Karibib area, that have been refolded by D3 deformation (refolded fold axial planes). This is similar to the model of Longridge *et al*. (2012) for inference folding to explain dome formation processes.

8.1.5 Damaran amphibolite dykes and granitoids

Field relationships, petrographic analysis, geochemical data and age constraints for the Damaran granitoids are generally consistent with those reported by previous studies. The granitoids were intruded between 550 Ma and 525 Ma. The amphibolite dykes identified within the field area are not Palaeoproterozoic in age but rather Damaran-associated amphibolite dykes that were emplaced during the Pan-African around 550 Ma. From U-Pb age data these dykes were emplaced, possibly during the early phases of collision (Fig. 8.1). The dykes appear as pre-kinematic intrusives (Goscombe *et al.,* 2017b) that can be linked to the 580 to 535 Ma Goas Suite (Milani *et al.,* 2015). These amphibolite dykes are broadly identifiable from remote sensed imagery, but field observations and petrographic analysis was required to confirm that they are not rafted Khan Formation semi-pelites. These Damaran amphibolites contain a foliation but this foliation could not distinguish between a pre-Damaran or Damaran emplacement age for the dykes, therefore, U-Pb was required to confirm the age relationship. Unradiogenic εHf and Th/Yb versus Nb/Th indicate that the amphibolite dykes may have had a juvenile source but crustal interaction occurred during the emplacement of the amphibolites. Therefore, these dykes are not products of reworking of mafic lower crust during the subduction of the Kalahari Craton beneath the Congo Craton (Milani *et al.,* 2015; Longridge *et al.,* 2018) but rather related to arc-magmatism during subduction or crustal assimilation. A possible subduction or crustal contamination signature was evident from LILE enrichment relative to the HFSE, HREE flattened depletion (Fig. 6.8) as well as notable depletions of Ba, Nb, Ta and Sr and enrichment of Th and Pb. Both scenarios are likely, as arc magmatism has been purported in the Damara Belt (McDermott, 1986) and crustal assimilation most likely took place as the dykes intruded continental crust, but neither scenario can be concluded based on this study.

Combined field, petrographic, geochemical and geochronological studies suggest that the red granites are equivalent to various red granites described by previous authors (Smith, 1965; Nex, 1997; Basson and Greenway, 2004; Longridge, 2012; Fremantle, 2017) and are anatectic granites associated with early metamorphism during the Damaran Orogen around 540 to 530 Ma (Goscombe *et al.,* 2017b), prior to the onset of D2. These syn-tectonic granites are extensive migrated partial melts (diatexites) that form through fractional crystallisation processes and act as final melts (enriched REE patterns and negative Eu anomalies) as described by Johannes *et al.* (2003). These granites also preserve metamorphic ages of *ca.* 560 Ma which are not uncommon for the Damara (Goscombe *et al.,* 2017b) and may be related to the Goas Suite. M1 metamorphism was constrained by the emplacement ages (535 Ma) and metamorphic ages (533 Ma) yielded from these granites as the red granites and Goas Suite (580 to 535 Ma; Milani *et al.,* 2015) are purported to be linked to M1 metamorphism (Longridge *et al.,* 2017).

The grey granites are also syn-tectonic granites that were most likely emplaced during the onset of early collision (Goscombe *et al.,* 2017b) and are correlated with the early Damaran granitoids (Nex and Kinnaird, 1995). No age constraints were established from this study and therefore the grey granites were most likely emplaced between 535 Ma and 525 Ma. This range was established from cross-cutting relationships of granitoids (red granites and type C′ SLG) with established crystallisation ages which provides estimates for the emplacement of the gey granites. These granites are formed by fractional crystallisation but show variable cumulate and final melt REE signatures with both positive and negative Eu anomalies (as described by Johannes *et al.,* 2003). Therefore, indicating that these granites crystallised from partial melt cumulates (as described by Johannes *et al.,* 2003) and migrated partial melts. Both the red and grey granites show a distinct granoblastic polygonal texture and display a well-developed foliation, which indicates that they were emplaced prior to D2 deformation and peak M2 metamorphism (M3 of Goscombe *et al.,* 2017b).

Remote sensing enabled the identification of a large portion of the SLGs depending on lateral extent and thickness. Their pink to white colour contrasts with the basement and supracrustal rocks, especially the Khan Formation. However, given their compositional varieties and heterogeneity the distinction between the SLGs is better accomplished in the field when cross-cutting relationships, mineralogy and modes of emplacement can be examined rather than through geochemistry and petrographic studies. In most cases the SLGs can be correlated to those described by other workers (Nex, 1997; Basson and Greenway, 2004; Fremantle, 2017), with the exception of type C′ SLG, which

are older than other SLGs of the same type. Types C', A and B are associated with D2 deformation (intrude D2 structures) and range from the oldest (C') to youngest (B), with regards to emplacement during D2 deformation (Fig. 8.1). Therefore, D2 deformation was dated using type C' SLG at 525 Ma. On the other hand, type E SLG was emplaced during D3 deformation (emplaced into D3 structures) but yielded no reliable ages but rather inherited ages for zircon derived from Palaeoproterozoic basement lithologies. Type F SLG cross-cut other structural features and intrusives and are associated with D4 deformation (occur along extensional faults/joints) and extension during orogenic collapse (Longridge, 2012). In general, the SLGs lack a granoblastic polygonal texture and therefore were interpreted as anatectic melts that formed as a response the high-temperature M2 metamorphism and extension during orogenic collapse (Longridge, 2012; Fuchsloch *et al.,* 2018).

All the Damaran granitoids were established to be Group I Damaran granitoids using the classification of McDermott *et al.,* 1996). They can be interpreted as products of biotite-dehydration melting that was either limited by the presence of biotite or plagioclase from Rb/Sr (0.4 – 5) and Ba/Sr (1.1 – 9.6) versus combined Fe_2O_3 + MgO (0.1 – 4.5) plots. The Damaran granitoids showed a fingerprint for subduction-related metasomatism or crustal assimilation. Specifically, LILE enrichment relative to HFSE coupled with a depletion of HREE (Kamber *et al.,* 2002; Williams *et al.,* 2004). Magma crust interaction was inferred from the Nb and Ta negative anomalies. A subduction-related multi-element signature is in agreement with arc magmatism dated around 560 Ma (Goscombe *et al.,* 2017b) and crustal reworking or assimilation would produce unradiogenic εHf values. However, distinguishing and concluding between the two is not possible.

Unradiogenic εHf values are distinctive for the Damaran granitoids. This suggests crustal reworking of variably aged crust and no new generation of crust during the Pan-African Orogeny, despite the voluminous emplacement of melt. New crustal generation was largely limited to the Archaean and early Mesoproterozoic, consistent with other Lu-Hf studies (McDermott *et al.,* 1989; Milani *et al.,* 2015; Longridge *et al.,* 2018). DM model ages of 1.6 Ga indicate a Kalahari Craton affinity in agreement with Longridge *et al.* (2018) who proposed that the Damaran Granitoids were sourced from reworking of the Kalahari Craton (DM model ages were typically younger than 2 Ga). However, the red granites and type C' SLGs show characteristically older Archaean DM model ages suggestive of a Congo Craton affinity indicating that the red granites and type C' SLG were reworked from Archaean crust rather than the younger Kalahari Craton as proposed by Longridge *et al.* (2018). This assumption was based on a model, which proposed that the Kalahari Craton was underthrust beneath the Congo Craton which lead to delamination and partial melting of the lower mafic component of the Kalahari Craton to produce Damaran granitoids (Longridge *et al.,* 2018). However,

the older DM model ages suggest that the Damaran granitoids had a varied source (Mesoproterozoic to Archaean), that is more similar to the Abbabis Complex and the Etusis Formation from this study, and possibly the Congo Craton.

8.1.6 Partial melting in the northern extent of the Palmenhorst Dome

A general distribution of metatexites and diatexites was produced from field mapping and textural classification of crystallised partial melts. Metatexites generally occur in the supracrustals and northern mapping area while diatexites increase in intensity towards the main Palmenhorst Dome in the south. This is consistent with a stratified crust showing an increase of partial melt towards the centre of the dome with SLGs and metatexites predominantly occurring within the supracrustal lithologies (Toe *et al.,* 2013).

The supracrustals typically occur as structurally controlled metatexites that formed from in situ to in-source melting, but also host migrated melt as intrusive SLGs. These metatexites intruded into higher crustal levels and become self-stabilising systems that sometimes develop into more pervasive intrusive melts (Hall and Kisters, 2012). Types A, B and C' SLGs vary from bedding/foliation parallel to intrusive SLGs metatexites and have shown varying crystallisation mechanisms. Rare Earth Element plots indicate that some of these SLGs were crystallised from in situ to in source cumulates (slight REE depletion and positive Eu anomaly in the sense of Johannes *et al.*, 2003) where residual melt migrated to form more final melts (REE enrichment and negative Eu anomaly as characterised by Johannes *et al.*, 2003). These SLGs also crystallised as more final melts (in the sense of Johannes *et al.*, 2003) that were most likely intrusive-type metatexites. However, this is not consistent across SLG types and variations occur within each type. This indicates that these melts have more of an interaction with their host lithologies (in situ to in source melting), which is mimicked by the REE patterns of the palaeosome (host rock) and leucosomes, which appear to have crystallised as cumulates (positive Eu anomaly; characterised by Johannes *et al.,* 2003) and the palaeosome has a depletion in Eu due to separation of plagioclase. So too, it has been proposed that the presence of new growth of garnet in the leucosome suggests in situ melting of the palaeosome (Ward *et al.,* 2008) which is commonly seen in metatexites defined by the type B SLGs. Therefore, these SLGs (typically types A and B SLG) compositions are often controlled by the host rock, whereas the intrusive SLGs (types C', E and F) can no longer be linked to their source lithologies.

The southern mapping area and basement lithologies contain more extensive melts (diatexites and coalesced SLGs) that are intrusive and crystallised as final melts in the sense of Johannes *et al.* (2003). Rare Earth Element plots (enriched with negative Eu anomaly) and bivariate major element plots

indicate that these granites, typically red granites, represent more final melts (in the sense of Johannes *et al.,* 2003) that had migrated and then crystallised through fractional crystallisation.

The grey granites have variable cumulate and final melt signatures (in the sense of Johannes *et al.,* 2003) which suggests that successive grey granites may have fractionated previous grey granite generations. A similar instance has been reported were the grey granite types show successive fractionation (Longridge, 2012). These granites are not always continuous bodies but appear to have intruded various basement lithologies to such an extent that remote sensing picked up a variation in the southern extent of the mapping area (southern domain 2). Due to their pervasive nature and final melt fractional crystallisation style, these intrusions cannot truly be linked to their sources and are not typical migmatites. However, due to their concentration in the cores of anticlines of basement lithologies they may have been sourced from the basement rocks or lower Nosib. However, these anatectic melts most likely migrated so it is difficult to establish this.

Based on textural classifications, a theoretical melt fraction (Renner *et al.*, 2000; Sawyer, 2008; Pawley *et al.,* 2015) was established for the various migmatite types described in the northern Palmenhorst Dome. An increase in melt fraction (both in situ and migrated) is proposed from the (1) bedding parallel metatexites through (2) sheeted granites, (3) sheeted leucogranites with rafted palaeosomes, to (4) diatexites/plutons (Fig. 3.40) and melt fraction generally increases towards the north. This also feeds into the structural model where increased heat from a concentration of melt enables these basement lithologies to fold into nappe-like structures during orogenic collapse.

Possible indicators for remnant partial melt were located in most of the basement and supracrustal lithologies suggesting that many of the lithologies in the field area could be possible candidates for sources of partial melt. The Abbabis Complex and lower Nosib Group have typically been proposed as sources for partial melt due to the increased migmatisation in the basement lithologies (Poli, 1997). Both melanosomes and leucosomes have been identified in the Abbabis Complex, which indicates that these lithologies could present a source for in situ melt. However, it is not exclusive to the basement lithologies and, therefore, the supracrustals cannot be excluded. The red and grey granites also exhibited limited possible relic melt textures indicating that these granitoids may have undergone melting after crystallisation. This is possible as the peak amphibolite to granulite facies thermal event was only initiated after the emplacement of these granites (Goscombe *et al.,* 2017b).

8.2 Future studies on the Abbabis Complex and the southern Central Zone:

- Remote sensing may be applied to other basement-cored domes in the sCZ to show compositional and mineralogical variations. Similar formations do not have the same spectral signature from one end of the sCZ to the other, making direct comparisons of the compositions difficult. However, remote sensing can be used as a first order discrimination tool to establish heterogenous components for the basement domes or identification of synclinal infolds. A similar approach can be used that was employed in chapter 2 where the infolds mapped by Longridge (2012) were used as a comparative tool for the northern extent of the Palmenhorst Dome.
- In order to determine with more certainty whether the Etusis Formation received contributions from the Abbabis Complex a larger collection of sample material is needed, including many of the lithologies from the heterogenous Abbabis Complex. The type locality yielded a simple stratigraphy for the basement complex and additional representation from each of the lithostratigraphic units would be more useful than just analysing the various granite-gneisses. Additionally, comparing εHf values for the Etusis Formation and Abbabis Complex is problematics since many of the published studies relied on inherited zircons, presumably from Abbabis Complex sources (Foster *et al.,* 2015; Milani *et al.,* 2015). Currently, only one published study used U-Pb and Hf isotope data from Abbabis Complex gneisses (Longridge *et al.,* 2018).
- Monazite geochronology should be used to date the Damaran granitoids as it is the most Pb-retentive accessory mineral (Cherniak *et al.,* 2004). Dating these granites using monazite would allow for increased accuracy on the dates produced for the emplacement of the intrusions and metamorphism. Seeing as some of these granites are localised partial melt, many of the analysed zircons are likely inherited, rendering interpretation of the age's problematic.

9. References

Ahrendt, H., Behr, H. J., Clauer, N., Porada, H., & Weber, K. (1983). K/Ar age determinations of the northern Damara Branch and their implications for the structural and metamorphic evolution of the Damara Orogen, South West Africa/Namibia. In R. M. Miller (Ed.), *Evolution of the Damara Orogen in South West Africa/Namibia* (Vol. 11, pp. 281-287): Special Publications of the Geological Society of South Africa.

Allsopp, H. L., Barton, E. S., Kröner, A., Welke, H. J., & Burger, A. J. (1983). Emplacement versus inherited isotopic age patterns: a Rb-Sr and U-Pb study of Salem-type granites in the central Damara Belt. In R. M. Miller (Ed.), *Evolution of the Damara Orogen* (Vol. 11, pp. 281-287): Special Publications of the Geological Society of South Africa.

Anders, E., & Grevesse, N. (1989). Abundances of the elements: Meteoritic and solar. *Geochimica et Cosmochimica Acta,* **53**, 197-214.

Anthonissen, C. J. (2009). *The mid-crustal architecture of a continental arc-a transect through the South Central Zone of the Pan-African Damara Belt, Namibia.* (unpublished M.Sc. Thesis), University of Stellenbosch, Stellenbosch.

Ashwal, L. D., Tucker, R. D., & Zinner, E. K. (1999). Slow cooling of deep crustal granulites and Pb-loss in zircon. *Geochimica et Cosmochimica Acta,* **63**, 2839-2851.

Ashworth, J. R. (1985). *Migmatites*. Glasgow: Blackie and Son.

Badenhorst, F. P. (1992). *The lithostratigraphy of areas 2115B and D in the Central Zone of the Damara Orogen, Namibia: with emphasis on facies changes and regional correlation*. (unpublished M.Sc. Thesis), University of Port Elizabeth, South Africa.

Barker, F. (1979). Trondhjemite: Definition, environment and hypotheses of origin. In F. Barker (Ed.), *Trondhjemiles, dacites and related rocks* (pp. 1-12). Amsterdam: Elsevier.

Barnes, J. F. H. (1981). *Some aspects of the tectonic history of the Khan-Swakop region of the Damara Belt, Namibia.* (unpublished Ph.D. Thesis), University of Leeds, Leeds.

Barnes, J. F. H., & Downing, K. H. (1979). Origin of domes in the central Damaran belt, Namibia. *Revue de Géologie Dynamique et de Géographie Physique,* **21**, 383-386.

Barnes, S. J., & Sawyer, E. W. (1980). An alternative model for the Damara Mobile Belt: Ocean crust subduction and continental convergence. *Precambrian Research,* **13**(4), 297-336.

Basson, I. J., & Greenway, G. (2004). The Rössing Uranium Deposit: a product of late-kinematic localization of uraniferous granites in the Central Zone of the Damara Orogen, Namibia. *Journal of African Earth Sciences,* **38**(5), 413-435.

Becker, T., & Schalk, K. E. L. (2008). The Sinclair Supergroup of the Rehoboth volcanic arc from the Sossusvlei-Gamsberg area to the Gobabis region. In R. M. Miller (Ed.), *The Geology of Namibia, Archaean to Mesoproterozoic* (Vol. 1, pp. 1-8 - 1-68). Windhoek: Geological Survey.

Black, L. P., Kamo, S. L., Williams, I. S., Mundil, R., Davis, D. W., Korsch, R. J., & Foudoulis, C. (2003). The application of SHRIMP to Phanerozoic geochronology; a critical appraisal of four zircon standards. *Chemical Geology*, **200**(1-2), 171-188.

Blaine, J. L. (1977). Tectonic evolution of the Waldau Ridge structure and the Okahandja Lineament in part of the Central Damara Orogen, west of Okahandja, South West Africa. *Bulletin of the Precambrian Research Unit, University of Cape Town,* **21**, 99.

Boardman, J. W., & Kruse, F. A. (1994). *Automated spectral analysis: A geological example using AVIRIS data, northern Grapevine Mountains, Nevada.* Paper presented at the Tenth Thematic Conference, Geologic Remote Sensing, San Antonio, Texas.

Bolhar, R., Ring, U., & Ireland, T. R. (2016). Zircon in amphibolites from Naxos, Aegean Sea, Greece: Origin, significance and tectonic setting. *Journal of Metamorphic Geology,* **35**(4), 413-434.

Bouvier, A., Jeffrey, D., Vervoort, J. D., & Patchett, P. J. (2008). The Lu–Hf and Sm–Nd isotopic composition of CHUR: constraints from unequilibrated chondrites and implications for the bulk composition of terrestrial planets. *Earth and Planetary Science Letters,* **273**, 48–57.

Brandt, R. (1985). Preliminary report on the stratigraphy of the Damara Sequence and the geology and geochemistry of the Damaran granites in an area between Walvis Bay and Karibib. *Communications of the Geological Survey of Namibia,* **1**, 31-43.

Brandt, R. (1987). A revised stratigraphy for the Abbabis Complex in the Abbabis Inlier, Namibia. . *South African Journal of Geology,* **90**, 314-323.

Briqueu, L., Lancelot, J. P., Valois, J. P., & Walgenwitz, F. (1980). Géochronologie U–Pb et gènese d'un type de minéralisation uranifère: les alaskites de Goanikontes (Namibie) et leur encaissant. *Bulletin des Centre de Récherches Exploration-production Elf-Aquitaine,* **4**, 759-811.

Bühn, B., Okrusch, M., Woermann, E., Lehnert, K., & Hoernes, S. (1995). Metamorphic evolution of Neoproterozoic manganese formations and their country rocks at Otjosondu, Namibia. *Journal of Petrology*, ***2***, 463-496.

Cecil, M. R., Gehrels, G., Ducea, M. N. & Patchett, P. J. (2011). U-Pb-Hf characterization of the central Coast Mountains batholith: Implications for petrogenesis and crustal architecture. *Lithosphere,* **3**(4), 247–260.

Chavez, P. S., Berlin, G. L., & Sowers, L. B. (1982). Statistical method for selecting landsat MSS. *Journal of Applied Photographic Engineer,* **8**(1), 23-30.

Cherniak, D. J., Watson, E. B., Grove, M., & Harrison, T. M. (2004). Pb diffusion in monazite: a combined RBS/SIMS study11Associate editor: Y. Amelin. *Geochimica et Cosmochimica Acta,* **68**(4), 829-840.

Clemens, J. D., Buick, I. S., Kisters, A. F. M., & Frei, D. (2017). Petrogenesis of the granitic Donkerhuk batholith in the Damara Belt of Namibia: protracted, syn-tectonic, short-range, crustal magma transfer. *Contributions to Mineralogy and Petrology,* **172**(7), 50.

Cottle, J. M., Larson, K. P. & Kellett, D. A. (2015). How does the mid-crust accommodate deformation in large, hot collisional orogens? A review of recent research in the Himalayan orogen. *Journal of Structural Geology*, **78**, 119-133.

Connelly, J. N. (2001). Degree of preservation of igneous zonation in zircon as a signpost for concordancy in U/Pb geochronology. *Chemical Geology,* **172**, 25-39.

Corfu, F., Hanchar, J. M., Hoskin, P. W., & Kinny, P. (2003). Atlas of zircon textures. *Reviews in mineralogy and geochemistry,* **53**(1), 469-500.

Corner, B. (2008). The Crustal Framework of Namibia Derived from an Integrated Interpretation of Geophysical and Geological Data. In R. M. Miller (Ed.), *The Geology of Namibia. Volume 1: Archaean to Mesoproterozoic* (pp. 2-1 – 2-19): Geological Survey of Namibia.

Coward, M. P. (1981). The junction between Pan African mobile belts in Namibia: Its structural history. *Tectonophysics,* **76**(1), 59-73.

Coward, M. P. (1983). The tectonic history of the Damaran belt. In R. M. Miller (Ed.), *Evolution of the Damara Orogen in South West Africa/Namibia* (Vol. 11, pp. 409-421): Special Publications of the Geological Society of South Africa.

Dalziel, I. W. D. (1991). Pacific margins of Laurentia and East Antarctica–Australia as a conjugate rift pair: evidence and implications for an Eocambrian supercontinent. *Geology,* **19**, 598–601.

Davis, G. H., & Reynolds, S. J. (1996). *Structural geology of rocks and regions*. New Jersey: John Wiley & Sons Inc.

De Kock, G. S. (1991). The mafic Audawib Suite in the Central Damara orogeny of Namibia: geochemical evidence for volcanic arc volcanism. *Journal of African Earth Sciences,* **12**, 593-599.

De Kock, G. S. (2001). A reappraisal of the Namibian Damara stratigraphy in part of the Southern Swakop Terrane and its implications to basin evolution. *South African Journal of Geology,* **104**, 115-136.

De Kock, G. S., & Botha, B. J. V. (1988). Komontwikkeling in die Damara-orogeen gedurende die afsetting van die Okomis-en Omusemaformasies aan die basis van die Swakopgroep, in die gebied suid-oos van Karibib, Namibia. *South African Journal of Geology,* **91**, 83-96.

De Kock, G. S., Eglington, B., Armstrong, R. A., Harmer, R. E., & Walraven, F. (2000). U-Pb and Pb-Pb ages of the Naauwpoort rhyolite, Kawaeup leptite and Okongava diorite: implications for the onset of rifting and orogenesis in the Damara belt, Namibia. *Communication of the Geological Survey of Namibia,* **12**, 81-88.

Downing, K. N. (1982). *The evolution of the Okahandja Lineament and its significance for Damara tectonics in Namibia.* (unpublished Ph.D. Thesis), University of Leeds, Leeds.

Downing, K. N., & Coward, M. P. (1981). The Okahandja lineament and its significance for Damaran tectonics in Namibia. *Geologische Rundschau,* **70**, 972-1003.

Foster, D. A., Goscombe, B. D., Newstead, B., Mapani, B., Mueller, P. A., Gregory, L. C., & Muvangua, E. (2015). U–Pb age and Lu–Hf isotopic data of detrital zircons from the Neoproterozoic Damara Sequence: Implications for Congo and Kalahari before Gondwana. *Gondwana Research,* **28**(1), 179-190.

Freemantle, G. G. (2017). *Primary urinium mineralisation of the central Damara Orogen, Namibia: A petrographic, geochemical and mineralogical account of the granite-hosted.* (unpublished Ph.D. Thesis), University of the Witwatersrand, South Africa.

Frimmel, H. E., Basei, M. S., & Gaucher, C. (2011). Neoproterozoic geodynamic evolution of SW-Gondwana: a southern African perspective. *International Journal of Earth Science,* **100**, 323-354.

Fuchsloch, W. C., Nex, P. A. M., & Kinnaird, J. A. (2018). Classification, mineralogical and geochemical variations in pegmatites of the Cape Cross-Uis pegmatite belt, Namibia. *Lithos,* **296-299**, 79-95.

Gerdes, A. & Zeh, A. (2006). Combined U–Pb and Hf isotope LA-(MC-)ICP-MS analyses of detrital zircons: comparison with SHRIMP and new constraints for the provenance and age of an Armorican metasediment in Central Germany. *Earth and Planetary Science Letters,* **249**, 47–61.

Gevers, T. W. (1931). An Ancient Tillite in South West Africa. *Transactions of the Geological Society of South Africa,* **34**, 1-17.

Gevers, T. W. (1963). Geology along the north-western margin of the Khomas Highlands, between Otjimbingwe-Karibib and Okahandja, South West Africa. *Transactions of the Geological Society of South Africa,* **66**, 199-251.

Goscombe, B., Foster, D. A., Gray, D., & Wade, B. (2017a). Metamorphic response and crustal architecture in a classic collisional orogen: The Damara Belt, Namibia. *Gondwana Research,* **52**, 80-124.

Goscombe, B., Foster, D. A., Gray, D., Wade, B., Marsellos, A., & Titus, J. (2017b). Deformation correlations, stress field switches and evolution of an orogenic intersection: The Pan-African Kaoko-Damara orogenic junction, Namibia. *Geoscience Frontiers,* **8**(6), 1187-1232.

Goscombe, B., Gray, D., & Hand, M. (2004). Variation in metamorphic style along the Northern Margin of the Damara Orogen, Namibia. *Journal of Petrology,* **45**, 1261-1295.

Goscombe, B., Grey, D., & Hand, M. (2005). Extrusional Tectonics in the Core of a Transpressional Orogen; the Kaoko Belt, Namibia. *Journal of Petrology,* **46**(6), 1203–1241.

Goscombe, B., Hand, M., & Gray, D. (2003). Structure of the Kaoko Belt, Namibia: progressive evolution of a classic transpressional orogen. *Journal of Structural Geology,* **25**(7), 1049-1081.

Gray, A. R., Foster, D. A., Meert, J. G., Goscombe, B. D., Armstrong, R., Trouw, R. A. J., & Passchier, C. W. (2008). A Damara Orogen perspective on the assembly of southwestern Gondwana. *Geological Society of London Special Publications,* **294**, 257-278.

Gray, D. R., Foster, D. A., Meert, J. G., Goscombe, B. D., Armstrong, R., Trouw, R. A. J., & Passchier, C. W. (2008). A Damara orogen perspective on the assembly of southwestern Gondwana. In R. J. Pankhurst, R. A. J. Trouw, B. B. Brito Neves, & M. J. De Wit (Eds.), *West Gondwana: Pre-Cenozoic Correlations Across the South Atlantic Region* (Vol. 294, pp. 257-278). Geological Society, London, Special Publications.

Green, A. A., Berman, M., Switzer, P., & Craig, M. (1988). A Transformation for Ordering Multispectral Data in Terms of Image Quality with Implications for Noise Removal. *IEEE Transactions on Geoscience and Remote Sensing,* **26**(1), 65-74.

Griffin, W. L., Wang, X., Jackson, S. E., Pearson, N. J., O'Reilly, S. Y., Xu, X. & Zhou, X. (2002). Zircon chemistry and magma mixing, SE China: in-situ analysis of Hf isotopes, Tonglu and Pingtan igneous complexes. *Lithos*, **61**, 237-269.

Haack, U., & Martin, H. (1983). Geochronology of the Damara Orogen – A Review. In H. Martin & F. W. Eder (Eds.), *Intracontinental Fold Belts* (pp. 839-846). Berlin: Springer Verlag.

Hall, D., & Kisters, A. (2012). The stabilization of self-organised leucogranite networks—Implications for melt segregation and far-field melt transfer in the continental crust. *Earth and Planetary Science Letters,* **355–356**, 1–12.

Hanmer, S., & McEachern, S. (1992). Kinematical and rheological evolution of a crustal-scale ductile thrust zone, Central Metasedimentary Belt, Grenville orogen, Ontario1. *Canadian Journal of Earth Sciences,* **29**, 1779-1790.

Harris, L. B., Koyi, H. A., & Fossen, H. (2002). Mechanisms for folding of high-grade rocks in extensional tectonic settings. *Earth Science Reviews,* **59**, 163-210.

Hartmann, O., Hoffer, E., & Haack, U. (1983). Regional metamorphism in the Damara Orogen: interaction of crustal motion and heat transfer. *Special Publication of the Geological Society of South Africa,* **11**, 233-241.

Hartnady, C. J., Joubert, P., & Stowe, C. (1985). Proterozoic crustal evolution of southwestern Africa. *Episodes,* **8**, 236-244.

Hawkesworth, C. J., Gledhill, A. R., Roddick, J. C., Miller, R. M., & Kroner, A. (1983). RbSr and KAr studies bearing on models for the thermal evolution of the Damara belt, Namibia. In R. M. Miller (Ed.), *Evolution of the Damara Orogen in South West Africa/Namibia* (Vol. 11, pp. 323-338): Special Publication of the Geological Society of South Africa.

Hawkesworth, C. J., & Kemp, A. I. S. (2006). Using hafnium and oxygen isotopes in zircons to unravel the record of crustal evolution. *Chemical Geology,* **226**(3), 144-162.

Hawkesworth, C. J., & Marlow, A. G. (1983). Isotope evolution of the Damara orogenic belt. In In R. M. Miller (Ed.), *Evolution of the Damara Orogen of South West Africa/Namibia* (Vol. 11, pp. 397-407): Special Publications of the Geological Society of South Africa.

Heinonen, A. P., Andersen, T., Rämö, O. T. (2010). Re-evaluation of Rapakivi Petrogenesis: Source Constraints from the Hf Isotope Composition of Zircon in the Rapakivi Granites and Associated Mafic Rocks of Southern Finland. *Journal of Petrology*, **51**(8), 1687–1709.

Henry, G. (1992). *The sedimentary evolution of the Damara Sequence in the lower Khan River valley, Namibia.* (unpublished Ph.D. Thesis), University of the Witwatersrand, South Africa.

Hoal, K. O., Hoal, B. G., Griffin, W. L., & Armstrong, R. A. (2000). Characterization of the age and nature of the lithosphere in the Tsumkwe region, Namibia. In R. M. Miller (Ed.), *Special Issue: Henno Martin Commemorative Volume* (Vol. 12, pp. 21-28): Communications of the Geological Survey of Namibia.

Hoffman, P. F. (2005). On Cryogenian (Neoproterozoic) ice-sheet dynamics and the limitations of the glacial sedimentary record. *South African Journal of Geology,* **108**, 557-577.

Hoffman, P. F., Hawkins, D. P., Isachsen, C. E., & Bowring, S. A. (1996). Precise U-Pb zircon ages for early Damaran magmatism in the Summas Mountains and Welwitschia Inlier, northern Damara belt, Namibia. *Communications of the Geological Survey Namibia,* **11**, 47-52.

Hoffman, P. F., Swart, R., Eckhardt, E., F., & Guowei, H. (1994). Damara Orogen of Northwest Namibia. *Geological excursion guide of the Geological Survey of Namibia, Windhoek*, 55.

Hoffmann, C. (1976). Granites and migmatities of the Damara belt, South West Africa. Petrography and melting experiments. *Geologische Rundschau,* **65**, 939-966.

Hoffmann, K. H. (1989). New aspects of lithostratigraphic subdivision and correlation of late proterozoic to early Cambrian rocks of the southern Damara Belt, and their correlation with central and northern Damara Belt and the Gariep Belt. *Communications of the Geological Survey Namibia,* **5**, 59-67.

Hoffmann, K. H., Condon, D. J., Bowring, S. A., & Crowley, J. L. (2004). U-Pb zircon date from the neoproterozoic Ghaub Formation, Namibia: constraints on Marinoan glaciation. *Geology,* **32**, 817-820.

Hofmann, A. W. (1988). Chemical differentiation of the Earth: the relationship between mantle, continental crust, and oceanic crust. *Earth and Planetary Science Letters,* **90**(3), 297-314.

Hoskin, P. W. O., & Black, L. P. (2000). Metamorphic zircon formation by solid-state recrystallization of protolith igneous zircon. *Journal of Metamorphic Geology,* **18**, 423-439.

Humphris, S. E. (1984). The mobility of rare earth elements in the crust. In P. Henderson (Ed.), *Rare Earth Element Geochemistry* (pp. 317–342). Amsterdam: Elsevier.

Inzana, J., Kusky, T., Higgs, G., & Tucker, R. (2003). Supervised classifications of Landsat TM band ratio images and Landsat TM band ratio image with radar for geological interpretations of central Madagascar. *Journal of African Earth Sciences,* **37**, 9–72.

Jackson, S. E., Pearson, N. J., Griffin, W. L., & Belousova, E. A. (2004). The application of laser ablation-inductively coupled plasma-mass spectrometry to in situ U–Pb zircon geochronology. *Chemical Geology*, **211**(1-2), 47-69.

Jacob, R. E. (1974). Geology and metamorphic petrology of part of the Damara Orogen along the lower Swakop River, South West Africa. *Bulletin of the Precambrian Research Unit, University of Cape Town,* **17**, 184.

Jacob, R. E., Kröner, A., & Burger, A. J. (1978). Areal extent and first U-Pb age of the Pre-Damaran Abbabis Complex in the central Damara be!t of South West Africa (Namibia)**. *Geologische Rundschau,* **67**, 708-718.

Jacob, R. E., Moore, J. M., & Armstrong, R. A. (2000). Zircon and titanite age determinations from igneous rocks in the Karibib District, Namibia: implications for Navachab vein-style gold mineralization. *Communications of the Geological Survey of Namibia,* **12**, 157-166.

Jacob, R. E., Snowden, P. A., & Bunting, F. J. L. (1983). Geology and structural development of the Tumas basement dome and its cover rocks. In R. M. Miller (Ed.), *Evolution of the Damara Orogen in South West Africa/Namibia* (Vol. 11, pp. 157-172): Special Publications of the Geological Society of South Africa.

Jacobs, J., Pisarevsky, S., Thomas, R. J., & Becker, T. (2008). The Kalahari Craton during the assembly and dispersal of Rodinia. *Precambrian Research, 160*.

Johannes, W., Ehlers, C., Kriegsman, L. M., & Mengel, K. (2003). The link between migmatites and S-type granites in the Turku area, southern Finland. *Lithos,* **68**(3), 69-90.

Johnson, S. D., Poujol, M., & Kisters, A. F. M. (2006). Constraining the timing and migration of collisional tectonics in the Damara Belt, Namibia: U-Pb zircon ages for the syn-tectonic Salem-type Stinkbank granite. *South African Journal of Geology,* **109**, 611-624.

Jung, S., Hoernes, S., & Mezger, K. (2000). Geochronology and petrology of migmatites from the Proterozoic Damara Belt — importance of episodic fluid-present disequilibrium melting and consequences for granite petrology. *Lithos,* **51**(3), 153-179.

Jung, S., Hoernes, S., & Mezger, K. (2002). Synorogenic melting of mafic lower crust: constraints from geochronology, petrology and Sr, Nd, Pb and O isotope geochemistry of quartz diorites (Damara orogen, Namibia). *Contributions to Mineralogy and Petrology,* **143**, 551-566.

Jung, S., Kröner, A., Hauff, F., & Masberg, P. (2015). Petrogenesis of Synorogenic diorite-granodiorite-granite complexes in the Damara Belt, Namibia: constraints from U-Pb zircon ages and Sr-Nd-Pb isotopes. *Journal of African Earth Sciences,* **101**, 253-265.

Jung, S., & Mezger, K. (2003). U-Pb garnet chronometry in high-grade rocks—case studies from the central Damara orogen (Namibia) and implications for the interpretation of Sm–Nd garnet ages and the role of high U–Th inclusions. *Contributions to Mineralogy and Petrology,* **146**, 382-396.

Jung, S., Mezger, K., & Hoernes, S. (2001). Trace element and isotopic (Sr, Nd, Pd, O) arguments for a mid-crustal origin of Pan-African garnet-bearing S-type granites from the Damara Orogen (Namibia). *Precambrian Research,* **110**, 325-355.

Jung, S., Mezger, K., & Hoernes, S. (2003). Petrology of basement-dominated terranes II. Contrasting isotopic (Sr, Nd, Pb and O) signatures of basement-derived granites and constraints on the source region of granite (Damara orogen, Namibia). *Chemical Geology,* **199**, 1-28.

Jung, S., Mezger, K., & Hoernes, S. (2004). Shear zone–related syenites in the Damara belt (Namibia): The role of crustal contamination and source composition. *Contributions to Mineralogy and Petrology,* **148**, 104–121.

Jung, S., Mezger, K., Masberg, P., Hoffer, E., & Hoernes, S. (1998). Petrology of an intrusion-related high-grade migmatite: implications for partial melting of metasedimentary rocks and leucosome-forming processes. *Journal of Metamorphic Geology,* **16**, 425-445.

Kamber, B. S., Ewart, A., Collerson, K. D., Bruce, M. C., & McDonald, G. D. (2002). Fluid-mobile trace element constraints on the role of slab melting and implications for Archaean crustal growth models. *Contributions to Mineralogy and Petrology,* **144**, 38-56.

Kennedy, W. Q. (1964). The structural differentiation of Africa in the Pan African (± 500 Ma) tectonic episode. *8th Annual Report of the Research Institute for African Geology*, 48-49.

Khoza, T. D., Jones, A. G., Muller, M. R. Evans, R. L., Miensopust, M. P. & Webb, S. J. (2013). Lithospheric structure of an Archean craton and adjacent mobile belt revealed from 2-D and 3-D inversion of magnetotelluric data: Example from southern Congo craton in northern Namibia. *Journal of Geophysical Research: Solid Earth*, **118**, 4378–4397.

Kinnaird, J. A., & Nex, P. A. M. (2007). A review of geological controls on uranium mineralisation in sheeted leucogranites within the Damara Orogen, Namibia. *Applied Earth Science,* **116**, 69-85.

Kinny, P. D., & Maas, R. (2003). Lu–Hf and Sm–Nd isotope systems in zircon. *Reviews in mineralogy and geochemistry,* **53**(1), 327-341.

Kirkland, C. L., Smithies, R. H., Woodhouse, A. J., Howard, H. M., Wingate, M. T., Belousova, E. A., Cliff, J. B., Murphy, R. C., & Spaggiari, C. V. (2013). Constraints and deception in the isotopic record; the crustal evolution of the west Musgrave Province, central Australia. *Gondwana Research*, **23**(2), 759-781.Kisters, A. (2005). Controls of gold-quartz vein formation during regional folding in amphibolite-facies, marble-dominated metasediments of the Navachab Gold Mine in the Pan-African Damara Belt, Namibia. *South African Journal of Geology,* **108**, 365-380.

Kisters, A. F. M., Jordaan, L. S., & Neumaier, K. (2004). Thrust-related dome structures in the Karibib district and the origin of orthogonal fabric domains in the south Central Zone of the Pan-African Damara belt, Namibia. *Precambrian Research,* **133**(3), 283-303.

Kleinhanns, I., Fullgraf, T., Wilsky, F., Nolte, N., Fliegel, D., Klemd, R., & Hansen, B. (2013). U-Pb zircon ages and (isotope) geochemical signatures of the Kamanjab Inlier (NW-Namibia): constraints on Paleoproterozoic crustal evolution along the southern Congo craton. *Geological Society London Special Publications, 389*.

Kretz, R. (1983). Symbols for rock-forming minerals. *American Mineralogist, 68*, 277-279.

Kröner, A. (1982). Rb–Sr geochronology and tectonic evolution of the Pan-African Damara belt of Namibia, south-western Africa. *American Journal of Science,* **282**, 1471-1507.

Kröner, A. (1984). Dome structures and basement reactivation in the Pan-African Damara belt of Namibia. In A. Kröner, R. Stuttgart, & N. Obermiller (Eds.), *Precambrian Tectonics Illustrated* (pp. 191-206.).

Kröner, A., Retief, E. A., Compston, W., Jacob, R. E., & Burger., A. J. (1991). Single-Age and conventional zircon dating of remobilised basement gneisses in the central Damara belt of Namibia. *South African Journal of Geology,* **94**, 379-387.

Kruger, T. & Kisters, A. (2016). Magma accumulation and segregation during regional-scale folding: The Holland's dome granite injection complex, Damara belt, Namibia, *Journal of Structural Geology*, **89**,1-18.

Kukla, C. (1993). Strontium isotope heterogeneities in amphibolite facies, banded metasediments— a case study from the Late Proterozoic KuisebFormation of the southern Damara Orogen. *Central Namibia: Geological Survey Namibia Memoir,* **15**, 139.

Kukla, P. A., & Stanistreet, I. A. (1991). Record of the Damaran Khomas Hochland accretionary prism in central Namibia: Refutation of an "ensialic" origin of a Late Proterozoic orogenic belt. *Geology,* **19**, 473-476.
Laben, C. A., & Brower, B. V. (2000). U.S.A. Patent No. 6,011,875. U. S. Patent.
Le lliitre, R. W., Bateman, P., Dudek, A., J., K., Lameyre Le Bas, M. J., Sabine, P. A., . . . Zanettin, B. (1989). *A classification of igneous rocks and glossary of terms*. Oxford: Blackwell.
Lehmann, J., Saalmann, K., Naydenov, K. V., Milani, L., Belyanin, G. A., Zwingmann, H., . . . Kinnaird, J. A. (2016). Structural and geochronological constraints on the Pan-African tectonic evolution of the northern Damara Belt, Namibia. *Tectonics,* **35**(1), 103–135.
Lehtonen, M. I., Manninen, T. E. T., & Schreiber, U. M. (Cartographer). (1995). The geology of the area between the Khan river and the Coast, and in the vicinity of Omdel Dam. Mapping Report and geochemical study. Map 2215A. Finnish-Namibian Geological mapping and maps project
Lillesand, T. M., Kiefer, R. W., & Chipman, J. W. (2004). *Remote sensing and image interpretation* (15th ed.). U.S.A: John Wiley and Son.
Longridge, L. (2012). *Tectonothermal Evolution of the southwestern Central Zone, Damara Belt, Namibia.* (unpublished Ph.D. Thesis), University of the Witwatersrand, South Africa.
Longridge, L., Gibson, R. L., Kinnaird, J. A., & Armstrong, R. A. (2011). Constraining the timing of deformation in the southwestern Central Zone of the Damara Belt, Namibia. In D. J. J. V. Hinsbergen, S. J. H. Buiter, T. H. Torsvik, C. Gaina, & S. J. Webb (Eds.), *The Formation and Evolution of Africa: A Synopsis of 3.8 Ga of Earth History*: Geological Society of London.
Longridge, L., Gibson, R. L., Kinnaird, J. A., & Armstrong, R. A. (2017). New constraints on the age and conditions of LPHT metamorphism in the southwestern Central Zone of the Damara Belt, Namibia and implications for tectonic setting. *Lithos,* **278-281**, 361-382.
Longridge, L., Kinnaird, J., Gibson, R., Hawkesworth, C., & Armstrong, R. (2018). Crustal recycling in the Damara Belt, Namibia, and interaction of the Congo and Kalahari Cratons – evidence from zircon U-Pb, Hf and O isotopes. *South African Journal of Geology,* **121**(3), 237-252.
Longridge, L., Kinnaird, J. A., Gibson, R. L., & Armstrong, R. A. (2014). AMPHIBOLITES OF THE CENTRAL ZONE: NEW SHRIMP U-PB AGES AND IMPLICATIONS FOR THE EVOLUTION OF THE DAMARA OROGEN, NAMIBIA. *South African Journal of Geology,* **117**(1), 67-86.
Ludwig, K. R. (2003). Isoplot 3.00. A geochronological toolkit for Microsoft Excel. *Berkeley Geochronology Center Special Publication, **4***.
Malone, S. J., Meert, J. G., Banerjee, D. M., Pandit, M. K., Tamrat, E., Kamenov, G. D., & Pradhan, V. R. (2008). Paleomagnetism and detrital zircon geochronology of the Upper Vindhyan sequence, Son Valley and Rajasthan, India: a ca. 1000 Ma closure age for the Purana basins. *Precambrian Research,* **164**, 137–159.
Marlow, A. G. (1983). Geology and Rb-Sr Geochronology of mineralised and radioactive granites and alaskites, Namibia. *Special Publication of the Geological Society of South Africa,* **11**, 289-298.
Marlow, A. G. M. (1981). *Remobilisation and Primary uranium genesis in the Damaran Orogenic Belt.* (unpublished Ph.D. Thesis), University of Leeds, Leeds.
Martin, H. (1965). *The Precambrian Geology of South West Africa and Namaqualand*. Cape Town: University of Cape Town.
Martin, H., & Porada, H. (1977). The intracratonic branch of the Damara Orogen in South West Africa II. Discussion of relationships with the Pan-African mobile belt system. *Precambrian Research,* **5**(4), 339-357.
Masberg, H. P., Hoffer, E., & Hoernes, S. (1992). Microfabrics indicating granulite-facies metamorphism in the low-pressure central Damara Orogen, Namibia. *Precambrian Research,* **55**, 243-257.
Masberg, P. (2000). Garnet growth in medium-pressure granulite facies metapelites from the central Damara Orogen: igneous versus metamorphic history. *Communications of the Geological Society of Namibia,* **12**, 115-124.
McDermott, F., Harris, N., & Hawkesworth, C. (1996). Geochemical constraints on crustal anatexis: A case study from the Pan-African Damara granitoids of Namibia. *Contributions to Mineralogy and Petrology,* **123**, 406-423.
McDermott, F., Harris, N. B. W., & Hawkesworth, C. J. (1989). Crustal reworking in southern Africa: constraints from Sr-Nd isotope studies in Archaean to Pan-African terrains. *Tectonophysics,* **161**, 257-270.
McDermott, F., & Hawkesworth, C. J. (1990). Intracrustal recycling and upper-crustal evolution: a case study from the Pan-African Damara mobile belt, central Namibia. *Chemical Geology,* **83**, 263-280.
McDermott, P. F. (1986). *Granite Petrogenesis and Crustal Evolution Studies in the Damara Pan-African Orogenic Belt, Namibia.* (unpublished Ph.D. Thesis), Open University.

Mehnert, K. R. (1968). *Migmatites and the Origin of Granitic Rocks*. Amsterdam, London, New York: Elsevier Publishing Company.

Merdith, A. S., Collins, A. S., Williams, S. E., Pisarevsky, S., Fodenc, J. D., Archibald, D. B., Müller, R. D. (2017). A full-plate global reconstruction of the Neoproterozoic. *Gondwana Research,* **50**, 84–134.

Mezger, K., & Krogstad, E. J. (1997). Interpretation of Discordant U-Pb Zircon Ages: An Evaluation. *Journal of Metamorphic Geology,* **15**, 127-140.

Milani, L., Kinnaird, J. A., Lehmann, J., Naydenov, K. V., Saalmann, K., Frei, D., & Gerdes, A. (2015). Role of crustal contribution in the early stage of the Damara Orogen, Namibia: New constraints from combined U–Pb and Lu–Hf isotopes from the Goas Magmatic Complex. *Gondwana Research,* **28**(3), 961-986.

Miller, R. M. (1983). The Pan-African Damara Orogen of South West Africa/Namibia. In R. M. Miller (Ed.), *Evolution of the Damara Orogen in South West Africa/Namibia* (Vol. 11, pp. 431-515): Special Publications of the Geological Society of South Africa.

Miller, R. M. (2008). *The Geology of Namibia*. Windhoek: Geological Survey of Namibia.

Nadeau, L., & Hanmer, S. (1992). Deep-crustal break-back stacking and slow exhumation of the continental footwall beneath a thrusted marginal basin, Grenville orogen, Canada. *Tectonophysics,* **210**, 215-233.

Nagel, R. (1999). *Eine Milliarde Jahre geologischer Entwicklung am NW-Rand des Kalahari Kratons.* (Dr. rer. Nat. thesis), Univ. Göttingen, Göttingen.

Nascimento, D. B., Schmitt, R. S., Ribeiro, A., Trouw, R. A. J., Passchier, C. W., & Basei, M. A. S. (2017). Depositional ages and provenance of the Neoproterozoic Damara Supergroup (northwest Namibia): Implications for the Angola-Congo and Kalahari cratons connection. *Gondwana Research,* **52**, 153-171.

Nash, C. R. (1971). Metamorphic petrology of the SJ Area, Swakopmund District, South West Africa. *Bulletin of the Precambrian Research Unit, University of Cape Town,* **9**, 77.

Nex, P. A. M. (1997). *Tectono-metamorphic setting and evolution of granitic sheets in the Goanikontes area, Namibia* (unpublished Ph.D. Thesis), National University of Ireland, Cork.

Nex, P. A. M., & Kinnaird, J. A. (1995). Granites and their mineralisation in the Swakop River area around Goanikontes, Namibia. *Communications of the Geological Survey of Namibia,* **10**, 51-56.

Nex, P. A. M., Kinnaird, J. A., & Oliver, G. J. H. (2001a). Petrology, geochemistry and uranium mineralisation of post-collisional magmatism around Goanikontes, southern Central Zone, Damaran Orogen, Namibia. *Journal of African Earth Sciences,* **33**(3), 481-502.

Nex, P. A. M., Oliver, G. J. H. & Kinnaird, J. A. (2001b). Spinel-bearing assemblages and P-T-t evolution of the Central Zone of the Damara Orogen, Namibia. *Journal of African Earth Sciences,* **32**(3), 471-498.

Norrish, K., & Hutton, J. T. (1969). An accurate X-ray spectrographic method for the analysis of geologic samples. *Geochemica et Cosmochimica Acta,* **33**, 431-454.

Oliver, G. J. H. (1994). Mid-crustal detachment and domes in the central zone of the Damara orogen, Namibia. *Journal of African Earth Science,* **19**, 331-344.

Oliver, G. J. H. (1995). The Central Zone of the Damara Orogen, Namibia, as a deep metamorphic core complex. *Communications of the Geological Survey of Namibia,* **10**, 33-41.

Oliver, G. J. H., & Kinnaird, J. A. (1996). The Rössing-SJ Dome, Central Zone, Damara Belt, Namibia: an example of mid-crustal extensional ramping. *Communications of the Geological Survey, Namibia,* **11**, 53-64.

Olsen, S. N. (1985). Mass balance in migmatites. In *Migmatites* (pp. 145-179). Boston, MA: Springer.

Ostendorf, J., Jung, S., Berndt-Gerdes, J., & Hauff, F. (2014). Syn-orogenic high-temperature crustal melting: Geochronological and Nd–Sr–Pb isotope constraints from basement-derived granites (Central Damara Orogen, Namibia). *Lithos,* **192-195**, 21-38.

Osterhus, L., Jung, S., Berndt, J., & Hauff, F. (2014). Geochronology, geochemistry and Nd, Sr and Pb isotopes of syn-orogenic granodiorites and granites (Damara orogen, Namibia) – arc-related plutonism or melting of mafic crustal sources? *Lithos,* **200-201**, 386-401.

Passchier, C., Kröner, A., Stuart. Myers, J., & Union of Geol. Sciences. - Commiss. on Tectonics, I. (1990). *Field Geology of High-Grade Gneiss Terrains*. Berlin: Springer-Verlag.

Pawley, M., Reid, A., Dutch, R., & Preiss, W. (2015). Demystifying migmatites: an introduction for the field-based geologist. *Applied Earth Science (Transactions of the Institutetution of Mining and Metallurgy, Section B),* **124**(3), 147-174.

Pearce, J. A. (2008). Geochemical fingerprinting of oceanic basalts with applications to ophiolite classification and the search for Archean oceanic crust. . *Lithos,* **100**, 14–48.

Petrus, J. A., & Kamber, B. S. (2012). VizualAge: A Novel Approach to Laser Ablation ICP-MS U-Pb Geochronology Data Reduction. *Geostandards and Geoanalytical Research,* **36**(3), 247-270.

Platt, J. P., & Behr, W. M. (2011). Grainsize evolution in ductile shear zones: Implications for strain localization and the strength of the lithosphere. *Journal of Structural Geology,* **33**, 537-550.

Poli, L. C. (1997). *Mid-crustal geodynamics of the Southern Central Zone, Damara Orogen, Namibia.* (unpublished Ph.D. Thesis), University of St Andrews, Scotland.
Poli, L. C., & Oliver, G. J. H. (2001). Constrictional deformation in the Central Zone of the Damara Orogen, Namibia. *Journal of African Earth Sciences,* **33**(2), 303-321.
Porada, H. (1979). The Damara-Ribeira Orogen of the Pan-African-Brasiliano cycle in Namibia (Southwest Africa) and Brazil as interpreted in terms of continental collision. *Tectonophysics,* **57**, 237-265.
Puhan, D. (1983). Temperature and Pressure of metamorphism in the Central Damara Orogen. In R. M. Miller (Ed.), *Evolution of the Damara Orogen in South West Africa/Namibia* (Vol. 11, pp. 219-223): Special Publications of the Geological Society of South Africa.
Rankin, W. (2015). *Cross-border correlation of the Damara Belt in Namibia and equivalent lithologies in northwestern Botswana from potential field and magnetotelluric interpretations.* (unpublished M.Sc. Thesis), University of the Witwatersrand, South Africa.
Renner, J., Evans, B., & Hirth, G. (2000). On the rheologically criticalmelt fraction. *Earth and Planetary Science Letters,* **191**(4), 585–594.
Richards, J. A. (1999). *Remote Sensing Digital Image Analysis: An Introduction*. Berlin, Germany: Springer-Verlag.
Rollinson, H. R. (1993). *Using Geochemical Data: Evaluation*. Longman, U.K.: Presentation, Interpretation.
Rubatto, D. (2017). Zircon: The Metamorphic Mineral. *Reviews in mineralogy and geochemistry,* **83**(1), 261-295.
Rubatto, D., & Gebauer, D. (2000). Use of cathodoluminescence for U–Pb zircon dating by ion microprobe: some examples from the Western Alps. In M. Pagel, V. Barbin, P. Blanc, & D. Ohnenstetter (Eds.), *Cathodoluminescence in geosciences* (pp. 373–400). Berlin, Heidelberg: Springer.
Rudnick, R. L., & Gao, S. (2003). Composition of the continental crust. In R. L. Rudnick (Ed.), *The Crust* (pp. 1–64). Oxford, U.K.: Elsevier–Pergamon.
Rumvegeri, B. T. (1991). Tectonic significance of Kibaran structures in Central and eastern Africa. . *Journal of African Earth Sciences,* **13**, 267-276.
Salminen, J., Hanson, R., Evans, D. A. D., Gong, Z., Larson, T., Walker, O., Gumsley, A., Söderlund, U. & Ernst, R. (2018). Direct Mesoproterozoic connection of the Congo and Kalahari cratons in proto-Africa: Strange attractors across supercontinental cycles. *Geology*, **46**(11), 1010-1014.
Sawyer, E. W. (1976). The geology of an area south-east of Walvis Bay: Lithology, sedimentation and field relationships. *Geological Survey of Namibia Regional Geology Reports, 3*.
Sawyer, E. W. (1981). Damaran structural and metamorphic geology of an area south-east of Walvis Bay, South West Africa/Namibia. *Memoir of the Geological Survey of South West Africa,* **7**, 94.
Sawyer, E. W. (2008). *Atlas of migmatites* (Vol. 9). Canada: NRC Research Press.
Schaltegger, U., Gebauer, D., & von Quadt, A. (2002). The mafic-ultramafic rock association of Loderio-Biasca (lower Pennine nappes, Ticino, Switzerland): Cambrian oceanic magmatism and its bearing on early Paleozoic paleogeography. *Chemical Geology,* **186**, 265-279.
Scherer, E., Munker, C., & Mezger, K. (2001). Calibration of the lutetium–hafnium clock. *Science,* **293**, 683–686.
Seth, B. (1999). *Crustal evolution of the Kaoko belt, NW Namibia.* (unpublished Ph.D. Thesis), Bayerischen Julius-Maximilians-Universität, Würzburg.
Shand, S. J. (1927). *Eruptive Rocks*. London: Thomas Murby & Co.
Simon, N., Ali, C. A., Mohamed, K. R., & Sharir, K. (2016). Best Band Ratio Combinations for the Lithological Discrimination of the Dayang Bunting and Tuba Islands, Langkawi, Malaysia. *Sains Malaysiana,* **45**(5), 659-667.
Simpson, C., & Wintsch, R. P. (1989). Evidence for deformation-induced K-feldspar replacement by myrmekite. *Journal of Metamorphic Geology,* **7**, 261-275.
Singletary, S. J., Hanson, R. E., Martin, M. W., Crowley, J. L., Bowring, S. A., Key, R. M., . . . Krol, M. A. (2003). Geochronology of basement rocks in the Kalahari Desert, Botswana, and implications for regional Proterozoic tectonics. *Precambrian Research,* **121**(1), 47-71.
Sláma, J., Košler, J., Condon, D. J., Crowley, J. L., Gerdes, A., Hanchar, J. M., Horstwood, M. S. A., Morris, G. A., Nasdala, L., Norberg, N., Schaltegger, U., Schoene, B., Tubrett, M. N. & Whitehouse,M. J. (2008). Plešovice zircon—a new natural reference material for U–Pb and Hf isotopic microanalysis. *Chemical Geology*, **249**(1-2), 1-35.
Smith, D. A. M. (1965). The geology of the area around the Khan and Swakop Rivers in South West Africa. *Memoir of the Geological Survey of South Africa, 3*, pp. 107.
Söderlund, U., Patchett, P. J., Vervoort, J. D., & Isachsen, C. E. (2004). The 176Lu decay constantdetermined by Lu–Hf and U–Pb isotope systematics of Precambrian mafic intrusions. *Earth and Planetary Science Letters,* **219**, 311–324.

South African Committee for Stratigraphy (SACS) (1980). Lithostratigraphy of the Republic of South Africa, South West Africa/Namibia, and Republics of Bophutshatswana, Transkei and Venda. In L. E. Kent (Ed.), *Stratigraphy of South Africa* (Vol. Handbook 8): Geological Survey of South Africa.

Sperner, B., Jonckheere, R., & Pfänder, J. A. (2014). Testing the influence of high-voltage mineral liberation on grain size, shape and yield, and on fission track and 40Ar/39Ar dating. *Chemical Geology,* **371**, 83-95.

Stammeier, J., Jung, S., Romer, R. L., Berndt, J., & Garbe-Schönberg, D. (2015). Petrology of ferroan alkali-calcic granites: Synorogenic high-temperature melting of undepleted felsic lower crust (Damara orogen, Namibia). *Lithos,* **224-225**, 114-125.

Stanistreet, I. G., & Charlesworth, E. G. (2001). Damaran basement-cored fold nappes incorporating pre-collisional basins, Kaoko Belt, Namibia, and controls on Mesozoic supercontinent breakup. *South African Journal of Geology,* **104**, 1-12.

Streckeisen, A. (1979). To each plutonic rock its proper name. *Earth Science Reviews,* **12**, 1-13.

Tack, L., Williams, I., & Bowden, P. (2002). *SHRIMP consraints on early post-collisional granitoids of the Ida Dome, central Damara (Pan-African) Belt, western Namibia*. Paper presented at the Abstracts of the 11th IAGOD Quadrennial Symposium and Geocongress, Windhoek, Namibia.

Taylor, S. R., & McLennan, S. M. (1985). *The Continental Crust: Its Composition and Evolution*. Oxford: Blackwell Scientific.

Toe, W., Vanderhaeghe, O., André-Mayer, A. S., Feybesse, J. L., & Milési, J. P. (2013). From migmatites to granites in the Pan-African Damara orogenic belt, Namibia. *Journal of African Earth Sciences,* **85**, 62-74.

Tran, H., Ansdell, K., Bethune, K., Watters, B., & Ashton, K. E. (2003). Nd isotope and geochemical constraints on the depositional setting of Paleoproterozoic metasedimentary rocks along the margin of the Archean Hearne craton, Saskatchewan, Canada. *Precambrian Research,* **123**, 1-28.

Valois, J.-P., & Walgenwitz, F. (1979). Pétrographie des alaskites et de la série metamorphique de Goanikontes, Namibie. *Bulletin of the Elf Exploration Production Research Center,* **3**, 351-367.

Veenhof, R. P., & Stel, H. (1991). A cleavage triple point and its meso-scopic structures: the Mustio Sink (Svecofennides of SW Finland). *Precambrian Research,* **50**(3-4), 269-282.

Vermeesch, P. (2018). IsoplotR: a free and open toolbox for geochronology. *Geoscience Frontiers,* **9**, 1479-1493.

Vervoort, J. D., & Kemp, A. I. (2016). Clarifying the zircon Hf isotope record of crust–mantle evolution. *Chemical Geology*, **425**, 65-75.

Volkmann, M. J., Richards, D. L., Wells, M., & Kasch, A. (Cartographer). (1988). Geological map of the Damara Orogen SW Africa/Namibia. Geological Survey of Namibia.

Ward, R., Stevens, G., & Kisters, A. (2008). Fluid and deformation induced partial melting and melt volumes in low-temperature granulite-facies metasediments, Damara Belt, Namibia. *Lithos,* **105**(3), 253-271.

Werner, C. D. (1987). Saxonian granulites - igneous or lithogenous. A contribution to the geochemical diagnosis of the original rocks in high-metamorphic complexes. In: Gerstenberger, H. (Ed.) *Contributions to the geology of the Saxonian granulite massif (Sachsisches Granulitgebirge)* (Vol. 133, pp. 221-250), Zfl-Mitteilungen.

Wiedenbeck, M. A. P. C., Alle, P., Corfu, F., Griffin, W. L., Meier, M., Oberli, F. V., von Quadt, A., Roddick J.C. & Spiegel, W. (1995). Three natural zircon standards for U-Th-Pb, Lu-Hf, trace element and REE analyses. *Geostandards newsletter*, **19**(1), 1-23.

Williams, H. M., Turner, S. P., Pearce, J. A., Kelley, S. P., & Harris, N. B. W. (2004). Nature of the Source Regions for Post-collisional, Potassic Magmatism in Southern and Northern Tibet from Geochemical Variations and Inverse Trace Element Modelling. *Journal of Petrology,* **45**(3), 555-607.

Wilson, A. H. (2012). A Chill Sequence to the Bushveld Complex: Insight into the First Stage of Emplacement and Implications for the Parental Magmas. *Journal of Petrology,* **53**, 1123-1168.

Wilson, T. J., Grunow, A. M., & Hanson, R. E. (1997). Gondwana assembly: The view from southern Africa and East Gondwana. *Journal of Geodynamic,* **23**(3/4), 263 – 286.

Winter, J. D. N. (2001). *An Introduction to Igneous and Metamorphic Petrology*: Prentice Hall.

York, D. (1969). Least-squares fitting of a straight line with correlated errors. *Earth and Planetary Science Letters*, 320-324.

10. Appendices

Appendix 1: Migmatite nomenclature used for field mapping

Migmatites are mixed rocks found in medium- to high-grade metamorphic areas that are heterogenous, composed of two (or more) parts with one part having formed as a result of partial melting (Mehnert, 1968; Ashworth, 1985; Sawyer, 2008). There are several ways to classify a migmatite including compositional (i.e. parts of a migmatite) and textural based schemes (Sawyer, 2008). The parts of a migmatite include the palaeosome and neosome (Sawyer, 2008), with the palaeosome constituting the protolith that was not affected by partial melting (Olsen, 1985), while the neosome is the component of the migmatite, which is usually quartzofeldspathic to feldspathic in composition, that has been newly formed by partial melting (Sawyer, 2008). The neosome can be broken into several parts namely the residuum, melanosome and leucosome and these are described based on the varying proportions of dark to light minerals (Mehnert, 1968). The residuum is a component of the neosome that is the remaining solid fraction, after partial melting, with the partial melt extracted (Mehnert, 1968). Melanosomes and leucosomes are the dark and light components of a migmatite, respectively (Mehnert, 1968; Sawyer, 2008). The melanocratic minerals are the residual fraction after melt has been removed to create the leucosome, which is segregations of melt made up primarily of quartz and feldspars (Mehnert, 1968; Sawyer, 2008). Furthermore, the neosome can be subdivided based on their source area. In situ and source melts are products of melt that are still within and have not migrated beyond there source layer, respectively (Sawyer, 2008). Leucocratic dykes or granitic intrusions are products of melt that have migrated from their source layers (Sawyer, 2008). In situ melts generally display diffuse contacts while the remaining types typically show discordant or sharp contacts and are detached from their residuum (Mehnert, 1968; Sawyer, 2008).

The most useful way to classify and determine the amount of melt fraction in a migmatite is from the textural classification used in Sawyer (2008). There are varying orders of classification from first to third order divisions. The first order division is between metatexites, transitional and diatexites, and generally describes the partial melt fraction. Second-order divisions are primarily based on the amount of and how the melt reacts to syn-anatectic strain (Sawyer, 2008). These second-division morphologies are subdivided into numerous types under metatexites and diatexites. With increasing melt and strain the types develop from patch to diatexite morphologies as a continuum between each type. Third-order classifications are separate from metatexites and diatexites because they occur in both and include fold-structured and vein structured migmatites (Mehnert, 1968). A schematic of this tiered classification scheme can be seen in table 10.1, with descriptions of key identifying features for the different morphological types.

Table detailing the textural morphologies of first to third-order divisions of migmatites after Sawyer (2008).

First-order Division		Metatexites palaeosome > neosome		Diatexites palaeosome < neosome	
		Heterogeneous Pre-partial melting features are preserved Palaeosome and neosome is present Low fraction of melt Low strain conditions		Neosome is dominant Melt is pervasive Pre-partial melting textures are absent Syn-anatectic-flow structures Palaeosome appears as rafts or is absent	
Second-order Division	*Syn-anatectic strain*				
	Low to None	patch	Higher generations of melt at discrete sites. Small, scattered patches of non-foliated insitu neosomes develop. Generally round or oval in shape. Even distribution of melanosome and leucosome. Occur in competent layers.	nebulite	Coalescence of patch migmatites. Large patches of neosome that have diffuse borders.
		dilation	Leucosome is located in dilatant structural sites (low-pressure). Occurs in competent layers in boudins and folds, for example. Short and restricted to particular layers.	schollen	Characterised by raft-like forms of remnants of palaeosomes, resister lithologies or melanosomes. This type is a common transition from metatexites and diatexites. In addition, with lower fraction melts. Little rotation of rafts but sometimes rounding of rafts is present. Flow foliations are present in the leucosome.
	Moderate	net	The essential feature is that the leucosomes occur in two or more intersecting systemetic sets so it looks like a net pattern outlining lozenge shaped palaeosome blocks.. Very common type. With further partial melting the palaeosome becomes a gneiss.	schlieren	Display well-developed flow-induced structures indicates by trains of platy and elongate minerals called schlieren. Rafts, resister lithologies or melanosomes may be present but they are generally less abundant. Parallelism is present between successive intrusions of leucosomes. Foliation or compositional banding is typically truncated at low angles.
	High	stromatic	Numerous thin and laterally persistent bands of leucosome that are parallel to the major foliation or compositional layering. Although they are not always concordant. Generally, leucosomes bands have a melanosomes along the boundary, although may be absent. Banding spacing is generally regular (*lit par lit*).	diatexite	Form under the highest fraction of melt and strain and are dominated by neosome. Remnant palaeosomes are rare and commonly absent. Pre-partial melt structures are only seen in scattered schollen. Show schlieren defined by platy minerals and banding may be present. Have cross cutting veins, leucocratic patches
Third-order Division	Morphologies not specific to metatexites and diatexites	**Fold-structured migmatites** Develop at low fractions of melt Controlled by relative competencies between layers Leucosomes develop in fold hinges, radial fractures, dilational sites parallel to folding and axial planar shears **Vein-structured migmatites** Contain one or more generations of discordant, leucocratic veins Usually superimposed on earlier metatexite or diatexite morphologies Some may be deformed but typically the yougest vein is usually undeformed and postdate peak partial melting events Contain mafic minerals generally parallel to the wall of the vein Intrusive types rather than insitu and in-source types			

In the field, a combination of these two schemes were used to describe the migmatites, while the textural classification was primarily used to determine the fraction of melt. This was done in order to see if there was varying partial melt fractions in certain areas to assess if it was an important factor in dome formation as Toe *et al.* (2013). Toe *et al.* (2013) established a tectonic stratification of the orogenic and the role of granitic intrusions and partial melts was attributed to crustal thickening and not the reason for dome formation in the southern Central Zone. Therefore, discerning whether

the northern extent of the Palmenhorst Dome has a stratification of the crust and the possible role of granitic melts, both in situ and intrusive, and partial melt in dome formation.

Appendix 2: Description of outcrops and localities for the samples collected in this study.

		Latitude	Longitude	Outcrop description
Sheeted leucogranites				
Type A	3.3I	-22.532115	14.998827	White partial melt parallel to foliation which cross-cuts pelitic schist. The sheeted leucogranite comprises fine-grained plagioclase and minor blebby quartz.
Type A	RO2L	-22.56697	14.974016	Thin sheeted leucogranite comprising plagioclase and K-feldspar with minor quartz and magnetite. Fine-grained sheeted leucogranite cross-cutting an amphibolite dyke.
Type B	KO4L	-22.609042	14.948939	Medium-grained plagioclase-rich sheeted leucogranite with accessory garnet. 1-2 m thick sheeted granite crossing cutting a grey granite.
Type B	7.1L	-22.574245	14.977711	White sheeted leucogranite with a biotite foliation and pegmatitic plagioclase in the core of a medium-grained sheeted granite. Comprises mainly plagioclase and biotite. Cross-cuts grey granite.
Type B	RO5L	-22.56697	14.974016	In situ partial melt pocket with diffuse contacts. Contains accessory garnet and amphibole within fine- to medium-grained plagioclase-rich intrusive.
Type C	KO7	-22.575932	14.977643	Pink medium- to coarse-grained sheeted leucogranite comprising K-feldspar and plagioclase. Smokey quartz is present and occurs as blebby inclusions within K-feldspar. Magnetite concentrated in pegmatitic cores. Cross-cuts basement banded-gneiss.
Type C	6.1L	-22.575666	14.975459	Folded coarse-grained sheeted leucogranite which anastomoses and cross-cuts amphibolite dykes. Contains a minor biotite foliation and also truncates the foliation in the amphibolite. Comprises K-feldspar and plagioclase with smoky quartz.
Type C	RO3	-22.56697	14.974016	Pink coarse-grained pegmatite which comprises K-feldspar, plagioclase and magnetite. Thick intrusive (2-3 m) cross-cutting grey granite.
Type E	PAO3L	-22.537797	14.973903	Pegmatitic euhedral K-feldspar and minor plagioclase which is deep pink in colour. Minor books of biotite are present. Does not contain a foliation. Cross-cuts basement orthogneisses with a diffuse contact.
Grey granites				
	7.1M	-22.574245	14.977711	Foliated tonalitic to granodioritic sheeted granitoid comprising biotite, plagioclase and quartz. Biotite forms foliation in hand-sample. Cross-cut by network of leucocratic plagioclase-rich veins.
	KO4M	-22.609042	14.948939	Pink to grey foliated granitoid (granodioritic) with a moderate biotite foliation. Comprises fine- to medium-grained quartz, plagioclase and biotite. Minor K-feldspar.
	RO5M	-22.56697	14.974016	Fine-grained granodioritic intrusive rock with plagioclase accumulations within a biotite, plagioclase and quartz-rich rock. Contains pockets of partial melt with accessory garnet which cross-cuts the foliation in the grey granite.
	RO1V	-22.56697	14.974016	Tonalitic fine-grained intrusive mainly comprising biotite and plagioclase. Has a dominant foliation.
	RO1H	-22.56697	14.974016	Fine- to medium-grained biotite and plagioclase granodiorite with intrusive and diffuse contacts. Has a moderately developed foliation.
Red granites				
	KO3	-22.609042	14.948939	Red medium-grained granite with a moderate biotite foliation. Comprises K-feldspar and quartz which is often granular or elongate.
	KO6	-22.574804	14.979386	Musky pink to red medium-grained granite comprising K-feldspar, quartz and minor plagioclase.
Chuos Formation				
	2.1	-22.665095	14.829592	Garnet-(cordierite-sillimanite)-biotite schist with continuous foliation. Displays bands of alternating biotite rich (7 cm) and garnet rich (4 cm) layers.
	2.2	-22.66282	14.829099	Flattened mafic and quartzo-feldspathic clasts (polymict) within a biotite and amphibole matrix. This meta-diamictite is matrix supported and shows elongation of the clasts.

3.1	-22.538093	15.019774	Chuos diamictite.
Rössing Formation			
LG-R1	-22.55128	14.948141	Red quarzitic schist with granular garnet and sillimanite porphyroblasts within a sheared quarzitic and feldspar-rich schist.
Khan Formation			
3.3H	-22.532115	14.998827	Calc-silicate which contains andradite garnet (chunky), diopside (chunky) and sphene (titanite). Tension gashes are cored by quartz and rimmed by feldspar.
3.4	-22.508119	14.991486	Semi-pelitic schist with chunky diopside and amphibole. This semi-pelitic is green in colour and fine- to medium-grained. Contains K-feldspar and has minor banding.
7.2	-22.573647	14.978388	Banded diopside-K-feldspar gneiss which has alternating bands of pink and green layers. The gneiss is fine- to medium-grained and has minor biotite which forms a platy mineral foliation parallel to banding.
Etusis Formation			
1.1	-22.670535	14.775218	Banded feldspathic quartzite with ilmenite concentrations along banding. Quartz is medium-grained and gritty while the feldspars are pink to white and are fine-grained.
PAO1	-22.536925	14.974057	Sillimanite-biotite-plagioclase-(cordierite) schist with a prominent sillimanite lineation (1-2 cm) which is parallel to the biotite foliation. This continuous foliation and lineation is commonly folded twice.
Amphibolite dykes			
6.1M	-22.575666	14.975459	Rafts of amphibole and plagioclase-rich fine-grained dyke within type C sheeted leucogranite. The dykes contain an amphibole foliation which is folded and cross-cut by the sheeted leucogranite. Concentrations of biotite along the intrusive boundary are melanosomes.
7.3	-22.572853	14.978523	Intensely foliated amphibolite dyke which comprises amphibole, biotite and plagioclase. The dark fine-grained dyke is cross-cut by multiple sheeted leucogranites.
RO2A	-22.56697	14.974016	Weakly foliated amphibolite dyke comprising mainly amphibole and biotite with minor plagioclase.
Basement Gneisses			
PAO2	-22.537742	14.973967	Augen to orthogneiss with associated quartzo-feldspathic vein (cross cut). Banding and platy biotite form a continuous foliation. Alternating leucocratic and melanocratic bands are finely to broadly spaced.
PAO3M	-22.537797	14.973903	Finely banded grey orthogneiss found within the high strain zone. Alternating biotite to plagioclase-rich layers are present forming a continuous and straight gneiss.
KO5			Granite-gneiss with a weakly defined biotite foliation. Pink K-feldspar and plagioclase segregations are faintly banded. This banding and foliation is folded and cross-cut by an axial planar foliation.
RO6	-22.554966	14.969109	Medium-grained granite-gneiss which has K-feldspar and plagioclase-rich segregations. These segregations have biotite accumulations along the diffuse edges between the K-feldspar, quartz and magnetite granite-gneiss. A faint biotite foliation is present.
Basement granites			
KO1	-22.609042	14.948939	Musky pink microgranite comprising K-feldspar and plagioclase with minor quartz. Quartz or plagioclase is sometimes aligned as a weak foliation.
KO2L	-22.609039	14.948941	Leucocratic segregation of the K02M comprising increased plagioclase and K-feldspar which has increased grain-sizes (medium- to coarse-grained).
KO2M	-22.609045	14.948938	Fine-grained musky pink granite with a biotite spaced foliation which comprises K-feldspar, plagioclase and quartz. Has cross-cutting brittle fractures associated with epidote and chlorite.

Appendix 3.A: Whole-rock geochemical data

Whole rock major element data for samples from this study

	SiO2	TiO2	Al2O3	Fe2O3	FeO	MnO	MgO	CaO	Na2O	K2O	P2O5	Cr2O3	NiO	LOI	Total
Sheeted leucogranites															
Type A															
3.3l	20.37	0.03	0.19	0.10	0.81	0.05	1.38	44.18	0.17	0.00	0.02	0.00	0.00	32.74	100.04
RO2L	68.34	0.64	15.43	0.45	3.60	0.05	1.31	3.62	4.18	1.69	0.20	0.00	0.00	0.58	100.09
Type B															
KO4L	76.44	0.04	12.55	0.05	0.38	0.01	0.07	0.37	2.07	8.00	0.08	0.01	0.00	0.29	100.34
RO5L	74.61	0.20	14.04	0.16	1.28	0.02	0.45	2.84	4.39	1.53	0.04	0.00	0.00	0.36	99.92
Type C															
KO7	72.62	0.25	13.73	0.27	2.18	0.05	1.15	2.56	3.98	2.03	0.09	0.00	0.00	1.05	99.95
6.1L	72.3	0.27	13.13	0.25	2.03	0.06	1.47	2.54	3.20	3.86	0.07	0.00	0.00	0.58	99.77
RO3	72.74	0.12	14.25	0.09	0.73	0.01	0.23	0.62	2.50	8.44	0.15	0.00	0.00	0.42	100.27
Type E															
PAO3L	58.53	0.79	17.94	0.69	5.62	0.10	2.42	1.08	2.31	9.93	0.18	0.00	0.00	0.75	100.34
Grey granites															
7.1M	71.22	0.40	15.43	0.11	0.86	0.08	0.80	2.76	4.46	2.84	0.13	0.00	0.00	0.90	99.99
KO4M	75.64	0.12	12.47	0.11	0.90	0.03	0.35	0.58	2.20	7.36	0.09	0.00	0.00	0.52	100.36
RO5M	63.85	1.12	15.87	0.65	5.20	0.08	2.74	3.56	4.23	2.44	0.21	0.00	0.00	0.31	100.26
RO1V	69.47	0.68	15.02	0.39	3.16	0.05	1.50	3.87	4.07	1.39	0.17	0.00	0.00	0.60	100.36
RO1H	58.37	1.48	16.30	0.84	6.84	0.13	3.63	5.88	3.86	1.93	0.26	0.01	0.00	0.82	100.35
Red granites															
KO3	65.32	0.80	15.57	0.50	4.04	0.08	1.60	2.42	3.54	4.03	0.22	0.00	0.00	1.68	99.80
KO6	70.70	0.50	13.94	0.28	2.27	0.04	0.68	1.32	2.85	6.09	0.21	0.00	0.00	0.80	99.67
Chuos Formation															
2.1	57.5	0.95	18.64	1.14	9.24	0.13	5.49	0.77	1.13	2.99	0.08	0.02	0.01	2.27	100.38
2.2	71.3	0.60	10.94	0.46	3.79	0.07	2.80	2.38	1.05	3.80	0.12	0.01	0.00	2.94	100.25
3.1	64.22	0.68	10.33	1.61	13.03	0.12	1.78	2.01	1.67	3.15	0.31	0.01	0.00	0.77	99.69
Khan Formation															
3.3H	63.76	0.57	10.47	0.24	1.92	0.05	2.12	9.75	6.24	0.10	0.14	0.00	0.00	4.93	100.30
3.4	61.88	0.58	11.05	0.45	3.68	0.13	5.22	9.12	1.95	4.36	0.16	0.01	0.00	1.52	100.11
7.2	52.06	1.86	16.74	1.12	9.10	0.23	5.27	7.16	3.51	2.31	0.33	0.00	0.00	0.55	100.24
Etusis Formation															
1.1	85.52	0.28	7.16	0.19	1.54	0.00	0.06	0.17	4.01	0.14	0.07	0.00	0.00	0.17	99.31
PAO1	73.51	0.45	17.62	0.51	4.09	0.05	1.09	0.25	0.28	1.58	0.06	0.00	0.00	0.55	100.05
Amphibolite dykes															
6.1M	53.45	0.90	14.83	0.90	7.28	0.28	6.50	8.37	3.86	1.94	0.18	0.02	0.00	1.20	99.71
7.3	58.91	1.43	16.40	0.79	6.45	0.12	3.41	5.25	3.81	2.73	0.37	0.00	0.01	0.62	100.29
RO2A	58.7	1.45	16.34	0.87	6.98	0.13	3.72	4.15	3.48	2.84	0.25	0.00	0.00	1.43	100.34
Abbabis Complex gneisses															
Grey orthogneisses															
PAO2	59.43	0.67	20.47	0.55	4.51	0.11	1.49	5.55	4.94	1.70	0.19	0.00	0.00	0.80	100.41
PAO3M	53.92	1.07	19.11	0.91	7.37	0.14	3.64	2.02	3.11	7.87	0.27	0.01	0.00	0.89	100.32
Orthogneisses															
KO5	67.70	0.59	15.01	0.51	4.08	0.06	1.20	2.31	3.46	4.29	0.20	0.00	0.00	0.67	100.08
RO6	74.05	0.28	12.85	0.26	2.06	0.04	0.34	1.69	2.97	4.29	0.05	0.00	0.00	0.94	99.82
Abbabis Complex granites															
KO1	60.80	1.35	16.88	0.76	6.17	0.12	2.71	4.58	3.45	2.27	0.30	0.01	0.00	0.71	100.09
KO2L	70.34	0.31	15.93	0.20	1.60	0.03	0.94	3.42	4.70	1.45	0.19	0.01	0.00	0.89	100.00
KO2M	48.7	3.60	15.41	1.67	13.49	0.22	5.42	3.41	3.06	3.56	0.43	0.01	0.01	0.37	99.34

Whole rock trace element data for samples from this study

	Sheeted leucogranites									Grey granites					Red granites	
	Type A			Type B			Type C		Type E							
	3.3I	RO2L	KO4L	7.1L	RO5L	KO7	6.1L	RO3	PAO3L	7.1M	KO4M	RO5M	RO1V	RO1H	KO3	KO6
Li	11.597	19.116	3.874	14.348	8.872	17.884	15.202	5.143	18.558	25.124	8.913	22.743	17.819	16.358	23.785	18.276
P	84.901	814.806	267.69	382.387	176.958	335.474	264.256	596.81	650.977	499.364	325.838	848.107	615.615	972.611	803.043	758.766
Sc	12.462	4.759	0.265	1.801	1.66	2.77	12.603	1.479	8.745	2.315	1.77	10.656	2.926	14.799	9.906	4.871
Ti	58.138	3911.548	198.004	1517.358	1343.143	1202.431	1596.393	716.84	4756.657	2435.245	695.858	6207.881	4027.615	9059.794	5063.507	2989.295
V	18.884	73.805	3.677	27.404	23.897	7.975	23.185	7.537	46.901	34.485	11.086	111.757	61.507	154.522	73.148	28.815
Cr	4.428	14.981	1.659	14.674	3.27	4.697	10.962	2.009	17.824	14.609	3.117	10.522	10.457	10.593	21.524	4.462
Co	3.202	10.475	0.709	3.483	4.265	2.913	9.55	2.263	13.388	9.331	2.165	18.577	13.185	30.316	8.377	5.278
Ni	41.176	14.892	2.482	13.439	8.568	8.203	13.606	4.462	11.792	19.305	5.53	24.9	18.821	31.428	10.482	4.597
Cu	2.081	9.775	4.054	7.962	5.17	3.799	52.67	9.632	5.277	10.667	8.875	24.387	28.194	49.552	11.367	22.747
Zn	7.172	59.895	8.082	15.264	19.884	38.464	38.262	12.271	74.233	21.342	22.833	71.602	50.665	103.816	74.17	33.283
Ga	1.503	21.591	12.173	14.101	19.196	12.746	18.788	14.93	22.367	21.909	14.548	19.899	17.062	20.79	18.791	18.139
Rb	0.176	95.059	354.744	95.533	78.101	91.32	185.162	342.429	401.194	137.539	347.269	195.483	89.187	144.845	193.68	287.484
Sr	406.332	224.836	88.979	236.188	146.677	47.253	152.673	122.659	75.956	309.957	103.308	156.695	226.863	247.844	120.724	76.714
Y	119.809	15.7	6.183	18.357	5.408	9.525	53.94	9.338	12.122	29.26	10.212	24.452	5.179	23.963	20.101	34.36
Zr	4.266	200.287	9.05	172.045	60.548	163.137	41.669	42.447	158.689	251.176	28.669	205.71	162.861	140.51	141.103	335.362
Nb	0.18	23.326	1.527	12.848	10.924	9.418	23.085	4.953	26.561	20.74	7.065	31.832	11.838	22.1	15.634	23.77
Ba	2.157	328.611	588.305	644.203	223.384	78.49	540.449	710.633	735.651	793.441	585.533	255.397	263.082	459.057	1147.284	591.195
Sn	0.362	2.122	0.494	6.603	1.097	2.668	4.561	0.655	8.154	8.1	1.336	4.118	1.083	2.732	4.381	6.354
Cs	0.032	3.055	2.345	1.027	1.214	2.23	1.414	1.34	10.64	1.441	2.186	5.923	2.238	2.683	0.938	1.921
La	83.692	50.472	6.231	20.781	9.314	43.525	41.245	19.054	22.285	29.352	9.068	26.316	25.271	31.345	45.795	136.363
Ce	135.897	113.047	14.763	57.518	15.703	72.435	82.755	38.22	52.437	93.951	18.117	54.983	70.631	78.427	89.11	304.955
Pr	13.508	11.147	1.345	9.567	1.492	8.154	9.591	3.956	5.228	13.54	1.958	6.338	4.43	8.438	10.144	34.325
Nd	47.878	39.685	4.822	37.309	5.089	26.647	36.095	13.556	19.803	54.521	6.876	23.866	14.947	32.883	37.658	118.68
Sm	9.116	6.527	1.488	7.245	1.129	4.757	8.91	3.1	4.145	10.792	2.053	5.143	2.157	6.696	7.178	21.092
Eu	1.359	1.379	0.902	1.379	0.545	0.547	1.239	1.141	1.053	1.923	0.993	1.064	0.684	1.752	1.873	1.398
Gd	14.374	6.827	1.295	6.228	1.17	5.144	10.244	2.996	4.147	9.478	2.028	5.758	2.805	7.392	7.334	20.914
Tb	2.139	0.696	0.187	0.728	0.156	0.536	1.605	0.346	0.499	1.147	0.316	0.778	0.23	0.898	0.857	2.153
Dy	14.378	3.229	1.085	3.476	0.911	2.216	9.459	1.714	2.494	5.602	1.798	4.279	1.042	4.665	4.224	8.91
Ho	3.639	0.578	0.217	0.643	0.191	0.347	1.838	0.317	0.457	1.035	0.363	0.877	0.194	0.901	0.793	1.405
Er	12.619	1.692	0.627	1.933	0.628	0.88	5.341	0.913	1.278	3.117	1.068	2.661	0.596	2.624	2.272	3.718
Tm	1.938	0.216	0.086	0.259	0.097	0.099	0.771	0.118	0.164	0.429	0.148	0.39	0.075	0.359	0.289	0.369
Yb	12.761	1.34	0.508	1.73	0.648	0.586	4.857	0.701	1.012	2.839	0.918	2.616	0.479	2.256	1.693	2.073
Lu	1.962	0.2	0.071	0.255	0.095	0.089	0.678	0.108	0.142	0.405	0.132	0.392	0.077	0.329	0.243	0.29
Hf	0.23	4.988	0.304	4	1.99	4.893	1.449	1.33	4.17	6.131	0.921	5.167	4.089	3.404	3.736	8.859
Ta	0.041	2.419	0.166	0.699	0.996	0.451	1.008	0.213	1.648	1.161	0.417	2.115	0.954	1.533	0.794	1.133
W	0.134	0.513	0.292	0.474	0.55	0.167	0.413	0.236	0.859	0.504	0.593	4.105	0.259	0.665	0.281	0.184
Pb	2.233	17.856	37.68	7.334	15.128	12.879	18.931	42.883	33.328	10.193	44.988	10.784	14.722	14.244	23.924	47.079
Th	0.199	20.098	3.837	24.47	23.98	49.729	10.536	13.126	11.858	26.817	3.865	20.368	14.685	15.813	17.48	124.039
U	0.207	4.862	0.841	4.054	9.328	4.532	2.505	2.475	2.706	6.13	1.383	7.357	3.515	4.057	1.416	6.373

	Chuos Formation			Khan Formation			Etusis Formation		Amphibolite dykes			Abbabis Complex gneisses				Abbabis Complex granites		
												Grey orthogneiss		Orthogneiss				
	2.1	2.2	3.1	3.3H	3.4	7.2	1.1	PAO1	6.1M	7.3	RO2A	PAO2	PAO3M	KO5	RO6	KO1	KO2L	KO2M
Li	87.753	54.151	49.625	26.185	22.324	30.904	1.789	24.434	37.957	26.95	40.756	15.829	25.348	26.647	4.865	34.726	21.286	58.688
P	243.483	402.095	1052.243	513.534	524.481	1216.148	218.345	210.489	773.138	1347.033	1022.363	750.134	1010.002	723.75	172.858	950.509	814.448	1724.264
Sc	22.861	7.007	7.22	6.712	7.949	17.951	2.216	4.14	30.063	12.029	19.048	7.365	14.48	9.262	2.951	10.05	2.361	29.511
Ti	5719.743	3617.624	4023.355	3608.816	3582.635	11365.649	1766.115	2704.951	5597.438	8703.53	8579.957	3977.585	6376.035	3711.129	1400.338	6871.323	2012.546	21215.31
V	166.12	69.555	74.396	85.808	68.894	178.364	23.306	31.664	81.324	133.829	144.388	42.359	58.629	53.587	16.439	115.622	30.856	419.748
Cr	126.452	45.704	35.482	39.348	43.822	8.299	8.039	33.93	81.435	24.944	12.336	17.54	21.386	17.259	5.098	13.159	9.515	72.036
Co	37.359	12.965	10.226	4.182	13.259	37.122	0.521	4.091	27.851	24.489	27.184	11.526	18.736	10.378	2.124	16.425	9.003	48.042
Ni	76.152	25.508	18.327	17.902	27.251	48.508	3.511	10.709	36.824	30.673	31.458	11.076	15.312	11.795	4.406	16.926	22.538	75.96
Cu	65.351	23.394	5.432	5.701	74.668	18.495	4.2	5.987	70.909	31.454	28.332	4.819	8.941	18.826	3.936	29.38	31.869	53.793
Zn	140.955	63.328	67.948	13.156	45.908	128.034	6.75	29.361	133.718	96.071	144.243	55.939	103.202	71.453	15.645	69.19	39.391	216.189
Ga	24.447	14.209	14.629	12.552	14.961	21.34	8.859	32.754	30.088	21.135	23.99	21.077	25.267	21.69	10.515	17.584	18.094	26.817
Rb	173.044	111.191	170.616	1.975	186.122	116.697	1.939	81.987	128.702	128.838	190.979	102.968	409.727	223.53	139.759	136.082	104.02	237.795
Sr	60.246	90.627	85.097	108.87	175.246	244.557	16.756	7.32	120.26	298.842	207.291	204.252	77.014	121.335	35.845	198.83	226.714	188.525
Y	17.054	16.023	13.806	34.651	29.223	33.8	9.563	12.302	140.699	31.968	53.259	18.694	23.513	15.999	9.233	32.196	6.253	24.674
Zr	42.704	105.514	144.558	140.126	134.901	201.958	48.255	99.255	78.929	214.031	171.832	131.545	238.346	101.67	143.506	194.791	33.12	244.987
Nb	13.781	14.64	17.418	15.215	17.9	25.765	14.376	11.215	77.772	36.147	43.407	18.701	33.77	23.267	9.714	34.692	4.268	43.339
Ba	303.528	528.92	616.043	2.769	891.268	482.301	28.835	120.3	169.843	573.459	505.73	207.175	611.824	605.526	258.833	418.95	95.501	264.576
Sn	1.565	2.791	3.302	2.212	3.564	2.677	2.287	9.506	14.001	1.004	5.09	5.034	11.384	3.422	4.613	6.229	0.735	4.588
Cs	13.507	1.728	4.476	0.141	1.861	2.844	0.035	7.158	2.099	2.681	5.362	8.153	13.882	1.756	0.994	2.738	1.717	8.12
La	22.719	27.907	17.302	17.782	36.204	31.723	59.709	51.023	350.174	43.129	25.407	42.498	51.894	36.004	29.178	53.176	11.824	16.512
Ce	47.389	64.887	38.529	49.319	82.112	70.922	106.808	110.256	655.122	102.463	65.746	96.631	110.196	68.375	54.647	103.27	26.895	36.195
Pr	5.604	6.581	4.248	5.736	9.382	8.275	10.871	12.02	63.267	10.643	7.925	9.571	12.044	7.524	5.934	12.408	2.57	4.54
Nd	21.055	24.033	16.151	22.782	33.825	31.939	34.105	42.28	188.852	39.858	34.128	34.152	45.292	27.003	20.195	44.616	9.845	19.806
Sm	4.335	4.841	3.851	5.05	7.031	7.042	4.726	7.949	33.691	7.951	9.523	5.861	8.775	5.241	3.481	8.419	1.881	5.03
Eu	0.918	1.143	1.132	0.819	1.646	2.333	0.608	0.844	2.214	2.077	1.537	1.28	1.446	1.301	0.602	1.745	1.045	1.575
Gd	4.721	5.176	4.051	6.352	7.416	8.142	5.073	8.59	40.758	8.865	10.643	6.59	9.359	5.506	3.862	9.321	2.154	6.002
Tb	0.618	0.626	0.538	0.913	0.964	1.149	0.481	0.898	5.028	1.135	1.626	0.746	1.088	0.671	0.427	1.197	0.248	0.843
Dy	3.4	3.28	2.912	5.544	5.28	6.3	2.09	3.662	26.925	6.069	9.56	3.714	5.215	3.325	2.001	6.152	1.231	4.732
Ho	0.685	0.615	0.554	1.164	1.02	1.27	0.353	0.527	5.061	1.208	1.927	0.673	0.91	0.612	0.353	1.204	0.227	0.942
Er	2.156	1.813	1.621	3.592	3.028	3.689	1.049	1.23	15.024	3.527	5.769	1.949	2.473	1.706	0.966	3.595	0.654	2.681
Tm	0.314	0.249	0.229	0.519	0.429	0.518	0.119	0.112	2.094	0.48	0.847	0.253	0.301	0.201	0.12	0.493	0.082	0.359
Yb	2.133	1.577	1.413	3.476	2.748	3.367	0.734	0.651	13.211	3.078	5.342	1.623	1.764	1.127	0.756	3.17	0.471	2.261
Lu	0.323	0.234	0.211	0.542	0.407	0.501	0.101	0.086	1.881	0.441	0.759	0.234	0.265	0.152	0.119	0.455	0.068	0.338
Hf	1.172	2.859	3.715	4.155	3.687	4.775	1.434	3.081	2.83	4.852	4.149	3.538	6.294	2.904	4.584	4.755	0.88	5.998
Ta	0.955	1.174	1.238	1.212	1.245	1.697	1.6	0.854	3.221	2.025	3.41	1.649	2.137	0.828	0.785	2.589	0.314	2.577
W	0.532	0.545	0.893	0.199	0.243	0.704	2.288	1.124	0.732	0.126	0.799	0.974	1.102	0.174	0.246	0.492	0.418	1.546
Pb	9.184	24.167	19.91	1.522	6.115	8.71	2.684	5.672	16.373	6.764	15.108	13.33	26.313	27.678	14.942	11.683	10.983	9.69
Th	9.532	14.145	6.868	12.809	18.908	9.057	24.647	26.909	94.78	14.682	8.824	17.586	25.293	19.356	26.365	17.891	7.125	2.671
U	2.293	2.687	1.832	4.313	3.379	3.345	1.834	3.463	9.651	2.237	3.464	3.288	3.797	2.201	4.384	2.932	2.918	3.036

Appendix 3.B: XRF and ICP-MS analytical procedures

XRF analytical procedures for major elements

Analyses were completed on fused disks for major elements using the Norrish Fusion (Norrish and Hutton, 1969) technique and in-house correction procedures. Milled samples were ignited for 40 minutes at 1000 $^{\circ}$C where loss of ignition (LOI) was calculated. Samples (035 *gm*) were then mixed with Johnson Matthey Spectrolflux 105 (2.5 *gm*) and fired once again at 1100 $^{\circ}$C for 40 minutes and then poured and pressed into a fused disk. Using a PANalytical PW2404 WD XRF spectrometer major elements were analysed with a Rh tube set at 50 kV and 50 mA. Analysis time was set at 40 seconds per element and 20 seconds per background. Precision is 1% for elements that are more than 5% and 5% for elements less than 5% by weight. Standard calibrations were made up using synthetic oxide mixtures and international standard rocks and in-house controls.

ICP-MS analytical procedures for trace elements

50 *mg* of milled sample was added to 3 *ml* mixture of Hf and HNO_3 (3:2), in a high-pressure vessel, and placed in a CEM Mars Express Microwave digester at 235 $^{\circ}$C and 35 bars for 40 minutes. Digested samples were then evaporated on a hot plate (70 $^{\circ}$C) until dry. 3 *ml* of concentrated HN03 was added and capped for 24 hours on a hot plate at 70 $^{\circ}$C and then dried. This process was carried out twice and then 100 *µl* of HNO_3 was added to dried sample ready for analysis. Reference standards were within 10%, for all elements, agreement of accepted values.

Appendix 3.C: Calibration standards and reference standards data

Measured whole rock major element data for calibration and reference standards

	SiO2	Al2O3	Fe2O3	FeO	MnO	MgO	CaO	Na2O	K2O	TiO2	P2O5	Cr2O3	NiO
Run 1													
BHVO2	49.88	13.66	1.25	10.1	0.17	7.29	11.39	2.23	0.52	2.7354	0.27	0.0489	0.0159
GSP2	67.41	15.12	0.5	4.04	0.04	0.98	2.15	2.81	5.48	0.6727	0.29	0.0007	0.0013
NIM-D	39.52	0.34	1.72	13.93	0.22	43.92	0.27	0.05	0.01	0.0289	0.01	0.4367	0.268
NIM-P	51.16	4.29	1.27	10.28	0.23	25.41	2.61	0.32	0.09	0.1966	0.02	3.5379	0.0758
DTS1	40.52	0.27	0.87	7.03	0.13	49.85	0.12	0.08	0	0.0122	0.01	0.6198	0.3156
Run 2													
BHVO2	50.03	13.71	1.24	10.08	0.18	7.29	11.46	2.24	0.52	2.7353	0.27	0.049	0.014
GSP2	67.35	15.15	0.5	4.02	0.04	0.98	2.15	2.81	5.47	0.6713	0.29	-0.001	-2E-04
NIM-D	39.29	0.34	1.72	13.93	0.22	43.87	0.26	0.04	0	0.0262	0.01	0.4346	0.2663
NIM-P	51.08	4.28	1.27	10.26	0.23	25.43	2.59	0.34	0.09	0.1923	0.02	3.4872	0.0715
DTS1	40.67	0.27	0.87	7.05	0.12	50.02	0.12	0.08	0	0.0112	0.01	0.6164	0.3141

Precision and accuracy testing for whole rock major element data (accepted concentrations for standards are from USGS standards)

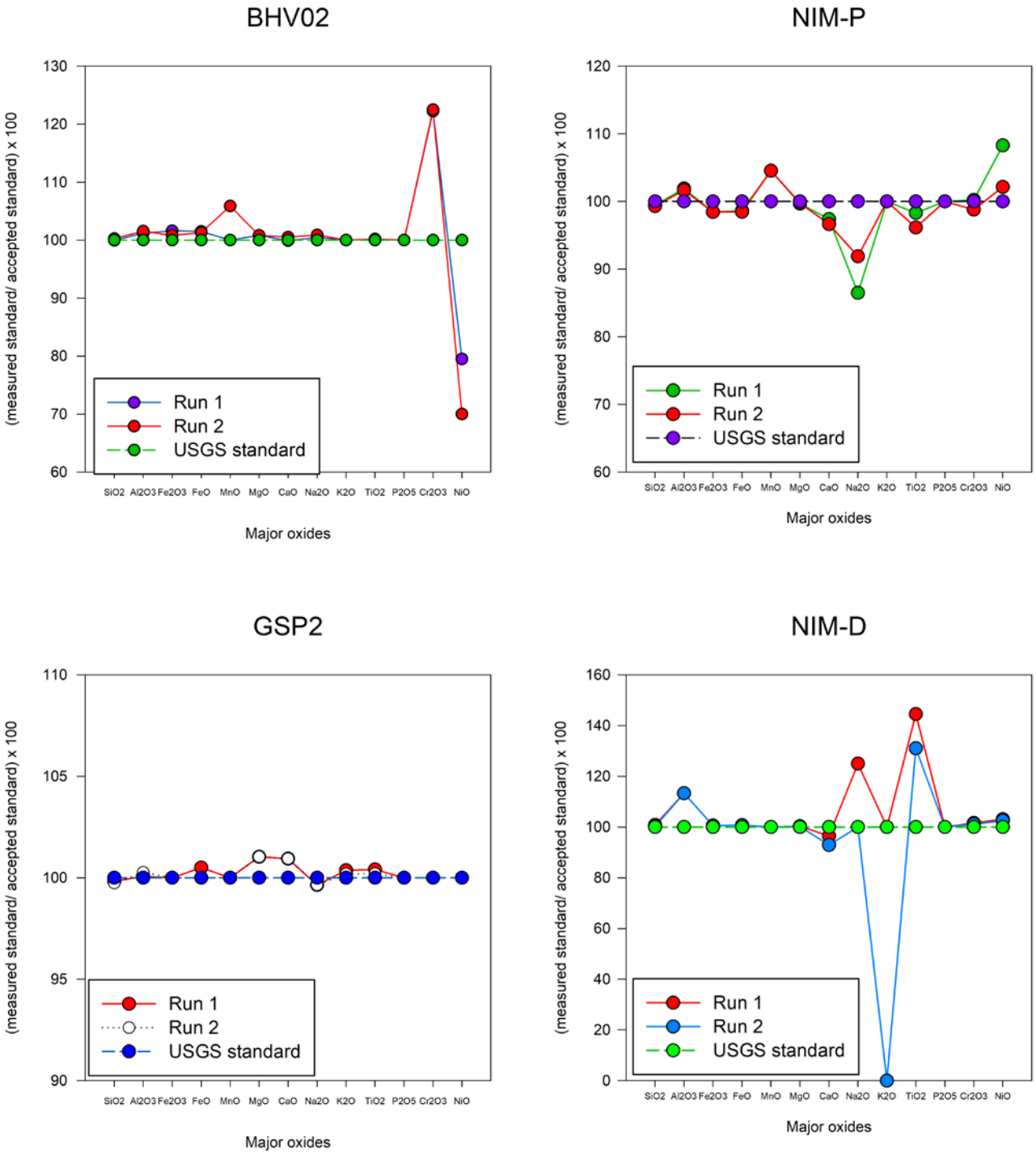


Figure showing the similarities between the measured reference standards and accepted USGS standards (normalised to 100%) for major whole rock XRF data. Measured BHV02 major oxides have discrepancies in Cr_2O_3 and NiO_2, measured NIM-P major oxides have discrepancies in Na_2O and NiO_2, measured GSP2 major oxides are consistent with measured standards while measured NIM-D major oxides have discrepancies in Al_2O_3, Na_2O, K_2O and TiO_2.

Measured whole rock trace element data for calibration and reference standards

	BHV02								GSP2			
	BHVO2.1	**BHVO2.2**	**BHVO2.1**	**BHVO2.2**	**BHVO2.1**	**BHVO2.2**	**BHVO2.1**	**BHVO2.2**	**GSP2**	**GSP2**	**GSP2**	**GSP2**
Li	4.421	4.361	4.218	4.151	4.253	4.229	4.241	4.087	34.792	34.583	31.429	33.11
P	1011.346	1007.2	975.544	979.673	932.189	938.045	1128.161	1117.043	1053.579	1049.98	1016.082	1221.593
Sc	28.136	26.038	27.642	25.756	28.999	29.11	28.836	29.145	3.521	3.681	3.546	3.82
Ti	17591.803	17339.828	17314.929	17394.262	17273.496	17078.423	17055.73	17119.737	4021.895	3962.956	4010.662	4026.306
V	334.048	325.701	329.732	328.519	328.739	327.694	324.895	327.541	53.284	53.531	53.47	54.283
Cr	308.517	283.565	308.314	283.417	289.062	284.405	285.852	284.124	19.99	20.286	20.931	21.012
Co	48.092	47.278	47.214	46.602	46.802	47.242	46.325	46.42	7.234	7.197	7.171	7.282
Ni	133.22	120.361	135.761	125.354	125.029	125.893	125.564	127.724	17.481	18.034	18.861	19.434
Cu	132.672	129.433	134.162	131.131	131.059	130.02	131.457	131.447	48.058	48.368	46.757	46.005
Zn	132.808	130.915	135.805	135.664	154.34	134.283	155.017	137.386	120.601	121.672	135.26	135.616
Ga	21.349	21.112	21.355	20.923	21.956	21.855	21.784	21.74	24.112	24.329	23.926	23.951
Rh												
Rb	8.651	7.982	8.795	7.699	9.203	8.826	9.883	9.092	166.251	167.243	138.423	139.544
Sr	393.306	372.77	388.982	368.467	396.199	394.545	396.625	397.299	156.547	163.407	128.182	135.353
Y	21.491	20.241	20.965	19.894	21.924	21.874	21.882	22.147	17.891	18.273	18.424	19.175
Zr	165.173	164.797	162.704	163.496	164.535	163.828	161.953	162.931	396.501	397.378	486.375	498.521
Nb	18.304	18.427	18.035	17.96	17.914	17.778	17.908	17.938	25.574	25.759	25.67	25.865
Ba	125.933	124.302	127.468	123.446	126.686	126.41	126.133	125.517	771.818	792.878	639.049	678.896
In												
Sn	1.785	1.778	1.93	1.753	1.775	1.786	1.787	1.768	6.703	6.545	6.531	6.257
Cs	0.087	0.076	0.086	0.072	0.091	0.088	0.094	0.088	1.037	1.062	0.988	0.986
La	14.103	13.529	14.227	13.388	13.973	14.021	14.164	14.152	129.947	132.271	128.491	133.433
Ce	35.808	34.79	35.957	34.375	35.084	35.223	35.115	35.403	393.769	402.054	378.848	388.574
Pr	4.965	4.773	4.964	4.736	4.898	4.912	4.924	4.963	41.558	42.67	41.203	42.629
Nd	22.164	21.323	22.566	21.576	21.861	21.885	21.957	22.159	148.595	154.79	150.931	153.13
Sm	5.478	5.311	5.613	5.279	5.46	5.571	5.614	5.642	19.96	20.314	19.812	20.643
Eu	1.954	1.858	1.965	1.874	1.976	1.978	1.986	2.006	1.872	1.998	1.99	2.048
Gd	6.281	6.036	6.348	5.992	6.454	6.404	6.424	6.436	16.78	18.399	18.288	19.025
Tb	0.878	0.838	0.875	0.817	0.88	0.886	0.891	0.89	1.341	1.429	1.416	1.476
Dy	4.587	4.372	4.627	4.364	4.688	4.695	4.635	4.715	4.714	4.96	4.89	5.078
Re												
Ho	0.849	0.808	0.867	0.788	0.845	0.864	0.871	0.867	0.694	0.711	0.714	0.751
Er	2.238	2.156	2.257	2.134	2.291	2.316	2.316	2.332	2.181	2.276	2.335	2.433
Tm	0.284	0.272	0.297	0.266	0.292	0.289	0.303	0.301	0.203	0.209	0.207	0.22
Yb	1.731	1.627	1.71	1.617	1.771	1.752	1.751	1.788	1.196	1.212	1.232	1.295
Lu	0.242	0.231	0.244	0.221	0.25	0.245	0.257	0.252	0.162	0.17	0.171	0.209
Hf	4.015	4.002	3.993	3.957	4.036	4.019	4.03	4.012	10.006	10.06	12.172	12.073
Ta	1.076	1.077	1.075	1.037	1.055	1.045	1.067	1.05	0.798	0.801	0.799	0.807
W	0.276	0.496	0.296	0.508	0.274	0.249	0.265	0.264	0.358	0.366	0.367	0.378
Pb	1.809	1.723	1.796	1.739	1.753	1.967	1.768	1.995	45.664	45.538	47.56	47.876
Bi												
Th	1.168	1.085	1.177	1.065	1.221	1.208	1.256	1.234	93.274	94.309	89.894	92.425
U	0.465	0.453	0.462	0.456	0.463	0.46	0.468	0.454	2.524	2.512	2.361	2.396

Precision and accuracy testing for whole rock trace element data (accepted concentrations for standards are from USGS standards)

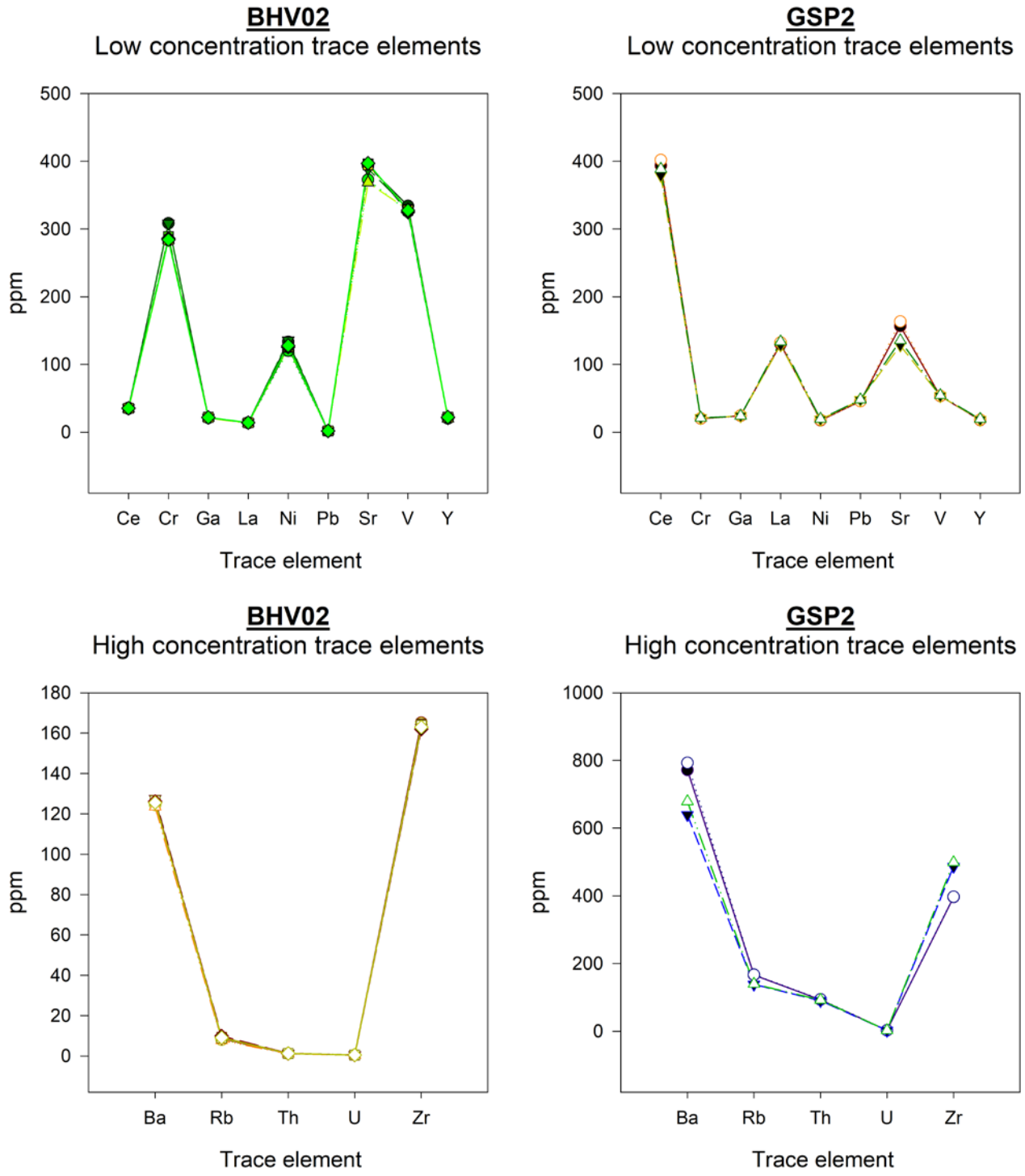


Figure showing the similarities in measured reference standards to accepted reference standards for selected trace elements (ppm).

Appendix 4.A: Summary of SELFRAG Lab experimental parameters

A summary of the experimental parameters for each sample is given in below. For each sample, a volume of 250 *ml* of rock aggregates were fragmented with varying energy and pulses.

Table summarising the SELFRAG Lab experiment information for each sample.

Sample ID (in the order processed)	Energy in J (activated pulses) All experiments set at 120Kv @ 5Hz with 200 initial pulses
K06	3.271×10^4 (300)
PA03	2.379×10^4 (200)
R06	3.251×10^4 (299)
K07	1.888×10^4 (197)
1.1	2.256×10^4 (190)
K05	2.280×10^4 (200)
7.3	2.123×10^4 (200)
PA01	2.566×10^4 (200)
PA02	2.233×10^4 (200)
R02	2.395×10^4 (200)

Appendix 4.B: Summary of methods and settings used for LA-ICP-MS

Analytical Protocols using LA-SF-ICPMS at Wits

Prepared by Robert Bolhar, date: 25 Feb 2019

Prior to laser ablation analysis zircons and other accessory minerals are to be separated and mounted in epoxy to be examined by backscattered (BSE) and cathodoluminescence (CL) imaging for selecting locations for analysis and to avoid cracks and inclusions.

U-Pb zircon: Instrumentation and Data Acquisition

U-Th-Pb measurements were carried out in the Earthlab at the University of the Witwatersrand, employing an Australian Scientific Instruments (ASI) Resonetics Resolution 193 nm ArF excimer (SE 155) system coupled to a Thermo Scientific Fisher sector-field ICPMS (Element XR). The U-Th-Pb measurements were performed in low resolution and electrostatic scanning (E-scan) modes. Data were acquired by single spot analysis (30 mm), using a laser repetition rate of 8 Hz and a fluence of 2.5 Jcm^{-2}. Total signal acquisition time was 65 sec to allow data processing and preparation for the next analysis, comprising 15 sec of pre- and post-ablation (gas blank) and 20 sec of ablation measurements. Laser sampling took place in a SE155 dual-volume ablation cell (Laurin Technic, Canberra, Australia) using a mixed He-Ar atmosphere and a small volume of N_2 to enhance signal stability and sensitivity. The following gas flows were applied: He (300-400 ml/min), Ar (800-1200 ml/min) and N_2 (2-4 ml/min), respectively. Zircon standard GJ1 (Jackson et al., 2004) served for calibration, and Temora-2 (Black et al., 2003, 2004) and Plešovice (Sláma et al., 2008) zircon certified reference materials (CMRs) were analysed as unknows to evaluate accuracy and precision. The LA-ICPMS system was tuned during line scans using NIST 612 glass for maximum sensitivity for ^{238}U and ^{206}Pb, while maintaining oxide levels (ThO^+/Th) < 0.5 % and the Th/U ratio >0.8. Typically, two analyses of the primary calibration standard were obtained at the beginning and end of a sequence, and 10-20 analyses of unknowns were followed by analyses of one primary calibration standard and two to four secondary standards for quality control purposes. Prior to each spot analysis surface material was removed using 2 laser pulses. The following masses were measured (60 samples per peak): ^{202}Hg, $^{204}(Pb+Hg)$, ^{206}Pb, ^{207}Pb, ^{208}Pb, ^{232}Th, ^{235}U, and ^{238}U. Magnet settling time was 0.001 sec, and sample times range from 0.0002 sec (^{235}U) to 0.003 sec (^{207}Pb). All isotopes were measured in pulse counting mode, except for ^{238}U (analog mode). A summary of instrument settings is provided in table 1.

U-Pb data reduction using iolite

Data reduction was performed using the iolite extension (http://www.iolite.org. au) to the software Igor Pro (http://www.wavemetrics.com), proceeding in a series of sequential steps, including data import, selection of integrations, baseline subtraction, drift and down-hole fractionation, calibration and error propagation (Paton et al., 2010, 2011). Additionally, the data reduction scheme (DRS) VizualAge (Petrus and Kamber, 2012; http://www.japetrus.net/va) was applied to more carefully select integrations in order to minimize discordance and to enable common lead correction, if necessary (Andersen, 2002).

U-Th-Pb data presentation and calculation of ages

Graphic presentation and calculation of Concordia and upper intercept ages was carried out using the software ISOPLOT-R (Vermeesch, 2018) and ISOTPLOT (Ludwig, 2003). Uncertainties on individual and mean/regressed ages are 2SE (standard error, absolute).

Trace elements in Silicates (and Glasses, Oxides, Carbonates): Instrumentation and Data Acquisition

Trace elemental analysis was carried out in the Earthlab at the University of the Witwatersrand, employing an Australian Scientific Instruments (ASI) Resonetics Resolution 193 nm ArF excimer (SE 155) system coupled to a Thermo Scientific Fisher sector-field ICPMS (Element XR). Measurements were performed in low resolution and electrostatic scanning (E-scan) modes. Data were acquired by single spot analysis (30-80 mm), using a laser repetition rate of 8 Hz and a fluence of 2.5 Jcm^{-2}. Total signal acquisition time was 65 sec to allow data processing and preparation for the next analysis, comprising 15 sec of pre- and post-ablation (gas blank) and 15 sec of ablation measurements. Laser sampling took place in a SE155 dual-volume ablation cell (Laurin Technic, Canberra, Australia) using a mixed He-Ar atmosphere and a small volume of N_2 to enhance signal stability and sensitivity. The following gas flows were applied: He (300-400 ml/min), Ar (800-1200 ml/min) and N_2 (2-4 ml/min), respectively. Synthetic glass NIST 612 (Jochum et al., 2011) served for calibration, while NIST 610 and 614 as well as USGS natural glasses BHVO2, BCR-2 and BIR-2 (Gao et al., 2002) were analysed as unknows to evaluate accuracy and precision. The LA-ICPMS system was tuned during line scans using NIST 612 glass for maximum sensitivity for ^{6}Li, ^{115}In and ^{238}In, while maintaining oxide levels (ThO^{+}/Th) <0.5 %. For internal standardization, the isotopes ^{43}Ca or ^{29}Si were used. Typically, two analyses of the primary calibration standard were obtained at the beginning and end of an experiment, and 10-20 analyses of unknowns were followed by analyses of one primary calibration standard and two to four analyses of the secondary standards for quality control purposes. Prior to

each spot analysis surface material was removed using 2 laser pulses. The following masses were measured (40 samples per peak): ^{29}Si, ^{43}Ca, ^{45}Sc, ^{47}Ti, ^{51}V, ^{53}Cr, ^{59}Co, ^{60}Ni, ^{65}Cu, ^{85}Rb, ^{88}Sr, ^{89}Y, ^{90}Zr, ^{93}Nb, ^{139}La, ^{140}Ce, ^{141}Pr, ^{146}Nd, ^{147}Sm, ^{151}Eu, ^{157}Gd, ^{159}Tb, ^{163}Dy, ^{165}Ho, ^{166}Er, ^{169}Tm, ^{174}Yb, ^{175}Lu, ^{178}Hf, ^{181}Ta, ^{208}Pb, ^{232}Th, ^{238}U. All isotopes were measured in pulse counting mode, except for ^{238}U (analog mode). A summary of instrument settings is provided in table 2.

Trace element data reduction using iolite

Data reduction was performed using the iolite extension (http://www.iolite.org. au) to the software Igor Pro (http://www.wavemetrics.com), specifically the data reduction scheme ("DRS") "X_Trace_Elements_IS", proceeding in a series of sequential steps, including data import, selection of integrations, baseline subtraction, drift and down-hole fractionation, calibration and error propagation (Paton et al., 2010, 2011).

Table 1: Operating conditions and data acquisation for U-Pb zircon

ICP-MS	
Instrument	magnetic sector
Manufacturer	Thermo Scientific Instruments
Model	Element XR
RF power [W]	1200-1400
Gas Flows	
Cooling (Ar [l/min]	16
Auxiliary (Ar) [l/min]	0.9-1.0
Sample (Ar) [l/min]	0.3-0.4
Carrier (He) [l/min]	0.9-1.1
Laser	
Instrument	ArF excimer
Manufacturer	Australian Scientific Instruments
Model	Resolution SE155
Wavelength [nm]	193
Spot size [microns]	30
Repetition Rate [Hz]	8
Laser Fluence [J/cm2]	2.5
Data Acquisition	
Resolution Mode	Low
Protocol	Time-resolved
Scan Mode	E-scan
Scanned Masses	202, 204, 206, 207, 208, 232, 235, 238
Settling Times	0.001
Sample Times	0.0002-0.003
Samples Per Peak	60
Detection Mode	Counting for all isotopes except 238 (analog)
Detector Deadtime [n sec]	18 (check)
Background (gas blank) [sec]	two times 15
Ablation Time [sec]	20
Standards	
Calibration (primary)	zircon GJ1
Internal	na
Control (secondary)	Temora-2, Plesovice, 91500
Data Reduction	
Software	iolite, in-built into Igor Pro
Data Reduction Scheme(s)	VizualAge

Table 2: Operating conditions and data acquisation for TE silicates

ICP-MS	
Instrument	magnetic sector
Manufacturer	Thermo Scientific Instruments
Model	Element XR
RF power [W]	1200-1400
Gas Flows	
Cooling (Ar [l/min]	16
Auxiliary (Ar) [l/min]	0.9-1.0
Sample (Ar) [l/min]	0.3-0.4
Carrier (He) [l/min]	0.9-1.1
Laser	
Instrument	ArF excimer
Manufacturer	Australian Scientific Instruments
Model	Resolution SE155
Wavelength [nm]	193
Spot size [microns]	30
Repetition Rate [Hz]	8
Laser Fluence [J/cm2]	2.5
Data Acquisition	
Resolution Mode	Low
Protocol	Time-resolved
Scan Mode	E-scan
Scanned Masses	29Si, 43Ca, 45Sc, 47Ti, 51V, 53Cr, 59Co, 60Ni, 65Cu, 85Rb, 88Sr, 89Y, 90Zr, 93Nb, 139La, 140Ce, 141Pr, 146Nd, 147Sm, 151Eu, 157Gd, 159Tb, 163Dy, 165Ho, 166Er, 169Tm, 174Yb, 175Lu, 178Hf, 181Ta, 208Pb, 232Th, 238U
Settling Times	0.001
Sample Times	0.0002-0.003
Samples Per Peak	60
Detection Mode	Counting for all isotopes except 238 (analog)
Detector Deadtime [n sec]	18 (check)
Background (gas blank) [sec]	two times 15
Ablation Time [sec]	20
Standards	
Calibration (primary)	NIST612
Internal	43Ca, 29Si
Control (secondary)	NIST610, 614, BHVO-2G, BIR-1G, BCR-2G
Data Reduction	
Software	iolite, in-built into Igor Pro
Data Reduction Scheme(s)	X_Trace_Elements_IS

References

Andersen, T. (2002). Correction of common lead in U–Pb analyses that do not report ^{204}Pb. *Chemical geology*, *192*(1-2), 59-79.

Black, L. P., Kamo, S. L., Allen, C. M., Aleinikoff, J. N., Davis, D. W., Korsch, R. J., & Foudoulis, C. (2003). TEMORA 1: a new zircon standard for Phanerozoic U–Pb geochronology. *Chemical geology*, *200*(1-2), 155-170.

Black, L. P., Kamo, S. L., Allen, C. M., Davis, D. W., Aleinikoff, J. N., Valley, J. W., ... & Foudoulis, C. (2004). Improved 206Pb/238U microprobe geochronology by the monitoring of a trace-element-

related matrix effect; SHRIMP, ID–TIMS, ELA–ICP–MS and oxygen isotope documentation for a series of zircon standards. *Chemical Geology*, *205*(1-2), 115-140.

Gao, S., Liu, X., Yuan, H., Hattendorf, B., Günther, D., Chen, L., & Hu, S. (2002). Determination of forty two major and trace elements in USGS and NIST SRM glasses by laser ablation inductively coupled plasma mass spectro-metry. *Geostandards Newsletter*, *26*(2), 181-196.

Jackson, S. E., Pearson, N. J., Griffin, W. L., & Belousova, E. A. (2004). The application of laser ablation-inductively coupled plasma-mass spectrometry to in situ U–Pb zircon geochronology. *Chemical Geology*, *211*(1-2), 47-69.

Jochum, K. P., Weis, U., Stoll, B., Kuzmin, D., Yang, Q., Raczek, I., ... & Günther, D. (2011). Determination of reference values for NIST SRM 610–617 glasses following ISO guidelines. *Geostandards and Geoanalytical Research*, *35*(4), 397-429.

Petrus, J. A., & Kamber, B. S. (2012). VizualAge: A novel approach to laser ablation ICP-MS U-Pb geochronology data reduction. *Geostandards and Geoanalytical Research*, *36*(3), 247-270.

Ludwig, K. R. (1999). Isoplot/Ex 2.01: a geochronological toolkit for Microsoft Excel. *Berkeley Geochronology Center, Berkeley, CA*.

Paton, C., Woodhead, J. D., Hellstrom, J. C., Hergt, J. M., Greig, A., & Maas, R. (2010). Improved laser ablation U-Pb zircon geochronology through robust downhole fractionation correction. *Geochemistry, Geophysics, Geosystems*, *11*(3).

Paton, C., Hellstrom, J., Paul, B., Woodhead, J., & Hergt, J. (2011). Iolite: Freeware for the visualisation and processing of mass spectrometric data. *Journal of Analytical Atomic Spectrometry*, *26*(12), 2508-2518.

Sláma, J., Košler, J., Condon, D. J., Crowley, J. L., Gerdes, A., Hanchar, J. M., ... & Schaltegger, U. (2008). Plešovice zircon—a new natural reference material for U–Pb and Hf isotopic microanalysis. *Chemical Geology*, *249*(1-2), 1-35.

Vermeesch, P. (2018). IsoplotR: a free and open toolbox for geochronology. Geoscience Frontiers, 9(5), 1479-1493.

Appendix 4.C: Measured U-Pb-Th geochronological data for the ten samples analysed in this study

					Isotopic ratios							Ages							
Spot analysis	Domain	U ppm	Th ppm	Pb ppm	207Pb/ 235U	2SE	206Pb/ 238U	2SE	Rho	207Pb/ 206Pb	2SE	207Pb/ 235U	2SE	206Pb/ 238U	2SE	207Pb/ 206Pb	2SE	Disc. %	Excl. from conc. calc.
Abbabis Complex granites and gneisses																			
K05-01	magmatic	160	181	1270	6.63	0.09	0.380	0.004	0.47	0.1268	0.0016	2063	13	2074	17	2057	13	-1	
K05-02	metamorphic	131	124	842	5.79	0.08	0.335	0.003	0.49	0.1256	0.0015	1942	12	1860	15	2036	11	9	
K05-03	magmatic	177	59	412	6.17	0.09	0.364	0.003	0.21	0.1231	0.0016	1997	12	1999	15	2002	15	0	
K05-04	magmatic	142	68	455	5.96	0.08	0.349	0.004	0.34	0.1241	0.0017	1968	12	1928	17	2017	16	4	
K05-05	magmatic	435	152	1024	5.87	0.08	0.348	0.003	0.37	0.1226	0.0015	1955	11	1922	13	1992	14	3	
K05-06	magmatic	309	60	427	6.64	0.15	0.384	0.004	0.31	0.1256	0.0026	2060	19	2092	19	2033	22	-3	
K05-07	metamorphic	395	60	555	7.15	0.14	0.375	0.004	0.36	0.1382	0.0026	2125	17	2050	18	2200	22	7	
K05-08	metamorphic	623	97	681	4.41	0.10	0.265	0.003	0.63	0.1205	0.0021	1710	18	1512	17	1959	20	23	
K05-09	resin	540	70	498	5.21	0.08	0.313	0.003	0.28	0.1206	0.0019	1852	13	1753	13	1963	16	11	X
K05-10	magmatic	70	142	872	2.65	0.06	0.200	0.003	0.72	0.0953	0.0015	1309	16	1176	14	1541	20	23	
K05-11	metamorphic	120	74	376	2.72	0.05	0.207	0.003	0.55	0.0952	0.0014	1330	13	1211	13	1535	17	21	
K05-12	metamorphic	75	79	619	5.80	0.14	0.334	0.006	0.72	0.1256	0.0020	1940	20	1857	28	2034	17	9	
K05-13	metamorphic	200	215	1195	2.63	0.20	0.177	0.009	0.97	0.1056	0.0028	1267	52	1044	50	1705	45	39	
K05-14	metamorphic	195	114	875	5.13	0.12	0.302	0.004	0.66	0.1220	0.0020	1835	19	1702	20	1986	19	14	
K05-15	metamorphic	149	50	421	6.01	0.11	0.349	0.004	0.48	0.1246	0.0020	1975	15	1930	19	2020	15	4	
K05-16	metamorphic	191	46	388	6.02	0.11	0.346	0.004	0.39	0.1258	0.0022	1975	16	1915	21	2040	18	6	
K05-17	metamorphic	121	59	196	1.30	0.02	0.133	0.001	0.32	0.0711	0.0011	847	9	804	7	956	20	15	
K05-18	metamorphic	200	34	178	2.78	0.14	0.200	0.008	0.97	0.0996	0.0016	1326	39	1169	45	1611	24	28	
K05-19	metamorphic	232	184	1370	6.69	0.10	0.373	0.004	0.50	0.1300	0.0017	2069	12	2044	18	2097	13	2	
K05-20	metamorphic	97	68	503	5.41	0.11	0.322	0.005	0.76	0.1217	0.0016	1883	17	1800	22	1980	15	9	
K05-21	magmatic	181	31	235	6.16	0.11	0.351	0.003	0.24	0.1274	0.0024	1995	17	1939	16	2057	19	6	
K05-22	magmatic	126	71	473	6.71	0.11	0.387	0.004	0.46	0.1258	0.0020	2070	15	2109	18	2043	16	-3	
K05-23	magmatic	132	133	842	6.61	0.09	0.380	0.004	0.51	0.1255	0.0015	2059	12	2074	20	2038	13	-2	
K05-24	magmatic	66	127	816	6.66	0.09	0.386	0.003	0.45	0.1251	0.0015	2068	11	2105	13	2034	13	-4	
K05-25	resin	102	124	592	3.31	0.05	0.226	0.002	0.49	0.1062	0.0014	1482	12	1311	9	1736	14	24	X
K05-26	metamorphic	91	24	122	1.74	0.21	0.142	0.011	0.98	0.0817	0.0039	954	71	850	59	1178	86	27	
K05-27	magmatic	81	44	264	6.29	0.14	0.374	0.004	0.38	0.1220	0.0023	2015	19	2048	20	1980	21	-4	
K05-28	metamorphic	131	62	186	1.63	0.05	0.151	0.002	0.78	0.0783	0.0016	981	16	907	9	1145	32	21	X
K05-29	metamorphic	113	46	284	6.05	0.18	0.348	0.006	0.59	0.1257	0.0031	1973	27	1928	27	2030	28	5	
K05-30	metamorphic	239	54	127	1.03	0.03	0.108	0.002	0.74	0.0688	0.0014	717	15	663	9	885	29	23	
K05-31	magmatic	186	66	369	5.96	0.09	0.353	0.003	0.36	0.1221	0.0016	1968	13	1948	16	1990	13	2	
K05-32	magmatic	153	77	454	6.07	0.10	0.359	0.004	0.63	0.1227	0.0014	1983	14	1977	19	1991	13	1	
K05-33	metamorphic	273	98	534	4.64	0.09	0.287	0.005	0.75	0.1169	0.0015	1752	16	1627	23	1909	11	15	
K05-34	metamorphic	135	239	1403	5.74	0.09	0.332	0.004	0.56	0.1252	0.0016	1935	13	1849	18	2032	13	9	
K05-35	magmatic	65	51	344	6.46	0.10	0.362	0.003	0.42	0.1296	0.0019	2040	14	1989	15	2093	16	5	
K05-36	magmatic	225	91	611	6.52	0.09	0.364	0.003	0.42	0.1297	0.0016	2047	12	2003	14	2098	12	4	
K05-37	magmatic	532	112	768	6.44	0.09	0.362	0.003	0.28	0.1292	0.0019	2037	12	1993	15	2086	14	4	
K05-38	metamorphic	319	131	828	5.51	0.07	v	0.003	0.30	0.1245	0.0016	1900	11	1797	13	2020	11	11	X
K05-39	resin	428	39	359	6.06	0.15	0.330	0.004	0.37	0.1338	0.0031	1984	22	1838	18	2149	26	14	X
K05-40	magmatic	360	112	756	5.76	0.10	0.336	0.003	0.38	0.1244	0.0020	1940	14	1867	16	2017	18	7	
R06-01	metamorphic	425	46	133	2.81	0.28	0.195	0.018	0.92	0.1045	0.0041	1888	20	1879	36	1898	16	35	
R06-02	metamorphic	1325	34	214	3.01	0.15	0.206	0.009	0.91	0.1057	0.0022	1153	20	1046	26	1359	21	33	

R06-07	metamorphic	364	47	119	2.04	0.11	0.167	0.008	0.91	0.0886	0.0020	1971	22	1942	40	2000	16	31	
R06-08	metamorphic	1435	22	253	1.77	0.09	0.155	0.007	0.92	0.0831	0.0017	1229	18	1103	24	1457	18	29	
R06-09	magmatic	515	57	162	4.14	0.31	0.251	0.017	0.93	0.1195	0.0033	1903	21	1875	37	1933	17	29	
R06-10	metamorphic	1437	35	208	1.59	0.11	0.145	0.009	0.89	0.0793	0.0026	1035	16	927	20	1271	19	28	
R06-11	magmatic	693	67	199	3.40	0.22	0.229	0.014	0.93	0.1077	0.0026	1812	24	1792	41	1834	18	27	
R06-12	metamorphic	1474	33	227	2.36	0.12	0.187	0.009	0.92	0.0915	0.0018	1129	19	995	23	1396	22	26	
R06-13	metamorphic	466	31	90	2.11	0.12	0.176	0.009	0.92	0.0869	0.0020	1410	19	1210	25	1727	18	25	
R06-14	magmatic	283	40	97	3.28	0.21	0.230	0.014	0.93	0.1035	0.0025	1999	23	2014	41	1983	18	23	
R06-15	metamorphic	586	35	136	1.76	0.12	0.159	0.010	0.90	0.0803	0.0023	1601	26	1482	40	1761	20	23	
R06-16	magmatic	1128	51	167	3.17	0.18	0.227	0.012	0.91	0.1012	0.0024	1359	37	1151	48	1705	34	22	
R06-17	magmatic	1514	40	194	3.84	0.25	0.258	0.016	0.94	0.1077	0.0023	966	22	875	25	1179	30	18	
R06-18	metamorphic	1397	59	292	4.33	0.27	0.278	0.016	0.91	0.1132	0.0029	1451	31	1375	46	1565	24	17	
R06-19	metamorphic	1295	65	268	4.07	0.24	0.271	0.014	0.91	0.1089	0.0027	1476	25	1333	36	1687	22	15	
R06-20	metamorphic	260	35	90	3.18	0.25	0.238	0.018	0.94	0.0969	0.0025	2015	25	2043	45	1986	19	13	
R06-21	metamorphic	603	56	127	5.65	0.35	0.332	0.019	0.91	0.1235	0.0032	1504	26	1328	36	1760	21	9	
R06-22	magmatic	1138	47	240	5.39	0.36	0.332	0.020	0.91	0.1178	0.0032	1451	22	1321	31	1647	22	5	
R06-25	metamorphic	547	11	139	5.62	0.33	0.340	0.018	0.90	0.1198	0.0030	1649	24	1548	37	1781	21	4	
R06-26	magmatic	340	42	108	5.51	0.27	0.338	0.015	0.92	0.1185	0.0023	1918	25	1886	44	1953	23	3	
R06-27	metamorphic	184	20	61	5.96	0.31	0.352	0.017	0.93	0.1230	0.0024	1998	26	1970	46	2027	23	3	
R06-28	magmatic	125	22	38	6.15	0.37	0.357	0.019	0.91	0.1249	0.0032	1924	27	1848	45	2008	22	3	
R06-29	magmatic	229	23	51	4.95	0.28	0.320	0.017	0.92	0.1121	0.0025	1662	31	1445	45	1949	24	3	
R06-30	metamorphic	475	47	121	5.95	0.37	0.353	0.020	0.91	0.1222	0.0032	1699	26	1579	39	1851	22	2	
R06-31	metamorphic	253	33	82	5.42	0.26	0.338	0.015	0.93	0.1162	0.0021	1968	27	1948	47	1989	22	1	
R06-32	metamorphic	460	54	160	6.16	0.32	0.367	0.017	0.92	0.1218	0.0025	2009	27	2068	50	1948	23	-2	
R06-33	metamorphic	330	21	102	6.28	0.35	0.373	0.019	0.91	0.1220	0.0028	1884	29	1847	49	1924	25	-3	X
R06-34	metamorphic	1690	20	242	6.23	0.39	0.378	0.021	0.91	0.1195	0.0031	1031	22	951	27	1203	28	-7	X
R06-35	metamorphic	953	12	304	5.28	0.35	0.347	0.021	0.91	0.1103	0.0030	1866	28	1922	50	1804	23	-8	X
PA02-01	metamorphic	126	97	712	6.42	0.11	0.368	0.004	0.26	0.3678	0.0021	2031	15	2018	20	2049	21	1	
PA02-02	magmatic	42	30	253	6.79	0.24	0.394	0.009	0.44	0.3941	0.0043	2079	33	2139	39	2035	32	-6	
PA02-03	magmatic	116	67	497	5.22	0.13	0.315	0.005	0.59	0.3149	0.0027	1852	20	1763	26	1965	19	11	
PA02-04	metamorphic	755	148	895	2.78	0.08	0.207	0.003	0.72	0.2070	0.0014	1343	21	1212	14	1548	35	21	
PA02-05	metamorphic	130	87	573	5.20	0.11	0.308	0.004	0.23	0.3083	0.0018	1847	18	1732	17	1979	21	12	
PA02-06	metamorphic	156	40	280	2.74	0.11	0.192	0.006	0.76	0.1922	0.0029	1328	29	1131	31	1673	28	32	
PA02-07	resin	233	39	313	3.24	0.27	0.212	0.013	0.97	0.2120	0.0065	1393	76	1228	69	1688	67	26	X
PA02-08	magmatic	206	95	661	5.42	0.11	0.327	0.004	0.60	0.3272	0.0019	1883	17	1824	18	1945	20	6	
PA02-09	resin	217	207	1302	6.25	0.09	0.364	0.003	0.30	0.3636	0.0016	2009	12	1999	15	2017	13	1	X
PA02-10	mixed domain	116	99	640	6.10	0.14	0.351	0.004	0.35	0.3510	0.0020	1984	20	1941	19	2030	22	4	X
PA02-11	resin	232	52	369	3.40	0.14	0.233	0.007	0.86	0.2334	0.0035	1488	33	1349	37	1705	25	22	X
PA02-12	magmatic	110	44	311	6.46	0.11	0.379	0.004	0.37	0.3788	0.0021	2040	16	2070	19	2019	17	-3	
PA02-13	resin	388	129	711	2.94	0.07	0.224	0.004	0.68	0.2241	0.0018	1390	17	1303	19	1527	17	14	X
PA02-14	mixed domain	607	240	1310	3.81	0.08	0.262	0.005	0.78	0.2620	0.0023	1590	17	1499	24	1720	17	13	X
PA02-15	magmatic	142	91	602	6.17	0.12	0.363	0.004	0.36	0.3625	0.0022	1998	18	1993	20	2001	21	0	
PA02-16	metamorphic	128	44	333	5.78	0.18	0.350	0.008	0.79	0.3504	0.0042	1935	27	1933	40	1945	20	0	
PA02-17	magmatic	97	67	464	5.81	0.15	0.339	0.004	0.34	0.3386	0.0022	1941	22	1879	21	2015	22	6	
PA02-18	metamorphic	210	13	109	1.56	0.07	0.147	0.003	0.61	0.1468	0.0016	950	25	882	18	1079	58	12	
PA02-19	resin	193	203	1395	6.78	0.10	0.389	0.004	0.54	0.3889	0.0018	2082	14	2117	16	2049	13	-4	X
PA02-20	resin	237	177	1177	6.57	0.09	0.379	0.004	0.29	0.3792	0.0018	2053	12	2072	17	2034	14	-2	X
PA02-21	resin	246	73	546	5.97	0.10	0.357	0.004	0.52	0.3565	0.0020	1969	14	1967	18	1979	14	1	X
PA02-22	magmatic	267	106	642	5.81	0.17	0.349	0.007	0.79	0.3494	0.0033	1940	24	1929	31	1953	19	1	
PA02-23	metamorphic	300	173	970	5.32	0.16	0.313	0.007	0.86	0.3133	0.0035	1862	26	1754	34	1991	18	12	
PA02-24	mixed domain	77	52	320	6.92	0.20	0.394	0.006	0.58	0.3940	0.0030	2092	25	2140	27	2059	26	-5	X

PA02-25	metamorphic	342	103	500	3.29	0.11	0.230	0.005	0.83	0.2299	0.0024	1468	25	1333	25	1674	28	20	
PA02-26	mixed domain	81	87	528	7.21	0.17	0.411	0.005	0.27	0.4105	0.0027	2131	21	2216	24	2065	21	-8	X
PA02-27	mixed domain	158	134	735	5.72	0.14	0.344	0.006	0.68	0.3439	0.0029	1928	21	1904	27	1966	17	3	X
PA02-28	metamorphic	78	31	224	6.09	0.14	0.374	0.006	0.44	0.3737	0.0031	1984	20	2049	29	1930	26	-6	
PA02-29	resin	75	66	481	7.16	0.19	0.401	0.006	0.15	0.4013	0.0032	2127	24	2173	29	2100	30	-5	X
PA02-30	magmatic	184	86	648	6.63	0.12	0.386	0.005	0.43	0.3858	0.0024	2063	16	2102	22	2024	17	-4	
PA02-31	metamorphic	95	79	600	6.62	0.15	0.383	0.006	0.37	0.3829	0.0028	2059	21	2088	26	2036	18	-3	
PA02-32	magmatic	113	84	707	5.98	0.18	0.352	0.008	0.72	0.3517	0.0039	1963	27	1939	38	2001	20	3	
PA02-33	metamorphic	162	18	167	2.20	0.07	0.167	0.004	0.61	0.1668	0.0019	1178	23	993	21	1550	28	36	
PA02-34	metamorphic	462	39	194	1.76	0.07	0.157	0.005	0.86	0.1568	0.0025	1022	26	937	28	1233	22	23	
PA02-35	metamorphic	75	4	64	2.42	0.14	0.194	0.006	0.74	0.1936	0.0032	1238	49	1138	35	1470	55	16	
PA02-36	resin	140	91	774	6.57	0.11	0.370	0.004	0.17	0.3697	0.0019	2053	14	2027	17	2088	20	3	X
PA02-37	magmatic	167	72	610	5.52	0.14	0.326	0.006	0.81	0.3260	0.0032	1900	22	1822	29	1994	22	10	
PA02-38	metamorphic	243	39	322	4.79	0.11	0.294	0.005	0.71	0.2936	0.0023	1778	19	1662	23	1926	18	14	
PA02-39	resin	211	72	476	3.30	0.09	0.218	0.003	0.38	0.2178	0.0015	1476	20	1270	15	1800	25	29	X
PA02-40	resin	114	118	703	6.10	0.15	0.342	0.005	0.49	0.3422	0.0025	1984	21	1896	24	2087	21	9	X
PA02-41	metamorphic	305	89	494	3.90	0.19	0.237	0.009	0.93	0.2374	0.0045	1588	41	1368	46	1916	26	29	
PA02-42	magmatic	421	111	621	2.96	0.07	0.208	0.003	0.63	0.2083	0.0016	1391	19	1219	17	1676	23	27	
PA02-43	metamorphic	469	447	2200	5.55	0.08	0.329	0.004	0.75	0.3294	0.0020	1909	12	1834	20	1975	11	7	
PA02-44	metamorphic	212	39	239	2.45	0.16	0.172	0.006	0.88	0.1718	0.0032	1227	45	1019	35	1602	55	36	
PA02-45	resin	472	439	2111	6.05	0.08	0.352	0.004	0.60	0.3517	0.0019	1981	12	1942	18	2006	12	3	X
PA02-46	resin	333	159	700	4.29	0.07	0.265	0.003	0.62	0.2650	0.0017	1689	14	1515	17	1895	16	20	X
Amphibolite dykes																			
7.3-01	metamorphic	37	40	129	1.40	0.04	0.082	19.800	0.02	0.1263	0.0073	874	33	505	10	2027	61	75	X
7.3-02	resin	47	68	164	1.11	0.00	0.078	34.100	0.07	0.1056	0.0053	754	25	482	9	1697	58	71	X
7.3-03	resin	59	89	204	1.05	0.01	0.077	44.500	0.00	0.1000	0.0050	717	25	477	8	1617	60	69	X
7.3-04	resin	390	156	425	0.80	0.00	0.098	77.850	0.45	0.0597	0.0013	596	11	602	8	588	25	-6	X
7.3-05	magmatic	1095	1162	2410	0.73	0.01	0.090	581.000	0.30	0.0593	0.0007	559	5	556	4	577	15	2	
7.3-06	metamorphic	37	50	116	1.24	0.04	0.077	25.050	0.17	0.1166	0.0077	799	37	478	11	1881	67	74	X
7.3-07	metamorphic	47	67	151	1.06	0.01	0.073	33.300	0.16	0.1062	0.0067	720	32	452	11	1731	65	73	X
7.3-08	magmatic	460	350	520	0.69	0.01	0.085	175.000	0.56	0.0592	0.0013	533	11	528	8	567	28	1	
7.3-09	metamorphic	928	659	1239	0.75	0.00	0.090	329.500	0.49	0.0604	0.0008	568	7	554	5	613	16	8	
7.3-10	magmatic	919	840	1522	0.68	0.01	0.085	420.000	0.22	0.0587	0.0008	529	5	523	4	549	18	2	
7.3-11	metamorphic	831	575	1150	0.70	0.01	0.088	287.500	0.43	0.0580	0.0009	540	7	543	5	530	19	-6	
7.3-12	resin	1079	1072	1900	0.68	0.03	0.083	536.000	0.35	0.0596	0.0007	528	5	514	3	591	15	11	X
7.3-13	metamorphic	673	493	940	0.73	0.01	0.090	246.500	0.25	0.0587	0.0010	556	7	557	4	558	18	-4	
7.3-14	magmatic	62	124	469	1.92	0.01	0.179	62.050	0.20	0.0779	0.0029	1078	26	1063	12	1133	42	3	X
7.3-15	magmatic	771	855	1670	0.73	0.01	0.092	427.500	0.32	0.0580	0.0009	557	6	566	5	529	18	-10	
7.3-16	magmatic	505	103	227	0.73	0.01	0.090	51.500	0.45	0.0591	0.0011	557	9	556	6	566	21	-2	
7.3-17	metamorphic	789	576	1051	0.68	0.01	0.085	288.000	0.16	0.0586	0.0008	529	6	525	3	550	18	2	
7.3-18	metamorphic	639	607	1148	0.70	0.01	0.087	303.500	0.19	0.0590	0.0009	541	6	538	4	564	19	1	
7.3-19	metamorphic	879	911	1658	0.69	0.01	0.085	455.500	0.24	0.0592	0.0009	534	6	526	4	573	19	6	
7.3-20	magmatic	664	391	684	0.70	0.07	0.086	195.500	0.27	0.0591	0.0010	541	8	535	4	567	22	2	
7.3-21	metamorphic	944	1080	1698	0.71	0.04	0.089	540.000	0.69	0.0581	0.0009	543	9	547	9	535	20	-5	
7.3-22	metamorphic	483	317	626	0.72	0.01	0.090	158.650	0.22	0.0578	0.0012	547	8	553	5	517	25	-14	X
7.3-23	metamorphic	1046	1061	1961	0.72	0.03	0.089	530.500	0.43	0.0585	0.0008	549	6	549	5	547	16	-2	
7.3-24	metamorphic	1060	981	1847	0.70	0.01	0.088	490.500	0.27	0.0579	0.0009	540	6	545	4	523	19	-8	
7.3-25	metamorphic	922	821	1524	0.70	0.01	0.087	410.500	0.22	0.0582	0.0010	537	7	538	4	534	19	-3	
7.3-26	magmatic	395	56	114	0.68	0.01	0.086	28.000	0.18	0.0577	0.0013	528	10	531	4	510	30	-14	X
7.3-27	metamorphic	26	25	89	1.96	0.01	0.082	12.630	0.16	0.1760	0.0120	1079	47	505	14	2576	75	80	X
7.3-28	metamorphic	42	47	129	1.25	0.02	0.076	23.260	-0.06	0.1200	0.0083	807	37	473	10	1948	69	75	X

7.3-29	magmatic	670	590	1235	0.72	0.04	0.089	295.000	0.19	0.0588	0.0010	551	8	549	4	568	21	-1	
7.3-30	magmatic	657	384	772	0.72	0.01	0.088	192.000	0.18	0.0592	0.0011	549	8	543	4	569	23	1	
7.3-31	metamorphic	693	100	225	0.71	0.00	0.088	49.900	0.16	0.0589	0.0012	544	8	541	4	558	27	-2	
7.3-32	metamorphic	911	741	1388	0.68	0.04	0.084	370.500	0.16	0.0586	0.0010	524	7	520	4	552	20	3	
7.3-33	magmatic	900	867	1740	0.72	0.03	0.089	433.500	0.39	0.0588	0.0009	550	7	548	4	565	22	0	
7.3-34	resin	65	95	187	1.04	0.01	0.072	47.400	-0.06	0.1038	0.0049	719	22	450	8	1694	58	72	X
7.3-35	metamorphic	42	63	156	1.37	0.01	0.077	31.500	-0.04	0.1308	0.0078	865	32	479	11	2087	65	76	X
R02-01	metamorphic	1080	885	89	0.72	0.02	0.091	0.003	0.92	0.0575	0.0007	1329	30	463	16	3264	33	-10	
R02-02	metamorphic	1363	866	109	0.70	0.02	0.088	0.002	0.87	0.0574	0.0007	589	14	551	12	739	42	-8	
R02-04	magmatic	2966	596	212	0.62	0.03	0.080	0.003	0.95	0.0561	0.0008	535	9	523	10	589	18	-8	
R02-05	magmatic	599	957	49	0.76	0.05	0.089	0.005	0.84	0.0624	0.0023	1872	30	664	15	3730	37	21	
R02-06	resin	53	2	4	2.49	0.17	0.075	0.003	0.56	0.2422	0.0140	536	5	543	6	506	13	88	X
R02-07	resin	126	19	8	1.62	0.07	0.073	0.002	0.60	0.1609	0.0053	842	20	416	6	2231	51	84	X
R02-08	mixed domain	8	1	1	16.70	0.45	0.193	0.004	0.85	0.6283	0.0091	2249	19	818	15	4044	14	81	X
R02-09	mixed domain	173	28	11	1.29	0.09	0.067	0.002	0.45	0.1403	0.0086	1607	61	608	28	3384	86	84	X
R02-10	resin	46	7	4	3.87	0.58	0.099	0.009	0.64	0.2837	0.0330	1270	25	464	9	3135	43	86	X
R02-11	resin	15	2	2	8.16	0.35	0.135	0.005	0.89	0.4378	0.0085	2918	13	1137	12	4575	10	85	X
R02-12	metamorphic	809	444	65	0.69	0.02	0.086	0.003	0.89	0.0579	0.0009	616	15	505	10	1047	46	-1	
R02-14	metamorphic	718	454	61	0.74	0.03	0.092	0.003	0.90	0.0585	0.0010	545	9	491	9	777	20	-3	
R02-17	magmatic	710	292	57	0.70	0.02	0.086	0.003	0.87	0.0593	0.0010	730	49	530	10	1408	166	9	
R02-18	metamorphic	416	500	31	0.65	0.02	0.079	0.002	0.85	0.0598	0.0011	-2040	-504	232	12	-7128	699	19	
R02-19	magmatic	269	249	20	0.66	0.02	0.079	0.002	0.83	0.0604	0.0012	2902	19	1144	19	4541	11	22	
R02-21	mixed domain	7	0	1	16.43	0.64	0.194	0.007	0.91	0.6139	0.0100	532	7	533	8	527	17	81	X
R02-25	magmatic	603	114	53	1.45	0.10	0.093	0.004	0.56	0.1135	0.0068	1797	15	611	8	3729	15	72	X
R02-26	mixed domain	17	1	2	6.15	0.27	0.110	0.004	0.87	0.4043	0.0088	605	20	495	7	1039	80	87	X
R02-27	magmatic	530	162	44	0.70	0.03	0.086	0.003	0.93	0.0586	0.0009	1998	19	675	12	3925	16	4	
R02-28	metamorphic	1178	76	83	0.61	0.03	0.075	0.003	0.91	0.0589	0.0010	1572	36	584	14	3380	56	18	
R02-29	magmatic	1170	231	91	0.83	0.05	0.081	0.003	0.67	0.0742	0.0035	1712	18	581	10	3654	20	54	X
R02-30	resin	370	84	28	0.71	0.03	0.079	0.003	0.90	0.0651	0.0012	538	7	529	8	577	18	38	X
R02-31	magmatic	866	139	73	0.79	0.05	0.089	0.004	0.75	0.0639	0.0026	228	30	307	6	-444	291	27	
R02-33	resin	24	1	2	2.70	0.22	0.075	0.005	0.86	0.2629	0.0111	551	7	561	8	510	13	89	X
R02-34	metamorphic	1649	143	140	0.74	0.03	0.091	0.004	0.87	0.0594	0.0014	909	22	571	11	1855	54	4	
R02-35	metamorphic	715	171	60	0.72	0.03	0.089	0.004	0.91	0.0585	0.0011	482	8	465	9	564	18	0	
Etusis Formation																			
1.1-01	magmatic	66	80	290	1.91	0.07	0.184	0.003	0.10	0.0753	0.0027	1078	24	1089	15	1062	47	-9	
1.1-02	magmatic	1115	399	1395	1.74	0.02	0.173	0.001	0.54	0.0730	0.0007	1023	6	1028	8	1014	10	-2	
1.1-03	metamorphic	406	139	835	6.25	0.10	0.365	0.005	0.85	0.1233	0.0010	2010	14	2008	23	2007	9	0	
1.1-04	metamorphic	54	41	271	5.66	0.11	0.343	0.006	0.66	0.1201	0.0019	1920	17	1901	29	1954	16	3	
1.1-05	magmatic	218	151	492	1.60	0.03	0.159	0.002	0.33	0.0727	0.0013	967	12	949	9	1009	22	6	
1.1-06	metamorphic	89	77	522	5.09	0.10	0.310	0.004	0.46	0.1188	0.0022	1830	17	1742	22	1934	21	10	
1.1-07	metamorphic	135	31	213	5.28	0.10	0.310	0.004	0.55	0.1228	0.0018	1862	16	1741	18	1997	17	13	X
1.1-08	resin	128	56	428	2.87	0.10	0.198	0.004	0.78	0.1053	0.0022	1367	25	1160	23	1709	26	32	X
1.1-09	magmatic	1524	1986	3330	1.18	0.02	0.109	0.002	0.86	0.0783	0.0008	787	11	665	13	1154	13	42	X
1.1-10	magmatic	64	109	373	1.78	0.06	0.175	0.003	0.01	0.0741	0.0029	1033	23	1038	13	1023	45	-8	
1.1-11	metamorphic	160	134	315	1.72	0.04	0.173	0.002	0.27	0.0720	0.0015	1013	13	1029	10	978	25	-8	
1.1-12	magmatic	251	154	506	1.71	0.04	0.172	0.002	0.50	0.0717	0.0013	1009	13	1024	9	974	20	-6	
1.1-13	metamorphic	129	127	421	1.57	0.05	0.159	0.003	0.26	0.0716	0.0022	957	19	955	14	968	37	-5	
1.1-14	magmatic	96	146	502	1.70	0.05	0.168	0.002	0.20	0.0732	0.0023	1001	20	1003	13	1004	36	-3	
1.1-15	magmatic	560	255	717	1.73	0.02	0.173	0.002	0.51	0.0728	0.0008	1020	8	1027	8	1007	13	-3	
1.1-16	metamorphic	291	182	606	1.74	0.03	0.172	0.002	0.44	0.0731	0.0011	1020	11	1024	8	1011	18	-2	
1.1-17	metamorphic	287	288	996	1.78	0.04	0.175	0.002	0.35	0.0738	0.0016	1035	15	1038	10	1029	26	-2	

1.1-18	magmatic	170	93	344	1.79	0.05	0.175	0.002	0.40	0.0738	0.0016	1038	16	1038	11	1037	23	-2	
1.1-19	magmatic	388	179	635	1.72	0.03	0.171	0.001	0.29	0.0730	0.0011	1015	10	1017	7	1011	18	-2	
1.1-20	metamorphic	351	172	592	1.73	0.03	0.171	0.002	0.42	0.0733	0.0012	1018	11	1018	10	1018	19	-1	
1.1-21	magmatic	424	349	1210	1.73	0.02	0.172	0.001	0.54	0.0730	0.0008	1018	8	1021	8	1014	12	-1	
1.1-22	magmatic	35	54	191	1.87	0.09	0.184	0.003	0.20	0.0740	0.0035	1059	30	1088	17	1025	56	-13	X
1.1-23	metamorphic	447	168	579	1.71	0.03	0.170	0.001	0.33	0.0730	0.0011	1011	10	1011	8	1011	17	-1	
1.1-24	magmatic	496	247	776	1.83	0.03	0.178	0.002	0.45	0.0744	0.0010	1053	9	1054	9	1052	15	-1	
1.1-25	metamorphic	487	148	533	1.72	0.02	0.171	0.001	0.29	0.0730	0.0010	1015	9	1016	8	1012	18	-1	
1.1-26	metamorphic	812	1094	3460	1.76	0.02	0.174	0.002	0.53	0.0736	0.0008	1031	8	1033	8	1029	14	-1	
1.1-27	magmatic	229	263	918	1.73	0.03	0.171	0.002	0.17	0.0734	0.0014	1017	12	1015	9	1014	21	-1	
1.1-28	metamorphic	96	51	398	6.34	0.16	0.370	0.007	0.77	0.1244	0.0019	2015	23	2025	33	2022	16	-1	
1.1-29	metamorphic	99	75	506	6.49	0.09	0.374	0.004	0.38	0.1257	0.0018	2042	13	2048	17	2040	16	0	
1.1-30	metamorphic	122	174	548	1.76	0.05	0.171	0.002	0.28	0.0743	0.0018	1025	17	1017	11	1045	26	0	
1.1-31	magmatic	1106	473	1513	1.73	0.02	0.171	0.002	0.67	0.0733	0.0006	1017	7	1015	8	1020	9	0	
1.1-32	metamorphic	425	441	992	1.75	0.03	0.172	0.002	0.39	0.0737	0.0010	1027	9	1025	9	1035	14	1	
1.1-33	metamorphic	285	96	340	1.69	0.03	0.168	0.001	0.47	0.0733	0.0011	1005	11	1003	8	1016	16	1	
1.1-34	metamorphic	306	132	424	1.69	0.03	0.167	0.002	0.46	0.0733	0.0011	1002	10	994	8	1017	19	1	
1.1-35	metamorphic	281	420	1125	1.73	0.03	0.169	0.002	0.42	0.0739	0.0013	1015	12	1006	10	1033	21	2	
1.1-36	metamorphic	277	154	538	1.73	0.03	0.169	0.002	0.24	0.0740	0.0013	1019	11	1008	8	1038	20	2	
1.1-37	magmatic	394	279	893	1.75	0.03	0.170	0.002	0.49	0.0740	0.0009	1024	9	1014	8	1043	18	2	
1.1-38	magmatic	112	362	1208	1.64	0.05	0.162	0.002	0.17	0.0737	0.0023	985	18	965	11	1022	34	3	
1.1-39	metamorphic	427	186	597	1.68	0.03	0.166	0.001	0.41	0.0735	0.0011	1001	9	989	8	1024	17	3	
1.1-40	metamorphic	332	250	717	1.60	0.03	0.160	0.002	0.57	0.0727	0.0011	970	11	956	11	1000	16	3	
1.1-41	metamorphic	400	39	154	1.76	0.02	0.171	0.002	0.46	0.0748	0.0009	1030	9	1016	9	1062	14	4	
1.1-42	metamorphic	592	204	669	1.67	0.02	0.164	0.001	0.33	0.0736	0.0010	996	8	980	8	1026	13	4	
1.1-43	metamorphic	252	67	470	6.00	0.08	0.350	0.003	0.60	0.1241	0.0013	1974	11	1934	16	2016	11	4	
1.1-44	magmatic	261	217	593	1.47	0.03	0.150	0.002	0.42	0.0711	0.0013	916	12	901	10	956	22	4	
1.1-45	metamorphic	297	182	732	1.83	0.03	0.174	0.002	0.33	0.0760	0.0013	1054	12	1034	9	1095	20	4	
1.1-46	magmatic	321	109	757	5.88	0.06	0.344	0.003	0.53	0.1234	0.0011	1957	9	1906	13	2008	9	5	
1.1-47	metamorphic	1325	290	1640	1.76	0.02	0.170	0.002	0.66	0.0750	0.0006	1030	8	1010	9	1068	10	5	
1.1-48	metamorphic	320	71	233	1.57	0.03	0.157	0.001	0.53	0.0725	0.0010	956	10	939	8	998	16	5	
1.1-49	metamorphic	235	149	448	1.56	0.04	0.155	0.002	0.43	0.0728	0.0016	949	15	928	11	999	27	5	
1.1-50	metamorphic	519	406	1341	1.57	0.02	0.156	0.001	0.32	0.0726	0.0010	957	9	937	8	1002	17	6	
1.1-51	magmatic	148	141	895	5.98	0.10	0.345	0.004	0.69	0.1253	0.0015	1971	15	1908	19	2033	13	6	
1.1-52	magmatic	148	83	572	5.61	0.09	0.333	0.004	0.42	0.1218	0.0019	1916	14	1854	20	1984	15	6	
1.1-53	metamorphic	153	316	1018	1.69	0.04	0.163	0.002	0.16	0.0750	0.0018	1003	15	975	10	1061	29	6	
1.1-54	magmatic	553	252	758	1.61	0.03	0.159	0.002	0.70	0.0734	0.0009	974	11	953	10	1026	14	7	
1.1-55	magmatic	524	614	512	1.61	0.03	0.158	0.001	0.52	0.0735	0.0011	972	10	947	8	1032	15	8	
1.1-56	metamorphic	352	251	926	5.69	0.15	0.331	0.007	0.92	0.1243	0.0012	1921	24	1841	35	2017	12	8	
1.1-57	metamorphic	1368	301	1513	1.89	0.03	0.175	0.002	0.82	0.0778	0.0007	1075	11	1041	12	1141	13	9	
1.1-58	mixed	143	120	389	1.43	0.04	0.144	0.002	0.32	0.0720	0.0018	896	15	867	12	978	28	9	X
1.1-59	metamorphic	133	87	608	5.67	0.09	0.329	0.004	0.51	0.1244	0.0019	1924	14	1831	18	2018	15	9	
1.1-60	metamorphic	150	143	493	1.52	0.05	0.150	0.004	0.70	0.0733	0.0017	931	20	900	20	1015	25	10	
1.1-61	magmatic	297	106	335	1.97	0.07	0.176	0.003	0.85	0.0799	0.0016	1095	23	1046	17	1190	33	11	X
1.1-62	magmatic	216	120	758	5.15	0.08	0.309	0.003	0.63	0.1205	0.0015	1841	14	1737	16	1963	13	11	X
1.1-63	resin	242	38	290	5.24	0.08	0.312	0.003	0.56	0.1214	0.0014	1856	12	1752	15	1978	12	11	X
1.1-64	metamorphic	349	30	90	4.56	0.06	0.290	0.003	0.64	0.1140	0.0011	1739	10	1642	15	1863	10	12	X
1.1-65	resin	189	117	185	1.59	0.03	0.154	0.002	0.38	0.0746	0.0012	964	11	923	9	1059	19	12	X
1.1-66	resin	1032	1259	3610	1.58	0.02	0.154	0.002	0.72	0.0744	0.0006	961	7	921	8	1049	10	12	X
1.1-67	metamorphic	1054	471	1309	1.44	0.02	0.144	0.002	0.62	0.0725	0.0009	905	9	868	10	993	14	12	X
1.1-68	metamorphic	117	63	211	1.13	0.05	0.118	0.003	0.56	0.0695	0.0023	761	22	721	16	889	46	12	X

1.1-69	metamorphic	511	131	839	4.87	0.05	0.300	0.003	0.70	0.1183	0.0009	1797	8	1689	13	1932	8	12	X
1.1-70	metamorphic	330	127	464	4.77	0.05	0.294	0.003	0.57	0.1172	0.0011	1777	10	1663	13	1919	10	13	X
1.1-71	metamorphic	355	159	732	3.28	0.06	0.240	0.003	0.79	0.0987	0.0011	1473	15	1386	16	1598	13	13	X
1.1-72	crack	604	181	621	2.03	0.03	0.179	0.002	0.58	0.0821	0.0009	1125	9	1063	8	1246	15	14	X
1.1-73	magmatic	216	61	356	3.80	0.07	0.256	0.003	0.64	0.1076	0.0016	1591	15	1470	14	1758	17	16	X
1.1-74	resin	87	95	538	5.05	0.10	0.296	0.004	0.37	0.1238	0.0023	1826	17	1671	18	2008	20	16	X
1.1-75	magmatic	121	120	275	1.34	0.04	0.135	0.002	0.36	0.0734	0.0024	859	18	814	11	1008	41	17	X
1.1-76	metamorphic	530	236	1098	2.24	0.03	0.183	0.002	0.59	0.0884	0.0010	1192	10	1083	9	1389	14	22	X
1.1-77	resin	146	85	289	1.11	0.03	0.123	0.001	0.27	0.0726	0.0016	756	12	748	8	1000	27	24	X
1.1-78	metamorphic	227	41	291	3.45	0.29	0.223	0.015	0.98	0.1064	0.0030	1436	73	1284	78	1718	51	27	X
PA01-01	resin	323	134	1157	4.57	0.12	0.289	0.005	0.91	0.1150	0.0015	1743	22	1636	25	1879	19	13	X
PA01-02	resin	469	24	225	3.35	0.06	0.245	0.003	0.83	0.0996	0.0010	1489	14	1411	18	1615	11	13	X
PA01-03	resin	65	29	268	4.40	0.12	0.278	0.005	0.46	0.1154	0.0030	1708	23	1579	23	1878	29	15	X
PA01-04	metamorphic	167	42	372	4.98	0.13	0.308	0.005	0.81	0.1176	0.0018	1809	22	1727	27	1917	17	10	
PA01-05	magmatic	208	60	505	4.65	0.07	0.296	0.003	0.58	0.1142	0.0013	1756	12	1673	14	1867	11	10	
PA01-06	metamorphic	227	35	307	2.97	0.05	0.217	0.002	0.69	0.0994	0.0015	1397	13	1266	10	1607	17	21	X
PA01-07	magmatic	211	121	1079	6.71	0.08	0.383	0.003	0.59	0.1268	0.0013	2073	10	2092	14	2052	11	-2	
PA01-08	magmatic	213	56	504	5.77	0.07	0.346	0.003	0.34	0.1217	0.0015	1941	11	1915	13	1979	12	3	
PA01-09	magmatic	152	64	480	6.22	0.09	0.358	0.003	0.54	0.1252	0.0015	2005	12	1974	16	2026	14	2	
PA01-10	magmatic	99	110	1054	6.60	0.10	0.385	0.004	0.40	0.1250	0.0018	2056	14	2100	16	2025	13	-4	
PA01-11	magmatic	425	34	234	2.21	0.06	0.185	0.003	0.72	0.0858	0.0015	1179	19	1095	16	1335	24	18	X
PA01-12	magmatic	309	84	726	3.43	0.08	0.240	0.004	0.84	0.1042	0.0013	1506	18	1383	20	1698	14	19	X
PA01-13	resin	354	6	29	0.76	0.02	0.095	0.001	0.12	0.0580	0.0014	573	10	587	6	521	31	-22	X
PA01-14	crack	263	9	90	2.40	0.06	0.197	0.003	0.71	0.0882	0.0016	1239	19	1160	15	1384	27	16	X
PA01-15	crack	242	87	703	4.24	0.05	0.273	0.002	0.24	0.1121	0.0015	1681	10	1558	11	1831	15	15	X
PA01-16	magmatic	209	94	825	6.22	0.10	0.374	0.004	0.55	0.1206	0.0016	2004	15	2049	18	1962	13	-5	
PA01-17	resin	527	79	586	2.27	0.07	0.188	0.003	0.83	0.0871	0.0015	1197	20	1109	16	1356	25	18	X
PA01-18	metamorphic	486	40	286	2.24	0.05	0.182	0.003	0.76	0.0889	0.0012	1190	14	1074	16	1398	17	23	X
PA01-19	metamorphic	206	114	912	5.43	0.13	0.331	0.006	0.85	0.1181	0.0015	1883	21	1842	30	1925	15	4	
PA01-20	magmatic	85	30	292	5.53	0.16	0.347	0.006	0.30	0.1153	0.0033	1897	25	1918	27	1873	28	-3	
PA01-21	metamorphic	183	78	628	6.41	0.09	0.371	0.003	0.25	0.1246	0.0017	2032	12	2034	13	2021	13	-1	
PA01-22	magmatic	158	75	676	6.09	0.11	0.357	0.005	0.67	0.1237	0.0017	1985	16	1966	24	2011	13	2	
PA01-23	resin	456	128	625	2.15	0.04	0.174	0.003	0.66	0.0893	0.0013	1161	13	1032	14	1407	17	27	X
PA01-24	magmatic	195	66	565	6.70	0.08	0.388	0.003	0.31	0.1247	0.0016	2070	11	2112	15	2024	12	-5	
PA01-25	resin	305	19	159	1.99	0.04	0.166	0.002	0.40	0.0869	0.0017	1108	14	991	10	1354	21	26	X
PA01-26	mixed	175	18	158	2.91	0.08	0.216	0.004	0.71	0.0973	0.0018	1379	20	1259	19	1569	20	19	X
Red granite																			
K06-01	metamorphic	641	74	178	0.68	0.01	0.084	0.001	0.28	0.0583	0.0008	526	6	521	4	539	19	2	
K06-02	magmatic	540	599	1474	0.69	0.01	0.086	0.001	0.40	0.0583	0.0010	534	8	534	4	531	24	-6	
K06-03	resin	575	231	522	0.68	0.01	0.086	0.001	0.42	0.0576	0.0011	527	8	530	5	510	23	-9	X
K06-04	metamorphic	459	369	1038	0.91	0.03	0.088	0.001	0.23	0.0748	0.0020	652	13	541	4	1042	47	45	X
K06-05	metamorphic	275	201	870	1.39	0.04	0.145	0.003	0.64	0.0700	0.0014	883	15	870	15	923	23	4	X
K06-06	metamorphic	669	81	539	0.90	0.02	0.090	0.001	0.67	0.0731	0.0015	652	12	553	5	1013	29	45	X
K06-07	magmatic	403	212	422	0.72	0.02	0.088	0.001	0.46	0.0600	0.0015	552	12	547	6	601	30	2	
K06-08	metamorphic	428	297	596	0.73	0.02	0.089	0.001	0.45	0.0602	0.0014	556	12	548	7	611	33	5	
K06-09	metamorphic	439	224	428	0.72	0.02	0.091	0.001	0.22	0.0579	0.0016	547	12	558	7	526	40	-31	
K06-10	metamorphic	480	99	212	0.70	0.02	0.088	0.001	0.24	0.0587	0.0013	538	9	543	5	551	25	-6	
K06-11	metamorphic	284	266	488	0.73	0.02	0.091	0.001	0.13	0.0591	0.0019	552	14	558	6	565	40	-15	
K06-12	magmatic	252	188	486	0.69	0.02	0.089	0.001	0.10	0.0576	0.0017	532	12	549	7	508	35	-28	
K06-13	metamorphic	2760	103	219	0.37	0.01	0.049	0.000	0.45	0.0562	0.0008	322	4	310	3	456	18	28	X
K06-14	metamorphic	3320	200	272	0.32	0.01	0.042	0.001	0.80	0.0559	0.0008	279	6	265	4	449	20	38	X

K06-15	metamorphic	464	266	385	0.70	0.02	0.087	0.001	0.19	0.0590	0.0015	536	11	540	5	567	30	-3	
K06-16	metamorphic	2520	320	553	0.67	0.01	0.084	0.001	0.75	0.0584	0.0007	518	8	521	8	544	16	3	
K06-17	magmatic	293	197	325	0.74	0.03	0.089	0.001	0.31	0.0606	0.0020	557	15	550	7	607	42	-8	
K06-18	magmatic	823	720	1380	0.70	0.02	0.088	0.001	0.26	0.0580	0.0013	534	10	543	5	529	27	-8	
K06-19	magmatic	322	229	362	0.73	0.03	0.091	0.001	0.20	0.0593	0.0020	558	15	559	7	578	37	-9	
K06-20	metamorphic	587	526	670	0.69	0.02	0.084	0.001	0.16	0.0597	0.0017	528	12	519	5	584	33	2	
K06-21	metamorphic	613	44	85	0.67	0.02	0.085	0.001	0.05	0.0579	0.0016	522	11	525	5	527	37	-19	
K06-22	magmatic	216	113	265	0.88	0.06	0.088	0.002	0.32	0.0723	0.0049	632	34	543	9	960	110	-8	X
K06-23	magmatic	633	231	334	0.70	0.02	0.086	0.001	0.09	0.0591	0.0016	538	11	532	6	565	34	-13	
K06-24	magmatic	668	342	506	0.70	0.02	0.088	0.001	0.14	0.0581	0.0015	537	11	542	5	521	33	-20	
K06-25	resin	16	119	162	0.68	0.35	0.106	0.009	0.23	0.0630	0.0300	470	200	646	51	1760	410	48	X
K06-26	resin	424	60	148	0.71	0.03	0.084	0.002	0.47	0.0612	0.0023	542	18	518	10	643	45	5	X
K06-27	resin	545	514	243	0.71	0.02	0.083	0.001	0.27	0.0615	0.0019	542	14	514	7	665	43	12	X
K06-28	magmatic	474	323	469	0.70	0.02	0.085	0.001	0.17	0.0598	0.0019	536	13	523	6	588	40	1	
K06-29	magmatic	219	149	266	0.79	0.04	0.090	0.002	0.05	0.0632	0.0032	585	23	556	9	725	64	-4	X
K06-30	resin	533	400	1561	3.75	0.09	0.241	0.004	0.79	0.1119	0.0016	1577	19	1390	22	1826	17	24	X
K06-31	magmatic	286	125	467	2.82	0.09	0.199	0.005	0.78	0.1012	0.0021	1354	25	1170	25	1652	22	29	X
K06-32	metamorphic	714	48	256	1.26	0.05	0.112	0.003	0.76	0.0799	0.0022	820	23	685	14	1180	40	41	X
K06-33	metamorphic	101	66	480	6.66	0.19	0.375	0.007	0.24	0.1277	0.0038	2057	26	2051	30	2058	31	0	X
K06-34	resin	338	329	549	0.70	0.03	0.086	0.001	0.21	0.0577	0.0026	532	20	532	8	571	54	-49	X
K06-35	metamorphic	2788	279	455	0.47	0.02	0.054	0.002	0.90	0.0628	0.0012	386	13	336	15	700	29	48	X
Sheeted leucogranites																			
K07-01	apatite	642	599	294	4.23	0.09	0.266	0.005	0.87	0.1164	0.0012	1676	17	1516	24	4	0	20	X
K07-02	magmatic	1860	413	272	2.82	0.26	0.206	0.013	0.99	0.0942	0.0030	1291	67	1199	67	5	0	20	X
K07-03	resin	3730	4000	156	0.69	0.02	0.080	0.002	0.94	0.0634	0.0007	530	13	494	13	13	0	29	X
K07-04	metamorphic	1088	926	684	3.90	0.15	0.265	0.009	0.97	0.1067	0.0012	1596	35	1513	44	4	0	13	
K07-05	metamorphic	3012	233	110	1.10	0.05	0.111	0.003	0.97	0.0718	0.0013	745	23	678	17	9	0	29	
K07-06	resin	3034	201	51	0.82	0.01	0.098	0.001	0.73	0.0611	0.0007	604	7	602	7	10	0	2	X
K07-07	magmatic	2292	203	51	0.67	0.01	0.083	0.001	0.76	0.0582	0.0007	518	8	516	6	12	0	-2	
K07-08	metamorphic	1980	145	38	0.82	0.03	0.096	0.003	0.95	0.0614	0.0009	600	19	588	17	10	0	5	
K07-09	metamorphic	2305	307	98	1.03	0.07	0.104	0.004	0.98	0.0691	0.0020	699	33	637	24	10	0	22	
K07-10	metamorphic	2625	302	76	0.76	0.02	0.090	0.001	0.85	0.0605	0.0008	571	10	555	8	11	0	5	
K07-11	magmatic	1447	147	25	0.70	0.01	0.086	0.001	0.48	0.0581	0.0008	536	7	533	6	12	0	-14	
K07-12	metamorphic	1270	449	189	1.64	0.15	0.138	0.009	0.98	0.0805	0.0027	936	58	829	50	7	0	28	
K07-13	metamorphic	1742	1376	839	3.01	0.04	0.208	0.002	0.67	0.1033	0.0012	1409	11	1217	13	5	0	27	
K07-14	metamorphic	3532	436	120	0.83	0.01	0.095	0.001	0.50	0.0627	0.0006	614	5	586	5	11	0	13	
K07-15	resin	2787	264	101	0.79	0.03	0.090	0.002	0.90	0.0625	0.0013	587	17	553	10	11	0	11	X
K07-16	metamorphic	376	573	241	1.64	0.04	0.161	0.002	0.05	0.0733	0.0017	982	14	963	8	6	0	-3	X
K07-17	metamorphic	1887	193	42	0.89	0.01	0.101	0.001	0.47	0.0634	0.0008	644	6	620	6	10	0	11	
K07-18	magmatic	987	663	643	4.88	0.07	0.291	0.004	0.81	0.1211	0.0009	1796	11	1645	18	3	0	17	X
K07-19	metamorphic	1370	62	44	4.05	0.04	0.263	0.002	0.64	0.1112	0.0008	1643	8	1505	12	4	0	17	
K07-20	resin	3290	350	253	1.44	0.02	0.126	0.001	0.65	0.0827	0.0010	905	9	766	7	8	0	38	X
K07-21	metamorphic	1726	147	39	0.96	0.02	0.107	0.001	0.67	0.0651	0.0008	681	8	654	8	9	0	13	
K07-22	metamorphic	163	364	210	3.56	0.09	0.240	0.003	0.50	0.1074	0.0023	1536	19	1387	17	4	0	20	
K07-23	metamorphic	1680	375	177	1.18	0.05	0.115	0.003	0.91	0.0739	0.0015	785	21	699	14	9	0	30	
K07-24	resin	88	108	48	1.90	0.07	0.185	0.003	0.19	0.0749	0.0028	1073	27	1093	17	5	0	-21	X
K07-25	magmatic	327	235	104	1.91	0.07	0.187	0.004	0.54	0.0743	0.0018	1077	22	1105	22	5	0	-14	X
K07-26	metamorphic	1063	303	68	0.65	0.01	0.082	0.001	0.40	0.0581	0.0011	510	8	507	5	12	0	-34	
K07-27	metamorphic	875	174	42	0.67	0.01	0.084	0.001	0.22	0.0577	0.0012	519	8	521	4	12	0	-15	
K07-28	resin	3824	270	54	0.64	0.01	0.081	0.001	0.44	0.0574	0.0007	503	5	505	4	12	0	-9	X
K07-29	metamorphic	2867	798	280	0.95	0.01	0.106	0.001	0.52	0.0657	0.0007	681	6	648	5	9	0	17	X

PA03-01	metamorphic	388	144	674	2.92	0.08	0.201	0.004	0.81	0.1035	0.0018	1379	22	1180	21	1683	19	30
PA03-02	metamorphic	120	108	632	6.65	0.14	0.393	0.005	0.48	0.1212	0.0023	2061	19	2136	25	1974	20	-8
PA03-03	metamorphic	355	28	159	4.28	0.07	0.285	0.003	0.38	0.1082	0.0015	1687	12	1615	15	1763	15	8
PA03-04	metamorphic	531	57	272	4.48	0.06	0.295	0.003	0.63	0.1091	0.0012	1725	11	1665	17	1783	12	7
PA03-05	metamorphic	169	99	544	5.62	0.12	0.342	0.005	0.54	0.1186	0.0021	1914	18	1895	23	1933	17	2
PA03-06	metamorphic	157	168	854	6.22	0.10	0.370	0.004	0.41	0.1214	0.0018	2008	14	2031	18	1980	15	-3
PA03-07	metamorphic	338	74	409	4.13	0.10	0.273	0.004	0.77	0.1087	0.0017	1655	19	1557	22	1776	20	12

Appendix 4.D: Measured U-Pb-Th data for calibration and reference standards (91500, Plesovice, GJ-1, Temora 2 and QGNG)

				Isotopic ratios							Ages						
Spot analysis	U ppm	Th ppm	Pb ppm	207Pb/ 235U	2SE	206Pb/ 238U	2SE	Rho	207Pb/ 206Pb	2SE	207Pb/ 235U	2SE	206Pb/ 238U	2SE	207Pb/ 206Pb	2SE	Disc. %
Experiment 1																	
91500-01	27	10	47	1.91	0.10	0.192	0.004	0.17	0.0722	0.0038	1065	36	1132	22	993	64	-40
91500-02	25	9	53	1.94	0.13	0.198	0.003	0.16	0.0723	0.0048	1073	44	1163	16	951	76	-69
91500-03	30	11	47	1.80	0.11	0.182	0.003	0.21	0.0719	0.0043	1037	37	1077	18	973	70	-36
91500-04	26	10	46	1.93	0.12	0.183	0.003	0.17	0.0765	0.0045	1069	40	1084	18	1092	68	-13
91500-05	24	8	40	2.00	0.12	0.193	0.004	0.20	0.0760	0.0044	1095	42	1135	21	1074	71	-23
91500-06	25	8	41	1.94	0.11	0.193	0.004	0.17	0.0734	0.0044	1084	41	1134	22	1021	74	-33
91500-07	28	10	47	1.96	0.11	0.189	0.004	0.23	0.0752	0.0041	1080	39	1116	22	1039	59	-19
91500-08	29	11	50	1.89	0.10	0.186	0.004	0.10	0.0750	0.0043	1062	38	1096	22	1046	69	-17
91500-09	24	8	46	1.95	0.13	0.188	0.004	0.13	0.0757	0.0052	1068	45	1108	23	1050	74	-31
91500-10	24	8	32	1.96	0.11	0.188	0.004	0.27	0.0757	0.0041	1083	38	1108	23	1060	68	-17
91500-11	24	9	31	1.98	0.13	0.193	0.004	0.14	0.0740	0.0050	1080	46	1138	23	1035	82	-40
91500-12	29	10	50	2.21	0.12	0.186	0.004	0.05	0.0869	0.0051	1168	40	1101	24	1318	73	11
91500-13	30	10	46	1.94	0.12	0.184	0.004	0.25	0.0777	0.0050	1074	44	1085	23	1105	75	-18
91500-14	25	9	41	1.96	0.13	0.189	0.004	0.24	0.0750	0.0046	1075	43	1120	23	1056	68	-19
91500-15	25	9	45	2.02	0.15	0.192	0.004	0.19	0.0766	0.0056	1084	51	1130	22	1079	86	-67
91500-16	27	10	47	1.91	0.10	0.192	0.004	0.17	0.0722	0.0038	1065	36	1132	22	993	64	-40
91500-17	25	9	53	1.94	0.13	0.198	0.003	0.16	0.0723	0.0048	1073	44	1163	16	951	76	-69
91500-18	30	11	47	1.80	0.11	0.182	0.003	0.21	0.0719	0.0043	1037	37	1077	18	973	70	-36
91500-19	26	10	46	1.93	0.12	0.183	0.003	0.17	0.0765	0.0045	1069	40	1084	18	1092	68	-13
91500-20	24	8	40	2.00	0.12	0.193	0.004	0.20	0.0760	0.0044	1095	42	1135	21	1074	71	-23
91500-21	25	8	41	1.94	0.11	0.193	0.004	0.17	0.0734	0.0044	1084	41	1134	22	1021	74	-33
91500-22	28	10	47	1.96	0.11	0.189	0.004	0.23	0.0752	0.0041	1080	39	1116	22	1039	59	-19
91500-23	29	11	50	1.89	0.10	0.186	0.004	0.10	0.0750	0.0043	1062	38	1096	22	1046	69	-17
91500-24	24	8	46	1.95	0.13	0.188	0.004	0.13	0.0757	0.0052	1068	45	1108	23	1050	74	-31
91500-25	24	8	32	1.96	0.11	0.188	0.004	0.27	0.0757	0.0041	1083	38	1108	23	1060	68	-17
91500-26	24	9	31	1.98	0.13	0.193	0.004	0.14	0.0740	0.0050	1080	46	1138	23	1035	82	-40
91500-27	29	10	50	2.21	0.12	0.186	0.004	0.05	0.0869	0.0051	1168	40	1101	24	1318	73	11
91500-28	30	10	46	1.94	0.12	0.184	0.004	0.25	0.0777	0.0050	1074	44	1085	23	1105	75	-18
91500-29	25	9	41	1.96	0.13	0.189	0.004	0.24	0.0750	0.0046	1075	43	1120	23	1056	68	-19
91500-30	25	9	45	2.02	0.15	0.192	0.004	0.19	0.0766	0.0056	1084	51	1130	22	1079	86	-67
Plesovice-01	254	30	33	0.39	0.02	0.054	0.001	0.12	0.0530	0.0023	333	12	336	4	400	41	-27
Plesovice-02	248	29	35	0.37	0.02	0.053	0.001	0.11	0.0510	0.0022	320	12	333	4	346	44	-86
Plesovice-03	244	28	34	0.40	0.02	0.054	0.001	0.03	0.0531	0.0023	337	12	340	4	392	49	-46
Plesovice-04	245	28	33	0.37	0.02	0.054	0.001	-0.03	0.0500	0.0022	320	12	339	4	304	42	-136
Plesovice-05	258	30	36	0.40	0.02	0.053	0.001	0.07	0.0536	0.0024	336	13	335	4	419	48	-97
GJ1-01	287	10	26	0.82	0.02	0.098	0.001	0.00	0.0604	0.0014	604	10	602	5	622	29	-1
GJ1-02	287	10	26	0.82	0.02	0.098	0.001	0.24	0.0604	0.0014	603	12	602	4	618	31	-2
GJ1-03	287	10	26	0.82	0.02	0.098	0.001	-0.04	0.0604	0.0016	603	11	602	5	613	39	-13
GJ1-04	287	10	26	0.82	0.02	0.098	0.001	0.08	0.0604	0.0016	603	12	602	5	625	33	-8
GJ1-05	287	10	26	0.82	0.02	0.098	0.001	0.18	0.0604	0.0015	603	12	602	5	609	35	-9
GJ1-06	287	10	26	0.82	0.02	0.098	0.001	0.17	0.0604	0.0014	604	11	602	5	603	32	-7
GJ1-07	287	10	26	0.82	0.02	0.098	0.001	0.20	0.0604	0.0015	603	11	602	5	616	33	-7
GJ1-08	287	10	26	0.82	0.02	0.098	0.001	-0.08	0.0604	0.0017	603	12	602	5	607	38	-12
GJ1-09	287	10	26	0.82	0.02	0.098	0.001	-0.09	0.0604	0.0015	605	10	602	5	608	30	-6

GJ1-10	287	10	26	0.82	0.02	0.098	0.001	0.11	0.0604	0.0016	603	12	602	5	609	30	-4
GJ1-11	287	10	26	0.82	0.02	0.098	0.001	0.10	0.0604	0.0016	603	11	602	5	618	33	-4
GJ1-12	287	10	26	0.82	0.02	0.098	0.001	0.21	0.0604	0.0017	603	13	602	5	607	35	-10
GJ1-13	287	10	26	0.82	0.02	0.098	0.001	0.18	0.0604	0.0017	603	13	602	6	605	36	-14
GJ1-14	287	10	26	0.82	0.02	0.098	0.001	0.15	0.0604	0.0018	604	13	602	5	606	35	-10
GJ1-15	287	10	26	0.82	0.02	0.098	0.001	0.07	0.0604	0.0016	603	11	602	6	617	31	-4
Experiment 2																	
Plesovice-01	233	34	45	0.39	0.02	0.054	0.001	0.11	0.0530	0.0020	337	10	340	4	386	38	-32
Plesovice-02	233	34	44	0.40	0.02	0.054	0.001	-0.01	0.0542	0.0025	340	13	339	4	432	45	-31
Plesovice-03	236	35	46	0.40	0.02	0.054	0.001	0.07	0.0538	0.0021	340	11	338	4	444	42	-6
Plesovice-04	236	34	45	0.40	0.02	0.054	0.001	0.18	0.0544	0.0021	341	11	337	4	442	41	-26
Plesovice-05	231	34	43	0.40	0.02	0.053	0.001	0.20	0.0550	0.0022	341	12	334	4	481	43	5
Temora2-01	84	36	54	0.52	0.03	0.067	0.001	0.09	0.0571	0.0034	418	21	415	7	634	67	-62
Temora2-02	123	84	119	0.52	0.03	0.068	0.001	0.04	0.0558	0.0028	418	17	421	6	523	54	-73
Temora2-03	64	29	45	0.56	0.04	0.068	0.001	0.13	0.0608	0.0038	445	22	421	8	669	57	18
Temora2-04	198	97	141	0.52	0.02	0.066	0.001	0.20	0.0566	0.0021	421	13	414	5	544	51	-43
Temora2-05	50	26	41	0.59	0.04	0.070	0.002	-0.06	0.0641	0.0050	466	29	434	9	818	81	-25
Temora2-06	175	154	217	0.51	0.02	0.066	0.001	0.15	0.0561	0.0023	417	14	414	5	496	51	-34
Temora2-07	186	167	237	0.53	0.02	0.066	0.001	0.17	0.0586	0.0024	431	14	413	5	567	44	10
Temora2-08	154	72	104	0.52	0.03	0.066	0.001	0.21	0.0568	0.0030	416	18	413	6	560	56	-7
GJ1-01	282	9	24	0.82	0.02	0.098	0.001	0.16	0.0612	0.0013	607	9	603	6	633	22	2
GJ1-02	293	10	26	0.81	0.02	0.097	0.001	0.23	0.0609	0.0014	601	10	597	6	630	26	1
GJ1-03	286	9	26	0.82	0.02	0.098	0.001	0.28	0.0604	0.0013	605	10	605	5	611	25	-3
GJ1-04	287	9	27	0.81	0.02	0.097	0.001	0.20	0.0598	0.0012	599	9	599	5	599	25	-6
GJ1-05	288	10	26	0.81	0.02	0.100	0.001	0.19	0.0589	0.0012	603	11	611	7	566	29	-16
GJ1-06	284	9	23	0.82	0.02	0.097	0.001	0.23	0.0612	0.0014	607	11	598	6	638	26	3
GJ1-07	289	10	26	0.81	0.02	0.098	0.001	0.17	0.0600	0.0013	604	10	603	5	605	24	-7
GJ1-08	288	10	26	0.83	0.02	0.098	0.001	0.18	0.0615	0.0016	613	12	601	5	654	34	0
GJ1-09	284	9	25	0.82	0.02	0.098	0.001	0.09	0.0605	0.0015	605	11	600	5	627	31	-4
GJ1-10	290	10	25	0.81	0.02	0.098	0.001	0.14	0.0604	0.0016	602	12	601	5	611	29	-7
GJ1-11	287	10	27	0.82	0.02	0.098	0.001	0.24	0.0607	0.0014	607	10	605	7	618	26	-4
GJ1-12	284	9	24	0.82	0.02	0.098	0.001	0.32	0.0604	0.0015	605	12	604	6	611	31	-7
GJ1-13	290	10	29	0.82	0.02	0.098	0.001	0.17	0.0608	0.0016	605	12	601	6	624	34	-4
GJ1-14	286	9	23	0.81	0.02	0.098	0.001	0.07	0.0601	0.0015	599	11	600	6	605	31	-11
GJ1-15	288	10	28	0.82	0.02	0.098	0.001	0.18	0.0609	0.0016	603	12	601	5	634	32	-2
GJ1-16	283	9	25	0.82	0.02	0.098	0.001	0.14	0.0608	0.0017	605	12	602	6	624	34	-8
GJ1-17	290	10	24	0.81	0.02	0.098	0.001	0.31	0.0597	0.0014	598	11	603	6	584	32	-15
91500-01	28	11	54	1.85	0.09	0.180	0.003	-0.02	0.0761	0.0039	1054	30	1064	17	1070	51	-4
91500-02	26	10	50	1.90	0.09	0.186	0.004	0.27	0.0742	0.0032	1067	30	1101	20	1043	51	-12
91500-03	28	12	52	1.95	0.08	0.181	0.003	-0.07	0.0790	0.0035	1091	27	1071	17	1164	46	5
91500-04	25	10	47	1.99	0.10	0.186	0.004	0.17	0.0769	0.0036	1096	32	1098	19	1113	59	-8
91500-05	27	11	48	1.96	0.10	0.182	0.003	0.10	0.0781	0.0039	1091	35	1079	17	1136	67	-15
91500-06	25	10	44	1.98	0.10	0.186	0.004	0.07	0.0777	0.0039	1091	33	1097	20	1129	56	-10
91500-07	24	9	41	1.99	0.09	0.190	0.004	0.11	0.0766	0.0038	1109	34	1121	24	1119	65	-11
91500-08	26	10	47	2.02	0.10	0.190	0.004	-0.01	0.0780	0.0043	1107	35	1117	21	1137	68	-13
91500-09	29	14	60	1.99	0.10	0.188	0.004	0.14	0.0772	0.0040	1103	33	1110	20	1107	49	-7
91500-10	29	13	60	2.07	0.11	0.190	0.004	0.16	0.0794	0.0042	1120	36	1122	20	1143	63	-10
91500-11	25	11	54	2.07	0.12	0.186	0.004	0.24	0.0813	0.0046	1121	40	1100	21	1187	69	-2
91500-12	27	11	48	1.98	0.12	0.189	0.004	0.29	0.0765	0.0044	1086	42	1115	22	1080	70	-37
91500-13	26	10	52	2.12	0.12	0.191	0.004	0.13	0.0806	0.0046	1137	39	1127	23	1194	63	-4
91500-14	25	10	50	1.97	0.11	0.187	0.004	0.09	0.0776	0.0045	1087	39	1105	21	1111	64	-8

91500-15	32	16	67	1.91	0.10	0.185	0.004	0.12	0.0756	0.0040	1065	37	1094	20	1061	68	-32
91500-16	27	11	51	2.02	0.10	0.190	0.004	0.08	0.0780	0.0041	1113	34	1120	22	1126	64	-9
91500-17	25	10	50	1.96	0.11	0.186	0.004	0.12	0.0775	0.0045	1091	37	1100	20	1081	75	-45
91500-18	24	9	41	2.13	0.13	0.191	0.004	0.18	0.0814	0.0051	1135	42	1126	22	1186	69	-4
91500-19	27	12	52	2.09	0.12	0.188	0.004	0.11	0.0809	0.0045	1129	38	1111	22	1189	63	0
Experiment 3																	
Plesovice-01	289	72	94	0.42	0.03	0.054	0.001	-0.16	0.0566	0.0038	350	19	341	6	564	76	-29
Plesovice-02	264	51	87	0.45	0.03	0.054	0.001	-0.12	0.0596	0.0041	368	20	339	6	690	82	-12
Plesovice-03	309	91	118	0.40	0.03	0.054	0.001	-0.12	0.0535	0.0035	336	18	340	6	511	59	-3
Plesovice-04	274	62	93	0.38	0.03	0.053	0.001	-0.09	0.0524	0.0037	326	19	335	6	528	70	-22
Plesovice-05	281	70	112	0.40	0.03	0.054	0.001	0.04	0.0541	0.0040	336	21	336	6	544	70	4
GJ1-01	294	10	36	0.82	0.02	0.098	0.001	0.24	0.0599	0.0011	605	9	602	4	599	28	-5
GJ1-02	292	10	31	0.81	0.02	0.098	0.001	0.07	0.0599	0.0013	601	10	601	4	597	26	-5
GJ1-03	273	9	27	0.83	0.02	0.098	0.001	0.14	0.0616	0.0015	612	11	600	5	655	30	3
GJ1-04	286	9	25	0.83	0.02	0.099	0.001	0.01	0.0611	0.0017	612	12	609	5	632	34	-3
GJ1-05	293	9	23	0.79	0.02	0.096	0.001	-0.05	0.0604	0.0020	588	14	593	6	620	41	-14
GJ1-06	288	10	19	0.79	0.03	0.098	0.001	0.06	0.0600	0.0021	589	16	602	6	592	42	-52
GJ1-07	281	9	22	0.80	0.03	0.098	0.001	0.16	0.0599	0.0021	597	16	603	6	599	41	-17
GJ1-08	290	10	24	0.82	0.03	0.099	0.001	0.22	0.0608	0.0022	605	17	605	7	618	45	-22
GJ1-09	287	9	25	0.82	0.03	0.097	0.001	0.14	0.0606	0.0021	602	17	598	7	624	47	-19
GJ1-10	288	10	23	0.84	0.03	0.098	0.001	0.10	0.0616	0.0024	616	18	605	8	663	52	-12
GJ1-11	285	10	27	0.82	0.03	0.096	0.001	0.10	0.0615	0.0026	602	19	591	7	661	47	-13
GJ1-12	293	9	22	0.83	0.03	0.100	0.001	-0.08	0.0600	0.0024	613	17	613	8	604	51	-30
GJ1-13	284	9	31	0.82	0.04	0.099	0.002	0.15	0.0590	0.0025	601	20	609	9	602	52	-32
GJ1-14	292	10	22	0.80	0.03	0.096	0.001	0.15	0.0607	0.0025	596	18	591	8	625	52	-38
GJ1-15	285	10	35	0.81	0.04	0.098	0.001	0.10	0.0595	0.0025	599	19	605	7	608	52	-39
91500-01	36	14	84	1.94	0.08	0.183	0.002	0.24	0.0774	0.0029	1092	26	1081	12	1096	45	-3
91500-02	36	14	77	1.98	0.10	0.186	0.003	0.18	0.0769	0.0037	1091	33	1098	13	1092	55	-7
91500-03	37	15	73	1.92	0.11	0.182	0.003	0.30	0.0755	0.0040	1066	38	1078	16	1087	52	-10
91500-04	23	7	34	2.10	0.17	0.190	0.005	0.09	0.0803	0.0069	1098	59	1122	26	1172	92	-34
91500-05	21	6	32	2.09	0.20	0.192	0.005	0.10	0.0801	0.0074	1083	66	1128	24	1150	120	-55
91500-06	21	6	30	2.03	0.18	0.204	0.007	0.19	0.0724	0.0060	1074	62	1193	36	1008	93	-64
91500-07	22	8	31	2.24	0.23	0.206	0.006	0.25	0.0821	0.0085	1155	79	1206	33	1200	100	-42
91500-08	22	8	35	2.28	0.23	0.208	0.007	0.31	0.0790	0.0073	1141	72	1214	38	1165	99	-40
91500-09	22	7	31	2.09	0.25	0.208	0.009	0.26	0.0742	0.0083	1064	81	1214	46	1110	100	-53
91500-10	26	9	39	1.95	0.22	0.208	0.007	0.20	0.0672	0.0071	1021	81	1213	38	980	100	-87
91500-11	24	10	44	2.12	0.24	0.208	0.008	0.21	0.0728	0.0081	1075	81	1216	40	1080	100	-100
91500-12	21	8	40	2.01	0.27	0.214	0.009	0.26	0.0670	0.0085	1042	92	1245	49	1000	130	-118
91500-13	25	8	53	2.06	0.24	0.204	0.008	0.38	0.0756	0.0092	1075	90	1192	43	1160	120	-37
Experiment 4																	
GJ-01	833	30	8	0.80	0.01	0.096	0.001	0.18	0.0599	0.0011	597	8	593	5	587	40	-27
GJ-02	827	29	9	0.81	0.02	0.099	0.001	0.26	0.0592	0.0011	600	8	608	5	559	39	-21
GJ-03	832	30	9	0.79	0.01	0.097	0.001	0.32	0.0597	0.0010	589	8	598	5	587	34	-13
GJ-04	862	30	10	0.76	0.01	0.094	0.001	0.39	0.0593	0.0010	573	8	579	6	563	37	-24
GJ-05	798	28	9	0.79	0.02	0.096	0.001	0.22	0.0594	0.0011	590	9	593	6	570	43	-45
GJ-06	837	32	9	0.79	0.01	0.096	0.001	0.15	0.0590	0.0011	589	8	589	5	554	39	-25
GJ-07	820	30	8	0.80	0.02	0.097	0.001	0.24	0.0590	0.0011	597	8	599	6	559	41	-26
GJ-08	848	30	9	0.77	0.02	0.094	0.001	0.23	0.0590	0.0012	579	9	580	5	550	44	-9
GJ-09	831	28	9	0.78	0.02	0.096	0.001	0.13	0.0591	0.0012	586	8	591	5	551	44	-33
GJ-10	837	32	9	0.78	0.01	0.096	0.001	0.11	0.0588	0.0010	586	7	594	5	545	38	-6
GJ-11	861	30	8	0.78	0.02	0.096	0.001	0.24	0.0588	0.0011	582	8	591	5	548	43	-32

GJ-12	897	29	9	0.78	0.02	0.096	0.001	0.39	0.0592	0.0011	585	9	590	5	561	41	-25
91500-01	80	30	15	1.82	0.07	0.180	0.003	0.13	0.0725	0.0027	1042	24	1064	14	967	76	0
91500-02	81	30	15	1.87	0.07	0.179	0.003	0.18	0.0761	0.0030	1064	24	1061	14	1052	76	-21
91500-03	79	30	15	1.90	0.07	0.178	0.003	-0.02	0.0784	0.0030	1071	24	1058	15	1099	78	-14
91500-04	80	30	15	1.87	0.07	0.182	0.003	0.13	0.0754	0.0029	1060	26	1076	14	1017	84	-26
91500-05	80	30	16	1.83	0.08	0.178	0.003	0.23	0.0747	0.0031	1045	28	1054	16	1002	84	-29
91500-06	79	30	13	1.76	0.07	0.179	0.003	0.15	0.0708	0.0030	1025	27	1062	15	895	88	-63
91500-07	81	30	15	1.91	0.07	0.177	0.002	0.22	0.0776	0.0028	1077	25	1050	12	1096	73	-8
91500-08	80	30	15	1.85	0.07	0.180	0.003	0.28	0.0742	0.0029	1051	27	1068	15	986	82	-18
91500-09	81	30	17	1.83	0.08	0.180	0.003	0.11	0.0742	0.0032	1045	28	1065	17	972	92	-28
91500-10	79	30	15	1.87	0.08	0.181	0.003	0.18	0.0751	0.0030	1060	27	1075	16	1005	85	-36
91500-11	80	30	14	1.84	0.07	0.179	0.003	0.13	0.0751	0.0029	1052	25	1058	14	1024	78	-35
91500-12	80	30	15	1.82	0.07	0.180	0.003	0.13	0.0725	0.0027	1042	24	1064	14	967	76	0
91500-13	81	30	15	1.87	0.07	0.179	0.003	0.18	0.0761	0.0030	1064	24	1061	14	1052	76	-21
91500-14	79	30	15	1.90	0.07	0.178	0.003	-0.02	0.0784	0.0030	1071	24	1058	15	1099	78	-14
91500-15	80	30	15	1.87	0.07	0.182	0.003	0.13	0.0754	0.0029	1060	26	1076	14	1017	84	-26
91500-16	80	30	16	1.83	0.08	0.178	0.003	0.23	0.0747	0.0031	1045	28	1054	16	1002	84	-29
91500-17	79	30	13	1.76	0.07	0.179	0.003	0.15	0.0708	0.0030	1025	27	1062	15	895	88	-63
91500-18	81	30	15	1.91	0.07	0.177	0.002	0.22	0.0776	0.0028	1077	25	1050	12	1096	73	-8
91500-19	80	30	15	1.85	0.07	0.180	0.003	0.28	0.0742	0.0029	1051	27	1068	15	986	82	-18
91500-20	81	30	17	1.83	0.08	0.180	0.003	0.11	0.0742	0.0032	1045	28	1065	17	972	92	-28
91500-21	79	30	15	1.87	0.08	0.181	0.003	0.18	0.0751	0.0030	1060	27	1075	16	1005	85	-36
91500-22	80	30	14	1.84	0.07	0.179	0.003	0.13	0.0751	0.0029	1052	25	1058	14	1024	78	-35
Experiment 5																	
91500-01	31	12	60	2.06	0.15	0.190	0.004	0.02	0.0799	0.0058	1124	47	1120	21	1151	88	-8
91500-02	35	14	65	1.82	0.13	0.187	0.006	0.11	0.0732	0.0058	1049	52	1106	31	996	91	-24
91500-03	31	12	66	1.98	0.11	0.183	0.003	0.07	0.0785	0.0042	1088	37	1082	18	1143	64	-3
91500-04	34	13	54	1.90	0.15	0.179	0.005	0.26	0.0775	0.0060	1066	51	1062	27	1124	88	1
91500-05	24	8	46	1.99	0.14	0.195	0.005	0.21	0.0734	0.0052	1088	49	1148	26	1028	63	-24
91500-06	30	11	57	1.92	0.13	0.187	0.004	0.20	0.0760	0.0050	1071	46	1101	23	1069	73	-26
91500-07	35	13	56	2.02	0.14	0.185	0.005	0.15	0.0803	0.0056	1096	49	1092	25	1170	86	-11
91500-08	26	10	40	2.06	0.17	0.192	0.005	0.22	0.0780	0.0066	1093	58	1135	27	1108	99	-34
91500-09	24	8	49	1.92	0.17	0.195	0.006	0.12	0.0720	0.0062	1055	60	1146	33	1060	87	-73
91500-10	36	15	50	1.86	0.16	0.178	0.005	0.26	0.0749	0.0062	1036	56	1055	28	1073	87	-42
91500-11	34	17	50	1.97	0.15	0.185	0.005	0.09	0.0762	0.0058	1071	52	1095	27	1085	81	-15
91500-12	28	11	54	2.02	0.13	0.193	0.004	-0.06	0.0761	0.0052	1095	43	1138	20	1060	79	-37
91500-13	32	12	59	1.94	0.10	0.190	0.004	0.10	0.0747	0.0042	1080	35	1118	20	1027	66	-32
91500-14	31	12	66	1.98	0.11	0.183	0.003	0.07	0.0785	0.0042	1088	37	1082	18	1143	64	-3
91500-15	31	11	55	1.92	0.12	0.179	0.004	0.16	0.0786	0.0049	1068	42	1058	20	1117	72	-21
91500-16	30	11	57	1.90	0.12	0.186	0.004	0.19	0.0758	0.0050	1068	46	1097	24	1069	76	-27
91500-17	35	13	56	2.02	0.14	0.185	0.005	0.11	0.0799	0.0056	1098	49	1091	25	1160	88	-12
91500-18	27	11	50	2.02	0.14	0.202	0.005	0.12	0.0722	0.0050	1100	48	1185	29	1026	74	-44
91500-19	26	10	40	2.06	0.17	0.192	0.005	0.22	0.0780	0.0066	1093	58	1135	27	1108	99	-34
91500-20	24	8	49	1.92	0.16	0.195	0.006	0.13	0.0720	0.0061	1057	59	1148	33	1063	86	-72
91500-21	36	15	51	1.89	0.16	0.178	0.005	0.25	0.0762	0.0063	1045	56	1055	27	1091	87	-40
91500-22	35	17	50	1.97	0.15	0.185	0.005	0.12	0.0766	0.0059	1074	52	1091	27	1100	82	-12
GJ1-01	287	10	26	0.82	0.02	0.098	0.001	0.20	0.0604	0.0013	605	11	602	5	629	27	2
GJ1-02	287	10	26	0.82	0.02	0.098	0.001	0.22	0.0604	0.0014	603	11	602	5	618	28	-4
GJ1-03	287	10	26	0.82	0.02	0.098	0.001	0.20	0.0604	0.0016	605	12	602	6	608	33	-7
GJ1-04	287	10	26	0.82	0.03	0.098	0.001	-0.02	0.0604	0.0019	602	14	602	5	604	41	-20
GJ1-05	287	10	26	0.82	0.03	0.098	0.001	0.05	0.0604	0.0019	602	14	602	6	606	37	-11

GJ1-06	287	10	26	0.82	0.03	0.098	0.001	0.12	0.0604	0.0022	603	17	602	6	603	47	-39
GJ1-07	287	10	26	0.82	0.03	0.098	0.001	0.11	0.0604	0.0022	601	16	602	6	599	44	-22
GJ1-08	287	10	26	0.82	0.03	0.098	0.001	0.09	0.0604	0.0020	602	15	602	6	605	37	-8
GJ1-09	287	10	26	0.82	0.03	0.098	0.001	0.11	0.0604	0.0021	604	17	602	7	615	45	-26
GJ1-10	287	10	26	0.82	0.03	0.098	0.001	0.05	0.0604	0.0020	602	15	602	6	609	42	-11
GJ1-11	287	10	26	0.82	0.03	0.098	0.001	0.18	0.0604	0.0025	600	19	602	8	627	45	-41
GJ1-12	287	10	26	0.82	0.03	0.098	0.002	0.12	0.0604	0.0022	602	16	602	9	606	48	-18
GJ1-13	287	10	26	0.82	0.03	0.098	0.001	0.18	0.0604	0.0019	602	14	602	6	599	43	-19
Experiment 6																	
QGNG-01	203	155	61	5.09	0.13	0.327	0.007	0.88	0.1127	0.0013	1834	11	1825	17	1844	10	-1
QGNG-02	186	130	55	4.84	0.15	0.317	0.008	0.86	0.1109	0.0017	1792	13	1774	21	1814	14	-3
QGNG-03	198	185	59	4.98	0.20	0.315	0.011	0.87	0.1147	0.0023	1816	17	1765	26	1875	18	-7
QGNG-04	219	61	65	4.61	0.18	0.305	0.011	0.92	0.1096	0.0017	1752	16	1718	27	1792	14	-5
QGNG-05	586	101	201	4.99	0.24	0.338	0.015	0.94	0.1072	0.0017	1817	20	1875	36	1752	14	8
QGNG-06	134	31	41	4.93	0.20	0.320	0.012	0.92	0.1116	0.0019	1807	17	1792	30	1825	14	-2
QGNG-07	466	76	141	5.07	0.23	0.342	0.013	0.86	0.1076	0.0025	1831	19	1895	32	1759	21	9
QGNG-08	483	81	145	5.12	0.26	0.342	0.015	0.85	0.1087	0.0029	1840	22	1896	36	1777	25	8
QGNG-09	304	55	94	5.17	0.35	0.340	0.021	0.91	0.1103	0.0031	1848	29	1887	50	1804	25	5
91500-01	86	27	14	1.94	0.08	0.167	0.006	0.84	0.0845	0.0020	1095	14	993	16	1303	22	-26
91500-02	87	28	14	1.75	0.07	0.165	0.006	0.85	0.0769	0.0017	1025	14	982	16	1119	21	-13
91500-03	85	9	14	1.75	0.07	0.167	0.006	0.92	0.0759	0.0012	1025	12	994	16	1093	15	-10
91500-04	81	8	13	1.75	0.09	0.170	0.008	0.91	0.0746	0.0016	1027	17	1012	22	1059	22	-5
91500-05	80	8	13	1.75	0.10	0.169	0.009	0.91	0.0750	0.0019	1028	19	1009	25	1069	24	-6
91500-06	80	8	12	1.76	0.12	0.168	0.010	0.90	0.0758	0.0021	1030	21	1002	27	1089	26	-9
91500-07	88	9	14	1.74	0.07	0.168	0.006	0.90	0.0752	0.0013	1023	13	999	17	1074	16	-8

Appendix 4.E: U-Pb concordia ages for reference standards

U-Pb concordia ages determined for various reference standards (91500, Plesovice, GJ-1, Temora 2 and QGNG) from the different sample runs (experiments 1 to 6). Concordia ages are within error of accepted ages for the various samples, except 91500 shows the least accuracy (to accepted published ages) but is relatively precise within and across the different experiments.

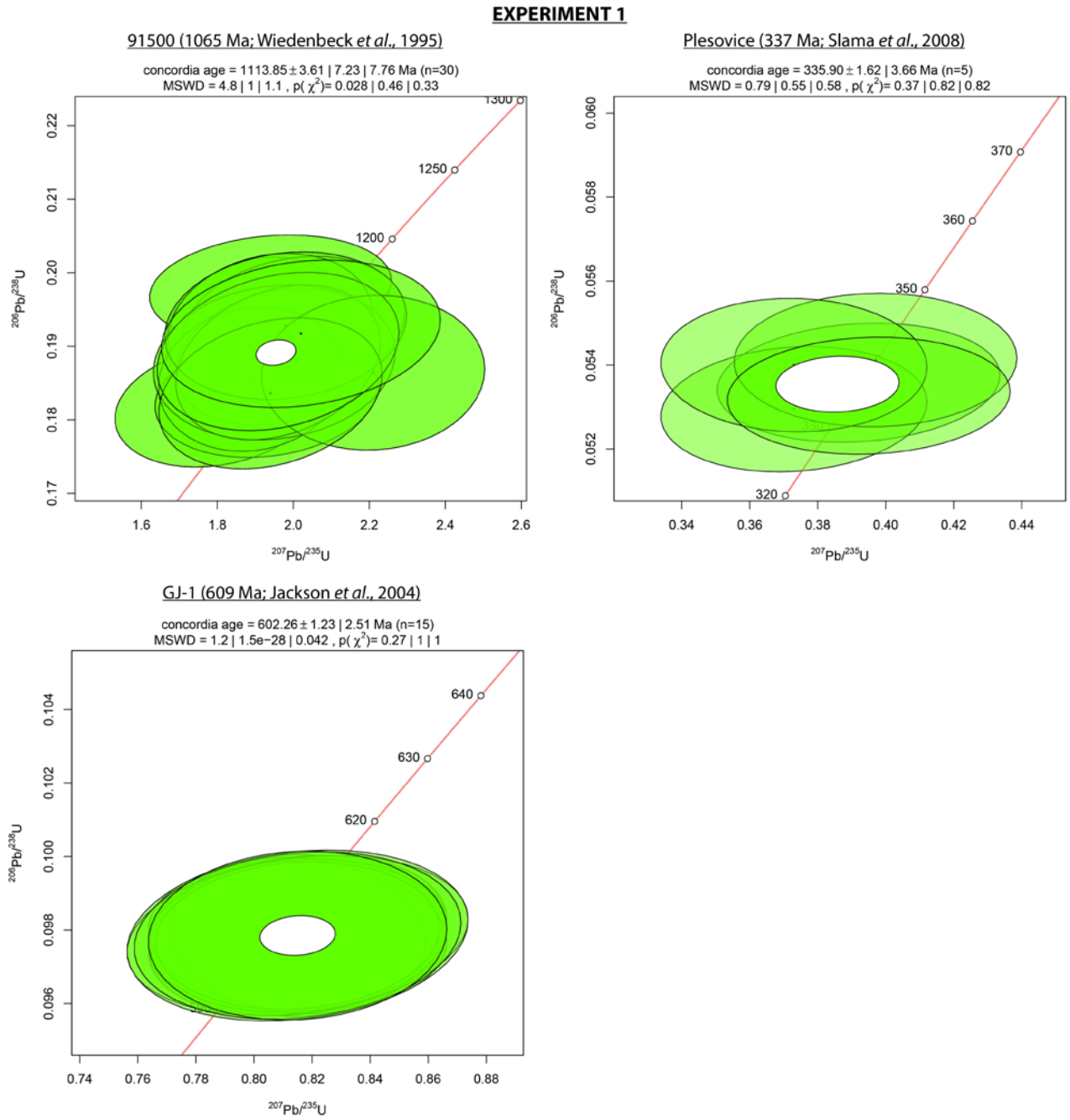


Figure showing the concordia ages of measured reference standard ages from experiment 1 compared with the accepted ages for the various standards.

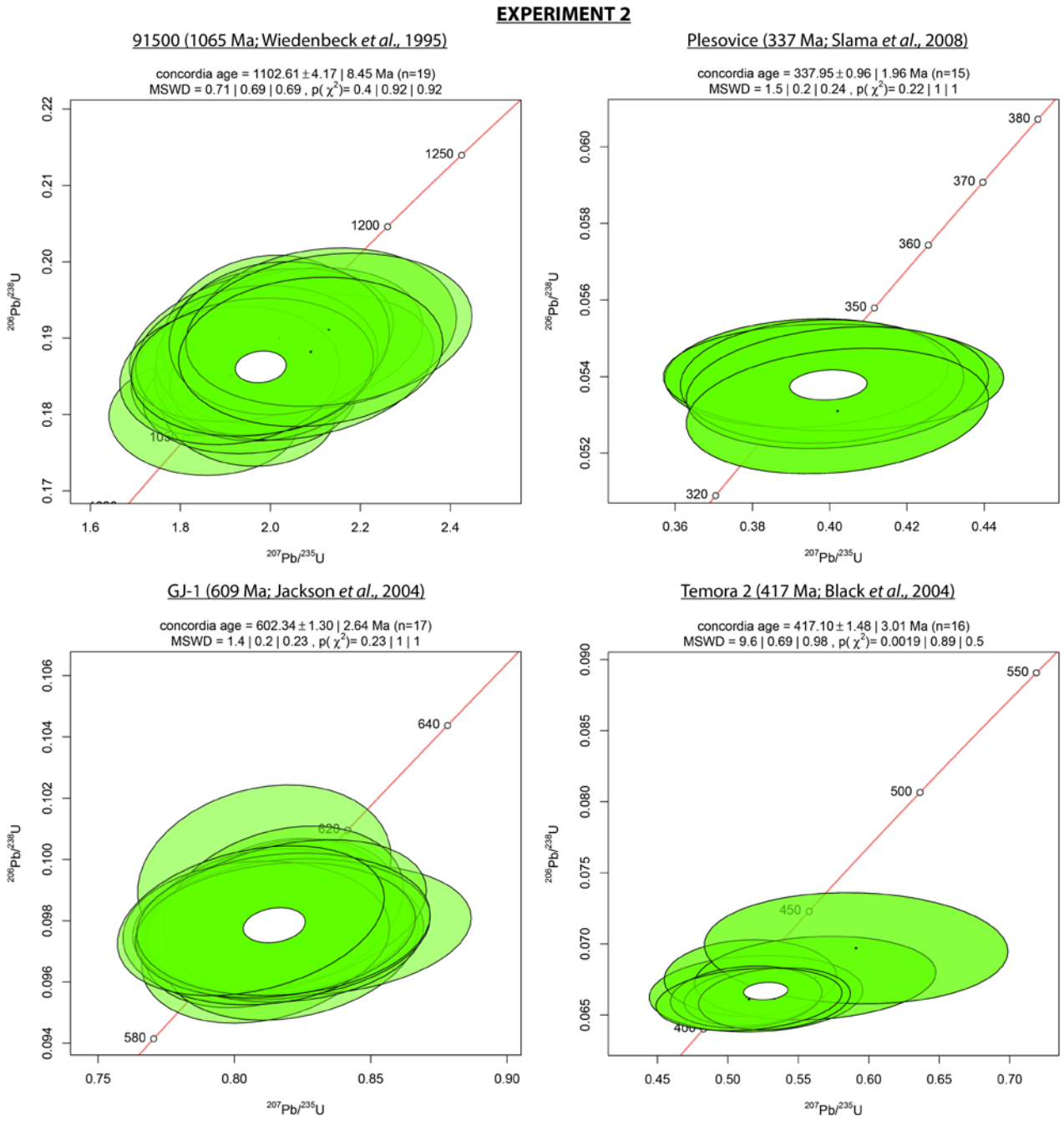


Figure showing the concordia ages of measured reference standard ages from experiment 2 compared with the accepted ages for the various standards.

EXPERIMENT 3

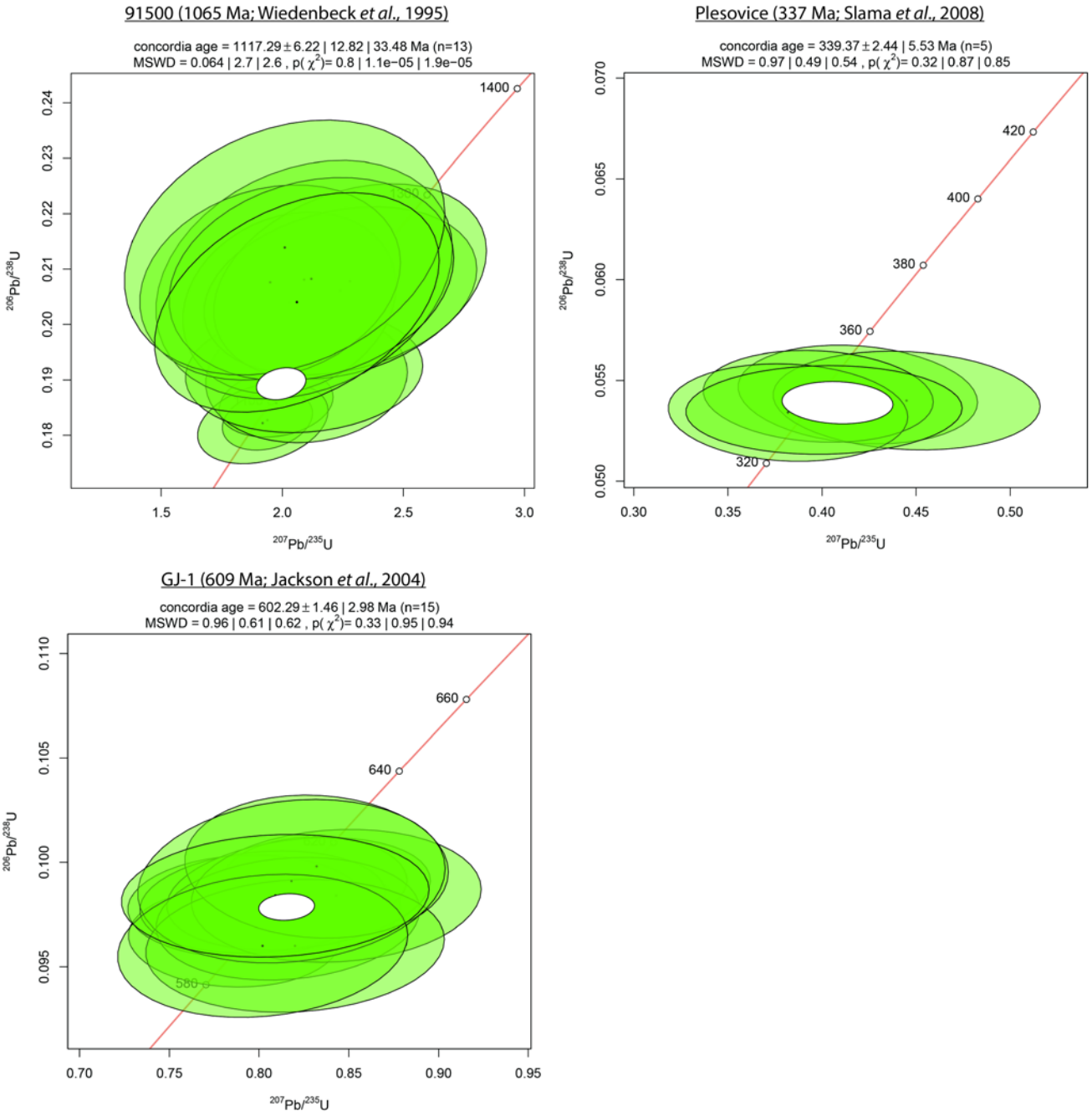


Figure showing the concordia ages of measured reference standard ages from experiment 3 compared with the accepted ages for the various standards.

EXPERIMENT 4

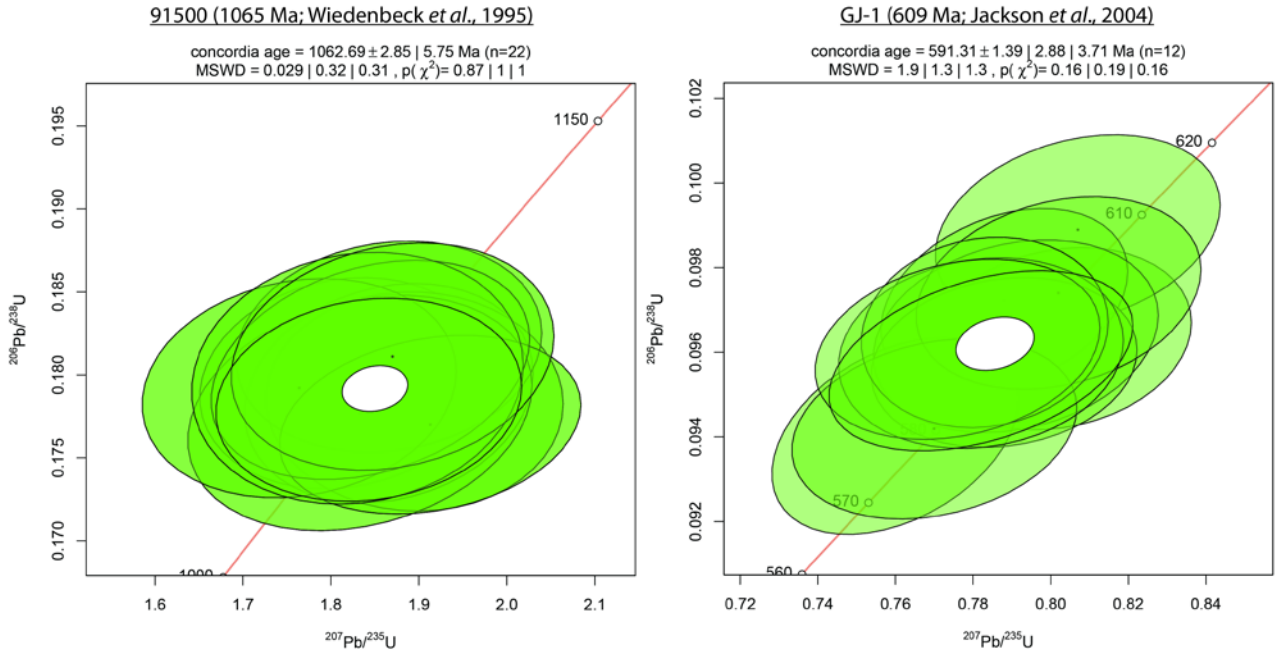


Figure showing the concordia ages of measured reference standard ages from experiment 4 compared with the accepted ages for the various standards.

EXPERIMENT 5

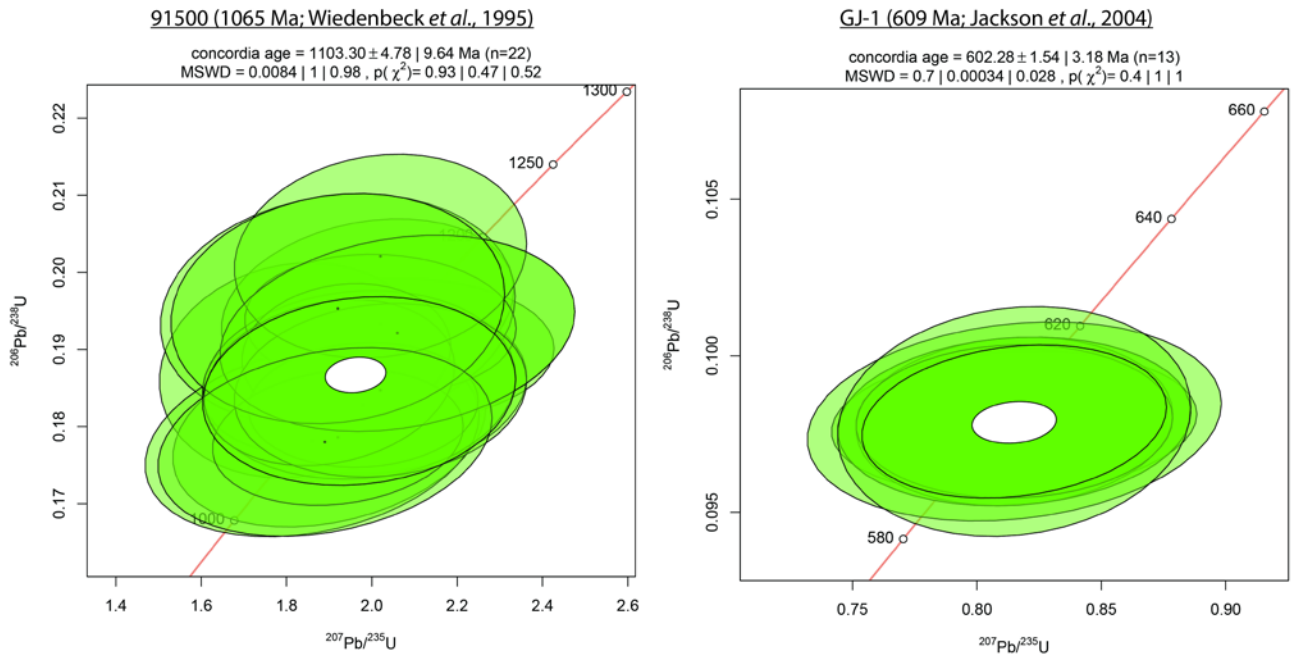


Figure showing the concordia ages of measured reference standard ages from experiment 5 compared with the accepted ages for the various standards.

EXPERIMENT 6

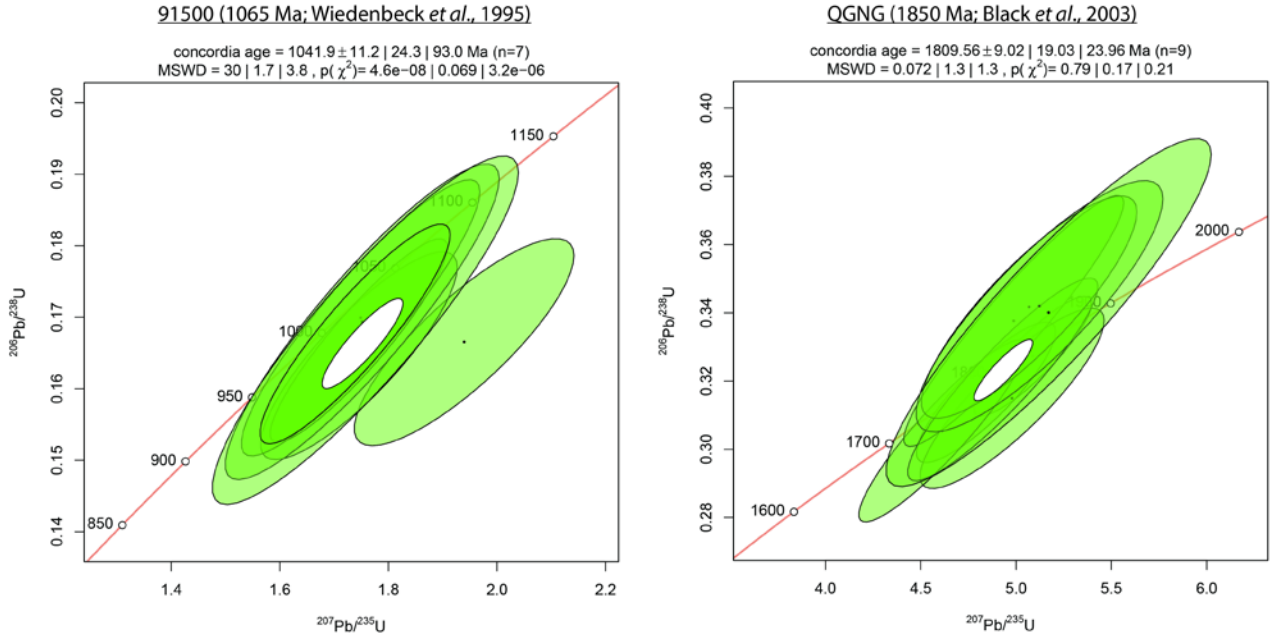


Figure showing the concordia ages of measured reference standard ages from experiment 6 compared with the accepted ages for the various standards.

Appendix 5.A: Summary of analytical procedures for Lu-Hf isotope experiments

LA MC-ICPMS method description for Hf analyses:

Prepared by Ms. Henriette Ueckermann

A 193nm ArF RESOlution SE excimer laser (Australian Scientific Instruments, Fyshwick) was coupled to a Nu Plasma II MC-ICPMS (Nu Instruments, Wrexham). The Nu Plasma II is equipped with 16 Faraday detectors allowing all isotopes of interest to be measured simultaneously

Plasma settings:	
RF Power	1300 W
Coolant gas flow	13.0 L/min
Auxiliary gas flow	0.88 L/min
Nebuliser gas flow	0.8 L/min
Laser He gas flow	0.25 L/min
Laser settings:	
Spot size	50 µm
Beam energy	4 mJ
Beam attenuation	50 %
Repetition rate	7 Hz
Fluence	3.25 J/cm^2
Blank signal	25 seconds
Ablation signal	70 seconds

Detector configuration:

H4 = 180Hf; H3 = 179Hf; H2 = 178Hf; H1 = 177Hf; Ax = 176Hf + 176Yb + 176Lu; L1 = 175Lu; L2 = 174Hf + 174Yb; L3 = 173Yb; L4 = 172Yb; L5 = 171Yb

Mass bias correction:

171Yb and 173Yb were used to calculate Yb mass fractionation and also used to correct for Lu mass fractionation; 179Hf and 177Hf were used to calculate Hf mass fractionation.

Interference corrections:

171Yb was used to calculate and correct for the 174Yb interference on 174Hf as well as for the 176Yb interference on 176Hf; 175Lu was used to correct for the 176Lu interference on 176Hf.

Accuracy evaluation:

Secondary standards were measured at regular intervals and treated as unknowns to evaluate the accuracy of the measurements. Zircon standards Mud Tank, Plesovice, 91500, Temora 2 and LV11 were used for this purpose.

Background correction:

Background signal is collected on mass prior to ablation, and subtracted from the signal.

Appendix 5.B: Measured Lu-Hf isotopic data for the ten samples analysed in this study

-	176Yb/ 177Hf'	SE	176Hf/ 177Hf	SE	178Hf/ 177Hf	SE	180Hf/ 177Hf	SE	176Lu/ 177Hf'	SE	Age (Ma)	SE	176Hf/ 177Hf (T)	eHf (T)	SE	T(DM) Ga
Abbabis Complex- gneisses and granites											**207Pb/ 206Pb**					
K05-1	0.02911512	0.000177	0.2814215	0.00000998	1.467247	0.0000121	1.886809	0.0000286	0.00078231	0.00000485	2036	6	0.281391306	-3.4	0.7	2.9
K05-2	0.03571279	0.000114	0.2814135	0.000011	1.46721	0.0000133	1.886803	0.0000288	0.000966354	0.00000259	2057	7	0.281375811	-3.5	0.8	2.9
K05-3	0.0225801	0.000205	0.2813734	0.00000916	1.467259	0.0000141	1.886807	0.0000315	0.000625463	0.00000499	2002	8	0.28134967	-5.7	0.7	3.0
K05-4	0.01648564	0.000154	0.2814081	0.00000788	1.467265	0.0000114	1.886808	0.000025	0.000497002	0.00000324	2017	8	0.2813891	-4.0	0.6	2.9
K05-5	0.0259	0.0000154	0.281393	0.0000108	1.467296	0.0000162	1.886779	0.0000348	0.000695064	0.00000042	2033	11	0.281366214	-4.4	0.8	3.0
K05-6	0.03721851	0.0000715	0.2814213	0.0000113	1.467243	0.0000141	1.886855	0.0000331	0.000995631	0.00000135	2034	7	0.281382911	-3.8	0.8	2.9
K05-7	0.02973677	0.000585	0.2813822	0.0000102	1.467243	0.0000126	1.886882	0.00003	0.000809573	0.0000149	2043	8	0.281350844	-4.7	0.7	3.0
K05-8	0.05577562	0.000101	0.281379	0.0000109	1.467272	0.0000135	1.886859	0.0000302	0.001460199	0.00000199	1959	10	0.281324813	-7.6	0.8	3.1
K05-9	0.0419654	0.000214	0.2813687	0.0000117	1.467262	0.0000135	1.886831	0.0000333	0.001134366	0.00000472	2097	7	0.281323581	-4.4	0.8	3.0
K05-11	0.0113099	0.0000847	0.2813406	0.0000113	1.467287	0.0000138	1.886894	0.0000314	0.00027452	0.00000229	2093	8	0.281329702	-4.3	0.8	3.0
K05-12	0.02401651	0.000058	0.2815958	0.0000115	1.467254	0.0000135	1.886799	0.000029	0.00079684	0.0000022	2020	8	0.281565292	2.4	0.8	2.5
K05-13	0.01800088	0.0000683	0.2813609	0.000012	1.467286	0.0000155	1.886883	0.0000354	0.000576311	0.00000273	1980	11	0.28133928	-6.6	0.9	3.0
K05-15	0.03012168	0.0000727	0.2813927	0.0000107	1.467252	0.0000146	1.886857	0.0000323	0.000948547	0.00000131	2038	7	0.281356053	-4.6	0.8	3.0
K05-16	0.01729548	0.0000459	0.2814032	0.0000103	1.467243	0.0000132	1.886699	0.0000292	0.000550294	0.00000176	1991	7	0.281382439	-4.8	0.7	2.9
K05-17	0.02376062	0.000441	0.2813657	0.0000107	1.467295	0.0000134	1.886878	0.0000287	0.000723631	0.0000127	2098	6	0.281336904	-3.9	0.8	3.0
K05-18	0.02402838	0.0000869	0.2814066	0.0000108	1.467268	0.0000161	1.886798	0.000034	0.00073775	0.00000175	2086	7	0.281377413	-2.8	0.8	2.9
R06-1	0.02554908	0.0000719	0.2815086	0.0000134	1.467285	0.0000153	1.88677	0.000037	0.000854786	0.00000271	1898	16	0.281477885	-3.5	1.0	2.8
R06-2	0.02231857	0.0000683	0.2814309	0.0000107	1.46724	0.0000137	1.886794	0.0000332	0.000697943	0.0000013	2000	16	0.281404448	-3.8	0.8	2.9
R06-3	0.03238191	0.0000602	0.2814166	0.000013	1.467277	0.0000167	1.886815	0.0000364	0.001012619	0.00000348	1933	17	0.28137953	-6.2	0.9	3.0
R06-4	0.03191544	0.000313	0.2814711	0.0000099	1.46727	0.0000143	1.886861	0.0000297	0.001116417	0.0000106	1834	18	0.281432359	-6.6	0.7	2.9
R06-5	0.02481392	0.000139	0.2814258	0.0000118	1.467243	0.0000162	1.886856	0.0000368	0.000764748	0.00000327	1983	18	0.281397067	-4.5	0.8	2.9
R06-6	0.01885879	0.0000421	0.2813437	0.0000155	1.467251	0.0000187	1.886861	0.0000428	0.000641305	0.00000162	1924	25	0.281320334	-8.5	1.1	3.1
R06-7	0.0197023	0.0000418	0.2814021	0.0000118	1.467265	0.0000145	1.886783	0.0000327	0.000615978	0.000000856	1948	23	0.281379372	-5.9	0.8	3.0
R06-8	0.02115642	0.0000947	0.2814131	0.0000111	1.467271	0.0000149	1.886752	0.0000358	0.000657578	0.00000199	1989	22	0.281388317	-4.6	0.8	2.9
R06-9	0.01526451	0.000032	0.2813878	0.0000108	1.467238	0.000014	1.886805	0.0000323	0.000491319	0.000000666	2027	23	0.281368923	-4.4	0.8	3.0
R06-10	0.02272678	0.0000452	0.281384	0.0000113	1.46728	0.000015	1.886904	0.0000352	0.000720091	0.00000176	1953	23	0.281357361	-6.6	0.8	3.0
R06-11	0.02386772	0.000242	0.2814265	0.00001	1.467249	0.0000122	1.886818	0.0000325	0.001025388	0.00000486	1804	23	0.28139151	-8.8	0.7	3.0
PA02-1	0.02056446	0.000243	0.2813867	0.00000736	1.467271	0.0000109	1.886868	0.0000243	0.000547374	0.00000569	2049	11	0.281365436	-4.1	0.5	2.9
PA02-2	0.01772214	0.0000909	0.2814268	0.00000593	1.467282	0.0000105	1.886857	0.0000229	0.00052867	0.00000167	2019	9	0.281406569	-3.3	0.4	2.9
PA02-3	0.01966819	0.000107	0.2813925	0.00000765	1.467283	0.0000107	1.886824	0.0000251	0.000533618	0.00000303	2035	16	0.281371915	-4.2	0.5	2.9
PA02-4	0.03911211	0.000231	0.2814001	0.00000713	1.467263	0.00000986	1.886819	0.0000233	0.001051236	0.00000582	2001	11	0.281360237	-5.4	0.5	3.0
PA02-5	0.02553901	0.000122	0.2814249	0.0000063	1.467249	0.00001	1.88685	0.0000225	0.000712134	0.00000331	2036	9	0.281397415	-3.2	0.4	2.9
PA02-6	0.02059289	0.0000753	0.281405	0.0000068	1.467275	0.00000994	1.886884	0.0000203	0.000587047	0.00000151	2024	9	0.281382479	-4.0	0.5	2.9
PA02-7	0.03362951	0.000321	0.2814866	0.00000766	1.467238	0.0000116	1.886864	0.0000243	0.000956823	0.00000618	1930	13	0.281451628	-3.7	0.5	2.8
PA02-8	0.04606871	0.000262	0.2814125	0.00000794	1.467278	0.0000107	1.886816	0.000024	0.001217971	0.00000776	2059	13	0.28136495	-3.8	0.6	2.9
PA02-9	0.03212601	0.000213	0.2814141	0.00000807	1.46726	0.0000113	1.886809	0.0000272	0.001004719	0.00000798	2017	7	0.281375691	-4.4	0.6	2.9
PA02-10	0.01288624	0.00004	0.2813832	0.00000542	1.467243	0.00000854	1.886846	0.0000206	0.000472988	0.000000599	2049	7	0.281364826	-4.1	0.4	2.9
PA02-11	0.04793456	0.000156	0.2814357	0.00000951	1.467108	0.000014	1.886674	0.0000299	0.001414918	0.00000327	2034	7	0.281381145	-3.8	0.7	2.9
Amphibolite dykes											**206Pb/ 238U**					
7.3-1	0.06556927	0.000882	0.2822965	0.0000143	1.467261	0.0000172	1.886764	0.0000386	0.001940447	0.000019	556	2	0.282276321	-5.6	1.0	1.7
7.3-2	0.03840281	0.000265	0.282288	0.0000126	1.467262	0.0000136	1.886814	0.0000321	0.001155821	0.00000828	528	4	0.282276604	-6.3	0.9	1.7

7.3-3	0.1060798	0.00127	0.2823175	0.0000165	1.467233	0.0000174	1.886765	0.0000393	0.00307102	0.0000377	554	3	0.282285709	-5.4	1.2	1.7
7.3-4	0.04860111	0.00175	0.2821892	0.0000314	1.467319	0.0000331	1.886935	0.0000621	0.00146774	0.0000414	543	2	0.282174301	-9.5	2.2	1.9
7.3-5	0.1013694	0.0013	0.2822839	0.0000166	1.467297	0.0000163	1.886846	0.0000377	0.003138434	0.0000449	557	2	0.282251228	-6.5	1.2	1.7
7.3-6	0.08998119	0.000583	0.2823064	0.0000143	1.467224	0.0000168	1.886743	0.0000386	0.002618247	0.0000117	538	2	0.282280093	-5.9	1.0	1.7
7.3-7	0.01958781	0.000303	0.2823063	0.00000986	1.467307	0.0000146	1.886823	0.000028	0.000666632	0.00000767	535	2	0.282299637	-5.3	0.7	1.6
7.3-8	0.06664319	0.00115	0.2823037	0.0000179	1.467296	0.0000222	1.886846	0.0000405	0.00195907	0.0000272	538	2	0.282284001	-5.8	1.3	1.7
7.3-9	0.06776484	0.000749	0.2822599	0.0000168	1.467273	0.0000242	1.886892	0.0000485	0.002018411	0.0000135	566	2	0.282238539	-6.8	1.2	1.8
7.3-10	0.08254991	0.00204	0.2822743	0.0000145	1.467265	0.0000155	1.886792	0.0000367	0.00236149	0.0000513	549	2	0.282250045	-6.7	1.0	1.7
7.3-11	0.08067928	0.00125	0.2823019	0.0000151	1.467284	0.0000185	1.886816	0.000041	0.00254263	0.0000436	543	2	0.282276075	-5.9	1.1	1.7
7.3-12	0.06288276	0.00072	0.2822567	0.0000266	1.467267	0.0000242	1.88682	0.0000527	0.001920129	0.0000274	602	4	0.282235079	-6.1	1.9	1.7
7.3-13	0.03022845	0.000648	0.282284	0.0000178	1.467174	0.0000186	1.886638	0.0000407	0.000996848	0.0000126	523	2	0.282274248	-6.4	1.3	1.7
7.3-14	0.07129217	0.00205	0.2823219	0.0000135	1.467201	0.0000149	1.886704	0.0000339	0.001974062	0.0000499	525	2	0.282302533	-5.4	1.0	1.6
7.3-15	0.06564639	0.00118	0.2822749	0.0000265	1.46728	0.0000343	1.887018	0.000122	0.00210026	0.0000428	556	3	0.282253087	-6.5	1.9	1.7
7.3-16	0.07784332	0.00082	0.2822546	0.0000221	1.46717	0.0000243	1.886698	0.0000546	0.002441226	0.0000187	526	2	0.282230594	-7.9	1.6	1.8
7.3-17	0.08350359	0.0012	0.2823065	0.0000174	1.467148	0.0000184	1.886707	0.0000454	0.002524712	0.0000249	547	5	0.282280677	-5.7	1.2	1.7
7.3-18	0.07422494	0.00191	0.2822176	0.0000448	1.467286	0.0000442	1.886903	0.000093	0.002310347	0.0000405	549	2	0.282193883	-8.7	3.2	1.8
7.3-19	0.06638564	0.00188	0.2823224	0.0000159	1.46714	0.0000164	1.886652	0.000036	0.001971909	0.0000472	545	2	0.282302324	-5.0	1.1	1.6
7.3-20	0.06550535	0.000637	0.2822009	0.0000214	1.467244	0.0000228	1.886837	0.0000484	0.002080414	0.0000217	541	2	0.282179872	-9.4	1.5	1.9
7.3-21	0.06043048	0.00071	0.2822986	0.0000141	1.467119	0.0000178	1.886669	0.0000352	0.001759156	0.0000184	520	2	0.2822815	-6.3	1.0	1.7
7.3-22	0.06447225	0.000826	0.2822983	0.0000138	1.467236	0.0000163	1.886797	0.0000347	0.001874581	0.0000206	548	2	0.282279106	-5.7	1.0	1.7
Etusis Formation- feldspathic quartzite											**207Pb/ 206Pb**					
1.1-1	0.03872329	0.000091	0.2814131	0.0000112	1.467266	0.000014	1.886844	0.0000303	0.001019818	0.00000267	1062	24	0.281392755	-25.6	0.8	3.5
1.1-2	0.04744381	0.000108	0.2817362	0.0000127	1.467284	0.0000152	1.886841	0.0000327	0.001317707	0.00000237	1954	8	0.281687428	5.2	0.9	2.3
1.1-3	0.02594501	0.0000599	0.2813887	0.0000116	1.467226	0.000016	1.886827	0.0000337	0.000695271	0.00000236	1004	18	0.281375594	-27.5	0.8	3.6
1.1-4	0.04310793	0.000148	0.2816994	0.0000096	1.467308	0.0000133	1.886907	0.000029	0.001179921	0.0000047	1029	7	0.2816766	-16.3	0.7	2.9
1.1-5	0.03128722	0.000162	0.2817229	0.0000104	1.467264	0.0000147	1.886802	0.0000305	0.000853907	0.00000428	1012	9	0.281706675	-15.6	0.7	2.8
1.1-6	0.03222698	0.0000738	0.2817208	0.0000104	1.46728	0.0000144	1.886915	0.000033	0.000916455	0.00000173	1011	9	0.281703403	-15.7	0.7	2.9
1.1-7	0.02800518	0.000129	0.2814152	0.0000106	1.467269	0.0000137	1.886789	0.0000302	0.000768781	0.00000358	1037	12	0.281400228	-25.9	0.8	3.5
1.1-8	0.02005239	0.0000465	0.2813876	0.0000132	1.467285	0.0000158	1.88683	0.0000352	0.000570203	0.0000013	1011	9	0.281376776	-27.3	0.9	3.6
1.1-9	0.03085767	0.000401	0.2817246	0.000011	1.467272	0.0000151	1.886898	0.0000332	0.000850628	0.00000948	1012	9	0.281708437	-15.5	0.8	2.8
1.1-10	0.03645516	0.000261	0.2817432	0.000012	1.467259	0.0000147	1.886841	0.0000319	0.00096932	0.00000559	1045	13	0.281724175	-14.2	0.9	2.8
1.1-11	0.02893213	0.000254	0.2817584	0.0000109	1.467251	0.0000148	1.886843	0.0000336	0.000786916	0.00000624	1022	17	0.281743298	-14.1	0.8	2.8
1.1-12	0.02225237	0.000255	0.2816785	0.0000155	1.467298	0.000019	1.886811	0.0000415	0.000622764	0.00000464	1043	9	0.281666301	-16.3	1.1	2.9
1.1-13	0.02430133	0.0000969	0.2817306	0.0000107	1.467261	0.0000143	1.886846	0.0000299	0.000675114	0.00000223	1033	11	0.281717503	-14.7	0.8	2.8
1.1-14	0.04763776	0.0000926	0.2818226	0.0000124	1.467302	0.0000148	1.886867	0.000036	0.001253942	0.00000164	1016	8	0.281798678	-12.2	0.9	2.6
1.1-15	0.06817919	0.00064	0.2817127	0.0000131	1.467255	0.0000165	1.886784	0.0000326	0.001737468	0.0000128	1035	7	0.281678928	-16.1	0.9	2.9
1.1-16	0.06463484	0.000531	0.2818225	0.0000131	1.467275	0.0000141	1.886839	0.0000319	0.00183266	0.00000686	1062	7	0.281785939	-11.7	0.9	2.6
1.1-17	0.02814605	0.000238	0.2817455	0.0000109	1.467259	0.0000132	1.88686	0.0000313	0.000802521	0.00000738	1026	7	0.281730038	-14.4	0.8	2.8
1.1-18	0.03792954	0.000178	0.2817625	0.0000138	1.467262	0.0000153	1.886897	0.0000358	0.001076666	0.00000517	2016	6	0.281721361	7.8	1.0	2.2
1.1-19	0.01356485	0.0000248	0.2817337	0.00000981	1.467278	0.0000141	1.886822	0.0000293	0.000494143	0.000000557	1095	10	0.281723533	-13.1	0.7	2.8
1.1-20	0.01591868	0.0000999	0.2816883	0.0000104	1.467281	0.0000142	1.886816	0.00003	0.000501471	0.00000207	2008	5	0.281669221	5.8	0.7	2.3
1.1-21	0.04988654	0.000548	0.2817477	0.0000113	1.467257	0.0000149	1.886736	0.0000325	0.001456174	0.0000148	1068	5	0.281718484	-13.9	0.8	2.8
1.1-24	0.02356713	0.000209	0.2817027	0.0000112	1.4673	0.0000149	1.886906	0.0000315	0.000637304	0.00000501	1190	17	0.281688437	-12.2	0.8	2.8
1.1-25	0.01425231	0.0000881	0.2817223	0.00000965	1.467238	0.0000124	1.886771	0.0000277	0.000461478	0.00000109	1015	13	0.281713505	-15.3	0.7	2.8
1.1-26	0.02548478	0.000175	0.2816904	0.0000109	1.467227	0.0000145	1.886781	0.0000327	0.000690592	0.00000411	1141	7	0.281675587	-13.8	0.8	2.8
1.1-27	0.01849814	0.000195	0.28165	0.0000107	1.467258	0.0000156	1.886801	0.0000324	0.000561663	0.00000474	2017	6	0.281628528	4.5	0.8	2.4
1.1-28	0.01786765	0.0000225	0.2817116	0.00000996	1.46724	0.0000136	1.886787	0.0000323	0.000632773	0.000000427	1061	15	0.281698988	-14.8	0.7	2.8
1.1-29	0.02673057	0.000183	0.2817734	0.0000133	1.467269	0.000015	1.886865	0.0000363	0.000870811	0.00000376	993	7	0.281757167	-14.2	0.9	2.7
1.1-30	0.0220219	0.0000534	0.2817123	0.0000103	1.467243	0.0000148	1.88685	0.0000272	0.00062676	0.00000145	1919	5	0.281689525	4.5	0.7	2.3
1.1-36	0.01482875	0.00016	0.2817061	0.000011	1.467216	0.0000137	1.886724	0.0000327	0.000464537	0.00000396	2018	8	0.281688332	6.7	0.8	2.2

1.1-37	0.03349728	0.000573	0.2817749	0.0000117	1.467152	0.0000136	1.886682	0.0000294	0.001094893	0.0000186	1934	11	0.281734797	6.4	0.8	2.2
1.1-38	0.03628516	0.000278	0.2817413	0.00000979	1.467214	0.0000139	1.886717	0.0000281	0.001107573	0.00000894	1009	11	0.281720317	-15.2	0.7	2.8
1.1-39	0.03671838	0.000101	0.2817348	0.0000106	1.467241	0.0000153	1.886789	0.0000328	0.00113357	0.00000502	1018	10	0.281713132	-15.2	0.8	2.8
1.1-40	0.03461441	0.000999	0.2817279	0.000012	1.467211	0.0000138	1.886735	0.0000332	0.001008878	0.0000269	1000	14	0.281708959	-15.8	0.9	2.9
1.1-41	0.03241876	0.000287	0.2814079	0.0000106	1.467197	0.0000129	1.886744	0.0000303	0.000935435	0.00000649	1014	5	0.281390099	-26.8	0.8	3.5
1.1-43	0.02934278	0.00012	0.2813848	0.00000926	1.467216	0.0000133	1.886781	0.0000308	0.000883776	0.00000309	1978	6	0.28135168	-6.2	0.7	3.0
1.1-44	0.02923676	0.0000702	0.2817569	0.0000102	1.467242	0.0000133	1.886752	0.0000286	0.000855231	0.00000296	1014	6	0.281740617	-14.3	0.7	2.8
1.1-45	0.01087509	0.000036	0.2816757	0.0000084	1.467214	0.0000116	1.88678	0.0000283	0.000423824	0.000000971	2008	10	0.281659571	5.4	0.6	2.3
1.1-46	0.02563977	0.00007	0.2817373	0.0000114	1.467219	0.0000149	1.886736	0.0000308	0.000767542	0.0000011	974	10	0.281723268	-15.9	0.8	2.8
Red granite											**206Pb/ 238U**					
K06-1	0.05454473	0.0000795	0.2818078	0.0000115	1.467279	0.0000149	1.886896	0.0000346	0.001439521	0.00000309	521	2	0.281793782	-23.5	0.8	3.0
K06-2	0.07662505	0.000438	0.2818067	0.0000133	1.467275	0.0000153	1.886883	0.0000336	0.00196627	0.00000918	534	2	0.281787069	-23.5	0.9	3.0
K06-3	0.07226603	0.000438	0.2817913	0.0000118	1.467245	0.0000136	1.886785	0.0000304	0.001809741	0.00000899	548	3	0.281772749	-23.6	0.8	3.0
K06-4	0.06632219	0.000371	0.2818132	0.0000105	1.467234	0.0000135	1.886811	0.0000277	0.00168789	0.00000794	519	2	0.281796818	-23.4	0.7	2.9
K06-5	0.07311072	0.000241	0.2818277	0.0000116	1.467284	0.0000145	1.886833	0.0000344	0.001880323	0.00000457	559	3	0.281808044	-22.2	0.8	2.9
K06-6	0.07065194	0.0000983	0.2818176	0.0000115	1.467254	0.000015	1.886843	0.0000286	0.001821585	0.0000029	543	3	0.281799099	-22.8	0.8	2.9
K06-7	0.04959216	0.000161	0.2817872	0.0000105	1.467278	0.0000137	1.886802	0.0000304	0.001272565	0.00000416	540	3	0.281774366	-23.8	0.7	3.0
K06-8	0.07326051	0.000608	0.2817995	0.0000118	1.467255	0.0000158	1.886785	0.000033	0.001850757	0.0000148	543	3	0.28178071	-23.5	0.8	3.0
K06-9	0.08059042	0.000317	0.2817828	0.0000121	1.467247	0.000014	1.886774	0.0000349	0.002010373	0.00000817	556	5	0.281761887	-23.8	0.9	3.0
K06-10	0.05180709	0.000572	0.2818454	0.0000108	1.467233	0.0000134	1.886869	0.0000303	0.001607848	0.0000109	547	3	0.281828973	-21.7	0.8	2.9
K06-11	0.05258625	0.00027	0.2817965	0.0000108	1.467242	0.0000146	1.88673	0.0000306	0.001637254	0.00000453	530	2	0.28178028	-23.8	0.8	3.0
K06-12	0.04379868	0.000512	0.2819249	0.0000111	1.467285	0.0000154	1.886824	0.0000338	0.001536145	0.0000152	521	4	0.281909941	-19.4	0.8	2.7
K06-13	0.05769208	0.000186	0.2817792	0.0000127	1.467263	0.0000148	1.886883	0.0000345	0.001695314	0.00000353	550	4	0.281761758	-24.0	0.9	3.0
K06-14	0.01683716	0.000168	0.2818298	0.00001	1.467267	0.000015	1.886837	0.0000299	0.000500378	0.00000419	518	5	0.28182496	-22.5	0.7	2.9
Sheeted leucogranites											**206Pb/ 238U**					
K07-1	0.03504204	0.000231	0.2817748	0.00000875	1.467259	0.0000131	1.886857	0.0000289	0.001013806	0.00000652	515.8	3	0.281765027	-24.6	0.6	3.0
											207Pb/ 206Pb					
PA03-1	0.04085685	0.000245	0.2814195	0.00000907	1.467296	0.000012	1.886831	0.0000271	0.001050154	0.0000053	1974	10	0.281380226	-5.3	0.6	3.0
PA03-4	0.02611065	0.000236	0.2814516	0.00000778	1.467268	0.0000104	1.886891	0.0000239	0.000693552	0.00000479	1980	8	0.281425582	-3.5	0.6	2.9
PA03-5	0.02111466	0.0000519	0.2814368	0.0000066	1.467286	0.000011	1.886888	0.0000244	0.000564782	0.00000164	1933	9	0.281416125	-4.9	0.5	2.9

Appendix 5.C: Measured Lu-Hf isotopic data for reference standards (LV11, Temora 2 and Mud Tank)

	176Yb/ 177Hf'	SE	176Hf/ 177Hf	SE	178Hf/ 177Hf	SE	180Hf/ 177Hf	SE	176Lu/ 177Hf'	SE
LV11										
LV11-1	0.208752	0.000146	0.282875	0.000013	1.467282	0.000013	1.886785	0.000026	0.003593	0.000001
LV11-2	0.214444	0.000165	0.282882	0.000014	1.467263	0.000014	1.886826	0.000029	0.003743	0.000000
LV11-3	0.202123	0.000200	0.282868	0.000013	1.467252	0.000014	1.886827	0.000029	0.003346	0.000001
LV11-4	0.202812	0.000182	0.282886	0.000012	1.467255	0.000013	1.886810	0.000028	0.003532	0.000000
LV11-5	0.182034	0.000229	0.282843	0.000012	1.467233	0.000012	1.886794	0.000027	0.003017	0.000001
LV11-6	0.1670601	0.000249	0.2828547	0.000012	1.467264	0.0000136	1.88685	0.000029	0.002824056	0.0000018
LV11-7	0.1303524	0.000228	0.2828407	0.000012	1.467225	0.0000122	1.886835	0.0000277	0.002210949	0.00000171
LV11-8	0.1485862	0.000151	0.282876	0.000012	1.467256	0.0000123	1.886886	0.0000286	0.002509201	0.000000449
LV11-9	0.1813502	0.00021	0.2828553	0.000013	1.467228	0.0000148	1.88677	0.0000312	0.003029707	0.000000414
LV11-10	0.1619323	0.000157	0.2828728	0.000013	1.467262	0.0000155	1.886806	0.0000319	0.002703825	0.000000444
LV11-11	0.1312685	0.00026	0.2828689	0.000012	1.467268	0.0000138	1.886811	0.0000281	0.002227219	0.00000227
LV11-12	0.1443321	0.000176	0.2828487	0.000013	1.467273	0.0000139	1.886875	0.0000291	0.002450237	0.000000784
LV11-13	0.1535898	0.000182	0.2828553	0.000013	1.467201	0.0000144	1.886873	0.000032	0.002600459	0.000000685
LV11-14	0.1669046	0.000271	0.2828684	0.000013	1.467256	0.0000134	1.886816	0.0000309	0.002815889	0.00000178
LV11-15	0.1711806	0.000254	0.2828698	0.000013	1.467252	0.0000145	1.886871	0.0000328	0.002857865	0.00000137
LV11-16	0.107851	0.000120	0.282827	0.000011	1.467255	0.000013	1.886744	0.000027	0.002078	0.000001
LV11-17	0.115222	0.000233	0.282823	0.000011	1.467296	0.000013	1.886828	0.000030	0.002254	0.000001
LV11-18	0.118371	0.000215	0.282813	0.000013	1.467247	0.000013	1.886830	0.000030	0.002343	0.000001
LV11-19	0.125752	0.000185	0.282818	0.000012	1.467272	0.000014	1.886873	0.000031	0.002489	0.000001
LV11-20	0.131256	0.000297	0.282810	0.000013	1.467240	0.000015	1.886714	0.000032	0.002553	0.000002
LV11-21	0.145808	0.000158	0.282816	0.000014	1.467276	0.000014	1.886806	0.000033	0.002832	0.000001
LV11-22	0.159332	0.000133	0.282832	0.000013	1.467201	0.000014	1.886738	0.000029	0.002903	0.000001
LV11-23	0.155496	0.000269	0.282817	0.000012	1.467148	0.000014	1.886658	0.000031	0.002834	0.000001
LV11-24	0.145468	0.000088	0.282863	0.000013	1.467141	0.000014	1.886654	0.000033	0.002685	0.000002
LV11-25	0.146576	0.000264	0.282841	0.000012	1.467202	0.000016	1.886769	0.000033	0.002681	0.000001
LV11-26	0.114256	0.000134	0.282837	0.000012	1.467248	0.000014	1.886760	0.000029	0.002103	0.000001
Temora 2										
TEM2-1	0.059599	0.000169	0.282705	0.000010	1.467259	0.000013	1.886872	0.000030	0.001610	0.000004
TEM2-2	0.077182	0.000048	0.282685	0.000010	1.467258	0.000013	1.886785	0.000025	0.002011	0.000001
TEM2-3	0.056323	0.000204	0.282710	0.000010	1.467275	0.000011	1.886866	0.000026	0.001459	0.000004
TEM2-4	0.049539	0.000332	0.282681	0.000009	1.467261	0.000012	1.886881	0.000025	0.001373	0.000008
TEM2-5	0.0816262	0.00197	0.2826854	0.000014	1.467266	0.0000152	1.886904	0.0000332	0.002232273	0.0000608
TEM2-6	0.073287	0.00123	0.2827151	0.000009	1.467239	0.0000126	1.886775	0.0000262	0.001925775	0.0000343
TEM2-7	0.0308553	0.000188	0.2826844	0.000009	1.467289	0.0000113	1.886877	0.0000251	0.000858945	0.00000611
TEM2-8	0.0380954	0.000702	0.282684	0.000009	1.467277	0.0000121	1.88688	0.0000293	0.000995625	0.0000171
TEM2-9	0.0567079	0.000948	0.2827045	0.000011	1.467227	0.0000134	1.886774	0.0000295	0.001475383	0.0000246
TEM2-10	0.0485485	0.000902	0.2826901	0.000009	1.467259	0.0000128	1.886825	0.0000283	0.001278942	0.0000233
TEM2-11	0.0889531	0.000121	0.2827077	0.000011	1.467246	0.0000128	1.886787	0.0000278	0.002313665	0.00000207
TEM2-12	0.0327583	0.000129	0.2826856	0.000010	1.467276	0.0000124	1.886829	0.0000295	0.000878286	0.00000202
TEM2-13	0.0399238	0.0000827	0.2827001	0.000009	1.467261	0.0000136	1.886836	0.0000307	0.001075093	0.00000298
TEM2-14	0.014909	0.000071	0.282658	0.000008	1.467276	0.000012	1.886734	0.000025	0.000471	0.000002
TEM2-15	0.062653	0.000124	0.282687	0.000009	1.467250	0.000011	1.886864	0.000023	0.002003	0.000005
TEM2-16	0.065443	0.000071	0.282675	0.000010	1.467245	0.000014	1.886776	0.000029	0.002051	0.000006
TEM2-17	0.037387	0.000041	0.282679	0.000009	1.467275	0.000012	1.886886	0.000028	0.001178	0.000003
TEM2-18	0.030980	0.000049	0.282673	0.000009	1.467276	0.000014	1.886821	0.000028	0.000992	0.000002
TEM2-19	0.030824	0.000277	0.282658	0.000010	1.467261	0.000013	1.886825	0.000030	0.000977	0.000010
TEM2-20	0.057002	0.000163	0.282711	0.000010	1.467160	0.000013	1.886646	0.000025	0.001609	0.000002
TEM2-21	0.029866	0.000060	0.282704	0.000008	1.467150	0.000011	1.886628	0.000026	0.000905	0.000001
TEM2-22	0.025876	0.000087	0.282698	0.000009	1.467182	0.000013	1.886724	0.000026	0.000771	0.000001
TEM2-23	0.046631	0.000084	0.282668	0.000010	1.467185	0.000013	1.886745	0.000029	0.001398	0.000003
TEM2-24	0.018921	0.000010	0.282698	0.000009	1.467242	0.000012	1.886789	0.000029	0.000563	0.000001
Mud Tank										
MT-1	0.001637	0.000004	0.282495	0.000007	1.467279	0.000012	1.886845	0.000024	0.000036	0.000000
MT-2	0.0016684	4.19E-06	0.2825144	0.000007	1.467245	0.000011	1.886835	0.0000255	3.70552E-05	5.46E-08
MT-3	0.0015755	4.26E-06	0.2825137	0.000007	1.467266	0.0000116	1.886836	0.0000234	3.52561E-05	4.86E-08
MT-4	0.0016036	4.73E-06	0.2824947	0.000008	1.467247	0.000012	1.886839	0.000026	3.55693E-05	6.07E-08
MT-5	0.001643	0.0000049	0.2825016	0.000008	1.467273	0.000012	1.886871	0.0000256	3.62085E-05	0.000000059
MT-6	0.0015995	4.85E-06	0.2825188	0.000008	1.46724	0.0000126	1.886754	0.000027	3.58093E-05	5.65E-08
MT-7	0.0013682	5.37E-06	0.2824809	0.000008	1.46728	0.0000116	1.886824	0.0000246	3.04722E-05	5.71E-08
MT-8	0.0014143	4.68E-06	0.2825116	0.000007	1.467283	0.0000125	1.886851	0.0000264	3.17892E-05	5.84E-08
MT-9	0.001082	0.000005	0.282512	0.000007	1.467229	0.000010	1.886787	0.000024	0.000028	0.000000
MT-10	0.001063	0.000005	0.282510	0.000007	1.467241	0.000011	1.886710	0.000026	0.000028	0.000000
MT-11	0.001071	0.000005	0.282514	0.000008	1.467253	0.000011	1.886770	0.000027	0.000029	0.000000
MT-12	0.001150	0.000006	0.282500	0.000008	1.467260	0.000013	1.886799	0.000026	0.000030	0.000000
MT-13	0.001151	0.000005	0.282501	0.000008	1.467161	0.000012	1.886747	0.000025	0.000028	0.000000
MT-14	0.001146	0.000005	0.282519	0.000008	1.467199	0.000012	1.886691	0.000026	0.000028	0.000000
MT-15	0.001170	0.000005	0.282492	0.000008	1.467218	0.000012	1.886714	0.000025	0.000029	0.000000

Appendix 5.D: Lu-Hf isotopic reference standards precision and accuracy testing

Comparison between measured reference standards (Temora 2, Mud Tank and LV11) and accepted ratios for reference standards. The measured reference standards are within error for accepted ratios for the reference standards.

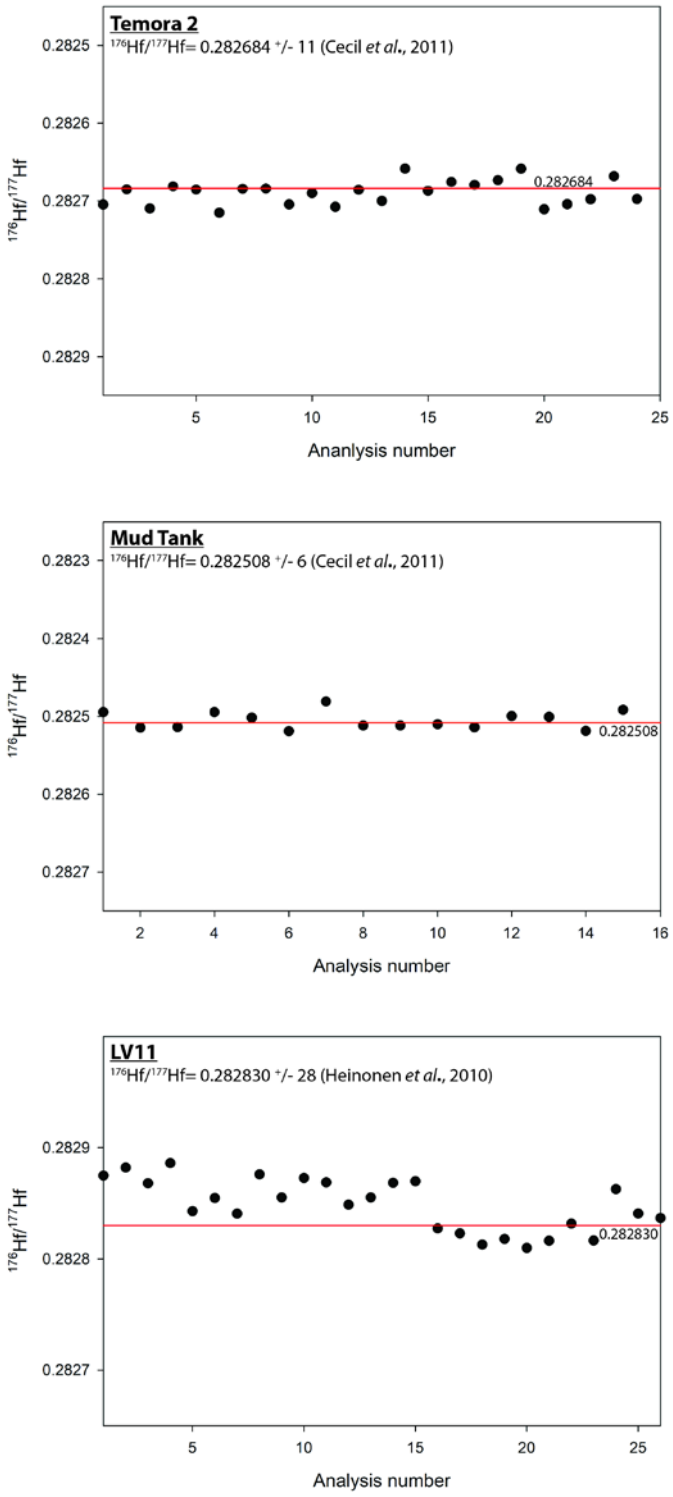


Figure showing the measured $^{176}Hf/^{177}Hf$ ratios for various reference standards compared with accepted reference standard ratios (red line).